Tawfik Abdo Saleh

Editor

Nanotechnology in Oil and Gas Industries

Principles and Applications

🐴 Springer

Topics in Mining, Metallurgy and Materials Engineering

Series editor
Carlos P. Bergmann, Porto Alegre, Rio Grande do Sul, Brazil

"Topics in Mining, Metallurgy and Materials Engineering" welcomes manuscripts in these three main focus areas: Extractive Metallurgy/Mineral Technology; Manufacturing Processes, and Materials Science and Technology. Manuscripts should present scientific solutions for technological problems. The three focus areas have a vertically lined multidisciplinarity, starting from mineral assets, their extraction and processing, their transformation into materials useful for the society, and their interaction with the environment.

More information about this series at http://www.springer.com/series/11054

Tawfik Abdo Saleh
Editor

Nanotechnology in Oil and Gas Industries

Principles and Applications

② Springer

Editor
Tawfik Abdo Saleh
Chemistry Department, and Center of Excellence
    in Nanotechnology (CENT)
King Fahd University of Petroleum and Minerals
Dhahran, Saudi Arabia

Preface

Nowadays, due to the different challenges presented in the oil and gas industry, different and modern technologies have arisen to accomplish production goals and environmental requirements. Nanotechnology in oil and gas industry is a fascinating subject of recent origin. Nanomaterials are involved in almost all stages in the oil and gas industry, including searching, drilling, production, processing, transport, and refining. Nanotechnology's focus areas include: in searching, signal and data processing; in drilling, the development of novel materials with great tensile strength and durability and drilling muds based on nanoparticles to control viscosity; in production and processing, the development of membranes, detectors, and separators (efficient and cost-effective materials for oil/water/gas separation are highly required); in transport, corrosion (improved inhibition), smart pipelines, and flow improvers with modified surfaces; and in refining, the development of catalysts, support materials with large surfaces, and improved efficiency and selectivity.

Principles and applications of nanotechnology in oil and gas industries book offers detailed, up-to-date chapters on the technological developments and nanomaterials in petroleum. The first chapter of the book encompasses the fundamentals and principles of the oil and gas industry. It highlights the upstream exploration and drilling sectors followed by midstream sectors. It also covers the downstream sectors with oil refinery processes. The second chapter gives an overview to nanotechnology applications in petroleum refining.

The other chapters describe the designing of effective nanomaterials and catalysts and desulfurization pathways with a focus on mechanisms of the upgrading and desulfurization process. These chapters introduce principles and advances in the nanomaterials in the refinery. Chapter 9 discusses the role of nanomaterials as an emerging trend toward the detection of winged contaminants. Chapter 10 discusses the biogas produced from different feedstocks in anaerobic digesters.

In this book, we have tried to cover many aspects of nanomaterials for the refinery, which is of current interest. This book is written for a large readership, including university students and researchers from diverse backgrounds such as chemistry, petroleum, materials science, physics, and engineering. It can be used

not only as a textbook for both undergraduate and graduate students but also as a review and reference book for researchers in these fields. We hope that the chapters of this book will provide the readers with valuable insight into state-of-the-art advanced and functional nanomaterials and technologies. However, it is possible that some topics have been left out owing to constraints on the size of the book. We trust that the preface will be useful to students, teachers, and researchers.

Dharan, Saudi Arabia   Tawfik Abdo Saleh

Acknowledgment

Contents

Chapter 1
Insights into the Fundamentals and Principles of the Oil and Gas Industry: The Impact of Nanotechnology

Tawfik Abdo Saleh and Saddam A. AL-Hammadi

Abstract Globally, crude oil is an invaluable source of energy and raw materials for major industries that are related to daily life. However, the oil and gas industry is facing a significant number of environmental, technical, and industrial challenges that require the development of different technologies to meet production goals, as well as industrial and environmental regulations. This chapter introduces a description of the petroleum industry from exploration up to petrochemical production and highlights the impact of nanotechnology in different but related processes. The oil and gas industry can be divided into three main categories: the upstream, midstream, and downstream sectors, which are also known as the refining process. The upstream and midstream sectors include oil exploration, production, and transportation. In these sectors, nanotechnology may contribute in developing more efficient, less expensive, and more environmentally sound technologies than those which are readily available, such as developing unique nano-based sensors for the oil well exploration process and synthesizing nanomaterials with a hydrophobic surface for scale inhibition in oil production tubes. The downstream sector and its related oil refinery processes include crude distillation, thermal cracking, fluid catalytic cracking, hydrofluoric acid alkylation, hydrotreating, hydrocracking, catalytic reforming, and the isomerization process. In the downstream sector, the contribution of nanotechnology is focused on developing catalysts with a high level of stability and performance that can be used in different catalysis processes in refinery plants, such as the fluid catalytic cracking and hydrotreating processes.

Keywords Crude oil • Nanotechnology • Oil and gas industry • Upstream • Midstream • Downstream and refining

T.A. Saleh (✉)
Chemistry Department, and Center of Excellence in Nanotechnology (CENT), King Fahd University of Petroleum and Minerals, Dhahran 31261, Saudi Arabia
e-mail: tawfik@kfupm.edu.sa; tawfikas@hotmail.com; http://faculty.kfupm.edu.sa/CHEM/tawfik/

S.A. AL-Hammadi
Chemical Engineering Department, and Center of Excellence in Nanotechnology (CENT), King Fahd University of Petroleum & Minerals, Dhahran 31261, Saudi Arabia

1 Overview

Crude oil is a complex mixture that contains different organic hydrocarbon molecules; generally, 83–87% carbon, 11–15% hydrogen, 0.05–6% sulfur, nitrogen 0.1–2%, oxygen 0.05–1.5%, and metals $< 0.1\%$. Several types of hydrocarbon molecules are present in crude oil with relative percentages of each varying from one oil type to another, thus determining the properties of each oil. The average range of the composition by weight includes hydrocarbon alkanes (paraffin-saturated chains) 15–60%, naphthenes (saturated rings) 30–60%, aromatics (unsaturated rings) 3–30%, and asphaltic 2–10%. The term petroleum covers

 (i) Naturally occurring unprocessed crude oil and
(ii) Petroleum products made up of refined crude oil

   Natural petroleum is refined into several types of fuels. Petroleum components can be separated using a fractional distillation technique. As shown in Fig. 1.1, the oil and gas industry facilities and systems can be classified into three sectors or stages:

  (i) Upstream
 (ii) Midstream
(iii) Downstream (Refining)
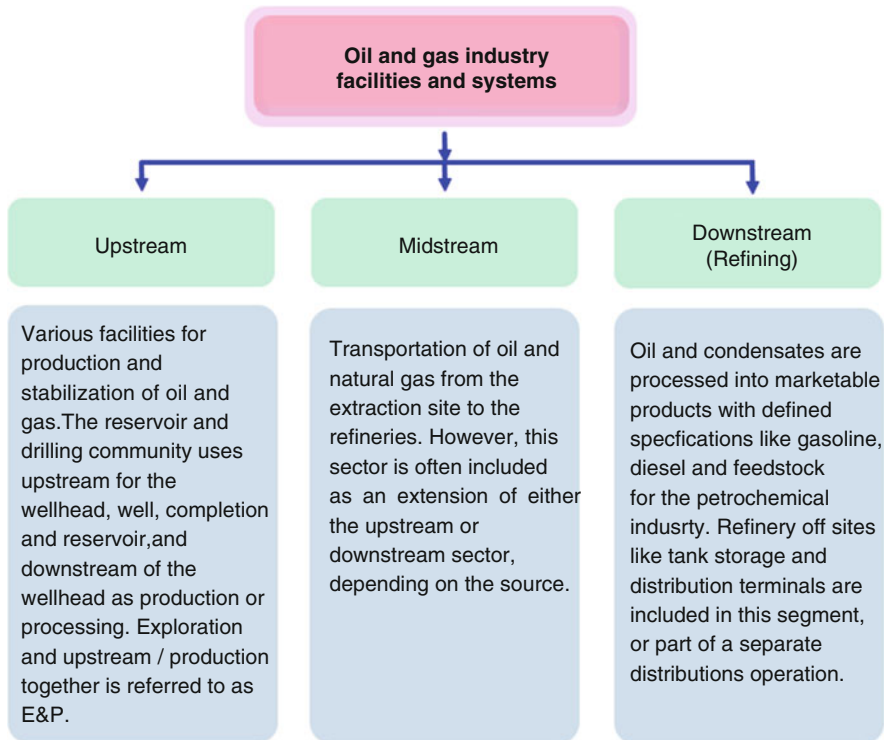
Fig. 1.1 General classification of oil and gas industry facilities and systems

2 Upstream Exploration and Drilling Sectors

The upstream exploration and drilling sectors of oil and gas process commonly involves the following:

2.1 Oil Well Exploration

Exploration can be defined as a searching for hydrogen deposits under the surface of the earth using different methods, and this process can be done by petroleum geologists. Due to the facts that the extraction of oil resources decays with time and the accessibility to the easily recoverable oil resources has been diminished significantly, more complicated techniques are required in order to enhance the field characterization performance and ultimately increase the amount of oil recovered. The extraction of oil and gas can be maximized by having sufficient information and a clear understanding of the targeted reservoir properties. Despite using any of the current sophisticated methods for oil recovery like thermal techniques, gas injection, water-flooding, and chemical flooding, a huge quantity of oil and gas will ultimately not be extracted. Besides the inefficiency of these methods of oil recovery, these conventional processes are not favorable economically (Himes et al. 2006; Jones 2015). Since the operations in the deep wells are carried out in a very harsh environment, conventional electrical sensors are not normally able to be sustained in such difficult conditions. The available techniques provide limited information, shallow penetration, and are not able to fulfill the reservoir's characterization requirements. Clearly, there is a necessity to use unconventional techniques and exceptional materials to overcome these technical challenges and to effectively explore unconventional oil and gas reservoirs. In addition, these techniques and materials should meet environmental regulations and address safety issues.

Researchers are trying to improve a new generation of sensors which are small and hard enough to sustain under harsh conditions and to provide accurate temperature, pressure, and oil and gas flow rate measurements. They also are able to penetrate deep into the wells and obtain a clear picture of the interaction between rocks and hydrogen deposits without being interrupted by the presence of electromagnetic fields. In addition, a high level of reservoir characteristics performance requires advanced computational and imaging techniques.

In nanotechnology, different synthesis methods can be used to produce effective nanomaterials which can contribute to making unique sensors and imaging contrast agents. The optical, magnetic, and electrical properties of these nanomaterials can be changed greatly when compared with their bulk counterparts. Besides, they can form percolated structures electrically and geometrically at low volume fractions. A combination of the nanoparticles and smart fluids can generate a very effective sensor that can work properly in very difficult conditions and

provide accurate measurements of temperature, pressure, oil flow rate, and stress in deep wells. Nanomaterial has great potential for use as markers for imaging when it is combined with advanced computational techniques and magnetic probes. The reservoir characterization and the pore sizing can be enhanced when the nanomaterial segregates into various fluid regions by chemical techniques. The pore size, high surface area, and mobility of the nanoparticles are absolutely essential in such imagining. Researchers are developing nanosensors which have the ability to provide information and data about fluid-type recognition, fluid-flow monitoring, and which are able to penetrate into deep wells and perform reservoir characterization. Furthermore, hyperpolarized silicon nanoparticles also have potential applications in oil imaging and exploration. A nano-CT machine could also play an important role in providing data on the pore-size distribution and images for shale and gas sand. The goal of nanotechnology in this field is to develop a nanorobot which is capable of comprehensively mapping and measuring the effective characteristics of the reservoir.

2.2 Wellheads and Drilling

The oil well exploration is followed by the drilling of a natural gas or oil well. Then, there should be a verification of whether the available natural gas is commercially suitable in terms of quantity. At this stage, the well can be completed to allow petroleum to be extracted to the surface.

Wellheads can be defined as components at the surface of an oil or gas well that provide the structural and pressure-containing interface for the drilling and production tools. Wellheads are used to provide the suspension point and pressure seals for the casing strings which run from the bottom of the hole-sections to the surface pressure control equipment. In this stage, the well hole is strengthened with casing, the pressure and temperature are evaluated for the formation, and the proper equipment is installed to ensure an efficient flow of natural gas from the well which is controlled with a choke (Devold 2013).

Nanotechnology offers innovative techniques for drilling processes which depend on water-based fluid. These methods could make a dramatic change in the drilling process performance, are low in cost, and can be applied using straightforward methods. Besides, nanotechnology-based solutions have less impact on the environment since the fluid used does not contain toxic chemical materials, which is the case with conventional fluid drilling. Nanomaterials can be applied to plug pores in the shale formation, which prevents the formation of a filter cake, which is usually responsible for fluid loss reduction and the formation of fractures. Nanoparticles can be added to the used drilling fluid to minimize the thickness of the filter cake by reducing the permeability of the shale formation. As a result, nanotechnology is a potential solution which could play an important role in increasing the drilling process quality and enhancing the wellbore stability.

Various nanotechnology techniques can be implemented to enhance the down-hole tool performance including the polycrystalline diamond compact bits. A nanodiamond is an interesting option to increase the PDC abrasion resistance and to boost its durability. One method to increase PDC diamond density and to decrease the metallic binder is that nanodiamond may reduce the localized micro-structural stress when its coefficient of thermal expansion CTE is compatible with that in the micron diamond.

Bit balling Nanomaterials drilling mud with the hydrophobic film forming capa-bility on the bit and stabilizer surfaces is used to eliminate the bit and stabilize balling. Due to their high surface area, nanomaterials fluid could be used for drilling in shale which is very reactive, highly pliable, and tenacious.

Due to the fine and very thin film forming capability of nanomaterials, the nanomaterials-based fluid may

 (i) Allow a reduction of the frictional resistance between the pipe and the borehole wall as a result of formation of a thin lubricating film in the wall-pipe interface.
(ii) Facilitate formation of an ultra-thin bed of a ball-bearing type surface between the pipe and the borehole wall which allows easy sliding of the drill string along the nanomaterial-based ball-bearing surface.

Removal of toxic gasses H_2S can diffuse to drilling fluid from formations during drilling of gas and oil wells. H_2S is to be eliminated from the mud to prevent corrosion of pipelines and equipment. For example, zinc oxide nanoparticles and bulk zinc oxide have the potential to remove H_2S from water drilling mud.

2.3   Logging While Drilling

Logging while drilling (LWD) is a method for the extraction and collection of data and information during the drilling process. It measures the formation properties, well geometry, and the drilling process properties. It makes measurements while the tools are drilling which provides directional surveys and drilling mechanics data. Compared with wireline measurement, LWD has similar measurement capa-bilities, although it differs in numerous other aspects. LWD can work in harsh environments. On the other hand, wireline measurements are small, delicate, powered through cable, offer high-speed performance, and are affected by the entirety of the challenging environment. The main advantage of these processes is monitoring and controlling the operations while the drilling is taking place.

There are many available LWD measurement techniques such as natural gamma ray (GR), borehole caliper, resistivity, and sonic and neutron porosity. Nowadays, the majority of the neutron porosity that is implemented in LWD uses He-3 detectors in order to detect neutrons in the whole. The main advantages of He-3

detectors are that they are mechanically robust, operate at high temperatures, and fulfill the well logging requirements; however, their available quantity is very limited and they could be depleted in the next few years. However, a good alternative for the He-3 detector is the Li-6 scintillation detector, which can be used as an LWD tool. This detector can be improved using nanotechnology techniques in order to work more efficiently and substantially. Nanostructured glass-ceramics of Li-6 scintillations can work far better than the current Li-6 scintillation materials. Nano-logging can be the main contributor in this field and can improve the next generation of LWD tools, especially in neutron porosity logging.

3 Upstream Production Sectors and Nanotechnology

3.1 *Manifolds/Gathering*

The well streams are brought to the main production facilities over a network of pipelines and manifold net systems. The aim of the pipelines is to allow for production setup or well sets. Thus, the best reservoir utilization well flow composition, such as gas, oil, and water, is selected from the available wells. For gas gathering systems, the individual gathering lines are metered into the manifold. However, for multiphase flows or combinations of gas, oil, and water, the inflated cost of the multiphase flow meters leads to the use of software flow rate estimators, where well test data is used to calculate the actual flow (Devold 2013).

Stimulation In viscoelastic surfactant stimulation fluid, high-molecular-weight cross-linked polymer fluids are being used to stimulate oil and gas wells. The advantages of such fluids are their exceptional viscosity, thermal stability, proppant transportability, and fluid leak-off control. On the other side, the disadvantages of such materials include the amount of polymer residue they leave behind which can damage formation permeability and fracture conductivity.

Therefore, the nanoparticles could be good alternatives because of their high surface morphology and high surface reactivity. These materials can stabilize fluid viscosity at high temperatures and produce a pseudo filter cake of viscous viscoelastic surfactant stimulation fluid which reduces the rate of fluid loss and improves fluid efficiency.

Scale inhibition The formation of scales inside the production tubing can be inhibited by using nanomaterials with a hydrophobic surface such as epoxy paint surfaces which can reduce the chances of scale deposition. An example of this type of material is nano SO_2/epoxy adhesive solution. Another example is nanomaterial coated with a low surface energy polymer, called aminopropyl.

3.2 Separation

In the case where the well produces a combination of gas, oil, and water, with various contaminants, then it is necessary to install the separation processes. The production separators are available in various forms and designs, with the classic variant being the gravity separator. Where the wells have pure gas production, for example, then the gas is taken directly for gas treatment and compression.

3.3 Gas Compression

In the case where the gasses from the separators have lost a significant degree of pressure, then the gasses should be recompressed for transportation. To facilitate this, turbine compressors gain their energy by using up a relatively small proportion of the natural gas which they compress. The turbine can serve to operate a centrifugal compressor, containing a type of fan which compresses and pumps the natural gas through the pipeline. Note that gas from a pure natural gas wellhead has sufficient pressure to feed directly to a pipeline transport system, thus there is no need for it to be recompressed.

3.4 Oil and Gas Storage and Export

The final step before the oil or gas leaves the platform consists of

  (i) Storage
 (ii) Pumps
(iii) Pipeline terminal equipment

   In production sites, the oil and gas is piped into a refinery terminal. Gas can be difficult to store locally, consequently, underground mines, caverns, and salt deposits are used to store gas. The gas pipeline is fed from the high-pressure compressors.
   On the other hand, on platforms with no pipelines, oil is then stored in onboard storage tanks to be transported using a shuttle tanker. The oil is stored in storage cells around the shafts on concrete platforms and in tanks on floating platforms. A separate storage tanker can be used for some floaters. Ballast handling is necessary to balance the buoyancy when the oil volume varies. For onshore, fixed roof tanks are usually used for crude and floating roofs for condensate. In addition, rock caverns are used. Oil pipelines are usually driven by separate booster pumps. For

long pipelines, intermediate compressor stations and pump stations are recommended to be used due to the distance involved in crossing mountain ranges (Devold 2013).

3.5 Midstream sectors

The midstream sectors involve

 (i) The transportation of oil and natural gas from the extraction site to the refineries by pipeline, rail, barge, oil tanker, or truck.
 (ii) Storage.
(iii) The wholesale marketing of crude or refined petroleum products.
(iv) Pipelines and other transport systems are utilized to move crude oil from production sites to refineries and deliver the various refined products to downstream distributors. Natural gas pipeline networks aggregate gas from natural gas purification plants and deliver it to downstream customers, like local utilities. This type may include natural gas processing plants which purify the raw natural gas and remove and produce elemental sulfur and natural gas liquids as finished end products.

4 Introduction to Downstream Sectors

The downstream sector usually includes the processes that are related to the crude oil refinery process, raw natural gas purification processes, and the network that is responsible for the marketing and distribution of these process products. The common products that are derived from the oil and natural gas are gasoline, petrol, kerosene, jet fuel, diesel oil, heating oil, fuel oils, lubricants, waxes, asphalt, natural gas, liquefied petroleum gas, and hundreds of petrochemicals (Leffler 2008; Fahim et al. 2009; Krylov et al. 1998; Vassiliou 2009; Meyers 2016). The material in the next sections is mainly focused on the oil refinery process and its configurations.

5 Oil Refinery Process

The downstream oil refinery processes are summarized in Fig. 1.2 (Jones and Pujado 1992). The discussion of each unit will be provided in the following main headings. A simple basic classification of oil refinery processes based on their nature is depicted in Fig. 1.3.
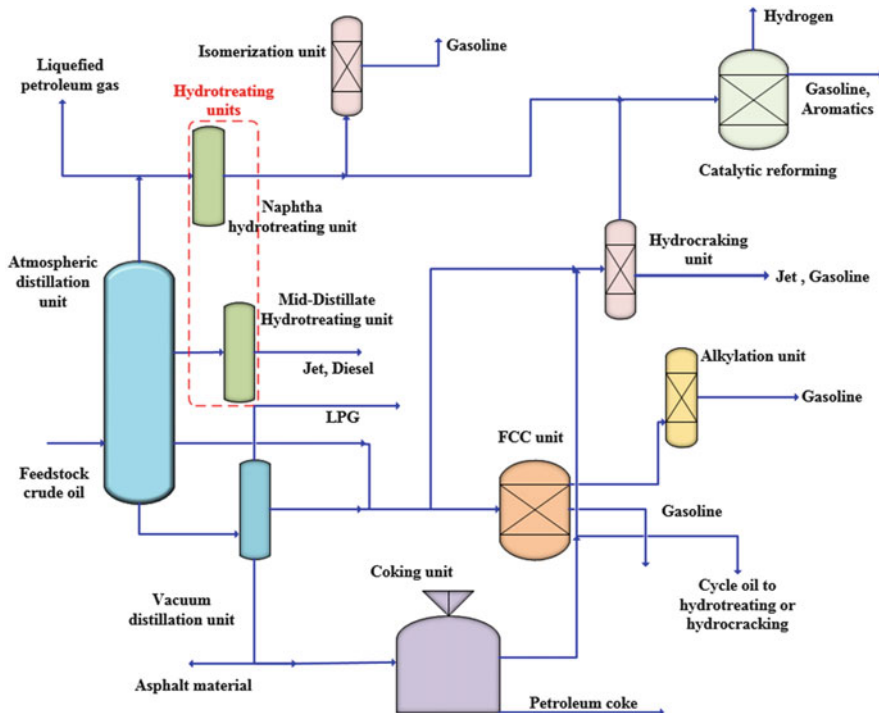
Fig. 1.2 A simplified block diagram of the refinery processes

5.1   Crude Distillation Unit

Crude oil contains a mixture of hydrocarbons with various boiling points. Thus, the distillation process can separate the crude oil into different hydrocarbon groups depending on their boiling point. In the oil refinery, there are two types of distillation unit which are, namely, atmospheric and vacuum distillation units (Jones 2006). Main types of crude distillation units in downstream sectors of oil refinery processes are presented in Fig. 1.4.

5.1.1   Atmospheric Crude Distillation Unit

The atmospheric crude distillation unit (ACDU) is the first unit in any petroleum refinery, where the processing of crude begins. In this unit, crude oil is distilled and separated into various valuable products (naphtha, kerosene, diesel, light and heavy oil, atmospheric gas oil (AGO)). These products are exposed to further processing downstream or become an input for conversion units in the rest of the refinery configuration. The main components of this unit are an atmospheric distillation
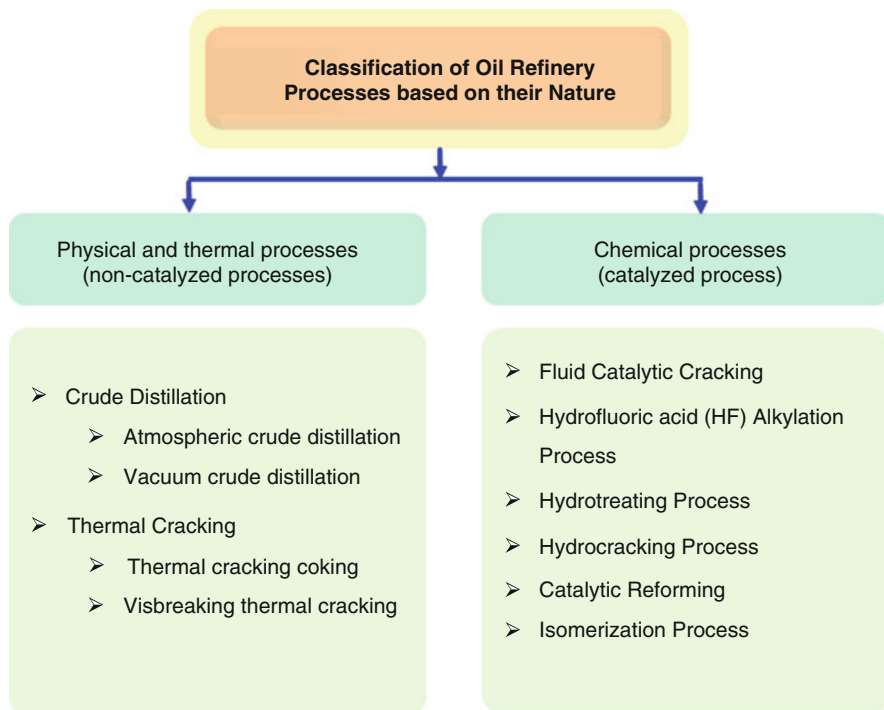
Fig. 1.3 Classification of oil refinery processes based on their nature

column, called a fractionation column, side stripper columns, a furnace, a desalter, integrated heat exchangers, and pump and crude oil storage, as shown in Fig. 1.5.

It is necessary to increase the temperature of the crude oil before entering the distillation column, and this can be done by using a series of heat exchangers or a preheat train where the heat is recovered from the column product streams and by exchanging with condensing streams from the fractionation column.

The crude oil usually contains salts, such as magnesium and chlorides of calcium, which have negative effects on the downstream refinery equipment due to the corrosive properties of these salts. Thus, the first goal of the atmospheric crude distillation unit (ACDU) is to remove the salt from the crude oil, reduce the causes of corrosion, prevent fouling, plug as much as possible, and to prepare the crude for further smooth processing. For this task, the crude oil is pumped to the first heat exchanger to increase its temperature up to (50–150°C) using recovered process heat. Increasing the crude oil temperature reduces its viscosity and surface tension, and this facilitates the subsequent mixing and separation processes. The crude oil is mixed with a water stream to dissolve the salt and the mixture is sent to the desalter drum to separate the salt water from the crude oil. This separation process occurs according to the electrostatic liquid/liquid separation mechanism, where a high voltage is applied to remove the suspended water salt globules from
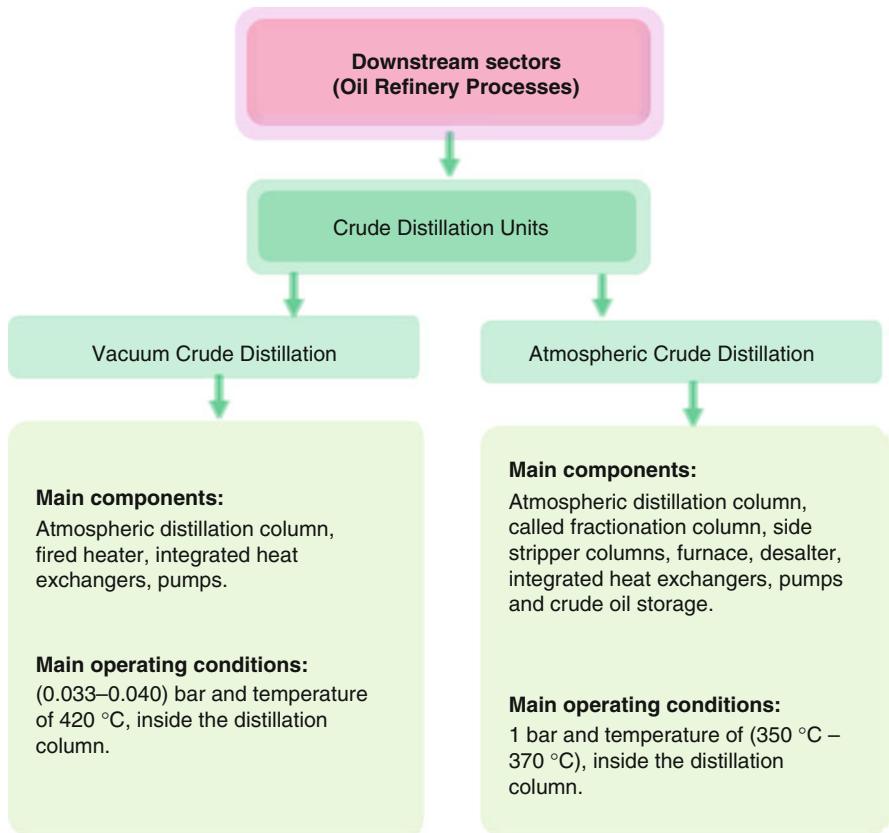
Fig. 1.4 Main types of crude distillation units in downstream sectors of oil refinery processes

the crude oil. The pressure inside the desalter drum must be maintained at a high value to prevent the partial vaporization of crude oil, resulting in the creation of a hazardous environment and unstable conditions. The effluent water from the desalter is disposed of by sending it to the oily water sewer.

The downstream of the desalter unit is heated further using another heat exchanger to a temperature of 200–280°C. Then, the crude oil temperature is increased up to (340–390°C) using a furnace (fired heater), resulting in vaporizing a portion of the crude oil and having a stream with two phases (liquid/gas). The heated crude oil is directed to the bottom part of the distillation column which is called the flash zone, where the two phases are separated.

At a pressure of about 1 bar and a temperature of (350–370°C) inside the distillation column, the vaporized portion of the crude oil moves up the column through trays, while the liquid portion leaves the flash zone of the column by a stream stripper section. In the distilling process, the crude oil should not be subjected to temperatures >370°C to avoid thermal cracking of the high-molecular-weight components forming the petroleum coke. The formation of coke may plug
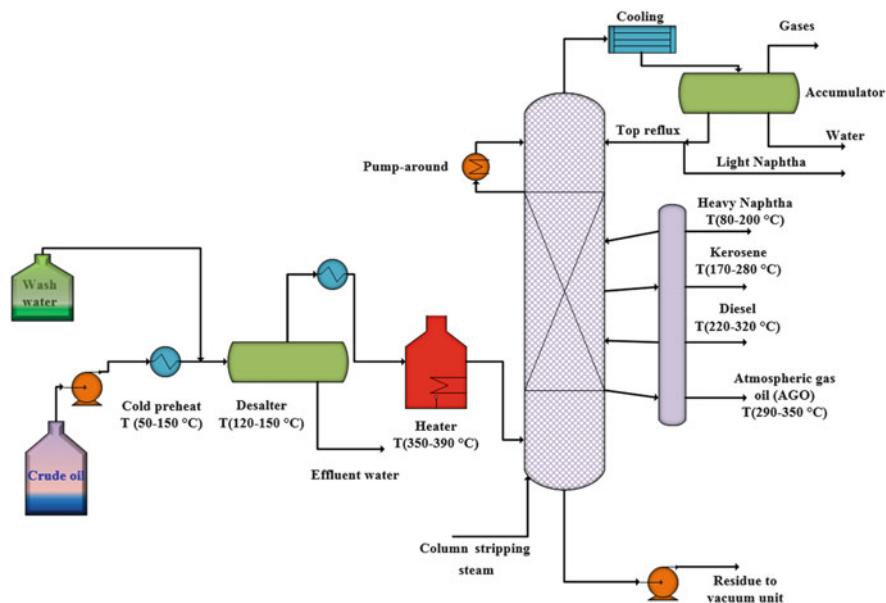
Fig. 1.5 The atmospheric crude distillation unit (ACDU)

the tubes in the furnace that heats the feed stream to the fractionation column, piping both from the furnace to the fractionation column and also in the column. The fractionation column inlet oil temperature is constrained between 370 and 380°C, producing residual oil from the bottom part of the fractionation column, where the hydrocarbons boil at a temperature higher than 370–380°C.

In every tray, the distillate vapor is in countercurrent contact with the liquid reflux stream which is generated from a condenser at the top of the distillation column and from the side stripper columns. The various fractions of the vaporized crude oil are gradually condensed with the column elevation on the trays based on their boiling point. As a result, the lighter portions of the crude oil condense on the higher trays, such as naphtha, methane, ethane, propane, and butane while the heavier portions, like fuel oils, condense on the lower ones. Using special trays (draw-off trays), distillate products are withdrawn from the side of the column into smaller side stripper columns. The side stream distillates are heavy gas oil, light gas oil (diesel), and kerosene (jet fuel), and they leave the atmospheric distillation column and enter the top of their respective stripper tower. Like the atmospheric distillation column, the stripper columns have between 4 and 6 fractionation trays, where there is liquid/vapor contact in every single tray. To draw off the hydrocarbons from the side stripper columns with specific properties, a steam is introduced at the bottom of the stripper column which exits at the top and enters into the distillation tower. The side stream stripper towers are usually compacted into one

column to make the flow from the side stream draw-off tray to its stripper tower more easy and direct.

The naphtha vapor leaves the top of the column and is collected in the overhead drum. The unestablished naphtha from the fractionation column is transferred to the naphtha stabilizer section to separate the stabilized overhead vapors which are condensed to recover liquefied petroleum gas (LPG). Then, LPG is treated in a caustic and amine treating unit. The stabilized naphtha then undergoes further separation to produce light, medium, and heavy naphtha. A portion of the side stream's product and naphtha vapor are condensed and returned as a liquid reflux to the distillation column.

The purpose of the flowing liquid reflux is creating a driving force for the separation of different crude fractions, controlling the temperature in the trays, and minimizing the heat loss in the column by recovering some energy from the condensed vapor streams. For further illustration, inside the tower are a series of trays that have perforations which allow the vapors to rise, as shown in Fig. 1.6. In a typical design, the trays are constructed with a device called a bubble cap which forces the vapor to bubble through a layer of collected liquid that is several inches deep on each tray. As it rises through the liquid, the vapor transfers some of its heat to the liquid. The heat transfer causes the vapor to cool slightly and some of the heavier components of the vapor to condense into a liquid. As a result of the heat transfer from the vapor, the liquid on the tray gains heat, some of its lighter components are driven off as a vapor which rises up to the next tray. This process is continuously repeated.

In the flash zone, the stripping steam flow is introduced into a countercurrent with the flow of the crude oil residue. This steam decreases the amount of liquid/vapor separation, resulting in enhancing the crude oil flashing (Gary et al. 2007).

The residual oil can't be distilled further due to the range of the temperature and pressure limitations in the atmospheric crude distillation unit (ACDU), so the residual is sent to the vacuum crude distillation unit (VCDU) for further distillation under different operating conditions.

Fig. 1.6 A tray in the atmospheric column with liquid/vapor contact
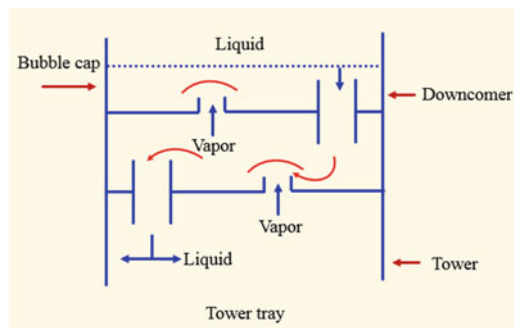
5.1.2 Vacuum Crude Distillation Unit

Vacuum distillation is a separation technique where the pressure is reduced above the liquid mixture, resulting in evaporation of the most volatile species when the pressure is less than their own vapor pressure. Vacuum crude distillation involves distillation of the atmospheric residue from the atmospheric crude distillation unit (ACDU) under vacuum in order to obtain additional useful products and to reduce the residual stock as much as possible. In a vacuum condition, distillation allows separation at lower temperatures, resulting in reducing the possibility of crude oil cracking and furnace tube coking, Fig. 1.7.

The vacuum crude distillation unit (VCDU) and atmospheric crude distillation unit (ACDU) are integrated specifically for utilizing the recovered heat and designing the integrated heat transfer system. The vacuum column has a larger diameter and a different internal structure than the atmospheric column. The internal design of the vacuum column should keep a pressure increasing from the top to the bottom of the column and the liquid/vapor contact should be excellent. As a result, the vacuum column contains packing materials and demister pads, which usually have a lower pressure drop compared to the trays that exist in the atmospheric column. This packing material consists of (1) structured sheet metal or (2) randomly dumped packing such as Raschig rings. However, the vacuum contains a few trays to draw off the product from the side of the column.
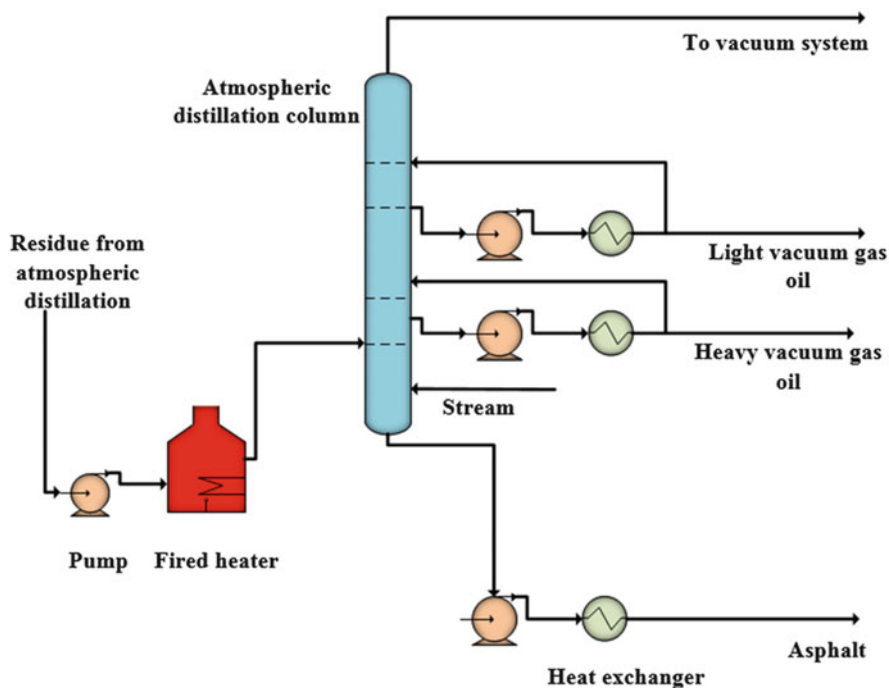
Fig. 1.7 A simplified diagram of the vacuum crude distillation unit (VCDU)

The vacuum condition is usually generated by a series of steam ejectors that are working from the top of the column. The ejectors remove inert and other vapors which exist in and pull a vacuum of about 5 mmHg absolute. The pressure in the vacuum column typically is kept at about (25–30) mmHg, and the temperature is maintained around 420°C.

Despite the difference in the operating conditions, the process configuration of the VCDU has somewhat the same configuration process as the atmospheric crude distillation unit (ACDU). The ACDU residue oil is preheated by a heat exchanger using recover heat from the hot stream products. Then, the residue oil is partially vaporized due to the increase in its temperature up to (400–430°C) using a fired furnace.

The two-phase stream enters the vacuum column and flashes at a feed point called the flash zone. The distilled vapor rises through the column and is condensed by the circulating liquid reflux moving down the column in the same manner as the cold reflux of the side stream in the ACDU. The products are taken off at the appropriate sections and are cooled by

  (i) Heat exchange with colder streams in the atmospheric unit
 (ii) By air coolers
(iii) As heating mediums to light end reboilers

The light vacuum gas oil is withdrawn from the top side of the column while the heavier vacuum gas oil leaves from the second side of the column. The light vacuum gas oil is directed to other conversion units in the refinery configuration for further processing or is used as a lube base stock. The vacuum residue can be either directed to a coke unit, a cracking unit, and a visbreaker unit or utilized to produce asphalt material.

5.2 Thermal Cracking Processes

The thermal cracking processes can be classified into the following main types: (a) coking and (b) visbreaking. The thermal coking process can be classified into various types including (1) the delayed coking process and (2) flexi-coking which is an improved version of conventional fluid coking. Table 1.1 summarizes different thermal cracking processes and their conditions. The following sections will discuss these types.

5.2.1 Thermal Cracking Coking Processes

Coking is an extreme form of the thermal cracking process, in which the heavy residue is completely converted from the low-cost material to valuable products. The common products of this process are naphtha, solid materials, gas oil, and coke. The coking process is suitable for processing heavy oil crudes like the Canadian heavy oil crudes. The delayed coking and fluid coking process are different types of

Table 1.1 Comparing between different thermal cracking processes and their conditions

Thermal cracking process	Process conditions
Delayed coking	Operates in semi-batch mode Moderate (482–515°C) heating at 6 bar Soak drums (452–482) coke walls Coked until drum solid Coke 25–40% on feed, yield 221°C, 30% on feed
Fluid coking	Operating conditions: 510–530°C and 0.7 bar Oil contact refractory coke Fluidized bed with steam-even heating Higher yield of light ends ($<C_5$), less coke yield
Flexi-coking	Licensed and commercialized by Exxon Research and Engineering Company Different fluidized beds are utilized to produce a lighter more valuable product from the heavy residue A large portion of the coke is converted to a low Btu gas The reactor temperature is maintained around (530°C)
Visbreaking	Mild operating conditions Mild (470–500°C) heating at 3.5–14 bar Reducing the fuel oil viscosity Low conversion (10%) to 221°C Two types: soaker and coil visbreaking process Heated coil or drum
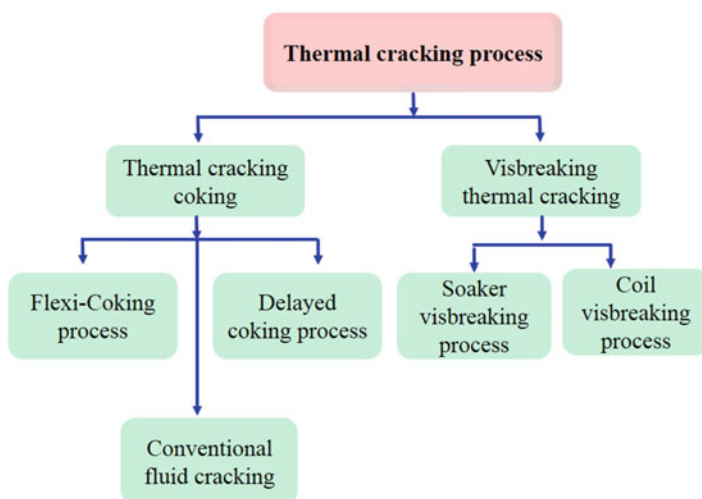
Fig. 1.8 Classification of the thermal cracking process

the coking process including (1) the delayed coking process and (2) flexi-coking; which are discussed in the following two sections. Figure 1.8 depicts the general classification of the thermal cracking process.

Delayed Coking Process

The delayed coking processing is a thermal cracking process, where the heavy residuum from the ACDU and VCDU is heated and converted into coke gas oil and petroleum coke in a batch-continuous process, Fig. 1.9. Like the ACDU and VCDU, a fired heater is used to increase the feed temperature up to (480–505°C), resulting in a mild cracking of the heavy residuum. The output stream of the furnace is routed to one of the coking drums with a temperature of around 500°C and a pressure of (2–3.5 bar). The coking drum usually takes (11–20 h) to be filled with oil residuum. The liquid/vapor mixture of the oil residuum is exposed to successive cracking until the total destruction of the heavy fractions is achieved. As a result of a long residence period, the coke is generated as a by-product from the rich carbon solid materials, and it is removed from the bottom part of the drum using high-pressure jets. The coke which is produced in the delayed coking process is called green coke and is classified as a sponge coke.

The feed stream is regularly switched between drums with one drum operating under the decoking process which is performed using high-pressure water jets. A cycle of events occurs at regular intervals depending on the delayed coking unit feed rate, drum size, and throughput capacity. Typically, delayed cokers run drum cycle times of about 12–16 h, with one drum filling online while its counterpart is off-line for stripping, cooling, and the decoking cycle.
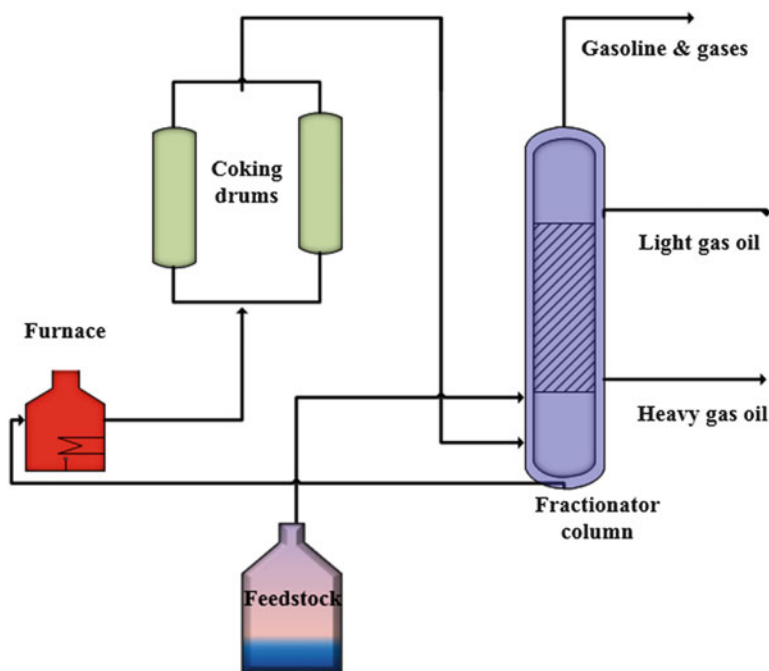
Fig. 1.9   A simplified diagram of the delayed coking process

The cracked vapor leaves from the top of the drum and is then directed to the fractionator column, where it is distilled and separated into the desirable distillate products (e.g., naphtha, kerosene, gas oil). The bottom of the fractionator column contains a reservoir where a combination between the fresh feed and condensed product vapor occurs in order to compensate for the feed of the coker heater.

Flexi-Coking Process

Flexi-coking is an improved version of the conventional fluid coking process, where the heavy residuum of oil from the atmospheric crude distillation unit (ACDU), vacuum crude distillation unit (VCDU), or fluid catalytic cracker (FCC) units is converted thermally to lighter and more valuable products using a continuous fluidized bed reactor, Fig. 1.10. This technology is licensed and commercialized by the Exxon Research and Engineering Company.

In conventional fluid coking, the oil residue is coked by being sprayed into a fluidized bed of hot, fine coke particles. For example, a shorter contact time with higher temperature coking might result in increased light and medium hydrocarbons with less cake generation. However, the product would have a lower value from economic point view (Rana et al. 2007).

Unlike the delayed coking process, a substantial portion of the coke is converted to a low Btu gas in the flexi-coking gasification process. The flexi-coking configuration has the capability of handling a wide range of feed types, particularly, feeds
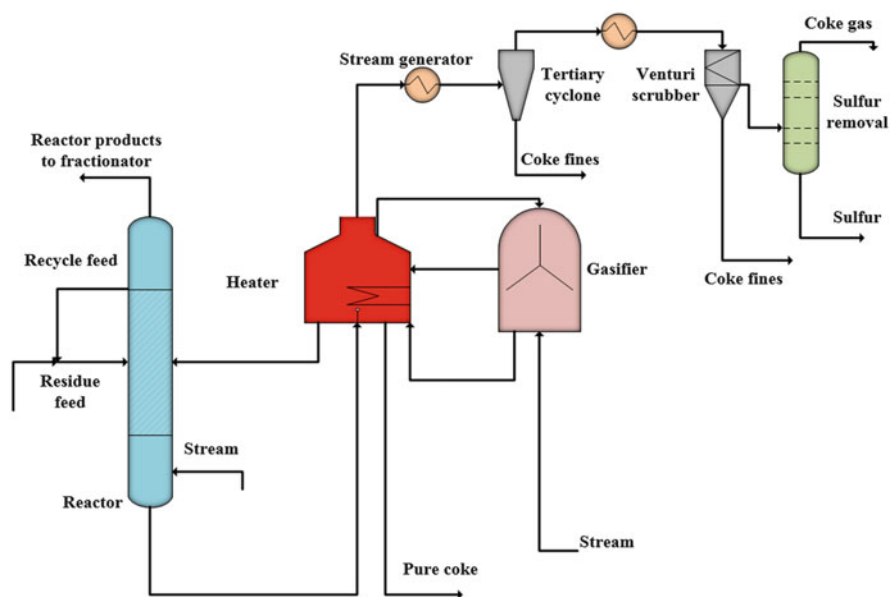
Fig. 1.10 A simplified flow diagram of the flexi-coking process

with high metals, sulfur, and Conradson Carbon Residue (CCR or Concarbon) content.

The heavy hydrocarbons are sprayed into the fluidized bed reactor, where they are cracked thermally, by a hot coke fluidized bed. This hot coke is circulating between the reactor and the heater vessel to maintain the reactor temperature at around (530°C) and to supply the sensible level of vaporization heat required for thermal cracking. The cracked vapor products leave the reactor section and enter the scrubber zone, where a portion of the vapor (usually fine coke and heavy oil particles) is condensed and recycled to the reactor zone. The reactor output flows to a conventional fractionator column for separation purposes.

A steam is injected into a baffled section at the reactor bottom to strip the coke is free from other reaction products. The coke is routed to the heater vessel, where its temperature is increased to about 600°C. The heating process is achieved using a coke fluidized bed, and its main goal is to transfer the heat to the reactor for the cracking process. The coke leaves the heater vessel and enters a gasifier, where it is converted to a low Btu gas which contains N_2, H_2, CO_2, and CO by a reaction with air and steam. The coke contains sulfur which is usually converted to H_2S and COS in the gasifier unit while the nitrogen is converted into NH_3 and N_2. This gas leaves the gasifier and enters the heater, where it is used to fluidize the coke bed and supply the reactor with the required heat energy. A coke purge stream is withdrawn from the heater and is usually about 0.5–0.9 wt % of the fresh feed. Most of the metals contained in the process feedstock are separated with this purged coke.

After leaving the heater, the coke gas is cooled using a steam generator and then enters a tertiary cyclone and venture scrubber, where the coke fines are collected. Finally, H_2S is removed from the coke gas in the sulfur removal unit (Stretford unit). As a result of the flexi-coking process, an upgrade in the low-quality fuel is achieved and a fuel gas with a lower heating value compared to natural gas is generated.

5.2.2 Visbreaking Thermal Cracking Process

The visbreaking process is a thermal cracking process under mild operating conditions, where the viscosity of the VCDU residuum is reduced by breaking the long chain molecules of the feedstock into shorter ones to obtain more valuable products and to meet the fuel oil specifications, Fig. 1.11. In the visbreaking process, the operating conditions of the thermal cracking are optimized in a way that breaks off the long paraffinic side chain attached to the aromatic rings into smaller molecules. As a result of this optimized process, the thermal cracking is not complete, the viscosity of the product is largely reduced, and the resulting fuel exhibits good stability. Under extreme operating conditions, the product has less stability and can be polymerized during storage which causes filter plugging and sludge formation.
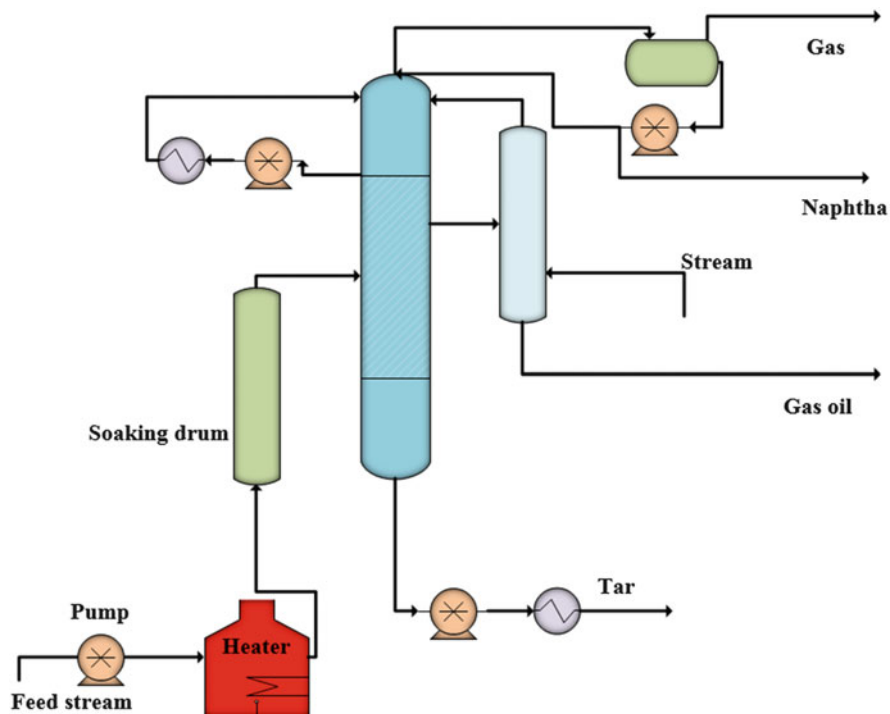
Fig. 1.11 A flow diagram of the Soaker Visbreaker unit

The principle reactions which occur during the visbreaking operation are:

- Cracking of the side chains attached to the cycloparaffin and the aromatic rings at the ring so the chains are removed or shortened into methyl or ethyl groups.
- Cracking of resins into light hydrocarbons (primarily olefins) and compounds which convert to asphaltenes.
- At temperatures above 480°C, there is some cracking of the naphthene rings. There is little cracking of the naphthenic rings below 480°C .

Thus, there are two types of visbreaking process: the soaker visbreaking process (Fig. 1.11) and the coil visbreaking process (Fig. 1.12). In the soaker visbreaker unit, thermal cracking is achieved at a relatively low temperature of about (427–443°C) and with a long residence time. However, the cracking is achieved at a high temperature of around (470–500°C) and a short residence time of about (1–3 min) in the coil visbreaker unit. Despite the similarity between the two units in the yield and properties of the product, the soaker visbreaker unit consumes less energy due to the relatively low temperature, and it can be operated for a long period of time (6–18 months) before being shut down for coal removal purposes compared to 3–6 months in the coil visbreaker unit. However, cleaning the coil
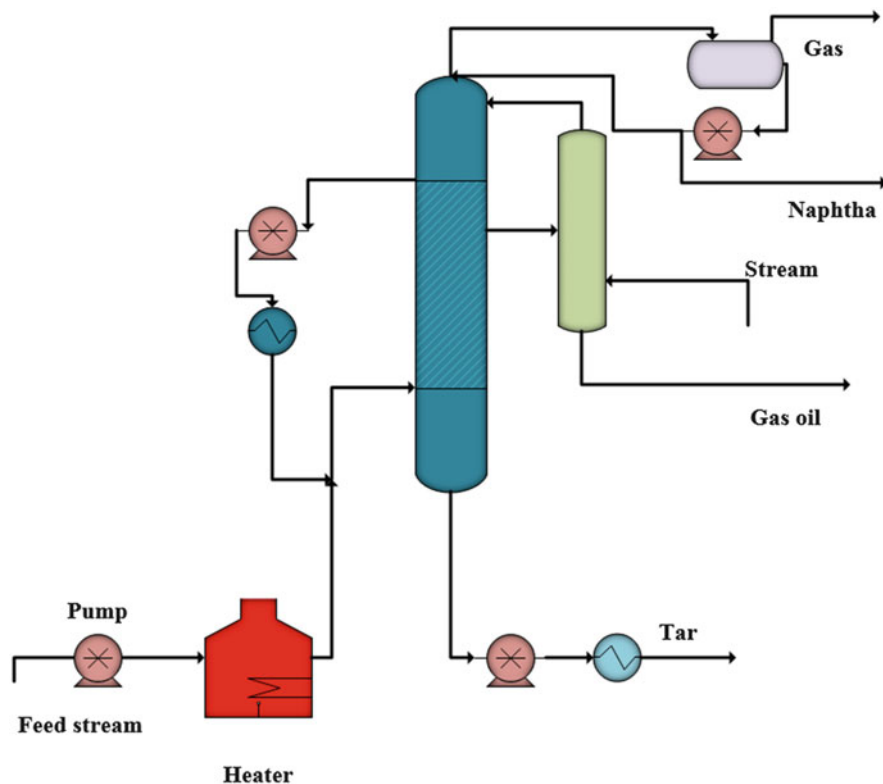
Fig. 1.12 A flow diagram of the Coil Visbreaker unit

visbreaker unit is much easier than the soaker visbreaker unit. Currently, the majority of the new refineries use the soaker visbreaker unit instead of the coil visbreaker unit (Sieli 1998).

5.3 Fluid Catalytic Cracking Unit

The fluid catalytic cracking unit is one of the most dynamic and complex processes in a refinery. In the fluid catalytic cracking unit, the high-boiling, high-molecular weight hydrocarbon fractions of petroleum crude oils are converted into valuable products, such as gasoline and olefinic gasses, Fig. 1.13.

Cracking of petroleum hydrocarbons can be performed by (1) thermal cracking and (2) catalytic cracking. Using catalytic cracking, more gasoline with a higher octane rating is produced with a by-product of olefinic-valuable gasses.

The common feedstock of an FCC unit contains atmosphere gas oil, vacuum gas oil, and a heavy stream, such as reduced crude oil.
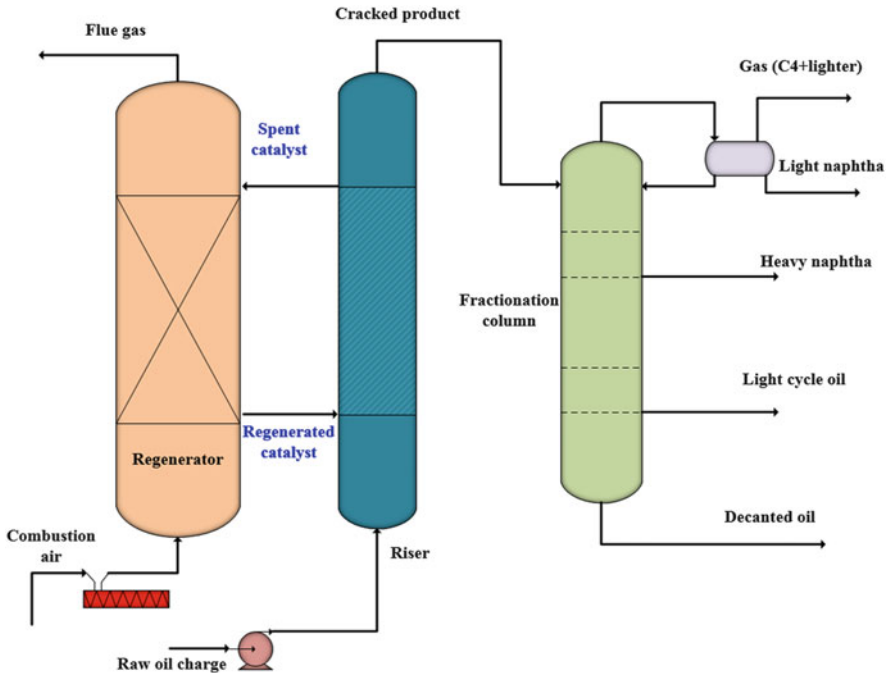
Fig. 1.13 A flow diagram of the fluid catalytic cracking unit (FCCU)

The feed usually contains major contaminants, such as carbon residue and metals. The fluid catalytic cracking process has two main steps: (1) the reaction and regeneration process and (2) the fractionation process.

5.3.1 Reaction and Regeneration Process

The fluid catalytic cracking unit (FCCU) is a circulating fluidized bed system which includes a reactor, regenerator, and a heterogeneous catalyst system. The reactor and regenerator vessels are connected to each other by transfer lines to enable the catalyst particles to flow between the two vessels for a continuous reaction and regeneration process. The feed to the unit along with the recycle streams is preheated to a temperature of 365–370°C. Then, the feed is allowed to flow to the riser, where it encounters hot regenerated catalyst at a temperature of 640–660°C.

In the inlet of the reactor vessel, cracking occurs owing to the contact of oil with the powder catalyst. To obtain a high surface contact area, the catalyst and oil are dispersed inside the reactor column. This provides complete cracking in the catalyst fluid bed in the reactor vessel. The catalyst fluidity can be maintained using a steam injection at the bottom part of the riser.

The cracked vapor effluent flows from the top section of the riser column to enter the recovery part of the plant. In this plant, the distillate products of cracking are

separated by fractionation and forwarded to either storage or for further treatment. The oil slurry stream from the recovery plant is returned back to the reactor as it is recycled. On a continuous basis, the catalytic materials from the reactor flow to the regenerator vessel where there is contact between the catalyst particles and an air stream that maintains the catalyst particles in a fluidized condition. The carbon that covers the catalyst particles is burned off by a reaction with the air which leads to a carbon conversion into gasses such as CO and CO_2.

The reactions that occur in the FCC unit are extremely exothermic which produces a huge amount of energy that increases the catalyst stream temperature up to $537°C$ and supplies the required heat for the oil cracking reaction.

5.3.2 The Fractionation Process

In the fractionation process, the output of the reactor-regeneration system is separated into different products. Liquefied petroleum gas and gasoline are removed overhead as vapor. Unconverted products such as light and heavy cycle oil flow out as a side stream. The overhead product is transferred to the stabilization section, where stabilized gasoline is separated from the light products from which liquefied petroleum gas is recovered.

The common products of the FCC unit contain light gasses, liquefied petroleum gas, gasoline, heavy and light cycle oil, and coke as a by-product which is consumed in the system regenerator to supply the reactor with the energy demand.

5.4 Hydrofluoric Acid Alkylation Process

The alkylation unit is one of the conversion units in the crude oil refinery where isobutane and alkenes with a low molecular weight are converted into alkylate, which is a high-octane gasoline, Fig. 1.14. The common catalysts for the alkylation reaction are sulfuric acid or hydrofluoric acid. Alkylation is catalyzed by liquid and solid acids, such as HF, $AlCl_3$-HCl, H_2SO_4, HF-BF_3, H_2SO_4-HSO_3F, BF_3—alumina, trifluoromethane sulfonicacid chlorided Pt alumina, ion exchange resins, and zeolites (Gary et al. 2007).

Based on the used catalysts, the unit may take the name of (1) sulfuric acid alkylation unit (SAAU), (2) hydrofluoric acid alkylation unit (HFAU) or hydrofluoric acid (HF) alkylation process (Fig. 1.15). The alkylation unit feedstocks usually contain olefins and isobutane. The catalytic cracking and coking operations are considered as the main source for the olefins in the alkylation process. Propene and butenes are the main olefins that are used. However, pentenes or amylenes are involved in some operations.

The process of hydrofluoric acid (HF) alkylation is achieved in four main steps including (1) feed pretreatment, (2) reaction, (3) fractionation, and (4) acid regeneration. These steps are highlighted in the following sections.
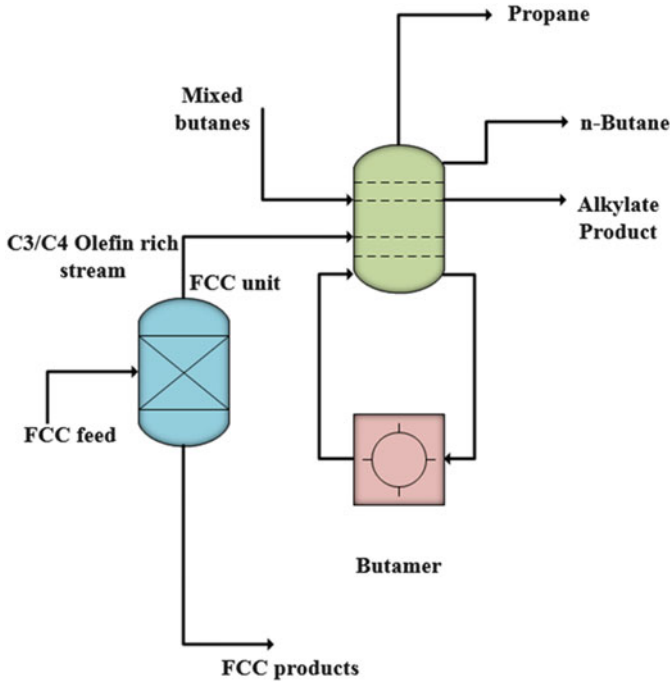
Fig. 1.14 A simplified block diagram of the location of the alkylation unit in the refinery configuration
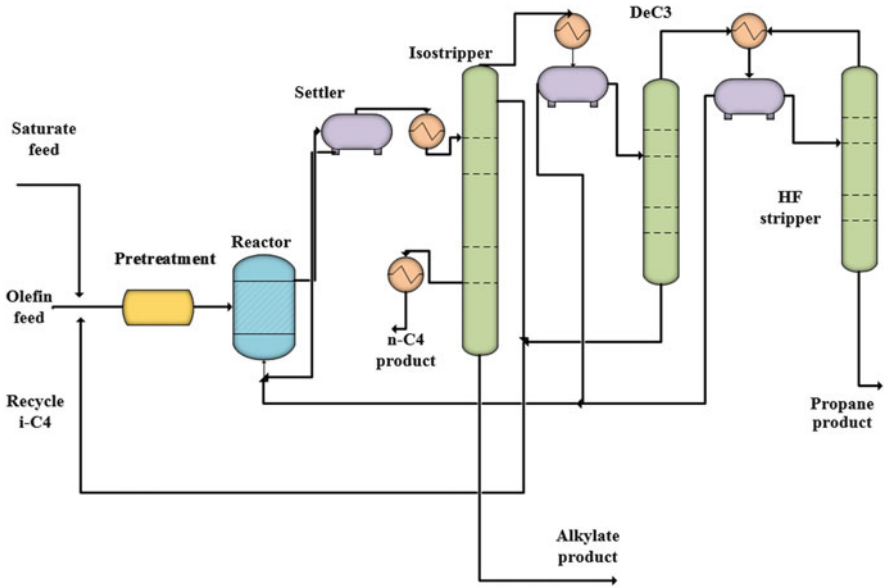
Fig. 1.15 Illustration of the hydrofluoric acid alkylation flow diagram

5.4.1 Feed Pretreatment

The alkylation unit olefin feed is generated from an FCC unit and contains butene, isobutene, and propene, in addition to amylenes, n-pentane, propane, n-butane, and noncondensables (ethane and hydrogen). The feed may also contain contaminants (such as water, methanol, and ethanol) which reduce the acid catalyst's efficiency by diluting its concentration or reacting with it. As a result, the acid consumption and the undesirable reaction products are increased. Therefore, in the hydrofluoric acid alkylation process, olefin feeds, which are produced from the FCC unit, are usually deethanized. Merox (mercaptan oxidation) is treated to remove H_2S and mercaptans and then dried.

5.4.2 Reactions

After the pretreatment of the olefin feed, it is combined with a huge amount of a recycled isobutane excess to supply a 6:14 isobutane to olefin molar ratio. Then, the combined stream is sent to the reactor column of the alkylation unit. The extreme exothermic heat that is generated from the reaction is removed using flowing cooling water in the reactor tubes, and this allows the reaction to occur in a temperature range from 27 to 38°C. The alkylation reaction occurs at a high rate of almost complete olefin conversion. The excess amount of nonreactive hydrocarbons, alkylate product, and isobutane that exist in the feed stream and the acid catalyst are transferred into the settler vessel. Using gravity, the dense acid phase and the hydrocarbons are separated from each other rapidly. Then, the dense acid phase is recycled to the reactor column while the hydrocarbons with the dissolved hydrofluoric acid flow out of the settler vessel into the isostripper column.

5.4.3 Fractionation

In the fractionation sector, the distillation process is utilized to separate the alkylate from the isobutene and acid catalyst. The unreacted isobutane is recycled and combined with the olefin feed before entering the reaction vessel. Propane is the main product of the distillation process and the n-butane flows off as a side product. Generally, the fractionation sector usually has a hydrofluoric acid stripper, a depropanizer, and an isostripper.

The isostripper is a column that has double side draws and its main function is to recover isobutane to increase the ratio of isobutane to olefin molar of the used reactor. The isostripper column consists of two reboilers. The goal of the upper reboiler is to increase the use of the low-pressure steam while the lower reboiler utilizes a heating medium which provides 200–230°C. Alkylate is withdrawn from the lower section of the column and then cooled and transferred to the product storage. Also, the isobutane is withdrawn from the column and recycled to the

reactor vessel while the n-butane is withdrawn from the side draw and sent to the product storage.

The depropanizer and hydrofluoric acid stripper separate propane from the recycled isobutene. The stream of the lower section of the depropanizer column is isobutane which is combined with the isobutane stream of the isostripper tower and recycled to the reactor vessel. In the upper part of the depropanizer column, the propane product and hydrofluoric acid are separated in the overhead receiver. The acid phase is recycled to the reactor sector and the acid which contains propane is sent to the hydrofluoric acid (HF) stripper column, where propane is stripped free of acid. The bottom stream of the HF stripper is a propane product treated with hot alumina to separate the organic fluorides, and then cooled and treated with potassium hydroxide pellets to remove traces of hydrofluoric acid and water.

5.4.4   Acid Regeneration

In the hydrofluoric acid alkylation process, a small stream of circulating acid is stripped with superheated isobutane in a small monel column called the acid regenerator. The regenerator overhead is hydrofluoric acid and isobutane that are recycled to the reactor; the regenerator bottom is polymer and the hydrofluoric acid–water azeotrope, which are neutralized with aqueous potassium hydroxide. In addition to the alkylate stream, the products leaving the alkylation unit include the propane and normal butane that enter with the saturated and unsaturated feed streams as well as a small quantity of tar produced by the polymerization reactions. The product streams leaving an alkylation unit usually contain grade propane liquid, normal butane liquid, C_5^+, and tar.

5.5   Hydrotreating Process

In the hydrotreating process called also catalytic hydrogen treating, objectionable materials such as sulfur, nitrogen, olefins, and aromatics are removed or reduced from the petroleum fractions. The terms hydrotreating, hydrodesulfurization, hydroprocessing, and hydrocracking are commonly used rather loosely in the industry because these processes are interconnected. In the processes of hydrodesulfurization and hydrocracking, for example, desulfurization and cracking operations occur at the same time. The common units under the hydrotreating process are shown in Fig. 1.16.

5.5.1   Applications of Hydrotreating

The removal of objectionable materials from crude oil fractions can be achieved by selecting a reaction between these objectionable materials and hydrogen gas in a
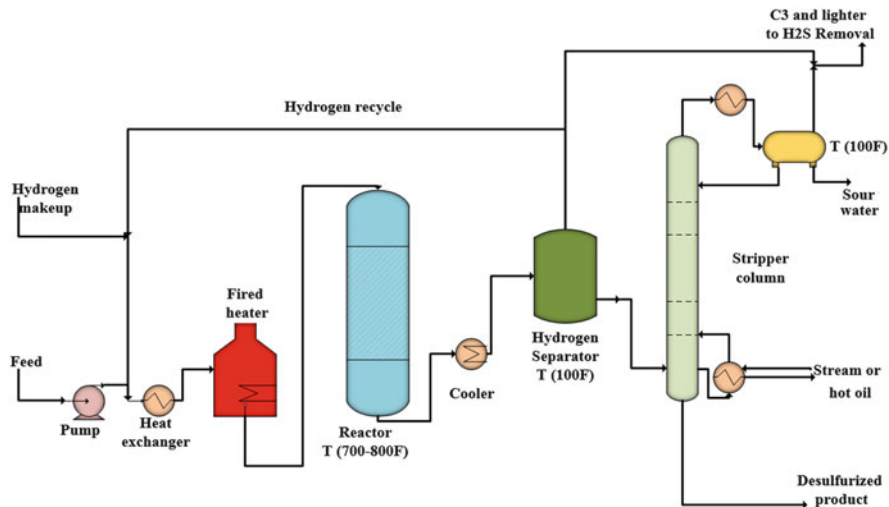
Fig. 1.16 A simplified diagram of the typical hydrotreating process unit

reactor at a high temperature (on average 300–500°C) and at moderate pressures. The lighter materials like naphtha are treated to be prepared for the next operation in the catalytic reforming units. However, jet fuel and heavy gas oil, in addition to other heavier distillates, are treated to meet the new stricter product quality standards regarding crude oil refinery products.

Many environmental regulations and constraints have been enforced on the oil industry to minimize the harmful materials in the refinery products as much as possible and to meet the new fossil fuel quality specifications.

Factors including the (1) type of feed, (2) desired cycle length, (3) and expected the quality of the products determine the type of design of a hydrotreater. Generally, the hydrotreating operates under the following conditions:

- Liquid hourly space velocity (LHSV) of 0.2–8.0.
- H_2 circulation of 300–4000 SCFB (50–675 Nm^3/m^3), where SCFB stands for the standard cubic feed hydrogen in the reactor per barrel of hydrocarbon feed.
- H_{2PP} of (14–138 bars).
- The start of run temperatures ranges between 290 and 370°C (Chianelli et al. 2002; Topsøe et al. 1996).

The common applications of hydrotreating are for:

(i) Naphtha (as a pretreatment process for the catalytic reformer unit): the objective is reducing or removing metals, nitrogen, and sulfur which can poison and deactivate the catalysts of the reforming process.
(ii) Kerosene and diesel: the objective is reducing or removing sulfur, in addition to saturating olefins and some of the aromatics, thereby improving the properties of the streams including the amount of kerosene diesel and the smoke point. This also provides storage stability.

(iii) Lube oil: the objective is reducing or improving the viscosity index, color, and stability while in storage.
(iv) Fluid catalytic cracker (FCC) feed: the objective is reducing or removing FCC yields while decreasing the catalyst usage and stack emissions.
 (v) Resids: the objective is reducing or removing sulfur to provide oils with low sulfur content which can affect conversion and pretreatment for the downstream process of conversion.

The recycled hydrogen and hydrogen makeup are mixed with the feed before entering the reactor vessel after the preheating process. The hydrotreating reaction is carried out at a temperature equal to or less than 427°C to avoid cracking. The hydrotreating process occurs in a fixed-bed reactor by a reaction between hydrogen gas and the oil in the presence of metal oxide catalysts. The common products of this reaction are hydrogen sulfide, saturated hydrocarbons, and ammonia. Then, the reactor products are cooled and sent to a hydrogen separator unit to separate the hydrogen from the oil. In the stripper column, the remaining hydrogen sulfides and light end products are removed from the oil. The gas is treated to remove hydrogen sulfide and recycled to the reactor (Gary et al. 2007).

5.5.2   Chemistry of the Hydrotreating Process

The chemical steps and reactions which occur during the hydrotreating process can be summarized as:

• Sulfur removal, desulfurization or hydrodesulfurization (HDS), where the organic sulfur compounds are converted to hydrogen sulfide (Saleh and Danmaliki 2016a, b).
• Nitrogen removal, denitrogenation or hydro-denitrogenation, where the organic nitrogen compounds are converted to ammonia.
• Organo-metallic, hydrodemetallation or hydrodemetallization, where the organo-metals are converted into the respective metal sulfides which are removed.
• Oxygen removal, where organic oxygen compounds are converted into water.
• Olefin saturation, where organic compounds containing double bonds are converted into their saturated homologues.
• Aromatic saturation, hydro-dearomatization, where some of the aromatic compounds are converted into naphthenes.
• Halides removal, where the organic halides are converted into hydrogen halides.

5.6   Hydrocracking Process

Hydrocracking processes are versatile catalytic refining processes which are performed for crude oil feedstock upgrading by adding hydrogen and removing

impurities. In the hydrocracking process, the weight of large molecules is converted into lower molecular weight by cracking until the desired boiling range is reached. The feed of the hydrocracking can range from heavy vacuum gas oils to atmospheric gas oils, while the products can range from heavy diesel to light naphtha.

The hydrocracking can usually be achieved by using various configuration processes including (1) single-stage process, (2) double-stage process, and (3) multi-stage processes, Figs. 1.17 and 1.18. These processes are highlighted in the following paragraphs.

5.6.1 Process Description and Classifications

The hydrocracking process can be classified into two types:

(i) The hydrocracking process where the cracking and treating are combined in one reactor is considered as a single-stage process. This single-stage process can be used for (1) a moderate degree of conversion or (2) for full conversion with a limited reduction in molecular weight such as the production of middle distillates from heavy distillate oils. The disadvantages of the single-stage unit include limitations in the conversion percentage and the deactivation and contamination of the used catalysts by undesirable materials.
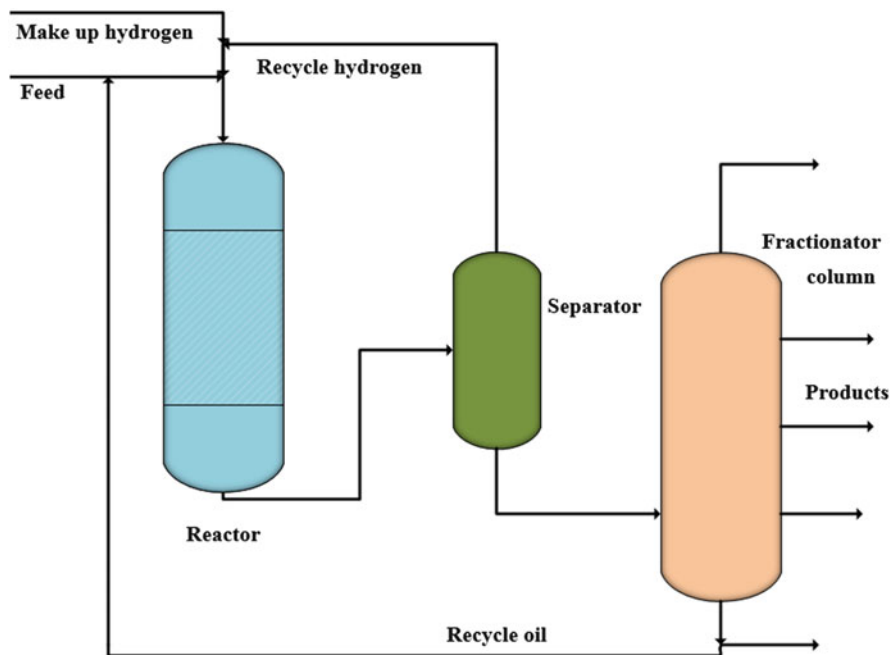
Fig. 1.17 A simplified diagram of the hydrocracking single-stage process
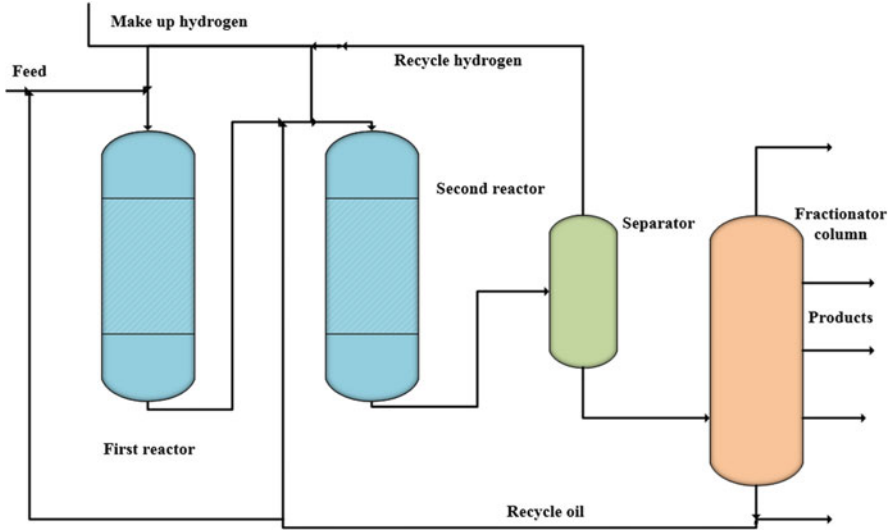
Fig. 1.18 A simplified diagram of the hydrocracking two-stage process

(ii) The hydrocracking process where the cracking reaction occurs in an additional reactor or reactors is considered as a multi-stage process. In the first reactor, the undesirable materials are separated from the unconverted hydrocarbons. Denitrogenation and desulfurization take place along with a limited amount of hydrocracking of the exothermic reactions. The catalyst is arranged in several fixed beds while the temperature of the reaction is controlled by injecting a portion of the recycle gas between these catalyst beds. The products of the first and second reactor are transferred into the hydrogen separation unit, where the hydrogen is separated and recycled. Then, they are sent to the fractionation column, where unconverted materials are removed and withdrawn from the lower section of the fractionation column.

5.6.2 Chemistry of the Hydrocracking Process

In the hydrocracking process, the heavy feedstock containing large molecular weight molecules can be converted into smaller molecular weight compounds. The reactions which occur in the hydrocracking units include (1) treating, called pretreating, and (2) cracking, or hydrocracking reactions which require a bifunctional catalyst, possessing the dual function of both cracking and hydrogenation. The reactions in hydrocracking can be classified into two categories:

 (i) Desirable reactions include the treating, saturation, and cracking reactions
(ii) Undesirable reactions include contaminant poisoning and coking of the catalyst

5.6.3   Advantages of Hydrocracking

Hydrocracking processes have several advantages including:

(a) Flexibility in terms of the production of gasoline and the middle distillates.
(b) The products are of a high standard.
(c) Relatively easy processes with the ability to handle a wider range of feedstock, like the cycle oils from other cracking units.
(d) Easy to control with the capability of handling various feedstock compositions.
(e) Limited by-product yield.
(f) Good conversion rate of the gas oil and residues into useful products.

5.7   Catalytic Reforming

In the catalytic reforming process, light crude oil distillates react with the hydrogen stream at a pressure of 3.5–34.5 bars and at an elevated temperature. In addition, there is the presence of platinum-based catalysts to increase the octane number of the hydrocarbon feed streams, Fig. 1.19. The paraffin-rich naphtha feed with low octane is converted into a liquid product which is rich in aromatic compounds with a high-octane number. In addition, hydrogen and light hydrocarbons are obtained as reaction by-products. Reformate can be used as a blending material for motor fuels, and as the main source of aromatics that are heavily used in the petrochemical industry (Pujadó and Moser 2006). The common feedstocks of the catalytic reforming unit are heavy straight-run gasolines, naphthas (82–190°C), and heavy hydrocracker naphthas.
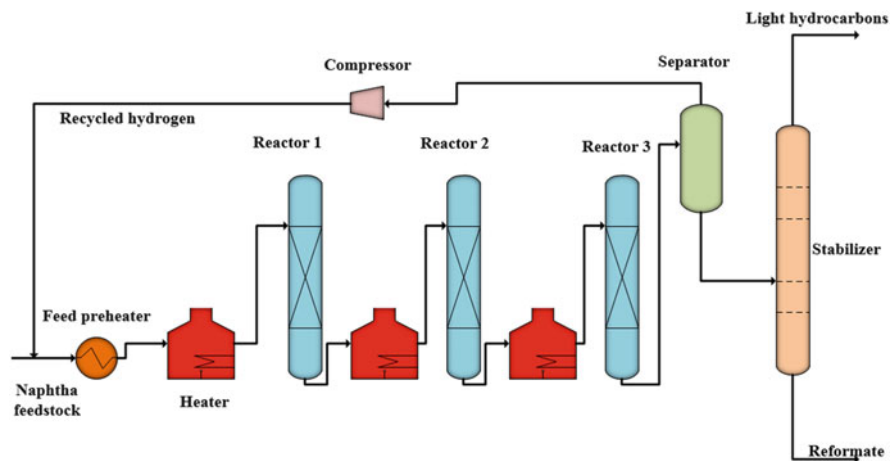
Fig. 1.19 General catalytic reforming flow diagram

5.7.1 Process Description

The first step generally is the naphtha feed preparation which involves removing the impurities and reducing catalyst degradation. Then, the actual reforming process step starts. A typical flow diagram is presented here. The reforming process includes the following steps:

– The reaction section comprising heat recovery, furnace, and rectors
– Hydrogen separation and recirculation
– The product recovery section or distillation

The naphtha feedstock is combined with the hydrogen generated by the reaction process itself, vaporized, and passed through a heat recovery train from the outgoing reaction products. Then, it enters a succession of the alternating furnace and fixed-bed reactors. The common catalysts that are used in these reactors are a platinum catalyst or a bimetallic (Pt- Rh) catalyst.

The product of the least fixed-bed reactor is cooled and transferred to a separator unit to remove the hydrogen stream which is recycled and mixed with the naphtha feedstock. Also, the excess of the hydrogen product is transferred to other units in the refinery plant. The liquid products from the bottom of the separator are sent to a stabilizer called a butanizer. This makes the bottom product which is called reformate, while the butanes and lighter paraffins pass overhead and are then sent to the other users.

The catalysts require regeneration after a certain time. Depending on the catalyst type and the severity of the reaction, the cycle time and method of regeneration varies. Some catalytic reforming systems continuously regenerate the catalysts.

5.7.2 Reactions

In catalytic reforming, reaction conditions should be selected to favor the desired reactions and inhibit the undesired reactions. Desirable reactions in a catalytic reformer form aromatics and iso-paraffins:

• Paraffins are isomerized and converted to naphthenes which are subsequently converted to aromatics.
• Olefins are saturated to form paraffins.
• Naphthenes are converted to aromatics.
• Aromatics are left essentially unchanged.

It should be noticed that the reactions which form undesirable products include:

• Dealkylation of side chains on naphthenes and aromatics to form butane and lighter paraffins.
• Cracking of paraffins and naphthenes to form butane and lighter paraffin.

Major reactions that take place during reforming include:

- Dehydrogenation of naphthenes to aromatics.
- Dehydrocyclization of paraffins to aromatics.
- Isomerization.
- Hydrocracking.

5.8 Isomerization Process

The isomerization process is mainly used to transform n-paraffins to iso-paraffins. The n-paraffins usually have a low-octane number whereas iso-paraffins have a high-octane number, Fig. 1.20. Hence, the main applications of the process are in producing high-octane blending components for gasoline in refineries. To obtain high-octane stock, the common process includes:

- Isomerization of butane to isobutane
- Isomerization of pentanes and hexanes into higher branched isomers

For a general description of the isomerization process, the common feed of the isomerization unit is a light straight-run gasoline stream high in C_5 and C_6^+ normal paraffins. The feed is sent to the deisopentanizer column which removes (1) iC_5
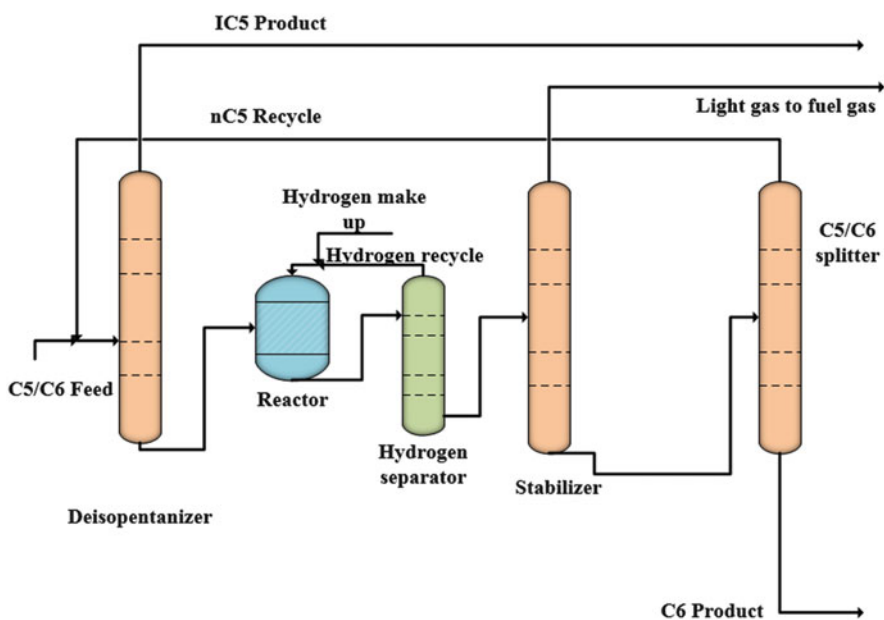
Fig. 1.20 Flow diagram of a typical isomerization unit

which exists in the streams and (2) iC_5 generated in the reactors which are recycled back to the feed stream as a portion of the nC_5 recycles. When the iC_5 enters the overhead of the deisopentanizer column, the balance of the feed stream is transferred to the isomerization unit. In this unit, hydrogen gas is introduced into the stream to drive the reaction to produce the desirable products and decrease the coke formation on the particles of catalysts. As with the previous units in the oil refinery, the stream is sent to the hydrogen separation unit to separate and return the hydrogen back to the feed stream of the reactor. In the stabilizer column, the light hydrocarbons that may be generated during the reactions are removed. The separated hydrocarbons flow from the upper part of the stabilizer column, then they are blended into the refinery fuel gas unit. The product stream leaves the lower part of the stabilizer column and enters a C_5/C_6 splitter column, where C_5s are sent out of the top of the column and recycled back. The nC_5 in the C_5s is reprocessed and the iC_5 can be sent out of the top of the deisopentanizer as a product. The C_6 and heavier components leave the bottom of the splitter and either go to gasoline blending or to the catalytic reforming unit.

5.9 Nanotechnology in Refining Processes

Nanotechnology is making a significant contribution to the oil refining and petrochemical industry, with potential solutions for the related challenges. For example, several forms and types of nanomaterials are being used as catalysts for several types of refinery and developing industry in various units.

One example is the development of mesoporous catalyst materials such as zeolite and alumina loaded with diverse types of nanoparticles as catalysts. Another example is the use of nanotechnology in removing harmful toxic substances such as nitrogen oxides, sulfur oxides, and related acids and acid anhydrides from vapor by using distinct types of nanofilters and nanoparticles. The removal of mercury from oil and gas is considered to be another challenge, where nanomaterials can play a key role in solving these types of the problem by using, for example, nanoparticles of metal oxides such as copper oxide. Nanotechnology further provides solutions for carbon capture and long-term storage. The removal of sulfur compounds from oil is another problem that is being investigated by scientists and engineers. Various nanomaterials are being developed and evaluated for such applications.

In the following chapters, the role of nanotechnology in solving different oil and gas-related problems is discussed along with several types of nanomaterials that are used for such applications.

References

Chianelli RR, Berhault G, Raybaud P, Kasztelan S, Hafner J, Toulhoat H (2002) Periodic trends in hydrodesulfurization: in support of the Sabatier principle. Appl Catal A 227:83–96

Devold H (2013) Oil and gas production handbook: an introduction to oil and gas production. Lulu.com

Fahim MA, Al-Sahhaf TA, Elkilani A (2009) Fundamentals of petroleum refining, 1st edn. Elsevier, Amsterdam. ISBN-13: 978-0444527851

Gary JH, Handwerk GE, Kaiser MJ (2007) Petroleum refining: technology and economics. CRC, Boca Raton, FL

Himes JF, Mehlberg RL, Pujadó PR, Ward DJ (2006) Gasoline components. In: Jones DSJ, Pujadó PR (eds) Handbook of petroleum processing. Springer, Dordrecht, pp 355–416

Jones DS (2006) The atmospheric and vacuum crude distillation units. In: Jones DSJ, Pujadó PR (eds) Handbook of petroleum processing. Springer, Dordrecht, pp 111–187

Jones DS (2015) An introduction to crude oil and its processing. In: Treese SA, Pujado PR, Jones DSJ (eds) Handbook of petroleum processing. Springer, Dordrecht, pp 1–45

Jones DSJ, Pujado PR (1992) Petroleum processing handbook. Springer, Dordrecht. ISBN: 978-1-4020-2820-5

Krylov NY, Bokserman AA, Stavrovsky ER (1998) The oil industry of the Former Soviet Union. CRC, Boca Raton, FL, p 187

Leffler W (2008) Petroleum refining in nontechnical language, 4th edn. PennWell, Tulsa, OK. - ISBN-13: 978-1593701581

Meyers RA (2016) Handbook of petroleum refining processes, 4th edn. McGraw-Hill, New York. ISBN-13: 978-0071850490

Pujadó PR, Moser M (2006) Catalytic reforming. In: Jones DSJ, Pujadó PR (eds) Handbook of petroleum processing. Springer, Dordrecht, pp 217–237

Rana MS, Samano V, Ancheyta J, Diaz JAI (2007) A review of recent advances on process technologies for upgrading of heavy oils and residua. Fuel 86(9):1216–1231

Saleh TA, Danmaliki G (2016a) Influence of acidic and basic treatments of activated carbon derived from waste rubber tires on adsorptive desulfurization of thiophenes. J Taiwan Inst Chem Eng 60:460–468

Saleh TA, Danmaliki G (2016b) Adsorptive desulfurization of dibenzothiophene from fuels by rubber tyres-derived carbons: kinetics and isotherms evaluation. Process Saf Environ Protect 102:9–19

Sieli GM (1998) Visbreaking the next generation. Foster wheeler publication

Topsøe H, Clausen BS, Massoth FE (1996) Hydrotreating catalysis, science and technology. Springer, Berlin

Vassiliou M (2009) Historical dictionary of the petroleum industry. Scarecrow (Rowman and Littlefield), Lanham, MD. 700 pp

Chapter 2
Nanotechnology Applications in Petroleum Refining

Ubong J. Etim, Peng Bai, and Zifeng Yan

Abstract Nanotechnology has successfully gained applications in many areas of life, thereby seen as the modern way of creating products, which results in high efficiency of use. In the petroleum processing industries, this revolution is no exception. The efficiency of a number of conversion processes improves upon application of materials with the nanometer scale dimension, which is caused by improvements and developments of better material properties as the particle size decreases. In this chapter, the applications of nanotechnology through nanocatalysis in petro-refining processes are highlighted. This is exemplified by discussing the applications of nanotechnology in several typical petroleum refining processes, including catalytic cracking, oxidative dehydrogenation of alkanes, and desulfurization. Other processes for the production of clean fuels are also briefly reviewed. The key benefits of "nano-tech" application in catalysis are based on the exposure of a large surface area for reaction, thereby reducing the tendencies to adverse and side reactions. The desire for an improved catalyst with high activity, low deactivation, and low coke formation to meet the growing demand for chemicals and fuels necessitates the increasing exploitation of nanoparticles as catalysts.

Keywords Nanotechnology • Nanomaterial • Nanocatalysis • Petroleum processing

1 Introduction

The quest for exploring and improving the properties of materials at atomic scales has driven scientists to a broad field of research known as nanotechnology. Fundamentally, at the nanoscale, the properties of materials between 1 and 100 nm provide new insights into improvements of the existing materials and ways to

U.J. Etim • P. Bai (✉) • Z. Yan (✉)
State Key Laboratory of Heavy Oil Processing, China University of Petroleum, Qingdao 266580, China

PetroChina Key Laboratory of Catalysis, China University of Petroleum, Qingdao 266580, China
e-mail: baipeng@upc.edu.cn; zfyancat@upc.edu.cn

designing novel ones with striking features can be successfully and effectively explored. Nanotechnology has successfully gained applications in many areas of life, resulting in improved efficiency of product creation and utilization. In the scientific world, the term "nano" is used as a prefix that means "billionth" or a factor of 10^{-9} or $1/10^9$. A nanometer, therefore, refers to a unit which indicates an order of spatial measurement that is one "billionth" of a meter.

Nanotechnology could be defined as the science, engineering, and application of materials at the nanoscale (i.e., at least one dimension measured in nanometer) (Zhou 2007). The nanoscale means dimensions in the order of 100 nm or less. With the increased sensitivity of analytical tools at the nanometer levels, nanoscience has thus brought one of the most incredible and remarkable revolutions into the world of material science, enabling diverse applications. The first mention of the idea and concept of nanoscience and nanotechnology is credited to a physicist, Richard Feynman, in 1959 during a talk to the American Physical Society, where he described the process in which scientist could be able to manipulate and control materials at the nanoscale. The talk titled "*There is plenty of room at the bottom*" allows humanity to benefit from the implication of materials to obtain miniaturization for applications of the previous technologies.

The impacts of nanotechnology in the society have been unambiguously and overwhelmingly felt in many areas through improved efficiency and high-quality products developed at reduced overhead cost, which increases demand. Thus, nanotechnology can be considered fundamental to the modern ways of life. Improved and efficient products which span all sectors of the society are immediate consequences of the intimate integration of the so-called nano-tech. Presently, nanotechnology is applied to all areas of life, and its applications are exploited in a number of industries, including electronics, materials and manufacturing, aerospace, photography, construction, chemicals as well as petroleum refineries. The oil and gas industries, from upstream through the midstream to downstream have gone through stages where chemical processes are facilitated because of the relevancy of employing materials with unique size-dependent properties.

1.1   Nanosize

Just how small is the *nanosize*? "Nano" is about as small as it gets in the world of regular physical, materials, and biological sciences (Lindsay 2009). Based on the units, things are measured in our everyday life, for instance, the diameter of a hydrogen atom is about one-tenth of a nanometer, so the nanometer scale is the smallest scale on which one might consider building blocks on a scale. Generally, atoms are smaller than a nanometer, one atom measures in the range of ~0.1–0.3 nm, depending on the type of the element. As could be seen in Fig. 2.1, several other objects exist at the nanometer scale. Examples include viruses (30–50 nm), DNA (2 nm), buckyballs (1 nm in diameter), carbon nanotubes (~1 nm in diameter), and many catalysts used in the production of fuels and petrochemicals are based on nanoparticles. The thickness of a sheet of paper is
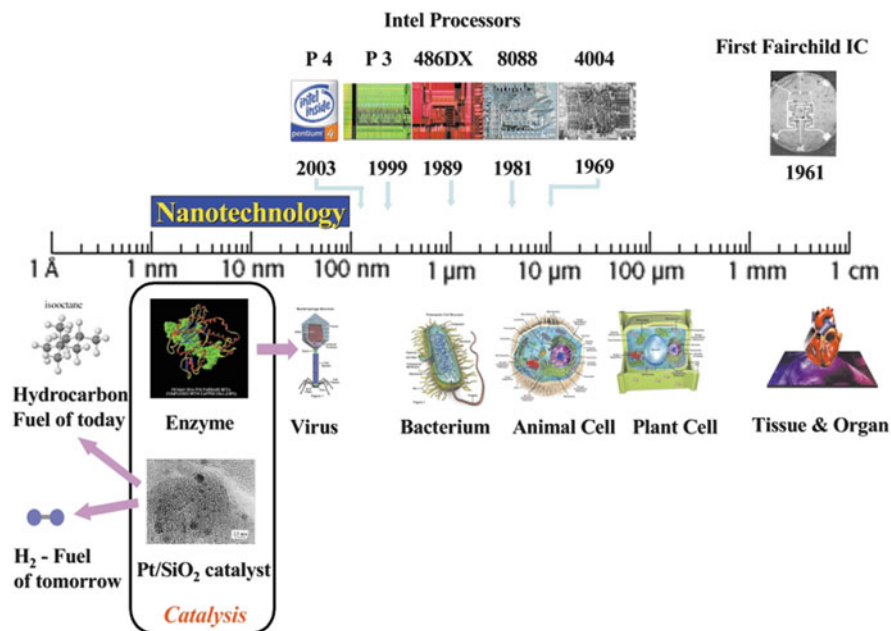
Fig. 2.1 Some nanometer-sized materials. Adapted from Grunes et al. (2003), with permission of the Royal Society of Chemistry

about 100,000 nm and the human hair is about 50,000–100,000 nm in diameter (Grunes et al. 2003). Objects and dimensions that are this small are difficult to measure with the conventional instruments and require special tools for analysis. So, the sensitivity of measurement is enhanced using powerful microscopic tools that permit the use of unique methods to allow for the visualization of surface features on the atomic scale, such as atomic force microscopy (AFM), scanning electron microscopy (SEM), transmission electron microscopy (TEM), and scanning tunneling microscopy (STM). These characterization tools have been frequently used to examine the nanostructure of model catalyst systems. Using STM, for example, it becomes possible to explain why doping Ni catalysts used for the steam reforming of methane with a small amount of gold reduces the tendency of such catalysts to deactivate because of carbon deposition (Besenbacher et al. 1998).

1.2 Nanomaterials

Nanomaterials possess unique properties derived from features present in them that are measurable on the nanometer scale. Examples of nanomaterials in use in modern industrial applications include carbon materials, metal oxides, and zeolites.

The preparation of materials at the nanoscale is feasible through careful design and controlled synthesis procedures. Generally, nanomaterials can be synthesized by two widely known methods, either by bottom-up or top-down approach. The bottom-up approach involves the formation of nanomaterials by reaction and assembly of the reactants in the presence or absence of structure directing agents (SDA). In the top-down approach, the bulk materials are broken down to smaller particle size by mechanical, thermal, or chemical methods. The former has the advantage of precise control of the particle size; however, the use of expensive precursors and surfactant increases cost. The latter has the disadvantage of nonuniform particle size. Faujasite zeolite nanosheets, for example, are synthesized by controlling the pore structure using SDA and crystallization temperature that allow for the formation of zeolite particles with interstitial pores between the nanosheet assemblies (Inayat et al. 2012; Mehlhorn et al. 2014; Yutthalekha et al. 2016). The most important property to optimize during the synthesis of nanomaterials is the surface area. The shape, size, and composition of the surface need to be controlled as well. These properties are of basic importance in applications involving catalysis because they are the determinants of catalyst activity and stability. Often, the surface area increases with a decrease in the dimension of a material. Thus, as the material size decreases, a greater portion of the atoms are found at the surface compared to the bulk material. Because growth and catalytic chemical reactions occur at materials surfaces, a given mass of nanomaterial reacts more compared to the same mass of bulk material. Additionally, materials that are inert in their bulk form are reactive when existing in nanoscale. Nanomaterials are expected to have a much greater surface area per unit volume compared with larger particles. This property makes them more chemically reactive because atoms at the surface of some materials do not have covalent bonds as they are in an energetically unstable state. Since more atoms located at the surface are in energetically unstable states, nanomaterials are more reactive compared to the bulk materials.

1.3   Nanoparticles

Nanoparticles in principle have sizes ranging between 1 and 100 nm (Rao et al. 2002). Their physical and chemical properties are intermediate those of the atom of an element and the bulk material. The beneficial aspect of this class of materials as compared with their bulk (microparticles greater than 1 μm) is often size-dependency of functions. As the size decreases and approaches the nanoscale, new and fascinating functional properties develop and become significant, such as color change and phase transformation. For example, the unique physical properties of nanoparticles allow high absorption of radiation in photovoltaic cells that are composed of nanoparticles than does in thin films of continuous sheets. Other examples of size-dependent property changes could be seen in quantum confinement in semiconductor particles, surface plasmon resonance in some metal particles, and in chemical reactivity that is utilized for image formation

Fig. 2.2 Schematic illustration of the ways to increase the surface area of dense solids. Adapted with permission from Valtchev and Tosheva (2013). Copyright (2013) American Chemical Society
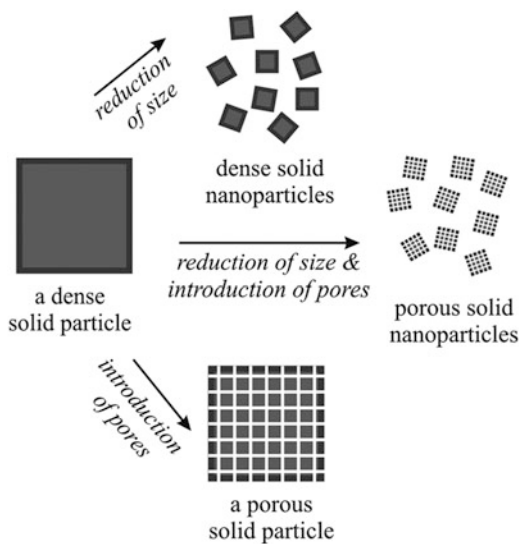
in photography (Lindsay 2009). Increasing the number of surface atoms in a material often increases surface-to-volume ratio and chemical potentials in the material (Zhou et al. 2009). The number of surface atoms in solid materials can be increased by (1) decreasing the size of bulk particles or (2) creating open pore network within the bulk of the material as illustrated in Fig. 2.2 (Valtchev and Tosheva 2013). Another unique method is to synthesize nanosized particles containing accessible and uniform nanopores. The size of nanoparticles is very instrumental in determining chemical properties. In catalysis, nanoparticles or nanomaterials play a vital role in improving chemical transformations.

1.4 Nanocomposites

A nanocomposite is a multiphase solid material in which at least one of the phases has one, two, or three dimensions of less than 100 nm. In other words, a nanocomposite material is composed of a bulk matrix and at least one nano-dimensional phase with properties different from those of the matrix. The properties of a nanocomposite differ considerably from those of the constituent and/or conventional composite materials due to dissimilarities in structure and chemistry, the exceptionally high surface-to-volume ratio of the reinforcing phase and/or its exceptionally high aspect ratio. A reinforcement surface area indicates that a small amount of nanoscale reinforcement has an observable effect on the macroscale properties of the nanocomposite. As an example, loading carbon nanotubes enhances the electrical and thermal conductivity of a conductor bulk material. Also, some nanomaterials result in enhancing optical, dielectric, and mechanical

characters and heat resistance. Examples of nanocomposites include porous media, colloids, gels, and copolymers. The mechanical, electrical, thermal, optical, electrochemical, and/or catalytic properties of a nanocomposite differ markedly from those of the individual component materials. Size limits for these effects have been proposed: size <5 nm finds applications in catalysis, <20 nm for making a hard magnetic nanomaterials soft, <50 nm for refractive index changes, as well as <100 nm to achieve super magnetism, mechanical strengthening or restricting matrix dislocation movement (Kamigaito 1991).

2   Nanocatalysis

The application of nanotechnology in petroleum refining is mainly driven by the creation of nanocatalysts that have led to improvement in the fields of both homogeneous and heterogeneous catalysis. Nanoparticles are important catalysts for petroleum processing and energy conversion. The performance of a catalyst is sensitive to particle size because the surface structure and electronic properties can change greatly with size (Zhou et al. 2009; Bell 2003). For example, the heat of adsorption for CO and the activation energy for CO dissociation both change with increasing the size of Ni particles, consequently, affecting the performance of Ni nanoparticles in the Fischer–Tropsch synthesis of hydrocarbons from synthesis gas (Bell 2003). Reducing the particle size of porous materials to nano-dimensions allows for the optimization of their applications in catalysis. Nanoporous materials show improved catalytic activity in diffusion-limited reactions, and manipulation of nanocrystalline suspensions using colloidal chemistry approach results in the preparation of 2D and 3D microporous materials with adjusted characteristics for catalytic reactions (Valtchev and Tosheva 2013).

Nanocatalysis involves the synthesis and characterization of supramolecular materials at the nanometer level and their controlled applications (Schlögl and Abd Hamid 2004). It differs from conventional catalysis since the materials are explicitly designed to a length scale much larger than that of a single active site. It has been demonstrated in various reactions that the use of nanocatalyst can decrease the energy requirements in chemical processes, resulting in a greener chemical industry. The contribution of nanoscience and nanotechnology may have been seen as a springing science in catalysis; however, it will be of beneficial interest to clarify that the selectivity principles by which heterogeneous catalytic reactions proceed rely exclusively on nanocatalysis, and the use of small particles in technical catalysis has been operated for ages (Schlögl and Abd Hamid 2004).

Nanoporous materials are fundamental to the modern petroleum refining and the petrochemical industry. Zeolites, for instance, are employed as key catalysts in petroleum refining. Zeolites are crystalline aluminosilicate materials with well-defined pore connection dependent on the particular topology. There are about 230 zeolite framework types ("Database of Zeolite Structures, http://www.iza-structure.org/databases/") of which the commonest ones employed in large
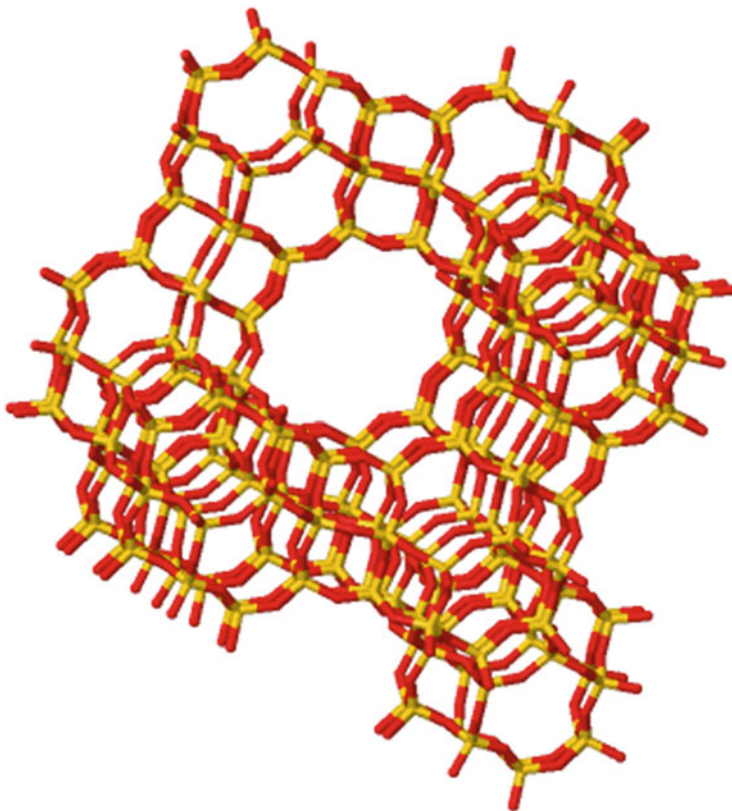
Fig. 2.3 Structure of zeolite Y (FAU). Constructed from ("Database of Zeolite Structures, http://www.iza-structure.org/databases/")

quantities in the petroleum refining and the petrochemical industry are zeolite Y and ZSM-5 of FAU and MFI topologies as in Figs. 2.3 and 2.4, respectively. Of special note is that these zeolites consist in nano-pores that allow for molecular sieving functionalities in them as shown in Fig. 2.5. So far, their excellent shape selective properties position them as one of the most important heterogeneous catalysts practically in use.

The relevant nano-pore sizes (0.74–1.2 nm in zeolite Y and 0.54–1.0 nm in ZSM-5) afford these zeolites the ability to screen heavier hydrocarbon molecules, allowing only those with a diameter less than or equal to their pore size to pass through. For more than five decades, zeolites have contributed immensely to the growth of the petroleum industry, being a catalyst for the transformation of less valued crude oil fractions to more valued and desirable products by a process known as fluid catalytic cracking (FCC). Although zeolites contain inherent nanosized pores that classify them as nanomaterials, they are usually of micrometer particle size. Controlling the synthesis conditions of the conventional micrometer-
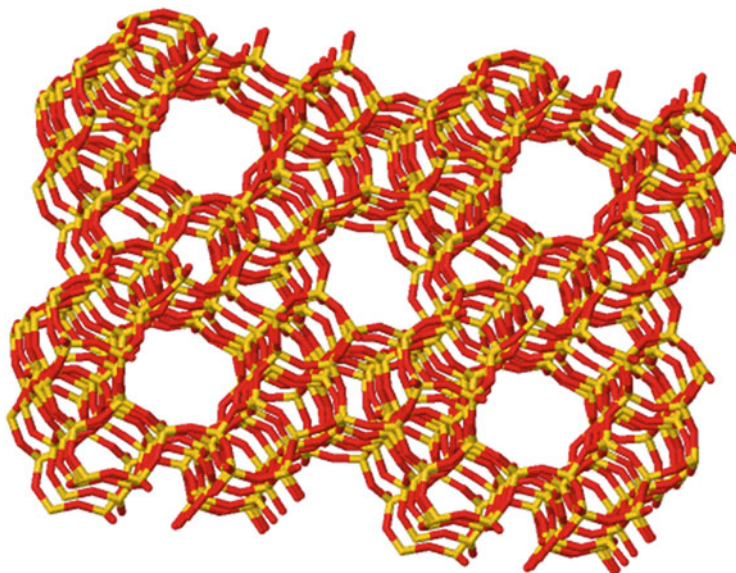
Fig. 2.4 Structure of zeolite ZSM-5 (MFI). Constructed from ("Database of Zeolite Structures, http://www.iza-structure.org/databases/")
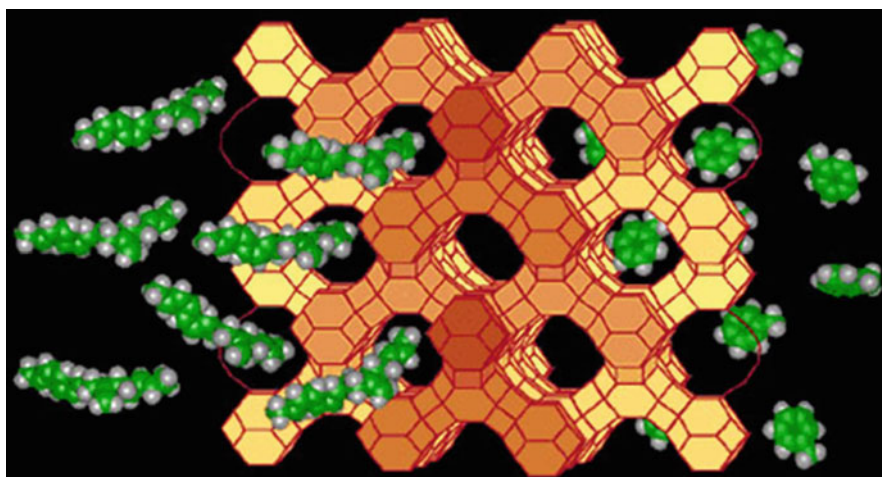
Fig. 2.5 Molecules diffusion through the zeolite Y pore ($\sim$7.4 Å). Adapted from ("Database of Zeolite Structures, http://www.iza-structure.org/databases/")

sized zeolite could result in entirely nanosized zeolites such as nanosheets. For practical applications in catalytic reactions, it is important to understand the differences between the nanocrystals and microcrystal zeolites. The nanocrystal zeolites exhibit high external surface area, which is advantageous for processing

bulky molecule that cannot penetrate through the small pores and channels of zeolites. In addition, they have shorter diffusion path lengths than the conventional micrometer-sized zeolite (Farcasiu and Degnan 1988; Weisz 1995).

2.1   Supported Metal Catalysis

2.1.1   Catalyst Support

The advances in the synthesis of materials for improved catalytic performance of various reactions have led to exciting strategies for creating catalyst particles that are of very small size. In most of the applications, these catalysts are sat on porous metal oxide supports, which have diameters in orders of a nanometer. This strategy contributes to the production of nanometer length scale catalysts that are very active and stable under various high reaction severities. Among the widely used support materials for catalyst fabrication, alumina and silica have received considerably most applications for reasons pertaining to cost-effectiveness and excellent physicochemical properties as catalyst supports. Aluminas are widely employed as standard supports for many metal and sulfide catalysts at the industrial scale. For catalysts requiring relatively low reaction temperature (less than 500°C), such as for hydrogenation using platinum, palladium, or metal sulfides as active phase, high surface area alumina can be used. For low-temperature reactions, such as partial oxidation reactions, transition aluminas are preferable. Stabilized aluminas with silica or alkali, alkali-earth, or rare earth cations (K^+, Ca^{2+}, La^{3+}, etc.) are extensively used for reactions requiring medium to high temperatures. An example is the case of some endothermic reactions such as steam reforming or partial oxidation reactions using platinum or rhodium catalysts. Silicas possess excellent mechanical and thermal stabilities and are also widely used as supports for industrial applications. Nickel and copper catalysts supported on silica are frequently used for hydrogenation reactions. In some other cases, silicas are used as stabilizers as a very little amount is required.

2.1.2   Particle Size Effect of Metal Oxide Supports

The influence of crystalline structure or particle size on the solid-state chemistry of materials, including metal oxides used as catalyst supports has received great attention recently. It has long been conceived but came to limelight at the birth of nanoscience and nanotechnology. Practically, nanostructured catalysts are more stable materials in comparison to its bulk counterparts for the reason that the surface-free energy predominates in the bulk. This was first reported for γ-Al_2O_3 with respect to corundum α-Al_2O_3 (McHale et al. 1997) and for other polymorphic systems such as anatase-TiO_2 with respect to rutile (Zhang et al. 2009) as well as tetragonal ZrO_2 in comparison to monoclinic zirconia (Zhang et al. 2006).

Therefore, the easy formation and stabilities of γ-Al_2O_3, anatase TiO_2, and tetragonal ZrO_2 at room temperature are because of their existence in the form of nanoparticles (Busca 2014). An unpromoted, size-selected Ag_3 clusters and ~3.5 nm Ag nanoparticles on alumina supports can catalyze direct propylene epoxidation with only a negligible amount of carbon dioxide formation and with high activity at low temperatures (Lei et al. 2010), whereas bulk Ag catalyst produces substantial amount of carbon dioxide. Density functional calculations show that, relative to extended silver surfaces, oxidized silver trimers nanoclusters are more active and selective for epoxidation reaction because of the open-shell nature of their electronic structure (Lei et al. 2010). Valence electrons in bulk metals form continuous bands, and upon reduction of the bulk material in a certain direction down to the nanometer scale, the motion of electrons in this direction is subject to confinement (Yang et al. 2015; Valden et al. 1998). In this regard, compared to bulk metals, nanoparticles exhibit much larger total exposed surface areas and various combinations of surface structures, and the electronic confinement effects within nanoparticles lead to major changes in the electronic structure (Valden et al. 1998; Haruta and Daté 2001). This raises the possibility of tuning the catalytic process. In this way, nanotechnology could provide an effective means through which the surface structure and electronic properties of supported nanocatalysts can be effectively controlled without changing their composition. A very small crystal size of the nanocrystalline zeolite contributes favorably to both the formation of a high external surface area, with no steric constraints, and to a faster diffusion of reactant molecules to the acid sites located within the zeolite micropores (Serrano et al. 2010). This feature leads to catalytic performance improvement. It is therefore clear that the activity and selectivity of catalyst nanoparticles are strongly dependent on their size and shape as well as surface and electronic structures.

Particle size reduction of the active metal offers an invaluable benefit to energy cost reduction. Au nanoparticles having dimensions less than 10 nm are often used for various applications including catalysis. In catalysis, selective oxidation of ethanol in oxygen catalyzed by SiO_2 supported Au shows an improved activity at a lower temperature than does the bulk Au catalyst (Zheng and Stucky 2006). This behavior, besides improved catalytic activity, demonstrates energy conservation that comes with smaller particle size catalyst. The size of Co particles plays a key role in determining its selectivity performance. Co nanoparticles with a mean diameter of 6–10 nm can improve the selectivity of C_{5+} hydrocarbons than the bulk Co (Bezemer et al. 2006). In the following sections, selected examples of petro-refining/chemical processes where nanotechnology finds immense applications are discussed.

3 Petroleum Refining Processes

3.1 Catalytic Cracking

Catalytic cracking occurs on solid acids catalysts. Its development in the late 1930s brought a revolution into the petroleum industry that was previously relied entirely on thermal cracking. The cracking catalysts are usually crystalline aluminosilicate solids with acid sites strong enough to cause the scission of carbon–carbon bond in hydrocarbon molecules. Unlike thermal cracking, the use of powder catalysts provides alternative routes for cracking by lowering the activation energy for the reaction. One of the areas where the application of nanoscience has a success story is the petroleum refining. As mentioned earlier, the use of zeolite catalyst in the FCC for the conversion of heavy crude oil fractions has been an important revolution in the petroleum industries since the 1960s, and its significant contributions are continuously felt hitherto. As of today, over seven million barrel of petroleum products and chemical are annually produced using the zeolite catalyst (Zhou 2007).

3.1.1 Nanozeolite

Crystalline zeolites have 3D networks of well-defined micropores (<1.2 nm). With these pore constraints, only molecules of comparable or size less than the pore aperture can access the active sites. Catalytic reactions are therefore restricted to the molecules having a diameter below the pore constraints. Thus, larger feed molecules are then crack on the external surface of the zeolite. The use of nanosized zeolite could overcome this limitation because as the ratio of external to internal number of atoms increases when the particle size decreases, the zeolite nanocrystals present a large external surface area and high surface activity (Vuong et al. 2010). The improved surface area exposes move acidic sites for catalytic reactions. This increases catalytic performance due to higher accessibility to active sites. Decreasing the zeolite crystallite size has been demonstrated to increase the conversion and the selectivity of gas oil (Rajagopalan et al. 1986). Compared with micron-sized, nanosized zeolites exhibit a higher activity, lower coking activity and longer life in many reactions. One of the pioneer studies that demonstrate the influence of zeolite crystal size on catalytic cracking was published in 1986 (Rajagopalan et al. 1986). NaY zeolite crystals size ranging from 60 nm to 0.65 μm was employed for catalytic conversion of gas oil in the FCC reaction. The catalyst containing the smallest particles exhibited improved activity and selectivity to gasoline and light cycle oil (LCO) as in Fig. 2.6a, b. These improved selectivities were attributed to the decreased diffusion resistance to the gas oil and produced gasoline in the nanosized zeolite. With nanozeolite, the conversion of hydrocarbons can be greatly improved. Vuong et al. (2010) synthesized a series of zeolite Y nanocrystals and compared their catalytic activity in a standard gas oil cracking test. It was found that small
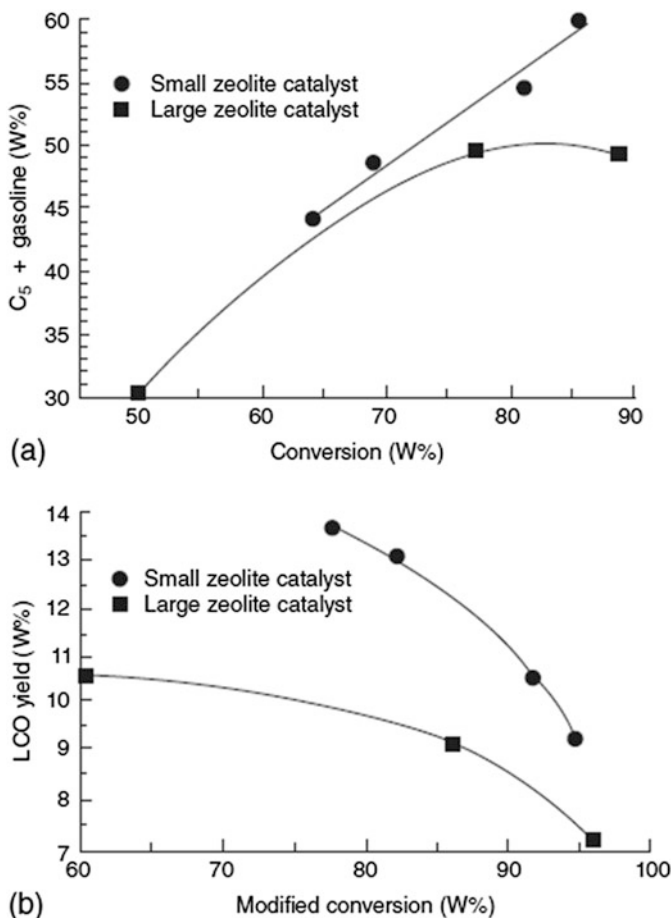
Fig. 2.6 Selectivity of heat-treated zeolite particles (2 h at 538°C) to (**a**) gasoline and (**b**) light cycle oil, LCO catalysts on west Texas heavy oil feed. Adapted from Rajagopalan et al. (1986) with permission from Elsevier. Copyright 1986 Elsevier publishers

nanosized zeolite (25, 40, and 100 nm)-based FCC catalysts exhibited higher catalytic activities compared to larger ones as illustrated in Fig. 2.7. A correlation is between gasoline selectivity in FCC feedstock conversion and zeolite particle size. This performance of zeolite catalysts followed the trend as: FCC-100 < FCC-40 < FCC-25, which can be explained by the cracking of FCC feed on the external surface of zeolite crystals.

The intrinsic properties of a catalyst can be modified by reducing the crystallite size. Nanosized ZSM-2 (~100 nm) has been recently prepared (Covarrubias et al. 2009). This type of zeolite possesses improved acidity, high surface area and maintains the structural stability that makes it highly attractive for catalytic applications. The nanosized ZSM-2 zeolite offers as an excellent catalyst support for
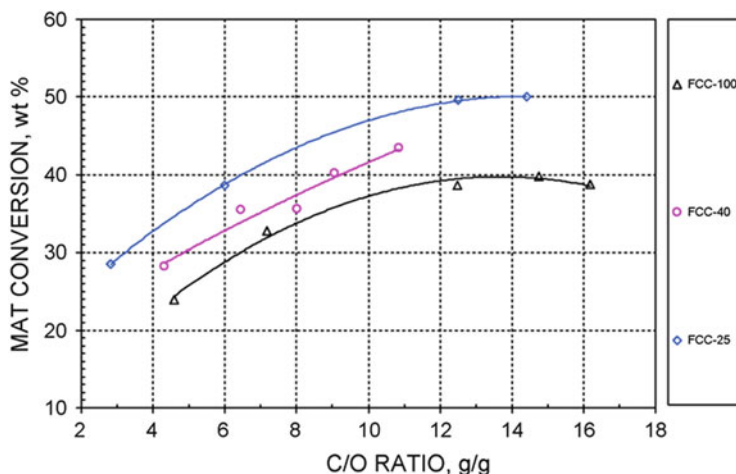
Fig. 2.7 MAT conversion curve for nanozeolites-based FCC catalyst. Adapted from Vuong et al. (2010) with permission from Elsevier. Copyright 2010 Elsevier publishers

metallocene polymerization. A nanoporous aluminosilicate (MMZ_{USY}) obtained from USY zeolite exhibits high thermal stability and accessibility for oil molecules in the conversion of bio-oil. When compared with MCM-41, the MMZ_{USY} showed excellent catalytic activity and selectivity due to improved surface acidity (Park et al. 2008). Catalytic cracking activity on the external surface of nanozeolites of FAU (zeolite Y) and MFI-type (ZSM-5) was evaluated in 1,3,5-triisopropylbenzene conversion and compared with conventional micron-sized zeolite Y and ZSM-5 crystals used as reference samples. Smaller crystal catalysts showed higher activities and an increase in conversion with the time of reaction. The conversion was high for zeolite Y, as it is related to high amounts of surface acid sites with respect to ZSM-5 (Morales-Pacheco et al. 2011). Nanosized zeolite Y crystals are employed in the selective catalytic reduction of NO_2 with urea (Li et al. 2005). The reaction rate is significantly higher than that of commercial FAU-type zeolite. The performance of nanosized crystallites when compared with that of commercial micrometer-sized zeolite Y is attributed to the larger external surface of zeolite nanocrystals rich in silanols, and extra-framework Al is found to be responsible for the higher reaction rate. Additionally, a decrease in the formation of undesired products like biuret and cyanuric acid is observed on the nanosized catalyst.

Light olefins, usually produced by the thermal cracking of naphtha, are an invaluable product of the petroleum industry and an important raw material for the petrochemical industry. Presently, an alternative method for producing light olefins in large quantities is by catalytic processes. An example is the use of methane as a source of methanol followed by methanol-to-olefin (MTO) reaction. The most often used catalysts for this reaction are ZSM-5 and SAPO-34. SAPO-34 shows higher selectivity to light olefins; however, it is rapidly deactivated due to coke deposition. A decrease in the crystal size of SAPO-34 is expected to reduce the

coke formation and thus increase the effectiveness factor (Valtchev and Tosheva 2013). Comparing the catalytic properties of nano- and micrometer-sized SAPO-34 crystals in the MTO reaction, the nanosized catalysts exhibit a longer catalyst lifetime, which is related to the enhanced diffusion and desorption of produced hydrocarbons, leaving the micropore space unblocked and thus limiting side reactions and coke formation (Hirota et al. 2010).

3.1.2 Synthesis of Nanozeolites

The synthesis of zeolite nanocrystals was somewhat challenging until recently when practical approaches have become feasible. Like the conventional micronsized zeolites which yield particles with dimension of about 1 μm, nanocrystal zeolites are also synthesized from clear solutions under hydrothermal conditions (Persson et al. 1994; Mintova et al. 2016; Schoeman et al. 1994). Special attention is required during preparation of the initial precursor gel to favor the nucleation and crystallization processes. The number of nuclei in the homogeneous precursor solution determines the crystal size. Therefore, a system with sufficient nucleation results in very small crystals (Mintova et al. 2016). Different methods can be adopted for the synthesis of zeolite nanocrystals, namely, hydrothermal crystallization, microwave, ultrasonic, confined space, seeding and use of microreactor (Askari et al. 2013; Jo et al. 2013; Pan et al. 2009; Jacobsen et al. 2000a, b; Schmidt et al. 2000; Sun et al. 2015, Lv et al. 2013, Hu et al. 2009, Kore et al. 2014; Gao et al. 2016). Hydrothermal crystallization is the most widely employed method because of the ease to control the crystallization process. The precursor gel solution is prepared in such a way to favor the nucleation over the growth of the crystals and to limit the aggregation between the growing crystals. Furthermore, a number of other factors have to be controlled to achieve the desirable nucleation. Such factors include polymerization process during preparation of the initial precursor gel, hydrothermal treatment temperature, the amount of the metal cation in the colloidal precursor solution, and the type and concentration of SDA. In addition, alkalinity of the gel solution, crystallization time, precursor gel molar composition, and zeolite particle source affect the particle size of the synthesized zeolites and direct the growth of the crystals to the desired zeolite structure (Covarrubias et al. 2009; Sun et al. 2015; Davis et al. 2015). High supersaturation and steric stabilization of the proto-nuclei in the presence of quaternary ammonium cations play crucial roles in the formation of non-aggregated zeolite nanocrystals (Covarrubias et al. 2009).

In zeolites formation mechanism, generally, amorphous particles are initially formed and then converted into crystals with changing size. Zeolite nuclei form in the center and grow outwards until the whole amorphous particles are transformed into crystalline ones. After heating at a high temperature, larger cubic crystals are obtained (Mintova et al. 1999). However, other mechanisms of nanozeolite crystals formation have been reported in the literature. Recently, it has been shown that very small sized EMT-typed zeolite can be synthesized from template-free Na-rich precursor system (Ng et al. 2012a, b). The resulting nanosized zeolite which exhibited a size of 15×4 nm along the a and c directions, respectively, was

possible due to the control of the polymerization process during the preparation of the initial suspension (Ng et al. 2012a, b) and the low-temperature hydrothermal treatment that limited the growth of the crystals and inhibited competitive zeolite structures. Hierarchical beta nanozeolites were synthesized from protozeolite seeds in the presence of an organosilane as a precursor. It was found that zeolite crystallization proceeded through a condensed step mechanism, gradually growing from the evolved nuclei. The organosilane played important roles as a mesoporogen and a growth inhibitor. The crystal size and mesopore properties of the prepared hierarchical beta nanozeolites strongly depended on the properties of seeds (Sun et al. 2015).

3.2 Oxidative Dehydrogenation of Alkanes

Oxidative dehydrogenation (ODH) of propane is an attractive option for propene production. In the presence of oxygen, the thermodynamic restrictions of dehydrogenation are overcome and the exothermic character of the reaction renders it an energetically efficient process (Karakoulia et al. 2009). Vanadia nanoparticles supported on various oxides ZrO_2, Al_2O_3, MgO, SiO_2, TiO_2, CeO_2, and Nb_2O_5 are active catalysts for the ODH of alkanes to olefins (Khodakov et al. 1998; Corma et al. 1992; Wachs and Weckhuysen 1997; Khodakov et al. 1999). A recent study shows that the ODH activity per atom of exposed V decreases with increasing size of the vanadia clusters (Khodakov et al. 1999). Support surfaces that covered with small V_2O_5 clusters containing V–O–V or V==O linkages lead to high dehydrogenation rates and selectivities. The composition of the support influences the speciation of different VOx species and V_2O_5 clusters, and thus the catalytic behavior of supported vanadia in ODH reactions (Khodakov et al. 1999). Also, the sizes of preselecting platinum clusters were demonstrated to greatly enhance ODH of propane to propylene (Vajda et al. 2009). Platinum nanoclusters stabilized on high surface area supports are 40–100 times more active for ODH of propane than previously reported for bulk platinum, in addition to exhibiting high selectivity to propylene over undesirable products. The superior performance of the nano-platinum catalyst as revealed by quantum calculations indicates that under-coordination of the platinum atoms is responsible for the high reactivity with extended surfaces (Vajda et al. 2009). The calculated transition states and intermediates in the reaction of C_3H_8 leading to the formation of propylene on the Pt_4 cluster are shown in Fig. 2.8. The "true" barrier to breaking the first C–H bond is only 0.42 eV. The corresponding barrier referenced to gas-phase propane (the "apparent" barrier) is slightly smaller (0.18 eV); this barrier is found to be smaller (0.05 eV) when recalculated on a Pt_8 cluster. In spite of the small magnitude of the energetic barrier, this step will probably be rate-limiting because of the very large entropic loss, and consequently, lower pre-exponential factor, associated with propane adsorption at high temperatures on the clusters. The other pathways are thermodynamically downhill to the formation of propylene, which binds to Pt_4 by its π bond (Vajda et al. 2009).
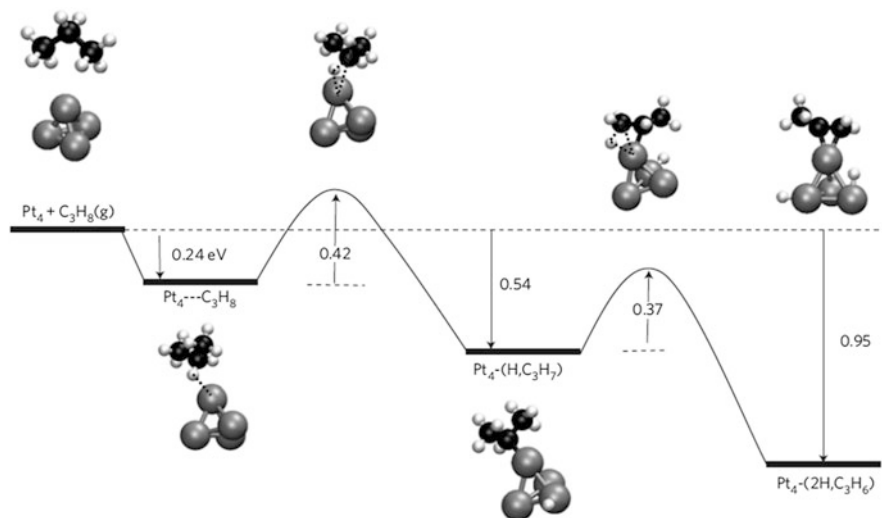
Fig. 2.8 Conversion of propane to propylene from DFT calculations for the dehydrogenation of propane on a Pt$_4$ cluster leading to the formation of propylene adsorbed on the cluster. Energies (in eV) of the equilibrium structures are relative to the reactants. Energy barriers for the transition state structures are relative to the preceding equilibrium structure ("true" barriers). The first barrier corresponds to breaking of the first C–H bond (on the CH$_2$ group) and the second barrier corresponds to breaking of the second C–H bond (on a CH$_3$ group). The *dotted lines* in the structures indicate partial bonds. Reprinted with permission from Macmillan Publishers Ltd. *Nature Chemistry* (Vajda et al. 2009), copyright 2009

3.3 Desulfurization of Petroleum

Due to stringent regulations by various environmental protection agencies across the world on the release of poisonous gases to the environment from petroleum exploitation, desulfurization of commercial fuels is widely practiced in order to reduce the sulfur content to less than 10 ppm in the refined petroleum products. In the upgrading of heavy oil via desulfurization, unsupported metal sulfide catalysts in its natural state are gaining serious attention. To increase the desulfurization capacity of these catalysts, the particles size need to reduce as much as possible to eliminate the introduction of toxic sulfur compounds to pre-sulfurize the hydrogenation catalysts. This simplifies the application process and improves the efficiency of the catalysts (Li and Zhu 2012). Several types of sulfur removal are carried out using metal catalysts. Catalysts based on molybdenum, cobalt, and nickel dispersed on different supports are effective catalysts for the removal of sulfur from petroleum and petroleum products (Li and Zhu 2012; Sudhakar 1998; Mohajeri et al. 2010). The composition, as well as particle size, can play an important role in the performance of the catalysts. A US patent 20100167915A1 (Mohajeri et al. 2010)

discloses that hydrodesulfurization (HDS) catalysts on nanostructured porous carbon supports are excellent for desulfurization of hydrocarbon feedstocks. A nanocomposite based on anatase-vanadium-polyphosphomolybdate ((TiO_2)/ (Bu_4N)$_4$H[$PMo_{10}V_2O_{40}$]) shows a good capacity to oxidatively desulfurize a simulated gas oil. The nano layer of the anatase phase with a particle size of 20 nm shows a high S conversion (more than 98%) (Rezvani et al. 2014). The high oxidative desulfurization (ODS) of gas oil proves an efficient, convenient, and a practical method for scavenging sulfur compounds with this nanocomposite material. Fe@Si–$PMo_{10}V_2$ nanostructured support as a catalyst for the ODS process selectively oxidizes sulfides to the corresponding sulfoxides and sulfones under mild reaction conditions. The catalyst also exhibits excellent activity to remove sulfur contents in model oil and shows a high potential as an effective catalyst for deep desulfurization of diesel. The presence of other compounds such as nitrogen and aromatic compounds can affect ODS conversion. An important characteristic of this nanocatalyst is its reusability after at least three ODS cycles with a good catalytic activity (Rafiee and Rezaei 2016). Reusability of the catalyst is an important consideration in the design of a catalyst for industrial applications. Silver supported on mesoporous silica nanoparticles exhibits excellent regeneration stability and maintains high activity up to six cycles (Hauser et al. 2016). This is due to the reduction of silver ions to silver nanoparticles within the mesochannels of the extra-framework aluminum. The good behavior of hematite (Fe_2O_3) nanoparticles for thiophene decomposition in desulfurization reaction is a result of the unique properties of the catalyst (Khalil et al. 2015). Among other factors, the size of the hematite nanocatalyst influences the ability of the catalyst to decompose thiophene. The catalytic performance increases with an increase in reaction temperature and the amount of the catalyst but decreases with the particle size and the presence of hydrogen donor. Hydrogen donor covers the surface of the catalyst and blocks the active sites. In this reaction, the catalytic process involves a cyclic phase transformation of some of the hematite to magnetite (Fe_3O_4) as thiophene is oxidatively decomposed into its products and reoxidation of magnetite to hematite in the presence of water as the source of active oxygen (Khalil et al. 2015). Recently, carbon materials have become excellent supports for various catalysts in different desulfurization reactions (Mohammed et al. 2017; Guo et al. 2017). Nanocatalyst composite structure was prepared on various carbon nanotube supports and the formation of network structure between metal catalysts and CNTs was observed (Mohammed et al. 2017). These supports enable the homogeneous spreading of the active CoMo particles within the bulk of CNTs. Experiments using these nanocatalysts reveal better results than the conventional catalyst (CoMo/Al_2O_3) in the removal of sulfur from gas oil. An improvement of about 10% in HDS over conventional catalyst was obtained after 10 h under conditions: 280°C of reactor temperature, 10 bar of system pressure, and $2\,h^{-1}$ of space velocity of gas oil, which were optimum conditions to remove sulfur from the gas oil (Mohammed et al. 2017). In an in situ experiment for upgrading heavy oil, different carbon

nanomaterials were utilized as catalysts in the HDS reaction with thiophene as a sulfur-containing model compound. The carbon nanocatalysts possessed an ultrahigh specific surface area and a good degree of graphitization. It was found that the graphitization degree of the carbon-based nanocatalysts is of great importance in the HDS reaction, contributing to catalytic activity. The performance of the carbon-based nanomaterials demonstrates the potential application of carbon nanomaterials as metal-free catalysts in in situ upgrading and recovery of heavy crude oil, which will contribute to a more sustainable chemistry in terms of production and refining of heavy crude oils (Guo et al. 2017).

Synergism of nanosized materials improves stability and recycling of catalysts for reusability (Hauser et al. 2016). Zeolites as supports for desulfurization catalysts synergistically contribute to excellent activities of the catalysts. Crystalline mordenite nanofibers support with a bundle structure containing parallel mesopore channels were tested for sulfur removal in HDS. Cobalt and molybdenum (CoMo) species were introduced into the mesopores and micropores of nano-bundles mordenite (NB-MOR). The NB-MOR supported CoMo catalyst (CoMo/NB-MOR) exhibited an unprecedented high activity (99.1%) as well as very good catalyst life in the HDS of 4,6-dimethyldibenzothiophene and diesel compared with a conventional γ-Al_2O_3 supported CoMo catalyst (61.5%). The spillover hydrogen formed in the micropores migrates onto nearby active CoMo sites in the mesopores, which could be responsible for the great enhancement of the HDS activity (Tang et al. 2013). These features are crucial for the design and preparation of multifunctional high activity catalysts for HDS, selective cracking, and hydrocracking (Tang et al. 2013). The alumina-nano Y zeolite (Al_2O_3-nY) composites reduce the metal-support interaction and heighten the MoS_2 stacking degree, shorten slabs, and enlarge corner Mo atoms. The addition of nanozeolite also enhances the overall acidity, which improves the HDS activity compared with NiMo/Al_2O_3 catalysts. Synergism of the hydrogenation activity and acid amounts is responsible for the improved activity (Yin et al. 2011, 2015). The differences in the basicity and/or acidity of support materials are important contributors to the performance of desulfurization catalyst (Zhang et al. 2015). A large amount of the strong basic sites can avoid the polymerization of catalyst species and form small oxide clusters. On Co-MoS_2/NS-MgO, after sulfidation, small MoS_2 clusters with shorter lengths and less stacking formed on the NS-MgO contribute to an increase in the sites available for Co-promotion, resulting in the Co-MoS_2/NS-MgO catalyst with a high HDS activity (Zhang et al. 2015).

3.4 Fisher–Tropsch Synthesis

Fischer–Tropsch synthesis (FTS) is one of the efficient ways to convert coal, biomass, and natural gas into hydrocarbon derivatives through the intermediacy of synthesis gas (a mixture of H_2 and CO) on supported metal catalysts (Jiao et al. 2016). The greatest challenge with this process in the production of olefins is low

conversion and selectivity to lighter olefins ($C_{2=}$ to $C_{4=}$). Towards overcoming these limitations, supported metal nanoparticles have shown high promise as an effective catalyst for increasing conversion of lower olefins (López and Corma 2012; Galvis et al. 2012). Conversion of syngas to C_2 through C_4 olefins with selectivity up to 60 w%, using catalysts that compose of iron nanoparticles, homogeneously dispersed on weakly interactive α-alumina or carbon nanofibers supports is reported (Galvis et al. 2012). The use of iron nanoparticles improves stability of the reaction performed at high temperature, which is necessary to shift product selectivity to lighter hydrocarbons that is lacking with bulk iron catalysts. At a high temperature, the undesirable Boudouard reaction, $2CO(g) \rightarrow C(s) + CO_2(g)$ (Steynberg and Dry 2004), leads to the deposition of carbon, which can block the active sites and induce fragmentation of the particles in bulk iron catalysts (Shroff et al. 1995). The mechanical and thermal instabilities of the bulk iron oxide catalysts also result in the plugging of the catalyst bed in fixed-bed operation or in the fouling of separation equipment in a fluidized-bed process (Galvis et al. 2012). Compared with bulk Fe, the nanoparticle Fe catalysts display improved catalytic performances under industrial relevant conditions as shown in Fig. 2.9. It is also very clear that the support type exhibits significant effects on the performance for nano-Fe catalyst. After an initial activation period, Fe/b-SiC, Fe/CNF, 25 wt%Fe/α-Al$_2$O$_3$, and Fe/γ-Al$_2$O$_3$ show stable catalytic activities for up to 60 h (Galvis et al. 2012). The stability maintained during this time fully complies with the requirements for the application of catalysts in fluidized-bed reactors relevant in industrial applications of the exothermic FTS to olefins process.

The supported and bulk Fe catalysts tested in the FTS reaction at 1 bar and 350 °C at low CO conversion (0.5–1%) restrict secondary hydrogenation of olefins as shown in Table 2.1 (Galvis et al. 2012). Catalytic activity is expressed as iron time yield (i.e., the number of CO moles converted to hydrocarbons per gram of iron per second). A high initial activity is observed for Fe/b-SiC and Fe/CNF over 15 h. In Table 2.2, the activities and product selectivities measured after 64 h of reaction at 20 bar are displayed. The CO_2 selectivity for all the samples is approximately 40% on the basis of CO converted. The promoted catalysts prepared using supports with low interaction with iron show high catalytic activities combined with high selectivities to the desired products (Galvis et al. 2012).

Cobalt nanoparticles supported on mesoporous zeolites are effective catalysts for FTS (Cheng et al. 2015; Peng et al. 2015; Sartipi et al. 2014). The cooperative interplay of the Co sites and the acid sites on the zeolite forms a bifunctional catalyst that exhibits better performance than a monofunctional catalyst. A bifunctional catalyst consisting of uniform-sized Co nanoparticles and mesoporous H-ZSM-5 has been demonstrated to be effective for CO hydrogenation and hydrocracking/isomerization reactions (Cheng et al. 2015). The bifunctional catalyst was found to be promising for the direct production of gasoline-range (C_{5-11}) hydrocarbons from syngas. The Bronsted acidity in the zeolite results in hydrocracking/isomerization of the heavier hydrocarbons formed on Co nanoparticles, while the mesoporosity contributes to suppressing the formation of lighter (C_{1-4}) hydrocarbons. The selectivity for C_{5-11} hydrocarbons could reach about 70% with a ratio of
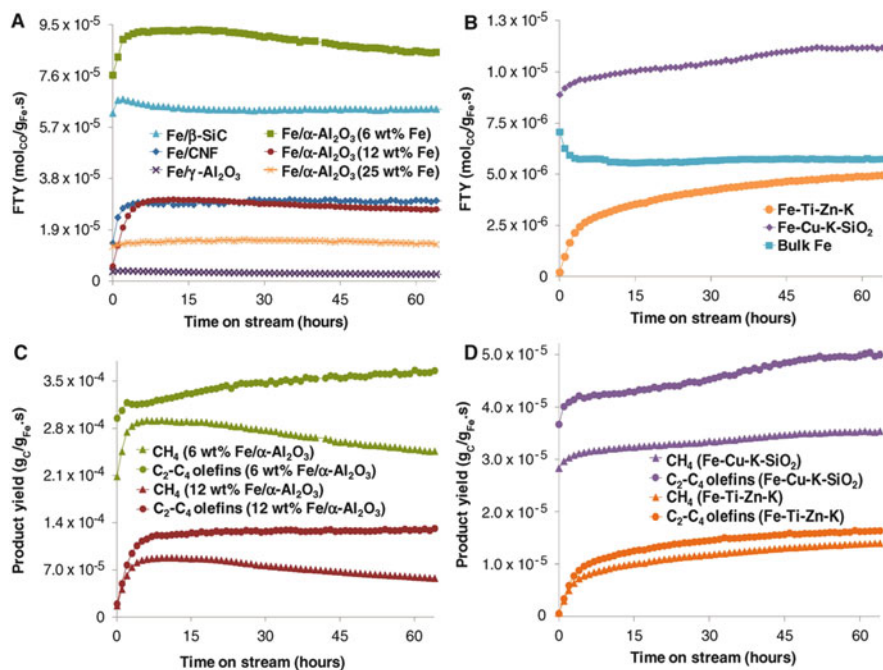
Fig. 2.9 (**a–d**) Catalytic performance of iron catalysts for the FTO process at 20 bar. Catalytic tests were carried out at $T = 340\,°C$, $P = 20$ bar, and a H_2/CO ratio of 1. Iron time yield is plotted above as a function of time for (**a**) Fe-supported catalysts and (**b**) bulk Fe catalysts. Methane and lower olefins yields are plotted below as a function of time for (**c**) Fe-supported catalysts and (**d**) bulk Fe catalysts. The product yields were obtained at CO conversion levels between 70 and 80%. Adapted from Galvis et al. (2012). Reprinted with permission from The American Association for the Advancement of Science

isoparaffins to n-paraffins of approximately 2.3 over this catalyst, and the former is markedly higher than the maximum value (ca. 45%) expected from the Anderson–Schulz–Flory distribution (Cheng et al. 2015).

3.5 Other Reactions

Nanozeolite clinoptilolite supported rhodium nanoparticles (Rh/NZ-CP) were tested in the hydrogenation of arenes, nitroarenes, and alkenes under moderate reaction conditions. The nanocatalyst contains 2 wt% Rh of particle sizes in the range of 5–20 nm distributed on the zeolite. The catalytic performance of Rh/NZ-CP improves significantly, and the catalysts could be regenerated by a simple process and reused for many times without significant decrease in activity and selectivity. The high catalytic activity, thermal stability, and reusability present the

Table 2.1 Product selectivity and catalytic activity at 1 bar

Sample[a]	FTY (10^{-6} mol$_{co}$/g$_{Fe}$.S)	Selectivity (%C)			
		CH_4	C_2–C_4 Olefins	C_2–C_4 Paraffins	C_{5+}
Fe/CNF	1.41	23	61	4	12
Fe/α-Al$_2$O$_3$ (12 wt%Fe)	0.65	22	61	4	13
Fe/β-SiC	6.52	31	58	4	7
Fe/SiO$_2$	0.14	38	56	5	1
Fe/γ-Al$_2$O$_3$	0.07	54	44	2	0
Fe-Ti-Zn-K	0.13	83	16	1	0
Fe-Cu-K-SiO$_2$	0.20	43	46	2	9
Bulk Fe	0.08	76	21	2	1

From Galvis et al. (2012). Reprinted with permission from The American Association for the Advancement of Science

[a]Catalytic tests were performed at 350°C and an H_2/CO ratio of 1; results after 15 h on stream are shown (CO conversion: 0.5–1.0%). The product mixture that was analyzed consisted of C_1–C_{16} hydrocarbons. Iron time yield (FTY) represents moles of CO converted to hydrocarbons per mol of Fe per second; %C is defined as carbon atoms in a product with respect to the total number of C atoms in the hydrocarbon mixture

Table 2.2 Catalytic performance at 20 bar

Sample[a]	FTY (10^{-5} mol$_{co}$/g$_{Fe}$.S)	Selectivity (%C)				
		CH_4	C_2–C_4 olefins	C_2–C_4 paraffins	C_{5+}	Oxygenates
Fe/CNF	2.98	13	52	12	18	5
Fe/α-Al$_2$O$_3$ (6 wt%Fe)	8.48	24	35	21	10	10
Fe/α-Al$_2$O$_3$ (12 wt%Fe)	2.66	17	39	19	14	11
Fe/α-Al$_2$O$_3$ (25 wt%Fe)	1.35	11	53	6	21	9
Fe/β-SiC	6.38	35	19	39	4	3
Fe/γ-Al$_2$O$_3$	0.25	49	33	11	1	6
Fe-Ti-Zn-K	0.49	24	28	29	10	9
Fe-Cu-K-SiO$_2$	1.12	26	36	12	18	8
Bulk Fe	0.57	30	32	18	14	6

From Galvis et al. (2012). Reprinted with permission from The American Association for the Advancement of Science

[a]Catalytic tests were performed at 340°C and a H_2/CO ratio of 1; results after 64 h on stream are shown. The product mixture that was analyzed consisted of C_1 to C_{10} hydrocarbons

catalyst as an attractive option when compared with the conventional (Baghbanian et al. 2015).

The catalytic cracking of *n*-hexane over nano-ZSM-5 zeolite (MFI-type zeolite, Si/Al = 150 and 240) catalysts was tested at reaction temperatures ranging from 823 to 923 K under atmospheric pressure (Konno et al. 2012). The catalysts, compared with the micron-sized zeolite, exhibited a higher *n*-hexane conversion

with stable activity up to 50 h (Table 2.3). The Thiele modulus and the effectiveness factors for the reaction using ZSM-5 zeolites with different crystal sizes are presented in Fig. 2.10 and Table 2.4. It can be clearly seen from Table 2.4 that the effectiveness factor for MFI (S)150, that is, small crystallite size MFI with Si/Al of 150 is 1.0, indicating that the catalytic reaction in MFI(S)150 proceeded under reaction-controlled conditions (Konno et al. 2012). The large external surface area and low diffusion resistance of the nanozeolites reduce the effect of pore plugging due to coke deposition (Yin et al. 2014). For this reason, the application of nanozeolite in the catalytic cracking of *n*-hexane is effective in stabilizing the catalytic activity. Similarly, in the cracking of *n*-hexane and naphthenes, (cyclo-hexane and methyl-cyclohexane), coke was readily formed from the beginning of the reaction leading to significant deactivation of the catalyst for micron-sized ZSM-5 (Konno et al. 2013). For ZSM-5 catalysts, regardless of the reactant, the nanoscale ZSM-5 exhibited a high conversion and a high light olefins yield with a stable activity. As a result, application of nanoscale ZSM-5 zeolites to the catalytic cracking of naphtha is effective and gives light olefins with high yield and excellent stable activity. Nanosized *β*-zeolites for the isomerization of hexane are also active with good selectivity to branched isomers because of the high external surface area of the small particles of the nanosized *β*-zeolites and the rapid diffusion of the reactants and products (Sakthivel et al. 2009).

In another report, methanol conversion to light olefins was investigated over SAPO-34 nanocatalyst with a crystal size of about 50 nm, and its catalytic proper-ties were compared with those of 600 nm SAPO-34 catalyst (Askari et al. 2012). The product distribution over the two catalysts was almost the same, but their deactivation behaviors differ considerably. SAPO-34 catalyst with large crystal deactivates faster than SAPO-34 nanocatalyst. This variation in the deactivation of the different SAPO-34 crystallites is attributed to the number of accessible cavities near their external surface and the diffusion limitation of the reactant and product molecules. Due to a shorter diffusion length, the residence time of the produced hydrocarbons is short, resulting in the long catalyst lifetime of the SAPO-34 nanocrystals. Incorporation of a stabilizer into active catalysts could influence their performance. Boron incorporation into H-ZSM-5 nanocatalyst results in the isomorphic substitution of B into the framework of H-ZSM-5 (Yaripour et al. 2015). The interaction between B species and H-ZSM-5 reduces the strong acid sites and generates new weak acid sites which modify the densities and distributions of acid sites on the [B]-HZSM-5. This raises the lifetime of the modified zeolite in MTO reaction up to 1300 h compared to that of the conventional reference sample 340 h (Yaripour et al. 2015). However, propylene selectivity does not change significantly with the substitution of B in H-ZSM-5. The deactivated catalysts reveal that incorporation of boron improves coke resistance of the ZSM-5 nanocatalyst. The considerable enhancements of the lifetime and catalytic stability are attributed to the reduction of strong/mild acid sites ratio as well as small crystal size of the [B]-H-ZSM-5 nanocatalyst. In summary, the boron-modified ZSM-5 nanocatalyst exhibits more stable catalytic performance and longer catalytic life-time for the MTO reaction.

Table 2.3 *n*-Hexane conversion, product yields, and coke amounts over the catalyst with different crystallite sizes

Catalyst	Time (h)	Conversion (C-mol%)	Light olefins yield (C-mol%)			Total olefin	BTX yield (C-mol%)	Others yield (C-mol%)	Coke amount of after 50 h (wt.%)
			C2=	C3=	C4=				
MFI(S)150	0.5	94.1	20.8	32.7	3.8	57.3	4.2	32.6	
	7	93.5	19.1	32.8	4	55.9	4.1	33.5	–
	50	82	13.2	29	4.7	46.9	4.5	30.6	59.1
MFI(M)150	0.33	92.2	22.8	30.3	6.6	59.7	4.3	28.2	
	7.5	93.1	20.8	32.4	7.3	60.5	3.9	28.7	–
	50	81	13.6	31.3	8.4	53.3	2.6	25.1	21.0
MFI(L)150	0.33	94.7	23.9	28.6	5.9	58.4	6.2	30.1	
	8.5	81	13.6	30.8	8.1	52.5	3.1	25.4	–
	50	48.3	6.2	19.5	6.3	32	1.5	14.8	7.5

Reprinted from Konno et al. (2012) with permission from Elsevier. Copyright 2012, Elsevier publishers

Fig. 2.10 Relationship between the Thiele modulus and the effectiveness factor in *n*-hexane cracking at 923 K over ZSM-5 zeolites (Si/Al = 150) with different crystal sizes. Adapted from Konno et al. (2012) with permission from Elsevier. Copyright 2012 Elsevier publishers

Table 2.4 Effectiveness factors of ZSM-5 zeolites (Si/Al = 150) with different crystal sizes in *n*-hexane cracking at 923 K

Sample	Reaction rate constant k (m^3 kg^{-1} s^{-1})	Thiele modulus ϕg (mc)	Effectiveness factor ηg (mc)
MFI(S)150	(1.04) 150^{-2}	(5.38) 150^{-2}	1
MFI(M)150	–	(8.97) 150^{-2a}	1
MFI(L)150	–	1.38^a	0.65
Coked MFI(S) 150	8.27 MFI^{-3}	9.03 MFI^{-1}	0.8
Coked MFI(L) 150	4.24 MFI^{-3}	2.41	0.41

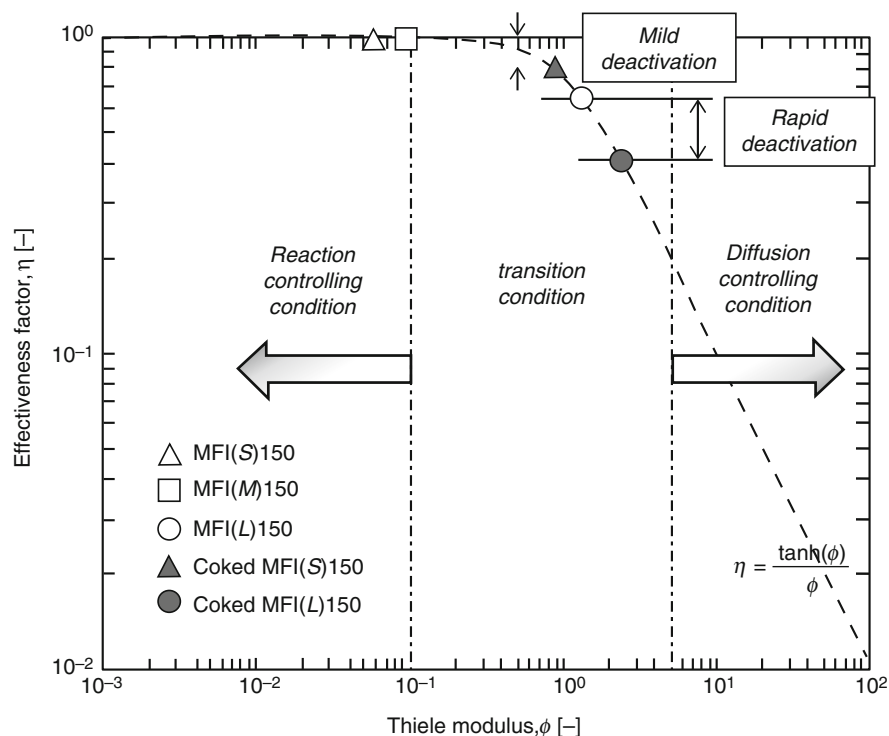Reprinted from Konno et al. (2012) with permission from Elsevier. Copyright 2012, Elsevier publishers
[a]Theoretical value calculated from reaction rate constant of MFI(S)150

4 Concluding Notes and Future Perspectives

The relationship between nanoscience/nanotechnology and catalysis offers huge opportunities for improvements in petroleum processing. The utilization of nanoporous materials as supports and as active catalysts and metal nanoparticles for catalysis traverses various petroleum refining processes. The tremendous benefits the nanoscale materials possess over their micron-sized counterparts are due to their intrinsic size-dependent properties. The formulation of ideal nanoparticles to improve a process efficiency requires careful designed and controlled experiments. The improvements of several features make them a better choice. The properties that make them ideal candidates for petroleum processing include a greater surface area to volume ratio due to tiny particle size, and thermal and catalytic stability. Although the physiochemical characteristics of nanoparticles, such as phase, structure, or behavior, may be influenced by the method of preparation and the nature of the environment in which the nanoparticles are subjected to, the extent of these factors on the particle properties can also be size dependent and therefore can be controlled. Phase transformation in a metal nanoparticle catalyst could lead to the catalyst deactivation. However, it is not true in the case of nanoporous materials such as zeolites. The large external surface area to volume ratio decreases the tendencies of coke formation, which causes catalyst deactivation. Metal catalysts or solid acidic catalysts (such as zeolite) are utilized extensively in the petroleum industry, for example, in catalytic cracking hydrocracking, hydrodesulfurization, isomerization, reforming, and dehydrogenation.

The desire for improved catalysts with high activity, low deactivation, and low coke formation to increase production to meet the growing demand for chemicals and fuels are increasingly necessitating the exploitation of nanoparticles as catalysts, and there are even more opportunities lying to be explored using the potentials of nanotechnology. The inherent stability of nanoparticle catalysts and their bifunctional catalysis potentials provide even more future opportunities for many applications, such as the catalytic application to renewable fuels. Nanotechnology will continue to improve the future of petroleum refining explorations and exploitations. It is expected that lower energy consumption, extended lifetime of catalyst system and reduced amount of materials and reuse of nanomaterials will offer more environmentally friendly catalysts in the future.

References

Askari S, Halladj R, Sohrabi M (2012) Methanol conversion to light olefins over sonochemically prepared SAPO-34 nanocatalyst. Micropor Mesopor Mater 163:334–342

Askari S, Alipour SM, Halladj R, Farahani MHDA (2013) Effects of ultrasound on the synthesis of zeolites: a review. J Porous Mater 20:285–302

Baghbanian SM, Farhang M, Vahdat SM, Tajbakhsh M (2015) Hydrogenation of arenes, nitroarenes, and alkenes catalyzed by rhodium nanoparticles supported on natural nanozeolite clinoptilolite. J Mol Catal A Chem 407:128–136

Bell AT (2003) The impact of nanoscience on heterogeneous catalysis. Science 299:1688–1691

Besenbacher F, Chorkendorff I, Clausen B, Hammer B, Molenbroek A, Nørskov JK, Stensgaard I (1998) Design of a surface alloy catalyst for steam reforming. Science 279:1913–1915

Bezemer GL, Bitter JH, Kuipers HP, Oosterbeek H, Holewijn JE, Xu X, Kapteijn F, van Dillen AJ, de Jong KP (2006) Cobalt particle size effects in the Fischer-Tropsch reaction studied with carbon nanofiber supported catalysts. J Am Chem Soc 128:3956–3964

Busca G (2014) Metal oxides as acid-base catalytic materials. Elsevier, Amsterdam

Cheng K, Zhang L, Kang J, Peng X, Zhang Q, Wang Y (2015) Selective transformation of syngas into gasoline-range hydrocarbons over mesoporous H-ZSM-5-supported cobalt nanoparticles. Chem Eur J 21:1928–1937

Corma A, Lopez-Nieto J, Paredes N, Perez M, Shen Y, Cao H, Suib S (1992) Oxidative dehydrogenation of propane over supported-vanadium oxide catalysts. Stud Surf Sci Catal 72:213–220

Covarrubias C, Quijada R, Rojas R (2009) Synthesis of nanosized ZSM-2 zeolite with potential acid catalytic properties. Micropor Mesopor Mater 117:118–125

Database of Zeolite Structures. http://www.iza-structure.org/databases/

Davis ME, García-Martínez J, Li K (2015) Mesoporous zeolites: preparation, characterization and applications. Wiley, Weinheim

Farcasiu M, Degnan TF (1988) The role of external surface activity in the effectiveness of zeolites. Ind Eng Chem Res 27:45–47

Galvis HMT, Bitter JH, Khare CB, Ruitenbeek M, Dugulan AI, de Jong KP (2012) Supported iron nanoparticles as catalysts for sustainable production of lower olefins. Science 335:835–838

Gao Y, Wu G, Ma F, Liu C, Jiang F, Wang Y, Wang A (2016) Modified seeding method for preparing hierarchical nanocrystalline ZSM-5 catalysts for methanol aromatisation. Micropor Mesopor Mater 226:251–259

Grunes J, Zhu J, Somorjai GA (2003) Catalysis and nanoscience. Chem Commun 9 (18):2257–2260

Guo K, Gu M, Yu Z (2017) Carbon nanocatalysts for aquathermolysis of heavy crude oil: insights into thiophene hydrodesulfurization. Energy Technol. doi:10.1002/ente.201600522

Haruta M, Daté M (2001) Advances in the catalysis of Au nanoparticles. Appl Catal A Gen 222:427–437

Hauser JL, Tran DT, Conley ET, Saunders JM, Bustillo KC, Oliver SR (2016) Plasma treatment of silver impregnated mesoporous aluminosilicate nanoparticles for adsorptive desulfurization. Chem Mater 28:474–479

Hirota Y, Murata K, Miyamoto M, Egashira Y, Nishiyama N (2010) Light olefins synthesis from methanol and dimethylether over SAPO-34 nanocrystals. Catal Lett 140:22–26

Hu Y, Liu C, Zhang Y, Ren N, Tang Y (2009) Microwave-assisted hydrothermal synthesis of nanozeolites with controllable size. Micropor Mesopor Mater 119:306–314

Inayat A, Knoke I, Spiecker E, Schwieger W (2012) Assemblies of mesoporous FAU-type zeolite nanosheets. Angew Chem Int Ed 51:1962–1965

Jacobsen CJ, Madsen C, Houzvicka J, Schmidt I, Carlsson A (2000a) Mesoporous zeolite single crystals. J Am Chem Soc 122:7116–7117

Jacobsen CJ, Madsen C, Janssens TV, Jakobsen HJ, Skibsted J (2000b) Zeolites by confined space synthesis—characterization of the acid sites in nanosized ZSM-5 by ammonia desorption and ^{27}Al/^{29}Si-MAS NMR spectroscopy. Micropor Mesopor Mater 39:393–401

Jiao F, Li J, Pan X, Xiao J, Li H, Ma H, Wei M, Pan Y, Zhou Z, Li M (2016) Selective conversion of syngas to light olefins. Science 351:1065–1068

Jo C, Jung J, Shin HS, Kim J, Ryoo R (2013) Capping with multivalent surfactants for zeolite nanocrystal synthesis. Angew Chem 125:10198–10201

Kamigaito O (1991) What can be improved by nanometer composites? J Jpn Soc Powder Powder Metall 38:315–321

Karakoulia SA, Triantafyllidis KS, Tsilomelekis G, Boghosian S, Lemonidou AA (2009) Propane oxidative dehydrogenation over vanadia catalysts supported on mesoporous silicas with varying pore structure and size. Catal Today 141:245–253

Khalil M, Lee RL, Liu N (2015) Hematite nanoparticles in aquathermolysis: a desulfurization study of thiophene. Fuel 145:214–220

Khodakov A, Yang J, Su S, Iglesia E, Bell AT (1998) Structure and properties of vanadium oxide-zirconia catalysts for propane oxidative dehydrogenation. J Catal 177:343–351

Khodakov A, Olthof B, Bell AT, Iglesia E (1999) Structure and catalytic properties of supported vanadium oxides: support effects on oxidative dehydrogenation reactions. J Catal 181:205–216

Konno H, Okamura T, Kawahara T, Nakasaka Y, Tago T, Masuda T (2012) Kinetics of n-hexane cracking over ZSM-5 zeolites—effect of crystal size on effectiveness factor and catalyst lifetime. Chem Eng J 207:490–496

Konno H, Tago T, Nakasaka Y, Ohnaka R, J-i N, Masuda T (2013) Effectiveness of nano-scale ZSM-5 zeolite and its deactivation mechanism on catalytic cracking of representative hydrocarbons of naphtha. Micropor Mesopor Mater 175:25–33

Kore R, Srivastava R, Satpati B (2014) ZSM-5 zeolite nanosheets with improved catalytic activity synthesized using a new class of structure-directing agents. Chem Eur J 20:11511–11521

Lei Y, Mehmood F, Lee S, Greeley J, Lee B, Seifert S, Winans RE, Elam JW, Meyer RJ, Redfern PC (2010) Increased silver activity for direct propylene epoxidation via subnanometer size effects. Science 328:224–228

Li YH, Zhu YQ (2012) Research progress of unsupported nano catalyst. Adv Mater Res 550–553:284–291. Trans Tech Publ

Li G, Jones CA, Grassian VH, Larsen SC (2005) Selective catalytic reduction of NO_2 with urea in nanocrystalline NaY zeolite. J Catal 234:401–413

Lindsay S (2009) Introduction to nanoscience. Oxford University Press, New York

López C, Corma A (2012) Supported iron nanoparticles as catalysts for sustainable production of lower olefins. ChemCatChem 4:751–752

Lv Y, Qian X, Tu B, Zhao D (2013) Generalized synthesis of core-shell structured nano-zeolite@ ordered mesoporous silica composites. Catal Today 204:2–7

McHale J, Auroux A, Perrotta A, Navrotsky A (1997) Surface energies and thermodynamic phase stability in nanocrystalline aluminas. Science 277:788–791

Mehlhorn D, Inayat A, Schwieger W, Valiullin R, Kärger J (2014) Probing mass transfer in mesoporous faujasite-type zeolite nanosheet assemblies. ChemPhysChem 15:1681–1686

Mintova S, Olson NH, Valtchev V, Bein T (1999) Mechanism of zeolite A nanocrystal growth from colloids at room temperature. Science 283:958–960

Mintova S, Grand J, Valtchev V (2016) Nanosized zeolites: Quo Vadis? C R Chim 19:183–191

Mohajeri A, Rashidi A, Jozani KJ, Khorami P, Amini B, Parviz D, Kalbasi M (2010) Hydrodesulphurization nanocatalyst, its use and a process for its production. U.S. Patent No. 20100167915

Mohammed MI, Razak AAA, Shehab MA (2017) Synthesis of nanocatalyst for hydrodesulfurization of gasoil using laboratory hydrothermal rig. Arab J Sci Eng 42 (4):1381–1387

Morales-Pacheco P, Domínguez J, Bucio L, Alvarez F, Sedran U, Falco M (2011) Synthesis of FAU (Y)-and MFI (ZSM5)-nanosized crystallites for catalytic cracking of 1, 3, 5-triisopropylbenzene. Catal Today 166:25–38

Ng E-P, Chateigner D, Bein T, Valtchev V, Mintova S (2012a) Capturing ultrasmall EMT zeolite from template-free systems. Science 335:70–73

Ng E-P, Goupil J-M, Al V, Fernandez C, Retoux R, Valtchev V, Mintova S (2012b) Nucleation and Crystal Growth Features of EMT-Type Zeolite Synthesized from an Organic-Template-Free System. Chem Mater 24:4758–4765

Pan Y, Ju M, Yao J, Zhang L, Xu N (2009) Preparation of uniform nano-sized zeolite A crystals in microstructured reactors using manipulated organic template-free synthesis solutions. Chem Commun 7233–7235. doi: 10.1039/b917949f

Park HJ, Jeon J-K, Kim JM, Lee HI, Yim J-H, Park J, Park Y-K (2008) Synthesis of nanoporous material from zeolite USY and catalytic application to bio-oil conversion. J Nanosci Nanotechnol 8:5439–5444

Peng X, Cheng K, Kang J, Gu B, Yu X, Zhang Q, Wang Y (2015) Impact of hydrogenolysis on the selectivity of the Fischer-Tropsch synthesis: diesel fuel production over mesoporous zeolite-Y-supported cobalt nanoparticles. Angew Chem 127:4636–4639

Persson AE, Schoeman BJ, Sterte J, Otterstedt JE (1994) The synthesis of discrete colloidal particles of TPA-silicalite-1. Zeolites 14:557–567

Rafiee E, Rezaei S (2016) Deep extractive desulfurization and denitrogenation of various model oils by $H_{3+n}PMo_{12-n}V_nO_{40}$ supported on silica-encapsulated γ-Fe_2O_3 nanoparticles for industrial effluents applications. J Taiwan Inst Chem Eng 61:174–180

Rajagopalan K, Peters AW, Edwards GC (1986) Influence of zeolite particle size on selectivity during fluid catalytic cracking. Appl Catal 23:69–80

Rao C, Kulkarni G, Thomas PJ, Edwards PP (2002) Size-dependent chemistry: properties of nanocrystals. Chem Eur J 8:28–35

Rezvani MA, Shojaei AF, Zonoz FM (2014) Anatase titania–vanadium polyphosphomolybdate as an efficient and reusable nano catalyst for the desulphurization of gas oil. J Serb Chem Soc 79:1099–1110

Sakthivel A, Iida A, Komura K, Sugi Y, Chary KV (2009) Nanosized β-zeolites with tunable particle sizes: synthesis by the dry gel conversion (DGC) method in the presence of surfactants, characterization and catalytic properties. Micropor Mesopor Mater 119:322–330

Sartipi S, Alberts M, Santos VP, Nasalevich M, Gascon J, Kapteijn F (2014) Insights into the catalytic performance of mesoporous H-ZSM-5-supported cobalt in Fischer-Tropsch synthesis. ChemCatChem 6:142–151

Schlögl R, Abd Hamid SB (2004) Nanocatalysis: mature science revisited or something really new? Angew Chem Int Ed 43:1628–1637

Schmidt I, Madsen C, Jacobsen CJ (2000) Confined space synthesis. A novel route to nanosized zeolites. Inorg Chem 39:2279–2283

Schoeman B, Sterte J, Otterstedt J-E (1994) Colloidal zeolite suspensions. Zeolites 14:110–116

Serrano DP, van Grieken R, Melero JA, García A, Vargas C (2010) Nanocrystalline ZSM-5: a catalyst with high activity and selectivity for epoxide rearrangement reactions. J Mol Catal A Chem 318:68–74

Shroff MD, Kalakkad DS, Coulter KE, Kohler SD, Harrington MS, Jackson NB, Sault AG, Datye AK (1995) Activation of precipitated iron Fischer-Tropsch synthesis catalysts. J Catal 156:185–207

Steynberg A, Dry M (2004) Fischer-Tropsch technology. Elsevier, Amsterdam

Sudhakar C (1998) Selective hydrodesulfurization of cracked naphtha using novel catalysts. U.S Patent No. 5770046

Sun W, Wang L, Zhang X, Liu G (2015) Controllable synthesis of hierarchical beta nanozeolites from tailorable seeds. Micropor Mesopor Mater 201:219–227

Tang T, Zhang L, Fu W, Ma Y, Xu J, Jiang J, Fang G, Xiao F-S (2013) Design and synthesis of metal sulfide catalysts supported on zeolite nanofiber bundles with unprecedented hydrodesulfurization activities. J Am Chem Soc 135:11437–11440

Vajda S, Pellin MJ, Greeley JP, Marshall CL, Curtiss LA, Ballentine GA, Elam JW, Catillon-Mucherie S, Redfern PC, Mehmood F, Zapol P (2009) Subnanometre platinum clusters as highly active and selective catalysts for the oxidative dehydrogenation of propane. Nat Mater 8:213–216

Valden M, Lai X, Goodman DW (1998) Onset of catalytic activity of gold clusters on titania with the appearance of nonmetallic properties. Science 281:1647–1650

Valtchev V, Tosheva L (2013) Porous nanosized particles: preparation, properties, and applications. Chem Rev 113:6734–6760

Vuong G-T, Hoang V-T, Nguyen D-T, Do T-O (2010) Synthesis of nanozeolites and nanozeolite-based FCC catalysts, and their catalytic activity in gas oil cracking reaction. Appl Catal A Gen 382:231–239

Wachs IE, Weckhuysen BM (1997) Structure and reactivity of surface vanadium oxide species on oxide supports. Appl Catal A Gen 157:67–90

Weisz PB (1995) Molecular diffusion in microporous materials: formalisms and mechanisms. Ind Eng Chem Res 34:2692–2699

Yang F, Deng D, Pan X, Fu Q, Bao X (2015) Understanding nano effects in catalysis. Natl Sci Rev 2:183–201

Yaripour F, Shariatinia Z, Sahebdelfar S, Irandoukht A (2015) Effect of boron incorporation on the structure, products selectivities and lifetime of H-ZSM-5 nanocatalyst designed for application in methanol-to-olefins (MTO) reaction. Micropor Mesopor Mater 203:41–53

Yin H, Zhou T, Liu Y, Chai Y, Liu C (2011) NiMo/Al_2O_3 catalyst containing nano-sized zeolite Y for deep hydrodesulfurization and hydrodenitrogenation of diesel. J Nat Gas Chem 20:441–448

Yin X, Chu N, Yang J, Wang J, Li Z (2014) Synthesis of the nanosized MCM-22 zeolite and its catalytic performance in methane dehydro-aromatization reaction. Catal Commun 43:218–222

Yin H, Liu X, Yao Y, Zhou T (2015) Nanosized HY zeolite-alumina composite support for hydrodesulfurization of FCC diesel. J Porous Mater 22:29–36

Yutthalekha T, Wattanakit C, Warakulwit C, Wannapakdee W, Rodponthukwaji K, Witoon T, Limtrakul J (2016) Hierarchical FAU-type zeolite nanosheets as green and sustainable catalysts for benzylation of toluene. J Clean Prod 142:1244–1251

Zhang YL, Jin XJ, Rong YH, Hsu TY, Jiang DY, Shi JL (2006) The size dependence of structural stability in nano-sized ZrO_2 particles. Mater Sci Eng A 438–440:399–402

Zhang H, Chen B, Banfield JF (2009) The size dependence of the surface free energy of titania nanocrystals. Phys Chem Chem Phys 11:2553–2558

Zhang L, Fu W, Xiang M, Wang W, He M, Tang T (2015) MgO Nanosheet assemblies supported CoMo catalyst with high activity in hydrodesulfurization of dibenzothiophene. Ind Eng Chem Res 54:5580–5588

Zheng N, Stucky GD (2006) A general synthetic strategy for oxide-supported metal nanoparticle catalysts. J Am Chem Soc 128:14278–14280

Zhou B (2007) Nanotechnology in catalysis volumes 3. Springer, New York

Zhou X, Xu W, Liu G, Panda D, Chen P (2009) Size-dependent catalytic activity and dynamics of gold nanoparticles at the single-molecule level. J Am Chem Soc 132:138–146

Chapter 3
Advances in Nanocatalyzed Hydrodesulfurization of Gasoline and Diesel Fuels

Tawfik Abdo Saleh and Ibrahim Munkaila Abdullahi

Abstract This chapter is aimed toward providing a general overview of the significant progress that desulfurization technology has brought to the oil and gas industries. Organosulfur compounds are known to release various environmentally harmful sulfur products into the atmosphere from the combustion engines of vehicles, leading to a serious environmental threat. Efficient removal of these sulfur compounds from diesel and gasoline fuels that we inevitably use in various capacities every day is therefore paramount. Various desulfurization technologies have been developed over the years to address this issue, and one of the most efficient and cost-effective approaches is transition metal-catalyzed hydrodesulfurization (HDS). Several nanocatalysts have been designed for this purpose. The chapter encapsulates some of the various ways in which these catalysts are being prepared, including doped nanocatalysts which are relatively unexplored for this application. It also includes a discussion and examples of their activities in the desulfurization reactions. The limitations are discussed, as well as possible ways to improve their sulfur removal efficiency. Furthermore, some of the commercially employed HDS catalysts, including feedstock, the reaction conditions they work best under, the type of reactor, and various factors affecting the hydrodesulfurization reactions are discussed, along with illustrations. The HDS mechanism is another important aspect of desulfurization that was thoroughly reviewed, including a discussion of the suggested pathways for the hydrodesulfurization of dibenzothiophenes (DBTs) and their derivatives, in addition to the toxic processes of HDS catalysts. Finally, the ongoing research on improved desulfurization processes, specifically the deep HDS of diesel and gasoline fuels in order to comply with the current standard for sulfur removal specifications, is also briefly addressed in this chapter.

Keywords Diesel and gasoline fuels • Nanocatalysts design • Mechanisms of hydrodesulfurization

T.A. Saleh (✉) • I.M. Abdullahi
Chemistry Department, and Center of Excellence in Nanotechnology (CENT), King Fahd University of Petroleum and Minerals, Dhahran 31261, Saudi Arabia
e-mail: tawfik@kfupm.edu.sa; tawfikas@hotmail.com; http://faculty.kfupm.edu.sa/CHEM/tawfik/

1   Introduction

Crude oil has been known to be one of the most substantial energy sources, serving as the most wide reaching of all sources. It comprises a mixture numerous organic compounds. The use of fuel for transportation is the key area where crude oils are primarily used substantially, e.g., gasoline in automobiles, diesel for some cars and trucks, and jet fuel for aircraft. Crude oils may have different forms of impurities present in them, but the most common of all are the sulfur compounds. Liquid (oil) fuels among other fuel types contain sulfur which ultimately resorts to direct sulfur (IV) oxide (SO_2) emission, in addition to other sulfate particulate matter (SPM) that endangers lives and property in public communities and promotes corrosion, reduces the life span of refinery engines. In addition, the emission control technology developed to meet NO_x and SPM emission specifications may be significantly affected by the presence of sulfur compounds in the diesel engines exhaust gases (Srivastava 2012). Various industrial catalysts such as sulfur-based transition metal catalysts have been widely employed in hydrotreatment refining applications of petroleum, e.g., hydrodesulfurization and hydrodenitrogenation, hence, these catalysts are considered industrially vital in the oil industry. These industrial catalysts are in general formed from Group VIII (Co or Ni) mixed with sulfides of an element in Group VIB (Mo or W). Commercial molybdenum catalysts promoted with Co- or Ni- commonly supported on alumina are employed in petroleum hydrotreatment applications. Some important characteristics of alumina support that makes it to be widely employed include high active metal phase dispersion (Vasudeven and Fierro 1996) and its excellent mechanical properties. Intensive researches since the last few decades have pointed out that its promising physical properties are owing to the rather strong chemical bonding interactions present between the transition metal oxides of precursor states and amorphous alumina (Topsøe and Clausen 1986).

Ultra-trace removal of sulfur has become highly attractive as a result of sulfur amount excessively increasing in the crude oils as well as decline in the allowable limit of the amount of sulfur in diesel and gasoline fuels by specifications regulatory bodies. Diesel and oil of low-sulfur content is highly desirable for a safe and friendly environment. The challenge of removing sulfur from FCC naphtha has predominated the recent gasoline desulfurization problem, contributing at least one-third of gasoline pool but over 90% of sulfur in gasoline; this sulfur results in the release of SO_x in air from combustion engines of vehicle leading to air pollution. It is essential that deep gasoline sulfur removal or diesel sulfur must be made, without any decrease in octane number nor loss in the yield of gasoline.

Hydrodesulfurization (HDS) is no doubt among the most regarded processes necessitated to produce diesel fuel of low-sulfur content to as low as below 0.05 wt. % which is in accordance with the reported raising challenge for the environmentally accepted clean fuel with the least increment in production cost. It has been previously reported that alkyl-dibenzothiophenes derivatives with 4- and/or 6-alkyl, for example, 4,6-dimethyl-dibenzothiophene (4,6-DMDBT), exhibited far lower

reactivity in HDS than the unsubstituted dibenzothiophene counterpart (Ma et al. 1995). Generally, the desulfurization of light fractions; constituting high proportion of reactive sulfur-based compounds, e.g., alkyl-benzothiophenes much easier and faster (less reaction time; first few minutes) than heavy fractions; constituting relatively less reactive sulfur-based compounds. For example, alkyl-dibenzothiophenes are difficult to desulfurize under regular HDS techniques (Ma et al. 1995).

2 Processes of Desulfurization Technology in Oil and Gas Industries

Modern refineries are highly integrated industrial plants, with primary assignment of efficiently converting various complex crude oil mixtures feed into high yields of desired valuable products. For this reason, more research efforts are considered to improve conventional hydrodesulfurization and develop substitutes for desulfurization technologies like oxidation-extraction called also oxidative desulfurization are always on the rise. Others are biodesulfurization and selective adsorption, for adequate removal of refractory sulfur compounds present in petroleum products (Srivastava 2012). Cracking, hydrogenation, reforming, blending, extraction, and distillation are some of the crucial physical and chemical processes employed in refineries to convert crude oil to higher value desirable products (Babich and Moulijn 2003). At present, in order for refineries to meet dynamic societal needs with regard to quality of products and other specifications, there is a need to upgrade the existing refining technologies, while researching for innovatively more advanced technologies. Co- and Ni-promoted MoS_2 have shown promising catalytic activity in HDS, and thus, a catalytic system of MoS_2 promoted with Co or Ni have widely been used in HDS catalytic processes. (Moses et al. 2009). The refinery streams of sulfur containing gasoline becomes an environmental threat when gasoline of S $\geq$ 30 ppm is produced, and the need to treat such gasoline becomes necessary. Advanced and conventional Co–Mo and Ni–Mo catalysts have demonstrated high degree of usefulness in their ability to remove sulfur reasonably at high level. On the other side, hydrogenation of unsaturated compounds (olefins) should be minimized as it leads to simultaneous fall in octane number of gasolines. Product yield and specifications are used to rate the efficiency of process applicability. Catalysis based on conventionally employed HDS technologies have been on the rise for better improvement, while in recent years, more sophisticated desulfurization techniques providing efficient ways of removing sulfur as well as increasing the octane number are highly desirable (Babich and Moulijn 2003; Saleh and Danmaliki 2016a).

The basic classifications of desulfurization could be grouped based on the following classes:

1. Nature of employed process; whether physical, chemical, or both
2. Organosulfur compounds fate during desulfurization
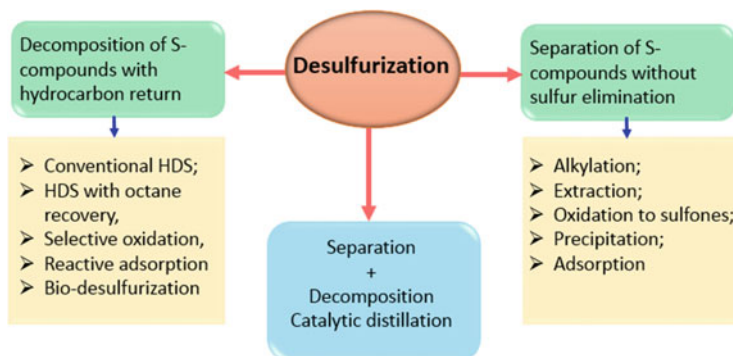
Fig. 3.1 Organosulfur compound-based classification of desulfurization process

3. The role played by hydrogen in the process

Starting with the organosulfur compounds transformation, the process can be subdivided into three main categories, depending on whether decomposition of the sulfur compounds takes place or not, refinery stream separation without sulfur elimination, or both processes (Fig. 3.1). In the first category, the organosulfur compounds decompose into solid sulfur or gaseous products, while the hydrocarbon, on the other hand, remains in the refinery streams and is recovered. The most common illustration of this specific process type is the conventional HDS.

The second category simply separates the organosulfur compounds from the refinery streams. Many processes like this usually transform the organosulfur compounds first into easily separable components from the refinery streams. However, the two challenges associated with desulfurization of streams by separation are that it may lead to the loss of some desired product as well as the disposal of the retained organosulfur molecules. In the third process type, decomposition in a single reactor, as well as separation of organosulfur compounds from streams in separation vessels are carried out simultaneously. The joint processes from the root for several technologies which may be very reliable for producing fuels of ultra-low sulfur contents at industrial scale. An interesting example of this special category of the process is the catalytic distillation desulfurization.

Another form of desulfurization processes which depends on the role hydrogen plays in sulfur removal, this classification is the one based on:

1. HDS processes
2. Non-HDS processes

HDS processes employ hydrogen for the decomposition of organosulfur compounds and sulfur elimination from refinery streams; this may involve several pre- or post-distillation treatments of refinery streams with hydrotreatment to enable the specifications of desired fuel maintained. On the other hand, hydrogen is not involved in the non-HDS processes.
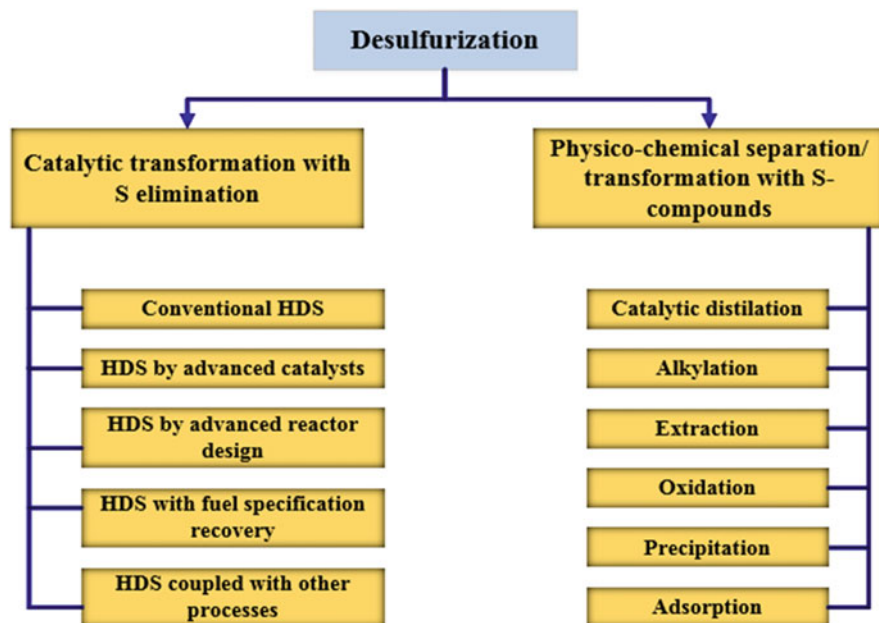
Fig. 3.2 Nature of a key process classification of desulfurization technologies for sulfur removal

The last but not the least form of the desulfurization processes classification is based on the nature of employed processes; physico-chemical processes (Fig. 3.2). Catalytic conversion of organosulfur compounds involving the elimination of sulfur is the most advanced and commercialized technologies. Examples of such technologies to maintain good fuel specifications are conventional hydrotreatment, hydrotreatment in reactor design in the presence of high active catalysts, and hydrotreatment combined with some chemical processes. One major characteristic of the technologies of the last-mentioned example is the employment of physico-chemical processes involving major step such as adsorption, extraction, distillation, alkylation, oxidation, or the combination of one or all of these processes, which has an entire different approach from the separation and/or to transformation of organosulfur compounds from refinery streams by catalytic HDS. For example, the adsorption process requires adsorbents which take up the sulfur molecules selectively from the crude oil sample. A nonreactive, porous substrate that permits the greatest surface area for adsorption is used to hold the active adsorbent. Adsorption is said to take place when there is attachment of sulfur molecules to the adsorbent on the substrate; this remains adsorbed and hence separated from the fuel. Although the method requires low temperature and pressure and may be relatively cheaper, it is not as promising as the catalytic transformation methods (Srivastava 2012).

HDS is a refining process that has a well-established commercialization protocol that involves heating the mixture of a feedstock and hydrogen, in the presence of a catalysts for the essence of sulfur removal. Both the streams from conversion units, e.g., fluid catalytic cracking (FCC) and hydrocracker units and distillate streams obtained during direct distillation of crude oil are desulfurized by the refineries. Depending on the nature and the design of the refinery, HDS can be carried out either before or after FCC. Although due to the poisoning effect of sulfur on Pt, HDS must be carried out before feedstock reforming. H_2S liberation occurs as a result of sulfur reduction occurring in the HDS reactor; this is gradually removed from the flue gas by amine scrubbing. Today, HDS is the most employed desulfurization technology employed although processes like caustic washing is performed as well, basically to remove low molecular weight thiols. Majority of HDS operations in addition to removing sulfur, also help to get rid of nitrogen compounds as well as some metal impurities. In order to meet up with the specifications of ultra-low sulfur on fuels that are produced from straight-run streams, refineries systematically control the appropriate catalysts selection as well as the hydrogenating conditions. The challenge, however, comes up when dealing with the desulfurization of other steams originating from the conversion units, which usually include the refracted sulfur compounds. The currently practiced HDS processes was improved for the removal of sulfur from the derivatives of DBT using a zeolite catalyst supported by nickel (Isoda et al. 2000). In this technology, mainly two steps are involved.

1. Passing hydrogen gas at a pressure of 250 Pa, at 270 °C for 1 h and is the optimum reaction condition for the first step.
2. Further desulfurization of the products is carried out by passing hydrogen gas at a pressure of 250 Pa, over a $CoMo/Al_2O_3$ catalyst at 300 °C for 2 h, for the removal of 4,6-DMDBT.

The need for a relatively elevated temperature, high pressure as well as several steps associated with this desulfurization process adds to the overall cost of running the refineries and hence are the major disadvantages of the process.

3　Hydrodesulfurization of Diesel and Gasoline Fuels

In refining process, sulfur compounds are generally unwanted, this is because aside having pollution and health effects from the sulfur oxide gases they produce, they usually turn some catalysts employed inactive in processing crude oil, as well as causing problems of pipeline corrosion in refining and pumping equipment. For these, desulfurization is highly necessary to have a safe fuel for various applications. Diesel fuel oil deep hydrodesulfurization (HDS) principally targeting alkyl-dibenzothiophenes such as 4-methyl- and 4,6-dimethyldibenzothiophenes for deep HDS was designed through various stages and fractional HDS to obtain a satisfactory sulfur level as well as the fluorescent color of desulfurization oil product was reported by I. Machida et al. The multi-stage hydrodesulfurization process of diesel
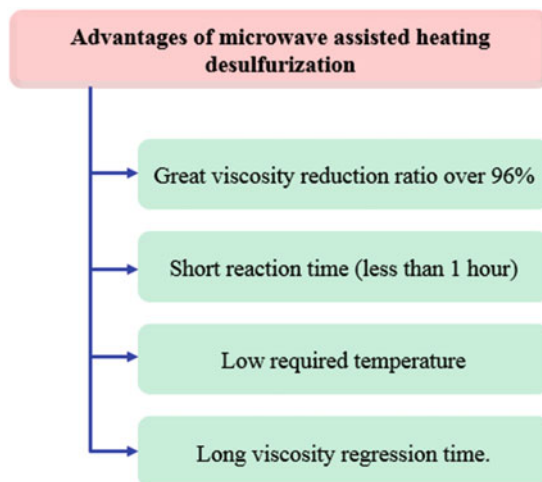
fuel is carried out at a 2.9 MPa pressure, initially over Co–Mo at 360 °C for a duration of 30 min, reducing the sulfur level to 0.092 wt.%. This is followed by carrying out the process over Ni–Mo at a temperature of 360 °C for a duration of 20 min, further decreasing the sulfur level to 0.035 wt.%, and finally, performing the process once again over the same Ni–Mo catalyst but this time, at a relatively lower temperature of 260 °C makes it possible to achieve an overall sulfur level of about 0.016 wt.% low and reaction time of 60 min. The results obtained satisfy the acceptable sulfur level as well as the reaction time (Mochida et al. 1996).

There are some important parameters that affect the deep HDS of diesel fuels. To start with, inorganic reactants and products including hydrogen, ammonia, and hydrogen sulfide if present could remarkably influence the hydrodesulfurization reaction rate as shown by numerous works that adopt model feed. However, for commercial units deep HDS, the partial pressures of these gasses encountered deviate considerably from those usually employed in model feed studies. Furthermore, unlike the data for many pure compounds, obtained in gas-phase or vapor-phase study, the hydrodesulfurization of gas oil is a liquid-phase reaction. And it is often not an easy task to correlate the data obtained at the interface gas-solid and liquid-solid, although, interestingly, another work finding illustrates that many similarities are exhibited with the hydrodenitrogenation of quinoline carried out in the liquid phase and vapor phase (Satterfield et al. 1975).

Several techniques can be used for upgrading heavy crude oil into lighter one. Although high temperatures are required for the methods usually in use, other setbacks include health-threatening environmental pollution as well as long reaction time. The use of carbon-based nanocatalysts in heavy crude oil upgrade was reported to have significant impact in the oil upgrading process by efficiently upgrading the heavy oil into lighter ones at a considerably lower temperature of about 150 °C. Microwave-assisted heating is used to elevate the temperature of crude oil. This proposed technique was found to have the advantages, shown in Fig. 3.3. Thus, upgrade transformation of heavy crude oil to lighter ones could be more environment-friendly and cost-effective (Li et al. 2014).

4 Nanocatalysts Design

The catalytic activities of most sulfides of transition metals have been tested towards HDS (Pecoraro and Chianelli 1981). When their activity was investigated individually towards HDS, they were found to vary across the periodic table over three orders of magnitude. Most of the metals of the second and the third rows were literally found to be the most active catalysts. This varying activity among the metals could be attributed to the structural nature as well as electronic properties. The employed catalysts in the refractory sulfur species desulfurization are designed in two possible approaches:

1. The first method relays on finding a catalyst that could selectively hydrogenate the refractory sulfur species among the major presence of polyaromatic hydrocarbons. In the presence of H_2S, Ru is one of the most promising noble metals reported to be highly active (Hirschon et al. 1987).
2. The second approach involves the elimination of the steric hindrance in DBT skeleton to the desulfurization by the isomerization of their methyl groups. A Co–Mo/Al_2O_3 catalyst-containing zeolite is more preferred as it exhibits slightly more promising activity than commonly employed Ni–Mo/Al_2O_3 and Co–Mo/Al_2O_3; this was justified from the higher conversion of 4,6-DMDBT it showed, confirmed from the analytical data of the product, which indicates the methyl groups disproportionation and isomerization (Mochida et al. 1996).

Trickle-flow experiments were carried out in accordance with the guidelines reported by van Looij et al. (van Looij et al. 1998; Sie 1995), using the catalysts: CoMo/Al_2O_3 and a NiMoP/Al_2O_3 (Criterion Catalyst Company). A stainless-steel reactor of an internal diameter of 15 mm was loaded with 20 mg catalyst, diluted with SiC, after which the drying of the catalyst takes place at 450 °C for a period of 2 h. The influence of internal mass transport on the reaction rate was minimized by adopting catalyst bodies of a sieve fraction of 180–600 μm: according to the reported study, an efficiency factor of >0.95 was obtained under the conditions employed (Gosselink and Stork 1987). Additionally, experiments have verified that the use of viz. 180–250 mm which are even much smaller catalyst bodies, virtually the same HDS activity observed, confirming that according to the reported investigations, the limitation associated with internal diffusion was negligible. Several catalytic systems have been designed for various HDS processes, most of which are Co-, Mo-, and Ni-based catalysts supported on alumina with one metal serving as promoter, commonly Mo. The reaction is carried out in specialized types of reactors with reactions optimized for each specific catalyst adopted. Table 3.1 below shows the summary of catalyzed that have been designed and applied in various capacities, the reaction system used and its optimum conditions.

The resistance of sulfur to noble metal catalysts has been an area of emphasis for several studies due to its significance in desulfurization processes (Cooper and Donnis 1996). In recent times, a novel strategy for the design of sulfur-resistant noble metal catalysts was proposed for the production of clean distillate fuels, by

Table 3.1 Optimal conditions for the removal of sulfur by HDS

Process	Sulfur compound feedstock	Catalyst	Reactor system	S Conc. Co (ppm)	Temp. (°C)	Pressure (MPa)	% S Removal	References
Deep HDS	Alkyl DBTs light oil	Co–Mo/An Al$_2$O$_3$	Packed bed	4000	300	–	67%	Kabe et al. (1993)
Three stage HDS	Alkyl DBTs diesel	CoMo + NiMo	Packed bed	7060	250	2.9	69%	Ma et al. (1994)
HDS	Alkyl DBTs heavy gas oil	Co–Mo–Al	Trickle bed	1800	360	5.5	20%	Yitzhaki et al. (1995)
Deep HDS	Alkyl DBTs gas oil	Co–Mo/γ–Al$_2$O$_3$	Fixed bed	13200	350	3	96%	Andari et al. (1996)
HDS	Alkyl DBTs heavy gas oil	Co, Ni, Mo, W supported on Al$_2$O$_3$/SiO	Trickle bed	13300	320	5.4	80%	Vradman et al. (1999)
In situ H2 generation	BT water/toluene emulsion	Mo	Batch autoclave	350	340	20	99.5%	Ng and Milad (2000)
Staged HDS	Alkyl DBTs medium cycle oil	NiMoS/Al$_2$O$_3$	Packed Bed	4900	340	5	97%	Shin et al. (2001)
Deep HDS	Alkyl DBTs light cycle oil	Co–Mo supported on MCM-41	Packed Bed	21900	350	4.5	57%	Turaga and Song (2003)
Lab Scale HDS	Alkyl DBTs middle distillates	NiMo/γ–Al$_2$O$_3$	Trickle bed	16740	350	4	90%	Pedernera et al. (2003)
Deep HDS	Alkyl DBTs gas oil	CoMo/Al$_2$O$_3$ + NiMo/Al$_2$O$_3$	Packed Bed	14350	340	3	98%	Choi et al. (2003)
HDS	Alkyl DBTs gas oil	NiMo sulfide on Al$_2$O$_3$–Si support	Packed Bed	11780	340	4.9	94%	Kunisada et al. (2004b)
Deep HDS	Alkyl DBTs gas oil	CoMoS and NiMoS	Batch autoclave	340	–	4.9	97%	Kunisada et al. (2004a)
Oil presaturated with H2	Alkyl DBTs diesel	CoMo	Two phase reactor	1200	400	7	99%	Schmitz et al. (2004)

(continued)

Table 3.1 (continued)

Process	Sulfur compound feedstock	Catalyst	Reactor system	S Conc. Co (ppm)	Temp. (°C)	Pressure (MPa)	% S Removal	References
Lab Scale Deep HDS	Alkyl DBTs diesel	P and Ni–Al$_2$O$_3$ supported Mo oxycarbides		520	340	4	50%	Costa et al. (2005)
HDS	Thiophene n-Heptane	FeS–MoS supported on Al$_2$O$_3$ and carbon		1000	280	0.1	30%	Hubaut et al. (2007)
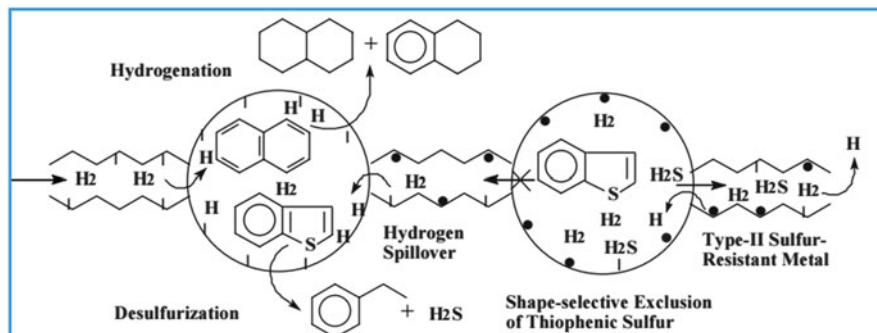
Fig. 3.4 Proposed novel concept for catalyst design based on shape-selective exclusion, hydrogen spillover, and two sulfur resistance types. The scheme represents internal surface metal particles as *black dots*

employing low-temperature hydrotreating of sulfur-containing distillates (Song 1999), diesel fuels, and jet fuels are examples. Special zeolites-supported noble metals were invoked in the proposed design concept, which utilizes the following (Song 1999):

- Selective exclusion based on shape
- Spillover of hydrogen
- Two sulfur resistance types

Noble metal particles bimodal distributions could be prepared from special zeolite supports. The pore sizes of the metals vary from small (pore opening of about 5 Å or less) to large (6 Å pore opening or larger).

Note: according to IUPAC recommendation, pores are classified as:

1. macropores: pores with widths exceeding about 50 nm
2. mesopores: pores of widths between 2 nm and 50 nm
3. micropores: pores with widths not exceeding about 2 nm

Some materials are categorized by small pores whereas others will be contained in large pores. It is of interest that distribution of the two pores is uniform or their systems interconnect, so that they are as close as possible. Size inhibition may occur when some relatively bigger organosulfur compounds, e.g., thiophenic molecules try to diffuse into the small pores leading to "selective exclusion based on shape." On the other hand, the larger pores (micropore or mesopore size range) would permit fast diffusion preferentially as well as allowing bulky polycyclic aromatic to reaction with sulfur compounds. The thiophenic molecules are small enough to penetrate the large pores but big enough to be blocked by the small pores. H_2 molecules, on the other hand, are very special in that, they are small enough to enter both pore types quite readily, get dissociatively adsorbed on the available metal around, and be conveyed between pore systems by means of spillover. This spillover hydrogen plays a vital role in recovering poisoned metal sites via the

elimination of R-S-R and R-S-H; this poisoning occurs when adsorbed sulfur deactivates the metal in the large pores. The classification of sulfur resistance based on types; type I implying resistance to organic sulfur compounds and type II implying resistance to inorganic H_2S is of paramount importance. A higher type II sulfur resistance is an expected property exhibited specifically by small pores metal species. Figure 3.4 shows an elegant scheme of the proposed novel concept (Song 1999).

5   Doped Nanocatalysts Preparations

Preparation approach for catalyst synthesis generally has a significant effect on the catalyst activity for any specific type of transformation or reaction. There are very limited reports in documented literature illustrating the effect of the method of catalyst preparation has on HDS. Although, it is yet to be well understood, the reasons why catalyst developed by one have better activity than that developed by another method. The effect CoMo/silica catalysts on thiophene HDS has been studied and reported (Venezia et al. 2002). Two possible methods can be used to prepare the catalysts, namely, incipient wetness impregnation/co-impregnation route and the complete sol-gel method; a control catalytic system was prepared by supporting the catalysts on a commercial silica, and the results were compared. The highest activity was found to be exhibited by the sol-gel silica supported catalyst with the two co-impregnatedly loaded metals in the presence of nitrilotriacetic acid. Equilibrium deposition filtration (EDF) technique was employed for the preparation of $CoMo/Al_2O_3$ catalyst by Mo precursor deposition, and the subsequent dry impregnation deposition of Co precursor; these gave rise to the catalysts with higher activity as compared to those prepared by the regular co-EDF and those by the technique of conventional impregnation (Papadopoulou et al. 2003).

The preparation of HDS catalysts can be done by the technique of incipient wetness impregnation of Ni–Mo(W) and Co–Mo(W) species over zirconium-doped siliceous MCM-41 (Rodriguez-Castellon et al. 2008). These catalysts were found to exhibit a very satisfactory activity within the temperature range of 300–340 °C, with conversion yields of 92.6% and 49.0%, respectively, for Ni–Mo(W) and Co–Mo(W). The catalysts promoted with Ni were found to exhibit better performance as compared to those catalysts promoted with Co in the DBT HDS reactions. Other catalysts prepared were Ti-loaded hexagonal mesoporous SBA-15 supported Co/Mo and Ni/Mo catalysts. The use of Ti-loaded SBA-15 material as catalysts support leads to the enhancement of the DDS route in this reaction, thus, more active than those of their Ti-free counterpart (Nava et al. 2007).

Other prepared catalysts reported are the unsupported types, example of such catalysts are the unsupported MoS_2 catalyst reported to have been prepared in situ, under moist condition, through the decomposition of ammonium thiomolybdate. Various characterization techniques were employed to fully characterize this

catalyst, these include; scanning electron microscopy (SEM), XRD, measurements of specific surface area were carried out using BET and BJH etc. The catalytic performance of the catalyst was studied on diesel oils HDS; such oils include LCO, SRGO, light cycle, and straight-run gas oil. Also, further investigation on some refractory sulfur compounds selected in oils was carried out on 4,6-dimethyldibenzothiophene (4,6-DMDBT), dibenzothiophene (DBT), and benzothiophene (BT). The preparation of MoS_2 catalysts was carried out via the decomposition of ammonium thiomolybdate precursor under moist condition in situ, in decalin (Trakarnpruk et al. 2008) as:

$$(NH_4)_2MoS_4 \rightarrow 2NH_3 + H_2S + MoS_2 + S$$
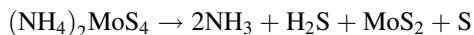
The occurrence of MoS_2 was confirmed by the XRD technique; the XRD pattern shows MoS_2 Phase (JCPDS-ICDD 3701492, 2 θ (Å) = 14 (002), 33 (100), 40 (103), and 58 (110) (Song et al. 2000a, b). The XRD pattern of the catalyst after the HDS reaction shows less crystallinity. Specific surface areas, total pore volume of the in situ prepared MoS_2 are determined using BET. The catalyst prepared in the presence of water shows high surface area of 544 m^2 g^{-1} and pore volume of 1.16 cm^3 g^{-1}. It was proposed that water helps dispersion of the precursor droplets in decalin under agitation (Trakarnpruk and Seentrakoon 2007). Specific surface area, total pore volume as well as elemental analysis (EDX) of the MoS2 catalyst before and after HDS reactions are reported. The surface area and pore volume of the catalyst after HDS reaction decreased considerably to 332 m^2 g^{-1} and 0.63 cm^3 g^{-1}, respectively. This might be attributed to sintering of MoS_2 crystallites. From EDX analysis, it shows the slight decrease of S/Mo ratio from 1.7 to 1.6. However, C/Mo ratio was increased from 5.9 to 7.1, the carbon detected in the catalyst before the HDS comes from decomposition of decalin which was used as solvent. This reveals contribution of decalin in the preparation of MoS_2 catalyst by in situ decomposition of ammonium thiomolybdate. The carbon increased in the catalyst after the HDS is derived from oil. Scanning electron microscopy (SEM) of the MoS_2 catalyst reveals a highly porous and rough surface. The water addition increases dispersion of MoS_2 generated from ammonium thiomolybdate precursor since it is insoluble in oil. The surface of the catalyst after the reaction is less porous.

6   Hydrodesulfurization Reactions

The HDS model compounds' reactions, Fig. 3.5, were carried using CoMo/carbon-supported catalyst and commercial CoMo/alumina support. Two independent reaction routes are possible, the first route start with desulfurization of DBT, and then hydrogenation, and the second requires the hydrogenation of DBT, followed by desulfurization. For all the catalysts studied, the selectivity was close at the same temperature. However, a dramatic change was reported in the preferred mechanistic
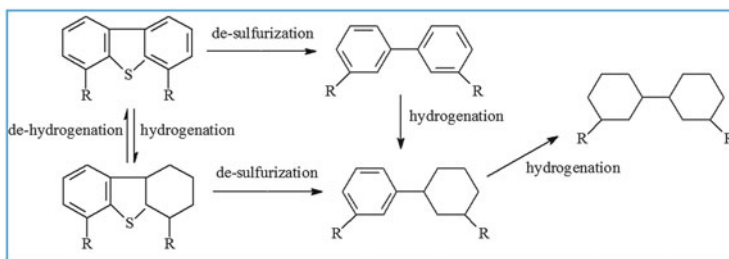
Fig. 3.5 HDS of dibenzothiophenes (DBT and derivatives) (R = H, CH$_3$, or any other alkyl group)

route for desulfurization of 4,6-DMDBT with temperature. At low temperature, the hydrogenative pathway is preferred, while at high temperature direct desulfurization predominates. The catalytic activity of carbon-supported CoMo catalyst was found to be more than that of the analogous alumina-supported catalysts for DBT. The most active preparation method was over three times more active for DBT HDS than a comparable commercial HDS catalyst. The major reason for its higher activity is the higher number of active sites the carbon-supported catalyst is suggested to be on it. Thus, the substrate/catalyst ratio may influence the activity difference of the two catalysts as described above with 4,6-DMDBT. In addition, the narrow pores of the present active carbon (12.5 Å) may have some hindrance on the diffusion of bulky 4,6-DMDBT. Mesoporous carbon of large surface area is an interesting support for heavier feedstocks (Farag et al. 2000).

7 Factors Affecting the Reactions

The influence of changes in the concentrations of polycyclic aromatic compounds, e.g., pyrenes, chrysenes, napthalenes, etc. on the rate of reaction kinetics of deep HDS in a trickle-flow system is negligible within the operating window of existing once. One of the key parameters of reaction rate inhibition in deep HDS is the use of trace amounts viz. within the range of ca. 0–30 ppm of organo-nitrogen compounds. It could be inferred from the reported literature that there is a strong resemblance between the behavior of trace amounts and high concentrations effect of basic organo-nitrogen compounds. An order of −0.15 with respect to basic organo-nitrogen compounds was calculated in commercial gas oil. In the presence of at least 10,000 ppm polycyclic aromatics, trace amounts (viz. ca. 0 ± 30 ppm) of basic organo-nitrogen compounds affects the kinetic rate of the overall HDS reaction in a significant way. It could be deduced from reported literature that the principal role of the basic organo-nitrogen compounds of relatively high concentrations in model feeds resemble closely the key role of trace amounts currently pinpointed in deep HDS of a highly complex mixture, e.g., gas oil. The influence of variations in the

concentration is negligible in bulky polycyclic aromatics, e.g., pyrenes, chrysenes, and naphthalenes (van Looij et al. 1998; Danmaliki and Saleh 2017).

Hydrogen sulfide is another factor that has been reported to have an effect on hydrodesulfurization reactions. Although it is important, it is of secondary importance even in the treatment of raw distillates in HDS. It is well known that hydrogenolysis reactions are more prone to H_2S poisoning as compared to hydrogenation. The HDS of β-DBTs requires hydrogenation which is a crucial step in HDS, while H_2S could assist in the enhancement of the hydrogenation process; this has been an under-acknowledged point in the past. An example of this was seen in the HDS of DBT on CoMo/Al_2O_3 catalyst. The HDS of 4,6-DMDBT over NiMo/C was observed to give a similar result (Sakanishi et al. 2000). This could be attributed to an increment in surface SH groups as a result of the dissociation of H_2S (Topsøe et al. 1996). H_2S modestly inhibits hydrogenation in the HDN of six-membered nitrogen heterocycles, which could improve the scission of C–N bond. The point of emphasis here is that there is less pronounced H_2S inhibiting effect in β-DBTs HDS than in that observed in DBT HDS. This is consistent with the known fact that hydrogenation is more important and hence plays a key role in β-DBTs HDS than hydrogenolysis.

The commercial NiMo/Al_2O_3 was reported to exhibit around three times higher activity than the commercially employed CoMo/Al_2O_3 catalyst in the HDS reaction pathways of 4,6-DMDBT in decalin. Again, this could be attributed to the higher hydrogenation activity of NiMo/Al_2O_3 catalyst as compared to CoMo/Al_2O_3. The low reactivity of 4,6-DMDBT, on the other hand, could be ascribed to steric hindrance. This (steric hindrance) is relieved by aromatic ring hydrogenation and therefore, catalysts with higher hydrogenation potential show better catalytic activity towards 4,6-DMDBT HDS.

Trickle-bed reactors are used to carry out the HDS reaction in refineries. The operating conditions of for these reactors usually requires H_2 gas pressure between 3.0 and 5.0 MPa and a temperature of range 300–450 °C, commonly employing CoMo/Al_2O_3 or NiMo/Al_2O_3 catalysts (Whitehurst et al. 1998; Saleh and Danmaliki 2016b). These severe conditions lead to excessive consumption of hydrogen, hydrogenating the available olefins, as well as decreasing octane rating. Linear or branched thiols referred to as recombinant mercaptans can be formed from the reaction of olefins with H_2S in the reactor under mild HDS conditions, forming typically a chain of 5–12 carbons long. Sulfur is maintained in the product due to the formation of recombinant mercaptans, restricting the HDS process effectiveness. A further extended research in catalysis and process designs of HDS are being carried out to improve the efficiency of sulfur removal, while maintaining the least specification of the fuel quality. For some special systems, e.g., fuel cells, atmospheric pressure is preferably the most suitable condition to carry out HDS reactions. Also, low H_2 to fuel ratio is essentially desirable for such systems to run the HDS reaction since hydrogen is crucial reactant in the fuel cell. In the case of phosphoric acid fuel cell (PAFC) on the other hand, natural gas is the crucial reactant for its operation; hence, the system also adopts HDS. HDS reaction in systems like direct carbonate fuel cell has also been studied. HDS reaction at

atmospheric pressure condition proceeds only via the less effective route; hydrogenolysis and not through the popular hydrogenation (HYD) route which is believed to be the efficient desulfurization route especially for refractory sulfur compounds, e.g., 4,6-DMDBT (Bartsch and Taniellian 1974). These HDS route mechanisms are discussed in coming section. Under certain conditions, temperatures >300 °C and atmospheric pressure, thermodynamic factors tend to limit hydrogenation of aromatic rings. There are a lot of merits, in that the catalysts active sites are usually unoccupied during the hydrogenation of aromatic compounds. Although the presence of aromatics themselves may lead to possible inhibition, this could be possible even in their unhydrogenated form. Great interest is laid on the studies that channels towards determining the optimal conditions, especially the operational pressure for the HDS unit to be applied for various fuel cell systems.

Hydrogen supply is another factor that affects this reaction. The solubility of hydrogen in hydrocarbon solvents swiftly appreciate with temperature raise. Also, the kinematic viscosity of hydrogen is relatively high. Hence, the order of its solubility as a function of solvent structure has a trend which decreases in the following order: hexadecane > bicyclohexyl > tetralin > 1-methylnaphthalene. It has been noticed and reported that the rates HDS 4,6-DMDBT and of DBT increases in the presence of hydrocarbon solvent, e.g., the use of cyclohexane solvent led to better rate enhancement than decaline and much lower rate in the absence of any solvent (Saleh et al. 2017). The HDS of 4,6-DMDBT was observed to experience a more pronounced solvent effect as compared to that of DBT HDS. This observed solvent effect corroborates the argument on hydrogen solubility, in that the solubility has a strong inverse relationship to solvent's specific gravity function, of which diffusivity can be used to justify. The hydrogenation of toluene studied was found to be affected by the effect of solvent. A study was conducted to screen the catalyst in deep HDS, and the variation in the activity of this catalyst in the study was observed to generally diminish with raise in hydrogen pressure. This compression effect could be associated with hydrogen "starvation" since more hydrogenative catalysts would experience more of the effect with fall in hydrogen pressure. At low hydrogen pressure of about 0.79 MPa, desulfurization of LCO with bulk was compared to that which takes place in the presence of a commercial HDS catalyst at 343 °C; the results showed that RuS_2 gave 220 ppmw from 1.47 wt.%, in contrast to 1680 ppmw that was obtained using the commercial catalyst (Ho 2004). This activity of RuS_2 is quite remarkable and could be linked to its structural feature; isotropic cubic. The surface SH groups density may be increased by disulfide $(S–S)^{-2}$ species from the effect of hydrogen cleavage from facile heterolytic. Depending on the structure of catalyst, steric hindrance may tend to become an issue; it appears to be more pronounced in RuS_2 catalysts than those of MoS_2 based having highly anisotropic layered structure. The key remaining question that may come up despite this interesting result is: will hydrogen supply be a problem for 10–15 ppmw sulfur regime at low pressures? The use of supercritical solvents attempted to put an end to the issue potential hydrogen supply (Ackerson and Byars 2000). This approach can best be proven when the rate limiting step is the hydrogen supply at high pressures.

Subsequently, the HDS of 4,6-DEDBT over a sulfided (catalyst A); CoMo/Al$_2$O$_3$-SiO$_2$ was employed to examine some elementary details of deep HDS (Ho 2004).

8 Mechanisms of Hydrodesulfurization in Diesel and Gasoline Fuels

Gasoline, jet fuels, and diesel are the three principal types of transportation fuels which may vary significantly in composition and properties, produced from various refinery streams. The typical sulfur compound types found in liquid fuels and their corresponding refinery streams for fuels are summarized in Table 3.2 (Song et al. 2000a, b). The reactivity ranking is obtained from well-tabulated experimental data and a large pool of literature information. Direct HDS through hydrogenolysis pathway occurs in compounds like disulfides, sulfides, thiols, and tetrahydrothiophene and other sulfur compounds with no structural conjugation between the π-electrons on the aromatic ring moiety and the lone pairs on S atom and the lone pairs on S atom of the compound. Significantly higher HDS reactivity has been shown by these sulfur compounds relative to those of thiophene because the former has weaker C–S bond as well as higher electron density on the S atom. The reactivity of 1- to 3-ring sulfur compounds increases in the order dibenzothiophenes < benzothiophenes < thiophenes (Vasudeven and Fierro 1996). Consequently, thiophenes found in naphtha are relatively far less reactive than the disulfides, sulfides, and thiols as such; in practical high-conversion processes, the latter can be essentially infinitely reactive. Similarly, in gas oils, the reactivity of (alkyl-substituted) sulfur-containing compounds such as 4-methyldibenzothiophene and 4,6-dimethyldibenzothiophene (4,6-DMDBT) are by far low relative to the others (Gates and Topsoe 1997; Kabe et al. 1992). Hence,

Table 3.2 Typical sulfur compounds and corresponding refinery streams for fuels (Song 2003)

Types of sulfur compounds	Refinery streams obtained	Corresponding fuels generated
Mercaptanes, RSH; sulfides, R$_2$S; disulfides, RSSR; thiophene (T) and its alkylated derivatives, benzothiophene	SR-naphtha; FCC naphtha; coker naphtha	Gasoline (BP range: 25–225 °C)
Mercaptanes, RSH; benzothiophene (BT), alkylated benzothiophenes	Kerosene; heavy naphtha; middle distillate	Jet fuel (BP range: 130–300 °C)
Alkylated benzothiophenes; dibenzothiophene (DBT); alkylated dibenzothiophenes	Middle distillate; FCC LCO; coker gas oil	Diesel fuel (BP range: 160–380 °C)
Greater than or equal to three-ring polycyclic sulfur compounds, including DBT, benzonaphthothiophene (BNT), phenanthro [4,5-b,c,d]thiophene (PT), and their alkylated derivatives and naphthothiophenes (NT)	Heavy gas oils; vacuum gas oil; distillation resides	Fuel oils (non-road fuel and heavy oils)
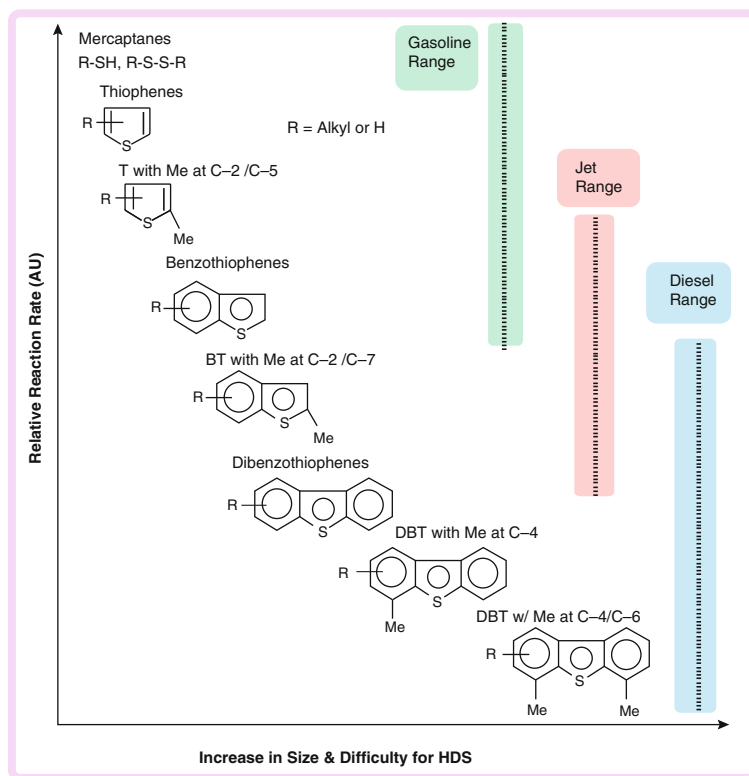
Fig. 3.6 The relationship between reactivity ring sizes and positions of alkyl substitutions on the ring of various organic sulfur compounds in HDS process

in deep HDS, the required conditions are the major factors that affect the transformation of these main methyl-substituted dibenzothiophenes. In 1997, it was reported that catalysts and reaction mechanisms are most appropriately studied using 4-methyldibenzothiophene and 4,6-DMDBT. In general, the most acceptable HDS mechanism for the reaction of DBT and 4,6-DMDBT takes place through two principal pathways, Fig. 3.6 (Song et al. 2000a). The first pathway requires the removal of sulfur in the absence of the aromatic rings abetting; this is otherwise called the hydrogenolysis pathway, while the second pathway on the other hand involves the preferentially hydrogenation of aromatic rings of DBT into 4H- or 6H-DBT intermediates before are finally desulfurized. This pathway is also called the hydrogenation desulfurization (HYD) route (Srivastava 2012).

Co–Mo–S model has for long provided a key basis for strategic developments of catalyst, shown in Fig. 3.7, specifically based in situ characterization techniques. Alumina support, commonly employed in hydrotreatment of catalysts, has the superiority that it allows quite easily a high Co–Mo–S structural dispersion, and in fact, the Co–Mo–S structure may not contain MoS_2 backbone as single MoS_2 layers. Reports based on the previously conducted research also suggested that the

Fig. 3.7 (**a**) Pictorial diagram showing alumina-supported Co–Mo–S, Co, and other Co sulfide structures. (**b**) Ball sphere model of a bulk-truncated, hypothetical simulated hexagonal MoS_2 nanocluster clearly showing the (0001) basal plane (Lauritsen et al. 2007)
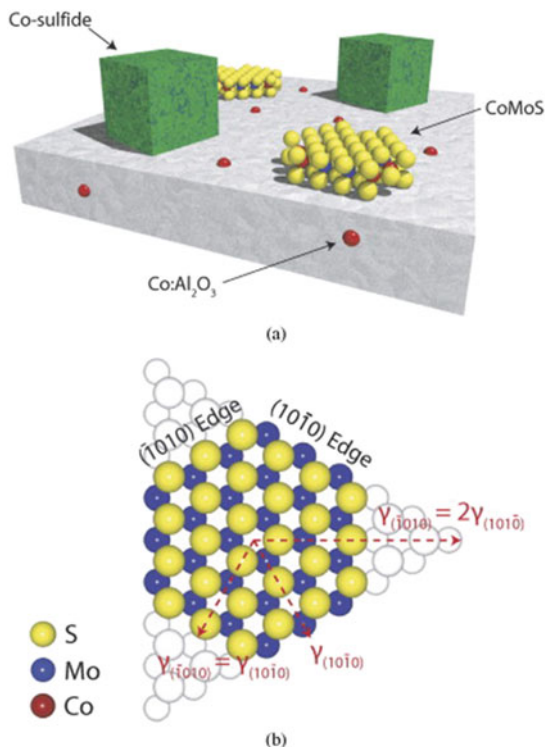
support may contain some of the promoter atoms or as separate promoter sulfide structures. Nevertheless, these are inactive structures, and therefore to avoid their formation, it is essential to have preparation and activation parameters control (Topsøe et al. 1981; Wivel et al. 1981). And because employing the use of alumina support enhances the development of small MoS_2 nanoclusters of high stability, which are usually characterized by high MoS_2 edge sites concentration, this is essential as it accommodates higher quantity of (Co) (Ni) which could be in the active Co–Mo–S (Ni–Mo–S) structure form. The support, in addition to its ability to stabilize small nanoclusters, could also have a direct interaction with the clusters, thereby influencing the intrinsic activity of the Co–Mo–S structures' active sites (Topsøe et al. 1996).

It has been observed that elevating the temperature of the sulfiding process from 400 to 600 °C brings about bond breakage yielding a modified Co–Mo–S structure and alumina as well and were found to have significantly promising per active site activity relative as compared to the lower temperature formed ones. These are referred to as Type II and Type I Co–Mo–S, respectively (Candia et al. 1984). Experimental results have been reported to show that in the structures of Type I category, Mo–O–Al bonds uniquely exist specifically between the Co–Mo–S structures and alumina support, hence, making the Co–Mo–S structure adopt some modified catalytic properties in many ways (Hinnemann et al. 2005). The bond to the support in the low-active Type I may be broken by high-temperature sulfiding,

perhaps transforming into the Type II category which are high active. However, since this method of treatment may as well lead to unplanned sintering as well as subsequent loss of crucial edge sites, it's an undesirable approach of producing Type II structures. There is therefore a need to find alternative methods of preparation; this may involve the addition of some additives or chelating agents, and alone side a weakly interacting support, e.g., carbon (Topsøe et al. 1996). Type II sites containing catalysts may form multi-stack MoS_2 structures, which could just be a side reaction product owing to the presence the very important weak support interactions, for example during hydrogenation reactions, the multi-stacks play an important role as only its top most layer will reveal the special brim sites. While in fact, single block piece of Type II Co–Mo–S structures catalysts could also be produced even for supports like carbon, which is a weakly interacting support, single slab structures may dominate (Carlsson et al. 2004). Other important advances were the possible existence of the structures Ni–Mo–S and Co–Mo–S in both low activity and high activity corresponding to Type I and Type II structures, respectively. However, there are several other atomic level features about Co–Mo–S that are yet to be known and understood, and consequently, for several years, it has been challenging to advance further as more information is required for fundamental understanding of the mechanism, for example, without atomic insight, it's virtually impracticable, to fully understand in great details the sites involved and how they are involved in the HYD and DDS pathways for HDS. Fortunately, more recent advancements in technology have changed this whole idea, and with special techniques like scanning tunneling microscopy (STM), well-resolved atomic images of MoS_2 nanoclusters can be provided (Helveg et al. 2000), Co–Mo–S and Ni–Mo–S (Lauritsen et al. 2007), and direct images of catalytically active edges can be obtained as well. Coupling this technique with DFT calculations (STM-DFT) provides a good avenue to generate electronic structure information, which demonstrate a key role in understanding catalysis and hence, more useful information can be unveiled. The small sulfide clusters may have uncommon sites with metallic-like feature, called "brim sites," located adjacent to the edges and appear bright in the STM images, which reveal a detailed insight into the Co and Ni promoter atom positions in Co–Mo–S and Ni–Mo–S structures. The STM results provide much more detailed insight, revealing the preferential occupation of the promoter atoms in very specific edge sites types, referred to as S-edges. It was also found that different modifications of Co–Mo–S and Ni–Mo–S might as well be present (Lauritsen et al. 2007). It has been shown that a detailed insight in the morphological of catalysts with high surface area can be obtained using high angle annular dark field scanning transmission electron microscopy (HAADF-STEM) (Carlsson et al. 2004). High-resolution electron tomography is another approach that may be used and interestingly, information on the catalyst morphology can be obtained even for the Ni–Mo–S structures consisting of single layers. The Ni–Mo–S crystals were found to exhibit the hexagonally truncated morphology and higher order truncations as well for this catalyst preparation (Lauritsen et al. 2007).

Dibenzothiophenes (DBT) and DBT derivatives substituted especially at the 4- and 4,6- positions of the ring structure are considered one of the most refractory

classes of sulfur compounds in gas oil (Girgis and Gates 1991; Beens and Tijssen 1997). The identification of a novel catalytic routes mechanism for the improvement of the efficiency of hydrodesulfurization of substituted dibenzothiophenes is crucial in achieving deep HDS. Houalla et al. (1980) reported two parallel reaction pathways they suggested for the hydrodesulfurization of DBT:

1. formation of biphenyl by C–S bonds direct hydrogenolysis
2. two steps formation of cyclohexylbenzene via hydrogenation of one of the benzenoid rings followed by their subsequent rapid hydrogenolysis

Several other studies (Houalla et al. 1980; Nagai et al. 1986), in addition to these, suggested that for the hydrogenation and hydrogenolysis transformations, other possible catalytic sites do exist. According to Landau et al., they reported that a higher desulfurization rate was obtained in the hydrogenation of 4,6-dimethyldibenzothiophene (4,6-DMDBT) (Landau et al. 1996). Accordingly, catalysts with higher activity towards hydrogenation also show promising activity in the hydrogenation of 4,6-DMDBT. In spite of that, the hydrogen-to-hydrogen sulfide ratio employed at least 380 Nl/Nl, which swiftly mismatch the standard commercial once-through trickle-flow reactors results: ca. 15–20 Nl/Nl, hence does not suitably serve as representative of a deep HDS. And this is because hydrogen sulfide not only heavily influences the absolute activity of HDS, but also tempers with the relative significance of the competitive hydrogenolysis and hydrogenation pathways, and the relative catalytic activities of the supported NiMo and CoMo catalysts in refractory compounds the hydrodesulfurization, such as 4-MDBT and 4,6-DMDBT (Lamure-Meille et al. 1995): Ma et al. found that at high hydrogen-to-hydrogen sulfide ratios NiMo catalyst has an advantage over a CoMo catalyst when employed in the hydrodesulfurization of 4-MDBT and 4,6-DMDBT; however, the catalysts activities were very much comparable at low hydrogen-to-hydrogen sulfide ratios. Consequently, the question remains open whether the use of NiMo catalyst in deep HDS provides any advantage over a CoMo catalyst at the low hydrogen-to-hydrogen sulfide ratios representative of commercial once-through trickle-flow HDS reactors.

Co-promotion of MoS_2 catalysts forms the Co–Mo–S phase, where (10 10) S-edges of MoS_2 particles assist in the incorporation of Co atoms, leading to the formation of Co–Mo–S edge and significantly varying the structural and hence catalytic properties of the catalyst (Besenbacher et al. 2008). An essential effect of the Co-promotion is that the produced Co–Mo–S equilibrium structure contains inherent sulfur vacancies, which means that at the start of the catalytic cycle, additional sulfur vacancies need not to be formed. The unpromoted S-edge, in contrasts with, Co-promotion ones, requires the creation of vacancies as the first step in a catalytic cycle since it has full S coordination at its equilibrium state. It is important to emphasize that unique coordinatively unsaturated sites (CUS) are available at equilibrium conditions in the Co–Mo–S edge, and for this reason, the catalysis requires no vacancy formation at the initiating step. The situation is very dissimilar in the case of the unpromoted S-edges catalysis, and research findings have stressed the fact that it is very vital to consider that initial vacancy creation and
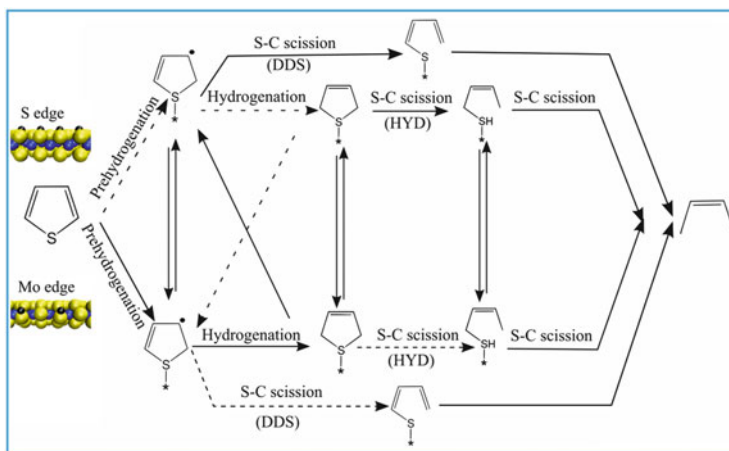
Fig. 3.8 Scheme showing the HDS of thiophene, reactions, and structures involved. Equilibrium structures are shown in atomic structures format at HDS conditions of the (10 10) and the (10 10) edge. The scheme shows an overview of the Co-promoted reactions, (10 10) edge marked with *red lines* and the non-promoted (10 10) edge indicated with *black lines* in the upper part of the scheme and in the lower part the reactions at the non-promoted (10 10) edge and in the middle the possible interactions between the two coexisting edges. The *dotted arrows* denote slow progressing reactions (Moses et al. 2008)

sulfur addition are two possible mechanisms both of which hydrodesulfurization (HDS) reactions can occur. The bright brim is a feature exhibited by Co–Mo–S active sites (Lauritsen et al. 2007) which are quite analogous to brim site of the Mo-edge. Turning to the catalytic activity, Fig. 3.8 provides a scheme showing the HDS of thiophene, reaction pathways, and structures involved, comparing an unpromoted MoS_2 and a promoted Co–Mo–S catalyst. The suitability of the Co–Mo–S edge for both C–S-scission and hydrogenation steps is the main consequence of the Co-promotion, whereas the unpromoted Mo- and S-edges are basically fitted for one of the two. The driving force for intermediates adsorption is thermodynamically controlled to transform from the (unpromoted) Mo-edge to the Co–Mo–S edge and thus, there is a high chance of hydrogenation occurring at both the Mo- and Co–Mo–S edges. The concluding remark here is that Co-promotion improves the catalytic properties of the catalyst towards hydrogenation. C–S-scission barriers are lower for Co–Mo–S than those for the non-promoted Mo-edge, but higher for the non-promoted S-edge. Although with the increasing hydrogenation activity and rise in adsorption energy of thiophene via the direct desulfurization (DDS) pathway, it is expected that Co–Mo–S brim site's activity rises higher than the unpromoted S-edged ones.

In MoS_2-based catalysts catalyzed hydrodesulfurization (HDS) reaction, various basic nitrogen-containing compounds, e.g., pyridine are popularly known to serve as inhibitors for this reaction. The interplay of density functional theory (DFT) calculations together with experimental data from scanning tunneling microscopy

(STM) revealed an atomic-scale insight into the nature of pyridine adsorption on MoS$_2$. Previous IR-spectroscopy and DFT studies were found to be in good agreement with the STM results obtained, which showed that the interaction of pyridine molecule itself with the MoS$_2$ nanoclusters is a very weak one or not even interacting at all. However, a significant adsorption enhancement observed in the presence of hydrogen is present at the MoS$_2$ edges, revealed by STM at the edges showing some adsorbed species. By analyzing the DFT energies obtained from calculation and simulated STM images, it could be concluded that these species are pyridinium ions located at the catalytically active brim sites. In addition to that, the results of DFT calculations for the vibrational modes of the adsorbed pyridinium species were found to agree quite well with those obtained from previously reported IR experiments on alumina-supported MoS$_2$ catalyst of high surface area. There is high level of similarity between these adsorption sites and the brim sites involved in hydrogenation reactions in HDS. Therefore, combining the STM results and DFT calculations reveals a novel atomic-scale insight into the inhibition mechanism of basic N-compounds in HDS and directly observing for the first time, the mode of adsorption of basic nitrogen compounds on the active catalytic MoS$_2$ edges. Furthermore, these results were in full support of the previously reported study correlating the affinity of the N-containing compounds for proton and their strength inhibitions.

The detailed information of the interaction of pyridine molecules at atomic scale with the active catalytic sites on MoS$_2$ nanoclusters has been studied using STM studies and DFT calculations. The pyridine molecules were found to be only adsorbed weakly on the MoS$_2$ edges as revealed by atom-resolved STM. In addition, the presence of SH groups on the edges leads to the observation of other chemisorbed species on the brim sites. These results were compared with DFT calculations and simulated STM images and the species were assigned to the adsorbed pyridinium ions on the brim site edges of the MoS$_2$ nanoclusters. Consequently, these results reveal the first direct observation of pyridinium ions. It was found that pyridinium adsorbed in an inclined fashion on top of the MoS$_2$ nanoclusters on the brim sites was the most suitable binding mode. In addition, there was a very good agreement between frequencies observed from previous IR studies on MoS$_2$/Al$_2$O$_3$ catalysts of high surface area and the calculated ones for pyridine and pyridinium ion. The findings that the peak at IR frequency of 1546 cm^{-1} could be best attributed to pyridinium ion further emphasize that the principal HDS inhibitor for the MoS$_2$ catalyst is not actually pyridine molecule itself, but rather the pyridinium ion. The fact that the previously reported DFT calculations revealed a very satisfactory activation barrier for pyridinium ion formation (Logadottir et al. 2006), in distinction to the experimental IR data gathered, could possibly be related to the effects of catalytic support that were not taken into consideration by the DFT calculations. A twofold effect of the adsorption of pyridinium ion on the sites of Mo-brim edge are known in the overall poisoning process of the HDS catalyst:

- The first adsorption effect is the assisted consumption of adsorbed hydrogen atoms, which could potentially improve hydrogenation reaction step.
- While the second effect is believed to occur due to blockage of the hydrogenation pathway sites by the strongly binded pyridinium species adsorbed on the MoS_2 brim sites.

According to some reported results in the literature, an even stronger poisoning effect were suggested for cyclic nitrogenous compounds heavier than pyridine, due to the more intrinsic delocalized *p*-character they have, van der Waals interaction with the MoS_2 nanoclusters is high promoted, and consequently, binding more strongly to the active catalytic brim sites (Beens and Tijssen 1997; Shih et al. 1992). These compounds also have better proton affinity, qualifying them as stronger inhibitors for the hydrogenation mechanistic pathway. Several other reports suggested that heavier N-cyclic compounds be further studied with Co- or Ni-promoted MoS_2 nanoclusters. In another study, active carbons supported NiMo sulfide (NiMo/C) was used in the desulfurization of 4,6-Dimethyldibenzothiophene 4,6-DMDBT into *n*-decane inside a microautoclave inserted in a sampling apparatus to essentially establish the kinetics and mechanism of hydrodesulfurization HDS by measuring the equilibrium between 4,6-DMDBT and corresponding tetrahydro derivative assisted by a computational curve fitting. At higher temperatures between 340 and 380 °C, regardless of the presence of carbon supports the (NiMo/C) catalysts was shown to exhibit relatively higher activity towards the HDS of 4,6-DMDBT than the commercially established NiMo/alumina catalyst (Sakanishi et al. 2000).

9   Deep Hydrodesulfurization of Diesel and Gasoline Fuels

The increasing rise in the standard for sulfur removal specifications has triggered continuous research for the further improvements in the processes of deep hydrodesulfurization (HDS) technology, of which were mostly carried out using fixed bed reactors. One of the major issues faced in deep desulfurization of diesel fuels is the troubles involved in removing refractory sulfur compounds, especially 4,6-dimethyldibenzothiophene, with conventional hydrodesulfurization processes. This issue engulfing deep HDS is exacerbated by the compounds: H_2S and polyaromatics inhibiting effects and those of nitrogen compounds as well. While on the other hand, selective HDS of thiophene compounds and derivatives with no significant loss of octane number is, in fact, a critical issue for gasoline deep desulfurization. The appropriate octane number can be retained by the isomerization of the paraffinic components of naphtha, as well as by olefinic components preservation in FCC naphtha (Song 2003). A more recent approach reported is the use of slurry reactor hydrodesulfurization (HDS) of diesel, which has proven to be more promising than the one conducted in a fixed bed reactor. This improvement was attributed to the high activity of the catalyst, online catalyst introduction, and elimination, and finally the uniform heating profile, thereby increasing the

efficiency the process. The HDS of straight-run diesel was carried out in a high-pressure autoclave under the following operating conditions: 3–5 MPa of pressure, at a hydrogen flow rate of 0.56–2.77 L min^{-1}, at temperature of 320–360 °C, using a NiMoS/Al$_2$O$_3$ catalyst, with a loading of 4.8–23.1 wt% in the reactor. The rate of reaction was observed to be sensitive to the amount of catalyst used as well as the hydrogen flow rate, pressure, and temperature employed (Deng et al. 2010). A set up was designed to carry out deep desulfurization using a steady-state model as a test plant for a catalytic trickle-bed reactor. This was developed to adequately model the hydrodesulfurization of vacuum gas oil with high sulfur compounds content. Kinetic study was conducted based on the experimental data of the sulfur content of the exit reaction mixture to estimate the kinetic parameters and was found to be in satisfactory agreement with the theoretical data obtained from the model. According to the experiments conducted, while keeping other parameters constant, a rise in pressure and the ratio of H$_2$/CH, as well as a fall in LHSV, enhance the effective removal of sulfur compounds from the gas oil. Also, an improved quality of gas oil product was obtained as shown by the analysis of physico-chemical characteristics of the products relative to the feedstock, such as a decrease in density and viscosity, as well as the increase in cetane index values. Also, the theoretical simulation study was conducted by keeping all other parameters constant and varying parameters such as pressure, the ratio of H$_2$/CH, and the LHSV. It was concluded that many design parameters offer the possibility of accepting the best process conditions for specific feedstock (Sertic-Bionda et al. 2005).

The desulfurization of alkyl-dibenzothiophenes can be achieved in two ways. The first takes place via the through direct extraction of sulfur, producing biphenyl-type products (BP). It is sometimes called the hydrogenolysis path. Hydrogenation is the second desulfurization path, in this approach, prehydrogenation of one of the aromatic rings leads to the formation of cyclohexylbenzene-type products (CHB). The ratio of the rate constants of these two paths is the measure of their relative importance. However, this ratio is not easily obtainable, and for that reason, another term is defined: hydrogenation index (γ), which may be expressed as the ratio of the weight percent of CHB to BP in the desulfurized product, mathematically stated as:

$$\gamma = \frac{\text{Wt.\%CHB in product}}{\text{Wt.\%BP in product}}$$

This definition can be better understood using an example for illustration. When applying the definition to the HDS of 4,6-diethyldibenzothiophene (46DEDBT), γ is the ratio of C4CHB (diethylcyclohexylbenzenes and isomers) to C4BP (diethylbiphenyls and isomers), even though C2CHB compounds such as ethylcyclohexylbenzene and dimethylcyclohexylbenzenes as well as C2BP, e.g., ethylbiphenyl and dimethylbiphenyls are formed as side products (Ho 2004). In a similar way, in 4,6-dimethyldibenzothiophene (46DMDBT) HDS, the ratio of C2CHB to C2BP is simply the γ. It is important to note that it is only reasonable to compare γ for different catalysts at constant HDS. It is only fortunate that, at

constant conditions of temperature and pressure, for highly hindered β-DBTs (e.g., 46DEDBT) at least, γ does not change significantly with space velocity (Ho 2004). Since in general, hydrogenolysis has a considerably higher activation energy relative to hydrogenation (Farag et al. 2000), γ swiftly falls with temperature. And γ on the other hand has a direct proportionality relationship with pressure, and this is because hydrogenation is a stronger dependent on hydrogen pressure (Bataille et al. 2000).

10   Conclusion

Despite the rigorous ongoing research on desulfurization and the considerable attention in some areas of desulfurization like oxidative desulfurization, the use of microbes for sulfur compounds metabolism and selective adsorption, the principal approach to sulfur removal remains the HDS method. Herein, we discussed some important processes of desulfurization technology in oil and gas industries and the various classifications of desulfurization and as well, the forms of hydrodesulfurization of diesel and gasoline fuels which is the focus of the chapter. Also, nanocatalysts design was another aspect that we try to consider, by looking at various catalyst reported for some specific desulfurization process and the conditions they work best in. In addition, doped nanocatalysts preparations was also a topic of interest. Furthermore, an example of hydrodesulfurization reaction was described, where a model example of dibenzothiophene was used, as HDS of thiophene, its derivatives, and closely related compounds are still relevant. Factors generally affecting hydrodesulfurization reactions were also considered. Most importantly, we pointed out some essential mechanisms of hydrodesulfurization in diesel and gasoline fuels, and some of the approaches to deep hydrogenation of diesel and gasoline fuels which provides a cost-efficient alternative to meeting the future specifications of world's environmental agencies regarding sulfur contents; however, it is important to note that more research still needs to be conducted to check for the suitability of future approaches to meet the sulfur limit specifications and address the problems that may hinder their feasibility.

References

Ackerson MD, Byars MS (2000). US Patents, 6,123,835
Andari MK, Abu-Seedo F, Stanislaus A, Qabazard HM (1996) Kinetics of individual sulfur compounds in deep hydrodesulfurization of Kuwait diesel oil. Fuel 75:1664–1670
Babich IV, Moulijn JA (2003) Science and technology of novel processes for deep desulfurization of oil refinery streams: a review. Fuel 82:607–631

Bartsch R, Taniellian C (1974) Hydrodesulfurization: I. Hydrogenolysis of benzothiophene and dibenzothiophene over CoO, MoO$_3$, Al$_2$O$_3$ catalyst. J Catal 35:353–358

Bataille F, Lemberton JL, Michand P, Perot G, Vrinat M, Lemaire M, Schulz E, Breysse M, Kasztelan S (2000) Alkyldibenzothiophenes hydrodesulfurization-promoter effect, reactivity and reaction mechanism. J Catal 191:409

Beens J, Tijssen R (1997) The characterization and quantitation of sulfur-containing compounds in (heavy) middle distillates by LC-GC-FID-SCD. J High Resol Chromatogr 20(3):131–137

Besenbacher F, Brorson M, Clausen BS, Helveg S, Hinnemann B, Kibsgaard J, Lauritsen J, Moses PG, Nørskov JK, Topsøe H (2008) Recent STM, DFT and HAADF-STEM studies of sulfide-based hydrotreating catalysts: insight into mechanistic, structural and particle size effects. Catal Today 130:86–96

Candia R, Clausen BS, Topsøe H (1984) Proceedings of the ninth Iberoamerican symposium on catalysis. Lisbon, Portugal, p 211

Carlsson A, Brorson M, Topsøe H (2004) Morphology of WS$_2$ nanoclusters in WS$_2$/C hydrodesulfurization catalysts revealed by high-angle annular dark-field scanning transmission electron microscopy (HAADF-STEM) imaging. J Catal 227:530–536

Choi KH, Kunisada N, Korai Y, Mochida I, Nakano K (2003) Facil ultra-deep desulfurization of gas oil through two-stage or layer catalyst bed. Catal Today 86:277–286

Cooper BH, Donnis BBL (1996) Aromatic saturation of distillates: an overview. Appl Catal A 137:203–223

Costa PD, Manoli JM, Potvin C (2005) Dje'ga-Mariadassou G deep HDS on doped molybdenum carbides: from probe molecules to real feedstocks. Catal Today 107–108:520–530

Danmaliki GI, Saleh TA (2017) Effects of bimetallic Ce/Fe nanoparticles on the desulfurization of thiophenes using activated carbon. Chem Eng J 307:914–927

Deng Z, Wang T, Wang Z (2010) Hydrodesulfurization of diesel in a slurry reactor. Chem Eng Sci 65:480–486

Farag H, Mochida I, Sakanishi K (2000) Fundamental comparison studies on hydrodesulfurization of dibenzothiophenes over CoMo-based carbon and alumina catalysts. Appl Catal A Gen 194–195:147–157

Gates BC, Topsoe H (1997) Reactivities in deep catalytic hydrodesulfurization: challenges, opportunities, and the importance of 4-methyldibenzothiophene and 4,6-dimethyl-dibenzothiophene. Polyhedron 16:3213

Girgis MJ, Gates BC (1991) Reactivities, reaction networks, and kinetics in high-pressure catalytic hydroprocessing Ind. Eng Chem Res 30(9):2021–2058

Gosselink J, Stork WHJ (1987) Catalyst Deactivation. Chem Eng Process 22:157

Helveg S, Lauritsen JV, Lægsgaard E, Stensgaard I, Nørskov JK, Clausen BS, Topsøe H, Besenbacher F (2000) Atomic-scale structure of single layer MoS$_2$ nanoclusters. Phys Rev Lett 84:951–954

Hinnemann B, Nørskov JK, Topsøe H (2005) A density functional study of the chemical differences between Type I and Type II MoS$_2$-based structures in hydrotreating catalysts. J Phys Chem B 109:2245–2253

Hirschon AS, Wilson RB Jr, Laine RM (1987) Ruthenium promoted hydrodenitrogenation catalysts. Appl Catal 34:311–316

Ho TC (2004) Deep HDS of diesel fuel: chemistry and catalysis. Catal Today 98:3–18

Houalla M, Broderick DH, Sapre AV, Nag NK, de Beer VHJ, Gates BC, Kwart H (1980) Hydrodesulfurization of methyl-substituted dibenzothiophenes catalyzed by sulfided Co-Mo/γ-Al$_2$O$_3$. J Catal 61:523–527

Hubaut R, Altafulla J, Rives A, Scott C (2007) Characterization and HDS activities of mixed Fe–Mo sulphides supported on alumina and carbon. Fuel 86:743–749

Isoda T, Takase Y, Kusakabe K, Morooka S (2000) Changes in desulfurization reactivity of 4,6-dimethyldibenzothiophene by skeletal isomerization using a Ni-supported Y-type zeolite. Energy Fuels 14:585–590

Kabe T, Ishihara A, Tajima H (1992) Hydrodesulfurization of sulfur-containing polyaromatic compounds in light oil. Ind Eng Chem Res 31(6):1577–1580

Kabe T, Qian WH, Ogawa S, Ishihara A (1993) Mechanism of hydrodesulfurization of dibenzothiophene on Co-Mo/Al2O3 and Co/Al2O3 catalyst by the use of radioisotope 35S. J Catal 143:239–248

Kunisada N, Choi KH, Korai Y, Mochida I, Nakano K (2004a) Effective supports to moderate H2S inhibition on cobalt and nickel molybdenum sulfide catalysts in deep desulfurization of gas. Appl Catal A 260:185–190

Kunisada N, Choi KH, Korai Y, Mochida I, Nakano K (2004b) Novel zeolite based support for NiMo sulfide in deep HDS of gas oil. Appl Catal A 269:43–51

Lamure-Meille V, Schulz E, Lemaire M, Vrinat M (1995) Effect of experimental parameters on the relative reactivity of dibenzothiophene and 4-methyldibenzothiophene. Appl Catal A Gen 131(1):143–157

Landau MV, Berger D, Herskowitz M (1996) Chemical and physical characterization of alumina-supported chromia-based catalysts and their activity in dehydrogenation of isobutane. J Catal 158(1):236–250

Lauritsen JV, Kibsgaard J, Olesen GH, Moses PG, Hinnemann B, Helveg S, Nørskov JK, Clausen BS, Topsøe H, Lægsgaard E, Besenbacher F (2007) Location and coordination of promoter atoms in Co- and Ni-promoted MoS2-based hydrotreating catalysts. J Catal 249(2):220–233

Li K, Hou B, Wang L, Cui Y (2014) Application of carbon nanocatalysts in upgrading heavy crude oil assisted with microwave heating. Nano Lett 14:3002–3008

Logadottir A, Moses PG, Hinnemann B, Topsoe NY, Knudsen KG, Topsoe H, Norskov JK (2006) A density functional study of inhibition of the HDS hydrogenation pathway by pyridine, benzene, and H2S on MoS2-based catalysts. Catal Today 111:44

Ma X, Sakanishi K, Mochida I (1994) Hydrodesulfurization reactivities of various sulfur compounds in diesel fuel. Ind Eng Chem Res 33(2):218–222

Ma X, Sakanishi K, Isoda T, Mochida I (1995) Quantum chemical calculation on the desulfurization reactivities of heterocyclic sulfur compounds. Energy Fuel 9:33–37

Mochida I, Sakanishi K, Ma X, Nagao S, Isoda T (1996) Deep hydrodesulfurization of diesel fuel: design of reaction process and catalysts. Catal Today 29:185–189

Moses PG, Hinnemann B, Topsøe H, Nørskov JK (2008) Corrigendum to the hydrogenation and direct desulfurization reaction pathway in thiophene hydrodesulfurization over MoS2 catalysts at realistic conditions: a density functional study. J Catal 260:202–203

Moses PG, Hinnemann B, Topsøe H, Nørskov JK (2009) The effect of co-promotion on MoS2 catalysts for hydrodesulfurization of thiophene: a density functional study. J Catal 268:201–208

Nagai M, Sato T, Aiba A (1986) Poisoning effect of nitrogen compounds on dibenzothiophene hydrodesulfurization on sulfided NiMoAl2O3 catalysts and relation to gas-phase basicity. J Catal 97(1):52–58

Nava R, Ortega RA, Alonso G, Ornelas C, Pawelec B, Fierro JLG (2007) CoMo/Ti-SBA-15 catalysts for dibenzothiophene desulfurization. Catal Today 127:70–84

Ng FTT, Milad IK (2000) Catalytic desulphurization of benzothiophene in an emulsion via in situ generated H2. Appl Catal A 200:243–254

Papadopoulou C, Vakros J, Matralis HK, Kordulis C, Lycourghiotis A (2003) On the relationship between the preparation method and the physicochemical and catalytic properties of the CoMo/γ-Al2O3 hydrodesulfurization catalysts. J Colloid Interface Sci 261:146–153

Pecoraro TA, Chianelli RR (1981) Hydrodesulfurization catalysis by transition metal sulfides. J Catal 67:430–445

Pedernera E, Reimert R, Nguyen NL, van Buren V (2003) Deep desulfurization of middle distillates: process adaptation to oil fractions' compositions. Catal Today 79–80:371–381

Rodriguez-Castellon E, Jimenez-Lopez A, Eliche-Quesada D (2008) Nickel and cobalt promoted tungsten and molybdenum sulfide mesoporous catalysts for hydrodesulfurization. Fuel 87:1195–1206

Sakanishi K, Nagamatsu T, Mochida I, Whitehurst DD (2000) Hydrodesulfurization kinetics and mechanism of 4,6-dimethyldibenzothiophene over NiMo catalyst supported on carbon. J Mol Catal A Chem 155:101–109

Saleh TA, Danmaliki GI (2016a) Influence of acidic and basic treatments of activated carbon derived from waste rubber tires on adsorptive desulfurization of thiophenes. J Taiwan Inst Chem Eng 60:460–468

Saleh TA, Danmaliki GI (2016b) Adsorptive desulfurization of dibenzothiophene from fuels by rubber tyres-derived carbons: kinetics and isotherms evaluation. Process Saf Environ Prot 102:9–19

Saleh TA, Sulaiman KO, AL-Hammadi SA, Dafalla H, Danmaliki GI (2017) Adsorptive desulfurization of thiophene, benzothiophene and dibenzothiophene over activated carbon manganese oxide nanocomposite: with column system evaluation. J Clean Prod 154:401–412

Satterfield CN, Modell M, Mayer JF (1975) Interactions between catalytic hydrodesulfurization of thiophene and hydrodenitrogenation of pyridine. AIChE J 21(6):1100–1107

Schmitz C, Datsevitch L, Jess A (2004) Deep desulfurization of diesel oil: kinetic studies and process-improvement by the use of a two-phase reactor with pre-saturator. Chem Eng Sci 59:2821–2829

Sertic-Bionda T, Gomzi Z, Šaric T (2005) Testing of hydrodesulfurization process in small trickle-bed reactor. Chem Eng J 106:105–110

Shih SS, Mizrahi S, Green LA, Sarli MS (1992) Deep desulfurization of distillates. Ind Eng Chem Res 31(4):1232–1235

Shin S, Yang H, Sakanishi K, Mochida I, Grudoski DA, Shinn JH (2001) Inhibition and deactivation in staged hydrodenitrogenation and hydrodesulfurization of medium cycle oil over NiMoS/Al2O3 catalyst. Appl Catal A 205:101–108

Sie ST (1995) Proceedings of the 210th ASC symposium on deactivation and testing of hydrocarbon-processing catalysts, Chicago, August 20–25, 6

Song C (1999) Designing sulfur-resistant, noble-metal hydrotreating catalysts. Chemtech 29 (3):26–30

Song C (2003) An overview of new approaches to deep desulfurization for ultra-clean gasoline, diesel fuel and jet fuel. Catal Today 86:211–263

Song C, Hsu CS, Mochida I (2000a) Chemistry of diesel fuels. Taylor & Francis, New York, 294 pp

Song C, Yoneyama Y, Kondam MR (2000b) Method for preparing a highly active, unsupported high-surface-area MoS_2 catalyst. U.S. Patent No. 6156693

Srivastava VC (2012) An evaluation of desulfurization technologies for sulfur removal from liquid fuels. RSC Adv 2:759–783

Topsøe H, Clausen BS (1986) Active sites and support effects in hydrodesulfurization catalysts. Appl Catal 25:273–293

Topsøe H, Clausen BS, Candia R, Wivel C, Mørup S (1981) In situ Mössbauer emission spectroscopy studies of unsupported and supported sulfided Co-Mo hydrodesulfurization catalysts: evidence for and nature of a Co-Mo-S phase. J Catal 68:433–452

Topsøe H, Clausen BS, Massoth FE (1996) Hydrotreating catalysis. In: Anderson JR, Boudart M (eds) Catalysis-science and technology, vol 11. Springer, Berlin

Trakarnpruk W, Seentrakoon B (2007) Hydrodesulfurization activity of MoS_2 and bimetallic catalysts prepared by in situ decomposition of thiosalt. Ind Eng Chem Res 46:1874–1882

Trakarnpruk W, Seentrakoon B, Porntangjitlikit S (2008) Hydrodesulfurization of diesel oils by MoS_2 catalyst prepared by in situ decomposition of ammonium thiomolybdate. Silpakorn U Sci Tech J 2(1):7–13

Turaga UT, Song C (2003) MCM-41-supported Co-Mo catalysts for deep hydrodesulfurization of light cycle oil. Catal Today 86:129–140

van Looij F, van der Laan P, Stork WHJ, DiCamillo DJ, Swain J (1998) Key parameters in deep hydrodesulfurization of diesel fuel. Appl Catal A Gen 170:1–12

Vasudeven PT, Fierro JLG (1996) A review of deep hydrodesulfurization catalysis. Catal Rev Sci Eng 38(2):161–188

Venezia AM, Parola VL, Deganello G, Cauzzi D, Leonardi G, Predieri G (2002) Influence of the preparation method on the thiophene HDS activity of silica supported CoMo catalysts. Appl Catal A 229:261–271

Vradman L, Landau MV, Herskowitz M (1999) Deep desulfurization of diesel fuels: kinetic modeling of model compounds in trickle-bed. Catal Today 48:41–48

Whitehurst DD, Isoda I, Mochida I (1998) Present state of the art and future challenges in the hydrodesulfurization of polyaromatic compounds. Adv Catal 42:345–357

Wivel C, Candia R, Clausen BS, Mørup S, Topsøe H (1981) On the catalytic significance of a Co-Mo-S phase in Co-MoAl2O3 hydrodesulfurization catalysts: combined *in situ* Mössbauer emission spectroscopy and activity studies. J Catal 68(2):453–463

Yitzhaki D, Landau MV, Berger D, Herskowitz M (1995) Deep desulfurization of heavy atmospheric gas oil with CoMoAl catalysts effect of sulfur adsorption. Appl Catal A 122:99–110

Chapter 4
Improvement of Hydrodesulfurization Catalysts Based on Insight of Nano Structures and Reaction Mechanisms

Hui Ge, Zegang Qiu, Zhenyu Ge, and Wenpeng Han

Abstract Two-dimensional (2D) layer materials have attracted surging interests since the discovery of the super properties of graphene in 2004. Hydrodesulfurization (HDS) catalysts which contain mainly 2D layer $Mo(W)S_2$ active phases with Co or Ni as promoters thus obtain new development chance. Combining characterization technologies with theory calculations, the catalytic structure, electronic properties, and reaction mechanisms have been largely revealed. These new insight understandings have facilitated the design and fabrication of high-performance HDS catalysts for not only ultra-deep desulfurization but also the quality improvement of different type of fuels. However, this needs the subtle tradeoff among different catalytic properties such as HDS, selective hydrogenation, hydrodenitrogenation, and hydrodearomatics for the achievement of the octane value retaining of gasoline, cetane number improvement of diesel, or polyaromatics saturation of heavy fuels, which still have a lot of technique challenges. The industrial application also requires the effective synergism between process and HDS catalysts.

Keywords 2D MoS_2 • Hydrodesulfurization • Promoters • Alumina • Support interaction

H. Ge (✉) • W. Han
State Key Laboratory of Coal Conversion, Institute of Coal Chemistry, Chinese Academy of Sciences, Taiyuan, Shanxi 030001, PR China
e-mail: gehui@sxicc.ac.cn

Z. Qiu
College of Chemistry and Chemical Engineering, Xi'an University of Petroleum, Xi'an, Shaanxi 710065, PR China

Z. Ge
School of Material Science and Engineering, Shandong University, Jinan, Shandong 250002, PR China

1   Introduction

Hydrodesulfurization (HDS) is one of the most important processes in the refinement of petroleum, by which the sulfur impurity is removed from hydrocarbons. Otherwise, upon fuel combustion, sulfur oxides are emitted, causing harmful sour rain. Although industrial Co(Ni)Mo(W) sulfide catalysts are effective to remove most organosulfur compounds, such as thiol, thioether, thiophenes, benzothiophenes, and dibenzothiophenes (DBT). It remains a tough challenge for HDS of 4,6-dimethyldibenzothiophene (4,6-DMDBT) analogs that have substitutions hindering the adsorption and reaction of sulfur heteroatoms. The situation becomes more serious by the continually increased sulfur content in the crude oils and more stringent sulfur limits for fuel products (Fujikawa et al. 2006). Meanwhile, the refining cost needs to be carefully controlled due to the decreased interests. Thus, catalysts must be effective to achieve ultra-deep desulfurization with affordable cost.

The last two decades have seen major advances in the characterization techniques and theory calculation which have helped us to understand active sites, elementary steps in reaction paths, and the interactions between active phases with supports in the $Mo(W)S_2$-based HDS catalysts. Since Novoselov (2004) discovered monolayer graphene with super properties, there emerges a researching wave to 2D MoS_2 analog materials. The newly acquired knowledge have opened up the way to rationally design and synthesize novel $Mo(W)S_2$-based catalysts for ultra-deep desulfurization of oil streams (Wang et al. 2013).

In this chapter, we review the recently obtained insights on the relation of structures with catalytic properties of HDS sulfide catalysts. And we present how the novel catalysts are designed and synthesized based on these understandings. And then we show that the newly developed catalysts are effectively applied in the ultra-deep desulfurization in petroleum refinement.

2   Relation of Structures of $Mo(W)S_2$-Based Catalysts with Activities

2.1   Structures of Layer $Mo(W)S_2$

$Mo(W)S_2$ materials have the unique "sandwich" structure composed of a metal layer between two sulfide layers. The "sandwich" layers are interacted by the weak Van der Waals forces and atoms in the layer are linked by the strong covalent bond. Thus, the bulk Mo(W) sulfides can be easily exfoliated into single- or few-layered 2D materials, which can be further tuned or assembled to heterostructures (Wang et al. 2015a).

According to the array of sulfur atoms in the layer and the stacking configurations, $Mo(W)S_2$ can form three phases (Fig. 4.1). 2H phase is thermodynamically stable, in which each layer rotate 180° and the layer configure is recovered every other layer. While 3R phase returns original configuration every three layers. Each
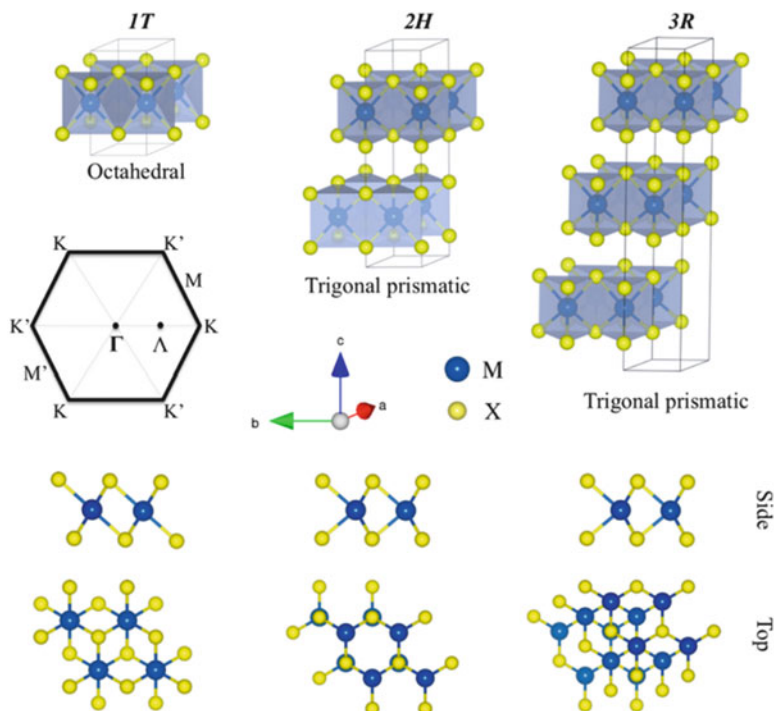
Fig. 4.1 Structure of MoS$_2$. They can crystallize in 1T (tetragonal), 2H (hexagonal), or 3R (rhombohedral) symmetry. The figure also shows the hexagonal Brillouin zone with the high symmetry k points (Reproduced from Heine 2015)

Mo or W atom is coordinated by six sulfur atoms in a trigonal prism for 2H and 3R phases. 1T-MoS$_2$ phase is metastable and six S atoms form a distorted octahedron around one metal atom (Heine 2015). Three phases can be transformed via intralayer or interlayer atomic gliding. For example, with intercalation of Li, 2H-MoS$_2$ can be converted to 1T-MoS$_2$ (Wang et al. 2014), which however gradually transforms back to 2H-MoS$_2$ at room temperature (Jiménez Sandoval et al. 1991).

2.2   Promoting Effect of Co or Ni to the Mo(W)S$_2$ Active Phase

Mo(W)S$_2$-based catalysts usually prepared with Co or Ni as promoters to improve the HDS activities. Topsøe (1981) suggested the so-called Co-Mo-S model where Co is located at the edge of Mo(W)S$_2$ slabs. Lauritsen et al. (2007) indeed observed the Co-Mo-S and Ni-Mo-S structures by STM (Fig. 4.2a–c). And they found that the promoter coordination leads to a morphology transformation from the triangle of unpromoted MoS$_2$ to the distorted hexagon.
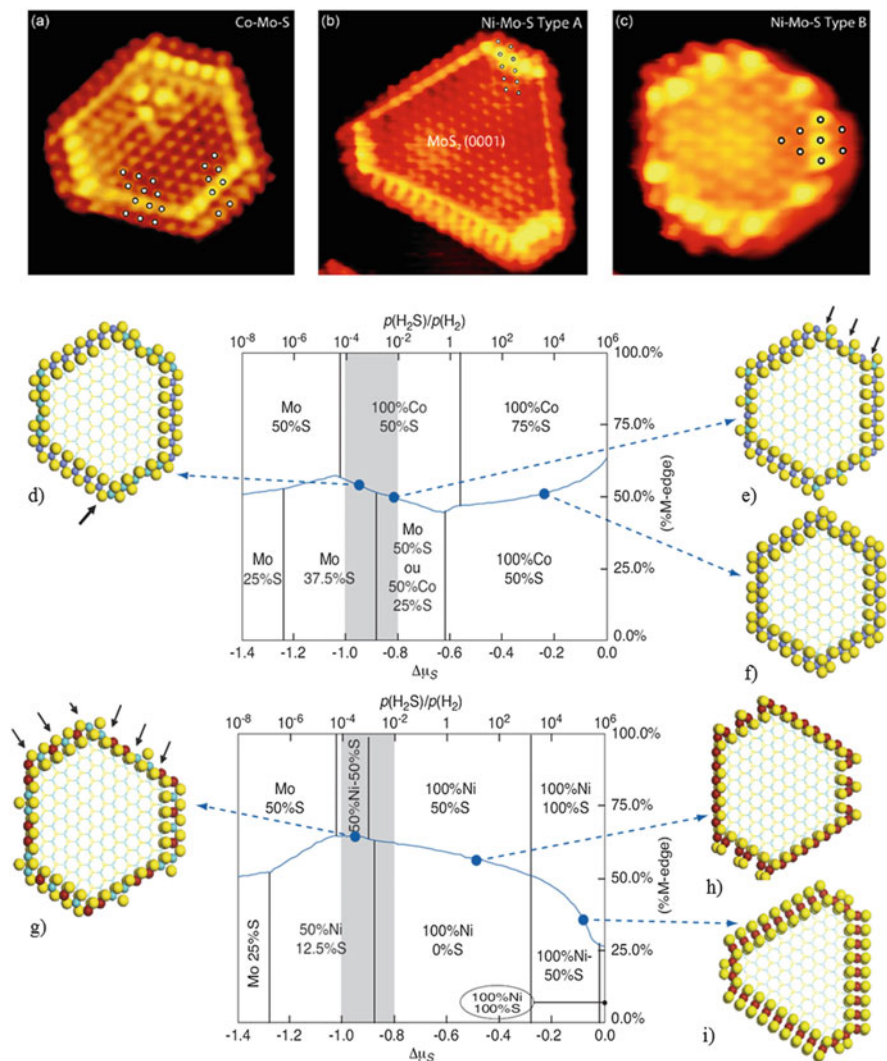
Fig. 4.2 STM images of a hexagonally truncated Co-Mo-S nanocluster (**a**) and Ni-Mo-S (**b, c**) supported on Au (111). Morphology diagrams for the Co-Mo-S (**d–f**) and Ni-Mo-S (**g–i**) nanocluster as a function of $\Delta\mu S$ and $p(H_2S)/p(H_2)$ at $T = 525$ K. The S-edge compositions are reported above the *blue line*, and the Mo-edge compositions are below this line. The *gray* region visualizes the range of usual HDS conditions (Adapted from Lauritsen et al. 2007; Krebs et al. 2009)

Fig. 4.2d–i shows that the equilibrium morphology of Co-Mo-S and Ni-Mo-S nanocluster under HDS conditions is a hexagon and a deformed hexagon, respectively. Ni is located in a square planar environment at both Mo and S edges. The same is true for the mixed Ni-Mo sites. Co is predominantly located in the

tetrahedral environment at the S-edge. However, mixed Co-Mo sites are preferentially located on the Mo-edge. The Co atoms on the edges of MoS_2 crystallites are 4-fold coordinated with either tetrahedral, pseudo-tetrahedral, or square planar structure depending on the sulfur coverage, type of substituted edge (S or Mo), and promotion degree (Castillo-Villalon et al. 2012).

The thermodynamic balance between the stability of promoted sites and promoter segregation effects is mainly driven by S-reductive conditions and can be interpreted by Le Chatelier's principle (Krebs et al. 2008a). Complete promoter segregation occurs under reductive conditions and at high temperature, corresponding to conditions not reached in HDS. Three sulfiding regimes characterized by the chemical potential of sulfur (µS) can be distinguished in Fig 4.2. In the high sulfiding regime (µS $\geq$ −0.25 eV), Co and Ni are stabilized on both edges. In the intermediate regime, i.e., traditional HDS conditions (−1.1 $\leq$ µS $\leq$ −0.25 eV), the selective affinity of the promoters for one type of edge is revealed. In the highly reductive environment (µS $\leq$ −1.1 eV), the mixed phase becomes unstable (Schweiger et al. 2002).

Different from the Co-Mo-S model. Delmon and Froment (1996) suggested the remote control mechanism illustrate the interaction of promoters with MoS_2 crystallites in bulky HDS catalyst. They found that in unsupported $Co(Ni)Mo(W)S_2$ system, the hydrogenation and HDS ability of MoS_2 or WS_2 can be significantly enhanced by the spillover hydrogen which is produced on the NiS_x or CoS_x phase. This synergetic effect is demonstrated by the experiments of stacked bed where the formation of Co-Mo-S phase was physically prohibited (Ojeda et al. 2003).

Ramos et al. (2012) suggested that increase of the contact between MoS_2 and Co_9S_8 improves the HDS activity of bi-component sulfide catalyst. Wang et al. (2016) reported the spillover hydrogen effect between the NiS_x and MoS_2 two phases played an important role on the high HDS performance of unsupported NiMo catalyst with high promoter loading. Villarroel et al. (2008) and Pimerzin et al. (2015) also evidenced that the synergism between Co(Ni) and Mo(W) sulfide phases leads the high catalytic activity of promoted sulfide catalysts.

2.3 Carburization of HDS Catalysts

Using dimethydisulfide (DMDS) instead of H_2/H_2S as sulfiding agent, Hallie (1982) observed that the HDS activity of gas/oil was apparently improved, which was explained by Kelty et al. (2007) as the formation of carbide-like structures at the edge of the active phase. By the analysis of spent HDS catalyst, Breysse et al. (2003) suggested that the "carbide" phase could present in between Co-Mo-S structures. And the cobalt promoter can facilitate the sulfur replacement by carbon at MoS_2 edges. Wen et al. (2006) showed by DFT calculation that carbon atom replacing sulfur atom at the edges of MoS_x cluster is a thermodynamically favored process. However, Tuxen et al. (2011) studied the carbonization of MoS_2-based catalysts by DMDS or dimethylsulfide. They could not observe the formation of carbide type phase. DFT calculation suggested that the carburization at $(Co)MoS_2$ edge by organic sulfiding agent is not favorable.
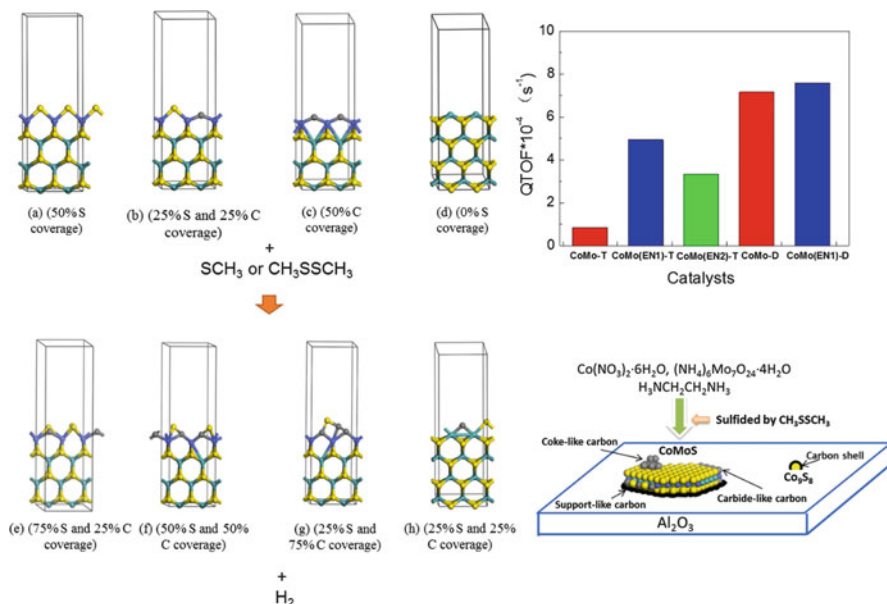
Fig. 4.3 Simultaneous sulfidation and carburization by CH_3S or CH_3SSCH_3 over $CoMo/Al_2O_3$ (Reproduced from Ge et al. 2014)

Recently, a combination of experiments and theory calculation, we carefully analyzed the process of carbonization of CoMo HDS catalyst. We found that the replacement of sulfur atoms at $(Co)MoS_2$ edge by the carbon atoms of DMDS molecule is indeed thermodynamic unfavored (Ge et al. 2014). However, the simultaneous sulfidation and carbidation on the unsaturated edges of $(Co)MoS_x(C_y)$ are possible (Fig. 4.3 and Table 4.1).

Carburization is not limited to the formation of carbide-like structures. Several carbon species may be simultaneously presented on the catalysts in real HDS conditions. Thus, the effect of carburization is usually an additive result of multi-carbon species. The organic chelating agents, such as EN, coordinated with Co^{2+} delays the sulfidation of cobalt promoters and facilitates the formation of Co-Mo-S active structures; on the other hand, the carbonization of chelating agent may coat the Co^{2+} retarding its access to the MoS_2 slabs. Ge et al. (2009) reported that the support-like carbon weakens the interaction between active metals and support which can improve the HDS activity. And coke-like carbon covers the active sites and suppresses the catalytic activity. Glasson et al. (2002) observed a positive effect of carbon bearing CoMo catalysts prepared with the addition of soybean oil for thiophene and crude oil desulfurization. They suggested that carbon deposits isolated the active particles resulting in a high dispersion. Similar positive results were found in CoMo catalyst presulfided by alkylpolysulfides (Alonso et al. 2002) and in MoS_2 catalyst produced by in situ decomposition of $(R_4N)_2MoS_4$ (Alvarez et al. 2004).

Table 4.1 The relative energy (eV) of simultaneous sulfidation and carburization by CH_3S or CH_3SSCH_3

Process	Edge	From	To	CH_3S	CH_3SSCH_3
a to e	S	50% S	75% S and 25% C	1.53	2.88
b to f	S	25% S and 25% C	50% S and 50% C	−0.57	0.78
c to g	S	50% C	25% S and 75% C	−1.65	−0.30
d to h	Mo	0% S	25% S and 25% C	−1.02	0.32

2.4   Interaction of Support with Active Phase

In refining industry, alumina is used almost exclusively as the support of HDS catalyst due to the excellent textural and mechanical properties and relatively low cost. However, the strong interaction between alumina support and metal sulfide phases can lead to the detrimental effect on the catalytic activities.

Hinnemann et al. (2005) revealed the nature and the influence of oxygen linkages between MoS_2-type nanocrystals and alumina support by DFT calculations. They show that oxygen linkages are predominantly present on the sulfur edge with the orientation approximately perpendicular to the MoS_2 sheets. Because Co promoters also present dominantly on the S edge, the formation of linkages compete with the incorporation of Co into the S edge (Byskov et al. 1999). Thus, if the S edge has been saturated with Co, the linkages to the support may not be likely formed. The DFT results also suggest that the oxygen linkages between the MoS_2-type structures and the support are not stable, but once Mo-O-Al linkages are formed, the activation energy for the bond breakage is quite high.

Both the structure and the reactivity of S edges can be severely influenced by the oxygen linkages. Many studies have shown that vacancy formation is a key step in the HDS process. But if existing the Mo-O-Al linkage, the vacancy formation becomes very endothermic. Thus Type I structures, which has a strong interaction between active phase and support, have a lower catalytic activity than Type II structures. And the transformation of Type I to Type II is suggested to associate with the breaking of Mo-O-Al linkages. The adsorption of hydrogen on sulfur edge sites above linkages is only slightly exothermic (−5 kJ/mol) compared to −52 kJ/mol on the S edge sites without linkages. Interestingly, the adsorption of hydrogen on a site neighboring to an edge site with a linkage is significantly more exothermic with −73 kJ/mol. Thus, the hydrogenation reactions can be influenced significantly.

Arrouvel et al. (2005) investigated how the active phase is influenced by different supports under reaction conditions. The coordination of MoS_2 with alumina support depends on the size of the active phase particles. Very small size MoS_2 particles (<15 Å) on γ-Al_2O_3 (110) and (100) surfaces exhibit Mo-O-Al bonds for both Mo- and S-edges. While for larger sizes (>15 Å), H bonds and van der Waals interactions can stabilize the particles parallel to the surface. For anatase-TiO_2 (101) and (001) surfaces, an epitaxial relationship is established between the Mo-edge and the support surfaces with the formation of Mo-O-Ti-S-Mo rings. But this epitaxy is not possible between the S-edge and the TiO_2 surface. The epitaxial MoS_2 clusters create edge-contacted particles in tilted or perpendicular orientations

owing to strong the interaction between the MoS_2 edge and TiO_2 planes. These perpendicularly arrayed MoS_2 particles are more active. Breysse et al. (2003) showed four times enhancement of the HDS activity of anatase-supported MoS_2 catalysts than alumina-supported ones. DFT calculation of adhesion energies of Mo_5CoS_n clusters on the two supports shows that Co promoters suppress the edge anchoring of active phase due to weakened edge interaction. And smaller size particles are stabilized on γ-alumina by the ligand effect of the promoter (Costa et al. 2007). Raybaud (2007) investigated the interface between MoS_x and support using DFT. It was revealed that the surface species and acid-basic properties are quantitatively correlated with the sulfo-reductive conditions (pH_2, pH_2S, pH_2O, and T) and the exposed surface of support. Under HDS conditions, the (110) surface of γ-alumina is highly hydroxylated, and the (001) surface of anatase (TiO_2) is partially hydroxylated and sulfide (Arrouvel 2004). They both present Brønsted sites. On the contrary, neither γ-alumina (100) nor the anatase (101) surfaces are hydrated or sulfided, thus only containing Lewis sites.

2.5 HDS Reaction Mechanism

Thiophene (C_4H_4S) is the main sulfur component in gasoline fuel and has been extensively used to investigate the reactivity and kinetics of HDS reactions (Fig. 4.6). Using the room temperature STM technique, it confirmed that interactions between thiophene molecules and MoS_2 clusters mainly occur at the edge domains. It is revealed that both sulfur vacancies on the edges and the interaction of flat-lying molecules with the "brim" sites are important for HDS reaction (Lauritsen et al. 2004). The desulfurization and the hydrogenation of thiophene may occur at the edge and brim, respectively.

Fig. 4.4d shows the schematic overview of the reaction pathways for thiophene HDS over unpromoted MoS_2 and Co-Mo-S catalysts. Co-promotion makes the Co-Mo-S edge suitable for both hydrogenation and C–S-scission, meanwhile the unpromoted Mo- and S-edges are primarily suited for one of the two. Hydrogenation is suggested to occur at both the Mo-edge and the Co-Mo-S edge. And Co promotors increase the hydrogenation properties of the catalyst. The C-S scission barriers on Co-Mo-S sites are higher than those on the non-promoted S-edge but lower than those on the non-promoted Mo-edge. However, due to the increased hydrogenation activity and adsorption energy of thiophene, the overall activity of the Co-Mo-S site is high. The equilibrium structure of Co-Mo-S has already contained sulfur vacancies. Thus, it is not necessary to form sulfur vacancies during the catalytic cycle. This is contrary to the unpromoted S-edge, which shows full S coordination in an equilibrium state and requires the creation of vacancies in the catalytic cycle.

Valencia et al. (2012) investigated the HDS reaction mechanism by DFT. The full chemical structures in the energetic profile of hydrogenation (HYD) and direct desulfurization (DDS) routes were shown in Fig. 4.5. The DBT-type compounds
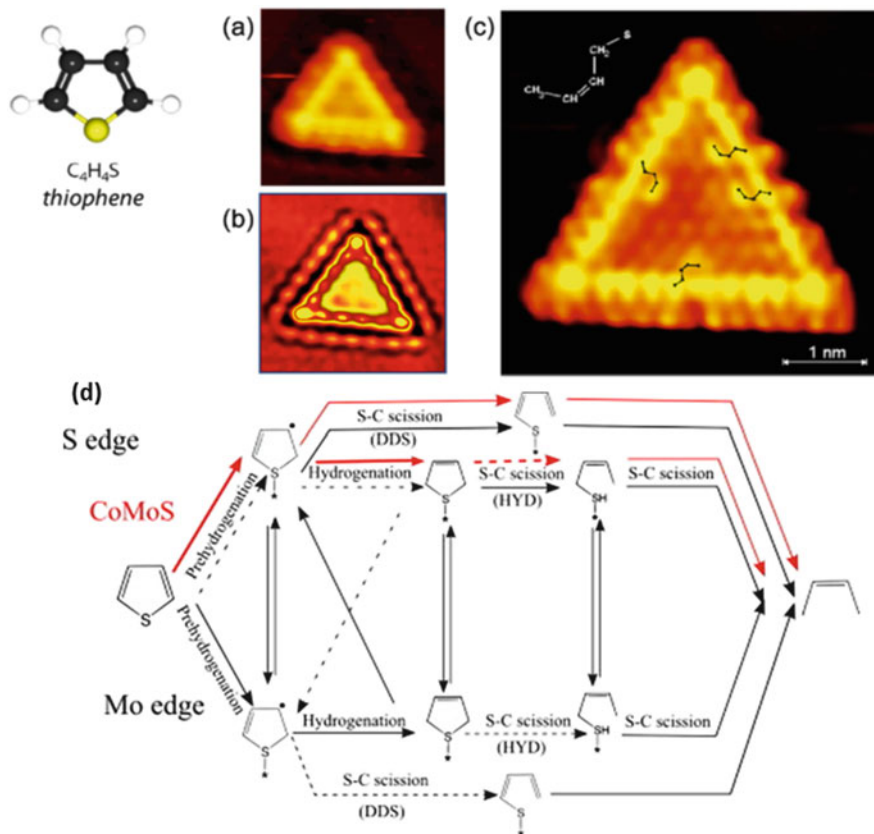
Fig. 4.4 Thiophene adsorption and reaction on unpromoted and Co-promoted MoS$_2$. (**a**) STM images of MoS$_2$ nanoparticle and after exposure to thiophene (**b**) and atomic hydrogen (**c**). (**d**) Schematic overview of the reactions and structures involved in the HDS of thiophene at the (-1010) S edge and the (10-10) Mo edge (Reproduced from Lauritsen and Besenbacher 2015; Moses et al. 2009)

exhibit high stability for both aromatic cycle and C-S bond. However, the HYD reaction route is more favored owing to lower energetic barriers compared with DDS reaction route.

Tuxen et al. (2012) highlighted the role of interactions of DBT with MoS$_2$ and Co-Mo-S for HDS reactions using STM and DFT (Fig. 4.6). The corner sites on the hexagonal CoMoS nanoparticles may play a main role in the DBT desulfurization.

Grønborg et al. (2016) recently revealed how 4,6-DMDBT is desulfurized via the DDS pathway over CoMo catalyst (Fig. 4.7). It is found that the direct chemisorption of the 4,6-DMDBT molecule on the CoMoS nanocluster is only possible at a vacancy in the corner position of the S-edge. But the formation of this vacancy is energetically unfavorable under HDS conditions and can be present only at very low frequency. Thus, 4,6-DMDBT is hard to be desulfurized. Interestingly,

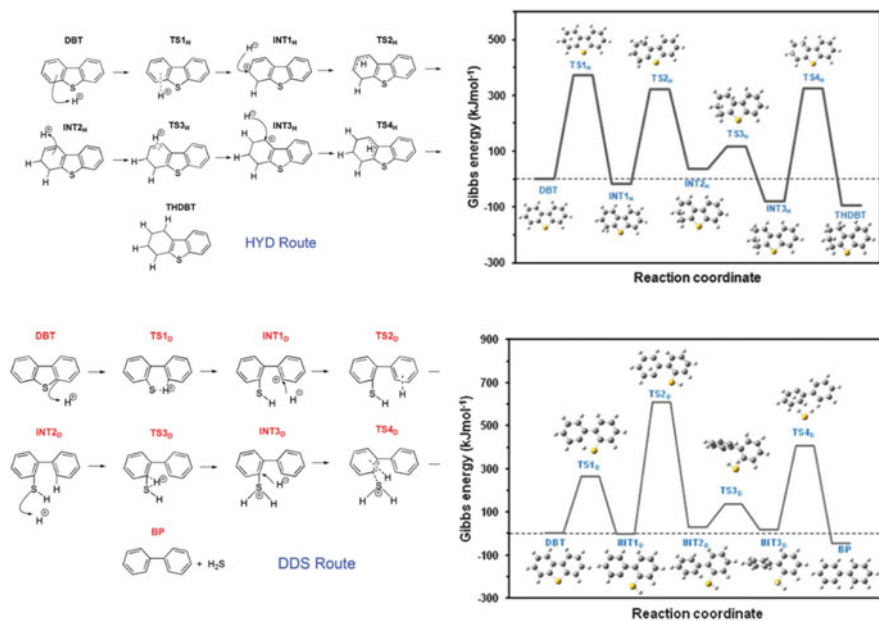**Fig. 4.5** Mechanism of HDS reaction route for DBT-type compounds (Reproduced from Valencia et al. 2012)
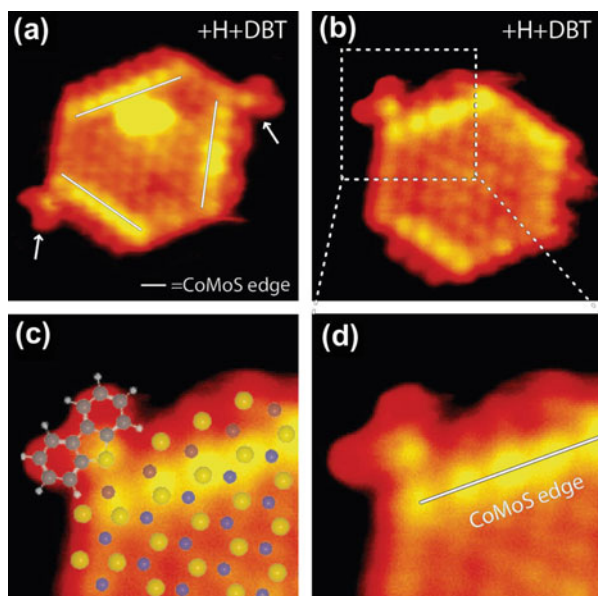

Fig. 4.6 STM images of Co-Mo-S nanoclusters after exposure to atomic hydrogen and subsequent dosing of DBT (Reproduced from Tuxen et al. 2012)
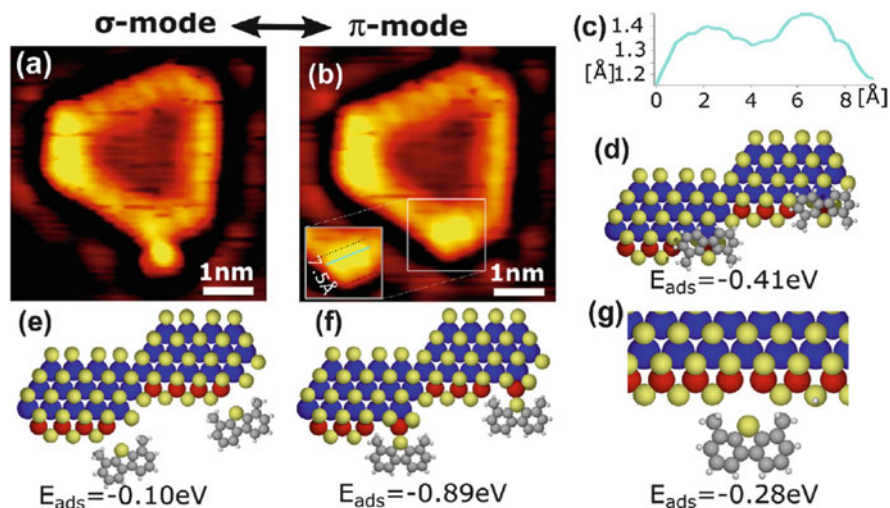
Fig. 4.7 STM image shows the transfer of 4,6-DMDBT adsorption between σ-model (**a**) and π-model (**b**). Line scan along the cyan line shown in the inset of the figure (**b**) revealing structural information (**c**). DFT calculations for 4,6-DMDBT adsorbed on top of a corner S-vacancy in π-mode (**d**), at corner-site without a corner vacancy (**e**) as well as at one corner vacancy (**f**). Ball model showing how the σ-mode is sterically impossible to occur in central corner vacancies (**g**) (Reproduced from Grønborg et al. 2016)

it is found that the σ-adsorption can transform reversibly into a π-like adsorption. This suggests the possibility to alternate between two configurations and between two reaction pathways, namely, on-top brim π-adsorption for HYD and the peripheral σ-chemisorption in cluster corner for DDS. Thus, both hydrogenation and direct desulfurization reactions can occur in the same adsorption process but in different configurations.

3 Design and Synthesis of Nano HDS Catalysts

3.1 Design of HDS Catalyst

The catalytically active phase in promoted catalysts is suggested to be Co(Ni)-Mo-S phase, where Co(Ni) atoms are located on the edges of the MoS_2 particles (Topsøe 2007). Another model, which is less preferred, is the so-called remote control theory (Delmon and Froment 1996).

Candia et al. (1984) found that there are two types of Co-Mo-S phases with distinctly different HDS activities, Co-Mo-S type I and type II, the latter with decreased support interaction exhibited about two times higher activity than the former. It is thus expected that highly active HDS catalysts should compose of highly dispersed Co-Mo-S type II phases. Conventionally, the alumina is used as

the support of HDS catalysts. However, the undesirable very strong metal–support interaction, which results in the type II structures, has urged new supports in order to achieve more efficient HDS reactions.

The surface energies play an essential role in the shape of the catalyst particles, the type of exposed facets, and consequently the catalytic activity. Elizabeth Cervantes-Gaxiola et al. (2013) observed that there is a direct correlation between the surface energies and DBT conversion for Ni-promoted catalysts. The DFT calculation shows surface energies in the sequence of $NiWS_2$ (0.1148 eV/Å^2) $< NiMoS_2$ (0.1221 eV/Å^2) $< NiMoWS_2$ (0.1336 eV/Å^2). The easiness of formation of mixed Mo and W catalyst surfaces is essential to the incorporation of promoter Ni in the active surface sites.

Hydrogenation to aromatics improves the quality of diesel with the increased cetane number. And the hydrogenation to polycyclic aromatics facilitates the hydrocracking of heavy fuels. However, inhibition of hydrogenation of olefins (HYDO) is preferred for gasoline fractions, which can avoid the loss of octane value.

It was observed that incorporating Co into Mo sulfide enhance the HDS activity apparently but has little effect on HYDO activity. This suggests the different active sites for these two reactions. Candia et al. (1984) reported that Type II Co–Mo–S phase with high stacking had better HDS/HYDO selectivity than the Type I Co–Mo–S one. Choi et al. (2004) reported HYDO occurring at the interfacial sites between sulfide phase and alumina support and HDS at the edge vacancies MoS_2 slabs. Mey et al. (2004) observed that addition of alkali reduces the HYDO activity more than the HDS one, which enhances the HDS/HYDO selectivity of CoMo/Al_2O_3. Recent results showed that the dispersion and stacking of supported $NiMoS_2$ crystallites influence the HDS/HYDO selectivity of FCC gasoline more than other factors, such as pore diameter or acidity (Fan et al. 2009). Li et al. (2010) found that longer average slab length of $(Co)MoS_2$ phases shows better HDS/OHY selectivity.

Krebs et al. (2008b) developed a kinetic model based on a Langmuir–Hinshelwood model with 2-methylthiophene (2-MT) and 2,3-dimetylbutyl-2-ene (23DMB2N) competing for the same catalytic active site (Fig. 4.8). It shows that the optimum of the selectivity volcano is shifted to the E(MS) value close to 145 kJ/mol, higher than the optima found for HYDO activities (close to 120–125 kJ/mol, dashed line in Fig. 4.8b). In particular, this model discovers that the CoMoS active phase (E(MS) ~143 kJ/mol) should be more selective than NiMoS (E(MS) ~128 kJ/mol).

Baubet et al. (2016) investigation of the relation of active structure of CoMoS catalysts with HDS activity and olefin hydrogenation selectivity. They observed that the structure of active phase was modified by the change of sulfiding conditions. And the HDS/HYDO selectivity is >2 for all the CoMoS catalysts and increases as a function of the sulfidation temperature (Table 4.2). The increasing HDS/HYDO selectivity is mainly due to the enhancement of the TOF of HDS reaction. And it is found that the HDS/HYDO selectivity can be influenced by the 2D shape driven by the activation-sulfidation conditions of the CoMoS catalyst.

Fig. 4.8 (**a**) Volcano-curves kinetic models of HYDO of 23DMB2N, (**b**) HDS/HYDO selectivity as a function of E (MS) (Reproduced from Krebs et al. 2008a)
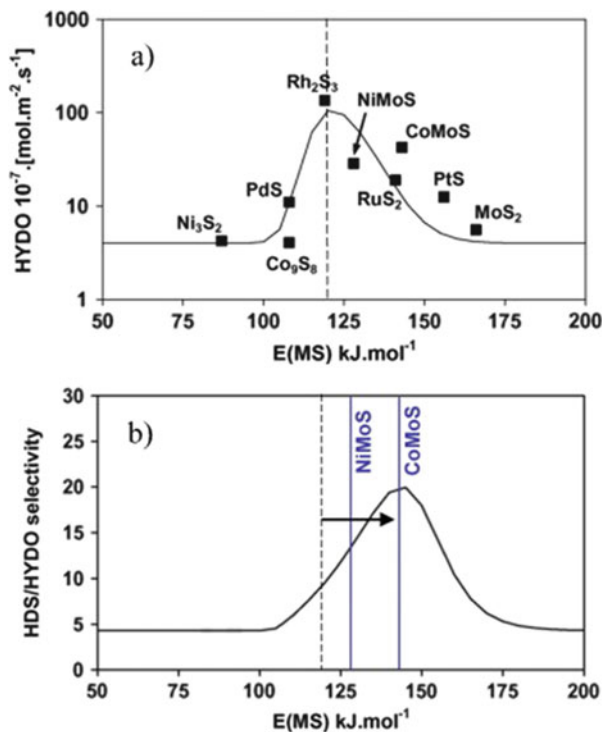
For diesel HDS catalysts, there needs a tradeoff between HYD and DDS functions. Although the HYD sites are preferred because of their intrinsically high activity for desulfurizing hindered DBTs, such as 4,6-DMDBT, they are however very vulnerable to nitrogen inhibition. On the other hand, the DDS sites, notwithstanding their low activity for the HDS of hindered DBTs, have the advantage of being more resistant to nitrogen inhibition.

As shown in Fig. 4.9, the DBT-HDS and 46DEDBT-HDS systems are nearly orthogonal to each other because the former requires a high hydrogenolysis (HYL) selective catalyst, while the latter requires a highly selective catalyst for hydrogenation of aromatics (HYA). For deep HDS, the required catalyst properties are a sufficiently high HYA activity combined with a sufficiently high resistance to N inhibition. Thus, an optimum industrial catalyst system should represent the best possible compromise between the two opposing requirements, represented by the gray area in Fig. 4.9.

Improvement of $Co(Ni)Mo(W)S_2$ catalysts for HDS of oil streams is a complicated process. Many parameters are necessary to consider (Fig. 4.10). Sufficient formation of Co(Ni)-Mo(W)-S active phases is usually pre-required for the ultra-deep HDS. Support properties determine the diffusion of feed and products influencing the kinetics of reactions. And they determine the formation of type I or II active phases. Additives modify support interaction and acid-base properties.

Table 4.2 HYDO and HDS rate constants (k and k')[a] and selectivity (S) of CoMoS/Al$_2$O$_3$ catalysts to 23DMB2N and 3-MT, as a function of the sulfidation conditions

	H$_2$S 250 °C	H$_2$S 350 °C	H$_2$S 400 °C	H$_2$S 475 °C	H$_2$S 550 °C	H$_2$S 625 °C	H$_2$S 700 °C	H$_2$S/H$_2$ 550 °C
k_{HDS}	1.04	1.06	0.98	2.14	2.18	1.68	0.71	1.52
k_{HYD}	0.36	0.36	0.32	0.44	0.34	0.19	0.07	0.50
S	2.89	2.94	3.06	4.86	6.41	8.84	10.14	3.04
2D shape*	nc	nc						
n $_{S-edge}$*	nc	nc	0.196	0.250	0.264	0.162	0.118	0.259
n $_{M-edge}$*	nc	nc	0.535	0.444	0.324	0.138	0.069	0.501
n $_{edge}$*	nc	nc	0.731	0.694	0.588	0.300	0.189	0.759
k'_{HDS}	nc	nc	1.34	3.08	3.71	5.60	3.76	2.00
k'_{HYD}	nc	nc	0.44	0.63	0.58	0.63	0.37	0.66

[a]Rate constant k is given in units of h^{-1} and rate constant k' is given in terms of h^{-1} mmol^{-1}; k' is normalized by the number of edge sites (expressed in mmol)
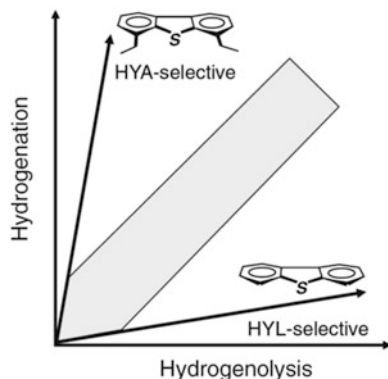
Fig. 4.9 Desired catalysts for diesel HDS lie inside the gray area that represents the optimum compromise between two opposing requirements (Ho and Qiao 2010)
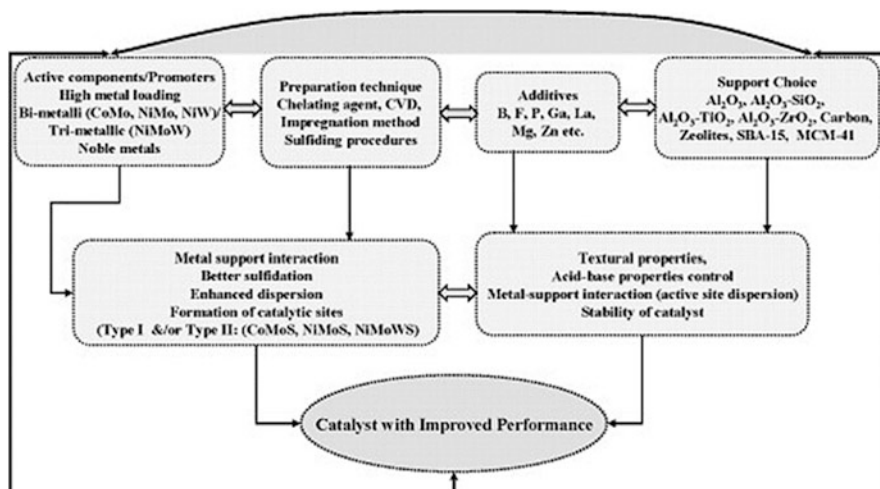
Fig. 4.10 Catalyst components and their key role to the HDS catalyst: a concept of acid-base supported catalyst (Reproduced from Stanislaus et al. 2010)

Preparation method and preparing parameters in the large extent determined the active structures and the final catalytic performance of HDS catalysts.

3.2   Synthesis of HDS catalysts

In the conventional impregnation method, the $Mo(W)S_2$-based active phases are generally yielded by sulfiding oxidic precursors which have been in advance prepared through three steps, e.g., impregnation on an alumina support, drying,

and calcination. The addition of chelating agents in the catalyst preparation is an effective way to improve catalytic activity. Many chelating ligands such as citric acid, nitrilotriacetic acid, glycol, 1,2-cyclohexanediamine-tetraaceticacid, ethylene diamine tetraacetic acid, and ethylene diamine have been used in preparation of HDS catalysts and evidenced to have a positive effect with proper contents (Lélias et al. 2010; Rana et al. 2007; Sun et al. 2003). To avoid the decomposition of a chelating agent, the obtained catalyst is usually free from calcination (Pashigreva et al. 2010).

It reveals that the usage of chelating agents increases the sulfidation temperature of promoters by the formation of thermally stabilized complexes. This facilitates the selective location of Co or Ni atoms on the edge sites of preformed MoS_2 particles to form the Co(Ni)-Mo-S structure and thus decrease the formation of separate Co or Ni sulfide particles, part of which may block the active sites of the catalyst.

The addition of P, B, and F change the acidity and support interaction of HDS catalysts. Phosphorus and boron increase the support acidity, weaken the interaction between Mo and Al, and enhance the Co decoration on the edge sites of MoS_2 particles. They can also increase the Mo and Co dispersion so as to improve the HDS activity (Rashidi et al. 2013). CO adsorption shows that the electron deficiency of the CoMoS sites increases with boron content. The hydrodenitrogenation (HDN) activity is strongly improved owing to the acidity enhancement. Meanwhile, for HDS, the extent of the beneficial effect of boron is smaller and limited to the boron addition smaller than 0.6 wt%. Increasing the support acidity enhances mainly the catalytic performances for the hydrogenation routes (Chen et al. 2013a).

Cosmo Oil Co., Ltd. developed highly active CoMo HDS catalyst, C-606A, for the production of ultra-low sulfur diesel fuels. The preparation method involves impregnation of the support with a solution containing $CoCO_3$, MoO_3, citric acid, and phosphoric acid, and air-drying without calcination. The commercial operation has demonstrated the excellent activity and stability of C-606A under industrial operating conditions (Fujikawa 2009).

Now alumina is still the most widely used support in preparation of HDS catalysts. Various nano-porous alumina has been synthesized with novel preparing methods. Wang et al. (2015b) synthesized hierarchy porous Al_2O_3 support by the "pH swinging" method. Pseudo-boehmite is synthesized with the pH value swinging between 10 and 2 with the alternative addition of sodium aluminate and aluminum nitrate at 45 °C. The prepared pseudo-boehmite was dried and calcined to obtain the alumina support. The pore sizes and pore distributions can be modified with pH swinging frequencies. CoMo catalyst using this alumina support with tri-modal pore distribution improved the HDS of FCC gasoline.

A hard-template method using polystyrene (PS) microbeads is a prospective technique for the preparation of hierarchical macro/mesoporous materials. The alumina support synthesized by this approach exhibited a bimodal pore size distribution of 9 nm mesopores and 250 nm macropores (Fig. 4.11). Compared with template-free method, the PS template increased the pore volume by 2.5 times and the specific surface area by 20%. The strong macroporous texture reduced the
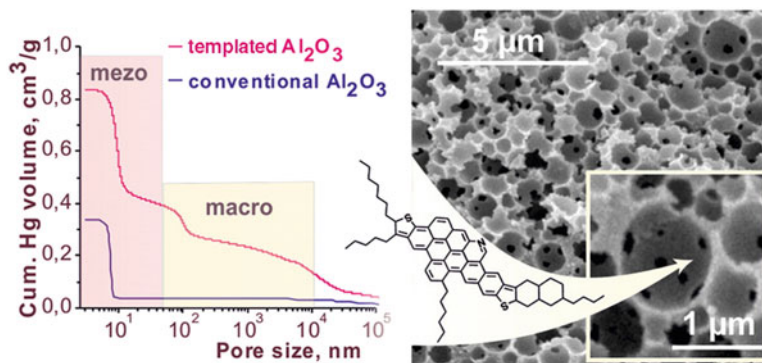
Fig. 4.11 A pair of mesoporous and hierarchical macro/mesoporous alumina-supported catalysts having distinct textural parameters have been chosen to elucidate the effect of texture on activity in HDS and hydride metal (HDM) of heavy tar oil possessing extremely high viscosity and sulfur content (Semeykina et al. 2016)

catalyst plugging during HDS of heavy tar. And the templated catalyst resulted in 56% higher HDS conversion that could be accounted for reducing diffusion limitations and increasing the availability of active sites (Semeykina et al. 2016).

Rashidi et al. (2010) prepared nanorod-like mesoporous γ-alumina by a surfactant-templating free sol-gel technique where aluminum isopropoxide was used as a precursor with ethanol, 2-propanol, or 2-butanol as solvents and sulfuric or hydrochloric acid as peptizing agents. The mesoporous alumina is a high surface area, large size, cylindrical pore shape, and high pore volume possessing an acidic texture and surface defects. These properties facilitate the Mo and Co dispersion and formation of the Type II Co–Mo–S phase, thus greatly enhancing the HDS activity.

Many other supports based on mixed oxides and zeolites have also been developed. La Parola et al. (2004) investigated CoMo catalysts supported on sol-gel prepared SiO_2-Al_2O_3 oxides with different Al/Si ratio. They reported that a maximum of activity was achieved for the mixed support in correspondence of Al/Si $\approx$ 2. The different strength and polarizability of Mo-O-Al or Mo-O-Si links are suggested responsible for the improved dispersion and reducibility of the Mo. For the mechanically mixed support of Al_2O_3 and SiO_2, the amount of SiO_2 modifies textural, acidity, and electronic properties of active phases. Increasing the SiO_2 content in the support decreased the interaction of the Mo and Ni phases with the support significantly influencing their dispersion. High SiO_2 content produced larger crystallites of MoS_2 (Leyva et al. 2012).

Sintarako et al. (2015) investigated the effect of ZrO_2 as a secondary support on DBT HDS activity over CoMo/Al_2O_3 catalysts. They found that ZrO_2 suppressed the inhibition of pyridine on the HDS activity of CoMo/Al_2O_3-based catalyst. CoMo/Al_2O_3-ZrO_2 catalyst with 10 wt% of ZrO_2 shown the best HDS performance which is ascribed to the decrease of the total amount of acid sites on CoMo/Al_2O_3-ZrO_2.

Mohanty et al. (2012) synthesized meso-structured alumina-silicate materials from ZSM-5 nanoclusters and used as catalysts support. The alumino-silicate materials exhibited different acid strength and textural properties depending on the time of hydrothermal treatment of the zeolite seeds. Synthesis with short treating time (4 h) showed properties similar to Al-SBA-15, whereas resembled ZSM-5 with 24 h long seeding time. The EXAFS study revealed that the highest sulfidation was achieved for the NiMo catalyst supported on mesoporous alumino-silicate synthesized from ZSM-5 seeds with 16 h of hydrothermal treatment, which gave higher HDS and hydrodenitrogenation (HDN) of light gas oil than NiMo/γ Al$_2$O$_3$.

Wan et al. (2010) prepared NiW catalysts supported on γ-Al$_2$O$_3$-MB-TiO$_2$ (denoted as AMBT) composites in which zeolite MB was synthesized from kaolin mineral. The characterization results showed that the additions of MB and TiO$_2$ reduced the interaction between the metal components and the composite support. And the overall acidity of the NiW catalysts was tuned by the incorporation of MB into the support. The high HDS activity of NiW/AMBT catalyst was attributed to the enhanced hydrogenation activity.

Gao et al. (2015) synthesized a series of ultra-small EMT and nano-sized EMT zeolites by a template-free system, and the micrometer-sized EMT, EMT/FAU, and FAU zeolites using 18-crown-6 as structure directing agent. CoMo catalysts using zeolite-incorporated alumina support exhibited high specific surface areas and pore volumes. Among the EMT zeolites involved catalysts, the micrometer-sized EMT-incorporated CoMo catalyst showed the highest HDS efficiency, but with the greatest loss of octane number due to the excessive olefin saturation. The EMT/FAU-incorporated CoMo catalysts possessed the suitable B and L acidity sites and excellent pore structures which made a good balance among HDS, hydroisomerization, and aromatization activities.

Heteropolyanions (HPA) have been used as precursors for preparing Mo or W HDS catalysts. The current attention was mainly focused on Keggin (Romero-Galarza et al. 2011) and Anderson (Palcheva et al. 2010) types HPA. These HPA were comprising edge-sharing octahedral Mo(W)O$_x$ surrounding a heteroatom. Waugh-type is another HPA, in which the Ni and the Mo atoms can be included in a single molecular entity. It features three triplets of Mo$_3$O$_{13}$ edge-sharing molybdenum octahedra condensation surrounding a central nickel atom. Cationic exchange of the ammonium cation in Waugh-type NiMo HPA with Ni^{2+} can give a Ni/Mo ratio of 0.45, which was very close to the optimal Ni/Mo = 0.5 reported for conventionally prepared HDS catalysts (Liang et al. 2014).

Ben Tayeb et al. (2010) deposited the W and Ni in the same entity of HPA on an amorphous silica–alumina support by incipient wetness impregnation. The best catalytic result was obtained over the catalyst based on the Ni$_4$SiW$_{11}$O$_{39}$ precursor, which was 30% more hydrogenating. This catalyst with the high Ni/W ratio allowed by the HPA salt stoichiometry has the better Ni promoting effect. And a good dispersion was also obtained.

Use of the cobalt salt of the HPA [Co$_2$Mo$_{10}$O$_{38}$H$_4$]$^{6-}$ for the preparation of CoMo HDS catalysts supported on Al$_2$O$_3$, TiO$_2$, and ZrO$_2$ shows that this cobalt

salt HPA leads to higher dispersion and higher promoting effect (Mazurelle et al. 2008). A close interaction between Co and Mo in the final catalyst can be achieved by impregnating Co-Mo HPA precursors (Martin et al. 2005).

Alsalme et al. (2016) prepared NiMo/SiO$_2$ HDS catalyst through the HPA route using Keggin type phosphomolybdates. The pre-catalyst retains intact Keggin structure of phosphomolybdic polyoxometalate possessing Brønsted and Lewis acidity. During in situ sufidation, the oxidic pre-catalysts transform into an active sulfidic phase with the loss of Keggin structure and catalyst acidity. And it shows higher thiophene conversion and higher butene selectivity than conventional industrial NiMo/Al$_2$O$_3$ catalyst with similar Mo loading.

North et al. (2015) fabricated bulk and supported Mo- and W-based catalysts containing Co or Ni as promoters and phosphorus as a modifier through the PHA route using Keggin type phosphomolybdates and phosphotungstates. Catalyst activity of thiophene HDS increases in the order of supports: SiO$_2$ < TiO$_2$ < γ-Al$_2$O$_3$. And CoMoP/γ-Al$_2$O$_3$ catalyst shows higher HDS activity and butene selectivity than the industrial catalyst of comparable composition.

Coelho et al. (2015) synthesized unsupported CoMgMoAl catalysts from CoMgAl-terephthalate layered double hydroxides which were prepared by ion exchange with ammonium heptamolybdate, followed by calcination at 723 K. The catalysts were sulfided in situ and subsequently tested in simultaneous thiophene HDS and cyclohexene hydrogenation (OHYD). Both the HDS and the OHYD activities of the catalysts increased with increasing Mg content, possibly due to improved Co/Mo ratio. And the HDS selectivity of the most active catalysts was higher than that of a commercial alumina-supported CoMo catalyst.

Højholt et al. (2011) developed a new approach for preparing bifunctional HDS catalysts by ion-exchanging CoMo$_6$ HPA onto the functionalized mesopore surface of a ZSM-5 zeolite. The obtained bifunctional catalyst displayed a significantly higher activity compared to the impregnated counterpart. The difference in HDS activity is attributed to an improved dispersion of the metals throughout the zeolite support, as illustrated in Fig. 4.12. Combining the intrinsic properties of the zeolites, such as acidity and size-selectivity, with the possibility to anchor catalytically active metal clusters in the close vicinity of these acid sites creates the novel type of bifunctional zeolite catalyst.

Hydrothermal synthesis using water or organic solvents can produce highly active nano-sized Mo-based sulfide particles. Yoosuk et al. (2010) prepared unsupported NiMo sulfide catalysts from ammonium tetrathiomolybdate and nickel nitrate by a hydrothermal synthesis method. The activity of these catalysts in the simultaneous HDS of DBT and 4,6-DMDBT is higher compared to that of the commercial NiMo/Al$_2$O$_3$ sulfide catalysts. Meanwhile, the unsupported NiMo sulfide catalysts showed higher activity for HYD pathway than the DDS pathway in the HDS of both DBT and 4,6-DMDBT. Higher temperature and higher H$_2$ pressure and addition of organic solvent increased the HDS activity. Higher preparation temperature increased HYD selectivity. The optimal Ni/(Mo+Ni) ratio for the NiMo sulfide catalyst was 0.5, higher than that for the conventional Al$_2$O$_3$-
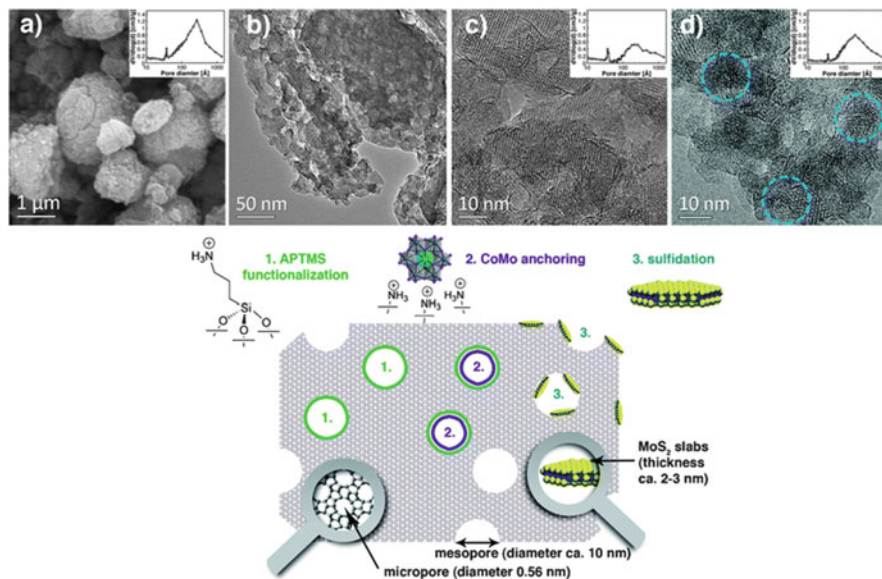
Fig. 4.12 Schematic illustration of the functionalization and anchoring of CoMo on hierarchical ZSM-5 with (**a**) SEM image of the parent hierarchical ZSM-5, (**b**) and (**c**) TEM images of the spent anchored catalyst, (**d**) TEM image of spent impregnated catalyst. The insets in a, c, and d part show the pore size distributions (Reproduced from Højholt et al. 2011)

supported NiMo sulfide catalysts. This was attributed to the high dispersion of the active species and more active NiMoS generated.

Lai et al. (2016a) synthesized uniform 3D NiMoS nanoflowers with self-assembled nanosheets *via* a simple hydrothermal growth method using elemental sulfur as sulfur sources. The HRTEM results indicate that the curve/short MoS_2 slabs on the nanosheets possess dislocations, distortions, and discontinuity, producing more Ni-Mo-S edge sites. The NiMoS nanoflower catalysts exhibited an excellent HDS activity for thiophene and 4,6-DMDBT. Liu et al. (2016) used a facile one-pot evaporation-induced self-assembly method to synthesize ordered mesoporous NiMo-Al_2O_3 catalysts with P123 as a structure-directing agent and anhydrous ethanol as solvent, which presented high HDS activities of DBT. By the hydrothermal method, Li et al. (2016) obtained a higher stacking layer number of $MoS_{2\pm x}$, where the S/Mo atomic ratio was controlled by adjusting the concentration of S and Mo precursors. It was observed that the catalysts with lower S/Mo ratio show a higher HDS/HYDO selectivity of gasoline due to larger sulfide crystallites exposed lower corner sites.

Hadj-Aissa et al. (2016) prepared $Co_9S_8@MoS_2$ unsupported catalysts by a solution reaction in ethylene glycol using cobalt sulfide seeds. The core-shell hybrid catalysts show high activity in HDS with an exceptionally high thermal stability. The catalytic sites takes place at the interface between the cobalt sulfide crystallites and the stacks of MoS_2 slabs. It is consistent with the NiWS system with nickel

sulfide covered with bent WS_2 slabs, where the active centers are located at the interface between nickel sulfide and WS_2 slabs (Le et al. 2008).

Shan et al. (2015) reported W-based hybrid nanocrystals as a precursor to prepare NiW/Al_2O_3 catalysts showing highly selective HDS performance of FCC naphtha. Singh et al. (2016a) synthesized ultra-small NiMo oxide nanoclusters ($\sim$2 nm) by colloidal synthesis using oleic acid and oleylamine as ligands, followed by incorporation of nanoclusters into the pores of γ-Al_2O_3 and calcination. Compared to the catalyst using wet impregnation method, the nanoclusters prepared sulfide catalyst showed enhanced catalytic activity for the DBT HDS. Using the same procedure, Co-promoted MoO_3 nanoclusters supported over γ-Al_2O_3 possessing increased Mo edge atoms presented improved HDS performance (Singh et al. 2016b).

Scott et al. (2015) prepared NiMoS nanoparticles of 100 nm with crystallite sizes 3–5 nm by precipitation from micro emulsions. These particles show good HDS conversion (50%) of a vacuum as oil, as well as an enhanced HDN activity compared to the $NiMo/Al_2O_3$ catalyst.

Gonzalez-Cortes et al. (2014) synthesized γ-alumina-supported NiMoW catalyst via the impregnation solution-based combustion method using urea as fuel for deep hydrotreating. This preparing method avoids the formation of $Al_2(MoO_4)_3$, $NiMoO_4$ or $NiWO_4$, instead of that it facilitates a strong interaction of NiO with MeOx species that could enhance the promoter effect of Ni on the edges of Mo (and/or W) sulfide. The presence of tungsten in the NiMo catalyst selectively enhances the HDS reaction rates through the hydrogenation pathway. This is attributed to the type II Ni-(Mo/W)-S structures and a combination of Ni, Mo, and W.

Recent years, ordered mesoporous materials have been extensively investigated as the support of HDS catalysts (Garg et al. 2008). The mesoporous supports can be coarsely classified as 2D channels, such as MCM-41, SBA-15, and HMS, and 3D channels, such as MCM-48, SBA-16, KIT-6, and FDU-12 (Fan et al. 2009). When the active phases are incorporated into the pores of the meso-porous support, their structural and electronic properties will be tuned by the confining effect of the pore size, as well as support interaction.

Zepeda et al. (2014) investigated the effect of Al and P additives in NiMo/HMS catalysts on HDS activity of thiophene and 4,6-DMDBT. It was found that NiMo/Al-HMS-P catalysts containing 1.0 wt% of P exhibited the best performance in both HDS reactions as a consequence of the proper balance between the active phase dispersion and hydrogenation ability.

Tang et al. (2013) introduced the Co and Mo into the mesopores and micropores of mordenite nanofibers. This CoMo catalyst exhibited an unprecedented high activity (99.1%) as well as very good catalyst stability in the HDS of 4,6-DMDBT compared with a conventional γ-alumina-supported CoMo catalyst (61.5%). This is due to that the spillover hydrogen formed in the micropores migrates onto nearby active CoMo sites in the mesopores.

Hao et al. (2016) used micro-mesoporous ZK-1 molecular sieves with different Si/Al ratios as supports for preparing Co-Mo catalysts. The CoMo/ZK-1 catalysts

show high surface areas ($\sim$700 m^2/g), large pore volumes, and hierarchical porous structures, which promote the dispersion of Co and Mo oxide phases on the ZK-1 supports. The TPR results show that the interactions between the Co and Mo oxide phases and the ZK-1 support are weaker than those in the CoMo/γ-Al$_2$O$_3$ catalyst. Under mild reaction conditions, the DBT HDS activity of CoMo/ZK-1 was higher than those of Co and Mo supported on ZSM-5, AlKIT-1, and γ-Al$_2$O$_3$.

4 Characterization of Synthesized Mo(W)S$_2$-Based Catalysts

Characterizations can reveal the relation of structures with the catalytic properties and assist the development of catalysts. Okamoto et al. (2004) developed an efficient technique to identify the maximum potential activity of HDS catalysts. They used Co(CO)$_3$NO as a probe molecule to coordinate on the edges of MoS$_2$ particles forming the Co-Mo-S active phases by CVD method (Fig. 4.13). The Co K-edge XANES results confirmed a selective formation of Co-Mo-S phase. Using this special "characterization," some important information can be obtained, such as maximum potential HDS activity, the extent of blocking of the active phase, the coverage of Co(Ni) atoms, and the dispersion of the MoS$_2$ particles in Co(Ni)Mo (W)S$_2$ catalysts.

It was found that Co(CO)$_3$NO molecules selectively adsorb on the vacant edge sites of MoS$_2$ particles if the contents of Ni or Co promotors are below the

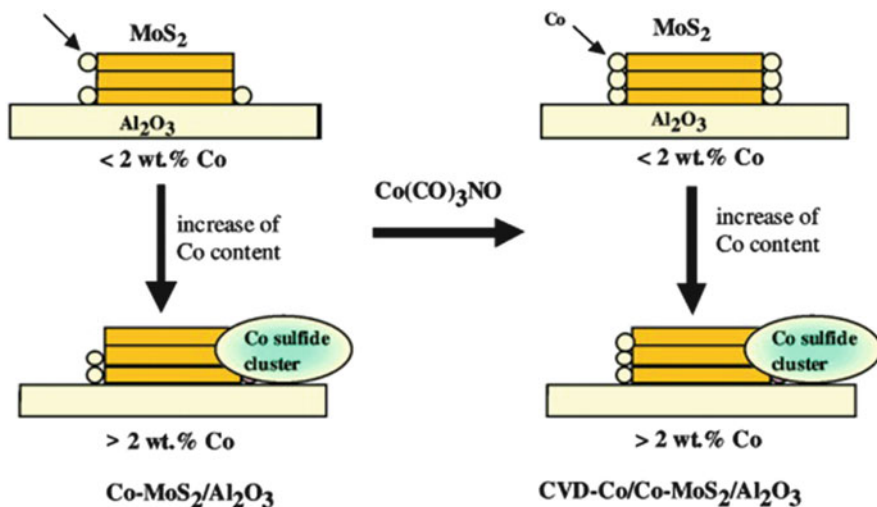**Fig. 4.13** Schematic surface models of Co–MoS$_2$/Al$_2$O$_3$ and CVD-Co/Co-MoS$_2$/Al$_2$O (Reproduced from Okamoto et al. 2004)

saturation threshold. The tested HDS activity of CVD-Co/MoS_2/Al_2O_3 is the maximum potential activity of $CoMoS_2$/Al_2O_3 at the situation that the edges of MoS_2 particles are fully occupied by Co atoms without any blocking by Co sulfide clusters (Okamoto 2003). If the MoS_2 edge has already been occupied by promoter Co(Ni) atoms, the $Co(CO)_3NO$ molecules are converted to less active, separate Co sulfide clusters, resulting in a decreased HDS activity.

Lai et al. (2016b) studied the effect of non-stoichiometric sulfur on the NiMoS structure of NiMo/Al_2O_3 and unsupported NiMo catalysts. Their results indicated the presence of reducible nonstoichiometric sulfur species (composed of S^{2-}, S_2^{2-}, and S^0) on the NiMoS surface and a sulfur dynamic equilibrium between the NiMoS edge and the gas phase. The S-S bonds on the NiMoS edge can be cleaved by hydrogen to form SH groups releasing H_2S. This leads to a significant increase of coordinatively unsaturated sites (CUS) on the NiMoS edge, beneficial for HDS activity. It was found that nonstoichiometric sulfur over the NiMoS/Al_2O_3 catalyst shows a higher H_2S partial pressure sensitivity than that over the unsupported NiMoS catalyst.

The sulfidation of supported NiW catalysts at different temperatures was shown in Fig 4.14. Conversion of tungsten oxides to WS_2 is more difficult than molybdenum oxides to MoS_2; therefore, typical sulfidation procedures result in mixed WO_xS_y and WS_2 phases. The former phase stabilizes Ni sulfide particles to form NiS-WO_xS_y, which is the precursor of the Ni-W-S phase. Mössbauer spectroscopy demonstrated that the NiS particles redisperse over the WS_2 edges when partly oxidic tungsten phases transform to WS_2. Owing to very slow W sulfidation, the Ni promoters end up in two phases, i.e., Ni-W-S and NiS–WO_xS_y phases, this in contrast to Co(Ni)Mo catalysts that mainly contain Co(Ni)–Mo–S phases after sulfidation. The NiS–WO_xS_y phase is deemed to perform well in liquid-phase HDS reactions whereas the Ni-W-S phase is most active for gas-phase HDS. The relative speciation of these two phases for alumina-supported NiW can be controlled by parameters as the calcination temperature and the sulfidation temperature and pressure. Chelating agents improve the edge occupation in NiW catalysts significantly by retarding Ni sulfidation. This is a more efficient formation of the Ni-W-S phase.

van Haande et al. (2015) studied morphology and structures of Ni-promoted mixed $Mo_xW_{(1-x)}S_2$/Al_2O_3 catalysts under different sulfidation and reaction conditions, as shown in Fig. 4.15. XPS and EXAFS showed that the slower sulfidation kinetics of W in activation process lead to the two-dimensional core-shell structure of $NiMo_xW_{(1-x)}$ sulfides with Mo located in the core and W in the shell. Increasing the H_2S/H_2 pressure during sulfidation distributed Mo and W more homogeneously, which was attributed to the favorable sulfidation of W under these conditions. And support interactions in the oxidic precursor plays a key role in the formation of these structures. Catalytic testing demonstrated that a core-shell structure is more active for thiophene HDS, whereas homogeneously mixed $Mo_xW_{(1-x)}S_2$ phase catalyzes the HDS of DBT.
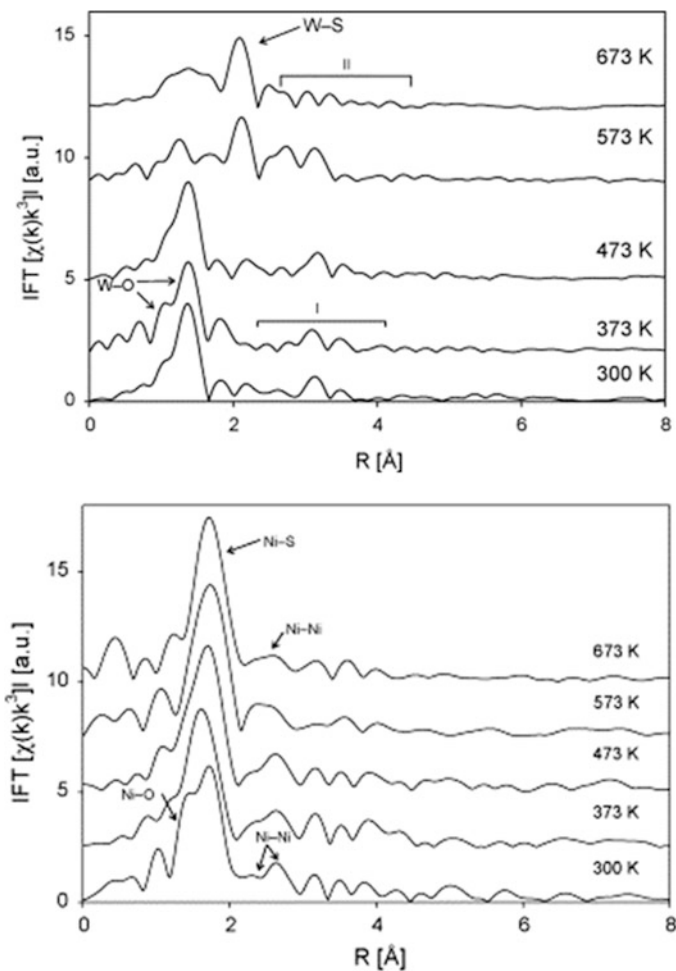
Fig. 4.14 W and Ni EXAFS k^3-weighted FT functions of NiW/Al$_2$O$_3$ after sulfidation at indicated temperatures, showing that W sulfidation starts at 573 K. Intervals I and II indicate the W–W contributions of WO$_3$ and WS$_3$, respectively. Ni is already completely sulfided at 573 K (Adapted from Hensen et al. 2007)

Nikulshin et al. (2014) investigated the effect of carbon on active phase morphology. Carbon varies the ratio of stacking number/linear size of active phase particles. As a result, the HYD/DDS selectivity of DBT is changed (Fig. 4.16). And the hydrogen uptake by the C-coated support could be a source of hydrogen for HDS reactions.
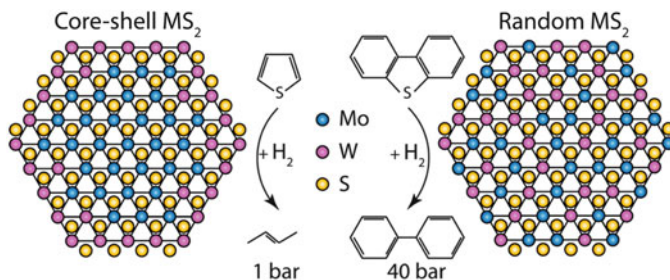
Fig. 4.15 Possible structures of the active phase in Ni-promoted $Mo_xW_{(1-x)}$ catalysts ($x \leq 1$) at different HDS environment. For the sake of clarity, Ni has been omitted from the drawings (Adapted from van Haande 2015)

5   Application of Mo(W)S$_2$-Based Catalysts for Deep Desulfurization

The synergy coordination of process technology with catalyst property is of critical importance for the industrial application of HDS catalysts. To tradeoff between ultra-deep HDS and octane containing in clean gasoline production, a two-stage fluid catalytic cracking (FCC) gasoline hydro-upgrading process is proposed with the selective HDS catalyst in the first reactor and the complemental HDS and octane recovery catalyst in the second reactor (Fig. 4.17). The full-range FCC gasoline is firstly separated into light and heavy cracked naphtha fractions (LCN and HCN) through distillation at 60 °C. LCN contains thiols as major sulfur-containing and most of the olefins with high-octane, and HCN contains mainly refractory sulfur-containing compounds (such as thiophenes, alkylthiophenes, and benzothiophenes) and low concentration of olefins. The LCN is treated with a 10% NaOH solution to remove the predominant C_2 and C_3 thiols. And the HCN is selectively desulfurized over a K and P modified Co-Mo/Al_2O_3 catalyst, followed by octane recovery over a Ni-Mo/HZSM-5 catalyst achieving hydroisomerization and aromatization of residual olefins as well as the compensating HDS. Finally, the hydro-upgraded HCN and caustic-treated LCN is blended again to obtain high-quality gasoline. The process endowed superior octane recovery ability while remarkably reducing the olefin content of FCC gasoline.

Control of the coordination patterns and the ratio of promoters/Mo(W), to a large extent, dominates the final performance of HDS catalysts, Zuo et al. (2004) studied the influence of Ni promoter amounts on thiophene HDS reaction of NiW catalysts. Compared with no-promoting catalysts they observed about 30 times drastic increase of activity for the catalyst with optimized Ni contents. It mainly correlates to the concentration of Ni-W-S phase. Meanwhile, the Ni promoters lead to a slight increase of stacking and length of WS$_2$ crystallites, as well as sulfidation of WO$_x$ precursors.

Figure 4.18 shows the effect on additional amount of Ni promoters on the HDS of different sulfur compounds over the NiMoS$_2$/γ-Al$_2$O$_3$ catalysts. It can be seen
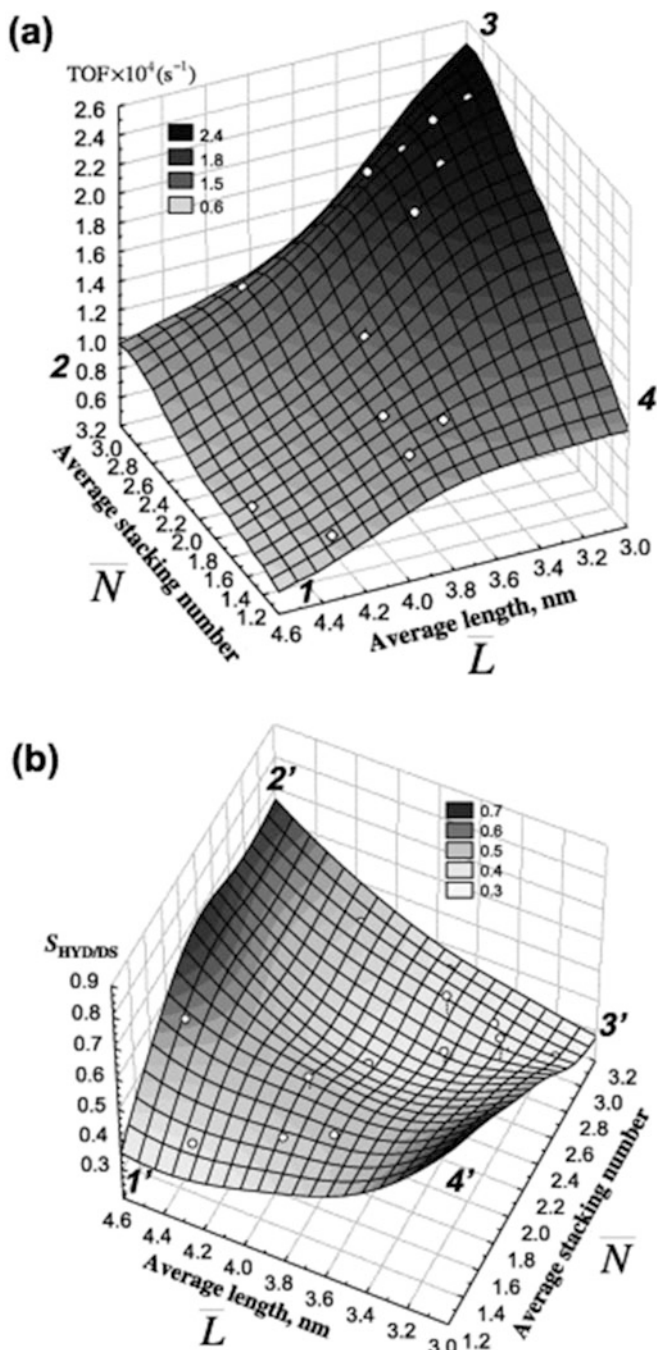
Fig. 4.16 3D dependences of TOF number (**a**) and HYD/DDS selectivity (**b**) in DBT HDS on average length and average stacking number of Co(Ni)MoS$_2$ particles in the catalysts (Reproduced from Nikulshin et al. 2014)
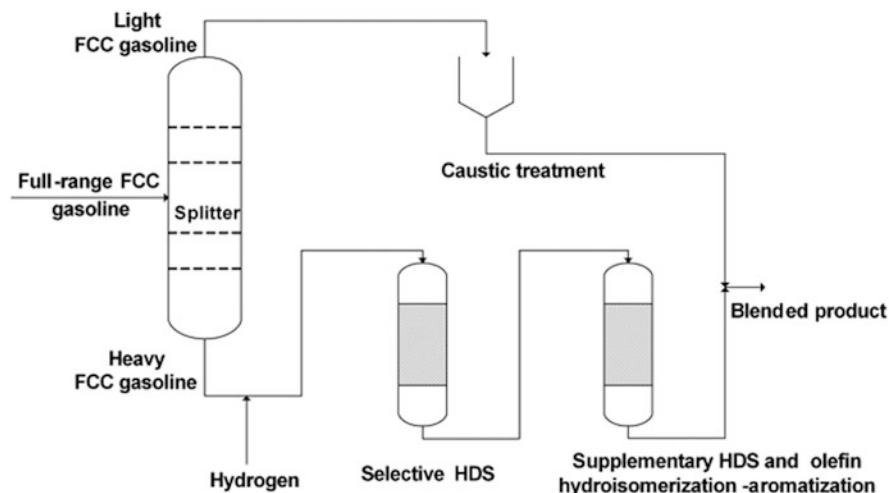
Fig. 4.17 Schematic diagram of the two-stage process for upgrade of FCC gasoline (Reproduced from Fan et al. 2013)

that the rate constant shows a volcano type with a maximum at Ni/(Ni + Mo) ≈ 0.33 where the NiMo catalyst is about 20 times higher active for DBT HDS than the Mo one. The rate constants of 4-methyldibenzothiophene (4-MDBT) and 4,6-DMDBT are dropped by roughly a factor of 2–3 and 4–6, respectively, owing to the steric hindering effect of substituents. Meanwhile, the DDS pathway of HDS of all three DBT derivatives is significantly enhanced by the addition of Ni, as shown in Fig. 4.18 (b), which is attributed to the formation of Ni-Mo-S phase.

Yin et al. (2016) studied the deep HDS of FCC and coking gas oils over highly loaded NiMoW catalysts compared with a commercial NiMo/γ-Al$_2$O$_3$ catalyst and a highly loaded NiMo catalyst. The observed that the FCC gas oil was relatively easier to process than coking gas oil. 4-MDBT had been totally removed when the coking gas oil was desulfurized to a level of 50 μg/g S. And only 4,6-DMDBT and 2,4,6-trimethyldibenzothiophene were detected in the deep HDS to a level less than 10 μg/g S. The highly loaded NiMoW catalyst had a higher activity than highly loaded NiMo and commercial NiMo/γ-Al$_2$O$_3$ catalyst, more suitable for the production of ultra-low-sulfur gas oils.

Peng et al. (2016) evaluated the deep desulfurization efficiency of stacking schemes for processing diesel feeds (Fig. 4.19). Results showed that the W-Mo-Ni/Mo-Co catalyst stacking is the most effective because of the following two reasons: (1) loading W-Mo-Ni catalyst on the upper bed of reactor not only facilitates the saturation of polyaromatics even but also provides low nitrogen feed for the bottom bed; (2) loading Mo-Co catalyst with alkyl transfer performance in the bottom bed favors the alkyl transfer reaction at high temperature, consequently improving the HDS efficiency.
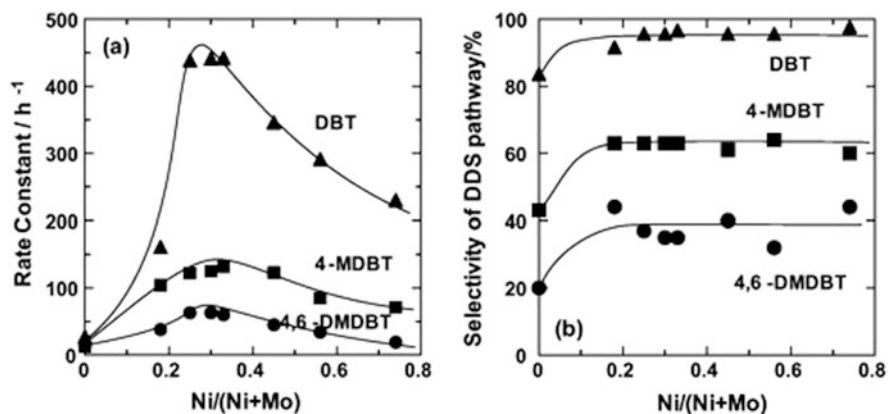
Fig. 4.18 Catalytic activities (**a**) and DDS selectivities (**b**) for HDS of DBTs over Ni-MoS$_2$/γ-Al$_2$O$_3$ catalysts. Reaction conditions: 2000 ppm sulfur, 3 MPa, 310 °C, LHSV = 300–3600 h^{-1}, H$_2$ flow rate = 200 cm^3 min^{-1} (Reproduced from Gao et al. 2011)
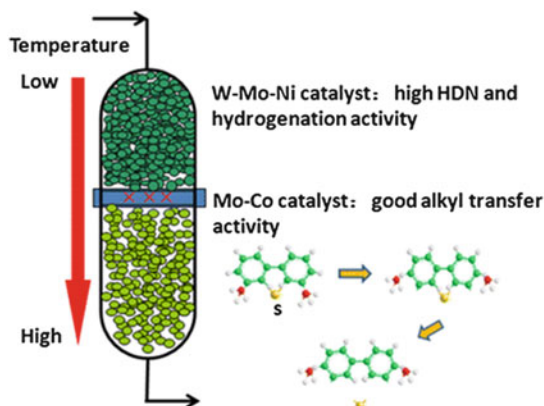
Fig. 4.19 Schematic deep HDS process in two-stage stacking bed (Reproduced from Peng et al. 2016)

To be confronted with the inhibition of nitrogen containing a compound to HDS, ExxonMobil Research and Engineering Co. developed a catalyst-zoning strategy that plays the strength of two catalysts with very different selectivity (Ho and Qiao 2010). For example, to treat light catalytic cycle oil (LCO), one catalyst used is a bulky Ni0.5Mn0.5Mo sulfide that has a very high HYA selectivity (Ho 2004). The other is sulfided CoMo/Al$_2$O$_3$ catalyst, which is HYL selective. The HDS activity of the bulky catalyst is more sensitive to N inhibition than that of the supported CoMo catalyst. A profitable way of using these two catalysts is to place Ni$_{0.5}$Mn$_{0.5}$Mo sulfide downstream of CoMo/Al$_2$O$_3$ in a stacked-bed reactor. Even a modest HDN by CoMo/Al$_2$O$_3$ catalyst can significantly dampen the N inhibition

impacts on the downstream bulky catalyst. And the bulk catalyst is relatively insensitive to the H_2S generated from the $CoMo/Al_2O_3$ catalyst. It noted that the 50/50 stacked bed outperforms a uniform mixed bed. This is because an effective ultra-deep HDS process requires a delicate balance between the hydrogenation function and tolerance of organonitrogen inhibition among catalysts. Cobalt as a promoter plays an important role in helping MoS_2-based catalysts combating organonitrogen inhibition.

A potential valorization of pyrolysis oils from lignocellulosic biomass is their co-hydrotreatment with petroleum cuts to produce transportation fuels (Pinheiro et al. 2009). Bui et al. (2009) investigated the impact of co-processing guaiacol, a representative oxygenated molecule of pyrolitic bio oils, with a straight run gas oil in an HDS process over the $CoMo/Al_2O_3$ catalyst. A decrease of HDS performance was observed at low temperature and high contact time. It was assigned to the formation of intermediate phenols competing with sulfur containing molecules for adsorbing on hydrogenation/hydrogenolysis sites. However, complete hydrodeoxygenation (HDO) of guaiacol was observed above 320 °C and HDS could proceed without any further inhibition.

Co-hydroprocessing of fossil fractions with lipids is an alternative pathway for integrating biomass in the transportation sector (Mercader et al. 2011). Bezergianni et al. (2014) evaluated $CoMo/Al_2O_3$ and $NiMo/Al_2O_3$ catalysts for hydroconversion of heavy atmospheric gas oil (HAGO) and waste cooking oil (WCO) mixtures. The results showed that the HDS efficiency depends primarily upon the reaction temperature and HAGO to WCO ratio. The HDS of NiMo catalyst is not affected by WCO, even in the 330 °C low temperature. However, the addition of WCO leads to strong deactivation of the CoMo catalyst. It was evident that NiMo type catalysts are more suitable for co-hydroprocessing of petroleum fractions with lipid-containing feedstocks.

Chen et al. (2013b) study the co-hydroprocessing of canola oil–heavy vacuum gas oil (HVGO) with different blending ratios under typical hydrotreating conditions over a commercial $NiMo/Al_2O_3$ catalyst. It was found that the HVGO–canola oil blend feeds had a higher conversion to the light product than the pure HVGO feed at similar operating conditions. However, the HDS and HDN were not affected by the addition of canola oil. Under similar conversion or light product yield, co-processing of HVGO–canola oil blends required lower temperature and/or pressure than the pure HVGO hydroprocessing, an implication of potential energy saving. It was also found that at the same conversion, the HVGO–canola oil blends generated more diesel but less gasoline than pure HVGO, an effective way to meet the fast increasing diesel demand. Vonortas et al. (2014) studied the effect of the refined and acidic vegetable oil content (0–30 wt%) on the co-hydroprocessing of their mixtures with gas oil over a $NiMo/Al_2O_3$ catalyst. It was found that 49–55% of the ester bonds are removed by the decarboxylation/decarbonylation pathway for both the refined and acidic vegetable oil. And the influence of the vegetable oil concentration on gas oil HDS of NiMo catalyst was negligible.

6 Conclusion

The advanced characterization techniques and DFT calculations have provided a fundamental understanding of surface reactions and highlighted the role of structures such as edge, corners, or single atom defects/vacancies as potential active sites in HDS catalysis. In particular, the atomic-scale insight into the Co-Mo-S active sites and "brim" edge has led to developing the better industrial HDS catalysts.

To supported CoMo, NiMo, and NiW catalysts, improvement can be achieved by increasing loading level of active metal (Mo, W, etc.); by adding one more transient metal (e.g., Ni to CoMo or Co to NiMo); and by incorporating a noble metal (Pt, Pd, Ru, etc.), but these methods may lead to the increase of cost and become unacceptable from economic perspective. Thus, enhancement of atomic efficiency of metals is more favored, such as the formation of as many as active centers with a limited amount of metals, control of active structures granting higher catalytic activity and synergy of different catalytic functions.

Apart from deep desulfurization, other catalytic properties are also important. Catalysts used for gasoline fraction HDS should suppress the hydrogenation to olefins avoiding the octane loss. But catalysts for diesel oil streams needs to have enough hydrogenation ability so as to achieve the desulfurization of refractory sulfur-containing compounds by HYD route and saturation of aromatics improving the cetane number. For the HDS of heavy fuels, a bi- or multi-functional catalyst is necessary to balance the hydrogenation of metal sites with cracking of acidic sites on support. Thus, the HDS catalysts require the fitful compromise among catalytic properties for specific type fuels.

Design and fabrication of HDS catalysts based on the rich understandings of active structures, the reaction mechanism, and kinetics as well as reaction engineering have become a trend with the fast advances in fundamental research and industrial application. To satisfy the demand of petroleum industry, it is also important to improve the synergism between HDS catalysts and the processes.

References

Alonso G, Berhault G, Aguilar A et al (2002) Characterization and HDS activity of mesoporous MoS_2 catalysts prepared by in situ activation of tetraalkylammonium thiomolybdates. J Catal 208:359–369. doi:10.1006/jcat.2002.3553

Alsalme A, Alzaqri N, Alsaleh A et al (2016) Efficient Ni-Mo hydrodesulfurization catalyst prepared through Keggin polyoxometalate. Appl Catal B Environ 182:102–108. doi:10.1016/j.apcatb.2015.09.018

Alvarez L, Espino J, Ornelas C et al (2004) Comparative study of MoS_2 and Co/MoS_2 catalysts prepared by ex situ/in situ activation of ammonium and tetraalkylammonium thiomolybdates. J Mol Catal Chem 210:105–117. doi:10.1016/j.molcata.2003.09.002

Arrouvel C (2004) Effects of P_{H2O}, P_{H2S}, P_{H2} on the surface properties of anatase TiO_2 and -Al_2O_3: a DFT study. J Catal 226:260–272. doi:10.1016/j.jcat.2004.05.019

Arrouvel C, Breysse M, Toulhoat H, Raybaud P (2005) A density functional theory comparison of anatase (TiO_2)- and gamma-Al_2O_3-supported MoS_2 catalysts. J Catal 232:161–178. doi:10.1016/j.jcat.2005.02.018

Baubet B, Girleanu M, Gay A-S et al (2016) Quantitative two-dimensional (2D) morphology-selectivity relationship of CoMoS nanolayers: a combined high-resolution high-angle annular dark field scanning transmission electron microscopy (HR HAADF-STEM) and density functional theory (DFT) study. ACS Catal 6:1081–1092. doi:10.1021/acscatal.5b02628

Ben Tayeb K, Lamonier C, Lancelot C et al (2010) Study of the active phase of NiW hydrocracking sulfided catalysts obtained from an innovative heteropolyanion based preparation. Catal Today 150:207–212. doi:10.1016/j.cattod.2009.07.094

Bezergianni S, Dimitriadis A, Meletidis G (2014) Effectiveness of CoMo and NiMo catalysts on co-hydroprocessing of heavy atmospheric gas oil-waste cooking oil mixtures. Fuel 125:129–136. doi:10.1016/j.fuel.2014.02.010

Breysse M, Afanasiev P, Geantet C, Vrinat M (2003) Overview of support effects in hydrotreating catalysts. Catal Today 86:5–16. doi:10.1016/S0920-5861(03)00400-0

Bui VN, Toussaint G, Laurenti D et al (2009) Co-processing of pyrolisis bio oils and gas oil for new generation of bio-fuels: hydrodeoxygenation of guaiacol and SRGO mixed feed. Catal Today 143:172–178. doi:10.1016/j.cattod.2008.11.024

Byskov LS, Nørskov JK, Clausen BS, Topsøe H (1999) DFT calculations of unpromoted and promoted MoS2-based hydrodesulfurization catalysts. J Catal 187:109–122. doi:10.1006/jcat.1999.2598

Candia R, Sørensen O, Villadsen J (1984) Effect of sulfiding temperature on activity and structures of Co-Mo/Al_2O_3 catalysts. Bull Soc Chim Belg 93:763–773

Castillo-Villalon P, Ramirez J, Castaneda R (2012) Relationship between the hydrodesulfurization of thiophene, dibenzothiophene, and 4,6-dimethyl dibenzothiophene and the local structure of Co in Co-Mo-S sites: infrared study of adsorbed CO. J Catal 294:54–62. doi:10.1016/j.jcat.2012.07.002

Chen W, Maugé F, van Gestel J et al (2013a) Effect of modification of the alumina acidity on the properties of supported Mo and CoMo sulfide catalysts. J Catal 304:47–62. doi:10.1016/j.jcat.2013.03.004

Chen J, Farooqi H, Fairbridge C (2013b) Experimental study on co-hydroprocessing canola oil and heavy vacuum gas oil blends. Energy Fuels 27:3306–3315. doi:10.1021/ef4005835

Choi J-S, Maugé F, Pichon C et al (2004) Alumina-supported cobalt–molybdenum sulfide modified by tin via surface organometallic chemistry: application to the simultaneous hydrodesulfurization of thiophenic compounds and the hydrogenation of olefins. Appl Catal Gen 267:203–216. doi:10.1016/j.apcata.2004.03.005

Coelho TL, Licea YE, Palacio LA, Faro AC (2015) Heptamolybdate-intercalated CoMgAl hydrotalcites as precursors for HDS-selective hydrotreating catalysts. Catal Today 250:38–46. doi:10.1016/j.cattod.2014.06.016

Costa D, Arrouvel C, Breysse M et al (2007) Edge wetting effects of gamma-Al_2O_3 and anatase-TiO_2 supports by MoS2 and CoMoS active phases: a DFT study. J Catal 246:325–343. doi:10.1016/j.jcat.2006.12.007

de Mercader FM, Groeneveld MJ, Kersten SRA et al (2011) Hydrodeoxygenation of pyrolysis oil fractions: process understanding and quality assessment through co-processing in refinery units. Energy Environ Sci 4:985–997. doi:10.1039/c0ee00523a

Delmon B, Froment GF (1996) Remote control of catalytic sites by spillover species: a chemical reaction engineering approach. Catal Rev 38:69–100. doi:10.1080/01614949608006454

Elizabeth Cervantes-Gaxiola M, Arroyo-Albiter M, Perez-Larios A et al (2013) Experimental and theoretical study of NiMoW, NiMo, and NiW sulfide catalysts supported on an Al-Ti-Mg mixed oxide during the hydrodesulfurization of dibenzothiophene. Fuel 113:733–743. doi:10.1016/j.fuel.2013.06.041

Fan Y, Shi G, Liu H, Bao X (2009) Morphology tuning of supported MoS_2 slabs for selectivity enhancement of fluid catalytic cracking gasoline hydrodesulfurization catalysts. Appl Catal B Environ 91:73–82. doi:10.1016/j.apcatb.2009.05.008

Fan Y, Shi G, Bao X (2013) A process for producing ultraclean gasoline by coupling efficient hydrodesulfurization and directional olefin conversion. AIChE J 59:571–581. doi:10.1002/aic.13832

Fujikawa T (2009) Highly active HDS catalyst for producing ultra-low sulfur diesel fuels. Top Catal 52:872–879. doi:10.1007/s11244-009-9228-y

Fujikawa T, Kimura H, Kiriyama K, Hagiwara K (2006) Development of ultra-deep HDS catalyst for production of clean diesel fuels. Catal Today 111:188–193. doi:10.1016/j.cattod.2005.10.024

Gao Q, Ofosu TNK, Ma S-G et al (2011) Catalyst development for ultra-deep hydrodesulfurization (HDS) of dibenzothiophenes. I: effects of Ni promotion in molybdenum-based catalysts. Catal Today 164:538–543. doi:10.1016/j.cattod.2010.10.016

Gao D, Duan A, Zhang X et al (2015) Synthesis of CoMo catalysts supported on EMT/FAU intergrowth zeolites with different morphologies and their hydro-upgrading performances for FCC gasoline. Chem Eng J 270:176–186. doi:10.1016/j.cej.2015.02.015

Garg S, Bhaskar T, Soni K et al (2008) Novel highly active FSM-16 supported molybdenum catalyst for hydrotreatment. Chem Commun:5310–5311. doi:10.1039/b809808e

Ge H, Li X, Qin Z et al (2009) Effects of carbon on the sulfidation and hydrodesulfurization of CoMo hydrating catalysts. Korean J Chem Eng 26:576–581. doi:10.1007/s11814-009-0098-6

Ge H, Wen X-D, Ramos MA et al (2014) Carbonization of ethylenediamine coimpregnated CoMo/Al_2O_3 catalysts sulfided by organic sulfiding agent. ACS Catal 4:2556–2565. doi:10.1021/cs500477x

Glasson C, Geantet C, Lacroix M et al (2002) Beneficial effect of carbon on hydrotreating catalysts. J Catal 212:76–85. doi:10.1006/jcat.2002.3781

Gonzalez-Cortes SL, Rugmini S, Xiao T et al (2014) Deep hydrotreating of different feedstocks over a highly active Al_2O_3-supported NiMoW sulfide catalyst. Appl Catal Gen 475:270–281. doi:10.1016/j.apcata.2014.01.045

Grønborg SS, Šarić M, Moses PG et al (2016) Atomic scale analysis of sterical effects in the adsorption of 4,6-dimethyldibenzothiophene on a CoMoS hydrotreating catalyst. J Catal 344:121–128. doi:10.1016/j.jcat.2016.09.004

Hadj-Aissa A, Dassenoy F, Geantet C, Afanasiev P (2016) Solution synthesis of core-shell Co_9S_8@MoS_2 catalysts. Catal Sci Technol 6:4901–4909. doi:10.1039/c6cy00311g

Hallie H (1982) Experience reveals best presuldiing techniques for HDS and HDN catalysts. Oil Gas J 80:69–74

Hao L, Xiong G, Liu L et al (2016) Preparation of highly dispersed desulfurization catalysts and their catalytic performance in hydrodesulfurization of dibenzothiophene. Chin J Catal 37:412–419. doi:10.1016/S1872-2067(15)61017-8

Heine T (2015) Transition metal chalcogenides: ultrathin inorganic materials with tunable electronic properties. Acc Chem Res 48:65–72. doi:10.1021/ar500277z

Hensen EJM, van der Meer Y, van Veen JAR, Niemantsverdriet JW (2007) Insight into the formation of the active phases in supported NiW hydrotreating catalysts. Appl Catal Gen 322:16–32. doi:10.1016/j.apcata.2007.01.003

Hinnemann B, Nørskov JK, Topsøe H (2005) A density functional study of the chemical differences between type I and type II MoS_2 -based structures in hydrotreating catalysts. J Phys Chem B 109:2245–2253. doi:10.1021/jp048842y

Ho TC (2004) Deep HDS of diesel fuel: chemistry and catalysis. Catal Today 98:3–18. doi:10.1016/j.cattod.2004.07.048

Ho TC, Qiao L (2010) Competitive adsorption of nitrogen species in HDS: kinetic characterization of hydrogenation and hydrogenolysis sites. J Catal 269:291–301. doi:10.1016/j.jcat.2009.11.012

Hojholt KT, Vennestrom PNR, Tiruvalam R, Beato P (2011) Tight bifunctional hierarchical catalyst. Chem Commun 47:12864–12866. doi:10.1039/c1cc15413c

Jiménez Sandoval S, Yang D, Frindt RF, Irwin JC (1991) Raman study and lattice dynamics of single molecular layers of MoS$_2$. Phys Rev B 44:3955–3962. doi:10.1103/PhysRevB.44.3955

Kelty SP, Berhault G, Chianelli RR (2007) The role of carbon in catalytically stabilized transition metal sulfides. Appl Catal Gen 322:9–15. doi:10.1016/j.apcata.2007.01.017

Krebs E, Silvi B, Raybaud P (2008a) Mixed sites and promoter segregation: A DFT study of the manifestation of Le Chatelier's principle for the Co(Ni)MoS active phase in reaction conditions. Catal Today 130:160–169. doi:10.1016/j.cattod.2007.06.081

Krebs E, Silvi B, Daudin A, Raybaud P (2008b) A DFT study of the origin of the HDS/HydO selectivity on Co(Ni)MoS active phases. J Catal 260:276–287. doi:10.1016/j.jcat.2008.09.026

Krebs E, Daudin A, Raybaud P (2009) A DFT study of CoMoS and NiMoS catalysts: from nano-crystallite morphology to selective hydrodesulfurization. Oil Gas Sci Technol - Rev IFP 64:707–718. doi:10.2516/ogst/2009004

La Parola V, Deganello G, Venezia AM (2004) CoMo catalysts supported on aluminosilicates: synergy between support and sodium effects. Appl Catal Gen 260:237–247. doi:10.1016/j.apcata.2003.10.020

Lai W, Chen Z, Zhu J et al (2016a) A NiMoS flower-like structure with self-assembled nanosheets as high-performance hydrodesulfurization catalysts. Nanoscale 8:3823–3833. doi:10.1039/c5nr08841k

Lai W, Xu Y, Ren Y et al (2016b) Insight into the effect of non-stoichiometric sulfur on a NiMoS hydrodesulfurization catalyst. Catal Sci Technol 6:497–506. doi:10.1039/c5cy01142f

Lauritsen JV, Besenbacher F (2015) Atom-resolved scanning tunneling microscopy investigations of molecular adsorption on MoS2 and CoMoS hydrodesulfurization catalysts. J Catal 328:49–58. doi:10.1016/j.jcat.2014.12.034

Lauritsen JV, Bollinger MV, Laegsgaard E et al (2004) Atomic-scale insight into structure and morphology changes of MoS2 nanoclusters in hydrotreating catalysts. J Catal 221:510–522. doi:10.1016/j.jcat.2003.09.015

Lauritsen JV, Kibsgaard J, Olesen GH et al (2007) Location and coordination of promoter atoms in Co- and Ni-promoted MoS(2)-based hydrotreating catalysts. J Catal 249:220–233. doi:10.1016/j.jcat.2007.04.013

Le Z, Afanasiev P, Li D et al (2008) Solution synthesis of the unsupported Ni–W sulfide hydrotreating catalysts. Catal Today 130:24–31. doi:10.1016/j.cattod.2007.07.002

Lélias MA, Le Guludec E, Mariey L et al (2010) Effect of EDTA addition on the structure and activity of the active phase of cobalt–molybdenum sulfide hydrotreatment catalysts. Catal Today 150:179–185. doi:10.1016/j.cattod.2009.07.107

Leyva C, Ancheyta J, Travert A et al (2012) Activity and surface properties of NiMo/SiO$_2$-Al$_2$O$_3$ catalysts for hydroprocessing of heavy oils. Appl Catal Gen 425:1–12. doi:10.1016/j.apcata.2012.02.033

Li M, Li H, Jiang F et al (2010) The relation between morphology of (Co)MoS$_2$ phases and selective hydrodesulfurization for CoMo catalysts. Catal Today 149:35–39. doi:10.1016/j.cattod.2009.03.017

Li P, Liu X, Zhang C et al (2016) Selective hydrodesulfurization of gasoline on Co/MoS$_{2\pm x}$ catalyst: effect of sulfur defects in MoS$_{2\pm x}$. Appl Catal Gen 524:66–76. doi:10.1016/j.apcata.2016.06.003

Liang J, Liu Y, Zhao J et al (2014) Waugh-type NiMo heteropolycompounds as more effective precursors of hydrodesulfurization catalyst. Catal Lett 144:1735–1744. doi:10.1007/s10562-014-1326-1

Liu H, Li Y, Yin C et al (2016) One-pot synthesis of ordered mesoporous NiMo-Al$_2$O$_3$ catalysts for dibenzothiophene hydrodesulfurization. Appl Catal B Environ 198:493–507. doi:10.1016/j.apcatb.2016.06.004

Martin C, Lamonier C, Fournier M et al (2005) Evidence and characterization of a new decamolybdocobaltate cobalt salt: an efficient precursor for hydrotreatment catalyst preparation. Chem Mater 17:4438–4448. doi:10.1021/cm0503634

Mazurelle J, Lamonier C, Lancelot C et al (2008) Use of the cobalt salt of the heteropolyanion $[Co_2Mo_{10}O_{38}H_4]^{6-}$ for the preparation of CoMo HDS catalysts supported on Al_2O_3, TiO_2 and ZrO_2. Catal Today 130:41–49. doi:10.1016/j.cattod.2007.07.008

Mey D, Brunet S, Canaff C et al (2004) HDS of a model FCC gasoline over a sulfided CoMo/Al_2O_3 catalyst: effect of the addition of potassium. J Catal 227:436–447. doi:10.1016/j.jcat.2004.07.013

Mohanty S, Mouli KC, Soni K et al (2012) Catalytic hydrotreatment using NiMo/MAS catalysts synthesized from ZSM-5 nano-clusters. Appl Catal Gen 419:1–12. doi:10.1016/j.apcata.2011.12.015

Moses PG, Hinnemann B, Topsøe H, Nørskov JK (2009) The effect of co-promotion on MoS_2 catalysts for hydrodesulfurization of thiophene: a density functional study. J Catal 268:201–208. doi:10.1016/j.jcat.2009.09.016

Nikulshin PA, Salnikov VA, Mozhaev AV et al (2014) Relationship between active phase morphology and catalytic properties of the carbon–alumina-supported Co(Ni)Mo catalysts in HDS and HYD reactions. J Catal 309:386–396. doi:10.1016/j.jcat.2013.10.020

North J, Poole O, Alotaibi A et al (2015) Efficient hydrodesulfurization catalysts based on Keggin polyoxometalates. Appl Catal -Gen 508:16–24. doi:10.1016/j.apcata.2015.10.001

Novoselov KS (2004) Electric field effect in atomically thin carbon films. Science 306:666–669. doi:10.1126/science.1102896

Ojeda J, Escalona N, Baeza P et al (2003) Synergy between Mo/SiO_2 and Co/SiO_2 beds in HDS: a remote control effect? Chem Commun:1608–1609. doi:10.1039/B301647C

Okamoto Y (2003) Preparation of Co–Mo/Al2O3 model sulfide catalysts for hydrodesulfurization and their application to the study of the effects of catalyst preparation. J Catal. doi:10.1016/S0021-9517(03)00029-0

Okamoto Y, Ochiai K, Kawano M, Kubota T (2004) Evaluation of the maximum potential activity of Co–Mo/Al2O3 catalysts for hydrodesulfurization. J Catal 222:143–151. doi:10.1016/j.jcat.2003.10.024

Palcheva R, Spojakina A, Jiratova K, Kaluza L (2010) Effect of co on HDS activity of alumina-supported heteropolymolybdate. Catal Lett 137:216–223. doi:10.1007/s10562-010-0361-9

Pashigreva AV, Bukhtiyarova GA, Klimov OV et al (2010) Activity and sulfidation behavior of the $CoMo/Al_2O_3$ hydrotreating catalyst: the effect of drying conditions. Catal Today 149:19–27. doi:10.1016/j.cattod.2009.07.096

Peng C, Guo R, Fang X (2016) Improving ultra-deep desulfurization efficiency by catalyst stacking technology. Catal Lett 146:701–709. doi:10.1007/s10562-015-1675-4

Pimerzin AA, Nikulshin PA, Mozhaev AV et al (2015) Investigation of spillover effect in hydrotreating catalysts based on $Co_2Mo_{10}-$ heteropolyanion and cobalt sulphide species. Appl Catal B Environ 168–169:396–407. doi:10.1016/j.apcatb.2014.12.031

Pinheiro A, Hudebine D, Dupassieux N, Geantet C (2009) Impact of oxygenated compounds from lignocellulosic biomass pyrolysis oils on gas oil hydrotreatment. Energy Fuels 23:1007–1014. doi:10.1021/ef800507z

Ramos M, Berhault G, Ferrer DA et al (2012) HRTEM and molecular modeling of the MoS_2-Co_9S_8 interface: understanding the promotion effect in bulk HDS catalysts. Catal Sci Technol 2:164–178. doi:10.1039/c1cy00126d

Rana M, Ramirez J, Gutierrezalejandre A et al (2007) Support effects in CoMo hydrodesulfurization catalysts prepared with EDTA as a chelating agent. J Catal 246:100–108. doi:10.1016/j.jcat.2006.11.025

Rashidi F, Kharat AN, Rashidi AM et al (2010) Fractal geometry approach to describe mesostructured boehmite and gamma-alumina nanorods. Eur J Inorg Chem 2010:1544–1551. doi:10.1002/ejic.200901103

Rashidi F, Sasaki T, Rashidi AM et al (2013) Ultradeep hydrodesulfurization of diesel fuels using highly efficient nanoalumina-supported catalysts: impact of support, phosphorus, and/or boron on the structure and catalytic activity. J Catal 299:321–335. doi:10.1016/j.jcat.2012.11.012

Raybaud P (2007) Understanding and predicting improved sulfide catalysts: insights from first principles modeling. Appl Catal Gen 322:76–91. doi:10.1016/j.apcata.2007.01.005

Romero-Galarza A, Gutiérrez-Alejandre A, Ramírez J (2011) Analysis of the promotion of CoMoP/Al_2O_3 HDS catalysts prepared from a reduced H–P–Mo heteropolyacid Co salt. J Catal 280:230–238. doi:10.1016/j.jcat.2011.03.021

Schweiger H, Raybaud P, Toulhoat H (2002) Promoter sensitive shapes of Co(Ni)MoS nanocatalysts in sulfo-reductive conditions. J Catal 212:33–38. doi:10.1006/jcat.2002.3737

Scott CE, Perez-Zurita MJ, Carbognani LA et al (2015) Preparation of NiMoS nanoparticles for hydrotreating. Catal Today 250:21–27. doi:10.1016/j.cattod.2014.07.033

Semeykina VS, Parkhomchuk EV, Polukhin AV et al (2016) CoMoNi catalyst texture and surface properties in heavy oil processing. part I: hierarchical macro/mesoporous alumina support. Ind Eng Chem Res 55:3535–3545. doi:10.1021/acs.iecr.5b04730

Shan S, Yuan P, Han W et al (2015) Supported NiW catalysts with tunable size and morphology of active phases for highly selective hydrodesulfurization of fluid catalytic cracking naphtha. J Catal 330:288–301. doi:10.1016/j.jcat.2015.06.019

Singh R, Kunzru D, Sivakumar S (2016a) Monodispersed ultrasmall NiMo metal oxide nanoclusters as hydrodesulfurization catalyst. Appl Catal B Environ 185:163–173. doi:10.1016/j.apcatb.2015.12.013

Singh R, Kunzru D, Sivakumar S (2016b) Co-promoted MoO_3 nanoclusters for hydrodesulfurization. Catal Sci Technol 6:5949–5960. doi:10.1039/c5cy02221e

Sintarako P, Praserthdam P, Thammongkol V et al (2015) The suppression of a basic nitrogen compound influence on hydrodesulfurization activity of dibenzothiophene in treated diesel over Al_2O_3 supported CoMo catalysts by ZrO2 as a secondary support. Catal Comm 62:89–94. doi:10.1016/j.catcom.2015.01.013

Stanislaus A, Marafi A, Rana MS (2010) Recent advances in the science and technology of ultra low sulfur diesel (ULSD) production. Catal Today 153:1–68. doi:10.1016/j.cattod.2010.05.011

Sun M, Nicosia D, Prins R (2003) The effects of fluorine, phosphate and chelating agents on hydrotreating catalysts and catalysis. Catal Today 86:173–189. doi:10.1016/S0920-5861(03)00410-3

Tang T, Zhang L, Fu W et al (2013) Design and synthesis of metal sulfide catalysts supported on zeolite nanofiber bundles with unprecedented hydrodesulfurization activities. J Am Chem Soc 135:11437–11440. doi:10.1021/ja4043388

Topsøe H (1981) In situ Mössbauer emission spectroscopy studies of unsupported and supported sulfided Co-Mo hydrodesulfurization catalysts: evidence for and nature of a Co-Mo-S phase. J Catal 68:433–452. doi:10.1016/0021-9517(81)90114-7

Topsøe H (2007) The role of Co–Mo–S type structures in hydrotreating catalysts. Appl Catal Gen 322:3–8. doi:10.1016/j.apcata.2007.01.002

Tuxen A, Gøbel H, Hinnemann B et al (2011) An atomic-scale investigation of carbon in MoS_2 hydrotreating catalysts sulfided by organosulfur compounds. J Catal 281:345–351. doi:10.1016/j.jcat.2011.05.018

Tuxen AK, Füchtbauer HG, Temel B et al (2012) Atomic-scale insight into adsorption of sterically hindered dibenzothiophenes on MoS_2 and Co–Mo–S hydrotreating catalysts. J Catal 295:146–154. doi:10.1016/j.jcat.2012.08.004

Valencia D, Peña L, García-Cruz I (2012) Reaction mechanism of hydrogenation and direct desulfurization routes of dibenzothiophene-like compounds: a density functional theory study. Int J Quantum Chem 112:3599–3605. doi:10.1002/qua.24242

van Haandel L, Bremmer M, Kooyman PJ et al (2015) Structure–activity correlations in hydrodesulfurization reactions over Ni-promoted $Mo_xW_{(1-x)}S_2$/Al_2O_3 catalysts. ACS Catal 5:7276–7287. doi:10.1021/acscatal.5b01806

Villarroel M, Baeza P, Escalona N et al (2008) MD//Mo and MD//W [MD = Mn, Fe, Co, Ni, Cu and Zn] promotion via spillover hydrogen in hydrodesulfurization. Appl Catal Gen 345:152–157. doi:10.1016/j.apcata.2008.04.033

Vonortas A, Kubicka D, Papayannakos N (2014) Catalytic co-hydroprocessing of gasoil-palm oil/AVO mixtures over a NiMo/gamma-Al$_2$O$_3$ catalyst. Fuel 116:49–55. doi:10.1016/j.fuel.2013.07.074

Wan G, Duan A, Zhang Y et al (2010) NiW/AMBT catalysts for the production of ultra-low sulfur diesel. Catal Today 158:521–529. doi:10.1016/j.cattod.2010.08.021

Wang L, He W, Yu Z (2013) Transition-metal mediated carbon–sulfur bond activation and transformations. Chem Soc Rev 42:599–621. doi:10.1039/C2CS35323G

Wang H, Lu Z, Kong D et al (2014) Electrochemical tuning of MoS$_2$ nanoparticles on three-dimensional substrate for efficient hydrogen evolution. ACS Nano 8:4940–4947. doi:10.1021/nn500959v

Wang H, Yuan H, Sae Hong S et al (2015a) Physical and chemical tuning of two-dimensional transition metal dichalcogenides. Chem Soc Rev 44:2664–2680. doi:10.1039/C4CS00287C

Wang T, Fan Y, Wang X et al (2015b) Selectivity enhancement of CoMoS catalysts supported on tri-modal porous Al$_2$O$_3$ for the hydrodesulfurization of fluid catalytic cracking gasoline. Fuel 157:171–176. doi:10.1016/j.fuel.2015.05.005

Wang W, Li L, Tan S et al (2016) Preparation of NiS2//MoS2 catalysts by two-step hydrothermal method and their enhanced activity for hydrodeoxygenation of p-cresol. Fuel 179:1–9. doi:10.1016/j.fuel.2016.03.068

Wen X-D, Cao Z, Li Y-W et al (2006) Structure and energy of Mo$_{27}$S$_x$C$_y$ clusters: a density functional theory study. J Phys Chem B 110:23860–23869. doi:10.1021/jp063323b

Yin C, Liu H, Zhao L et al (2016) Study for the production of ultra-low sulfur gas oils on a highly loaded NiMoW catalyst. Catal Today 259:409–416. doi:10.1016/j.cattod.2015.04.028

Yoosuk B, Song C, Kim JH et al (2010) Effects of preparation conditions in hydrothermal synthesis of highly active unsupported NiMo sulfide catalysts for simultaneous hydrodesulfurization of dibenzothiophene and 4,6-dimethyldibenzothiophene. Catal Today 149:52–61. doi:10.1016/j.cattod.2009.05.001

Zepeda TA, Infantes-Molina A, de Leon JND et al (2014) Hydrodesulfurization enhancement of heavy and light S-hydrocarbons on NiMo/HMS catalysts modified with Al and P. Appl Catal -Gen 484:108–121. doi:10.1016/j.apcata.2014.06.033

Zuo D, Vrinat M, Nie H et al (2004) The formation of the active phases in sulfided NiW/Al$_2$O$_3$ catalysts and their evolution during post-reduction treatment. Catal Today 93–95:751–760. doi:10.1016/j.cattod.2004.06.078

Chapter 5
Selective Sulfur Removal from Liquid Fuels Using Nanostructured Adsorbents

Diana Iruretagoyena and Raul Montesano

Abstract In recent years, there has been an increasing pressure to develop strategies to reduce the level of sulfur in transportation fuels due to stringent environmental regulations. Currently, hydrodesulfurization (HDS) is the most mature (pre-FCC) technology to remove sulfur from gasoline and diesel. However, conventional HDS can hardly produce ultra-low sulfur fuels while maintaining important fuel requirements (i.e., oxygen content, overall aromatic content, olefin content for gasoline, and cetane number for diesel). As a consequence, improvement of existing HDS processes and development of new desulfurization technologies is needed. In this regard, selective adsorption removal of sulfur (SARS) is a promising emerging approach for ultra-deep desulfurization of refinery streams by means of solid adsorbents. Contrary to HDS, SARS is usually carried out at low temperatures and pressures with minimal hydrogen consumption, preventing olefin hydrogenation and thus maintaining the properties of the fuels. This chapter presents a general overview of SARS. Emphasis is given to the use of nanostructured materials as sulfur adsorbents. Section 5.1 introduces the chapter presenting a general description of HDS, SARS and other emerging desulfurization technologies. Section 5.2 describes the two main groups of SARS (adsorption desulfurization and reactive adsorption desulfurization). Subsequently, the three main mechanisms for sulfur adsorption (π-complexation, direct sulfur–adsorption site interactions, and bulk incorporation in reactive adsorption desulfurization) are reviewed. Section 5.3 gives an overview of relevant literature concerning the use of promising groups of nanostructured adsorbents for SARS including zeolites, MOFs, mesoporous silicas, and carbon-nanostructured adsorbents. Finally, Sect. 5.4 gives some concluding remarks.

D. Iruretagoyena (✉)
Department of Chemical Engineering, Imperial College London, South Kensington Campus, London SW7 2AZ, UK
e-mail: d.iruretagoyena09@imperial.ac.uk

R. Montesano
Department of Chemical Engineering, Imperial College London, South Kensington Campus, London SW7 2AZ, UK

Haldor Topsoe A/S, Haldor Topsoe Allé 1, 2800 Kongens Lyngby, Denmark

1 Introduction

In recent years, there has been an increasing pressure to develop strategies to reduce
the level of sulfur in transportation fuels due to stringent environmental regulations.
The European Parliament has set a limit of 10 ppm of sulfur in gasoline and diesel
since 2009 while the Environmental Protection Agency (EPA) has adopted the
same limit in the Clean Air Act (Tier 3) effective from January 2017. In most
refineries, gasoline and diesel are formed by blending the corresponding straight-
run distillates with additional naphtha and diesel coming from cracking processes
(fluid catalytic cracking FCC, hydrocracking and thermal cracking of the vacuum
residue). The product from the cracking units contributes with ca. 48% of the
gasoline and 39% of the diesel pools, but amounts to 97% and 63% of the sulfur
content, respectively. Evidently, treatment of cracking streams is essential to meet
the low sulfur limits in current regulations and therefore emphasis has been given to
pre- and post-FCC desulfurization in recent years.

Hydrodesulfurization (HDS) is the most mature (pre-FCC) technology to
remove sulfur from gasoline and diesel. In this process, hydrogen reacts with the
organosulfur compounds to produce sulfur-free hydrocarbons and
H_2S. Conventional HDS is carried out at high temperatures (300–400 °C) and
hydrogen partial pressures over sulfided $CoMo/Al_2O_3$ and $NiMo/Al_2O_3$ catalysts.
The reactivity of the sulfur-containing compounds depends on the steric hindrance
and the electron density of the sulfur atom and decreases in the following order:
mercaptans, sulfides, disulfides, thiophenes, and benzothiophenes (and their
alkylated derivatives), and polynuclear sulfur compounds. It is possible to meet
the ultra-low sulfur levels imposed on gasoline by current regulations under severe
HDS conditions and using improved catalyst formulations (Topsøe et al. 1999;
Gutierrez et al. 2015) but higher temperatures lead to an increased catalyst deacti-
vation by coke deposition while higher H_2 partial pressures enhance the undesired
hydrogenation of unsaturated hydrocarbons, lowering the octane number. The
gasoline can be upgraded in a subsequent stage (isomerization + alkylation) but
to the detriment of the process economics. In the case of diesel, the competitive
adsorption between sterically hindered sulfur compounds and polyaromatics
decreases the desulfurization rate at low sulfur contents, and therefore, extremely
large catalyst volumes are required for deep HDS.

From the discussion above it is evident that conventional HDS can hardly
produce ultra-low sulfur fuels while maintaining important fuel requirements
(i.e., oxygen content, overall aromatic content, olefin content for gasoline, and
cetane number for diesel). As a consequence, improvement of existing HDS
processes and development of new desulfurization technologies is needed. Prom-
ising approaches for industry have been reviewed by Babich and Moulijn (2003)

and Song (2003) and include HDS with fuel specification recovery (Javadli and de Klerk 2012) and catalytic distillation (Ju et al. 2015), shifting the boiling point by alkylation (Arias et al. 2008), desulfurization via extraction (Farzin and Miran 2015), selective oxidation (Seeberger and Jess 2010), and selective adsorptive desulfurization (Menzel et al. 2016). This chapter presents a general overview of selective adsorption for removal of sulfur compounds (SARS). Emphasis is given to the use of nanostructured materials as sulfur adsorbents. Section 5.2 describes the two main groups of SARS (adsorption desulfurization and reactive adsorption desulfurization). Subsequently, the three main mechanisms for sulfur adsorption (π-complexation, direct sulfur–adsorption site interactions, and bulk incorporation in reactive adsorption desulfurization) are reviewed. Section 5.3 gives an overview of relevant literature concerning the use of promising groups of nanostructured adsorbents for SARS including zeolites, MOFs, mesoporous silicas, and carbon-nanostructured adsorbents. Finally, Sect. 5.4 gives some concluding remarks.

2 Selective Adsorption Removal of Sulfur Compounds

Selective adsorption removal of sulfur (SARS) is an emerging approach for ultra-deep desulfurization of refinery streams by means of solid adsorbents. SARS is most often regarded as a complementary step to conventional HDS for FCC naphtha and diesel, or as a final treatment to the blended pools. Contrary to ultra-deep HDS, SARS is usually carried out at low temperatures and pressures with minimal hydrogen consumption, preventing olefin hydrogenation and thus maintaining the properties of the fuels (e.g., octane and cetane numbers). In addition, the milder operating conditions of SARS potentially decrease the cost of the process, particularly considering the lower H_2 consumption, which is one of the most expensive items in ultra-deep HDS. Selective adsorption removal is conceived as a cost-effective strategy to reach ultra-clean fuel levels, removing the less reactive species that remain after conventional HDS. The main challenge of SARS is to find suitable solid adsorbents for the process, with high adsorption capacity, fast kinetics, adequate stability and renewability, and high selectivity for organosulfur compounds in the presence of competing species such as olefins and aromatics. SARS can be classified into two groups depending on the type of interaction between the organosulfur compound and the adsorbent: adsorption desulfurization and reactive adsorption desulfurization.

2.1 Adsorption Desulfurization

Adsorption desulfurization involves a weak interaction between the organosulfur molecules and the adsorbent (parallel adsorption via π-electrons of the aromatic rings) at low temperature (below 300 °C), low pressure (near atmospheric), and in
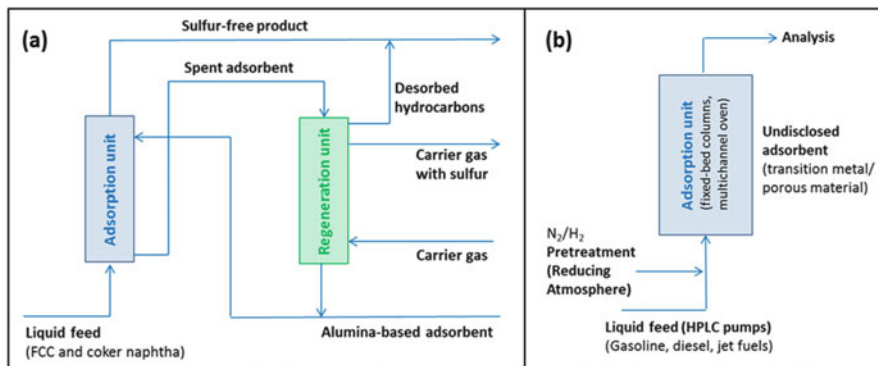
Fig. 5.1 Schematic representation of (**a**) IRVAD (adapted from Irvine 1998), (**b**) PSU-SARS processes (adapted from Velu et al. 2005)

the absence of hydrogen. The low heats of adsorption involved allow the adsorbed molecules to be easily desorbed by moderate changes in the process conditions, for instance, flushing the spent adsorbent, increasing temperature or decreasing pressure. In adsorptive desulfurization processes, the sulfur molecules are recovered during regeneration in a concentrated stream which can be treated easily downstream.

Research in adsorptive desulfurization has focused on the use of pure and modified activated carbons (Thaligari et al. 2016), CoMo-catalysts (Kim et al. 2016), alumina (Ullah et al. 2016), silica (Rodrigues et al. 2014), and zeolites (Lee and Valla 2017). Two main processes have been developed but have not been implemented in the industry yet. The IRVAD process consists of a moving bed of alumina-based adsorbent which is counter-currently brought into contact with FCC and coker naphta, Fig. 5.1a (Irvine 1998). The process operates at 240 °C and pilot tests have shown 90% reduction in the sulfur content. The spent adsorbent is regenerated at a slightly higher temperature and recirculated back to the adsorber. The alumina composition is optimized to improve hydrocarbon recovery during desorption. The PSU-SARS process operates between ambient temperature and 250 °C using an undisclosed adsorbent, most likely a transition metal complex supported on a zeolite, Fig. 5.1b (Velu et al. 2005). Experiments in laboratory scale showed that less than 20 ppmw remained in gasoline, jet fuel, and diesel treated with the developed adsorbents.

2.2 Reactive Adsorption Desulfurization

In reactive adsorption desulfurization, the sulfur atom from the organosulfur compound interacts strongly with the adsorption sites, remaining bounded to the surface. The organic molecule is hydrogenated and desorbed to the fuel stream without further structural changes. A schematic representation of this desulfurization process is given in Fig. 5.2. The operating conditions for reactive adsorption
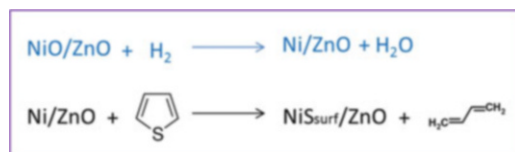
Fig. 5.2 Schematic representation of reactive adsorption desulfurization of thiophene using Ni/ZnO (adapted from Babich and Moulijn 2003)

are more severe than for nonreactive adsorption desulfurization, requiring the presence of H_2 at temperatures between 300 and 400 °C and pressures between 2 and 20 bar. However, less hydrogen (and with lower purity) is required compared to ultra-deep HDS and the fact that sulfur is captured by the adsorbent prevents possible recombinations between H_2S and the hydrocarbons in the stream. During regeneration, sulfur is recovered as H_2S, S or SO_2, depending on the procedure applied.

Most of the research regarding reactive desulfurization has dealt with metallic particles (mainly Ni) dispersed on metal oxides (ZnO, Al_2O_3, SiO_2) (Tawara et al. 2001; Park et al. 2008). ConocoPhillips developed a process called S-Zorb SRT which consists in a fluidized bed of adsorbent operating between 340–410 °C and 2–20 bar, requiring hydrogen purity above 50% (Song 2003; Babich and Moulijn 2003). The adsorbent is undisclosed but is known to be based on reduced metals and metal oxides that are sulfided during operation (most likely $Ni/ZnO + SiO_2 + Al_2O_3$). This technology can remove sulfur to levels below 10 ppmw from naphtha and diesel in a single step. Regeneration is carried out in a separate vessel. The process was implemented in Borger Refinery in Texas in 2001 and a second unit came online in Ferndale, Washington in 2003. The technology was bought by Sinopec in 2007.

2.3 Mechanisms of Sulfur Adsorption

2.3.1 π-Complexation

Donor–acceptor complexes are known to form between the π-electron system of aromatic rings (i.e., benzene and thiophene) and adsorption sites with electron–donor character. Here, the aromatic ring adsorbs parallel to the solid surface, preventing any steric hindrance from alkyl groups (Hernandez-Maldonado et al. 2005). Common examples of adsorbents that form π-complexes are alumina (Irvine 1998) and activated carbon (Salem 1994). The electron density of the aromatic species is influenced by the nature of the substituent groups and therefore differences in electron affinity exist between organosulfur molecules and sulfur-free aromatics. However, low selectivities for sulfur removal are often observed due

Fig. 5.3 Interaction
between
methylbenzothiophene on
PdCl$_2$/carbon (adapted from
Wang and Yang 2007)
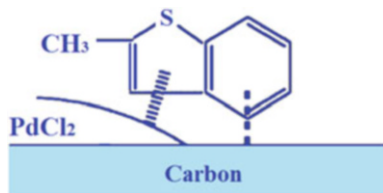
to the low concentration of the organosulfur compounds and to the abundance of
sulfur-free aromatics that remain in the fuels after conventional HDS (Salem 1994).

The selectivity of π-complexation increases by the incorporation of dispersed
metal ions on the adsorbents. The empty *s*-orbitals of transition metal cations can
form π bonds with a lone electron pair of sulfur while their *d*-orbitals can back-
donate electron density to the antibonding π-orbitals of the thiophene rings
(Hernandez-Maldonado et al. 2005). This results in a stronger adsorption of sulfur
molecules and hence higher selectivity and capacity. An increased selectivity
towards thiophenic molecules for Cu$^+$ exchanged zeolites was predicted by molec-
ular orbital calculations and corroborated experimentally (Takahashi et al. 2002).
PdCl$_2$ supported on activated carbon showed the high capacity to remove
benzothiophene from model jet fuel. A synergetic effect was proposed between
the carbon support and the Pd^{2+} ions where the thiophene ring interacts with the
metal through π-complexation while the benzene ring adsorbs strongly on the
carbon support, Fig. 5.3 (Wang and Yang 2007).

2.3.2 Direct Sulfur–Adsorption Site Interactions

The relatively high selectivity of some solid adsorbents towards trace organosulfur
compounds in fuels after HDS cannot be explained solely by the π-complexation
mechanism. Considering the eight possible configurations of thiophene in organo-
metallic complexes (Sanchez-Delgado 1994), Song and coworkers (Velu et al.
2005) pointed out that while six of them involve interactions with the π-electrons
of aromatic rings (and therefore are not selective for thiophene over benzene
cycles), the η$_1$S and S-μ$_3$ configurations are formed via direct sulfur–metal inter-
actions, see Fig. 5.4. The authors showed by molecular orbital calculations that the
highest occupied molecular orbital (HOMO) of thiophene (TP), benzothiophene
(BT), and dibenzothiophene (DBT) is localized more on the sulfur atom, whereas
the HOMO of alkylbenzenes and naphthalene is localized more on the conjugated
ring (Ma et al. 2002). Consequently, preferential adsorption is likely to take place
through the interaction of the HOMO on sulfur and the lowest unoccupied molec-
ular orbital (LUMO) on surface (metal) species. Suitable selective adsorption
centers are Lewis acid sites, functional groups with electron donor properties, and
surfaces with electronic defects.
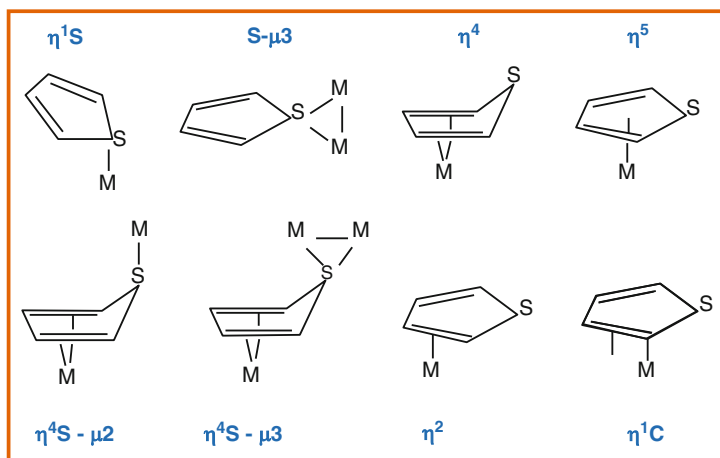
Fig. 5.4 Possible adsorption configurations of thiophene in organometallic complexes (adapted from Ma et al. 2002)

2.3.3 Bulk Incorporation in Reactive Adsorption Desulfurization

The reactivity of organosulfur compounds during reactive adsorption desulfurization has been reported to be higher for substituted thiophenes and benzothiophenes than for thiophene (Babich and Moulijn 2003), indicating that the reaction mechanism (i.e., coplanar adsorption, see above) is different from HDS reactions (Hernandez-Maldonado et al. 2005). In the presence of organosulfur compounds, there is a thermodynamic drive for some supported and bulk metal oxides (e.g., CuO, ZnO, MoO$_3$, NiO, Al$_2$O$_3$, MnO, and Co$_3$O$_4$) to incorporate sulfur in the form of metal sulfides, resulting in high theoretical capacities (Babich and Moulijn 2003). In practice, high sulfur uptakes have only been observed when metals are dispersed on the metal oxides (Tawara et al. 2001). A synergetic mechanism for reactive sulfur adsorption on Ni/Me$_x$O$_y$ has been tentatively proposed where hydrogenolysis of the organosulfur compound is catalyzed by the Ni sites, and the produced H$_2$S is rapidly re-adsorbed on ZnO which is then sulfided to ZnS, Fig. 5.5.

3 Nanostructured Adsorbents for Selective Adsorption Removal of Sulfur Compounds

As mentioned above, the main challenge of SARS is to find suitable solid adsorbents for the process, with high sulfur capacity at low temperatures and pressures, fast adsorption–desorption kinetics, adequate renewability and with high selectivity to adsorb sulfur in the presence of competing species such as aromatics, olefins, and

Fig. 5.5 Schematic representation of hydrogenolysis of thiophene using Ni/ZnO (adapted from Babich and Moulijn 2003)
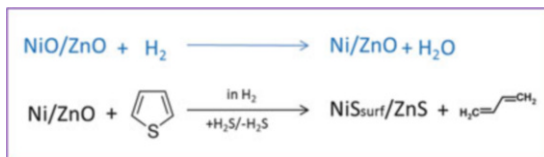
cyclic paraffinic hydrocarbons. In response to these demanding requirements, a range of potential sulfur adsorbents have been investigated including activated carbons, ionic liquids, supported metals, metal oxides, zeolites, and metal organic frameworks (MOFs). The desulfurization performance of each group of materials depends mainly on their chemical composition, the specific structure, and physico-chemical properties. In this context, the use of nanostructured adsorbents for SARS is particularly attractive since their high surface area and porosity improves the diffusion of sulfur compounds to the actives sites of the solid, facilitating parallel adsorption via π-electrons of the aromatic rings. In addition, it is possible to tune their adsorption properties by functionalization and by deliberate creation of defects during their synthesis. This section provides an overview of relevant literature concerning the use of promising nanostructured adsorbents for SARS including zeolites (Sect. 5.3.1), MOFs (Sect. 5.3.2), mesoporous silicas, and carbon-nanostructured adsorbents such as carbon nanotubes and graphene-like materials (Sect. 5.3.3).

3.1 Zeolites

Zeolites are crystalline aluminosilicates formed by a network of tetrahedral SiO_4 and AlO_4^- linked by shared oxygen atoms. The substitution of Si^{4+} by Al^{3+} in the ionic structure generates higher electron density on the bridging O atoms, which needs to be balanced by the addition of a positive ion, typically H^+ (Brønsted sites) or metal cations (Lewis sites). A remarkable characteristic of zeolites is the occurrence of a well-defined nano-pore structure that turns them into effective molecular sieves of the very large surface area. Their large surface area, their sieving properties, and the possibility to tailor the Brønsted and Lewis character by tuning their composition render zeolites very interesting materials for adsorption applications.

Most of the research concerning the use of zeolites for SARS has focused on investigating the adsorption performance of Y zeolite. Besides showing strong acidity and an excellent hydrothermal stability, Y zeolite is attractive because its cage-like cavities (~13 Å) interconnected by a wide 3D pore system (diameter 7.4 Å) (Kunhao et al. 2015) are able to accommodate large molecules such as alkylated dibenzothiophene, Fig. 5.6. Many studies have dealt with the removal of sulfur from model diesel, gasoline, and jet fuels comprising a variety of organosulfur compounds such as thiophene, benzothiophene, dibenzothiophene,
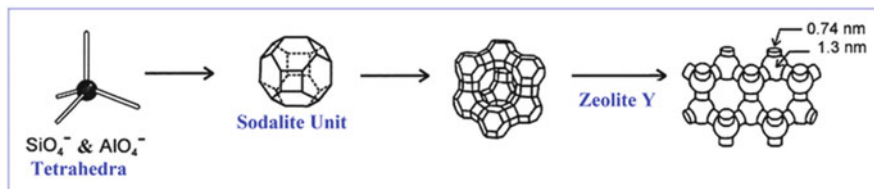
Fig. 5.6 Schematic representation of Y zeolite (adapted from Weitkamp 2000)

and 4,6-dymethildibenzothiophene (~1–800 ppmw S). Typically, the experiments have been carried out at low adsorption temperatures (20–150 °C) and pressures (1–2 bar). Depending on the operating conditions, the synthesis method and the pretreatment, the adsorption capacity of Y zeolites ranges from ~0.1 to 15 mgS g_{ads}^{-1}.

Many studies have shown that Y zeolites exchanged with transition metal ions (Cu^+, Ni^+, Zn^{2+}, Pd^{2+}, and Ag^+) exhibit higher capacities and selectivities to adsorb sulfur compared to NH_4Y and NaY zeolites, mainly due to the formation of stronger π-complexation bonds between the organosulfur compounds and the transition metals. Yang et al. (2001) synthesized Cu^+Y and Ag^+Y zeolites for the removal of thiophene in the presence of benzene and found higher sulfur capacities and selectivities compared to activated carbon, modified alumina, and other zeolite structures. The desulfurization performance decreased in the order $Cu^+Y \approx Ag^+$ Y > Na-ZSM-5 > activated carbon > NaY > modified alumina ≈ H-USY. In a subsequent study, Yang et al. (Hernandez-Maldonado et al. 2005) synthesized a monolayer CuCl/γ-Al_2O_3 adsorbent and studied its performance in the desulfurization of commercial diesel and jet fuels containing 140 and 365 ppmw S, respectively. Although CuCl/γ-Al_2O_3 showed a lower capacity than Cu^+Y, it was more stable. Cu^+Y is easily oxidized to $Cu^{2+}Y$ by oxygenates and moisture in the fuel, losing its π-complexation ability. Xue et al. (2005) studied the removal of thiophene and benzothiopene from model gasoline containing toluene and heptane and ranked the desulfurization performance as $Ce^{4+}Y$ > Ag^+Y > Cu^+Y > Na^+Y. Bhandari et al. (2006) reported that Ni^+Y and Cu^+Y zeolites have higher adsorption capacities for benzothiophene and 4,6-dimethyldibenzothiophene (DMDBT) than Y zeolites containing Fe^{2+}, Zn^{2+}, and Na^+ with the trend: $Ni^{2+}Y$ > Cu^+Y > Fe^{2+} Y > $Zn^{2+}Y$ > Na^+Y. In a more recent work, Zhang et al. (2008) assessed the removal of dibenzothiophene and 4,6-dimethyldibenzothiophene using various Na^+ Y exchanged zeolites and found that the adsorption capacities decreased in the order: AgY ≈ CuZnY > ZnNdY > ZnY > CuY > NiNdY ≈ NaY.

There are some discrepancies in the ranking of the desulfurization performance obtained for the same Y zeolites in the works mentioned above. This suggests that the capacities and selectivities of the materials do not depend exclusively on their chemical composition but can be influenced by other factors such as the type of sulfur species, the method used to synthesize the zeolite and the experimental adsorption methods. In general, it has been found that Ce-exchanged Y zeolites show high capacities and selectivities for organosulfur compounds over aromatics since adsorption occurs mainly via direct sulfur–metal (S–M) interactions rather

than via π-complexation (Velu et al. 2005; Song et al. 2014a). Hernandez-Maldonado et al. (2005) and Dastanian and Seyedeyn-Azad (2010) reported that vapor phase (VPIE) and solid-state (SSIE) ion exchange techniques lead to more efficient adsorbents compared to the conventional liquid phase ion exchange method (LPIE). The authors found that VPIE and SSIE minimize cation hydrolysis effects, avoiding unwanted species into the zeolite framework that result in low sulfur uptakes. Dastanian and Seyedeyn-Azad (2010) and Bakhtiari et al. (2016) showed that the stirring time, calcination temperature, and aging period used during the synthesis of Y zeolites play important roles in the final sulfur adsorption properties. The variations in the capacities and selectivities reported by different authors can also be attributed to the specific adsorption methodology used. Traditionally, batch (Song et al. 2014b), fixed-bed (breakthrough-type) (Velu et al. 2005; Hernandez-Maldonado et al. 2005; Bhandari et al. 2006), and flow calorimetry (Ng et al. 2005) tests have been used to investigate the sulfur adsorption properties of Y-zeolites.

Zeolites Y exhibit higher selectivities for substituted thiophenes and benzothiophenes than for thiophene in the following order 4,6-DMDBT > 4-M-DBT > DBT > BT > TP, indicating that selectivity increases with the π-electron density of the aromatic rings (Hernandez-Maldonado et al. 2005; Song et al. 2014a). Some authors have studied the competitive adsorption of organosulfur compounds in the presence of nitrogen heterocycles, aromatics, and olefins (Song et al. 2014a; Han et al. 2016; Ng et al. 2005). FT-IR studies on Ag^+Y, $Ce^{4+}Y$, and $Ag^+Ce^{4+}Y$ carried out by Song et al. (2014a) demonstrated that nitrogen-containing organics such as pyridine adsorb more preferentially than organosulfur compounds due to stronger interactions with the acid sites of the zeolite. In addition, pyridine occludes the pores of the zeolites reducing the space available for adsorption of thiophenic molecules. The authors reported that the uptake of organosulfur compounds by Ag^+Y zeolites decreases in the presence of aromatics and olefins since they also form π-complexes, leading to competitive adsorption. They found that the decrease in sulfur uptake was minimal for $Ag^+Ce^{4+}Y$ zeolites since alongside π-complexation, adsorption occurs via S–M interaction. Many authors have shown that the adsorption equilibrium of ion-exchanged Y zeolites can be adequately described by simple Langmuir and Freundlich isotherms and by more advanced models such as the Langmuir–Freundlich (Sips) isotherm (Xue et al. 2005; Takahashi et al. 2002; Yang et al. 2001; Bakhtiari et al. 2016). The heat of adsorption of Y zeolites ranges from 10 to 40 kJ mol^{-1}, decreasing linearly with the sulfur coverage (Lee and Valla 2017; Yang et al. 2001; Ng et al. 2005). Lee and Valla (2017) found that, in comparison to NaY, Y zeolites exchanged with transition metal ions exhibit higher heats of adsorption, revealing a stronger interaction between the species and the metal ions. In general, ion-exchanged Y zeolites exhibit fast sulfur adsorption kinetics which can be described by pseudo-first order models. Song et al. (2014b) assessed the performance of Cu^+Y and $Cu^+Ce^{4+}Y$ zeolites between 20 and 100 °C and found an optimal sulfur uptake around 50 °C. While there is a thermodynamic drive for adsorption at low temperatures, the

existence of a maximum sulfur capacity can be explained by low diffusion rates below 50 °C.

3.2 Metal Organic Frameworks

Metal organic frameworks (MOFs) are highly ordered materials consisting of metallic nodes (ions or clusters) coordinated to rigid organic molecules to form one-, two-, or three-dimensional networks, Fig. 5.7. The possibility to choose among various metallic centers and organic linkers (that can be functionalized) allow the physicochemical properties of MOFs to be tuned for a particular application. In the specific case of catalysis, gas storage, and adsorption, the most attractive features of MOFs are their high specific surface area (10,400 $m^2\ g^{-1}$), their large pore apertures (98 Å), their low density (0.13 $g\ cm^{-3}$), and their ability to accommodate guest molecules (Chughtai et al. 2015).

In recent years, there has been an increasing interest in exploiting the adsorption properties of MOFs to remove pollutants from water and fossil fuels. In the case of fossil fuels, most studies have used model diesel and gasoline to assess the performance of different MOFs in the removal of organosulfur compounds, in particular thiophene, benzothiophene, dibenzothiophene, and alkylsubstituted dibenzothiophenes. Experiments are usually carried out at atmospheric pressure and at relatively low adsorption temperatures (20–100 °C). Depending on the type of MOF and on the solvent and the operating conditions used, the adsorption capacities range from 2 to 112 mgS g_{ads}^{-1}, which are significantly higher than those of Y zeolites.

Cychosz et al. (2008) pioneered the use of MOFs for SARS studying the removal of BT, DBT, and DMDBT from isooctane with five different materials: MOF-5, MOF-177, HKUST-1, UMCM-150 and MOF-505. MOF-5 and MOF-177 are constructed from $Zn_4O(COO)_6$ secondary building units (SBUs) while HKUST-1, UMCM-150, and MOF-505 are Cu paddlewheel structures. The authors did not find any correlation between the surface area of the materials and the amount of sulfur adsorbed. Conversely, they observed that the adsorption performance of all three Cu materials was clearly superior to the Zn frameworks. UMCM-150 and MOF-505
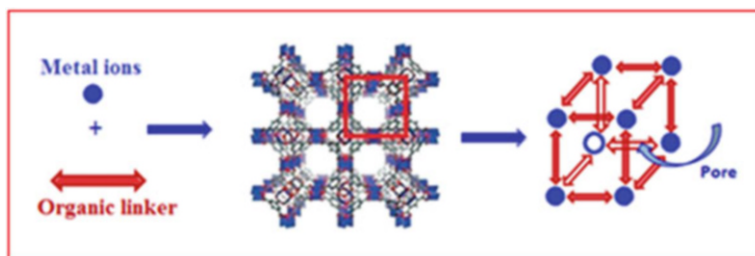
Fig. 5.7 Schematic representation of MOFs synthesis (adapted from Chughtai et al. 2015)

were the MOFs with the highest sulfur uptake which was ascribed to the presence of coordinatively unsaturated Cu-metal sites. Blanco-Brieva et al. (2013) assessed the sulfur adsorption performance of Fe-BTC ($C_9H_3FeO_6$), MIL-53 (Al) (Al(OH) $C_8H_4O_4$), and HKUST-1 ($Cu_3(C_9H_3O_6)_2$) MOFs and found that HKUST-1 exhibited the highest BT and DBT uptake due to a very strong interaction between the sulfur atom and the open Cu sites. Similar results were reported by Peralta et al. (2012) using real FCC naphtha and various types of MOFs as adsorbents. The authors observed that HKUST-1 and CPO-27-Ni exhibited the highest sulfur uptake and explained their results based on the presence of accessible coordinatively unsaturated metal sites. They also demonstrated that HKUST-1 and CPO-27-Ni have higher capacity and are more selective than Y zeolites in the presence of other aromatic compounds.

It has been reported that the adsorption capacity of MOFs can be significantly enhanced by the incorporation of transition metals after the synthesis. Khan et al. (2016) found that the BT uptake of MIL-47 doubled when it was impregnated with a $CuCl_2$ solution. The authors attributed the enhancement to the formation of π-complexes between the organosulfur compounds and Cu^{1+} ions produced during the pretreatment of the sample. Shi et al. (2011) reported a significant increase in the adsorption capacity of MOF-5 when it was impregnated with $Mo(CO)_6$. However, the authors did not observe any proportional trend between the amount of sulfur adsorbed and the content of $Mo(CO)_6$ in the sample, probably due to pore blockage at the molybdenum loadings used.

It has been reported that the sulfur uptake of MOFs decreases in the presence of other organic species (particularly aromatics) due to competitive adsorption. Cychosz et al. (2008) measured the BT, DBT, and DMDBT adsorption isotherms of five MOFs in isooctane and isooctane/toluene mixtures, and observed a fivefold decrease in the organosulfur uptake when toluene was present. Nevertheless, MOFs were found to be more selective towards sulfur molecules compared to a commercial NaY zeolite used as a benchmark. Shi et al. (2011) reported that a $Mo(CO)_6$/ MOF-5 reduced its DBT adsorption capacity by 90% in the presence of benzene. Contrary to these works, in a desulfurization study using real gasoline, Peralta et al. (2012) found that the sulfur uptake was not influenced by sulfur-free aromatic molecules but decreased significantly in the presence of olefins and nitrogen compounds. In a recent study, Khan and Jhung (2012) measured the sulfur capacity (DBT and DMDBT) of a series of MOFs with a MIL-53 topology in the presence of diethyl ether and water, which are oxygen-containing molecules that are usually present in gasoline and diesel pools. They observed a significant enhancement in the adsorption performance which was attributed to the structural flexibility of the MIL-53 material. In agreement with these observations, other authors have suggested that the breathing/flexibility properties of MOFs play a key role in the discrimination between thiophenic and nitrogen compounds (Van de Voorde et al. 2013). The availability and nature of open metal sites in MOFs also seem to be crucial factors with regard to the selective adsorption of nitrogen- and sulfur-containing organics. Maes et al. (2011) assessed the sulfur adsorption performance of a vast range of MOFs and found that MOFs with hard Lewis open metal sites (Fe^{3+}, Cr^{3+}, Al^{3+}) exhibit strong uptake of N-compounds and only weak affinity

for sulfur, whereas materials exposing soft Lewis open metal sites (Cu^{2+}, Co^{2+} and Ni^{2+}) were highly selective to S-compounds.

Contrary to Y-zeolites, the sulfur uptake of MOFs decreases significantly during regeneration with inert gases at high temperature, mainly due to a loss in crystallinity and porosity. However, MOFs can be effectively regenerated by polar solvents such as ethanol, methanol, and isopropanol (Blanco-Brieva et al. 2013). Blanco-Brieva et al. (2013) investigated the multicycle stability of HKUST-1 after adsorption of DBT. It was found that the adsorption capacity and crystallinity of the HKUST-1 adsorbent remained constant after several adsorption-regeneration cycles using methanol as a solvent. Although more comprehensive studies are needed to understand the adsorption equilibria and kinetics of organosulfur compounds on MOFs, it has been reported that Langmuir isotherms and pseudo-second order models can adequately describe the equilibrium and kinetics of the materials, respectively (Khan and Jhung 2012).

3.3 Mesoporous Silicas and Carbon-Nanostructured Adsorbents

Mesoporous silicas and some nanostructured carbons are receiving intense attention as solid adsorbents due to their large specific surface area, adequate pore size distribution, and unique chemical properties. Capacities above 20 mgS g_{ads}^{-1} have been reported for SARS, which is significantly larger than those observed with promoted Y zeolites.

In a pioneering work using nanostructured carbons, Nazal et al. (2015) assessed the removal of DBT from model diesel fuel using multi-walled carbon nanotubes (MWCNTs) and graphene oxide (GO), and found that the capacity of the materials was significantly increased by promoting them with 5 and 10% Al_2O_3 nanoparticles. They attributed the enhancement to the introduction of Lewis acidity. Fallah et al. (2015) demonstrated that the passivation of carbon nanoparticles with polyethylene glycol (PEG-200) enhanced the porosity and introduced acidic functional groups on the carbon framework that result in high adsorption capacities of BT, DBT, and DMDBT. GO has been used as support for hydrotalcites (HTs) and was shown to increase the DBT uptake compared to the unsupported materials, Fig. 5.8 (Menzel et al. 2016). The enhancement is attributed to an improved particle dispersion which favors the accessibility of sulfur to the adsorption sites. The HT/GO hybrids exhibited good regenerability and selectivity in the presence of biphenyl.

The surface chemistry, i.e., the presence of functional groups and acid sites, has been found to be as crucial for mesoporous silicas as for carbon nanostructures. Anbia and Karami (2015) compared the adsorption performance of a nanoporous carbon prepared using Al-SBA-15 as a template (CMK-3) with that of SBA-15 and Al-SBA-15. The following order in DBT uptake was found: CMK-3 > Al-SBA-

Fig. 5.8 Sulfur capacity of HT and HT/GO (adapted from Menzel et al. 2016)
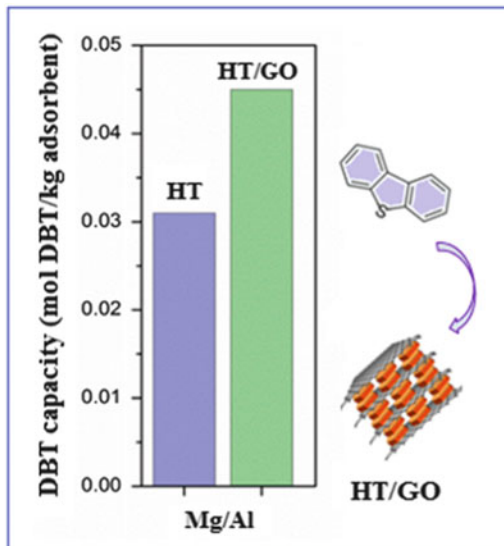
15 > SBA-15. CMK-3 exhibited the highest uptake (40 mgS g_{ads}^{-1}) due to a larger mesopore volume and specific surface area. The adsorption capacity of SBA-15 was significantly enhanced by the addition of Al due to the formation of Brønsted and Lewis sites of medium acidity. The presence of transition metals in the mesoporous silica structures has also been shown to enhance the sulfur capacity of the adsorbents. $PdCl_2$/SBA-15 was reported to have an increased capacity for benzothiophene and showed good regenerability by isooctane flushing (Rodrigues et al. 2014). Ag-impregnated mesoporous aluminosilicate nanoparticles (Al-MCM-41) prepared using a plasma treatment also exhibited remarkable sulfur uptakes from commercial jet fuel JP-8 (41 mgS g_{ads}^{-1}) and were very stable upon adsorption–desorption cycles (Hauser et al. 2016). The performance of Ag-Al-MCM-41 was superior to Ag-MCM-41 since the presence of intraframework Al introduced Brønsted acidity and aided in the dispersion and retention of Ag ions.

So far, very little attention has been given to the competitive adsorption of organosulfur compounds using mesoporous silicas and carbon nanostructures. General trends indicate that GO and MWCNTs adsorb selectively thiophenic molecules in the presence of aromatics and olefins such as benzene, naphthalene. and cyclohexene (Fallah et al. 2015). Similar to Y zeolites, preliminary studies suggest that the carbon nanostructures exhibit higher selectivities for substituted thiophenes than for thiophene (Khaled 2015). It has also been observed that the DBT uptake of GO is significantly enhanced in the presence of oxidizing agents such as *n*-octanal (Zhang and Wang 2017).

Mesoporous silicas and nanostructured carbons are typically regenerated using solvents such as ethanol, acetonitrile, toluene, and heptane (Nazal et al. 2015; Fallah et al. 2015; Khaled 2015) or by thermal treatment in air. In the case of carbonaceous adsorbents, the temperature should be maintained below 350 °C to

prevent the combustion of the materials under the oxidizing atmosphere. For both types of materials, the sulfur adsorption equilibria have been adequately described by Freundlich and Langmuir isotherms whereas pseudo-second order and linear driving force models have been used to describe the adsorption kinetics (Khaled 2015; Xiong et al. 2015).

4 Concluding Remarks

Selective adsorption removal of sulfur (SARS) is a promising technology for ultra-deep desulfurization of refinery streams. Contrary to conventional hydrodesulfurization (HDS), SARS is carried out at low temperatures and pressures with minimal hydrogen consumption. This prevents olefin hydrogenation and thus maintains the properties of the fuels (e.g., octane and cetane numbers). SARS is also a cost-effective strategy to remove heavy thiophenic compounds that remain after HDS. However, the main challenge of SARS is to find suitable solid adsorbents for the process, with high sulfur capacities, fast adsorption–desorption kinetics, adequate regenerability, and with high selectivity to adsorb sulfur in the presence of competing species.

Among the range of potential sulfur adsorbents, the use of nanostructured materials for SARS is particularly attractive since their high surface area and porosity improves the diffusion of sulfur molecules to the active sites. In addition, it is possible to tune their adsorption properties by functionalization and by deliberate creation of defects during their synthesis. The most widely studied nanostructures for selective sulfur removal are zeolites, metal organic frameworks (MOFs), mesoporous silicas, and carbon nanostructures. All of them show capacities that are at least in the range of precompetitive and commercial adsorbents. The performance of the different nanomaterials depends on the chemical composition, the nature of the sulfur molecules in the fuels, the presence of competing species, and the operating conditions. Zeolites have the advantage that the acid–base properties can be modified in a very controlled way by changing their bulk composition or through the incorporation of transition metals. The highest uptakes, however, have been reported for MOFs, but the stability of these structures during regeneration remains a big challenge. In contrast, nanostructured carbons and mesoporous silicas exhibit better regenerability and have adsorption properties that can be readily tuned but have relatively low capacities and selectivities.

Research efforts are still needed to get a deeper understanding of sulfur adsorption/desorption to allow better design of adsorbents. Investigation of competitive adsorption, and the influence of regeneration conditions on the stability and performance of the adsorbents in multicycle experiments are research areas that deserve particular attention. Likewise, the mechanical properties of the nanostructures need to be assessed and potentially improved by the use of binders.

References

Anbia M, Karami S (2015) Desulfurization of gasoline using novel mesoporous carbon adsorbents. J Nanostruct Chem 5(1):131–137

Arias M, Laurenti D, Geantet C, Vrinat M, Hideyuki I, Yoshimura Y (2008) Gasoline desulfurization by catalytic alkylation over silica-supported heteropolyacids: from model reaction to real feed conversion. Catal Today 130(1):190–194

Babich I, Moulijn J (2003) Science and technology of novel processes for deep desulfurization of oil refinery streams: a review. Fuel 82(6):607–631

Bakhtiari G, Abdouss M, Bazmi M, Royaee SJ (2016) Optimization of sulfur adsorption over Ag-zeolite nanoadsorbent by experimental design method. Int J Environ Sci Technol 13 (3):803–812

Bhandari VM, Hyun Ko C, Geun Park J, Han S-S, Cho S-H, Kim J-N (2006) Desulfurization of diesel using ion-exchanged zeolites. Chem Eng Sci 61(8):2599–2608

Blanco-Brieva G, Campos-Martin JM, Al-Zahrani SM, Fierro JLG (2013) Efficient solvent regeneration of Basolite C300 used in the liquid-phase adsorption of dibenzothiophene. Fuel 113:216–220

Chughtai AH, Ahmad N, Younus HA, Laypkov A, Verpoort F (2015) Metal-organic frameworks: versatile heterogeneous catalysts for efficient catalytic organic transformations. Chem Soc Rev 44(19):6804–6849

Cychosz KA, Wong-Foy AG, Matzger AJ (2008) Liquid phase adsorption by microporous coordination polymers: removal of organosulfur compounds. J Am Chem Soc 130 (22):6938–6939

Dastanian M, Seyedeyn-Azad F (2010) Desulfurization of gasoline over nanoporous nickel-loaded Y-type zeolite at ambient conditions. Ind Eng Chem Res 49(22):11254–11259

Fallah RN, Azizian S, Dwivedi AD, Sillanpää M (2015) Adsorptive desulfurization using different passivated carbon nanoparticles by PEG-200. Fuel Process Technol 130:214–223

Farzin N, Miran B (2015) Efficient desulfurization of gasoline fuel using ionic liquid extraction as a complementary process to adsorptive desulfurization. Pet Sci 12(2):330–339

Gutierrez C, Contreras L, Mancilla J, Elguezabal A (2015) Unsupported and supported non-promoted ruthenium sulfide catalyst with high catalytic activity for hydrocarbon hydrotreatments and its method. US 8987165 B2

Han X, Li H, Huang H, Zhao L, Cao L, Wang Y, Gao J, Xu C (2016) Effect of olefin and aromatics on thiophene adsorption desulfurization over modified NiY zeolites by metal Pd. RSC Adv 6 (78):75006–75013

Hauser JL, Tran DT, Conley ET, Saunders JM, Bustillo KC, Oliver SRJ (2016) Plasma treatment of silver impregnated mesoporous aluminosilicate nanoparticles for adsorptive desulfurization. Chem Mater 28(2):474–479

Hernández-Maldonado AJ, Yang FH, Qi G, Yang RT (2005) Desulfurization of transportation fuels by π-complexation sorbents: Cu(I)-, Ni(II)-, and Zn(II)-zeolites. Appl Catal B Environ 56 (1–2):111–126

Irvine RL (1998) Process for desulfurizing gasoline and hydrocarbon feedstocks. US 5,730,860

Javadli R, de Klerk A (2012) Desulfurization of heavy oil. Appl Petrochem Res 1(1):3–19

Ju F, Liu C, Meng C, Gao S, Ling H (2015) Reactive adsorption desulfurization of hydrotreated diesel over a Ni/ZnO-Al$_2$O$_3$-SiO$_2$ adsorbent. Energy Fuels 29(9):6057–6067

Khaled M (2015) Adsorption performance of multiwall carbon nanotubes and graphene oxide for removal of thiophene and dibenzothiophene from model diesel fuel. Res Chem Intermed 41 (12):9817–9833

Khan NA, Jhung SH (2012) Remarkable adsorption capacity of CuCl$_2$-loaded porous vanadium benzenedicarboxylate for benzothiophene. Angew Chem Int Ed 51(5):1198–1201

Khan NA, Yoon JW, Chang J-S, Jhung SH (2016) Enhanced adsorptive desulfurization with flexible metal-organic frameworks in the presence of diethyl ether and water. Chem Commun 52(56):8667–8670

Kim H, Lee C, Kim M, Oh J, Song S, Jang S, Yoon C, Han J, Yoon S, Nam S, Choi D, Shul Y, Ham H (2016) Preparation of CoMo/Al$_2$O$_3$, CoMo/CeO$_2$, CoMo/TiO$_2$ catalysts using ultrasonic spray pyrolysis for the hydro-desulfurization of 4, 6-dimethyldibenzothiophene for fuel cell applications. Int J Hydrogen Energy 41(41):18846–18857

Kunhao L, Breaver M, Speronello B, Garcia-Martinez J (2015) Surfactant-templated mesostructuring of zeolites: from discovery to commercialization. In: Garcia-Martinez J, Kunhao L (eds) Mesoporous zeolites. Wiley-VCH, Cham, pp 321–347

Lee KX, Valla JA (2017) Investigation of metal-exchanged mesoporous Y zeolites for the adsorptive desulfurization of liquid fuels. Appl Catal B Environ 201:359–369

Ma X, Sun L, Song C (2002) A new approach to deep desulfurization of gasoline, diesel fuel and jet fuel by selective adsorption for ultra-clean fuels and for fuel cell applications. Catal Today 77(1–2):107–116

Maes M, Trekels M, Boulhout M, Schouteden S, Vermoortele F, Alaerts L, Heurtaux D, Seo Y-K, Hwang YK, Chang J-S, Beurroies I, Denoyel R, Temst K, Vantomme A, Horcajada P, Serre C, De Vos DE (2011) Selective removal of N-heterocyclic aromatic contaminants from fuels by Lewis acidic metal–organic frameworks. Angew Chem Int Ed 50(18):4210–4214

Menzel R, Iruretagoyena D, Wang Y, Bawaked SM, Mokhtar M, Al-Thabaiti SA, Basahel SN, Shaffer M (2016) Graphene oxide/mixed metal oxide hybrid materials for enhanced adsorption desulfurization of liquid hydrocarbon fuels. Fuel 181:531–536

Nazal MK, Khaled M, Atieh MA, Aljundi IH, Oweimreen GA, Abulkibash AM (2015) The nature and kinetics of the adsorption of dibenzothiophene in model diesel fuel on carbonaceous materials loaded with aluminum oxide particles. Arab J Chem. doi:10.1016/j.arabjc.2015.12.003

Ng FTT, Rahman A, Ohasi T, Jiang M (2005) A study of the adsorption of thiophenic sulfur compounds using flow calorimetry. Appl Catal B Environ 56(1–2):127–136

Park JG, Ko CH, Yi KB, Park J-H, Han S-S, Cho S-H, Kim J-N (2008) Reactive adsorption of sulfur compounds in diesel on nickel supported on mesoporous silica. Appl Catal B Environ 81 (3–4):244–250

Peralta D, Chaplais G, Simon-Masseron A, Barthelet K, Pirngruber GD (2012) Metal–organic framework materials for desulfurization by adsorption. Energy Fuels 26(8):4953–4960

Rodrigues AKO, Ramos JET, Cavalcante CL Jr, Rodríguez-Castellón E, Azevedo DCS (2014) Pd-loaded mesoporous silica as a robust adsorbent in adsorption/desorption desulfurization cycles. Fuel 126:96–103

Salem ABSH (1994) Naphtha desulfurization by adsorption. Ind Eng Chem Res 33(2):336–340

Sánchez-Delgado RA (1994) Breaking CS bonds with transition metal complexes. A review of molecular approaches to the study of the mechanisms of the hydrodesulfurization reaction. J Mol Catal 86(1):287–307

Seeberger A, Jess A (2010) Desulfurization of diesel oil by selective oxidation and extraction of sulfur compounds by ionic liquids-a contribution to a competitive process design. Green Chem 12(4):602–608

Shi F, Hammoud M, Thompson LT (2011) Selective adsorption of dibenzothiophene by functionalized metal organic framework sorbents. Appl Catal B Environ 103(3–4):261–265

Song C (2003) An overview of new approaches to deep desulfurization for ultra-clean gasoline, diesel fuel and jet fuel. Catal Today 86(1–4):211–263

Song H, Cui X-H, Song H-L, Gao H-J, Li F (2014a) Characteristic and adsorption desulfurization performance of Ag–Ce bimetal ion-exchanged Y zeolite. Ind Eng Chem Res 53 (37):14552–14557

Song H, Chang Y, Wan X, Dai M, Song H, Jin Z (2014b) Equilibrium, kinetic, and thermodynamic studies on adsorptive desulfurization onto CuICeIVY zeolite. Ind Eng Chem Res 53 (14):5701–5708

Takahashi A, Yang FH, Yang RT (2002) New sorbents for desulfurization by π-complexation: thiophene/benzene adsorption. Ind Eng Chem Res 41(10):2487–2496

Tawara K, Nishimura T, Iwanami H, Nishimoto T, Hasuike T (2001) New hydrodesulfurization catalyst for petroleum-fed fuel cell vehicles and cogenerations. Ind Eng Chem Res 40 (10):2367–2370

Thaligari S, Srivastava V, Prasad B (2016) Adsorptive desulfurization by zinc-impregnated activated carbon: characterization, kinetics, isotherms, and thermodynamic modeling. Clean Technol Environ Policy 18(4):1021–1030

Topsøe H, Knudsen KG, Byskov LS, Nørskov JK, Clausen BS (1999) Advances in deep desulfurization. In: Hideshi H, Kiyoshi O (eds) Studies in surface science and catalysis, vol 121. Elsevier, Amsterdam, pp 13–22

Ullah R, Bai P, Wu P, Zhang Z, Zhong Z, Etim UJ, Subhan F, Yan Z (2016) Comparison of the reactive adsorption desulfurization performance of Ni/ZnO-Al$_2$O$_3$. Adsorbents prepared by different methods. Energy Fuels 30(4):2874–2881

Van de Voorde B, Munn AS, Guillou N, Millange F, De Vos DE, Walton RI (2013) Adsorption of N/S heterocycles in the flexible metal-organic framework MIL-53(FeIII) studied by in situ energy dispersive X-ray diffraction. Phys Chem Chem Phys 15(22):8606–8615

Velu S, Ma X, Song C, Namazian M, Sethuraman S, Venkataraman G (2005) Desulfurization of JP-8 jet fuel by selective adsorption over a Ni-based adsorbent for micro solid oxide fuel cells. Energy Fuels 19(3):1116–1125

Wang Y, Yang RT (2007) Desulfurization of liquid fuels by adsorption on carbon-based sorbents and ultrasound-assisted sorbent regeneration. Langmuir 23(7):3825–3831

Weitkamp J (2000) Zeolites and catalysis. Solid State Ion 131(1–2):175–188

Xiong J, Zhu W, Li H, Ding W, Chao Y, Wu P, Xun S, Zhang M, Li H (2015) Few-layered graphene-like boron nitride induced a remarkable adsorption capacity for dibenzothiophene in fuels. Green Chem 17(3):1647–1656

Xue M, Chitrakar R, Sakane K, Hirotsu T, Ooi K, Yoshimura Y, Feng Q, Sumida N (2005) Selective adsorption of thiophene and 1-benzothiophene on metal-ion-exchanged zeolites in organic medium. J Colloid Interface Sci 285(2):487–492

Yang RT, Takahashi A, Yang FH (2001) New sorbents for desulfurization of liquid fuels by π-complexation. Ind Eng Chem Res 40(26):6236–6239

Zhang Y, Wang R (2017) Nanocarbon materials for oxidative-adsorptive desulfurization using air oxygen under mild conditions. Diam Relat Mater 73:161–168

Zhang ZY, Shi TB, Jia CZ, Ji WJ, Chen Y, He MY (2008) Adsorptive removal of aromatic organosulfur compounds over the modified Na-Y zeolites. Appl Catal B Environ 82(1–2):1–10

Diana Iruretagoyena obtained her Ph.D. under the supervision of Professor David Chadwick and Professor Klaus Hellgardt in the Department of Chemical Engineering (2014) at Imperial College London, where she currently works as Research Associate. Her research focuses on the interfaces of reaction engineering, applied catalysis, separation processes, and materials science combining laboratory experiments and modelling work. Diana's research has resulted so far in a number of scientific publications and has been presented at international conferences and seminars. In addition, she was awarded the Julia Higgins Centenary Prize 2014 from the Department of Chemical Engineering.

Raul Montesano obtained his Ph.D. under the supervision of Professor David Chadwick in the Department of Chemical Engineering (2014) at Imperial College London, where he was awarded the Townend Prize. Currently, he works as a Research Engineer in R&D Chemicals at Haldor Topsøe.

Chapter 6
Nano-MoS$_2$ and Graphene Additives in Oil for Tribological Applications

Yufu Xu, Yubin Peng, Tao You, Lulu Yao, Jian Geng, Karl D. Dearn, and Xianguo Hu

Abstract Nano-additives have attracted lots of attentions in recent years due to their special performances. A traditional lubricating additive MoS$_2$ with nano-scale and a novel additive graphene were reviewed in this chapter. The synthesis methods, properties, and tribological applications of these two kinds of nano-additives dispersed in media have been reported. Nano-MoS$_2$ has three main nanostructures including nano-ball particles, nano-sheets, and nano-tubes. The wide accepted lubricating mechanisms for the MoS$_2$ nano-balls, nano-sheets, and nano-tubes are nano-bearing effects, slippery roles, and combined actions of rolling and sliding, respectively. Exfoliation and transfer seem to be the main pattern for MoS$_2$ nano-balls. For graphene, the adsorption and tribo-reaction account for its lubricating properties. A synergistic lubricating effect for using graphene and MoS$_2$ together dispersed in oil was found. Graphene was proved to extend the retention of MoS$_2$ on the surfaces and prevent the oxidation of MoS$_2$. Simultaneously, MoS$_2$ prevented the graphene from being ground into small and defective platelets. Both of them help to form a thicker adsorbed and tribo-film which result in a lower friction and wear. Other properties and applications of nano-MoS$_2$ and graphene are also reviewed. It shows that these two nano-additives have diverse functions and great potential for industrial applications.

Keywords Nano-MoS$_2$ • Graphene • Nano-additives • Tribological application

Y. Xu (✉) • Y. Peng • T. You • J. Geng • X. Hu
Institute of Tribology, School of Mechanical Engineering, Hefei University of Technology, Hefei 230009, China
e-mail: xuyufu@hfut.edu.cn

L. Yao
School of Chemistry and Chemical Engineering, Hefei University of Technology, Hefei 230009, China

K.D. Dearn
Department of Mechanical Engineering, School of Engineering, University of Birmingham, Edgbaston, Birmingham B152TT, UK

1   Introduction

A general demand from Society for a more sustainable and environmentally friendly development has led to an increasing interest and a growing corpus of work on energy-saving and emission reduction technologies (Price et al. 2011). The internal combustion engine is one such technology that has seen huge improvements in fuel efficiency, reduced overall energy consumption and emissions, and a key aspect of this has been improvements to the lubrication system (Abdelaziz et al. 2011).

   With the development of the nanotechnologies, the use of nano-additives added to base oils has been shown to reduce friction and wear due to their excellent lubricating effects. Some common solid particle lubricants such as nano-MoS_2 and graphene have made the transition from concept to the application and are showing great potential in the industry. However, there still exists a gap between the scientists and industrial engineers, relating to a general willingness to use the newly formulated additives (Zhmud and Pasalskiy 2013). If emissions and fuel consumption targets are to be met, then nano-additives, added to lubricant formulations will be a vital component for industry to deploy to meet these objectives.

   In this chapter, the progress and particularly the tribological behaviors of some key nano-additives dispersed in base oil are reviewed, and the trends in future developments of nano-additives are discussed in order to accelerate their application.

2   An Introduction to and the Tribological Behavior of Nano-MoS_2

Molybdenum disulfide (MoS_2) has a layered two-dimensional structure. Its crystal structure contains 1T-MoS_2, 2H-MoS_2, and 3R-MoS_2. 1T-MoS_2, per unit cell, has an octahedral structure with S atoms and one Mo atom; 2H-MoS_2 has a hexagonal structure and two S-Mo-S units per primitive cell, and 3R-MoS_2 has a hexagonal structure and three S-Mo-S units per primitive cell. Their respective structures are shown in Fig. 6.1. Among these MoS_2 crystals, 1T and 3R-MoS_2 are metastable and 2H-MoS_2 is stable under normal conditions. But no matter which crystal, each S atom is surrounded by 3 Mo atoms, and each Mo atom is surrounded by six S atoms consisting of S-Mo-S covalent bonds (Dickinson and Pauling 1923), such that the atom ratio of Mo and S is 1:2.

   The layered structure of MoS_2 has excellent tribological properties which are attributed to a combination of its low Van der Waals force between the molecule layers and strong covalent bond in the molecule. When MoS_2 bears a shear stress, molecular layers slide easily over one another. This is the reason that MoS_2 has been widely used as a solid lubricant and used as an additive of lubricating oils. It
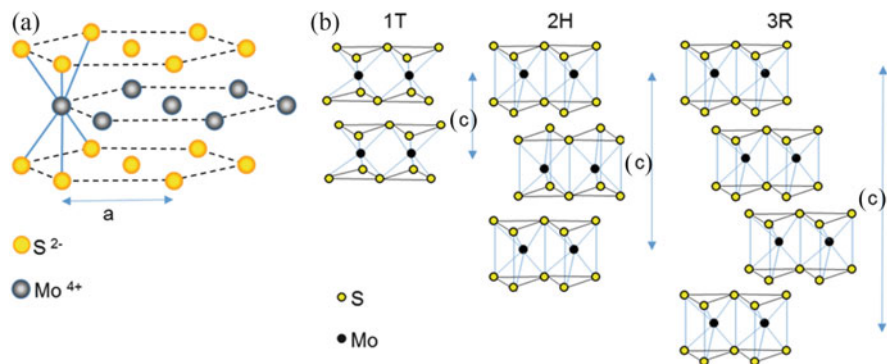
Fig. 6.1 Hexagonal structure of MoS$_2$ (**a**), a schematic illustration of the 1T- MoS$_2$ (**b**), 2H-MoS$_2$, and 3R-MoS$_2$, and the repeat unit of the MoS$_2$ layers (**c**) (Ye et al. 2015)

has been proved that the size of MoS$_2$ particles has a significant effect on their performances and so in the following section some typical nanostructures of MoS$_2$ are reviewed.

2.1 MoS$_2$ Particles: Nano-balls

Compared with MoS$_2$ sheets, MoS$_2$ nano-ball particles have some particular characteristics, including no dangling bonds that make them more stable. Additionally, the small size of the MoS$_2$ nanoparticles may result in some other enhanced physical properties.

2.1.1 Preparation of MoS$_2$ Nano-balls

Rosentsveig et al. (2009) used a four-step method to produce an inorganic fullerene-like (IF) MoS$_2$, which constitutes a typical nano-ball particle. The process includes four consecutive steps: (1) Evaporation of the molybdenum oxide (MoO$_3$) powder at a temperature of between 700 and 750 °C; (2) the reduction and condensation of the vapor into MoO$_{3-x}$ nanoparticles at 780 °C; (3) the sulfurization of the first few layers of the oxide nanoparticles; (4) the complete sulfurization of the nanoparticles with a slow diffusion-controlled reaction at a temperature above 840 °C. This method allows the sulfurized degree to be controlled (Fig. 6.2); it is however a complex procedure that consumes a large amount of energy.

Precipitation is another popular approach used for producing MoS$_2$ nano-balls due to the relatively gentle synthesis conditions. As an example, Huang et al. (2005) added 28 g Na$_2$S and 5 g (NH$_4$)$_2$MoO$_4$ into 250 mL distilled water, allowing the reaction to occur over an hour. During the reaction, hydrochloric acid was added to
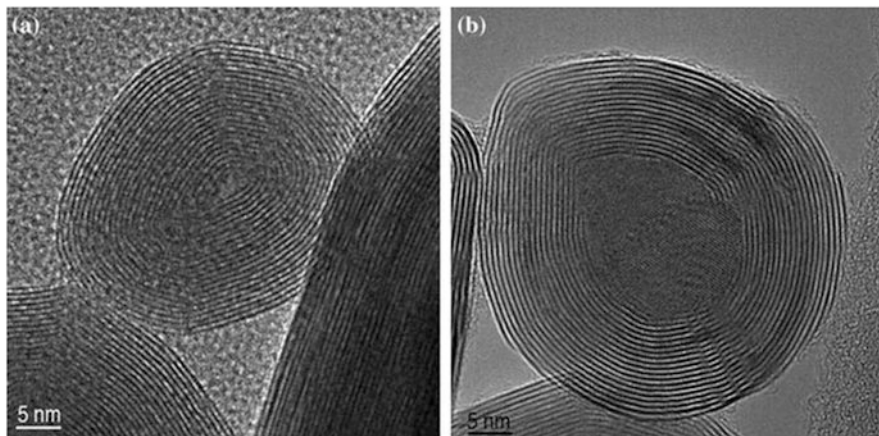
Fig. 6.2 TEM images of IF-MoS$_2$ nanoparticles with no oxide (**a**) and remaining oxide (MoO$_2$) in the core (**b**) (Rosentsveig et al. 2009)
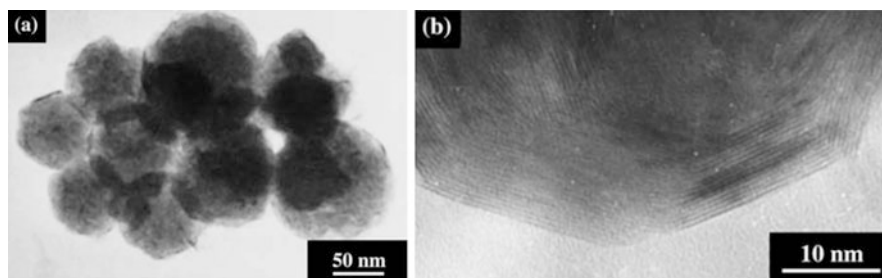
Fig. 6.3 TEM images of the IF-MoS$_2$ nanoparticles from produced using precipitation methods (Huang et al. 2005)

the solution in order to control the acidic pH. After this, the as-prepared MoS$_3$ precursor was desulfurized in a gas mixture of hydrogen-argon at 1173 K for 8 h. The final nano-balls had diameters varying from 70 to 120 nm (Seen from Fig. 6.3).

Hu et al. (2007) prepared molybdenum sulfide particles with Na$_2$MoO$_4$ and CH$_3$CSNH$_2$ by a quick (c. 5 min) homogenous precipitation technique in an alcohol–water solution at 82 °C. The resultant amorphous MoS$_x$ nano-ball particles were then desulfurized under H$_2$ flow at an elevated temperature for 50 min. This method seems to be another alternative method that can be used to synthesize nano-ball MoS$_2$.

2.1.2 Characterization of MoS$_2$ Nano-balls

Transmission electron microscopy (TEM) can be used to observe MoS$_2$ nanoparticles, operating levels of resolution that are much higher than light
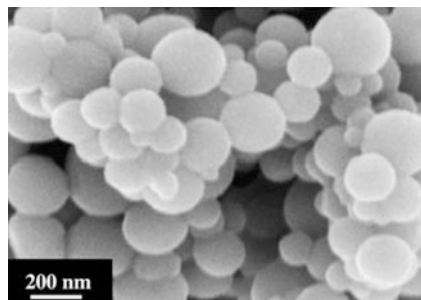
Fig. 6.4   SEM image of MoS$_3$ precursor (Huang et al. 2005)
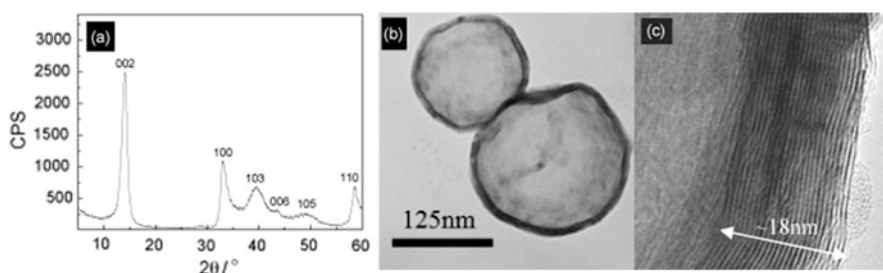
Fig. 6.5   XRD (**a**), TEM (**b**), and HRTEM (**c**) of the MoS$_2$ nano-ball particles (Hu et al. 2009b)

microscopes, due in part to the small de Broglie wavelength of electrons. It can also be used to show structure, morphology, and to check the aggregation of nanoparticles.

Scanning electron microscopy (SEM) is another effective tool to observe the form of nanoparticles. As an example, Fig. 6.4 (Huang et al. 2005) shows a MoS$_3$ precursor produced by Huang, with a clear spherical shape, with a diameter of ~150 nm. However, the aggregation of the nanoparticles is severe as no dispersing media can be used with this method.

X-ray powder diffraction (XRD) can be used to assess the crystal structure of MoS$_2$ nanoparticles. The work of the Institute of Tribology at Hefei University of Technology has proved that the MoS$_2$ nanoparticles have the similar XRD spectra in Fig. 6.5 with the standard curve of MoS$_2$ in PDF number 37-1492. Its holly structures are also shown in TEM in Fig. 6.5.

The crystallinity and shape of MoS$_2$ nano-balls are the main characteristics that affect frictional properties. These two properties are governed by the parameters and conditions selected during synthesis. Crystallinity governs the order degree of a MoS$_2$ layer which is composed of closed shells nano-balls. Perfectly crystalline MoS$_2$ nano-balls have a well-crystalline order with few defects present in closed shells, whereas poor crystallinity shows some extent of disorder with many point defects (Fig. 6.6). Moreover, perfectly crystalline MoS$_2$ nano-balls will have good physical properties. The shape of a MoS$_2$ nano-ball is not a perfect sphere most of the time. There are corners of the structure which are likely to induce stress
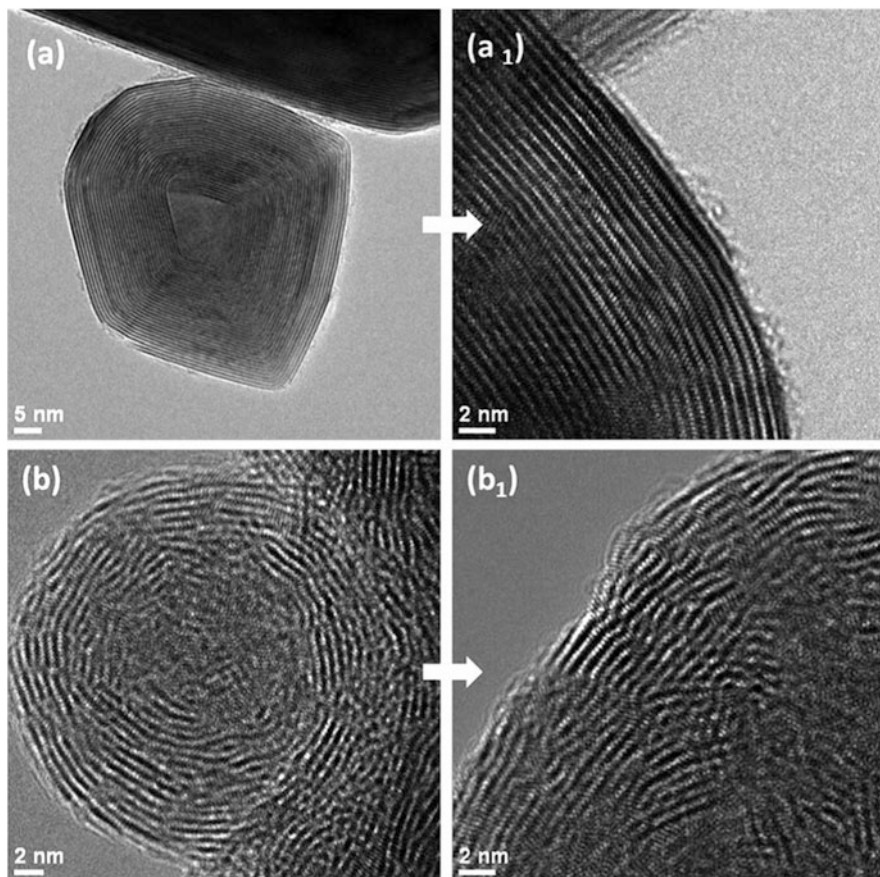
Fig. 6.6 HRTEM images of perfect (**a**, **a$_1$**) and incomplete crystalline MoS$_2$ nano-balls (**b**, **b$_1$**) (Lahouij et al. 2014)

concentrations. With this in mind, therefore the more perfectly crystalline and spherically shaped that the MoS$_2$ nano-ball is the higher the ability resist deformation (Lahouij et al. 2014).

2.1.3   Dispersion of MoS$_2$ Nano-balls in Base Oil

MoS$_2$ nanoparticles have lots of functions including lubrication, catalysis (Li et al. 2011b), functional materials, and so on (Radisavljevic et al. 2011). Among them, one of the most important functions for MoS$_2$ seems to be lubrication. Usually, it is used as an additive in base oil or grease. Thus, the choice of the base oil is very important for improving the lubricating properties of MoS$_2$ nanoparticles. For example, an industrial oil composed of many fractions of hydrocarbons has been

used for dispersing MoS$_2$ nanoparticles (Aralihalli and Biswas 2013). However, the industrial oil has contained many other additives with a variety of roles. To reduce the effects of the other additives, paraffin oil is often chosen as a base oil for use with MoS$_2$ nanoparticles (Huang et al. 2005) because of the similar components with traditional mechanical oils. Poly alpha olefin (PAO) has attracted lots of attention, with excellent thermal stability and anti-oxidation properties, as a base oil with MoS$_2$ nanoparticles in recent years (Rosentsveig et al. 2009). Moreover, Xu et al. have tried some renewable bioenergies, such as bio-oil, as the base oil for MoS$_2$ micro-sheets, which have also shown good lubricating effects.

It has been reported that the addition of the nanoparticles on their own in base oil has little effect on the tribological properties of a tribo-systems. But it takes effect after using a dispersing agent (Aralihalli and Biswas 2013; Desai and Banat 1997; Moshkovith et al. 2006). This suggests that the selection of the dispersive agent and method of mixing are very important. Zhou et al. (2008) used an extractant Cyanex 301 (di-(2,4,4-trimethylpentyl) dithiophosphinic acid) to modify the surface of MoS$_2$ nano-hollow spheres in liquid paraffin. Results showed that the modified MoS$_2$ had better extreme pressure, antiwear, and antifriction properties than commercial MoS$_2$. Sorbitol monooleate was selected by Huang et al. (2005) as the dispersing agent for IF-MoS$_2$ in paraffin oil. The mixture was stirred with a high-speed dispersion machine before ultrasonic treatment.

Dispersant agents can be grafted or adsorbed on nanoparticles with ultrasonication or stirring. The chemical affinity between dispersants and nanoparticles is the main factor that affects the dispersion. When chemical affinity is low, the particles can be easily separated from the base oil and the nanoparticles will agglomerate again under the effect of friction (Aralihalli and Biswas 2013).

It is important not to increase the concentration of dispersants to levels that are too high in the lubricant. Under such conditions, though the nanoparticles will be well dispersed, a large amount of dispersant agent will reduce the life of the lubricant and increase friction. As shown in Fig. 6.7, the tribological benefits of MoS$_2$ were eliminated when 5% dispersant was used. However, when the dispersant concentration was adjusted to 0.05%, the friction coefficient decreased. The reason for this is that with high concentrations of dispersants, MoS$_2$ nanoparticles cannot be adsorbed on the rubbing surface and reduce the friction coefficient (Rabaso et al. 2014a).

2.1.4 Comparison with Micro-MoS$_2$

MoS$_2$ nanoparticles have better lubricating properties than MoS$_2$ micro-particles (Hu et al. 2010). According to the Risdon's investigation (Risdon and Gresty 1975), the energy consumed on transportation in the USA during the period 1963–1974 can be reduced by 4.4% with a proper dispersion of 1% weight commercial molybdenum disulfide in the engine oil. Thus, it can be inferred that more fuel can be saved by the introduction of nano-MoS$_2$. Hu's results (Hu et al. 2010)
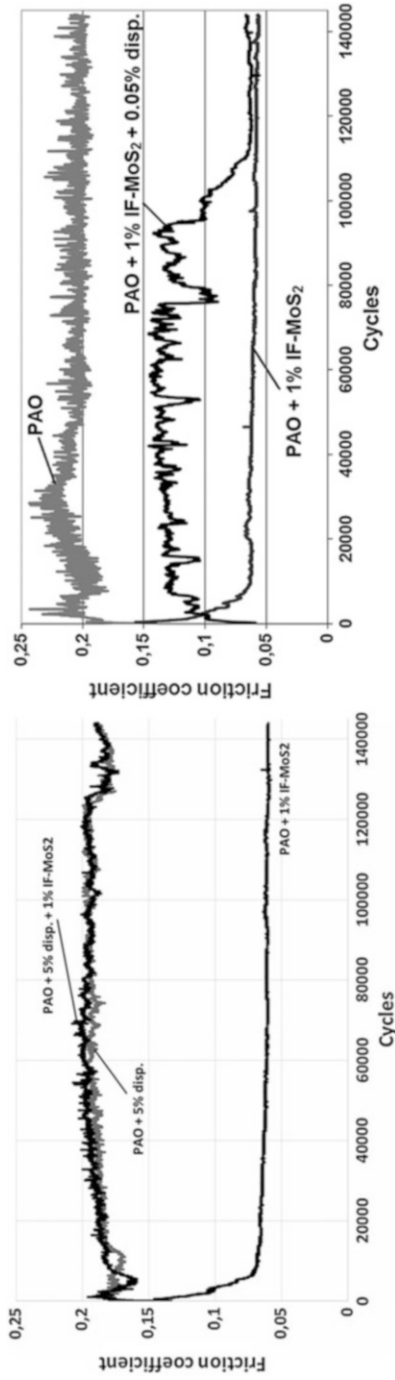
Fig. 6.7 Friction coefficient of PAO + 1% IF-MoS$_2$ + 5% dispersant (*left*), and PAO + 1% IF-MoS$_2$ + 0.05% dispersant (*right*) (Rabaso et al. 2014a)
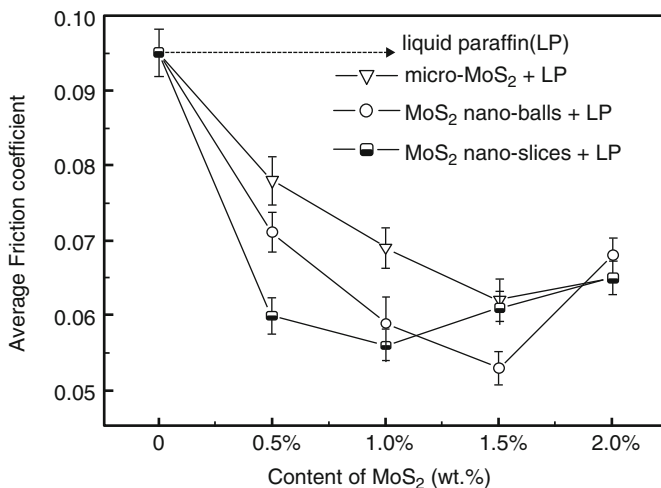
Fig. 6.8 Effects of the concentration of MoS$_2$ on the average friction coefficient (Hu et al. 2010)

showed that the addition of MoS$_2$ nano-balls in liquid paraffin at a concentration of 1.5 wt% resulted in a better antifriction and antiwear properties than micro-MoS$_2$. Figure 6.8 shows a friction coefficient reduction of 21% and 10%, respectively, when compared to those of 1.5% micro-MoS$_2$ and 1.0% nano-slices.

2.1.5 Effect of ZDDP on Tribological Properties

ZDDP (Zinc Dialkyl Dithiophosphates) is an important oxidation and corrosion inhibitor often found in fully formulated lubricating oil which extends the oxidation resistance of lubricating oil. It also has excellent antiwear properties but has no effect on friction. Lamellar MoS$_2$ nanoparticles derived from nano-sheets or the exfoliation of nano-balls are easily oxidized to MoO$_3$ which degrade the friction-reducing properties of MoS$_2$. When ZDDP and MoS$_2$ nanoparticles exist together, both friction coefficient and wear are reduced significantly. It is believed that there is a synergistic effect between ZDDP and MoS$_2$: the MoS$_2$ is believed to be embedded into ZDDP chemical reaction film and therefore reinforces its antiwear effect, at the same time, the ZDDP film provides protection for the MoS$_2$ from being oxidized resulting in the improvement of the antifriction behaviors (Tomala et al. 2015; Aldana et al. 2014).
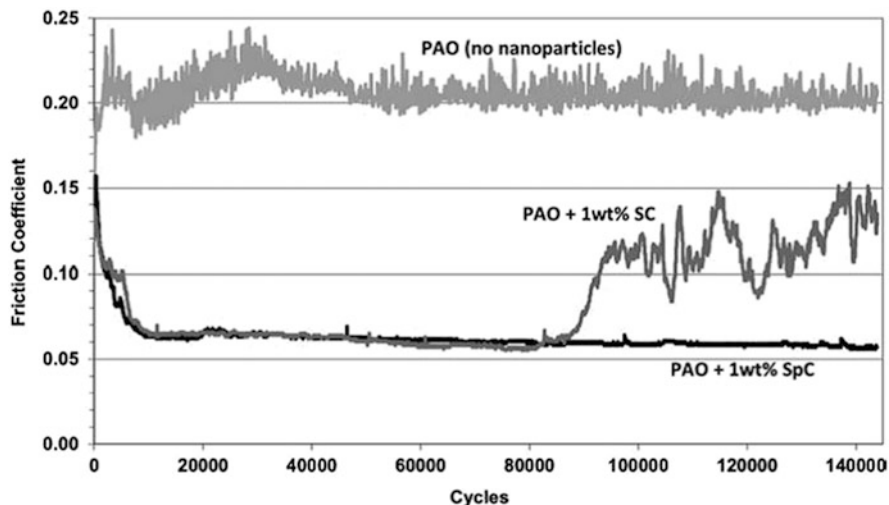
Fig. 6.9 Friction coefficient of perfect (SC) and poorly crystalline (SpC) on HFRR (Rabaso et al. 2014b)

2.1.6 Effect of Crystallinity on Tribological Properties

The tribological properties of MoS_2 nano-balls to some extent are dependent on its structural characteristics and particularly its crystallinity. MoS_2 nano-balls that are perfectly crystalline have a better ability to resist deformation, whereas MoS_2 with incomplete crystallinity are easily deformed and exfoliated under the similar sliding conditions (Lahouij et al. 2014). Rabaso et al. (2014b) compared the frictional properties of MoS_2 with poorly crystalline structures with similar average diameters (150 nm). They found that perfect MoS_2 nano-balls played a significant role in friction-reduction during running in, however, the friction coefficient increased after this due to the lack of perfect MoS_2 nano-balls. On the contrary, poorly crystalline MoS_2 maintained a stable low friction coefficient as shown in Fig. 6.9. The difference is because poorly crystalline can be easily exfoliated and transferred onto the rubbing surfaces forming an adsorbed layer. Perfect crystalline nanoparticles were much harder to exfoliate before being squeezed out from the rubbing interfaces, thanks to the better physical properties. In addition to the frictional process, the MoS_2 adsorbed film formed during the early stages of rubbing was gradually worn off. Due to the two reasons above, there were few MoS_2 particles remaining between the frictional interfaces resulting in the increase of the friction coefficient.

Fig. 6.10 A MoS$_2$ nano-ball bearing two different forms of pressure: isotropic (**a**), normal stress (**b**) (Joly-Pottuz et al. 2006)

(a)   (b)
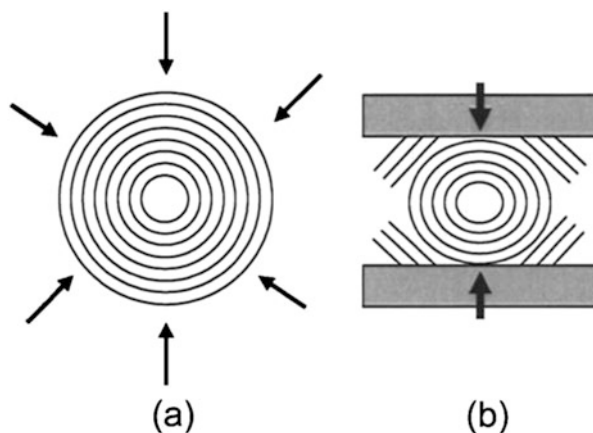
2.1.7 Effect of Different of Pressure on Exfoliation Behavior

MoS$_2$ nano-balls can be ruptured under a high normal stress on the frictional interfaces. However, this will not happen in oil though oil pressure might be much higher than critical ruptured normal stress. That is because oil pressure is isotropic and the shape of the nano-ball is quasi-spherical which makes bearing force of MoS$_2$ uniform (Fig. 6.10) (Joly-Pottuz et al. 2006).

2.1.8 Tribological Mechanisms

MoS$_2$ nano-balls have excellent lubricating properties as lubricating oil additives. There are three main frictional mechanisms that can explain this property: rolling, sliding, and exfoliation-transfer (third body) as shown in Fig. 6.11 (Tevet et al. 2011).

1. Rolling: MoS$_2$ nano-balls roll as a ball bearing across frictional interfaces under relatively low normal stress. The roller is dependent on the shape of nano-balls which should be quasi-spherical structures.
2. Sliding: Similar to nano-sheets, friction happens between external surfaces of the nano-balls under higher normal stress. The behavior of sliding is due to the shape of nano-MoS$_2$ particles, which is not perfectly spherical but of a faceted polyhedron structure. The corner of the faceted polyhedron structure can be easily distorted by asperities on the rough mating surfaces.
3. Exfoliation and transfer (third body): Exfoliation is the main action of behavior under high normal stress resulting in deformation and even rupture of the nano-balls. Under the combined effects of the normal stress and shear stress, the external surface of the nano-ball particles can be exfoliated producing MoS$_2$
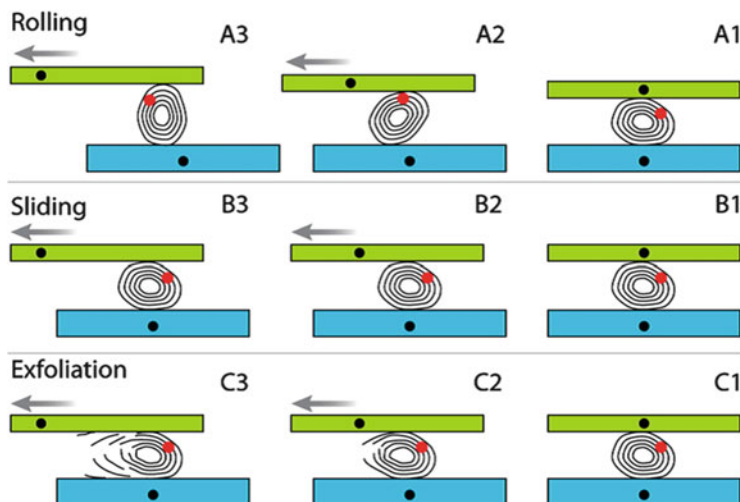
Fig. 6.11 Schematic of the three main tribological mechanisms of MoS$_2$ nano-balls: rolling (**a**), sliding (**b**), and exfoliation and transfer (third body) (**c**) (Tevet et al. 2011)

nano-sheets which can be adsorbed on the rubbing surfaces providing a protective layer and reduced the friction coefficient.

Among these three behaviors, rolling is generally accepted as the most prevalent mechanisms of friction reduction, because they cannot be detected directly only by micro-frictional tests on the single MoS$_2$ nano-balls.

Particle size and crystalline perfection of the MoS$_2$ nano-balls are the most important factors that affect tribological behavior (Rosentsveig et al. 2009). Generally, due to a nano-bearing effect, the small MoS$_2$ nanoparticles have better antiwear and friction reducing properties than larger nanoparticles. However, with the decrease of particle size, the aggregation effects of the MoS$_2$ can increase and chemical stability reduces, which might result in reduced lubricity. Hence, the particle size is very important in the efficacy of the additives. It is believed that exfoliation, rolling friction, and third body transfer of MoS$_2$ sheets into surface asperities are the prevalent mechanisms that can explain the excellent tribological properties of MoS$_2$ nanoparticles (Rosentsveig et al. 2009).

There are no active dangling bonds in the closed-structure MoS$_2$; consequently, the oxidation temperature of MoS$_2$ nano-ball particles is ~100 $^\circ$C higher than that of 2H-MoS$_2$. Moreover, under some testing conditions, the MoS$_2$ nano-ball particles had better lubricating properties than MoS$_2$ nano-sheets. This was ascribed to the chemical stability of the layer-closed spherical structure of nano-balls. The detailed mechanisms for this are shown in Fig. 6.12. In air or when used in liquid paraffin nano-sheets, due to the rim-edge site of the nano-sheets, they are easier to oxidized into MoO$_3$, there was a poor lubrication. MoS$_2$ nano-ball particles are relatively stable and can bear the shearing via rolling and elastic deformation.
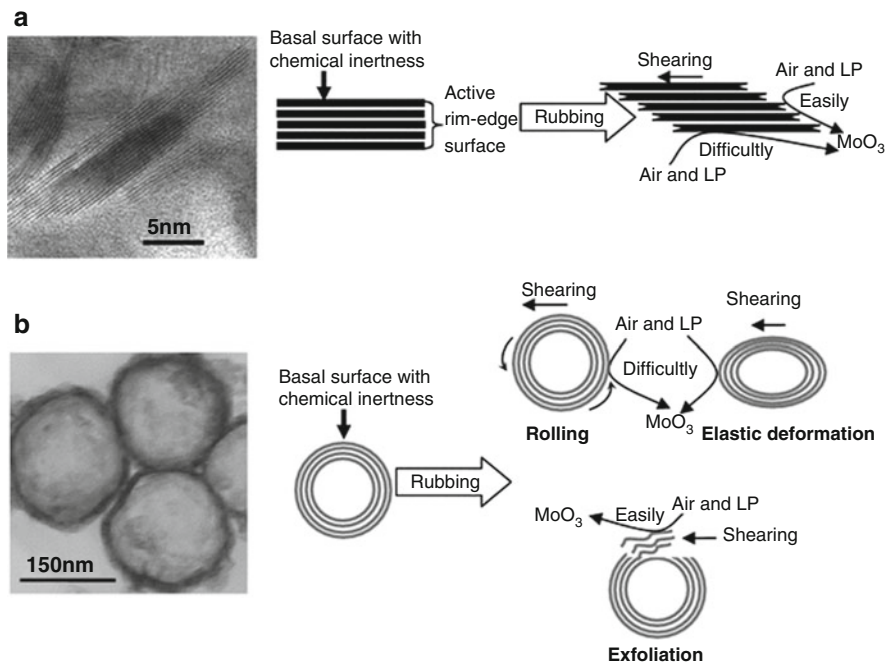
Fig. 6.12 TEM images and schematics of the lubrication mechanisms of MoS$_2$ nano-slices (**a**) and MoS$_2$ nano-balls (**b**) (Hu et al. 2010)

2.2   MoS$_2$ Nano-sheets

In recent years, the study of graphene-like two-dimensional layered materials has attracted great interest due to the successful exploration of graphene (Zhang et al. 2016b; Huang et al. 2012; Xu et al. 2013). Among them, MoS$_2$ nano-sheets are the popular research molecular as a result of their distinct structure and superior properties. Functionalization, hybridization, and modification of MoS$_2$-based nano-sheets have seen them used widely in various applications. Here, the preparation, characterization, and properties of nano-sheets are reviewed.

2.2.1   Preparation of MoS$_2$ Nano-sheets

It has been demonstrated that most of the methods for preparing 2-D nano-material such as graphene are effective for MoS$_2$ nano-sheets. The classic and straightforward way to prepare the nano-sheets is micro-mechanical cleavage (Radisavljevic et al. 2011). Using this top-down approach, a high-quality 2-D nano-material can be obtained (Lopez-Sanchez et al. 2013). However, the shortcomings of this method are also obvious. The productive efficiency is low and it is difficult to synthesize the
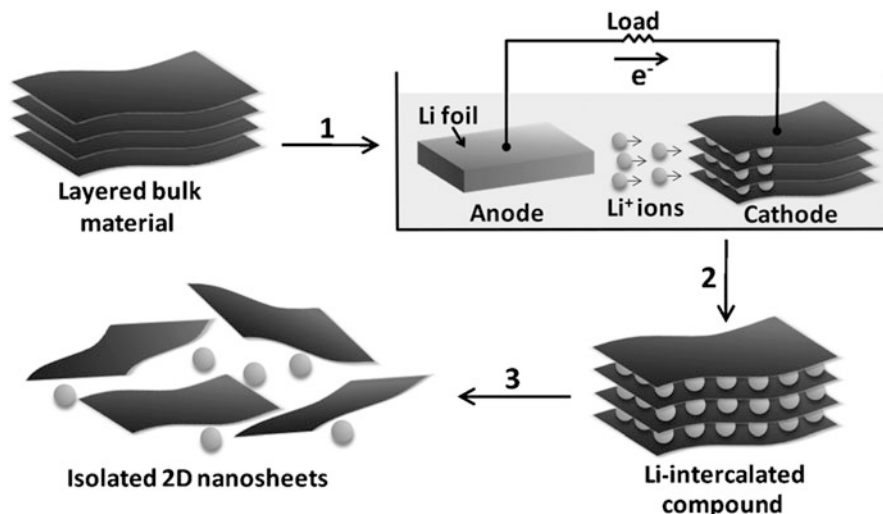
Fig. 6.13 Schematic illustration of electrochemical lithiation and exfoliation process for the fabrication of 2D nano-sheets from layered bulk crystals (Zeng et al. 2011)

2D nano-sheets in large quantities. Moreover, the geometry can be very difficult to control precisely.

Ion-intercalation exfoliation is another popular method that can be used for the preparation of MoS_2 nano-sheets. As shown in Fig. 6.13, there are three steps in this method: (1) introduction of Li^+ ions into the interlayer of bulk MoS_2; (2) immersion of Li_xMoS_2 nano-sheets into water; and (3) ultrasonic processing of the solution.

Bottom-up methods have been used to fabricate MoS_2 nano-sheets with desired size and thickness. Choudhary et al. (2014) adopted a sputter–chemical vapor deposition (CVD) technology to synthesize large-area, high-quality, and layer-controlled MoS_2 nano-sheets on Si-based substrates. They also demonstrated that the single-layer MoS_2 over an area of 2 inches wafers with the domain size of 10–15 μm^2, showing good potential in future flexible, high-temperature, and radiation hard electronics/optoelectronics. Although CVD is an effective method for producing high-quality MoS_2 nano-sheets, there are some obvious disadvantages with the synthesis conditions, such as high temperatures, the requirement for a vacuum, and specific substrates, which restrict the practical applications of MoS_2 nano-sheets (Zhang et al. 2016b).

Owing to specific merits such as cheap raw materials, size and thickness controllable, high productive efficiency and no requirements on the substrates, solution-based methods have become prevalent in recent years. Smith et al. (2011) prepared MoS_2 nano-sheets through 1.5 mg mL^{-1} sodium cholate as a surfactant to exfoliate bulk MoS_2 in aqueous solutions. In a typical run, ultrasonic treatment can be used for the solution lasting 30 min, followed by centrifugation at 1500 rpm for 90 min.

2.2.2 Application of MoS$_2$ Nano-sheets

One of the most important applications for MoS$_2$ nano-sheets is a substitute of noble metal catalysts such as Pt/C. It has been proved that the active edges of MoS$_2$ can be used as the active center for electro-catalysis (Zhang et al. 2016a). Electro-catalytic performance can be improved by reducing the dimension and by exposing the edges of the 2-D MoS$_2$.

Efficient energy storage is an important challenge for sustainable development. MoS$_2$ nano-sheets can be used in energy storage devices. One such application is in Li-ion batteries, which have been shown to be a highly efficient energy storage system. Although the charge capacity of the bulk MoS$_2$ is easy to reduce after use, after intercalating Li-ion into the interlayer of MoS$_2$, fewer layers of nano-sheets, the composites exhibited a high energy density capacity of 750 mA h g^{-1} even after 50 cycles (Du et al. 2010). Na ion intercalation in MoS$_2$ sheets has also shown promising results. Bang and his coworkers (2014) reported a simplest method for enhancing the productive efficiency of MoS$_2$ nano-sheets in 1-methyl-2-pyrrolidinone with the assistant of sodium hydroxide. They also proved that at the high current densities, the exfoliated MoS$_2$ electrode exhibited better capacities than the pristine particle electrode (Fig. 6.14), indicating improved properties of the exfoliated MoS$_2$ nano-sheets with the reduced diffusion lengths of Na ions.

Wu et al. (2012) used electrochemically reduced single-layer MoS$_2$ nano-sheets for sensor applications. It was found that the prepared MoS$_2$ nano-sheets had good conductivity and high electrochemical sensitivity to detect glucose and
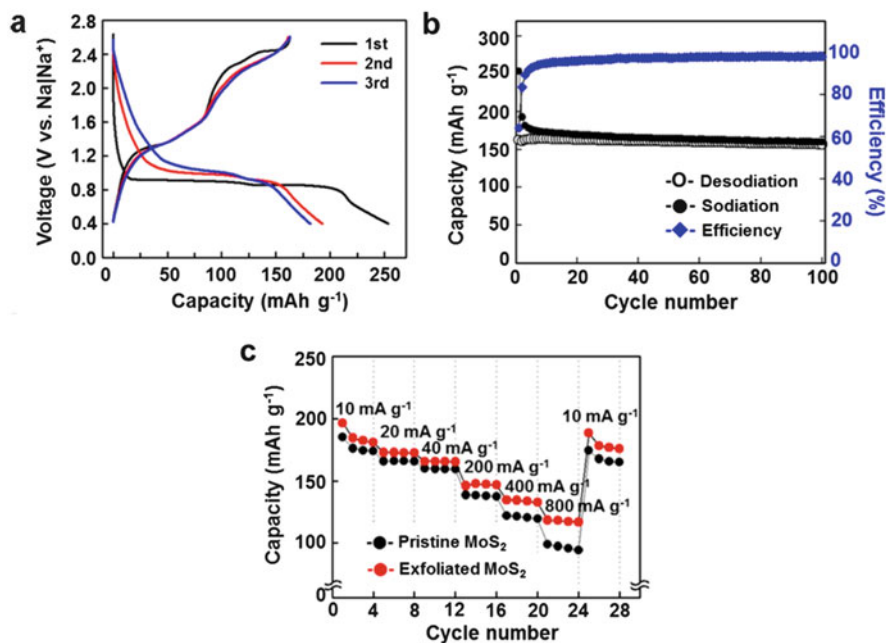
Fig. 6.14 Charge–discharge curves (**a**) and the cycling properties and their coulombic efficiencies of the MoS$_2$ nano-sheets (**b**); the rate capability of pristine MoS$_2$ powder and the prepared MoS$_2$ nano-sheets at various current densities (**c**) (Bang et al. 2014)
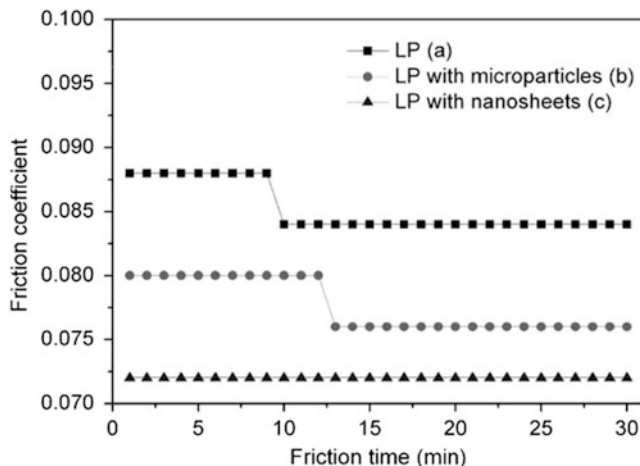
Fig. 6.15 Friction coefficient of the base oil with different additives: Without additives (**a**), MoS_2 micro-particles (**b**), and MoS_2 nano-sheets (**c**) (Wu et al. 2010)

biomolecules. Thus, reduced MoS_2 nano-sheets can be used in the development of novel electrode materials and can supply a novel platform for the sensing applications. Li et al. (2012) used MoS_2 film-based field-effect transistors to detect NO at room temperature. The results showed that a single-layer MoS_2 nano-sheet had a rapid response to NO, but the current was unstable. A few-layer (less than 5) MoS_2 nano-sheet assembly presented both stable and sensitive responses to NO up to 0.8 ppm.

Another important application for MoS_2 nano-sheets is as lubricating additives. According to Wu et al. (2010), with the addition of MoS_2 nano-sheets in liquid particles with concentration of 1.5 wt%, the friction coefficients decreased significantly and are shown in Fig. 6.15. In addition, MoS_2 nano-sheets have a lower and more stable friction coefficient than commercial MoS_2 micro-particles with the size of 3–5 mm, owing to the surface effect just as can be seen graphene (Huang et al. 2006). This can be explained by the fact that MoS_2 nano-sheets have a larger surface area and higher chemical activity, which makes them easier to adsorb on to rubbing surfaces in the form of a stable tribo-film, reducing the friction and wear.

Hu et al. (2009a) prepared MoS_2 nano-sheets with a thickness of 30–70 nm via a monolayer-restacking process and studied tribological behaviors on a four-ball tribometer. Experimental results indicated that MoS_2 nano-sheets had better antifriction, antiwear, and extreme pressure properties than micro-MoS_2 (Fig. 6.16). The excellent tribological properties of MoS_2 nano-sheets were attributed to a surface effect, dimension effect of the nanoparticles, and a complex tribo-film composed of MoO_3 and $FeSO_4$ on the worn surfaces.
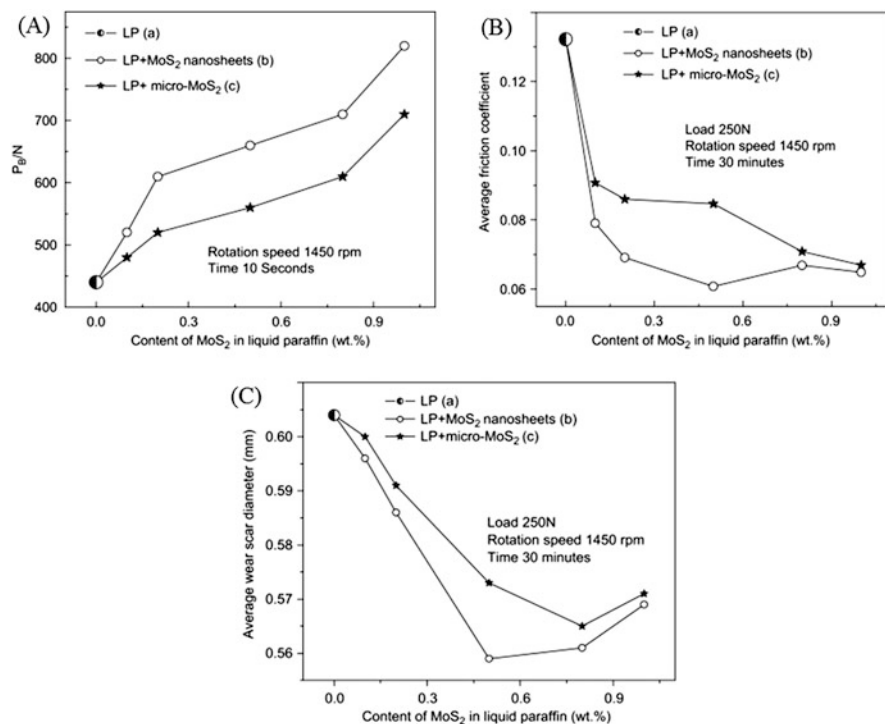
Fig. 6.16 P$_B$ values (**a**), average friction coefficient (**b**) and wear scar diameter (**c**) of liquid paraffin with MoS$_2$ nano-sheets and MoS$_2$ micro-sheets (Hu et al. 2009a)

2.2.3   Tribological Mechanisms of MoS$_2$ Nano-sheets

As shown in Fig. 6.17, there are some S dangling bonds on the rim of MoS$_2$ nano-sheets. When they enter into frictional interfaces, MoS$_2$ nano-sheets could be adsorbed onto the frictional interfaces forming an adsorbed film depending on the formation of S-O or S-Fe bonds. The O and Fe came from the oxide layer on the surfaces of the substrate. The adsorbed film prevented frictional interfaces from direct contact and improved the tribological properties.

Due to the chemical activity of dangling bonds, MoS$_2$ nano-sheets could be oxidized to MoO$_3$ and progressively sulfated, where oxygen might come from air or water during the sliding process. Fleischauer and Lince (1999) compared tribological properties of a typical MoS$_2$ film in which the sulfur was substituted for different contents of oxygen. They found that friction coefficient increased with increases in oxygen content at first, up to a saturation point of 3% followed by a decrease. It is still higher than pure MoS$_2$ when oxygen content exceeded the critical value (Fig. 6.18).

Fig. 6.17 Schematic illustration of possible formation mechanisms of MoS_2 adsorbed film on the iron oxide layer (**a**) and the metal atom (**b**) (Tannous et al. 2011)
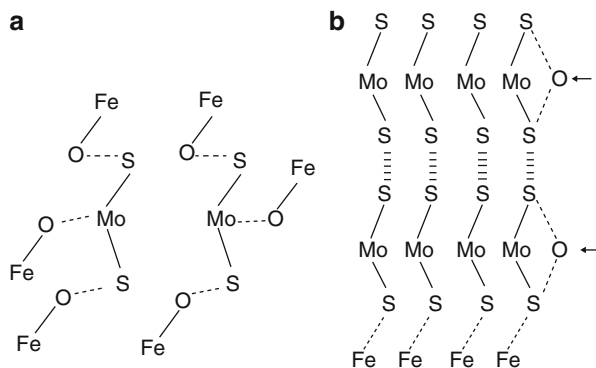
Fig. 6.18 Variation of friction coefficient with the oxygen concentration in the film (Fleischauer and Lince 1999)
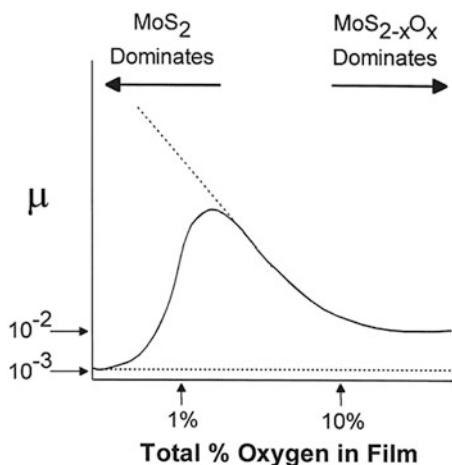
Onodera et al. (2009) drew similar conclusions by simulating single sheet MoS_2 lubrication with computational chemistry methods. They proposed that the excellent tribological properties of MoS_2 sheets were attributed to the increase of coulombic repulsion energies between the two sulfur layers reacting with the iron surfaces as shown in the Fig. 6.19. With oxygen introduced into MoS_2, coulombic interaction energy reduced and roughness of MoS_2 layer increased. These resulted in the rising of the friction coefficient. MoS_2 layers became flat again and decreased the friction coefficient with further increases in oxygen contents.

2.3 *MoS$_2$ Nano-tubes*

The MoS_2 nano-tubes, an analog of carbon nano-tubes, are considered to derive from lamellar compounds (Chen et al. 2001; Dresselhaus et al. 1996). The discovery
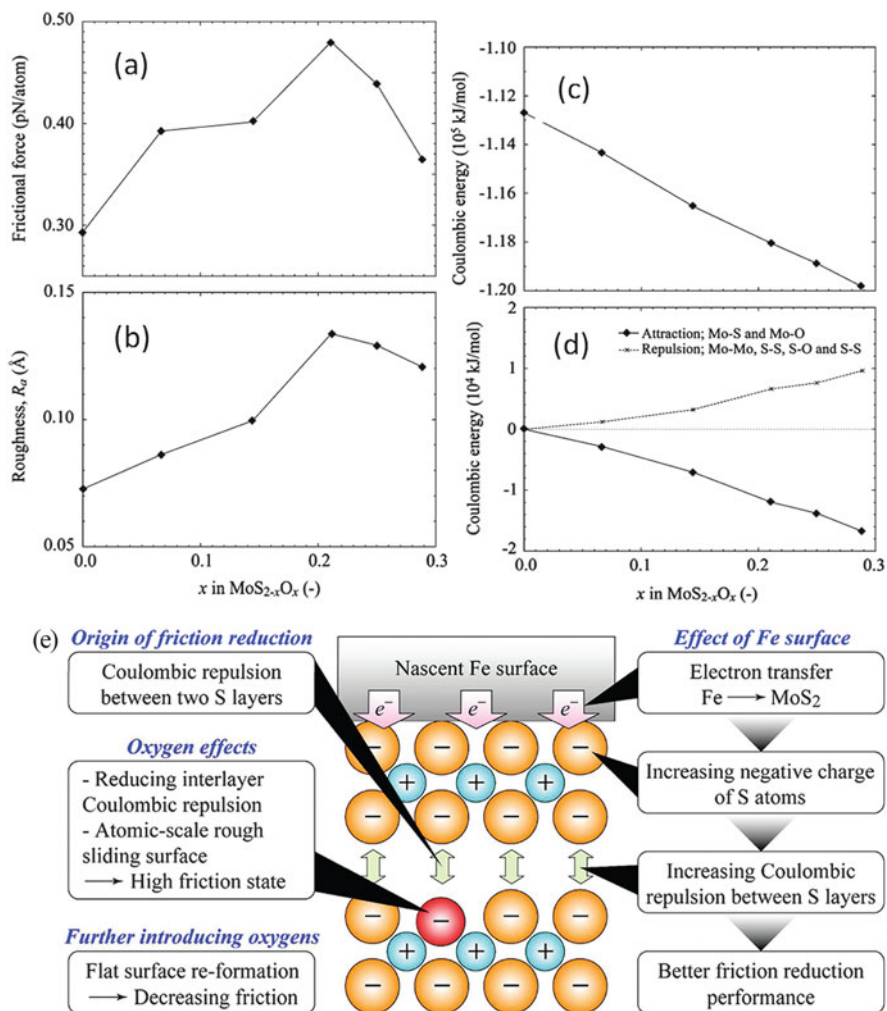
Fig. 6.19 Average frictional force (**a**), Ra of top MoS₂ layer on sliding surface (**b**); total interlayer coulombic interaction energy (**c**); coulombic attractive and repulsive energies (**d**) along with oxygen concentration in MoS₂ structures; schematic illustration (**e**) for lubricating properties of MoS₂ single sheet (Onodera et al. 2009)

of the carbon nano-tube has aroused great interest for the one-dimensional nano-tubes such as MoS₂ due to their small dimensions, high anisotropy, and special tube-like structures (Remskar et al. 2001). In this section, the preparation, characterization, and application of MoS₂ nano-tube will be described and discussed.

2.3.1 Preparation and Characterization of MoS$_2$ Nano-tube

Remskar et al. (2001) used 5 wt% C$_{60}$ as a catalyst during the production process. In a typical run, the reaction conditions were controlled as follows: reaction time: 22 days; temperature: 1010 K; reactor: silica ampoule; pressure: 10^{-3} Pa. The SEM and TEM images of the nano-tubes are shown in Fig. 6.20. The conversation rate was about 15% for MoS$_2$ nano-tubes.

Template synthesis is another path to obtain MoS$_2$ nano-tubes. Zelenski and Dorhout (1998) used aluminum oxide templates to prepare near-mono-dispersed MoS$_2$ nano-tubules. As shown in Fig. 6.21, the fibers in the picture were synthesized in 0.1 M (NH$_4$)$_2$MoS$_4$ DMF solutions. They were separated from the template by the dissolution of the template using 1.0 M NaOH solutions. Figure 6.21b presents an end-on view of the nano-tubes and confirms their hollow nature.

Nath et al. (2001) developed a simple synthesis method of MoS$_2$ and WS$_2$ nano-tube. The first step was to prepare MoS$_3$ precursors via decomposition of (NH$_4$)$_2$ MoS$_4$ at 400 $^{\circ}$C in an argon atmosphere. Then, the precursors were heated at 1200–1300 $^{\circ}$C under H$_2$ atmosphere. MoS$_2$ nano-tubes were formed, and the TEM images are shown in Fig. 6.22. It can be seen that the external diameter of the nano-tube is about 20–30 nm, and the wall thickness is about 10–15 nm. There are also some onion-like clusters in the Figure, suggesting the existence of an intermediate stage between MoS$_3$ precursors and MoS$_2$ nano-tubes (Margulis et al. 1993). Feldman et al. (1995) used the gas-phase reaction between MoO$_3$ and H$_2$S in a reducing atmosphere at high temperature and also got high-rate growth of MoS$_2$ nano-tubes.
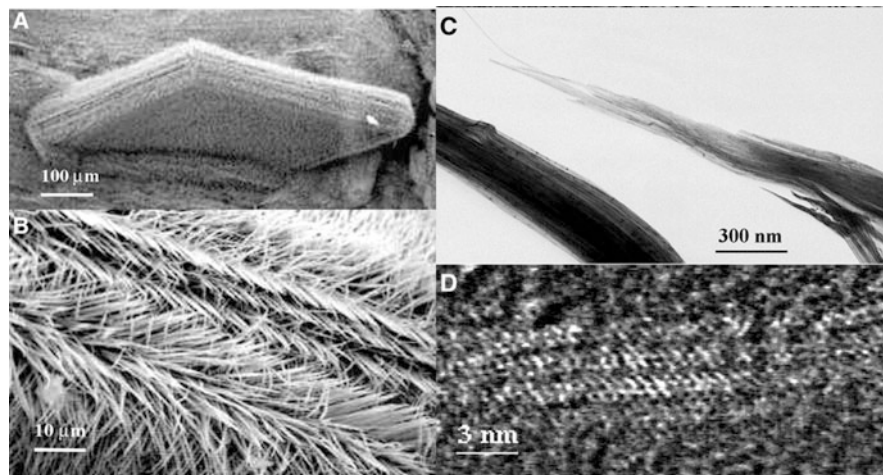
Fig. 6.20 SEM and TEM images on different length scales. (**a**) Bundles appear to self-assemble into various different microscopic structures. (**b**) The bundles end in sharp points. (**c**) A split tip of a bundle terminating in strands ~4 nm wide. (**d**) Expanded electron transmission view of a strand composed of an only few individual nano-tubes (Remskar et al. 2001)
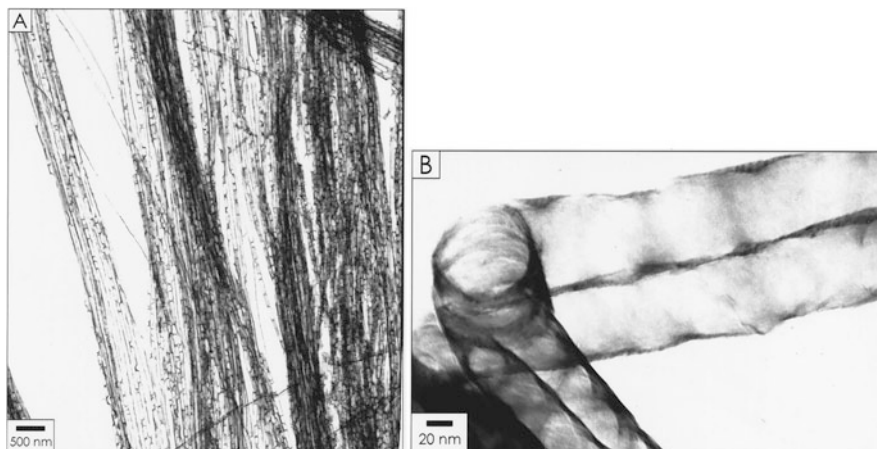
Fig. 6.21 A TEM image of the MoS$_2$ tubes after the dissolution of the aluminum oxide template (**a**). A TEM image of a bend in a tubule of MoS$_2$ emphasizing the hollow nature of the tubules (**b**) (Zelenski and Dorhout 1998)
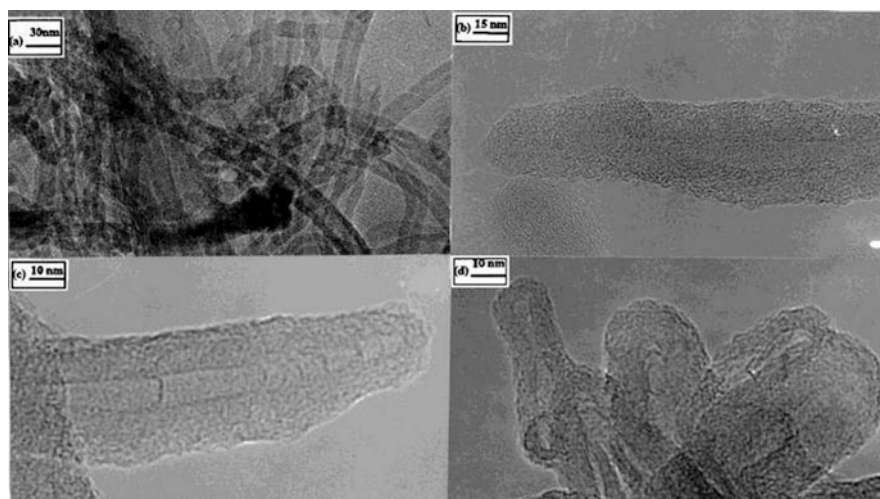
Fig. 6.22 TEM images of MoS$_2$ nano-tubes: (**a**) Images of several nano-tubes; (**b**) and (**c**) high-resolution images of the nano-tubes; and (**d**) nested-shell and onion-like clusters with a hollow core (Nath et al. 2001)

2.3.2   Applications of MoS$_2$ Nano-tubes

Besides the synthesis and characterization of MoS$_2$ nano-tubes, studies have been focused on a great number of particular properties and applications (Deepak and

Fig. 6.23 Catalytic
abilities of MoS$_2$ nano-
tubes (Chen et al. 2002)
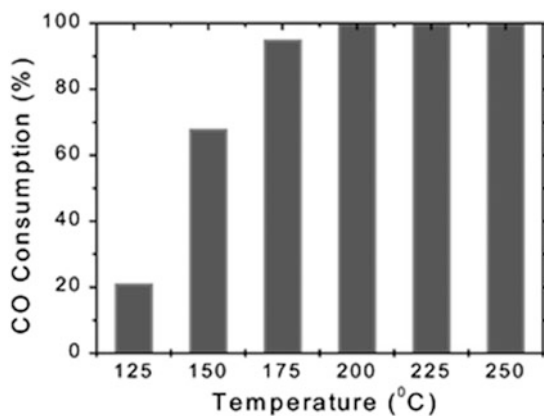
Jose-Yacaman 2010), for instance, mechanical properties (Hassanien et al. 2005),
field emission properties (Nemanič et al. 2003), in hydrogen storage applications
(Chen et al. 2003) and as catalysts (Chen et al. 2002).

Chen et al. (2002) synthesized an open-ended MoS$_2$ nano-tube and used it as the
catalyst of methanation of CO and H$_2$ at relatively low temperatures (Fig. 6.23).
Techniques such as this contribute to new ways of reducing the environmental load
resulting from CO emissions. By analyzing the shear and Young's moduli of the
MoS$_2$ nano-tubes, Kis et al. (2003) used an atomic force microscope to study the
interaction between the MoS$_2$ nano-tubes, finding the MoS$_2$ nano-tube ropes were
highly anisotropic and very weak.

Chen et al. (2001) prepared MoS$_2$ nano-tubes by heating (NH$_4$)$_2$MoS$_4$ in hydro-
gen/thiophene. They studied the electrochemical properties. It was found that the
highest capacity was 260 mAh g^{-1} because of a highly nano-porous structure,
suggesting a potential application in electrochemical catalysis and high-energy
batteries.

Analogously to MoS$_2$ nano-tube, WS$_2$ nano-tubes, can be used for tips in
scanning-probe microscopy (Rothschild et al. 1999). They have been successfully
applied in the inspection of microelectronics circuitry. With improvements in
productivity for producing these, the application of MoS$_2$ nano-tubes will widen
to include nanolithography, photocatalysis, sensors, and others (Tenne 2006).

MoS$_2$ nano-tubes also have excellent lubricating properties whether as lubricat-
ing oil additives or prepared as self-lubricating composite materials (Mertens and
Senthilvelan 2016; Zhou et al. 2007). However, due to their thin and long structure
and chemical inertness, MoS$_2$ nano-tubes are hard to disperse in lubricating oil
which limits their tribological application. Modification, treatment, or the addition
of a dispersion agent is an effective method to improve dispersion in oil of nano-
tube (Khalil et al. 2016; Chen et al. 2005). Kalin et al. (2012) investigated the
frictional properties of MoS$_2$ nano-tubes as oil additives. They found that the
lubrication mechanism was mainly exfoliation and deformation which was similar
to that of MoS$_2$ nano-balls. Exfoliated nano-sheets were adsorbed onto the rubbing

surfaces, and compacted and deformed to form a boundary film. With these two combined effects, MoS$_2$ nano-tubes reduce friction and wear significantly.

3   Graphene and Its Tribological Applications

Graphene, just like the structured MoS$_2$, is a 2-D layered material with sp^2-bonded carbon, that has received substantial attention (Novoselov et al. 2004; Li et al. 2009; Bonaccorso et al. 2015) due to its good conductivity, excellent mechanical properties, potential applications in electrochemical energy storage (Raccichini et al. 2015), microelectronics, and lubricating additives (Wu et al. 2015; Yao et al. 2014). In this section, the preparation, characterization, and applications of graphene are reviewed to give a view on the increasingly wide scope of applications.

3.1   Preparation and Characterization of Graphene

Graphene was firstly prepared by Geim et al. at the University of Manchester in 2004 by using tape (Novoselov et al. 2004). This was the work for which they were awarded the Nobel Prize in Physics in 2010. From this point, graphene has attracted substantial research attention such that its synthesis, characterization, its unique structures, and superior properties are well studied.

3.1.1   Exfoliation in Liquid or Gas

Exfoliation of graphite in liquid or gas is a physical method to obtain graphene. Hernandez et al. (2008) demonstrated that dispersion and exfoliation of graphite in *N*-methyl-pyrrolidone to obtain graphene-blended solutions with a concentration of 0.01 mg ml^{-1}. However, the yield of single-layer graphene was low at about 1%.

3.1.2   Modified Mechanical Exfoliation

Recently, in order to improve the yield of production of single-layer graphene, Xu et al. (2016) used a friction-induced exfoliation from graphite to graphene in esterified bio-oil. They dispersed flake graphite into the esterified bio-oil and then measured the tribological response of the dispersed graphite after ultrasonication for 20 min. Testing was performed on a ring-on-plate tribometer. It was found that

both load and sliding speed had an important effect on the quality of the graphene. Higher loads and lower sliding speed were helpful to form the single-layer graphene. In addition, higher loads also contributed to friction and wear reduction in the tribosystem due to the formation of a thicker tribofilm.

3.1.3 Epitaxial Growth

Due to the low efficiency of the mechanical exfoliation method, epitaxial growth has become one of the most important methods to produce the graphene film on certain substrates such as SiC and transition metals (Oshima and Nagashima 1997). Yang et al. (2013) used a plasma-assisted deposition epitaxial growth method to obtain the single-domain graphene on hexagonal boron nitride. The graphene was produced at ~500 °C. A schematic illustration of this process is shown in Fig. 6.24, suggesting a typical edge growth of carbon atoms. The sp^2 carbon structure of the graphene was confirmed by Raman spectra in Fig. 6.24b. The AFM images also showed the existence of single-layer graphene.

Fumihiko and Hiroki (2011) grew graphene on a SiC (0001) substrate under the temperatures varying from 600 to 915 °C by thermal decomposition of a cracked-ethanol source. This is an example of one kind of gas-source molecular beam epitaxy (MBE) methods. The experimental results showed that higher temperatures were helpful to prepare high-quality single-layer graphene. Unfortunately, the growth rate decreased with the increase in temperatures. Moreover, there was a network of fin-like ridge shapes of graphene (Fig. 6.25).

However, the epitaxial growth method for producing graphene has some disadvantages. For instance, it requires some harsh conditions, including high temperature, high vacuum, special atmosphere, and substrates. The synthesized graphene is also hard to separate from the substrate. It is also hard to produce graphene on a large scale in the industry.

3.1.4 Chemical Vapor Deposition

Chemical vapor deposition (CVD) has been used to produce high-quality thin films on substrates in the semiconductor industry. In recent years, this technique has also been applied to synthesize graphene. The principle is to deposit volatile precursors onto the substrate.

A single- and few-layer (less than 10) graphene film with a large area (~cm^2) was prepared by Reina et al. over a Ni surface using CVD technology (Reina et al. 2008). But the lateral size was limited to 20 μm. The domain boundaries have proved adverse to the transport properties. Thus, graphene with a larger area is still the pursuit of the scientists. Li et al. (2011a) prepared single crystal graphene with a domain size of up to 0.5 mm (Fig. 6.26), which were grown at low-pressure and high-temperature chemical vapor deposition (8 mTorr at 1035 °C) on copper-foil enclosures using methane as a precursor. The flow rates and partial pressures of the
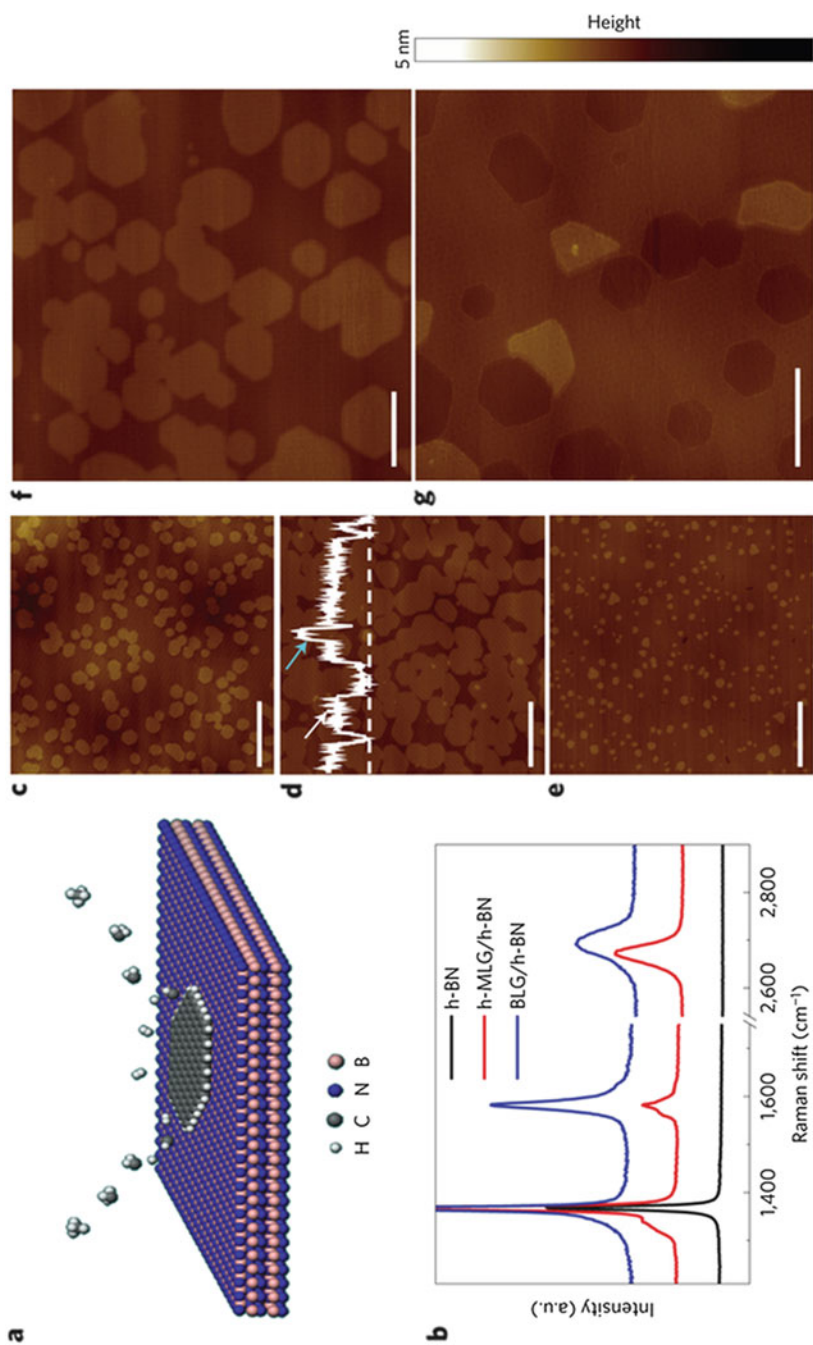
Fig. 6.24 Schematic illustration of the growth mechanism (**a**); Raman spectra for hexagonal MLG (h-MLG) grains (*red*), BLG film (*blue*), and bare h-BN surface (*black*) (**b**). (**c**–**e**) AFM images of as-grown graphene on h-BN at different stages including small grains nucleation (**c**), coalescence of grains (**d**), and continuous monolayer graphene with some second-layer nuclei on top. A height profile was extracted along the dashed white line cut in **d**, with *white* and *cyan* arrows indicating the first and second layer, respectively. The scale bars in **c**–**e** are 500 nm. **f**, **g**, Zoom-in AFM image of as-grown graphene showing aligned hexagonal grains (**f**) or pits after plasma etching (**g**). The scale bars in **f**, **g** are 200 nm (Yang et al. 2013)
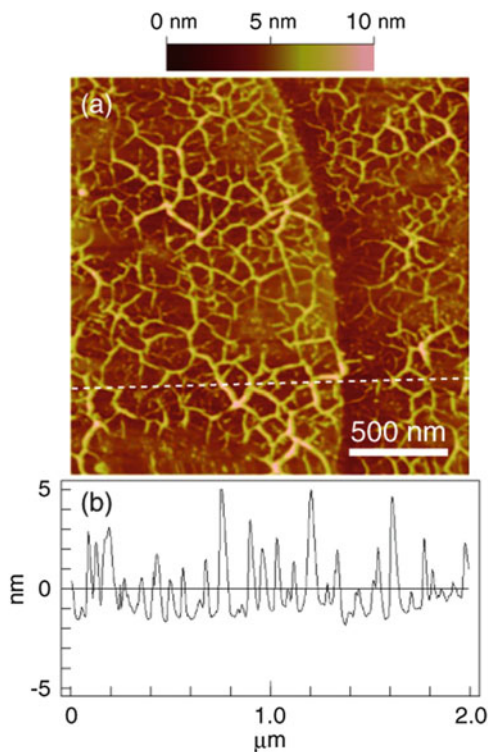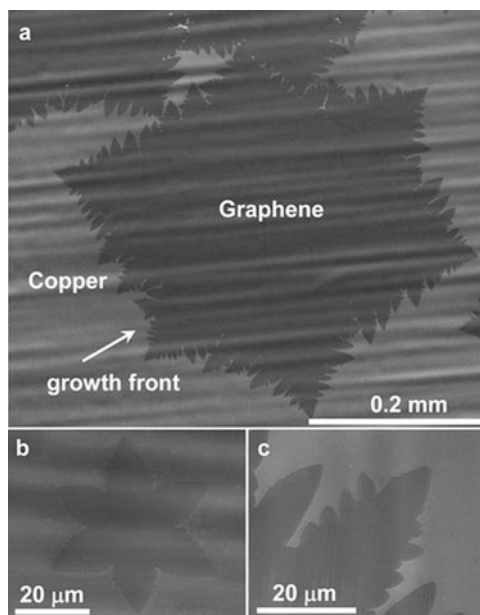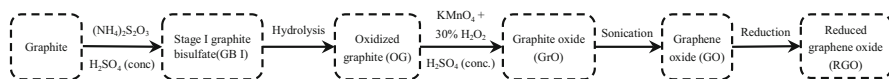
Fig. 6.27 The preparation process of reduced graphene oxide (Tkachev et al. 2012)

methane were less than 1 sccm and 50 mTorr, respectively. The transport properties of the graphene film were measured, and the mobility of the films was found to be a little bit higher than 4000 cm^2 V^{-1} s^{-1}, indicating further improvements for this graphene film should be possible.

CVD methods can produce high-quality graphene with a large area, with the products easily separated or transferred from substrates. In addition, CVD-derived graphene can be processed at relatively low temperatures and ambient pressure. However, the thickness of the graphene is hard to control and the yield remains low.

3.1.5 Reduced Graphene Oxide

A reduced graphene oxide method for the production of graphene in aqueous solution has attracted great interests due to its low cost, easy processability, and high efficiency. The process includes three steps: (1) preparation of oxide graphite from graphite using strong oxidants such as concentrated sulfuric acid, concentrated nitric acid, and potassium permanganate; (2) ultrasonic process for separating the lattices of oxide graphite; (3) reduction of the graphene oxide with reducers such as hydrazine hydrate and sodium borohydride.

Tkachev et al. (2012) used a modified Hummers method to prepare graphite oxide and then synthesized the graphene oxide by ultrasonic processing. The final reduced graphene oxide was obtained after the appropriate amount of graphene oxide and ethanol was mixed and reacted at 200–380 °C for 10–90 h. A typically detailed process for preparing reduced graphite oxide is shown in Fig. 6.27.

3.2 Properties and Applications of Graphene

Graphene has become a star molecule over the last c.10 years because of the ability to its particular structure and properties such as electrochemical, mechanical, and other properties. The progress of the main properties of graphene is reviewed in this section.

3.2.1 Electrochemical Properties

Electrons in graphene have a character that can be described by a linear dispersion relationship. It has been confirmed that at room temperature the electron mobility of

single-layer graphene amounts to $15,000$ m^2 V^{-1} s^{-1}. Therefore, graphene has many potential applications in microelectronic devices (Geim and Macdonald 2007). Geim and Macdonald (2007) noted that the conductivity of graphene was much higher than that of single-walled carbon nano-tubes by about 60 times. In addition, they found that graphene had higher surface negative charge, better stability, and signal-to-noise ratio than single-walled carbon nano-tubes, indicating the potential of graphene in the detection of some small molecules such as dopamine and serotonin by graphene electrodes.

Shan et al. (2016) used graphene to increase the conductivity and electrochemical stability of MoS$_2$ since MoS$_2$ has a high theoretical specific capacity (about 670 mA h g^{-1}) but low cycle charging performance. A unique film–foam–film structure was designed to solve this problem. The experimental results showed that the appropriate structures resulted in a high, reversible Li storage capacity of 1200 mA h g^{-1} and a longer lifetime, suggesting its potential application in high-energy-density batteries.

3.2.2 Mechanical Properties

With the potential application of graphene in nanoelectromechanical systems, the mechanical properties of monolayer or few-layer graphene (less than 5) have aroused great interest. Frank et al. (2007) used an atomic force microscope to measure the effective spring constants of the graphene sheets with a thickness between 2 and 8 nm ranging from 1 to 5 N m^{-1} and Young's modulus of graphene sheets is 0.5 TPa, which is a half of bulk graphite.

Young's modulus was studied by molecular dynamics and was predicted higher than 1 TPa (Van Lier et al. 2000). According to Lee et al. (2008) and Zhu et al. (2010), Young's modulus and fracture strength of a defect-free graphene were 1.0 TPa and 130 GPa, respectively, being measured by an AFM indentation approach (Fig. 6.28).

3.2.3 Optical Properties

Of main interest for graphene is the comparison of the permittivity features. Falkovsky (2008) investigated the transmittance of graphene in the optical region and found that optical properties were affected by the interband electron transitions. Moreover, the transmittance of graphene in the visible spectrum range was not affected by the frequency and had a constant value depending on its fine structure.

3.2.4 Extreme Pressure Properties

The extreme pressure value (P_B) of oil is an important parameter when evaluating the load carrying capacity of lubricating oil. Nano-scale lubricating particles being
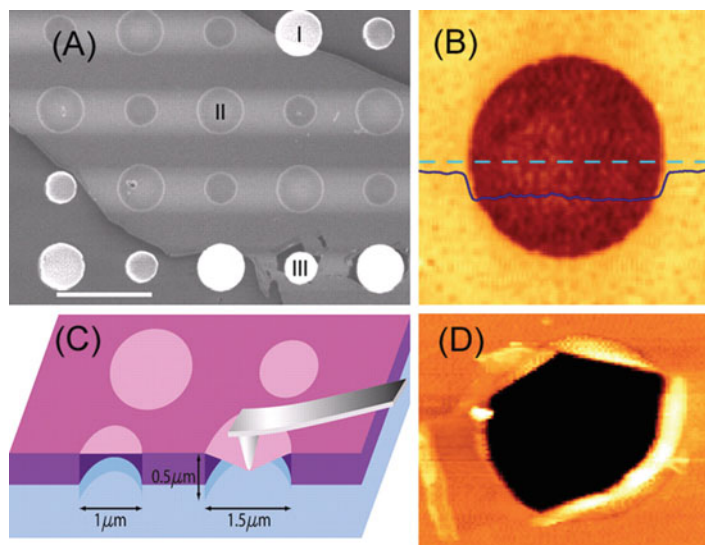
Fig. 6.28 Images of graphene membranes: SEM images of a large graphene flake spanning an array of circular holes 1 μm and 1.5 μm in diameter. Scale bar, 3 μm (**a**). Non-contact mode AFM image of one membrane (**b**). Schematic of nanoindentation on suspended graphene membrane (**c**). AFM image of a fractured membrane (**d**) (Lee et al. 2008)
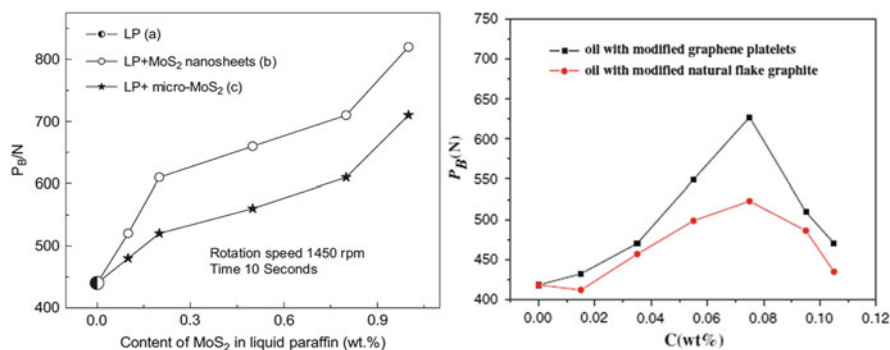
Fig. 6.29 Effect of concentration of MoS₂ nano-sheets (*left*) (Hu et al. 2009a) and graphene (*right*) on the P_B value (Lin et al. 2010)

mixed with oil can penetrate into rubbing surface during sliding and protect rubbing surfaces from contacting directly and can form an adsorbed layer. Because of the excellent antiwear properties, nanoparticles with a low concentration can improve P_B values significantly. As shown in Fig. 6.29, comparing with the base oil or base oil with flake graphite, MoS₂ nano-sheets and graphene can increase P_B value to approximately 2 and 1.6 times, respectively, at optimum concentrations (Hu et al. 2009a; Lin et al. 2010).

3.2.5 Dispersion Properties

The advantage of nanoparticles is that they can penetrate into mating surfaces during the frictional process even in severe boundary lubrication. However, nanoparticles tend to agglomerate due to nanometric size effects. The size of the agglomeration might amount to a few microns which make the particles much less likely to penetrate into frictional interfaces, and so they cannot reduce the friction and wear of the tribosystem. Therefore, the dispersive properties of the nano-lubricating additives are very important. Modification treatments are a chemical reaction method to graft a modifier on the nanoparticles to improve the dispersive properties. The modifiers commonly have an oleophylic functional group of long chain alkane. Although graphene has excellent tribological properties, the dispersion of graphene in oil is poor which leads to coagulation and precipitation of graphene quickly because of chemical inertness.

The modification is an effective approach to forming stable dispersions and preventing aggregation of graphene. Lin et al. (2010) modified graphene by using stearic and oleic acids. The modifiers, cyclohexane and dried graphene, were heated and stirred at 80 °C for 5 h. There were some residual oxygen-containing functional groups, as a result of the incomplete diminution of reduced graphene oxide, that could react with carboxyl groups of stearic and oleic acids. Therefore as a result of the long chain molecular structures of stearic and oleic acids, modified graphene has better dispersive properties than the pristine graphene as shown in Fig. 6.30.
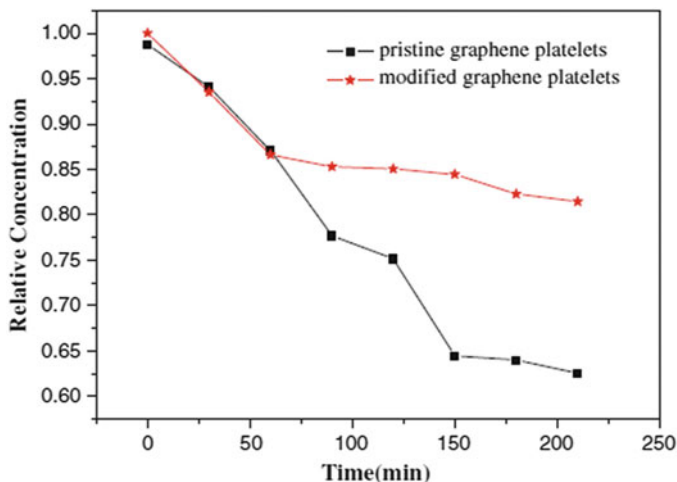
Fig. 6.30 Dispersive stability of graphene in lubricating oil (Lin et al. 2010)

3.2.6 Tribological Properties and Applications of Graphene

Graphene has excellent tribological properties as lubricating oil additive in part due to its layered structure similar in many respects to MoS$_2$. Eswaraiah et al. (2011) synthesized ultrathin graphene with a thickness of ~2 nm via reducing graphene oxide with focused solar radiation. The tribological properties were investigated by using a four-ball tribometer. They found that the ultrathin graphene dramatically reduced average coefficient friction and wear loss at a relative low concentration in a formulated engine oil as shown in Fig. 6.31. Also, graphene can significantly improve the load capacity of a lubricant owing to its excellent antiwear performances especially at a concentration of 0.025 mg mL^{-1}. In addition, graphene in the base oil could be adsorbed on the frictional interfaces and formed a physically adsorbed film. The adsorbed film protected the rubbing surfaces and reduced wear and the coefficient of friction.

According to the results in Fig. 6.31, graphene has an optimal concentration. The antifriction and antiwear behaviors deteriorated when the concentration of graphene exceeded the optimal concentration. This can be explained by the fact that graphene can form an adsorbed film protecting frictional interfaces at an
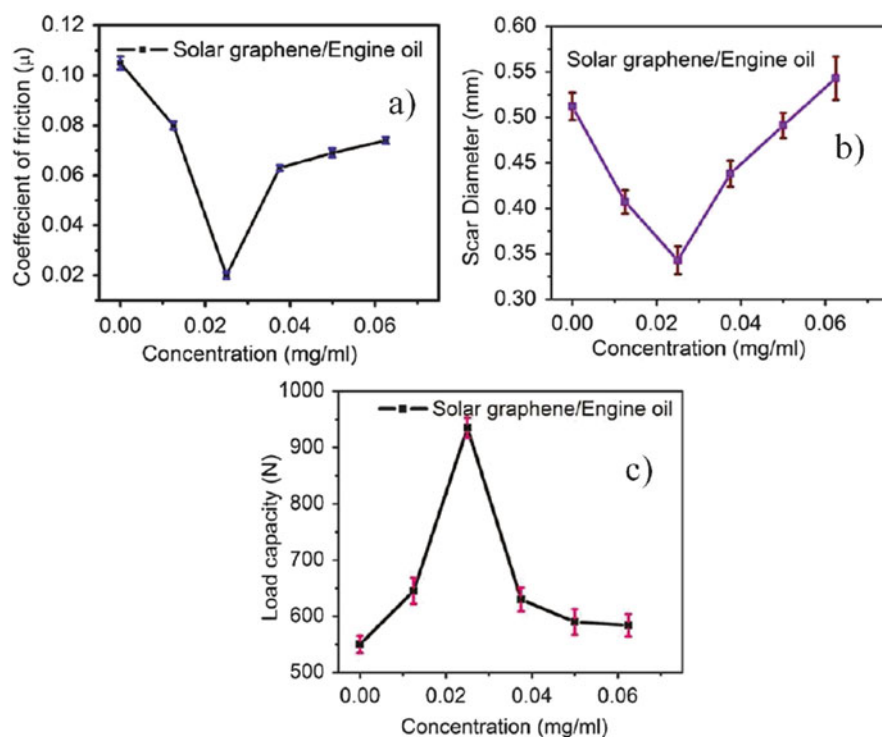
Fig. 6.31 Tribological properties of graphene dispersed in engine oil: Coefficient of friction (**a**), wear scar diameter (**b**), and load capacity (**c**) (Eswaraiah et al. 2011)
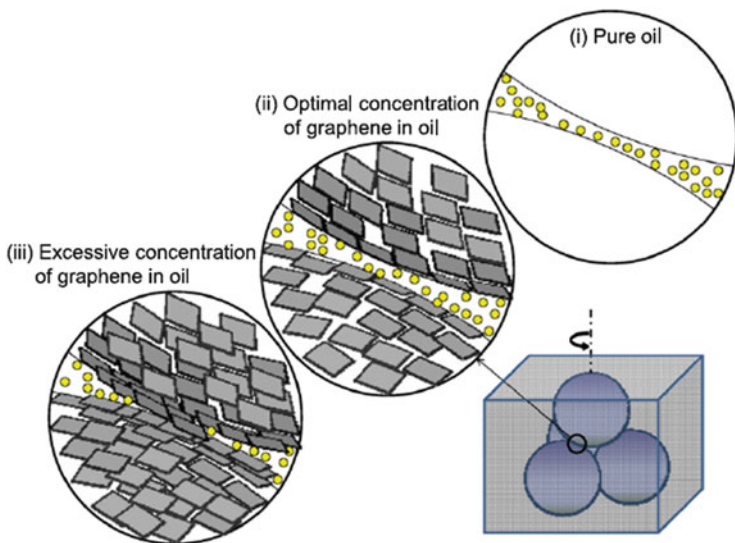
Fig. 6.32 Schematic of the lubrication mechanisms of graphene as oil additives at different lubricating states (Zhang et al. 2011)

optimal concentration. However, when the concentration exceeded the critical value, the lubricating oil in the friction region is reduced by the aggregation of graphene, which makes the oil film discontinuous and reduces the lubricating effects. The corresponding lubrication mechanisms of graphene as an oil additive in the different lubricating state are shown in Fig. 6.32 (Zhang et al. 2011).

4   Synergistic Lubricating Behaviors of Graphene and MoS$_2$

Previous studies (Kalin et al. 2012; Wang et al. 2014; Rabaso et al. 2014b; Marquart et al. 2013; Kogovšek et al. 2013; Zhang et al. 2012; Xu et al. 2015b) have shown that the tribological mechanisms of MoS$_2$ are interlayer slippage, rolling deformation, and a slippery exfoliation. But the MoS$_2$ particles are easily removed during the frictional process, which affects their long-term effects. Considering good adhesive and lubricating properties of graphene (Lin et al. 2011; Kandanur et al. 2012; Berman et al. 2013; Zhang et al. 2014; Fan and Wang 2014), the joint use of graphene and MoS$_2$ seems to be a good choice. Currently, graphene/MoS$_2$ composites have been selected as a photoresponsive coating (Huang et al. 2014), electrochemical sensors (Feng et al. 2014), catalyst supports (Zhai et al. 2015) and for lithium storage (Ma et al. 2014). Xu et al. (2015a) have systematically
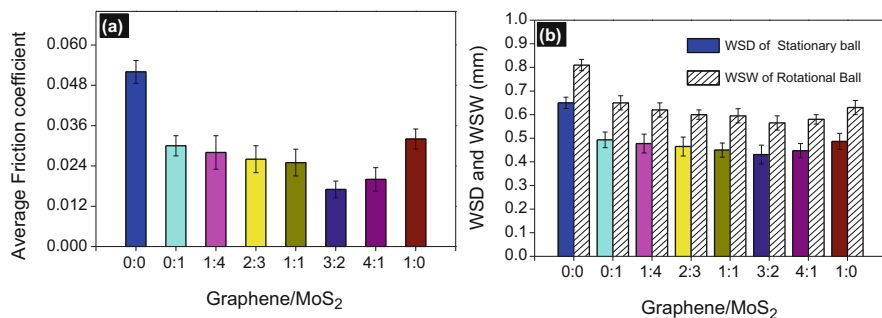
Fig. 6.33 Average friction coefficient (**a**) and WSD and WSW (**b**) of graphene and MoS$_2$ dispersed in base oil with different mass ratio (Xu et al. 2015a)

studied the lubricating properties of graphene/MoS$_2$ composites; the results and tribological mechanisms are reviewed in detail in the following sections.

4.1 Tribological Behaviors

Tribological tests were performed on a four-ball tribometer. The dispersive media was bio-oil and detailed frictional conditions were as follows: concentration of the additives: 0.5 wt%; Load:300 N; Rotating speed: 1000 rpm; Sliding time: 30 min. As shown in Fig. 6.33, the MoS$_2$/graphene composite had a lower friction coefficient and wear loss including wear scar diameter (WSD) and wear scar width (WSW) than MoS$_2$ or graphene. This suggested a clear synergistic lubricating role of graphene/MoS$_2$ composites.

The effect of the loads on the tribological behavior of the graphene/MoS$_2$ composite is shown in Fig. 6.34. The friction coefficient, WSD and WSW of esterified bio-oil (EBO), increased with load, due to the smaller micro-intervals between the friction pairs under higher loads (Xu et al. 2014b). There was a great decrease in the friction coefficient and wear loss of the EBO with graphene/MoS$_2$ composite additives, up to 300 N. Exceeding this load, the friction coefficient and wear loss remained stable or increasing. At the same time, for the same load, the EBO with graphene/MoS$_2$ composite additives showed the best lubricity in all the four lubricants. This confirms the synergistic lubricating effects between graphene and MoS$_2$.

4.2 Friction and Wear Mechanisms

In order to explore the friction and wear mechanisms of the graphene/MoS$_2$ composites, XPS spectra of the typical elements on the rubbed surfaces are
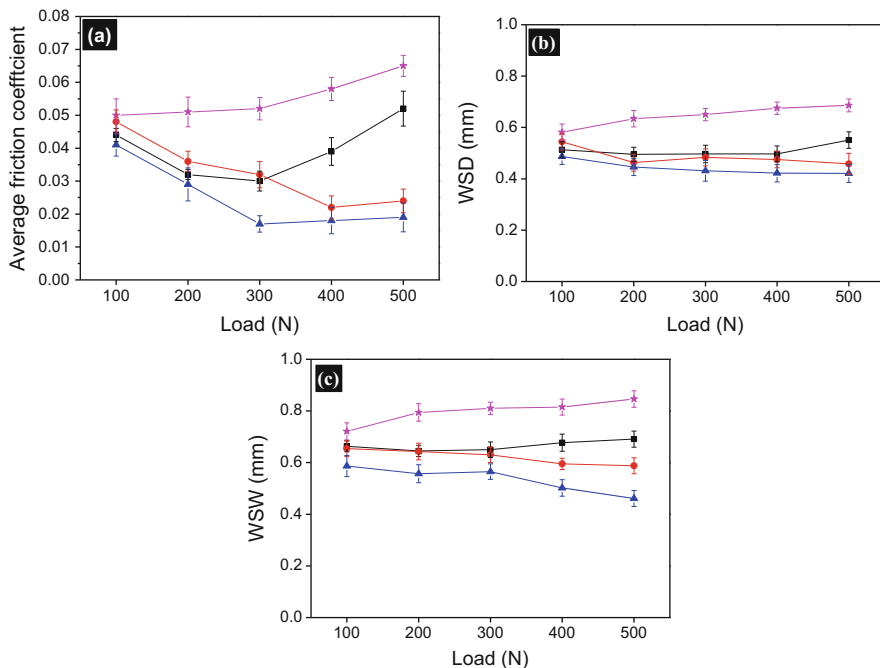
Fig. 6.34 Average friction coefficient (**a**), WSD (**b**), and WSW (**c**) of steel specimens under different loads (Xu et al. 2015a). Notes: *Filled star* EBO; *Filled circle* EBO+0.5 wt% graphene; *Filled square* EBO+0.5 wt% MoS$_2$; *Filled triangle* EBO+0.3 wt% graphene+0.2 wt% MoS$_2$

shown in Fig. 6.35. The position of the two C1s peaks suggested the existence of carbon or sp^3 C (C–C/C–H) and sp^2 C (C=C/C=O) (Xu et al. 2014a), respectively. This indicated that the adsorbed film was made from carbon or organics, coming from the graphene or base oil. The largest areas of C1s peaks of graphene/MoS$_2$ blends suggested the formation of the thickest adsorbed film containing graphene and organics. The O1s peak can be ascribed to hydroxides or sulfates, confirming the existence of an adsorbed film with organics or a tribo-film with sulfates. The O1s peak at 530.3 eV was attributed to Fe$_2$O$_3$, suggesting the tribo-oxidation of the substrate during sliding. The Fe2p peaks belonged to Fe$_2$O$_3$, and no simple Fe^0 peak was found, confirming the existence of a complete tribo-oxide film on the rubbing surfaces. The Cr2p peaks belonged to Cr$_2$O$_3$ and CrN, respectively. This confirmed a tribo-oxidation and tribo-reaction during the sliding process.

For graphene/MoS$_2$ lubrication, the two main Mo3d peaks at 232.6 and 235.8 eV were ascribed to MoO$_3$ (Hu et al. 2009b). Another peak at 229.7 eV was ascribed to Mo3d of MoS$_2$, but this peak was not detected for MoS$_2$ lubrication. Moreover, the two S2p peaks at 169 eV and 161.6 eV were indexed to SO$_4^{2-}$ and MoS$_2$, respectively (Moulder et al. 1995). When MoS$_2$ was used independently (c), the peak at 161.6 eV in the curve was very weak, suggesting that MoS$_2$ was easily
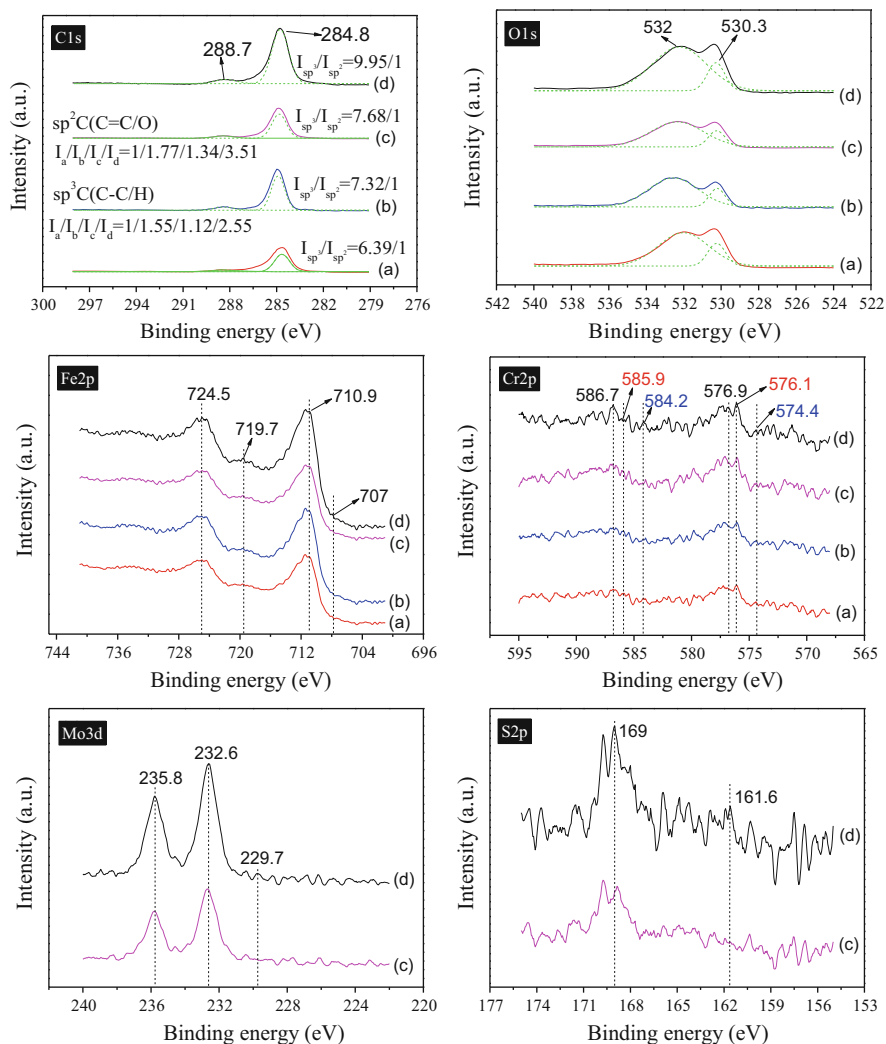
Fig. 6.35 XPS spectra of the worn surfaces of the rotating specimen lubricated by base oil (**a**), base oil with graphene additives (**b**), base oil with MoS$_2$ additives (**c**), base oil with graphene/MoS$_2$ composite additives (**d**) (Xu et al. 2015a)

oxidized during sliding. That is, the introduction of graphene was helpful to the adhesion of the MoS$_2$ on the frictional surface and further prevents the oxidation of MoS$_2$.

The friction and wear mechanisms were summarized as follows. For graphene, the main antifriction and antiwear components were the small graphene particles, and ploughing was the dominant form of wear. For MoS$_2$, the MoS$_2$ with the smaller surface area was the main lubricant but it is easy to be removed from the

frictional surface or oxidized. For graphene/MoS$_2$ composites, a thicker tribo-film was formed to play an antifriction and antiwear role. The synergistic lubricating effect of graphene and MoS$_2$ allows complete graphene and unoxidized MoS$_2$ to remain on the sliding surfaces.

5 Conclusions

In summary, in this chapter, two kinds of nano-additives MoS$_2$ and graphene have been reviewed. The preparation methods, properties, and applications have also been discussed. Both MoS$_2$ and graphene have various functions and applications and their tribological properties have been explored this chapter. For MoS$_2$, different structures have different physical properties. Nano-MoS$_2$ showed obvious advantages over the more conventional micro-MoS$_2$. In a widely accepted opinion, rolling is the main antifriction and antiwear mechanism for nano-MoS$_2$ particles. The slippery role is the friction-reducing mechanism of MoS$_2$ nano-sheets and the combined actions of rolling and sliding account for the excellent lubricating effect of MoS$_2$ nano-tubes. However, exfoliation and transfer cannot be ignored when explaining the tribological behaviors of nano-MoS$_2$. More combined applications of nano-MoS$_2$ with different structures require further study.

As for graphene, good adsorption onto the frictional surfaces is helpful to the lubricating behaviors of graphene. However, the effects of the layer, area, and defects in the graphene on the tribological behaviors still remain unknown and need further clarification in the future. The graphene/MoS$_2$ composites showed excellent synergistic lubricating effect. The mechanisms were attributed to the protective roles of the graphene preventing the oxidation of MoS$_2$ and also MoS$_2$ preventing graphene being destroyed and reduced into small, defective additives. The MoS$_2$ used in the composites was micro-MoS$_2$, nano-MoS$_2$ composites needed to be studied further. To conclude, both graphene and MoS$_2$ as lubricating additives have a bright future and more specialized applications will be researched and found.

References

Abdelaziz EA, Saidur R, Mekhilef S (2011) A review on energy saving strategies in industrial sector. Renew Sust Energy Rev 15:150–168
Aldana PU, Vacher B, Le Mogne T, Belin M, Thiebaut B, Dassenoy F (2014) Action mechanism of WS$_2$ manoparticles with ZDDP additive in boundary lubrication regime. Tribol Lett 56:249–258

Aralihalli S, Biswas SK (2013) Grafting of dispersants on MoS$_2$ nanoparticles in base oil lubrication of steel. Tribol Lett 49:61–76

Bang GS, Nam KW, Kim JY, Shin J, Choi JW, Choi SY (2014) Effective liquid-phase exfoliation and sodium ion battery application of MoS$_2$ nanosheets. ACS Appl Mater Interfaces 6:7084–7089

Berman D, Erdemir A, Sumant AV (2013) Few layer graphene to reduce wear and friction on sliding steel surfaces. Carbon 54:454–459

Bonaccorso F, Colombo L, Yu GH, Stoller M, Tozzini V, Ferrari AC, Ruoff RS, Pellegrini V (2015) Graphene, related two-dimensional crystals, and hybrid systems for energy conversion and storage. Science 347:1246501

Chen J, Kuriyama N, Yuan HT, Takeshita HT, Sakai T (2001) Electrochemical hydrogen storage in MoS$_2$ nanotubes. J Am Chem Soc 123:11813–11814

Chen J, Li SL, Xu Q, Tanaka K (2002) Synthesis of open-ended MoS$_2$ nanotubes and the application as the catalyst of methanation. Chem Commun 1722–1723

Chen J, Li SL, Tao ZL (2003) Novel hydrogen storage properties of MoS$_2$ nanotubes. J Alloys Compd 356:413–417

Chen CS, Chen XH, Xu LS, Yang Z, Li WH (2005) Modification of multi-walled carbon nanotubes with fatty acid and their tribological properties as lubricant additive. Carbon 43:1660–1666

Choudhary N, Park J, Hwang JY, Choi W (2014) Growth of large-scale and thickness-modulated MoS$_2$ nanosheets. ACS Appl Mater Interfaces 6:21215–21222

Deepak FL, Jose-Yacaman M (2010) Recent highlights in the synthesis, structure, properties, and applications of MoS$_2$ nanotubes. Isr J Chem 50:426–438

Desai JD, Banat IM (1997) Microbial production of surfactants and their commercial potential. Microbiol Mol Biol Rev 61:47–64

Dickinson RG, Pauling L (1923) The crystal structure of molybdenite. J Am Chem Soc 45:1466–1471

Dresselhaus MS, Dresselhaus G, Eklund PC (1996) Science of fullerenes and carbon nanotubes: their properties and applications. Academic Press, New York

Du GD, Guo ZP, Wang SQ, Zeng R, Chen ZX, Liu HK (2010) Superior stability and high capacity of restacked molybdenum disulfide as anode material for lithium ion batteries. Chem Commun 46:1106–1108

Eswaraiah V, Sankaranarayanan V, Ramaprabhu S (2011) Graphene-based engine oil nanofluids for tribological applications. ACS Appl Mater Interfaces 3:4221–4227

Falkovsky LA (2008) Optical properties of graphene. J Phys Conf Ser 129:012004

Fan XQ, Wang LP (2014) Highly conductive ionic liquids toward high-performance space-lubricating greases. ACS Appl Mater Interfaces 6:14660–14671

Feldman Y, Wasserman E, Srolovitz DJ, Tenne R (1995) High-rate, gas-phase growth of MoS$_2$ nested inorganic fullerenes and nanotubes. Science 267:222

Feng QL, Duan KY, Ye XL, Lu DB, Du YL, Wang CM (2014) A novel way for detection of eugenol via poly (diallyldimethylammonium chloride) functionalized graphene-MoS$_2$ nano-flower fabricated electrochemical sensor. Sens Actuat B Chem 192:1–8

Fleischauer PD, Lince JR (1999) A comparison of oxidation and oxygen substitution in MoS$_2$ solid film lubricants. Tribol Int 32:627–636

Frank IW, Tanenbaum DM, van der Zande AM, McEuen PL (2007) Mechanical properties of suspended graphene sheets. J Vac Sci Technol B 25:2558–2561

Fumihiko M, Hiroki H (2011) Molecular beam epitaxial growth of graphene and ridge-structure networks of graphene. J Phys D Appl Phys 44:435305

Geim AK, Macdonald AH (2007) Graphene: exploring carbon flatland. Phys Today 60:35

Hassanien A, Tokumoto M, Mrzel A, Mihailovic D, Kataura H (2005) Structural and mechanical properties of MoS$_2$-I$_x$ nanotubes and Mo$_6$S$_x$I$_y$ nanowires. Phys E 29:684–688

Hernandez Y, Nicolosi V, Lotya M, Blighe FM, Sun ZY, De S, McGovern IT, Holland B, Byrne M, Gun'Ko YK (2008) High-yield production of graphene by liquid-phase exfoliation of graphite. Nat Nanotechnol 3:563–568

Hu KH, Wang YR, Hu XG, Wo HZ (2007) Preparation and characterisation of ball-like MoS$_2$ nanoparticles. Mater Sci Technol 23:242–246

Hu KH, Liu M, Wang QJ, Xu YF, Schraube S, Hu XG (2009a) Tribological properties of molybdenum disulfide nanosheets by monolayer restacking process as additive in liquid paraffin. Tribol Int 42:33–39

Hu KH, Wang J, Schraube S, Xu YF, Hu XG, Stengler R (2009b) Tribological properties of MoS_2 nano-balls as filler in polyoxymethylene-based composite layer of three-layer self-lubrication bearing materials. Wear 266:1198–1207

Hu KH, Hu XG, Xu YF, Huang F, Liu JS (2010) The effect of morphology on the tribological properties of MoS_2 in liquid paraffin. Tribol Lett 40:155–165

Huang HD, Tu JP, Zou TZ, Zhang LL, He DN (2005) Friction and wear properties of IF-MoS_2 as additive in paraffin oil. Tribol Lett 20:247–250

Huang HD, Tu JP, Gan LP, Li CZ (2006) An investigation on tribological properties of graphite nanosheets as oil additive. Wear 261:140–144

Huang X, Qi XY, Boey F, Zhang H (2012) Graphene-based composites. Chem Soc Rev 41:666–686

Huang ZY, Han WJ, Liu XJ, Qi X, Zhong JX (2014) Graphene/MoS_2 hybrid structure and its photoresponse property. Ceram Int 40:11971–11974

Joly-Pottuz L, Martin JM, Dassenoy F, Belin M, Montagnac G, Reynard B, Fleischer N (2006) Pressure-induced exfoliation of inorganic fullerene-like WS_2 particles in a Hertzian contact. J Appl Phys 99:023524

Kalin M, Kogovšek J, Remškar M (2012) Mechanisms and improvements in the friction and wear behavior using MoS_2 nanotubes as potential oil additives. Wear 280–281:36–45

Kandanur SS, Rafiee MA, Yavari F, Schrameyer M, Yu ZZ, Blanchet TA, Koratkar N (2012) Suppression of wear in graphene polymer composites. Carbon 50:3178–3183

Khalil W, Mohamed A, Bayoumi M, Osman TA (2016) Tribological properties of dispersed carbon nanotubes in lubricant. Fuller Nanotub Carbon Nanostruct 24:479–485

Kis A, Mihailovic D, Remskar M, Mrzel A, Jesih A, Piwonski I, Kulik AJ, Benoît W, Forró L (2003) Shear and Young's moduli of MoS_2 nanotube ropes. Adv Mater 15:733–736

Kogovšek J, Remškar M, Mrzel A, Kalin M (2013) Influence of surface roughness and running-in on the lubrication of steel surfaces with oil containing MoS_2 nanotubes in all lubrication regimes. Tribol Int 61:40–47

Lahouij I, Vacher B, Dassenoy F (2014) Direct observation by in situ transmission electron microscopy of the behaviour of IF-MoS_2 nanoparticles during sliding tests: influence of the crystal structure. Lubr Sci 26:163–173

Lee CG, Wei XD, Kysar JW, Hone J (2008) Measurement of the elastic properties and intrinsic strength of monolayer graphene. Science 321:385–388

Li XS, Cai WW, An JH, Kim S, Nah J, Yang DX, Piner R, Velamakanni A, Jung I, Tutuc E (2009) Large-area synthesis of high-quality and uniform graphene films on copper foils. Science 324:1312–1314

Li XS, Magnuson CW, Venugopal A, Tromp RM, Hannon JB, Vogel EM, Colombo L, Ruoff RS (2011a) Large-area graphene single crystals grown by low-pressure chemical vapor deposition of methane on copper. J Am Chem Soc 133:2816–2819

Li YG, Wang HL, Xie LM, Liang YY, Hong GS, Dai HJ (2011b) MoS_2 nanoparticles grown on graphene: an advanced catalyst for the hydrogen evolution reaction. J Am Chem Soc 133:7296–7299

Li H, Yin ZY, He QY, Li H, Huang X, Lu G, Fam DWH, Tok AIY, Zhang Q, Zhang H (2012) Fabrication of single- and multilayer MoS_2 film-based field-effect transistors for sensing NO at room temperature. Small 8:63–67

Lin JS, Wang LW, Chen GH (2010) Modification of graphene platelets and their tribological properties as a lubricant additive. Tribol Lett 41:209–215

Lin LY, Kim DE, Kim WK, Jun SC (2011) Friction and wear characteristics of multi-layer graphene films investigated by atomic force microscopy. Surf Coat Technol 205:4864–4869

Lopez-Sanchez O, Lembke D, Kayci M, Radenovic A, Kis A (2013) Ultrasensitive photodetectors based on monolayer MoS_2. Nat Nanotechnol 8:497–501

Ma L, Ye JB, Chen WX, Chen DY, Yang Lee J (2014) Gemini surfactant assisted hydrothermal synthesis of nanotile-like MoS_2/graphene hybrid with enhanced lithium storage performance. Nano Energy 10:144–152

Margulis L, Salitra G, Tenne R, Tallanker M (1993) Nested fullerene-like structures. Nature 365:113–114

Marquart M, Wahl M, Emrich S, Zhang G, Sauer B, Kopnarski M, Wetzel B (2013) Enhancing the lifetime of MoS$_2$-lubricated ball bearings. Wear 303:169–177

Mertens AJ, Senthilvelan S (2016) Mechanical and tribological properties of carbon nanotube reinforced polypropylene composites. Proc Inst Mech Eng Part L-J Mat Des Appl 0:1–12

Moshkovith A, Perfiliev V, Lapsker I, Fleischer N, Tenne R, Rapoport L (2006) Friction of fullerene-like WS$_2$ nanoparticles: effect of agglomeration. Tribol Lett 24:225–228

Moulder JF, Stickle WF, Sobol PE, Bomben KD (1995) Handbook of X-ray photoelectron spectroscopy. Physical Electronics Inc., Eden Prairie, MA

Nath M, Govindaraj A, Rao CNR (2001) Simple synthesis of MoS$_2$ and WS$_2$ nanotubes. Adv Mater 13:283–286

Nemanič V, Žumer M, Zajec B, Pahor J, Remškar M, Mrzel A, Panjan P, Mihailovič D (2003) Field-emission properties of molybdenum disulfide nanotubes. Appl Phys Lett 82:4573–4575

Novoselov KS, Geim AK, Morozov SV, Jiang D, Zhang Y, Dubonos SV, Grigorieva IV, Firsov AA (2004) Electric field effect in atomically thin carbon films. Science 306:666–669

Onodera T, Morita Y, Suzuki A, Koyama M, Tsuboi H, Hatakeyama N, Endou A, Takaba H, Kubo M, Dassenoy F, Minfray C, Joly-Pottuz L, Martin JM, Miyamoto A (2009) A computational chemistry study on friction of h-MoS$_2$. Part I. Mechanism of single sheet lubrication. J Phys Chem B 113:16526–16536

Oshima C, Nagashima A (1997) Ultra-thin epitaxial films of graphite and hexagonal boron nitride on solid surfaces. J Phys Condens Matter 9:1–20

Price L, Levine MD, Zhou N, Fridley D, Aden N, Lu HY, Mcneil M, Zheng NN, Qin YN, Ping Y (2011) Assessment of China's energy-saving and emission-reduction accomplishments and opportunities during the 11th Five Year Plan. Energy Policy 39:2165–2178

Rabaso P, Dassenoy F, Ville F, Diaby M, Vacher B, Le Mogne T, Belin M, Cavoret J (2014a) An investigation on the reduced ability of IF-MoS$_2$ nanoparticles to reduce friction and wear in the presence of dispersants. Tribol Lett 55:503–516

Rabaso P, Ville F, Dassenoy F, Diaby M, Afanasiev P, Cavoret J, Vacher B, Le Mogne T (2014b) Boundary lubrication: influence of the size and structure of inorganic fullerene-like MoS$_2$ nanoparticles on friction and wear reduction. Wear 320:161–178

Raccichini R, Varzi A, Passerini S, Scrosati B (2015) The role of graphene for electrochemical energy storage. Nat Mater 14:271–279

Radisavljevic B, Radenovic A, Brivio J, Giacometti V, Kis A (2011) Single-layer MoS$_2$ transistors. Nat Nanotechnol 6:147–150

Reina A, Jia XT, Ho J, Nezich D, Son H, Bulovic V, Dresselhaus MS, Kong J (2008) Large area, few-layer graphene films on arbitrary substrates by chemical vapor deposition. Nano Lett 9:30–35

Remskar M, Mrzel A, Skraba Z, Jesih A, Ceh M, Demšar J, Stadelmann P, Lévy F, Mihailovic D (2001) Self-assembly of subnanometer-diameter single-wall MoS$_2$ nanotubes. Science 292:479–481

Risdon TJ, Gresty DA (1975) An historical review of reductions in fuel consumption of United States and European engines with MoS$_2$. SAE Technical Paper

Rosentsveig R, Gorodnev A, Feuerstein N, Friedman H, Zak A, Fleischer N, Tannous J, Dassenoy F, Tenne R (2009) Fullerene-like MoS$_2$ nanoparticles and their tribological behavior. Tribol Lett 36:175–182

Rothschild A, Cohen SR, Tenne R (1999) WS$_2$ nanotubes as tips in scanning probe microscopy. Appl Phys Lett 75:4025–4027

Shan TT, Xin S, You Y, Cong HP, Yu SH, Manthiram A (2016) Combining nitrogen-doped graphene sheets and MoS$_2$: a unique film-foam-film structure for enhanced lithium storage. Angew Chem 128:12975–12980

Smith RJ, King PJ, Lotya M, Wirtz C, Khan U, De S, O'Neill A, Duesberg GS, Grunlan JC, Moriarty G (2011) Large-scale exfoliation of inorganic layered compounds in aqueous surfactant solutions. Adv Mater 23:3944–3948

Tannous J, Dassenoy F, Lahouij I, Le Mogne T, Vacher B, Bruhács A, Tremel W (2011) Understanding the tribochemical mechanisms of IF-MoS$_2$ nanoparticles under boundary lubrication. Tribol Lett 41:55–64

Tenne R (2006) Inorganic nanotubes and fullerene-like nanoparticles. J Mater Res 21:2726–2743

Tevet O, Von-Huth P, Popovitz-Biro R, Rosentsveig R, Wagner HD, Tenne R (2011) Friction mechanism of individual multilayered nanoparticles. Proc Natl Acad Sci USA 108:19901–19906

Tkachev SV, Buslaeva EY, Naumkin AV, Kotova SL, Laure IV, Gubin SP (2012) Reduced graphene oxide. Inorg Mater 48:796–802

Tomala A, Vengudusamy B, Rodríguez Ripoll M, Naveira Suarez A, Remškar M, Rosentsveig R (2015) Interaction between selected MoS_2 nanoparticles and ZDDP tribofilms. Tribol Lett 59:1–18

Van Lier G, Van Alsenoy C, Van Doren V, Geerlings P (2000) Ab initio study of the elastic properties of single-walled carbon nanotubes and graphene. Chem Phys Lett 326:181–185

Wang CQ, Li HS, Zhang YS, Sun Q, Jia Y (2014) Effect of strain on atomic-scale friction in layered MoS_2. Tribol Int 77:211–217

Wu ZZ, Wang DZ, Wang Y, Sun AK (2010) Preparation and tribological properties of MoS_2 nanosheets. Adv Eng Mater 12:534–538

Wu SX, Zeng ZY, He QY, Wang ZJ, Wang SJ, Du YP, Yin ZY, Sun XP, Chen W, Zhang H (2012) Electrochemically reduced single-layer MoS_2 nanosheets: characterization, properties, and sensing applications. Small 8:2264–2270

Wu KH, Cheng HH, Mohammad AA, Blakey I, Jack K, Gentle IR, Wang DW (2015) Electron-beam writing of deoxygenated micro-patterns on graphene oxide film. Carbon 95:738–745

Xu MS, Liang T, Shi MM, Chen HZ (2013) Graphene-like two-dimensional materials. Chem Rev 113:3766–3798

Xu YF, Zheng XJ, Hu XG, Dearn KD, Xu HM (2014a) Effect of catalytic esterification on the friction and wear performance of bio-oil. Wear 311:93–100

Xu YF, Zheng XJ, Yin YG, Huang J, Hu XG (2014b) Comparison and analysis of the influence of test conditions on the tribological properties of emulsified bio-oil. Tribol Lett 55:543–552

Xu YF, Peng YB, Dearn KD, Zheng XJ, Yao LL, Hu XG (2015a) Synergistic lubricating behaviors of graphene and MoS_2 dispersed in esterified bio-oil for steel/steel contact. Wear 342:297–309

Xu ZY, Xu Y, Hu KH, Xu YF, Hu XG (2015b) Formation and tribological properties of hollow sphere-like nano-MoS_2 precipitated in TiO_2 particles. Tribol Int 81:139–148

Xu YF, Geng J, Zheng XJ, Dearn KD, Hu XG (2016) Friction-induced transformation from graphite dispersed in esterified bio-oil to graphene. Tribol Lett 63:1–11

Yang W, Chen GR, Shi ZW, Liu CC, Zhang LC, Xie GB, Cheng M, Wang DM, Yang R, Shi DX, Watanabe K, Taniguchi T, Yao YG, Zhang YB, Zhang GY (2013) Epitaxial growth of single-domain graphene on hexagonal boron nitride. Nat Mater 12:792–797

Yao J, Shi XL, Zhai WZ, Ibrahim AMM, Xu ZS, Chen L, Zhu QS, Xiao YC, Zhang QX, Wang ZH (2014) The enhanced tribological properties of NiAl intermetallics: combined lubrication of multilayer graphene and WS_2. Tribol Lett 56:573–582

Ye MX, Winslow D, Zhang DY, Pandey R, Yap YK (2015) Recent advancement on the optical properties of two-dimensional molybdenum disulfide (MoS_2) thin films. Photonics 2:288–307

Zelenski CM, Dorhout PK (1998) Template synthesis of near-monodisperse1 microscale nanofibers and nanotubules of MoS_2. J Am Chem Soc 120:734–742

Zeng ZY, Yin ZY, Huang X, Li H, He QY, Lu G, Boey F, Zhang H (2011) Single-layer semiconducting nanosheets: high-yield preparation and device fabrication. Angew Chem Int Ed 50:11093–11097

Zhai CY, Zhu MS, Bin D, Ren FF, Wang CQ, Yang P, Du YK (2015) Two dimensional MoS_2/graphene composites as promising supports for Pt electrocatalysts towards methanol oxidation. J Power Sources 275:483–488

Zhang W, Zhou M, Zhu HW, Tian Y, Wang KL, Wei JQ, Ji F, Li X, Li Z, Zhang P, Wu DH (2011) Tribological properties of oleic acid-modified graphene as lubricant oil additives. J Phys D Appl Phys 44:205303

Zhang WY, Demydov D, Jahan MP, Mistry K, Erdemir A, Malshe AP (2012) Fundamental understanding of the tribological and thermal behavior of Ag-MoS_2 nanoparticle-based multi-component lubricating system. Wear 288:9–16

Zhang LL, Pu JB, Wang LP, Xue QJ (2014) Frictional dependence of graphene and carbon nanotube in diamond-like carbon/ionic liquids hybrid films in vacuum. Carbon 80:734–745

Zhang G, Liu HJ, Qu JH, Li JH (2016a) Two-dimensional layered MoS$_2$: rational design, properties and electrochemical applications. Energy Environ Sci 9:1190–1209

Zhang X, Lai ZC, Tan CL, Zhang H (2016b) Solution-processed two-dimensional MoS$_2$ nanosheets: preparation, hybridization, and applications. Angew Chem Int Ed 55:8816–8838

Zhmud B, Pasalskiy B (2013) Nanomaterials in lubricants: an industrial perspective on current research. Lubricants 1:95–101

Zhou SM, Zhang XB, Ding ZP, Min CY, Xu GL, Zhu WM (2007) Fabrication and tribological properties of carbon nanotubes reinforced Al composites prepared by pressureless infiltration technique. Compos Part A Appl Sci Manuf 38:301–306

Zhou XD, Shi HQ, Fu X, Wu DM, Hu ZS (2008) Tribological properties of Cyanex 301-modified MoS$_2$ nano-sized hollow spheres in liquid paraffin. Ind Lubr Tribol 60:147–152

Zhu YW, Murali S, Cai WW, Li XS, Suk JW, Potts JR, Ruoff RS (2010) Graphene and graphene oxide: synthesis, properties, and applications. Adv Mater 22:3906–3924

Chapter 7
Hydrodesulfurization (HDS) Process Based on Nano-catalysts: The Role of Supports

Alimorad Rashidi, Fatemeh Mohammadzadeh, and Sedigheh Sadegh Hassani

Abstract Nowadays, market demand of middle distillate such as naphtha, kerosene, and diesel fractions with low sulfur content is augmented. Sulfur oxides which are released to the air by combustion of this kind of fuels are one of the critical problems of the environment. Hydrodesulfurization (HDS) is one of the most important catalytic processes which have been offered for solving these kinds of difficulties.

Conventional HDS catalysts are MoS_2 together with some metals from the transition metal series supported on γ-Al_2O_3 that are promoted by either cobalt or nickel.

A lot of research has been focused on HDS catalysts improvement for different industries, where they investigated various catalyst supports, active phases, and catalyst synthesis methods.

Recently, nano-materials are extensively used for catalytic HDS process. Carbon nanostructures such as carbon nanotubes (CNTs) draw scientists' attention because of their high mechanical strengths, purities, and thermal stability.

In this work, an overview of HDS process and various types of catalysts for removal of sulfur compounds from fuels is indicated. In addition, improved catalysts using nanotechnology including carbon nanotubes, graphene, and nano-alumina are investigated.

Keywords Hydrodesulfurization • Nano-catalyst • Carbon nanotubes • Graphene • Nano-alumina • Sulfur compounds

A. Rashidi (✉) • S. Sadegh Hassani
Nanotechnology Research Center, Research Institute of Petroleum Industry, Tehran, Iran
e-mail: rashidiam@ripi.ir

F. Mohammadzadeh
Process Engineering Section, Petroleum Engineering Department, Iranian Offshore Oil Company, Tehran, Iran

1   Introduction

In the last few decades, requirements to healthier and cleaner transportation fuels have become one of the most important subjects of discussion. Natural gas, fossil fuel, and some refined petroleum products (gasoline, kerosene, fuel oils, and diesel fuel) contain various sulfur compounds such as sulfides, thiols, thiophenes, benzothiophenes, and alkyl-substituted derivatives, most of which come from fluid catalytic cracking (FCC) unit (Babich and Moulijn 2003). These compounds not only are dangerous for the environment but could also poison the reforming catalyst and corrode the refinery equipment. In 2005, the European Union and US regulation restricted the sulfur content in gasoline and diesel to 30–50 ppm, while this amount was reduced to 10 ppm in 2010 (Deng et al. 2010) and it is expected to be less than 5 ppm in 2020 (Castillo-Araiza et al. 2015). On the other hand, the demand for high-quality petroleum grows up increasingly.

Implementation of environmental legislation to enhance the quality of oil along with market demand for low sulfur gasoline and high octane number has made great efforts to improve the quality of fuels. Hydrotreating process (HDT) which includes a sequence of important processes such as hydrodesulfurization (HDS), hydrodenitrogenation (HDN), and hydrodearomatization (HAD) for light and middle distillates, and hydrodemetallization (HDM) and hydrodeasphaltenization (HDAs) for heavy oils are fundamental techniques to remove or decrease sulfur components. These processes lead to more qualified productions and feedstocks (Nikulshin et al. 2016).

Middle distillate fraction has been more interest due to the importance of producing clean gasoline, jet and diesel fuels, and kerosene for the environment. Hence, many researchers have been focused on the sulfur removal from engine fuel using catalytic hydrodesulfurization process.

2   Hydrodesulfurization Process

Hydrodesulfurization (HDS) is an important catalytic process in which the sulfur compounds are converted to hydrocarbons and hydrogen sulfide that can easily be separated from natural gas and refined petroleum products; in this way, sulfur dioxide (SO_2) emissions from fuel combustion can be decreased.

Sulfur, even in low concentrations, poisons the precious metal catalysts (platinum and rhenium) in the catalytic reforming units which are used to upgrade the octane rating of the naphtha streams.

In this regard, in the industrial HDS process, the resulted hydrogen sulfide (H_2S) gas has been converted to sulfuric acid (H_2SO_4) and elemental sulfur.

The general conditions for HDS process are, temperature: 500–825 °F, hydrogen pressure: 150–3000 psig, hydrogen flows: 250–10000 SCF/bbl, feed space velocity: 0.5–5.0 volumes of liquid per volume of catalyst per hour (Schuman and Shalit

1971). The process conditions depending on the type of cutting oil and its sulfur compounds will be different. The fraction boiling up to 160 °C usually contains alkane thiols, aliphatic sulfides, and alicyclic sulfides that easily react with hydrogen in conventional hydrotreating process and completely removed. More complex thiophenes and bicyclic sulfides are found in higher boiling fractions. These compounds are more difficult to convert via hydrotreating. Hydrodesulfurization mechanism of thiophenic compounds is carried out via two pathways. In a first way, the sulfur atoms are directly removed from the ring and in this way, the ring is broken (hydrogenolysis pathway). In a second way, the aromatic ring is hydrogenated and then sulfur atoms are removed (hydrogenation pathway). Both pathways occur simultaneously and some parameters such as feed compound, reaction condition, and type of catalyst determine the predominant reaction (Babich and Moulijn 2003). Experimental results show that acidic supports facilitate the ring opening of hydrogenated intermediates and thus are suitable for this procedure (Santes et al. 2005). Many studies have been conducted to investigate the mechanism of HDS reactions through the integration of experimental results with the theoretical models (Krebs et al. 2008).

Thermodynamic data for the hydrogenation of sulfur compound which leads to the production of hydrocarbons and hydrogen sulfide shows that this reaction is possible thermodynamically over a wide range of temperatures. Nevertheless, the hydrogenation behavior of various sulfur compounds is probably different from the standpoint of thermodynamic, for example, the hydrogenation of saturated sulfur compound is favored at high temperature while increasing the temperature will decrease the thermodynamic driving force for thiophens. However, there is no thermodynamic limitation for hydrogenation of diverse sulfide compounds, although decreasing the reaction rate and the interference of competitor reactions cause problems in the implementation of the process (Schuman and Shalit 1971).

In this conventional process which is run out industrially, the warm oil fraction is mixed with hydrogen gas and then passed through the catalytic reactor; in this way the sulfur compounds with various structures and molecular weight are hydrogenated.

In the most usual cases, HDS process is carried out in fixed bed reactors with the cocurrent supply of oil stream and hydrogen. This reactor structure design causes to produce a mixed gas with inappropriate relative concentration. The high concentration of H_2S at the outlet reactor inhibits the complete sulfur removal (Babich and Moulijn 2003). Furthermore, the relatively large size of catalyst used in fixed bed reactor causes pressure drop and decreasing the internal diffusion and production of extreme heat because of exothermic reactions which can lead to creating hot spots and catalyst deactivation consequently.

In the recent years, some of the refining units exploit slurry reactors due to some advantages including simple construction and lower cost, efficient temperature control, less pressure drop, better performance of the catalyst, discharging the used catalysts, and bringing the fresh catalysts concurrently (Deng et al. 2010). Countercurrent operation is another new reactor system that could provide a preferable concentration profile. In this system, the oil feed is entered into the

reactor at the top and the hydrogen gas at the bottom and H_2S gas is removed at the top that prevents the reentry at the reactor outlet. The ebullated bed reactor is another type of HDS reactor that is designed especially for heavy refinery steams. This reactor benefit is good heat transfer and less coke formation. In another new approach, a combination of hydrotreating with other reactions as aromatizing and octane boosting is taken into consideration (Babich and Moulijn 2003).

Non-HDS based desulfurization technology is another approach that does not use hydrogen for desulfurization of sulfur compound from oil. In this way, sulfur is removed by shifting the boiling point through alkylation, extraction, adsorption, precipitation, and selective oxidation methods (Babich and Moulijn 2003).

Researchers try to promote the HDS process via different aspects such as construction of catalysts with high activity and lifetime, improving the design of reactors, and recently using a new internal catalyst to realize countercurrent flow (Deng et al. 2010; Song and Ma 2003).

3 Industrial HDS Catalysts and Their Activity

A well-known catalyst which is traditionally used in HDS process is Co–Mo, Ni–Mo or W crystallites that are well dispersed over alumina support (El Kady et al. 2010). The binary sulfide catalysts are highly regarded too because these systems cause very strong catalytic synergies. For example, individual Mo or Co sulfides shows very low activity as an HDS catalyst, but when combine to each other present very high activity (Okamoto 2008). A complete review of preparation of catalyst methods for HDS process is presented in some papers (Toulhoat and Raybaud 2013; Souchay 1969; Von Pope 1983; Campos-Martin et al. 2009; Vrinat et al. 2005; Dhar et al. 2003). In order to reduce the sulfur content of diesel and gas oil fuels, less than 15 ppm and 10 ppm, respectively (Bigdeli and Fatemi 2015; Michel et al. 2012), catalysts with higher strength are required.

The development of new catalysts is required for the optimization of HDS process. The synthesis method, activation procedure, type of support and active compound, promoter and posttreatment can affect the catalyst performance.

It is proven that sulfur and olefin compounds compete with each other on the catalyst and this is while hydrogenation of olefins causes to drop in octane number. Therefore, to keep a high octane number it is necessary to eliminate or limit the olefins reaction by using selective catalysts (Fontaine et al. 2010).

Improving selectivity has a key role in catalyst performance and could be fulfilled by adding diverse promoters to the catalyst composition (Mey et al. 2004), poisoning the hydrogenation sites selectively (Hatanaka 2005), balancing the basic–acidic properties of the support, and the amount of H_2S in feed (Fontaine et al. 2010). However, it should be noted that increasing the amount of H_2S has an inhibiting effect on both hydrodesulfurization and hydrogenation of olefins.

Type and quality of support also lead difference in catalyst performance via dispersing active component over and affecting the metal–support interaction

which in turn influence the catalyst functionalities. In order to select of an appropriate catalyst some criteria such as promoting effect on the active phase are important. For example, Co and Ni sulfides effects on active phase of MoS_2 lead to the formation of "CoMoS" or "NiMoS" phases, respectively (Toledo-Antonio et al. 2009).

Moreover, surface area, thermal stability, pore diameter, pore volume, geometrical functions, acidity, and mechanical strength are considered as key parameters for catalyst performances. Many materials were studied and experimental results showed that γ-Al_2O_3 is an ideal support with favorable characteristics, because it possesses high surface area, thermal stability, and regeneration. Also, its pore structures can be controlled simply (Nikulshin et al. 2014). However, the severe interaction between alumina and catalytic metals occurs that causes difficult sulfidation of components. Furthermore, acidic and basic sites on this support form coke (Stanislaus et al. 2010).

Generally, two types of sites are observed on traditional catalysts based on Al_2O_3 support: monolayer MoS_2 slabs that are so-called Type I and multilayer or highly stacked MoS_2 slabs which named Type II (Toledo-Antonio et al. 2009). Type II of CoMoS or NiMoS is a highly active site (Nikulshin et al. 2014) because strong bonds between molybdenum and the support are observed (Coelho et al. 2014) while the majority of sites belongs to the type I in alumina-supported catalysts. However, it is extremely complicated to constitute them.

In order to form these active slabs, increase Mo oxides dispersion, improve catalyst acidic characteristics, and reduce the interaction between catalysts components and supports, some additives like P and B are applied (Villarroel et al. 2009; Klimova et al. 2010; Dumeignil et al. 2006; Ferdous et al. 2004; Robles et al. 1999).

The other materials like MgO (Trejo et al. 2008), C (Nikulshin et al. 2014), TiO_2 (Guo et al. 2013), SiO_2 (Valencia and Klimova 2011; Gutiérrez and Klimova 2011), ZrO_2 (Vrinat et al. 1994), zeolite-like Na-Y, USY, and hybrid of alumina with them (Saih et al. 2005; Ren et al. 2016; Cui et al. 2013) exhibit superior performance as a support. Some of these oxides such as ZrO_2 and TiO_2 represent good reactivity (Escobar et al. 2008). For example, in Mo/TiO_2 catalysts, TiO_2 has a role as an accelerator in reduction and sulfidation of Mo because of its redox and semiconducting characteristics (Caero et al. 2003). However, because of their low surface area, weak thermal stability, and unfavorable mechanical characteristics, their commercial application is restricted (Faro and dos Santos 2006).

Investigation shows that mixed oxides (TiO_2/Al_2O_3 and ZrO_2/Al_2O_3) are suitable as a support due to their larger surface area than the oxides alone (Robles et al. 1999). However, catalysts based on mixed oxides are deactivated fast.

4   Nano-catalyst in HDS Process

Recently, nanotechnology has been extensively considered as a useful technology in various industries and preparation of nano-materials has attracted more and more attention (Gutiérrez and Klimova 2011; Mohammadi Meman et al. 2014; Morales-Ortũno et al. 2015). Thus, many reports have been published about the synthesis of nano-materials and many kinds of nano-catalysts for developing the HDS process.

Nano-particles with the high surface area as active phase of catalysts are extensively used for catalytic reactions (Aghabozorg et al. 2015).

Parviz et al. (2011) reported preparation of unsupported MoO_3 and $Co–MoO_3$ catalysts in the presence of different organic additives such as urea ($CO(NH_2)_2$), PEG200 ($HO(C_2H_4O)nH$), EDTA ($C_{10}H_{16}N_2O_8$), and sorbitol ($C_6H_{14}O_6$). Various kinds of MoO_3 microstructures and nanostructures were obtained by utilizing different additives. They clearly showed that nanostructure and promoted catalysts had excellent response in the hydrodesulfurization reaction of naphtha than microstructure catalysts. They observed that the amount of sulfur of the feed was reduced from 2420 to 24 ppm when urea-prepared promoted catalyst was utilized.

Ren et al. (2016) studied HDS of dibenzothiophene and 4,6-dimethyldibenzothiophene feed on NiW-ETS-10/Al_2O_3 and NiW-ETS–Ti Reach /Al_2O_3 (ETS-10 is the microporous titanosilicate) catalysts at 260 °C. They recognized the WS_2 slabs of NiW-AT-ETS/Al_2O_3 had an average length of 2.66 nm and layer number of 3.3 nm which showed more slabs and shorter slab length than the original one. They demonstrated that weak interaction between WS_2 as active phase and alumina supports was due to the presence of Ti species. They also reported that NiW-ETS–Ti Reach/Al_2O_3, which was named as NiW-AT-ETS/Al_2O_3, had higher activity in HDS of DBT and 4,6-DMDBT. They supposed that shorter length of WS_2 active phase leads to higher stacked layers and better dispersion of active sites on support in comparison of NiW-ETS-10/Al_2O_3 which was named as NiW-ETS-origin/Al_2O_3 were the reasons for 96.5% and 86.9% activities of DBT and 4,6-DMDBT hydrodesulfurization, respectively.

5   Types and Roles of Supports

5.1   Nano-alumina Support

The potential of alumina support in catalytic activity can be improved by controlling its size and morphology in the mesopore size (Lee et al. 2016; Rashidi et al. 2010, 2012). In this regard, by altering the physical and chemical properties of support, the activity and selectivity of prepared catalysts can be optimized (Aghabozorg et al. 2015).

F. Rashidi et al. have prepared some new catalysts using micro- and nano-alumina support with CoMoP and CoMoB active metals in hydrodesulfurization
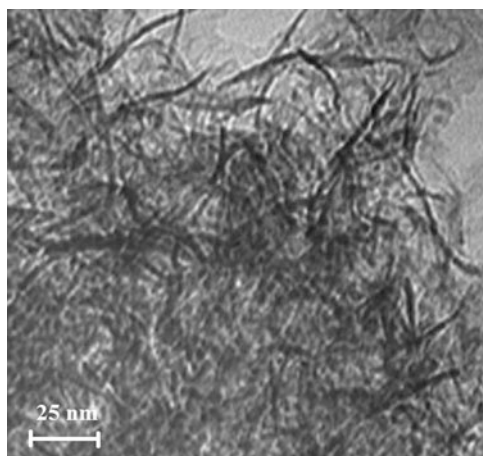
Fig. 7.1 TEM micrograph of the nano-γ-Al$_2$O$_3$ prepared with 2-propanol and sulfuric acid
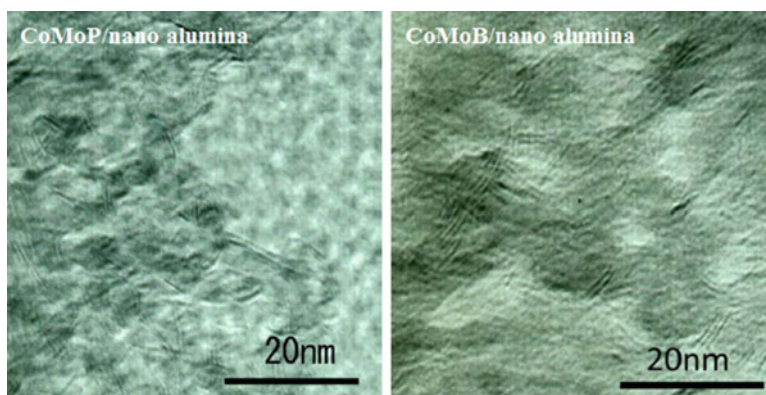
Fig. 7.2 HRTEM images on nano-catalysts Co–Mo/nano-alumina

of straight-run light gas oil (SRLGO) with 13500 ppm sulfur compounds (Rashidi et al. 2013). TEM micrographs of the nano-γ-Al$_2$O$_3$ prepared with 2-propanol and sulfuric acid are shown in Fig. 7.1. Also, Fig. 7.2 shows HRTEM images on nano-catalysts Co–Mo/nano-alumina.

Synthesized nano-alumina support was characterized using Accelerated Surface Area and Porosimetry System (ASAP), where the surface area, pore size, and pore volume are compared with commercial alumina support and presented in Table 7.1.

Also, the synthesized catalyst performance was investigated and compared with the commercial catalyst. They stated that presence of P and B in the catalyst structure increased the acidity of the catalyst by diminishing the interaction between metals and support and also caused Co metals placed on the edge of MoS$_2$ particles.

Table 7.1 Physical properties of the supports

Sample	Surface area (m^2/g)	Pore volume (cm^3/g)	Pore size (Å)
New nano-γ-Al$_2$O$_3$	403.05	1.69	104.59
Commercial-γ-Al$_2$O$_3$	246.20	0.50	70.30

They claimed that among the prepared catalysts, CoMoPB/nanoAl$_2$O$_3$ with a better dispersion of Mo and Co showed the higher activity than others and was able to decrease the sulfur content of diesel fuel to below 10 ppm.

They attributed the gasoil HDS activity to the stacking number and Co/Mo ratios of the CoMoS sites of the catalysts. They deduced that the active species of CoMoS II placed on the edges of MoS$_2$ slabs. In addition, they found that higher Co/Mo ratio caused higher Co efficiency. These results lead to the further HDS responsiveness. Also, Co and Mo dispersion and the stabilization of metals were improved via acidic nature of nano-alumina.

Liu and coworkers' (2012) experiments displayed higher HDS response for 4,6-DMDBT when bimodal mesoporous nanorod γ-Al$_2$O$_3$ support was prepared by the hydrothermal process. They used different quantities of PEG for better γ-Al$_2$O$_3$ crystal growth. Their studies indicated that supports with a higher amount of PEG (24 g PEG) had higher stacking layer number and higher activity. Their experiments revealed that bimodal mesoporous nanorod alumina had high surface area, lower lattice defects, and lower support interactions. This reason led to the higher dispersion of active phases and increasing the acidic sites. They reported that CoMo-BMA-4 had 98.5% conversion.

Wang and coworkers (2016) synthesized mesoporous alumina supports with crystal forms of γ, θ, and δ using boehmite sol and PEG and tested them in hydrodesulfurization of DBT and 4,6-DMDBT and compared their activities with commercial one. The θ and δ were obtained by thermal treatment of γ-alumina at high temperatures. They discovered that NiMo/δ-Al$_2$O$_3$ had higher conversion and catalytic response in all cases (99.6% conversion of DBT and 65.8% conversion of 4,6-DMDBT) at 613 K, 4.0 MPa, 200 ml/ml (Hydrogen/oil), and 150/h. They expressed several reasons for these phenomena. For example, characterization results declared δ-Al$_2$O$_3$ supports had a larger pore size (18.3 nm), surface area (114 m^2/g), and pore volume (0.56 cm^3/g) than the other supports. They had open pore channel so Ni–Mo metals could be impregnated easier in these channels. It caused better dispersion and stacking of a number of active sites over these catalysts.

This kind of prepared catalyst with moderate acid sites could facilitated the transformation of the reactants to the active sites and thus improved HDS of DBT and 4,6-DMDBT. Also, appropriate textural properties and suitable metal support interaction (MSI) of NiMo/δ-Al$_2$O$_3$ were reported.

5.2 Carbon Nanotubes Support

Also, carbon nanotubes (CNTs) as a novel nano-material are promising candidates because of their special properties such as high surface area (300–1500 m^2/g), thermal stability, high mechanical strength, electronic properties, and several adsorption sites (Thi Vu et al. 2012; Nakhaei Pour et al. 2010; Graham et al. 2009).

Generally, they are classified in two groups, single-walled which are monolayer graphene sheets that are rolled into a cylinder and multiwalled carbon nanotubes that contain rolled up multilayer graphene with diameters from 2 to 25 nm. Before hydrogenation process, the ends of the multiwall or single wall CNTs are opened for catalyst application (Yu et al. 2008). Several kinds of nano-particle such as Pt and Pd (Kiani et al. 2013) can be entered in and/or deposited on the CNTs structure to improve their activity as catalysts.

In Pawelec et al. article (2006), CNT supported CoMo catalysts performance had comprised with activated carbon or γ-Al$_2$O$_3$ supported catalysts in HDS of thiophene or dibenzothiophene. It was reported that CoMo/CNT had supreme activity due to their nanosized and electron donor aspects.

Nakhaei Pour et al. (2010) compared Co–Mo/SWCNT and alumina Co–Mo/γ-Al$_2$O$_3$ as the catalyst supports during hydrodesulfurization process of naphtha. They characterized synthesized SWNT using BET and XRD, which are shown in Fig. 7.3. and Table 7.2.
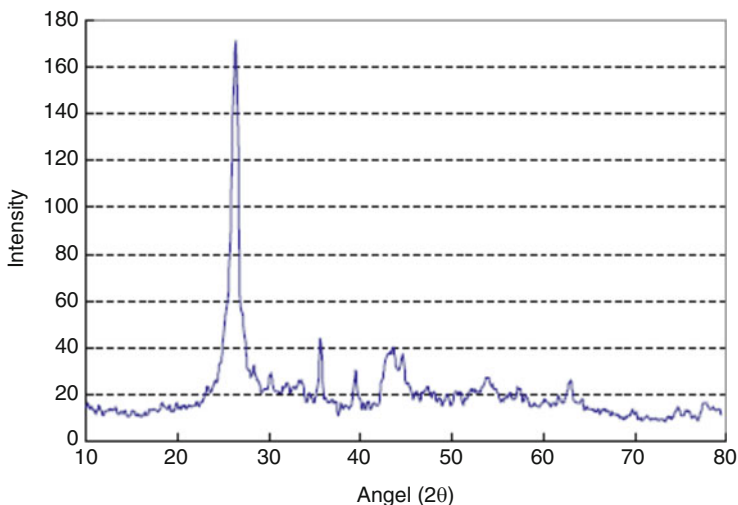
Fig. 7.3 XRD of Co–Mo/SWCNT catalysts after reaction

Table 7.2 Physical properties of SWCNT support

Sample	Surface area BET (m^2/g)	Pore volume (cm^3/g)	Pore size (Å)
SWCNT	303.25	0.76	10.02

XRD graph showed carbon as catalysts support and molybdenum sulfide of consumed catalysts after reaction. They deduced Mo contents were converted to the molybdenum sulfide.

They observed that MoO_2 and MoO_3 were the active sites on the CNT and γ-Al_2O_3 supports, respectively. They reported that carbon nanotubes had hydrophobic nature which resulted in weak interaction between Co/Mo and support. In calcinations stage, CNT caused reduction of Mo through heat treatment because Mo oxides gathered on the surface of support preliminary.

They claimed that comfortable reduction of active metals on the CNT supports was performed which facilitated the dispersion of Co–Mo particles on support and improved the acidity of CNT. Therefore, high isomerization and the cracking reaction of sulfur compounds could be observed in these kinds of catalyst that leads to the enormous HDS responsible behavior.

Results showed that CNT supported catalysts adsorbed high quantity of sulfur at operating temperature above 583 K since active phases on this catalyst were reduced more comfortably.

Khorami and Kalbasi (2011) investigated on the HDS of naphtha by multiwall carbon nanotube supported Co–Mo catalyst in a fixed bed reactor. The operational condition of the reactor was reported as below: 310 °C, 15 bar and liquid hourly space velocity: 4/h. They acquired catalyst with 10–20 nm clusters and support with 10 nm pore diameters that improved Co/Mo particles dispersion on the support. The activity of catalyst with total amounts of Co and Mo about 7% weight percent was examined for HDS of naphtha with 1270 ppm sulfur species like methylisopropylsulfide, t-amylmercaptan, isoamylmercaptan, ethyl sec butyl sulfide, etc. It was observed that all of the sulfur compounds displayed 88% conversion regardless of their molecular weights.

Shang et al. (2007) synthesized MoO_3/CNT, Co–Mo/CNT with different atomic ratio of Co/Mo and γ-Al_2O_3 supports and examined their behavior in hydrodesulfurization of dibenzothiophene. As the other researchers' reports, they revealed that Co–Mo/CNT had higher activity than Co–Mo based γ-Al_2O_3 catalyst due to the weak interaction of CNT support with metals spices, unlike γ-Al_2O_3 supports. They also postulated that reducibility of catalysts was depended on the atomic ratios of Co/Mo. They tested their catalysts with 0–1 atomic ratios of Co/Mo and concluded that the more atomic ratio, hence 0.7, lead to the more active spices in the catalysts. For MoO_3/CNT catalysts, they observed well dispersion of Mo on CNT catalysts when the catalyst loading was lower than 6% and proper scattering of MoO_2 particles when catalyst loading was 8%. MoO_2 particles have a more effective role on sulfidation process than MoO_3 because of their comfortable conversion capability.

In another research (Chen et al. 2004), DBT adsorption on sulfide and oxide of Co–Mo catalysts on CNT, activated carbon (AC) and γ-Al_2O_3 were studied. Characterization using NH_3-TPD technique indicated the higher activity of sulfide catalyst than oxides since a number of acidic sites on sulfide compounds were more than ones on oxide catalysts. Moreover, despite AC has higher surface area and pore

volume than CNT and γ-Al$_2$O$_3$, CoMoS/AC showed weaker acidity because a number of acidic sites were decreased after CoMoS and CoMoO loading on the AC. They found that the activity of CoMoS/CNT was about 97%. It means that almost all (90%<) of the DBT molecules were adsorbed on CoMoS/CNT. They deduced it may be related to the CoMoS/CNT end-on mode and presence of several onion vacancies (vacant orbit which is electron acceptor) in the MoO$_2$ metals as active phases.

Soghrati et al. (2012) prepared Co–Mo catalyst supported on CNT-coated cordierite monoliths (2Al$_2$O$_3$: 5SiO$_2$: 2MgO) and tested them in HDS of naphtha.

FESEM results of CNT-coated monolith determined the good distribution of CNTs on the monolith which caused to attain catalysts with the higher surface area, pore volume and mesoporous layer of CNTs with adhesion properties. A comparison of CoMo/monolith (A), CoMo/CNT, and CoMo/FACNT (CNT-coated monoliths) revealed that FACNT supported CoMo catalysts had higher activity than the others. Besides, when the metal content of the catalysts (CoMo) was increased to 10 wt%, the S conversion reached to 98.08%. It means that sulfur content of naphtha declined from 2670 to 53 ppm at 310 °C.

Eswaramoorthi et al. (2008) survived the effect of NiMo/MWCNTs catalysts on gas oil which was obtained from Athabasca bitumen. They evaluated their catalysts in different Ni and Mo contents of catalysts in various temperatures which showed different results in HDN and HDS of gas oil. Experimental results illustrated the reduction of Mo elements from Mo^{6+} to Mo^{4+} and Mo^0 in two steps and different temperatures. By increasing the amount of Ni, for example, for 0–4.5 wt% Ni/12 wt% Mo/MWCNTs, well dispersion of MoO$_3$ particles was seen. In addition, when Ni content increased to 3 wt% over 12 wt% Mo/MWCNTs, the number of active sites of MoS$_2$ enhanced. In addition, the catalysts activity of MWCNT support was higher than that of Al$_2$O$_3$ at low temperatures (345–360 °C) but at higher temperatures (375 °C) they displayed equal value. They believed that it was due to the catalysts tendency to have maximum activity at higher temperatures.

5.3   Graphene Support

In the recent years, graphene as a new carbon material with a planar sheet with sp^2 carbon–carbon bonds attracts the scientist attentions due to their high specific surface area, supreme mechanical, electronic and thermal properties, high elasticity, and good mobility (Rao et al. 2009; Zhu et al. 2010).

Some articles investigate graphene performance as catalyst support (Hajjar et al. 2016a) in HDS process. Z. Hajjar et al. (2016b) have synthesized graphene by CVD technique in atmospheric pressure and 900–1000 °C and with solid camphor (C$_{10}$H$_{16}$O), hydrocarbon source that contains hexagonal and pentagonal rings like methyl carbon, and methane gas as carbon precursors. They obtained a 5-layer graphene with a high yield of 90%. They conclude from BET results that obtained graphene from camphor had higher specific surface area and pore volume than

Table 7.3 Physical properties of the graphene support

Sample	Surface area (m^2/g)	Pore volume (cm^3/g)	Pore size (Å)
Graphene	850	2.11	100
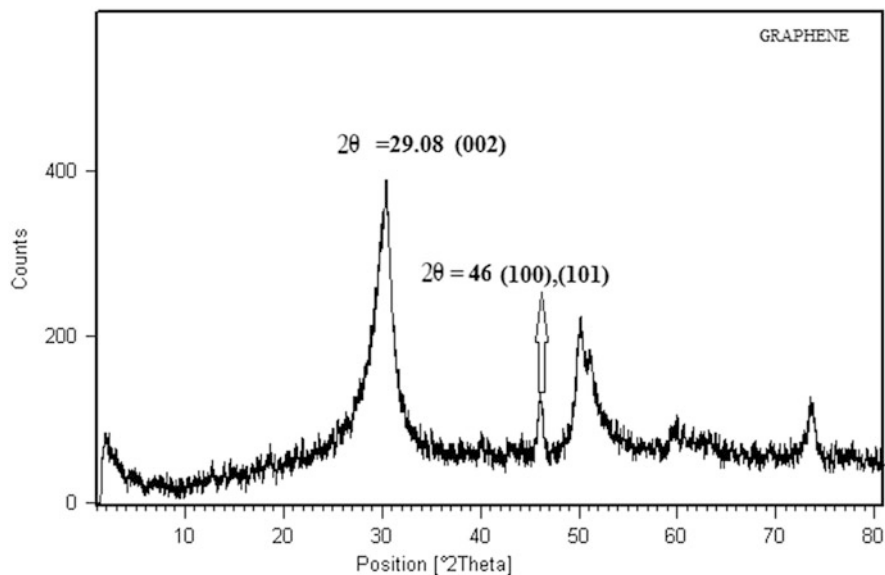
Fig. 7.4 XRD pattern of Graphene

methane precursor. They declared that more acidic sites were observed on the camphoric based catalysts. The physical characterization of the synthesized graphene is shown in Table 7.3.

Furthermore, from XRD patterns (Fig. 7.4), it could be observed, the graphene sample clearly shows the (002) reflection associated to 2Θ about ~29.8 which indicate graphene sheet and (100) and (101) reflections associated to 2Θ about 46 that overlap together.

Also, the Raman spectrum of graphene, Fig. 7.5, shows three main peaks G, D, and 2D. The I_D/I_G, the ratio D and G band intensities, is an important parameter to show carbon structure disordering and heteroatom doping, which higher value is reflective of more defects formation in graphene structure and heteroatom existence (Sun et al. 2015; Yuezeng et al. 2013).

They have also expanded their studies on the other synthesis methods of graphene (Hajjar et al. 2015). They have employed in situ and simultaneous chemical exfoliation method in graphene oxide–MoS_2 composite synthesis in order to accelerate the synthesis procedure. They claimed that smaller and more uniformly dispersed particles and higher and stronger acidic sites were obtained via this method.
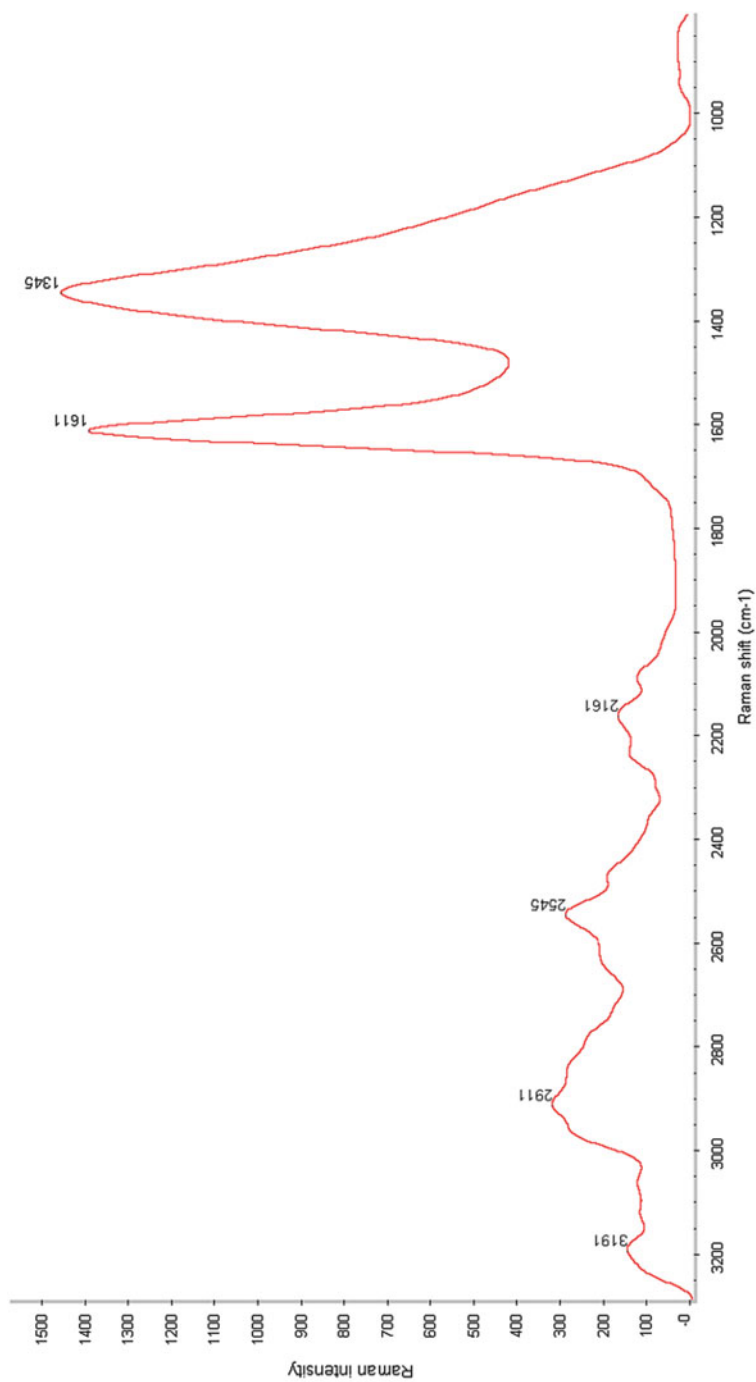
Fig. 7.5 Raman spectra of porous graphene

In both cases, catalysts were compared with industrial Co–Mo/γ-Al$_2$O$_3$ supported catalysts for HDS of naphtha with 1350 ppm sulfur content. The obtained results showed better reduction of active materials on graphene-based catalysts at lower temperature due to the weaker interaction between supports and Co–Mo metals. Their experience revealed that graphene-based catalyst had higher activity than industrial ones in hydrodesulfurization. Results showed that catalytic conversion of both cases was 100% while industrial catalyst had 92.6% conversion. BET results were obviously showed that specific surface area and pore size of graphene were higher than γ-Al$_2$O$_3$. In the first case, the number of active species on graphene-based catalysts perceived to be decreased at a lower temperature which was attributed to the weaker interaction of carbon-based supports with metals as catalysts. In the second article, sulfidation was performed by feed at first and so MoS$_2$ was formed initially and could act as active phase. Graphene oxides have weak interaction between supports and catalyst.

6   Conclusion

Sulfur compounds which are released to the air by combustion of fuels are one of the critical problems of the environment. Hydrodesulfurization as an important catalytic process is used to solve this problem. To reduce a number of sulfur compounds in oil stocks, improved processes and novel active catalysts have been introduced. The improved catalysts activity can be achieved by controlling the size, surface area, porosity, active phase dispersion, morphology, surface composition, and thermal stability.

In the HDS process, the most important applicable supports are nano- and mesoporous materials such as carbon nanotubes, graphene, and γ-Al$_2$O$_3$.

The γ-Al$_2$O$_3$ is an important support for HDS process. It has bimodal pore structures, i.e., the smaller pore with high surface area for HDS reactions and the larger pores for bulky reactants to diffuse in pores. In these supports, it is significant to produce fourfold (Al^{IV}) and fivefold (Al^V) aluminum acid centers in order to have better chemical reactions. By controlling the size of them in nano or meso scale, a lower amount of coke is obtained. By controlling the morphology and slab stacking numbers of active species in alumina-supported catalysts in nano and meso scales, suitable MoS$_2$ slab layers can be obtained and complete conversion achieved

Moreover, graphene and CNT supports have high surface area. Therefore, dispersion of nanoclusters over catalysts is increased and lower loading of metals on catalysts surfaces is needed which leads to economical costs.

References

Aghabozorg HR, Sadegh Hassani S, Rashidi AM (2015) Nanocatalysts preparation, characterization, and their application in oil and gas processes. In: Kharisov BI, Kharissova OV, Ortiz-Mendez U (eds) CRC encyclopedia. Taylor and Fransis, Boca Raton, FL, pp 100–107

Babich IV, Moulijn JA (2003) Science and technology of novel processes for deep desulfurization of oil refinery streams: a review. Fuel 82:607–631

Bigdeli S, Fatemi S (2015) Fast carbon nanofiber growth on the surface of activated carbon by microwave irradiation; a modified nano-adsorbent for deep desulfurization of liquid fuels. Chem Eng J 269:306–315

Caero LC, Romero AR, Ramirez J (2003) Niobium sulfide as a dopant for Mo/TiO$_2$ catalysts. Catal Today 78:513–518

Campos-Martin JM, Rojas S, Oyama ST, Gott T, Zhao H, Lee Y-K (2009) Transition metal phosphide hydroprocessing catalysts: a review. Catal Today 143:94–107

Castillo-Araiza CO, Chávez G, Dutta A, de los Reyes JA, Nuñez S, García-Martínez JC (2015) Role of Pt–Pd/γ-Al$_2$O$_3$on the HDS of 4,6-DMBT: Kinetic modeling & contribution analysis. Fuel Process Technol 132:164–172

Chen H, Zhou X, Shang H, Liu C, Qiu J, Wei F (2004) Study of dibenzothiophene adsorption over carbon nanotube supported CoMo HDS catalysts. J Nat Gas Chem 13:209–217

Coelho TL, Licea YE, Palacio LA, Faro AC Jr (2014) Heptamolybdate-intercalated CoMgAl hydrotalcites as precursors for HDS selective hydrotreating catalysts. Catal Today 250:38–46

Cui Q, Zhou Y, Wei Q, Yu G, Zhu L (2013) Performance of Zr- and P-modified USY-based catalyst in hydrocracking of vacuum gas oil. Fuel Process Technol 106:439–446

Deng Z, Wang T, Wang Z (2010) Hydrodesulfurization of diesel in a slurry reactor. Chem Eng Sci 65:480–486

Dhar GM, Srinivas BN, Rana MS, Kumar M, Maity SK (2003) Mixed oxide supported hydrodesulfurization catalysts—a review. Catal Today 86:45–60

Dumeignil F, Sato K, Imamura M, Matsubayashi N, Payen E, Shimada H (2006) Characterization and hydrodesulfurization activity of CoMo catalysts supported on sol-gel prepared Al$_2$O$_3$. Appl Catal A Gen 315:18–28

El Kady FYA, Abd El Wahed MG, Shaban S, Abo El Naga AO (2010) Hydrotreating of heavy gas oil using CoMoc-Al2O3 catalyst prepared by equilibrium deposition filtration. Fuel 89:3193–3206

Escobar J, Barrera MC, De Los Reyes JA, Cortés MA, Santes V, Gómez E, Pacheco JG (2008) Effect of Mo and Co loading in HDS catalysts supported on solvo-thermally treated ZrO$_2$–TiO$_2$ mixed oxides. Catal Today 133–135:282–291

Eswaramoorthi I, Sundaramurthy V, Das N, Dalai AK, Adjaye J (2008) Application of multi-walled carbon nanotubes as efficient support to NiMo hydrotreating catalyst. Appl Catal A Gen 339:187–195

Faro AC Jr, dos Santos ACB (2006) Cumene hydrocracking and thiophene HDS on niobia-supported Ni, Mo and Ni–Mo catalysts. Catal Today 118:402–409

Ferdous D, Dalai AK, Adjaye J (2004) A series of NiMo/Al$_2$O$_3$ catalysts containing boron and phosphorus Part I. Synthesis and characterization. Appl Catal A Gen 260:137–151

Fontaine C, Romero Y, Daudin A, Devers E, Bouchy C, Brunet S (2010) Insight into sulphur compounds and promoter effects on Molybdenum-based catalysts for selective HDS of FCC gasoline. Appl Catal A Gen 388:188–195

Graham UM, Dozier A, Khatri RA, Bahome MC, Jewell LL, Mhlanga SD, Coville NJ, Davis BH (2009) Carbon nanotube docking stations: a new concept in catalysis. Catal Lett 129:39–45

Guo C, Wu Y, Wang X, Yang B (2013) Effect of the support calcination temperature on selective hydrodesulfurization of TiO2 nanotubes supported CoMo catalysts. J Energy Chem 22:517–523

Gutiérrez OY, Klimova T (2011) Effect of the support on the high activity of the (Ni)Mo/ZrO2–SBA-15 catalyst in the simultaneous hydrodesulfurization of DBT and 4,6-DMDBT. J Catal 281:50–62

Hajjar Z, Kazemeini M, Rashidi AM, Bazmi M (2015) In situ and simultaneous synthesis of a novel graphene-based catalyst for deep hydrodesulfurization of naphtha. Catal Lett 145:1660–1672

Hajjar Z, Kazemeini M, Rashidi A, Tayyebi S (2016a) Artificial intelligence techniques for modeling and optimization of the HDS process over a new graphene based catalyst. Phosphorus Sulfur Silicon Relat Elem 191:1256–1261

Hajjar Z, Kazemeini M, Rashidi AM, Bazmi M (2016b) Graphene based catalysts for deep hydrodesulfurization of naphtha and diesel fuels: a physiochemical study. Fuel 165:468–476

Hatanaka S (2005) Hydrodesulfurization of selective catalytic cracked gasoline. Catal Surv Asia 9:87–93

Khorami P, Kalbasi M (2011) Hydrodesulfurization activity of CoMo catalyst supported on multi wall carbon nanotube: sulphur species study. J Exp Nanosci 6:349–361

Kiani M, Aghabozorg H, Jafari Jozani K, Rashidi AM, Mohsennia M (2013) Preparation and characterization of carbon nanotubes supported Ni_2P for hydrodesulfurization (HDS) of naphtha. Phosphorus Sulfur Silicon 188:1254–1261

Klimova T, Vara PM, Lee IP (2010) Development of new NiMo/g-alumina catalysts doped with noble metals for deep HDS. Cataly Today 150:171–178

Krebs E, Silvi B, Daudin A, Raybaud P (2008) A DFT study of the origin of the HDS/HydO selectivity on Co(Ni)MoS active phases. J Catal 260:276–287

Lee X, Feng J, Guo J, Wang A, Prins R, Duan X, Chen Y (2016) Preparation of Ni_2P/Al_2O_3 by temperature programmed reduction of a phosphate precursor with a low P/Ni ratio. J Catal 334:116–119

Liu X, Li X, Yan Z (2012) Facile route to prepare bimodal mesoporous γ-Al_2O_3 as support for highly active CoMo-based hydrodesulfurization catalyst. Appl Catal B Environ 121–122:50–56

Mey D, Brunet S, Canaff C, Maugé F, Bouchy C, Diehl F (2004) HDS of a model FCC gasoline over a sulfided CoMo/Al2O3 catalyst: effect of the addition of potassium. J Catal 227:436–447

Michel V, Dorothée L, Christophe G (2012) Use of competitive kinetics for the understanding of deep hydrodesulfurization and sulfide catalysts behavior. Appl Catal B Environ 128:3–9

Mohammadi Meman N, Pourkhalil M, Rashidi AM, Zare Nezhad B (2014) Synthesis, characterization and operation of a functionalized multi-walled CNT supported MnOx nanocatalyst for deep oxidative desulfurization of sour petroleum fractions. J Ind Eng Chem 20:4054–4058

Morales-Ortũno JC, Ortega-Domínguez RA, Hernández-Hipólito P, Bokhimi X, Klimova TE (2015) HDS performance of NiMo catalysts supported on nanostructured materials containing titania. Catal Today 271:127–139

Nakhaei Pour A, Rashidi AM, Jafari Jozani K, Mohajeri A, Khorami P (2010) Support effects on the chemical property and catalytic activity of Co-Mo HDS catalyst in sulfur recovery. J Nat Gas Chem 19:91–95

Nikulshin PA, Salnikov VA, Mozhaev AV, Minaev PP, Kogan VM, Pimerzin AA (2014) Relationship between active phase morphology and catalytic properties of the carbon–alumina-supported Co(Ni)Mo catalysts in HDS and HYD reactions. J Catal 309:386–396

Nikulshin P, Mozhaev A, Lancelot C, Blanchard P, Payen E, Lamonier C (2016) Hydroprocessing catalysts based on transition metal sulfides prepared from Anderson and dimeric Co2Mo10-heteropolyanions, a review. C R Chim 19:1276–1285

Okamoto Y (2008) A novel preparation-characterization technique of hydrodesulfurization catalysts for cleaner fuels. Catal Today 132:9–17

Parviz D, Kazemeini M, Rashidi AM, Jafari Jozani K (2011) Naphtha hydrodesulfurization over micro and nanostructure MoO_3 catalysts. Sci Iran C 18:479–485

Pawelec B, La Parola V, Navarro RM, Murcia-Mascarós S, Fierro JLG (2006) On the origin of the high performance of MWNT-supported PtPd catalysts for the hydrogenation of aromatics. Carbon 44:84–98

Rao CNR, Sood AK, Subrahmanyam KS, Govindaraj A (2009) Graphene: the new two-dimensional nanomaterial. Angew Chem Int Ed 48:7752–7777

Rashidi F, Nemati Kharat A, Rashidi AM, Lima E, Lara V, Valente JS (2010) Fractal geometry approach to describe mesostructured boehmite and Gamma-alumina nanorods. Eur J Inorg Chem:1544–1551

Rashidi F, Lima E, Rashidi H, Rashidi AM, Guzmane A (2012) Cooperative effect of gold nanoparticles with CUS aluminum from nanoalumina support in the catalysis of an electron transfer reaction. Appl Catal A Gen 417–418:129–136

Rashidi F, Sasakia T, Rashidi AM, Nemati Kharat A, Jafari Jozani K (2013) Ultra deep hydrodesulfurization of diesel fuels using highly efficient nanoalumina-supported catalysts: impact of support, phosphorus, and/or boron on the structure and catalytic activity. J Catal 299:321–335

Ren S, Li J, Feng B, Wang Y, Zhang W, Wen G, Zhang Z, Shen B (2016) A novel catalyst of Ni, W-surface-Ti-rich-ETS-10/Al$_2$O$_3$: its role and potential of HDS performance for steric hindered sulfur compound 4,6-DMDBT. Catalysis Today 263:136–140

Robles JM, Castellón ER, López AJ (1999) Characterization of Ni, Mo and Ni–Mo catalysts supported on alumina-pillared a-zirconium phosphate and reactivity for the thiophene HDS reaction. J Mol Catal A Chem 145:169–181

Saih Y, Nagata M, Funamoto T, Masuyama Y, Segawa K (2005) Ultra deep hydrodesulfurization of dibenzothiophene derivatives over NiMo/TiO$_2$-Al$_2$O$_3$. Appl Catal A 295:11–22

Santes V, Herbert J, Cortez MT, Zárate R, Díaz L, Swamy PN, Aouine M, Vrinat M (2005) Catalytic hydrotreating of heavy gasoil FCC feed on alumina–titania-supported NiMo catalysts. Appl Catal A Gen 281:121–128

Schuman SC, Shalit H (1971) Hydrodesulfurization. Catal Rev Sci Eng 4(1):245–318

Shang H, Liu C, Xu Y, Qiu J, Wei F (2007) States of carbon nanotube supported Mo-based HDS catalysts. Fuel Process Technol 88:117–123

Soghrati E, Kazemeini M, Rashidi AM, Jafari Jozani K (2012) Preparation and characterization of Co-Mo catalyst supported on CNT coated cordierite monoliths utilized for naphtha HDS process. Proc Eng 42:1484–1492

Song CS, Ma XL (2003) New design approaches to ultra-clean diesel fuels by deep desulfurization and deep dearomatization. Appl Catal B Environ 41:207–238

Souchay P (1969) Ions mineraux condenses. Masson

Stanislaus A, Marafi A, Rana MS (2010) Recent advances in the science and technology of ultra sulfur diesel (ULSD) production. Catal Today 153:1

Sun Z, Masa J, Weide P, Fairclough SM, Robertson AW, Ebbinghaus P, Warner JH, Tsang SCE, Muhlerb M, Schuhmann W (2015) High-quality functionalized few-layer graphene: facile fabrication and doping with nitrogen as a metal-free catalyst for the oxygen reduction reaction. J Mater Chem A 3:15444–15450

Thi Vu TH, Thi Nguyen TT, Thi Nguyen PH, Do MH, Au HT, Nguyen TB, Nguyen DL, Park JS (2012) Fabrication of photo catalytic composite of multi-walled carbon nanotubes/TiO$_2$ and its application for desulfurization of diesel. Mater Res Bull 47:308–314

Toledo-Antonio JA, Cotres-Jacome MA, Angeles-Chavez C, Escobar J, Barrera MC, Lopez-Salinas E (2009) Highly active CoMoS phase on titania nanotubes as new hydrodesulfurization catalysts. Appl Catal B Environ 90:213–223

Toulhoat H, Raybaud P (2013) Catalysis by transition metal sulfides, from molecular theory to industrial application. Editions Technip, Paris, p 151

Trejo F, Rana MS, Ancheyta J (2008) CoMo/MgO–Al$_2$O$_3$ supported catalysts: an alternative approach to prepare HDS catalysts. Catal Today 130:327–336

Valencia D, Klimova T (2011) Effect of the support composition on the characteristics of NiMo and CoMo/(Zr)SBA-15 catalysts and their performance in deep hydrodesulfurization. Catal Today 166:91–101

Villarroel M, Baeza P, Gracia F, Escalona N, Avila P, Gil-Llambías FJ (2009) Phosphorus effect on Co//Mo and Ni//Mo synergism in hydrodesulphurization catalysts. Appl Catal A Gen 364:75–79

Von Pope MT (1983) Heteropoly and isopoly oxometalates. Springer, Berlin

Vrinat M, Hamon D, Breysse M, Durand D, Courieres T (1994) Zirconia and alumina supported molebdenum based catalysts: a comparative study in hydrodesulfurization and hydrogenation reactions. Catal Today 20:273–282

Vrinat M, Bacaud R, Laurenti D, Cattenot M, Escalona N, Gamez S (2005) New trends in the concept of catalytic sites over sulfide catalysts. Catal Today 107–108:570–577

Wang X, Zhao Z, Zheng P, Chen Z, Duan A, Xu C, Jiao J, Zhang H, Cao Z, Ge B (2016) Synthesis of NiMo catalysts supported on mesoporous Al_2O_3 with different crystal forms and superior catalytic performance for the hydrodesulfurization of dibenzothiophene and 4,6-dimethyldibenzothiophene. J Catal 344:680–691

Yu Z, Fareid LE, Moljord K, Blekkan EA, Walmsley JC, Chen D (2008) Hydrodesulfurization of thiophene on carbon nanofiber supported Co/Ni/Mo catalysts. Appl Catal B Environ 84:482–489

Yuezeng S, Zhang Y, Zhuang X, Li S, Wu D, Zhang F, Feng X (2013) Low-temperature synthesis of nitrogen/sulfur co-doped three-dimensional graphene frameworks as efficient metal-free electrocatalyst for oxygen reduction reaction. Carbon 62:296–301

Zhu Y, Murali S, Cai W, Li X, Suk JW, Potts JR, Ruoff RS (2010) Graphene and Graphene Oxide: Synthesis, Properties, and Applications. Adv. Mater. 22:3906–3924

Chapter 8
Mechanisms of Desulfurization by Nanomaterials

Waqas Ahmad and Imtiaz Ahmad

Abstract A variety of materials are used as catalyst and adsorbent during the desulfurization of petroleum products, and nanomaterials also find its application in this field. In different desulfurization process, the behavior of nanomaterials towards desulfurization is different. In the case of hydrodesulfurization process, the catalyst used are CoMo or NiMo sulfides supported on various supports. The catalysts bear anion vacancy or coordinatively unsaturated sites, where the sulfur compounds adsorb and react with hydrogen, to set free sulfur as H_2S. The structure of the catalyst deeply influences its HDS activity; rim and edge model proposed suggests that the rim and edge sites of the catalysts sheets stacked together are more active for HDS of larger molecules. The activity of the catalysts enhances with reducing its crystalline structure. The catalysts used in oxidative desulfurization (ODS) include supported and unsupported metal oxides, polyoxmetalates, and transition metals as cations. During ODS reactions, the catalysts either act as an oxygen carrier, by converting into peroxo species or then enhance the dissociation of the oxidant to boost up the selective oxidation of the sulfur compounds. In adsorptive desulfurization, the adsorbent materials selectively retain the sulfur compounds by π-complexation or physical adsorption. In some cases, the adsorbents assist in cracking of sulfur compounds during the adsorption process.

Keywords Nanocatalysts • Desulfurization mechanism • Hydrodesulfurization • Sulfides catalysts • Oxidative desulfurization • Polyoxometalates • Adsorptive desulfurization • Reactive adsorption

1 Introduction

Nanomaterials have brought a revolution with a variety of technological applications including electronics, medicines, molecular biology, polymers, fabrics, glass, food products, automotive, sensors, coating, and catalysis. The same has found its place in oil and gas industries. In the petroleum industry, desulfurization of the

---
W. Ahmad (✉) • I. Ahmad
Institute of Chemical Sciences, University of Peshawar, 25120, Peshawar, KPK, Pakistan
e-mail: waqasaswati@yahoo.com

petroleum products is a challenging job. The obnoxious effects of sulfur in petroleum in the form of corrosion problems, catalysts deactivation, and environmental pollution necessitates eliminating sulfur to the minimum level (Ahmad 2015). At the present, catalytic hydrodesulfurization (HDS) is the sole industrial technology to cater the desulfurization of petroleum; however, research is underway to find more effective and convenient techniques. Among the developing desulfurization techniques, adsorptive desulfurization, oxidative desulfurization (ODS), and bio-desulfurization (BDS) are worth mentioning (Campos-Martin et al. 2010; Song and Ma 2003).

Owing to their high catalytic and adsorption activities, nanomaterials are extensively used for desulfurization of petroleum products. In some techniques like HDS and catalytic ODS, nanomaterials are used as catalysts whereas in adsorptive desulfurization these are used as adsorbent materials. So far a variety of nano-sized materials has been used as catalysts in industrial processes or in research experiments for desulfurization of petroleum distillate fractions. This chapter gives an insight of various desulfurization techniques and the action mechanism for various nanomaterials catalyst or adsorbent used in each technique. The aims of this chapter include the following:

1. To elaborate the basic principles of hydrodesulfurization (HDS), oxidative desulfurization (ODS), and adsorptive desulfurization (ADS)
2. To highlight the various types of nanomaterials catalyst used in each of the above desulfurization techniques
3. To explain the mechanism of action for nanomaterials during each desulfurization process

2   Hydrodesulfurization Catalysts

Hydrodesulfurization (HDS) is currently the only industrial process used for removal of sulfur from petroleum distillate fractions with the prime objectives to reduce the sulfurous emission in products and avoid the poisoning of noble metal catalysts by sulfur during the downstream processing of the products. In HDS process, the feed is treated with gaseous hydrogen under high pressure at an elevated temperature in the presence of catalysts in fixed bed or fluidized bed reactor. The sulfur is removed in the form of gaseous H_2S in the flue gasses, and the H_2S is used to produce elemental sulfur by clause process. The typical operating conditions of the HDS process are: hydrogen pressure 30–3000 psi, temperature 300–500 °C, hydrogen flow/recycle rate 250–10,000 SCF/bbl, and feed space velocity of 0.5–5 V/V/hr. The process conditions may be varied based on the sulfur content of the feed, the nature of the feed, and the degree of desulfurization required (Javadli and Klerk 2012). The catalysts used are metal sulfides, commonly CoMo and NiMo sulfides supported on γ-alumina, alumina-silica, or zeolite supports (Furimsky 1996; Knudsen et al. 1999; Ma et al. 1994; Shafi and Hutchings 2000; Vasudevan and Fierro 1996). Commonly used supports for the active phase

catalysts are silica-alumina molecular sieves and mesoporous silica molecular sieves such as MCM-41, zeolites, metal oxides, titania (TiO_2), carbon and composites of these materials, etc. (Olguin et al. 1997; Segawa et al. 2000; Song and Ma 2003). The main characteristics of the support materials are dispersion ability of active phase and possession of Lewis and Bronsted acidic sites which play an important role towards increasing the catalyst efficiency.

Generally, the active catalysts components are Co-Mo-S, Ni-Mo-S, and Mo-Ni-W-S, and various metals such as W, Ni, Fe, and Co are added to the catalyst as promoters. The promoters influence the binding energy of the metal-sulfur bond, and the strength of this bond is an important factor in enhancing the efficiency of the catalyst. The addition of some noble metals like Pd, Ru, and Pt to the active catalytic species has been found to markedly increase the catalyst efficiency; however, these are very susceptible to poisoning by sulfur (Song and Ma 2003). New commercial developments in the HDS catalysts brought some modification in the catalyst with improved efficiency such as CoMo and NiMo based STARS (Super Type II Reactive Sites) and NEBULA (New bulk activity) by Akzo Nobel catalyst preparation technology (Brevoord et al. 2000; Conference Exhibition 2000; Mayo et al. 2001; Song and Ma 2003), and Criterion NiMo and CoMo CENTINEL catalysts, by criterion catalyst and technologies (WS 2001).

Nanostructured noble and non-noble metal phosphide, nitrides, and carbides have been developed as novel high activity HDS catalysts. Reduction of metal chlorides or oxides in a hydrogen atmosphere under controlled temperature is a common route for the synthesis of nano-metallic phosphides. These catalysts show enhanced catalytic activity than the conventional Mo, Ni, W, Co sulfides, specifically NiP shows the highest activity than other metal phosphides due to its high intrinsic activity and a high degree of dispersion. Phosphide also shows resistance to inhibition in hydrodenitrogenation. Some noble metal phosphides, e.g., Rh, Pd, Ru, and Pt phosphides, have shown enhanced HDS activity and stability than non-noble metal phosphides. Metal nitrides are produced by reducing the metal precursors in NH_3 or the N_2 environment. Similarly, metallic carbides are prepared by reducing metal precursors in acetylene followed by in nitrogen under controlled temperatures. Metallic nitrides and carbides catalysts offer the advantage of the high acidity of the support material. However, the major drawback of metal phosphides, carbides, and nitrites is their low degree of dispersion of the active sites per unit mass of the catalyst. Also initially these catalysts show high HDS activity but later the activity declines as the active sites are sulfurized during the HDS process (Liu et al. 2013).

Under the conditions of the HDS process, the main hydrodesulfurization reaction involves the addition of H_2 to the hydrocarbon molecules, during which the sulfur atom is converted to H_2S, which is removed in gaseous forms in the flue gasses. The removal of N and O atom from the hydrocarbon molecules also occurs in the same way, besides the saturation of olefins also occurs similarly. The hydrodesulfurization of nonaromatic sulfur compounds, i.e., sulfides and thiols, occurs through cleavage of C–S bond and subsequent formation of S–H and C–H bonds.

However, in the case of thiophenic compounds, the reaction is complex and is shown to proceed through two pathways, hydrogenation and hydrogenolysis. Hydrogenation involves the successive addition of the H atoms to all the atoms of the molecules including sulfur atom, which leads to subsequent cleavage of the ring and removal of sulfur as H_2S from the ring. Whereas, hydrogenolysis proceeds by selective addition of hydrogen to the sulfur and carbon atoms at C–S bond resulting in subsequent cleavage of the C–S bond and removal of sulfur as H_2S (Scheme 8.1). Generally, both pathways occur simultaneously but depend on the catalysts selectivity which can prefer any of these two, generally, $NiMO/Al_2O_3$ favor the hydrogenolysis whereas $CoMo/Al_2O_3$ favor hydrogenation pathway (Knudsen et al. 1999; Ma et al. 1994; Vasudevan and Fierro 1996).

The alkylated benzo and dibenzothiophenes are resonance stabilized due to electron donating effects of the alkyl groups, besides because of the steric hindrance created by alkyl groups, these compounds are resistant to HDS reactions under normal operating conditions. The alkylated benzo and dibenzothiophenes are therefore termed as refractory sulfur compounds. The HDS reactivity of various sulfur
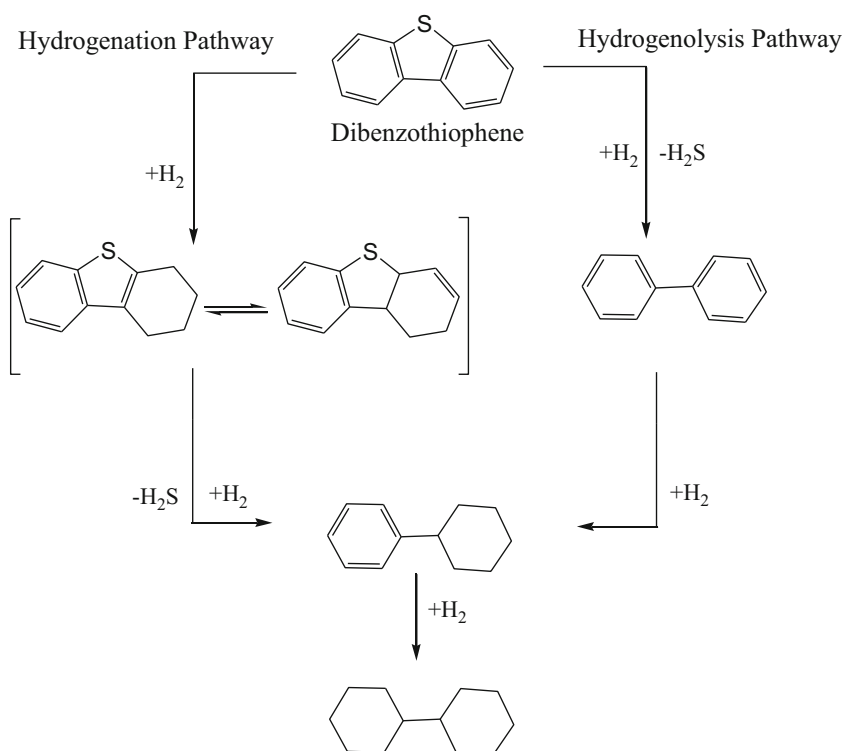
Scheme 8.1 Hydrogenation and hydrogenolysis pathways for hydrodesulfurization of dibenzothiophene

compounds is shown to be increasing in the following order (Gates and Topsøe 1997; Shafi and Hutchings 2000).

$$4,6 - R_2 - DBT < 4 - R - DBT < R - DBT < DBT < R - BT < BT$$
$$< R - Th < Th$$
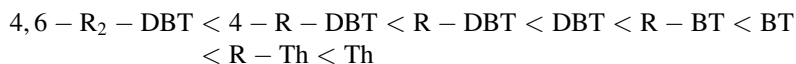
$$(Th = thiophene, R = Alkyl\ group)$$

The mechanism of the hydrodesulfurization reactions in the presence of sulfided catalyst has been studied by a number of researchers (Babich and Moulijn 2003; Kubota et al. 2014; Song and Ma 2003). Earlier workers proposed that the acidic sites on the catalysts do not take part in the HDS reaction, rather the CoMo and NiMO provide the active sites for the reaction. Lipsch et al. studied the mechanism of the hydrodesulfurization over CoMo catalyst and suggested that MoO_3 is mainly responsible for desulfurization reaction (Lipsch and Schuit 1969). During prior activation of the catalyst by reduction and sulfidation with H_2 and H_2S, anion vacancies are formed through reductive removal of bonded oxygen atoms in MoO_3. The anion vacancy also called coordinatively unsaturated sites, where the molybdenum centers are stabilized at the edges of MoS_2 crystallites. The sulfur compounds, i.e., thiophene, adsorbs at the anion vacancy site, at the transfer of hydrogen leads to cleavage of one C-S bond resulting in ring opening (Owens and Amberg 1961). The transfer of hydrogen atom further leads to the breaking of the C–S bond, removing S as H_2S and the resulting butadiene desorbs (Owens and Amberg 1961). Further saturation of C=C bond or butadiene may occur at the same site or another site (Scheme 8.2).

There are a large number of research studies which reveals that activity of the HDS catalyst is greatly dependent on the structure of the catalyst. It has been shown that in crystallites of MoS_2 catalyst, the most active sites are located on the edge planes and the basal planes are relatively inert. According to Rim and Edge model,
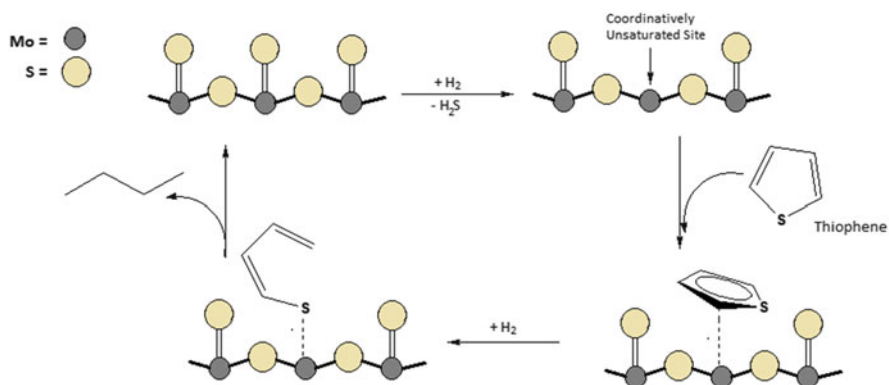
Scheme 8.2 Mechanism of HDS of thiophene over MoS_2
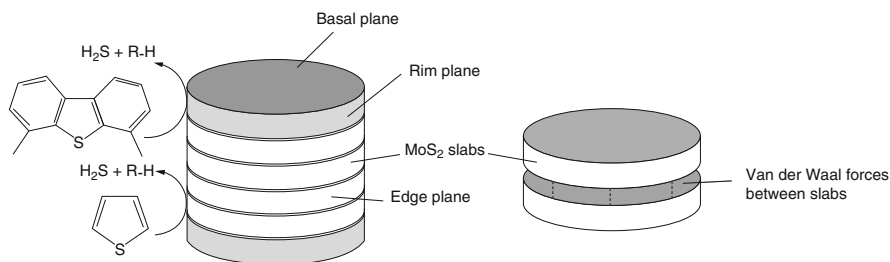
Scheme 8.3 Rim–Edge model of MoS$_2$ and HDS of sulfur compounds

proposed by Daage and Chianelli, unsupported MoS$_2$ crystallites have layered structure in which sheets of MoS$_2$ are stacked one above other and held together by weak Van der Waal forces. The hydrogenation of large molecules which show steric hindrance occurs on the top and bottom layers of MoS$_2$ slabs, called rim sites. Whereas the hydrogenation and hydrogenolysis of the sulfur compounds are catalyzed on all edge planes, the basal planes are considered catalytically inactive. In the case of single or bilayers, the selectivity is dominated by the presence of coordinative instauration. For smaller sulfur compounds, where the no steric interference is involved, there is no rim and edge effects, and the molecule is catalyzed at all active sites on the surface (Daage and Chianelli 1994) (Scheme 8.3).

Jhonsen et al. reported that when the MoS$_2$ sheets are dispersed by exfoliation, they offer high catalytic activity (Joensen et al. 1986). In the case of exfoliated MoS$_2$, the fraction of edge sites is greater, where the hydrogenolysis of C–S bond occurs (Thian 2008).

Tuxen et al. investigated the influence of size on the activity of MoS$_2$ nanoclusters and role of edge and corner sites for adsorption of model sulfur compounds, i.e., dibenzothiophene and 4,6-dimethyldibenzothiophene, during hydrodesulfurization reactions. The adsorption phenomenon was studied by high-resolution STM, using different sizes of MoS$_2$ nanocluster, which revealed that the size of the nanoclusters is the main factor that influences the adsorption behavior and selectivity and the threshold value for the size of nanocluster was 6 Mo atoms on the cluster edge. In the case of large nanoclusters, with Mo atoms above the threshold value, the S vacancy is formed on the cluster edges but due to sterical hindrance DBT cannot bind at these sites. Whereas in the case of nanocluster smaller than the threshold value, the S vacancies are formed at corner site where strong adsorption of DBT can occur without any hindrance. The high desulfurization activity is thus related to the size of the catalysts (Tuxen et al. 2010).

3 Oxidative Desulfurization (ODS)

Oxidative desulfurization (ODS) involves the selective oxidation of organic sulfur compounds in petroleum, and consequently the removal of the oxidized compounds from the feed by solvent extraction or adsorption over solid adsorbent (Campos-

Martin et al. 2010; Javadli and Klerk 2012). During oxidation step, the organosulfur compounds are converted into more polar oxidized form, i.e., sulfones; owing to their high polarity, sulfones can be easily separated from nonpolar oil phase through extraction with polar solvents or adsorption over solid adsorbents. For ODS process no specific high-temperature high-pressure reactor is required and it can be operated under mild conditions, i.e., low temperature and ambient pressure with high efficiency, also the process does not require expensive hydrogen, therefore the process is more economic than hydrodesulfurization.

The important factor in the ODS is the selective oxidation of the sulfur compounds in the nonpolar hydrocarbon phase, therefore very selective oxidants are required to attain high efficiency. The most commonly used oxidants in the ODS of liquid fuels include organic peracids, hydroperoxides, molecular oxygen, ozone, hydrogen peroxide, etc. (Campos-Martin et al. 2010; Gaofei et al. 2009). The removal of oxidized sulfur compounds from the oil phase is also a key step towards high efficiency of the ODS process, which can be effectuated by solvent extraction of the adsorption process. Most commonly the solvent extraction is used which is easy, less time consuming and does not require energy. The commonly used solvents for extraction of oxidized sulfur compounds in the ODS include dimethyl formamide, acetonitrile, dimethyl sulfoxide, toluene, methanol, ethanol, etc.; sometimes blends of different solvents are used to enhance the extraction efficiency. Whereas the adsorbents most commonly used for removal of oxidized sulfur compounds from the feed oil include silica, alumina, activated carbon, etc.

In ODS process, the reactivity of the sulfur compounds towards oxidation increases with increasing the electron density on the sulfur atom in the organosulfur compounds. Higher the electron density on the sulfur atom, more readily it can be oxidized through an electrophilic attack on the oxygen atom. Since the alkyl groups act as electron donating groups, therefore the presence of alkyl side chains in the aromatic sulfur compounds increases the electron density on sulfur compounds and in turn increases its reactivity towards oxidation. Among various aromatic sulfur compounds, the reactivity order is given as (Otsuki et al. 2000):

$$4, 6 - DMDBT > 4 - MDBT > DBT > BT > Th$$

In the case of HDS, the reactivity of sulfur compounds decreases with increasing alkyl side chains due to steric hindrance, and the reactivity order in sulfur compounds is the reverse of ODS. Therefore, the sulfur compounds which are highly resistant to be treated through HDS can be easily removed through ODS process.

A variety of catalysts are used in the ODS to improve the efficiency of the oxidant and thereby enhance the selective oxidation of sulfur compounds in the feed oil. The use of catalysts increases the extent of desulfurization by many folds, for the same oxidation system. The presence of catalyst also reduces the consumption of oxidant during ODS process. Mostly, the heterogeneous catalyst offers high activity than the homogenous catalyst since the separation and recycling of the homogeneous catalysts are difficult, therefore heterogeneous catalysts are

commonly used in ODS process. The catalysts used in ODS can be divided into three categories, bases on the structure and mechanism of oxidation. These are:

1. Supported and unsupported metal oxides
2. Nanostructured POM
3. Transition metal ions or salts

The mechanism of oxidation for these catalysts primarily depends upon the nature of the oxidants with which they are used. Some catalysts directly participate in the reaction through the active site and some provide their surface area for the reaction; however, in general, all these catalysts transport oxygen from the oxidant to the sulfur atom, no matter whatever the oxidant is used.

3.1 Supported and Unsupported Metal Oxides

A number of metals oxides either in supported form or unsupported form has been investigated for catalyzing the ODS reactions, which have shown promising results. The most commonly used metal oxides for ODS of model and real oil in the presence of different oxidant systems include the oxides of Mo, V, W, Cu, Ce, Ti, etc. in unsupported form or supported on various supports like alumina, silica, titania, etc. (Al-Shahrani et al. 2007; Caero et al. 2005; Chica et al. 2006a; García-Gutiérrez et al. 2006; González-García and Cedeño-Caero 2009; Ishihara et al. 2005; Maciuca et al. 2008; Wang et al. 2003). Studies have revealed that during the ODS process, these metal oxides form an intermediate peroxo species with the oxidant, which selectively oxidizes the organosulfur compound.

Gracia et al. investigated the ODS of model sulfur oil and diesel oil in the presence of polymolybdates supported on alumina, i.e., MoO_x/Al_2O_3, using H_2O_2 as an oxidant in acetonitrile solvent. It was proposed that during the ODS reaction the heptamolybdate and octamolybdate form a hydroperoxomolybdate species by nucleophilic attack of H_2O_2. The peroxy oxygen behaves as strong electrophiles and by nucleophilic attack of a sulfur atom, the hydroperoxymolybdate oxidizes the sulfur compounds to respective sulfoxides and then sulfone. During oxidation of sulfur compounds, the hydroperoxymolybdate species get reduced, which is then reoxidized by the oxidant (García-Gutiérrez et al. 2006). It has been shown that polyoxomolybdates in the presence of H_2O_2 in the ratio of $H_2O_2/Mo < 1$ leads to formation of $[Mo_7O_{22}(O_2)_2]^{6-}$ and $[Mo_8O_{24}(O_2)_2(H_2O)_2]^{4-}$ crystalline species, based on hepta and octamolybdate framework, in which the terminal oxygens (bridging oxo) are substituted by peroxogroups (Larking and Stomberg 1972; Trysberg and Stomberg 1981). The substitution of peroxo group in mono and di-peroxohepta molybdate at terminal Mo atom has been confirmed by ^{17}O-NMR (Pettersson et al. 2003). The formation of peroxomolybdate species is found to be dependent on temperature which helps in decomposition of H_2O_2, pH, polar solvent, and concentration of H_2O_2. Different types of molybdates supported on alumina were investigated for ODS of model oil, and it was shown that by

$$\left[Mo_nO_{2n+10}\right]^{(20-2n)-}$$
Hepta/octa molybdate

H_2O_2 H_2O_2

H_2O H_2O

$$\left[Mo_nO_{2n+8}(O_2)_2(H_2O)_{2n-14}\right]^{(20-2n)-}$$
Di-peroxo molubdate

H_2O

H_2O_2

$$\left[Mo_nO_{2n+9}(O_2)(H_2O)_{n-7}\right]^{(20-2n)-}$$
Mono-peroxo molybdate
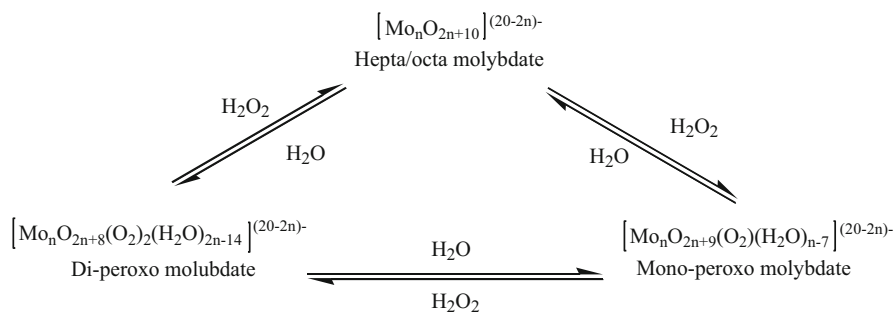
Scheme 8.4 The equilibrium between octa/hepta molybdate, mono-peroxo molybdate, and di-peroxomolybdate

nucleophilic attack of hydrogen peroxide on bridging oxo ligands of hepta and octamolybdates on alumina surface, a hydroperoxymolybdate group is formed. The hydroperoxomolybdate species on the reversible loss of water molecule leads to the formation of a monoperoxo species, in which by coordination to high valent Mo atom, the peroxo group is activated electrophilically. Similarly, by a subsequent nucleophilic attack of H_2O_2 and loss of water molecule, a diperoxo species may also be formed. The mono and diperoxo species remain in equilibrium with the hepta and octamolybdate precursor. Further, the oxidation of sulfur compounds involves the nucleophilic attack of sulfur atom on the peroxo group of mono or diperoxo species to form sulfoxide, whereas the monoperoxo species is regenerated to polymobdate and the diperoxo species is regenerated to monoperoxo species. In the similar manner, the sulfoxide is oxidized into sulfone in the second attack on the peroxospecies (García-Gutiérrez et al. 2008). Vegara-Mendez et al. verified this mechanistic hypothesis using DFT analysis in water and acetonitrile as solvents and concluded that the reactive peoxymolybdate intermediate could be formed during the ODS reaction in water and acetonitrile phases (Vergara-Méndez et al. 2011) (Scheme 8.4).

Molybdates are also used as ODS catalysts with oxidants other than H_2O_2, commonly with organic hydroperoxides, air, or molecular oxygen. A variety of hydroperoxides is used as efficient oxidants for ODS of the model and real oil samples including tertiary-butylhydroperoxide (TBPH), cumenehydroperoxide, cyclohexanoneperoxide, and tert-amylhydroperoxide (Chang et al. 2010; Chica et al. 2006b; Zhou et al. 2009a, 2006b). In ODS reactions based on hydroperoxide oxidation system, oxides of Mo supported on various supports has been widely used (Chica et al. 2006b; Ishihara et al. 2005; Venkateshwar Rao et al. 2007; Wang et al. 2003) (Scheme 8.5).

Wang et al. used molybdate MoO_3 supported on alumina and many other oxides supported on alumina including CrO_3, V_2O_5, Nb_2O_2, ZrO_3, NiMO, NiCoMo, etc. for ODS of model oil and kerosine oil in the presence of t-butylperoxide as oxide, in which MoO_3 was found to be the most effective catalyst. It was suggested that oxidation of sulfur compounds is carried out by a peroxo complex formed by MoO
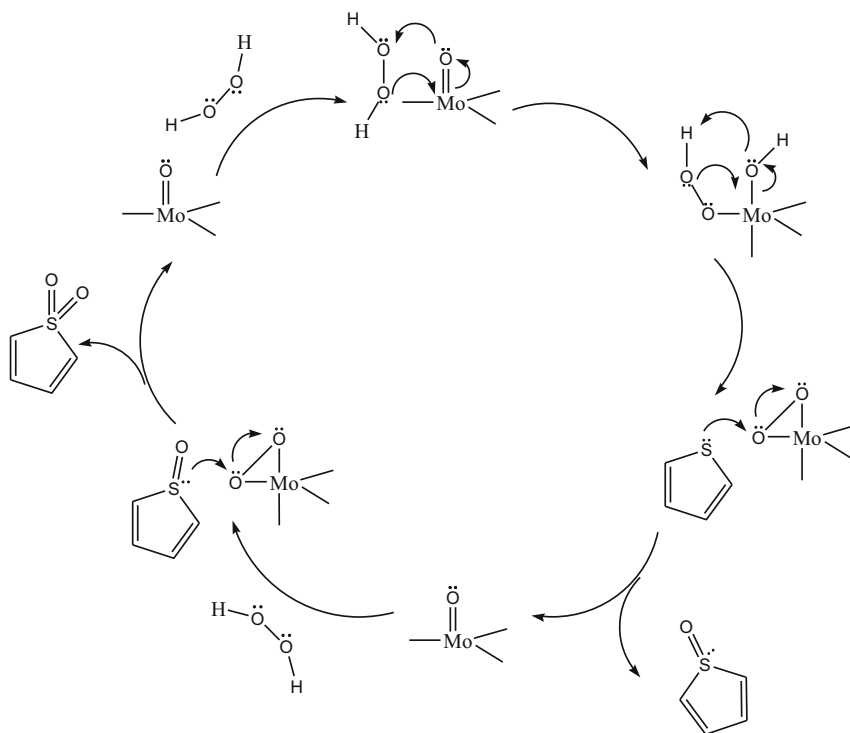
Scheme 8.5 Mechanism of oxidation of thiophene by molybdates

and t-butylperoxide (Wang et al. 2003). When MoO_3 is dispersed on alumina, due to the polarization of Mo–O bond the coordination of hydroperoxide with Mo–O bond is promoted. A five-membered peroxo complex is formed, in which the electrophilicity of the peroxo oxygen is enhanced, and leads to oxidation of sulfur compounds (Scheme 8.6).

Besides molybdates, other metal oxides such as tungstates and vanadates are also reported to follow the similar mechanism for ODS, involving formation of peroxocomplexes in the presence of H_2O_2 or hydroperoxides as oxidants (Al-Shahrani et al. 2007; González-García and Cedeño-Caero 2009, 2010; Yan et al. 2007; Yazu et al. 2004). The detailed mechanism of the ODS catalyzed by tungstates in the presence of H_2O_2 as oxidant is provided by Gracia et al. (García-Gutiérrez et al. 2014). In this study, ODS of diesel oil was investigated by several types of tungsten compounds such as Tungsten (VI) oxide, tungstic acid, ammonium tungstate, ammonium metatungstate, and phosphotungstic acid supported on various supports such as alumina, silica, titania, titania–alumina, and zirconia. It was shown that the mechanism of ODS by tungstates is similar to that followed by molybdates as discussed above. Here the reaction of H_2O_2 with polyoxotunstates in solution produces polynuclear peroxo complexes. The electrophilic attack of H_2O_2
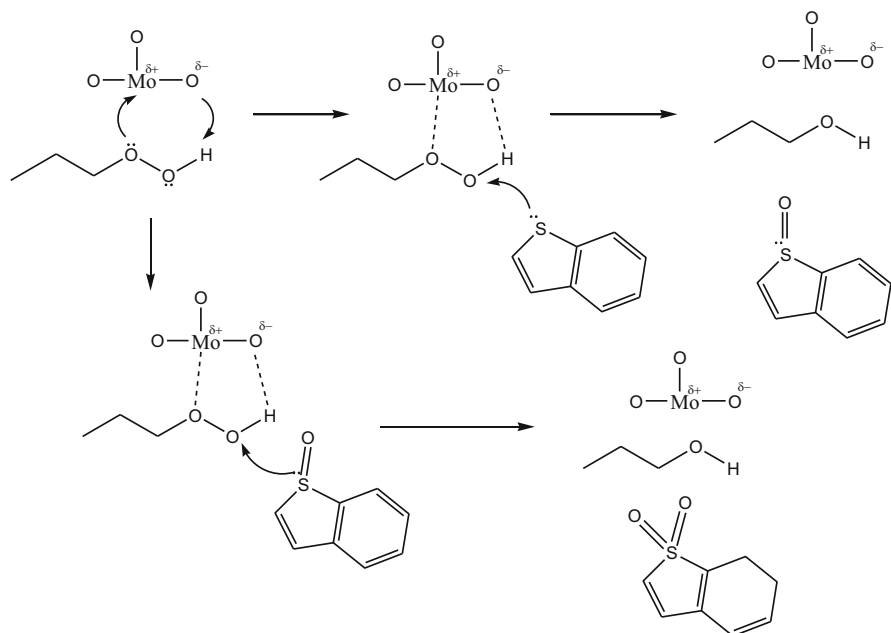
Scheme 8.6 Oxidation of sulfur compounds by MoO$_3$ and t-BuOOH

on the bridging oxo ligands of polyoxotungstate leads to formation of peroxopolyoxotugstates, like [H$_2$W$_{12}$O$_{33}$(O$_2$)$_7$]$^{6-}$ and [H$_2$W$_{12}$O$_{39}$(O$_2$)]$^{6-}$. One such peroxo complex anion [H$_2$W$_{12}$O$_{39}$(O$_2$)]$^{6-}$ has been isolated as its salt and characterized by FT-IR, ^{1}H-NMR, and polarographic studies to have Keggin type structure. The monoperoxoanion formed undergoes reversible loss of water molecule to form a hydroperoxytungstate intermediate. The sulfur compound is stepwise oxidized to respective sulfoxide and sulfone by nucleophilic attack of sulfur atom on the peroxo group of the intermediate, regenerating the tungstate anion.

Supported and unsupported metal oxides are also used for ODS of the model and commercial oil in the presence of air or molecular oxygen as oxidant. However, the ODS under air or molecular oxygen occurs at a relatively high temperature and high pressure than usually required in the presence of H$_2$O$_2$ and organic hydroperoxides. The ODS using air or O$_2$ as oxidants involves the formation of hydroperoxide which further carries out the oxidation of sulfur compounds, therefore a source of hydroperoxide is also required in the reaction medium. The alkyl aromatics present in the oil feed serve as a hydroperoxide source. In order to study the mechanism of formation of hydroperoxide during ODS with molecular oxygen or air, the model reaction has been studied in the presence of alkyl benzenes as a source of hydroperoxide. The generation of hydroperoxide occurs at elevated temperature (up to 140 °C) and follows free radical mechanism as shown in the reaction scheme (Sundararaman et al. 2010). Once the hydroperoxide is formed, it leads to oxidation of sulfur compounds in the way how the organic peroxides work (Scheme 8.7).
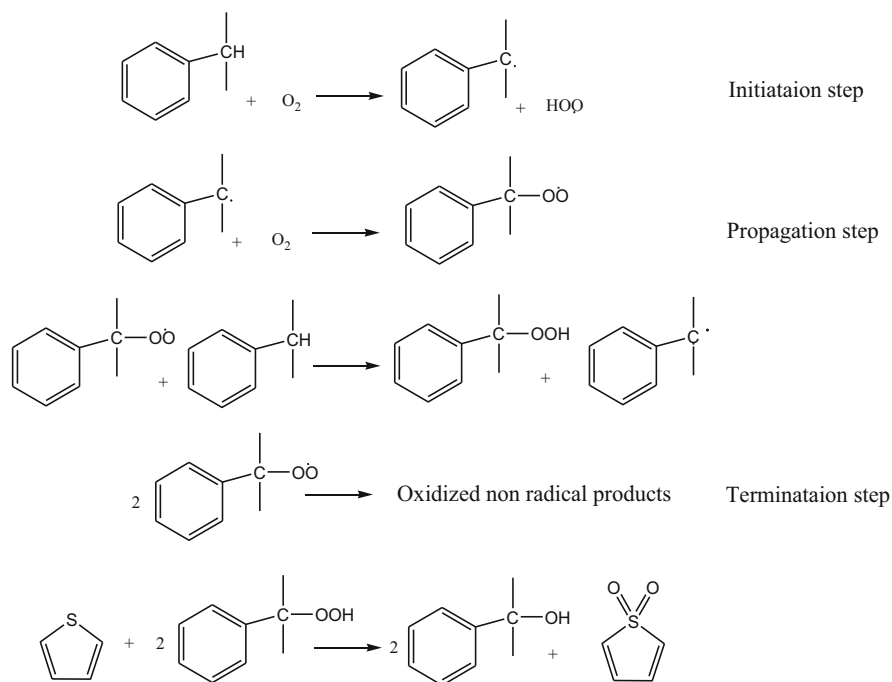
Scheme 8.7 Oxidation of thiophene by molecular oxygen

Sundraman et al. studied the ODS of jet fuel and diesel fuel using O_2 as oxidant in the presence CuO unsupported and supported on alumina at a temperature range of 100–140 °C, and concluded that the process involves the in situ formation of hydroperoxides utilizing the alkyl aromatic in the feed oil (Sundararaman et al. 2010). The extent of desulfurization in the diesel oil was higher than the jet fuel oil. Because of the higher aromatic content in diesel oil, a number of hydroperoxides produced was higher in diesel oil as determined by peroxide number, which in turn led to high desulfurization. The formation of hydroperoxides was found to depend upon the catalyst and the temperature. The ODS of Cold lake bitumen using air as oxidant at 150 °C resulted in 47% of sulfur removal (Javadli and de Klerk 2011). The ODS of diesel oil using air oxidation at a temperature range of 230–300 °C under pressure of 0.1 MPa in the presence of MnO_2 and Co_2O_3 supported on Al_2O_3 catalyst led to decrease in the sulfur content from 400 to 60 ppm (Sampanthar et al. 2006). It was shown that during the ODS process the aromatic content of the feed decreased from 46.4% to 12.5%, probably due to consumption in hydroperoxides formation. Whereas the olefin contents decreased from 2.4% to 3.6%, which was resulted by the free radical mechanism involved. Generally, the oxidation of sulfur compounds by so generated hydroperoxide leads to the formation of sulfoxide and sulfone, but under conditions of high temperature and high pressure of oxygen, overoxidation of sulfur compounds occurs which leads to cleavage of molecule and removal of the sulfur atom as SO_2. The release of the SO_2 during the ODS reaction
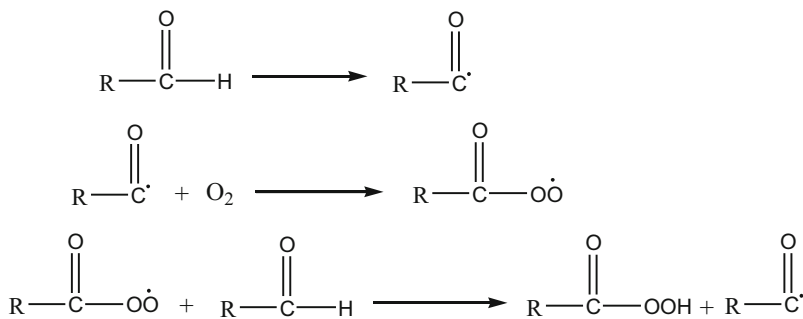
Scheme 8.8 Formation of peracids by aldehydes and molecular oxygen

was confirmed by purging the outlet gasses through the $AgNO_3$ solution which led to the formation of $AgSO_3$. The ODS of model oil by air under 0.1 MPa pressure and 400 °C temperature using CuO/Al_2O_3, ZnO/Al_2O_3, and Cu and Pt/CeO_2 also revealed that sulfur is removed as SO_2 (Lu et al. 2008). Fe(III) nitrates and bromides loaded on activated carbon also showed high efficiency in ODS of jet oil using air at 0.1 MPa pressure and 50 °C temperature (Ma et al. 2007), and the efficiency of catalyst was found to increase with increasing the Fe loading on the catalyst.

An initiator or sacrificial agent may be used to readily generate the hydroperoxides, at low temperature and pressure. The most commonly used initiator compounds for ODS process include various types of aldehydes, such as isobutyraldehyde, benzaldehyde, n-octanal and hexanal, etc. (Guo et al. 2011; Murata et al. 2003; Venkateshwar Rao et al. 2007; Zhou et al. 2009b). During this process the aldehydes are oxidized to peracids by O_2, and peracids further oxidize the sulfur compounds to respective sulfoxide and sulfones. The formation of peracids by the interaction of aldehydes and O_2 occurs stepwise, initially, an acyl radical is formed which further oxidizes to peroxy-acyl radical and finally to peracid as shown in the reaction scheme below (Saleh 2015) (Scheme 8.8).

The metal oxides catalysts used for catalyzing the ODS reaction using air or O_2 follow the same mechanism as reported for hydroperoxides. The peroxide or hydroperoxide formed by auto-oxidation of alkyl aromatics forms a metal oxide and hydroperoxide complex (Dooley et al. 2013). The metalloperoxy complex formed leads to oxidation of sulfur compounds in a similar way as discussed in the case of peroxides.

3.2 Polyoxometalates (POM) Catalysts

Polyoxometalates (POM) are the anionic cluster of metal oxides of group VI and V metals, i.e., Mo, W, V, and Ge, associated with various cation as their salt (Long et al. 2010). POM are termed as heteropolyoxometalates when some other

$$\text{POM} + \text{Oxidant-O} \longrightarrow \left[\text{POM-O}\right]$$

$$\text{Subtrate} + \text{POM-O} \longrightarrow \text{Products-O} + \text{POM}$$
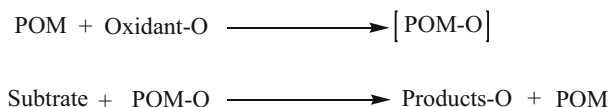
Scheme 8.9 Oxidation by polyoxometalates (POM)

heteroanions are also associated such as SO_4^{-2} or PO_4^{-2}. Structurally the POM consists of anionic clusters made of metal oxo species linked through bridging oxygen atoms together. Mostly the clusters contain three metals (group V and VI) in their high oxidation state in case of isopolyoxometalates, where no other hetero-atom is present, or in the case of heteropolyoxometalates, a heteroatom like P, Si, B, Al, Si, and Ge, may also be present. Based on the structure, POM is of different types which include Lindqvist type POM $[M_6O_{19}]^{n-}$, Anderson type $[XM_6O_{24}]^{n-}$, Keggin type $[XM_{12}O_{40}]^{n-}$, and Wells-Dawson type POM $[X_2M_{18}O_{62}]^n$. Here X represents heteroatom, M stands for metal, and n shows the overall charge on the cluster (Briand et al. 2003; Putaj 2012). POM have large molecular structure and possess versatile characteristics including high oxidation-reduction potential, proton acidity, thermal stability, and high reactivity of lattice oxygen, due to which they are used in a variety of fields including catalysis (Long et al. 2007).

POM are extensively used in the ODS reactions as catalysts for selective oxidation of organosulfur compounds, where they show superior activity as compared to other catalysts. The oxidation reactions involving POM as catalysts follow two types of mechanisms. The first type mechanism involves electron transfer oxidation, in which the substrate is oxidized and the POM is reduced, the reduced POM is then reoxidized by O_2. In this case, mostly no oxygenation occurs, or may occur but oxygen only works as an electron acceptor. The second type mechanism proceeds through formation of active metal proxo species, by the interaction of POM with a primary oxidant such as H_2O_2. The peroxo complex oxidizes the substrate by cleavage of a peroxo bond (Neumann et al. 1995) (Scheme 8.9).

The POM is reoxidized by the oxidant. Studies have shown that ODS reaction involving POM occurs through the second type of mechanism where the activated peroxo POM species is formed. In ODS reaction, a highly reactive transient species, the polyoxoperoxo complex is formed by transfer of oxygen from H_2O_2 to the POM molecule. The peroxo complex formed oxidizes the sulfur compounds successively to sulfoxides followed by sulfone, and itself gets reduced to POM species. The POM is again reoxidized by H_2O_2 to form another peroxo complex which is ready for further oxidation (Te et al. 2001). A generalized mechanism can be presented similar to that verified by Arichi et al. (Arichi et al. 2008) using isotopic investigation and GCMS techniques, in which the hydrogen peroxide acts as O-donor to POM, rather than directly oxidizing the substrate. During interaction of H_2O_2 and POM, H_2O_2 decomposes to form a MOO* peroxo species. The peroxo complex cleaves homolytically to generate a reactive electrophile species. The sulfur compound is oxidized by nucleophilic attack on the peroxo complex, and the POM is regenerated (Scheme 8.10).
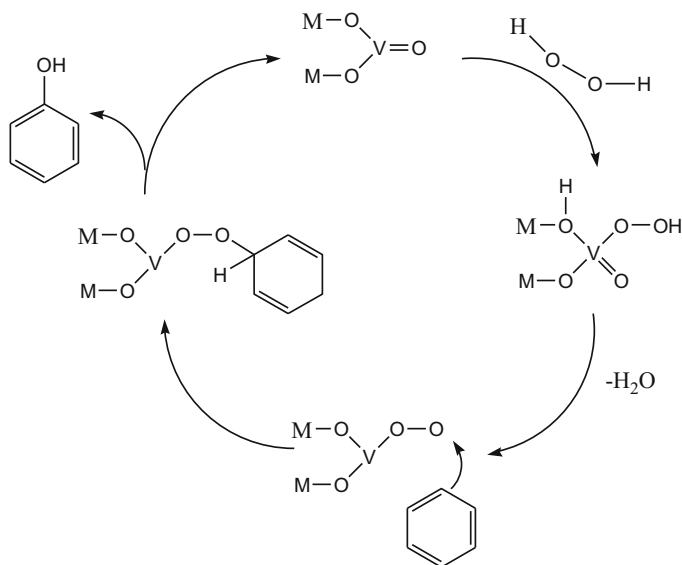
Scheme 8.10 Mechanism of oxidation by vanadium species

For ODS application, POM is mostly used in a supported and unsupported form with H_2O_2 as the oxidant, and in the presence of a nonpolar solvent such as acetonitrile and methanol (Gaofei et al. 2009). Since POM are soluble in the aqueous phase, therefore a biphasic medium is required which is formed by the addition of a polar solvent like acetonitrile and methanol to the nonpolar oil phase. In such a biphasic medium, the sulfur compounds are oxidized by the aqueous phase oxidant and POM. A variety of POM has been studied for ODS of the model and real oil samples in the biphasic medium. ODS of light oil was tested with tungstophosphoric acid (TPA) in the presence of H_2O_2 as an oxidant in acetonitrile-oil (4:1) biphasic medium, which led to decrease in the sulfur level from 300 to 112 ppm at 60 °C, (Yazu et al. 2001). The same oxidation system, i.e., TPA/H_2O_2, also showed high efficiency in tetradecane-ethanol (Yazu et al. 2003) and octane-acetic acid (Yazu et al. 2007) biphasic systems. Studies reveal that among different Keggin type POM catalysts containing Si and P as heteroatoms, containing tungstic and molybdic acid shows high desulfurization efficiency (Te et al. 2001), also among P-based POM containing different metals, i.e., Mo, W, and V, those containing W and Mo (i.e., $H_3PW_6Mo_6O_{40}$) are showed to be more efficient towards ODS of diesel oil in a biphasic medium, attaining up to 97 % sulfur removal (Wang et al. 2010).

Since the POM molecules have large molecular size, therefore due to the interaction of bulky POM structure and alkyl groups in the alkylated sulfur compound, steric hindrance is experienced which leads to decreased reactivity of alkylated sulfur compounds. Hence in the ODS reactions using POM catalysts, the alkylated sulfur compounds have lower reactivity than those with no alkyl groups. As such the order of reactivity among various sulfur compounds in
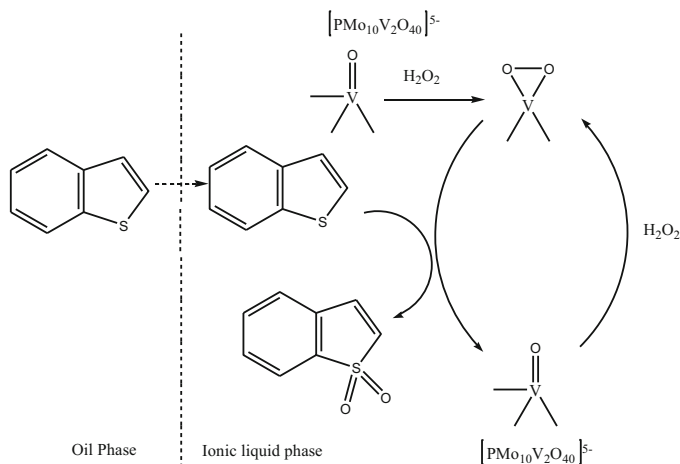
Scheme 8.11 Oxidation of sulfur compounds by vanadium-based POM in the presence of ionic liquids

POM/H_2O_2 oxidation system is same as reported for HDS reactions, i.e., 4,6-DMDBT < 4-MDBT < DBT.

In order to increase the ODS efficiency of the POM, its surface area can be increased by dispersion or support it on suitable materials. Studies have shown that reactivity of POM in terms of desulfurization efficiency drastically increases by supporting on various support materials such as different anion exchange resins (AER), silica, alumina, and mesoporous silicates (Xue-Min et al. 2007; Yang et al. 2007; Yazu et al. 2003; Zhang et al. 2005). It has been observed that in the case of real oil samples, the ODS efficiency of the POM catalysts is low, in which the aqueous phase oxidant cannot access completely to the sulfur compounds due to phase transfer limitations. Alternately in order to attain high desulfurization, excess amount of oxidant is required. In order to eliminate the phase transfer limitations and avoid the biphasic system, various techniques are used such as a combination of POM and ionic liquids, application of surfactants with POM catalysts, or using amphiphilic catalysts. The ODS of model oil was studied in the presence of heteropolyanion-based ionic liquid, i.e., ([Hmim]$_5$PMo$_{10}$V$_2$O$_{40}$), synthesized by the reaction of molybdovanadophosphoric acid (H$_5$PMo$_{10}$O$_{40}$) and N-methylimidazole, which showed 99% of sulfur removal under O/S ratio of 4:1. It was shown that during the desulfurization process, the sulfur compounds shift from oil phases to the ionic liquid phase where oxidation of sulfur compounds occurs, without any nonpolar solvent. Since H_2O_2 is miscible with the ionic liquid, it reacts with (PMo$_{10}$O$_{40}$) to form peroxospecies, and the peroxo complex oxidizes the sulfur compounds to respective sulfones. Many another type of ionic liquids and heteroplyacids have been studied for ODS (Zhang et al. 2013; Zhu et al. 2011) (Scheme 8.11).

Likewise, various types of surfactants such as tertaoctyl-ammonium bromide and hexadecyltrimethyl-ammonium bromide (CTAB) are also used during the ODS by
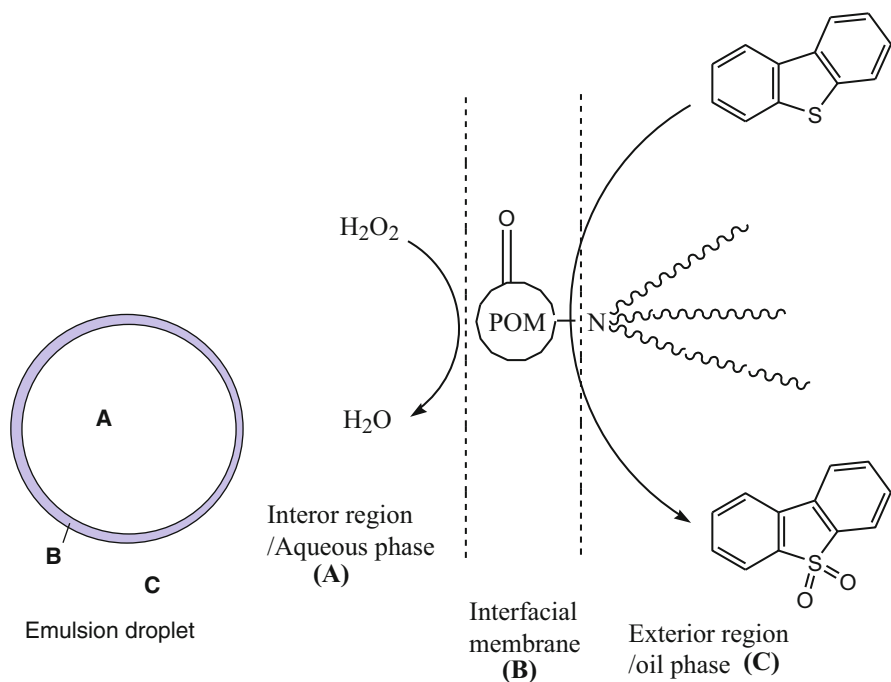
Scheme 8.12 Oxidation of DBT in emulsion droplet system

POM/H_2O_2 system, which has shown high ODS results under a limited amount of H_2O_2 and short reaction duration (Collins et al. 1997). However, the most notable approach is the application of quaternary ammonium salts of POM called amphiphilic or emulsion catalysts, which consists of hetero polyoxometalate anion combined together with a quaternary ammonium surfactant cation. Amphiphilic or emulsion has shown promising desulfurization efficiency in the presence of H_2O_2, and these catalysts eliminate the phase transfer limitations by the formation of an emulsion or tiny droplet during the ODS reaction which provides the intimate contact of the catalysts, oxidant, and sulfur compounds in the nonpolar oil phase. The emulsion or amphiphilic catalysts comprise two parts, i.e., the hydrophilic part which is the POM cluster and the lipophilic part which is the surfactant molecule consisting of the long alkyl group. In the emulsion system formed of tiny droplets, the lipophilic part of the catalysts is dispersed in the oil phase exterior to the droplet, and the hydrophilic POM part is captured at the interfacial membrane of the droplet, whereas the aqueous phase H_2O_2 is retained in the interior of the droplet. The POM is oxidized to peroxo complex by the interaction with H_2O_2, whereas the interaction of a sulfur compound and the peroxo complex occurs at the interface, where sulfur compounds are oxidized to respective sulfone. At the completion of the reaction, the emulsion breaks where the oxidized sulfur compounds and the amphiphilic catalysts are separated from the oil. The emulsion catalysts can be reused for a number of cycles, without losing its catalytic efficiency (Jiang et al. 2011) (Scheme 8.12).

Variety of an emulsion or amphiphilic catalysts has been investigated for ODS of various distillate fraction, which have shown remarkable efficiency. Phosphotungstate-based emulsion catalyst $[(C_{18}H_{37})_2N(CH_3)_2]_3[PW_{12}O_{40}]$ in the presence of H_2O_2 has been reported to decrease the level of sulfur in diesel oil to around 1 ppm from initial of 500 ppm sulfur (Li et al. 2004). Quaternary ammonium salt of sodium phosphotungstate $[C_{18}H_{37}N(CH_3)_3]_4[H_2NaPW_{10}O_{36}]$ has been shown to reduce the sulfur content of hydrotreated diesel from 500 to 1 ppm and that of straight run diesel from 6000 to 30 ppm, with O/S ratio of 3 under mild conditions (Lü et al. 2006). Similarly one study reports that among different Mo, W, and V containing emulsion catalyst, i.e., $[PV_2Mo_{10}O_{40}]^{4-}$, $[W_6O_{19}]^{2-}$, $[V(VW_{11})O_{40}]^{4-}$, and $[PVW_{11}O_{40}]^{4-}$, with same tetrabutylammonium cation, used for ODS of gas oil, the most efficient catalysts were found to be containing $[V(VW_{11})O_{40}]^{4-}$ anion, which attained about 90% of sulfur removal (Komintarachat and Trakarnpruk 2006). A number of studies have revealed that among different quaternary ammonium cations used for preparation of emulsion catalysts, the most suitable are di- or tri-methylhexadecyl ammonium cations, i.e., $C_{16}H_{33}NH^+$ $(CH_3)_2$ and $C_{16}H_{33}N^+(CH_3)_3$, which can generate the appropriate emulsion system required for high efficiency in ODS reactions (Gao et al. 2006; Imtiaz et al. 2013; Jiang et al. 2009; Li et al. 2004, 2005; Lu et al. 2007, 2010; Zhang et al. 2010).

Interesting fact about the emulsion catalysts is that reactivity order of the various sulfur compounds is same as for ODS process in the presence of per acids as oxidants, i.e.,

$$BT < 5 - MBT < DBT < 4,6 - DMDBT$$

This order shows that the stearic hindrance arising due to the interaction of POM catalysts and alkyl groups in alkylated sulfur compounds is eliminated due to the emulsion system (Collins et al. 1997; Te et al. 2001). This indicates that in the emulsion system better contact of sulfur compounds and the oxidants occurs.

3.3 Transition Metal Ions or Salts

A number of research reports describe the ODS of oil feed in the presence of transition metal ions as salts or supported form in the presence of different types of oxidants. Such catalysts are commonly used in the presence of H_2O_2 or per acids but also with other oxidants. These catalysts promote the decomposition of the oxidant species, which enhances the rate of oxidation of sulfur compounds. Dai et al. investigated the ODS of diesel oil using Fenton's reagent as a catalyst in the presence of H_2O_2/acetic acid oxidation system using ultrasonication (US) (Dai et al. 2008). The mechanism of the reaction was shown to involve a number of reactions in which the Fenton's reagent dissociates H_2O_2, to generate active hydroxyl radicals which are more reactive than H_2O_2 oxidant, and accelerate the oxidation of sulfur compounds. The metal ion can also consume the hydroxyl radicals, therefore when

the concentration of the metal ions is above the optimum value, the ODS efficiency declines. Results indicated that the optimum value for Fe^{2+}/H_2O_2 was 0.05 mol/mol. Furthermore, in the presence of US-Fenton's reagent, the efficiency of the ODS was found to be increased 2.17 times than in simple H_2O_2/acetic acid oxidation system (Scheme 8.13).

Riad et al. reported the ODS of light gas oil using H_2O_2 in the presence of Zn incorporated to hydroxyapatite catalysts prepared by ion exchange and wet impregnation methods (Riad and Mikhail 2012). It was shown that the catalysts prepared by ion exchange method show high efficiency than the other, by attaining 89% of sulfur removal. The author suggested that the Zn exchanged hydroxyapatite follows the mechanism similar to Fenton's reaction, where the hydrogen peroxide is decomposed by the Zn^{2+} ion to produce hydroxyl radical. The hydroxyl radical further oxidized the sulfur compounds to respective sulfoxide and then sulfone. Similarly, the ODS of model oil and various real oil samples including untreated naphtha, light gas oil, heavy gas oil, and Athabasca bitumen was studied in the air-assisted performic acid oxidation system in the presence of Fe^{2+} exchanged on the ZSM-5 zeolite. The level of desulfurization was increased in the presence of a catalyst, which was attributed to the dissociation of H_2O_2 and formation of hydroxyl radical by the catalysts via Fenton's mechanism.

Various other types of catalysts have also been found to enhance the desulfurization yield by similar mechanism of promoting the formation of hydroxyl radical, these include EDTA, Na, and Mg-silicates (Hao et al. 2005), silica gel (Chen et al. 2006), molecular sieves loaded with various metal oxides (Chen et al. 2007), transition metal salts (de Souza et al. 2009), and sodium bicarbonate (Deshpande et al. 2004). Activated carbon was found to increase the desulfurization level in case of fuel oil from 60% to 95% in the presence of H_2O_2/formic acid oxidation system (Yu et al. 2005). Zhu et al. reported that activated carbon possesses both reducing sites and oxidizing sites which perform the same action as Fe^{2+} and Fe^{3+} ions in Fenton's reagents during decomposition of H_2O_2. The reducing sites transfer electrons to H_2O_2 to form $HO^{\cdot}$ (hydroxyl) radical which oxidizes the sulfur compounds. However, the competitive reaction that occurs involves the reaction of

$$Fe^{2+} + H_2O_2 \longrightarrow Fe^{3+} + OH^- + OH^{\cdot}$$

$$Fe^{2+} + OH^{\cdot} \longrightarrow Fe^{3+} + OH^-$$

$$OH^{\cdot} + H_2O_2 \longrightarrow HOO^{\cdot} + H_2O$$

$$Fe^{3+} + HOO^{\cdot} \longrightarrow Fe^{2+} + O_2 + H^+$$
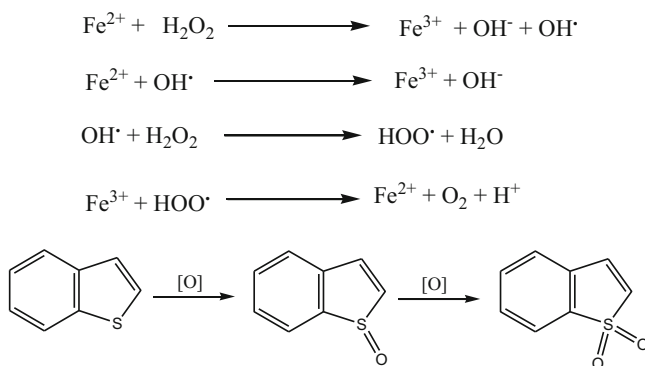
Scheme 8.13 Oxidation of sulfur compounds by Fenton's mechanism
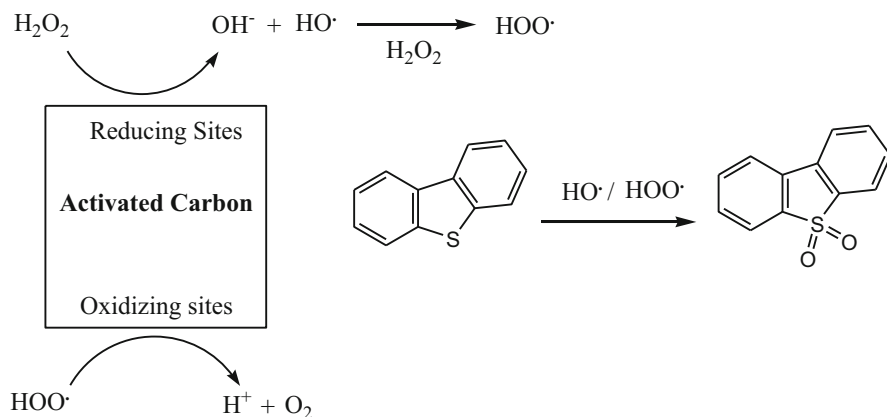
Scheme 8.14 Oxidation of DBT in the presence of HCOOH/H_2O_2 over activated carbon

hydroxyl radical with the H_2O_2 molecule to produce hydroperoxy radical (HOO·) and the oxidation of hydroperoxy radical to O_2 and H^+ by the oxidizing site on the activated carbon. The competitive reactions may be inhibited by adjusting the pH (Scheme 8.14).

Since reaction accelerates the ODS processes by promoting the formation of hydroxyl radicals, therefore less amount of oxidant is required while using these catalysts.

4   Adsorptive Desulfurization

In adsorptive desulfurization (ADS) various solid adsorbent materials are used to selectively remove sulfur compounds from petroleum. The adsorptive desulfurization is a very simple process which does not require much energy and can be operated in column or batch mode. During the contact of feed and the adsorbent, the sulfur compounds are selectively retained by the adsorbent, the desulfurized feed is separated, and the feed is recycled to attain more desulfurization till the sulfur breakthrough occurs. The efficiency of the process is primarily dependent on the process conditions and the characteristics of the adsorbent material, such as its adsorption capacity, mechanical stability, selectivity, and regeneration capability. A variety of adsorbent materials has been used for desulfurization of various petroleum distillate fractions such as gasoline, naphtha, diesel oil, jet fuel oil, and model oil which has shown promising efficiency. Commonly used adsorbent materials in this process include carbon-based adsorbents (Haji and Erkey 2003; Kim et al. 2006; Sano et al. 2004a, b), different types of zeolites (Hernández-Maldonado and Yang 2002; McKinley and Angelici 2003; Mikhail et al. 2002; Salem 1994; Salem and Hamid 1997; Velu et al. 2003), silica, alumina, metal

organic framework (MOF) (Brieva et al. 2010; Irvine et al. 1999), reduced metals (Bonville Jr et al. 2000; Fukunaga et al. 2003; Lesieur et al. 2002; Ma et al. 2005a, b), metal sulfides (Ma et al. 2003), metal oxides, and modified composite oxides (Turk and Gupta 2001; Watanabe et al. 2004; Zhou et al. 2006a) etc. Metal oxides and composite materials come in the category of the nanostructured materials, which show enhanced desulfurization efficiency.

Mechanistically, the adsorptive desulfurization can be divided into two categories, i.e., physical adsorption and reactive or chemical adsorption.

4.1 Physical Adsorption

Adsorptive desulfurization using carbon-based adsorbents and zeolites exhibits physical adsorption in which the sulfur compounds are retained from the feed by the adsorbent through physical interaction or Van der Waal forces. In such case, the sulfur compound binds up to the adsorbent in its original form or structure via physical forces such as hydrogen bonding or electrostatic attraction. Since such forces are weaker, the adsorbent material can be regenerated at the cost of low energy and the sulfur compounds can be recovered without any change in its structure. The adsorbent can be regenerated by physical processes such as heating, dissolution, or steam stripping.

Adsorptive desulfurization using activated carbon has been investigated by a number of researchers (Haji and Erkey 2003; Rakesh Kumar and Srivastava 2012), but the adsorption mechanism is not fully explored. Kostas et al. investigated the adsorptive desulfurization of model oil using nanoporous carbons of different nature (Triantafyllidis and Deliyanni 2014) and showed that the mechanism of adsorption is influenced by the surface properties and the texture of the activated carbon. The study revealed three possible factors responsible for the adsorption of sulfur compounds on the activated carbon. The volume of micropores of the activated carbon smaller than 10 Å is of the same dimension as the size of 4,6-DMDBT, which can be retained on the surface. The oxygenated functional groups on the surface of activated carbon interact the oxidized S compounds (sulfones) through hydrogen bonding. Besides the interaction between the delocalized π electrons of the aromatic sulfur compounds and that of aromatic rings of the activated carbon also provide a means of attachment. Kim et al. also ascribed the adsorption of sulfur compound (4,6-DMDBT) on activated carbon to the interaction through hydrogen bonding between the sulfur atoms and the surface oxygen functional groups (Kim et al. 2006). Sano et al. presented the same conclusion and reported that the adsorption of the sulfur compounds is enhanced when the oxygen functional groups on the surface of activated carbon are increased by chemical oxidation (Sano et al. 2004b). Scheme 8.15 describes the mechanism for physical adsorption of sulfur compounds over activated carbon.

Due to electron donating effect of the alkyl substituents in the aromatic sulfur compounds, the electron density is increased over the aromatic ring. It is, therefore,
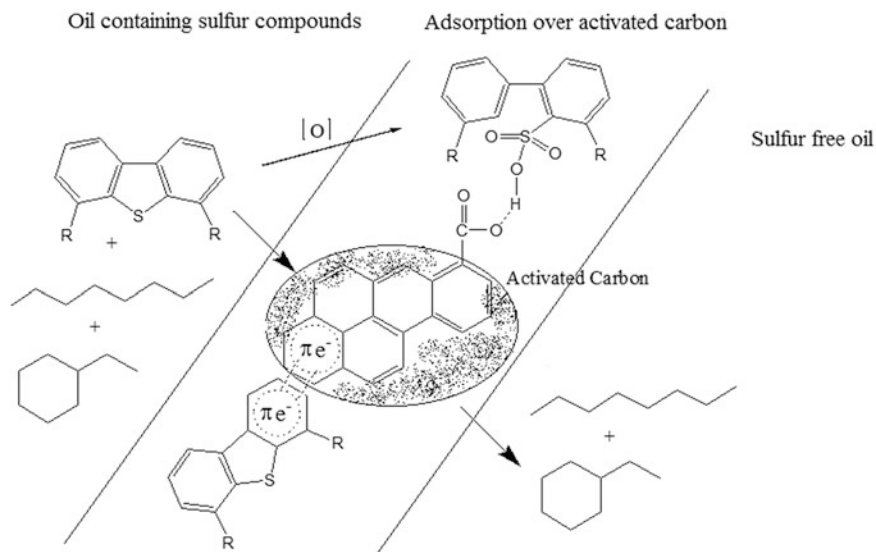
Scheme 8.15 Adsorption mechanism of sulfur compounds over activated carbon

the alkyl substitution in sulfur compounds exhibits synergistic effect during physical adsorption rather than declining desulfurization by posing stearic hindrance, which is the common observation in other desulfurization techniques (Kim et al. 2006). However, this phenomenon also contributes in the limited selectivity of physical adsorptive desulfurization, because the non-sulfur aromatic compounds also show the similar behavior.

4.2 Chemical or Reactive Adsorption

In this type of adsorption, chemical bonding is responsible for binding the sulfur compounds to adsorbent as a result of chemical reaction. In this process, the nature of the sulfur compounds is altered, mostly by decomposition, whereas the sulfur atom is bound to the adsorbent as sulfide. It has been shown that the selectivity of the desulfurization by reactive adsorption is very high but in this process, the regeneration of the adsorbent is very difficult (Hernández-Maldonado and Yang 2004a, c). Since the sulfur is bound to the adsorbent through chemical bonding, regeneration of adsorbent cannot be effectuated by physical processes. The adsorbent can be regenerated by reduction or strong heating in air (oxidation), where the sulfur may be removed as H_2S or sulfur oxides; however, the form of sulfur removed also depends upon the nature of adsorbent and sulfur compounds (Babich and Moulijn 2003).

Scheme 8.16 Adsorption of sulfur compounds by π-complexation
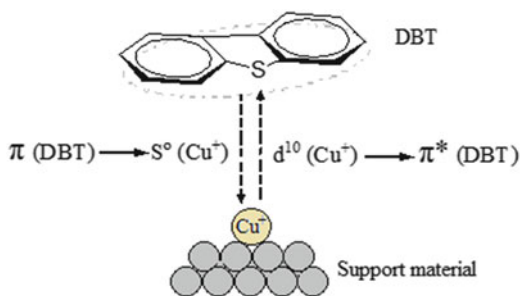
Based on the route of chemisorption, desulfurization by reactive adsorption can further be classified into two categories. The first category involves a direct reaction between sulfur atom and the adsorbent reactive site, whereas the second involves cracking of the sulfur compounds and the sulfur atom released further adsorbed on the adsorbent through a chemical reaction.

4.2.1 Adsorption Involving π-Complexation of Sulfur Compounds

The former type of reactive adsorption is exhibited by composite materials or metal supported zeolites, in which π-complexation is established between the metal atom in the adsorbent and organosulfur compounds, whereby the sulfur compound is removed from the oil stream. The interaction by π bonding is relatively stronger than the Van der Waal's attractive forces of physical adsorption, therefore the desulfurization efficiency is high in this case. A number of transition metals including Ag, Cu, Co, Zn, Ni, Ce, etc. supported on various supports like zeolite Y, MCM-41, and silica gel have been used for this purpose (Hernández-Maldonado et al. 2005; Hernández-Maldonado and Yang 2002; Ma et al. 2005b; McKinley and Angelici 2003; Tian et al. 2005; Velu et al. 2003). Clay-based adsorbents like bentonite modified with $KMnO_4$ or loaded with π-complexation species such as Fe^{+3}, Cu^{+1}, and Cu^{+2} are also used for desulfurization of model gasoline (Tang et al. 2011).

The π-complexation mechanism has been explained by adsorption of 4,6-DMDBT over Cu^+ loaded on Fujasite (Hernández-Maldonado and Yang 2004b). During complexation between Cu^+ with outer electronic configuration $3d^{10}4s^0$ and sulfur atom in aromatic ring, the thiophenic ring forms σ bond by donating π electrons to the empty s orbital of the Cu^+, in turn, the d orbital of cation back donate electrons to the π* orbital of the thiophenic ring (Hernández-Maldonado and Yang 2004c). It has been confirmed through experimental data and molecular orbital calculations that the π-complexation of Cu ions with sulfur-containing aromatic rings is stronger than with simple aromatics, i.e., containing no sulfur atom (Takahashi et al. 2002) (Scheme 8.16).

Cu and Ag exchanged faujasite zeolites, i.e., Ag-Y and Cu(I)-Y, have been found to efficiently remove thiophenes from the mixture of liquid hydrocarbons.

For feed containing 760 ppmw sulfur or 2000 ppm thiophene in n-octane, the order of breakthrough and adsorption capacities for different zeolites was reported to be as (Hernández-Maldonado and Yang 2003b):

$$\begin{aligned} Cu(I) - Y > Ag - Y > H - Y > Na - Y \& Cu(I) - Y > H - Y > Na - Y \\ > Ag - Y \end{aligned}$$
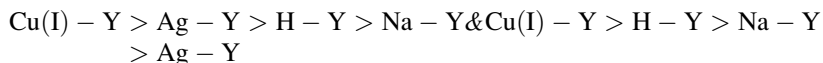
Application of Cu(I)-Y in combination with activated carbon as guard bed layer can perform as more efficient desulfurization system, capable of reducing the sulfur content of commercial gasoline and diesel to less than 0.28 ppmw (Hernández-Maldonado and Yang 2003a). Similar layered bed adsorbents consisted of Cu(I)-Y, activated carbon, and activated alumina (Selxorb) have been studied for desulfurization of diesel fuels at ambient pressure and temperature, which show desulfurization level up to 76 ppbw. The layered bed adsorbents containing alumina and Cu (I)-Y can be regenerated by calcination in air at 350 °C, followed by auto-reduction of the Cu species. The organosulfur compounds can also be recovered with solvent elution using CCl$_4$ and N,N-DMF solvents (Hernández-Maldonado et al. 2004). A hybrid material, as-synthesized mesoporous silica (SBA-15) containing Cu$_2$O was used to efficiently adsorb thiophene from model oil by π-complexation (Kou et al. 2015). Recently SiO$_2$-NiO aerogels with different Si/Ni ratios have also been found to be efficient adsorbents for removal of thiophenic sulfur from model oil. The maximum saturation adsorption capacities of 6.46 and 2.13 mgS/g were attained for thiophene and benzothiophene, respectively, using SiO$_2$-NiO aerogel with Si/Ni of 23 (Chen et al. 2016).

4.2.2 Adsorption Involving Cracking of Sulfur Compounds

A number of adsorptive desulfurization processes are based on this mechanism, where during the adsorption process, the sulfur compounds are cleaved by high temperature or by H$_2$ and the sulfur atom released during cracking chemically reacts with the adsorbent. This technique is actually a combination of hydrodesulfurization and adsorption. The adsorbent used in this process are commonly transition metal supported on basic oxides; however, most favorite adsorbent is NiO and ZnO, or nickel-based materials supported on silica, alumina, etc.

A commercial desulfurization process based on reactive adsorption called IRVAD process, developed by Black and Veatch Pritchard Engineering Company, uses selective adsorbents containing alumina for adsorption of sulfur from petroleum (Babich and Moulijn 2003; Song and Ma 2003; Yang et al. 2003). In this process, in a multistage reactor, the feed is allowed to contact countercurrently with the adsorbent in 4:1 ratio, at 240 °C and atmospheric pressure. In pilot plant experiments using cooker naphtha and FCC gasoline as feed, the process operated with 90% desulfurization efficiency (Babich and Moulijn 2003). The s-zorb process, developed by Phillips Petroleum Co. (USA), utilizes simultaneous
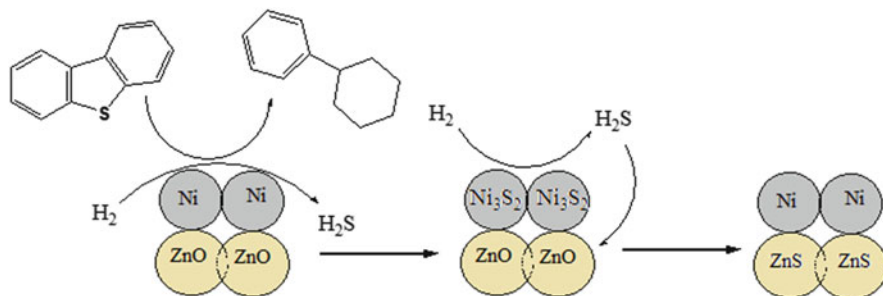
Scheme 8.17 Reactive adsorption of sulfur compounds over Ni supported on ZnO in the presence of H_2

hydrotreatment and adsorption. In this process, the feed, i.e., gasoline or diesel, is charged into fluidized bed reactor along with the adsorbent and gaseous hydrogen at 2–20 bars pressure and 340–410 °C temperature, under which the sulfur is bound to the adsorbent (Song and Ma 2003; Velu et al. 2003). The adsorbent composition is undisclosed; however, it is thought that it consists of ZnO and NiO loaded on silica or alumina (Gyanesh et al. 2000). The process is capable of attaining 98 % desulfurization, and in the case of using gasoline the sulfur content was decreased from 1100 ppmw sulfur to 25 ppm, with about 3 % reduction in olefin content of the feed.

The mechanism of desulfurization by reactive adsorption involving degradation of sulfur compounds has been investigated by Lichun et al. using Ni/ZnO as an adsorbent for model oil containing DBT (Huang et al. 2011). The reactive adsorption was tested in N_2 and H_2 atmosphere with 0.9 MPa pressure and temperature of 250 °C, which revealed that in the former case the adsorption rate was very slow and desulfurization efficiency was poor, whereas in the presence of H_2 the adsorbent shows high activity and capacity. The role of hydrogen was found to be decomposition of DBT over the surface of Ni, leading to the formation of Ni_3S_2, and later the sulfur is transferred to ZnO with the regeneration of Ni species. The proposed mechanism for the reactive-adsorptive desulfurization completes in three steps. The first step involves the cracking or decomposition of sulfur compounds, i.e., DBT, over the Ni surface and the sulfur released during decomposition reacts with Ni to form Ni_3S_2. In the second step, the hydrogenation of Ni_3S_2 leads to the formation of H_2S with regeneration of Ni species, whereas in the third step the H_2S is adsorbed by ZnO, to form ZnS (Scheme 8.17).

During the process, ZnO not only serves to adsorb the sulfur released from regeneration of Ni but also functions as a cocatalyst for cracking of sulfur compounds by Ni, the phenomenon has been reported by other researchers as well (Babich and Moulijn 2003; Bezverkhyy et al. 2009; Fan et al. 2010; Tawara et al. 2000, 2001). New advancement is going on the confirmation of the mechanism and improvement of the structural stability and reactivity of the Ni/ZnO adsorbent (Meng et al. 2012; Ullah et al. 2016; Wen et al. 2012). Rooh Ullah et al. used

Ni/ZnO dispersed on alumina to increase the stability of the catalyst, and they suggested the regeneration of the ZnS formed in the last step by oxidation under high temperature where ZnS is converted into ZnO (Ullah et al. 2016).

References

Ahmad W (2015) Sulfur in petroleum: petroleum desulfurization techniques. In: Saleh TA (ed) Applying nanotechnology to the desulfurization process in petroleum engineering. IGI Global. Retrieved from https://books.google.com.pk/books?id=oGa2CgAAQBAJ

Al-Shahrani F, Xiao T, Llewellyn SA, Barri S, Jiang Z, Shi H et al (2007) Desulfurization of diesel via the H_2O_2 oxidation of aromatic sulfides to sulfones using a tungstate catalyst. Appl Catal B Environ 73(3–4):311–316. doi:10.1016/j.apcatb.2006.12.016

Arichi J, Eternot M, Louis B (2008) Synthesis of V-containing Keggin polyoxometalates: versatile catalysts for the synthesis of fine chemicals? Catal Today 138(1–2):117–122. doi:10.1016/j.cattod.2008.04.036

Babich IV, Moulijn JA (2003) Science and technology of novel processes for deep desulfurization of oil refinery streams: a review. Fuel 82(6):607–631. doi:10.1016/S0016-2361(02)00324-1

Bezverkhyy I, Safonova O, Afanasiev P, Bellat J-P (2009) Reaction between thiophene and Ni nanoparticles supported on SiO_2 or ZnO: in situ synchrotron X-ray diffraction study. J Phys Chem C 113(39):17064–17069

Bonville Jr, L. J., DeGeorge, C. L., Foley, P. F., Garow, J., Lesieur, R. R., Preston Jr, J. L., & Szydlowski, D. F. (2000). Method for desulfurizing a fuel for use in a fuel cell power plant: Google patents.

Brevoord E, Gerritsen LA, Plantenga FL (2000) Paper presented at the the European refinery technology conference, 13–15 Nov 2000, Rome, Italy

Briand LE, Baronetti GT, Thomas HJ (2003) The state of the art on Wells–Dawson heteropoly-compounds: a review of their properties and applications. Appl Catal A Gen 256(1):37–50

Brieva GB, Campos-Martin JM, Al-Zahrani SM, Fierro JLG (2010) Removal of refractory organic sulphur compounds in fossil fuels using MOF sorbents. Glob NEST J 12:296–304

Caero LC, Hernández E, Pedraza F, Murrieta F (2005) Oxidative desulfurization of synthetic diesel using supported catalysts: part I. Study of the operation conditions with a vanadium oxide based catalyst. Catal Today 107–108(0):564–569. doi:10.1016/j.cattod.2005.07.017

Campos-Martin JM, Capel-Sanchez MC, Perez-Presas P, Fierro JLG (2010) Oxidative processes of desulfurization of liquid fuels. J Chem Technol Biotechnol 85(7):879–890. doi:10.1002/jctb.2371

Chang J, Wang A, Liu J, Li X, Hu Y (2010) Oxidation of dibenzothiophene with cumene hydroperoxide on MoO3/SiO2 modified with alkaline earth metals. Catal Today 149 (1–2):122–126. doi:10.1016/j.cattod.2009.04.026

Chen L, Guo S, Zhao D (2006) Oxidation of thiophenes over silica gel in hydrogen peroxide/formic acid system. Chin J Chem Eng 14(6):835–838

Chen LJ, Guo SH, Zhao DS (2007) Oxidative desulfurization of simulated gasoline over metal oxide-loaded molecular sieve. Chin J Chem Eng 15(4):520–523

Chen J, Zhang B, Miao G, Men J (2016) New SiO2–NiO aerogel sorbents for desulfurization by π-complexation: influence of molar ratio of Si/Ni. Ind Eng Chem Res 55(17):5036–5042. doi:10.1021/acs.iecr.6b00211

Chica A, Corma A, Dómine ME (2006a) Catalytic oxidative desulfurization (ODS) of diesel fuel on a continuous fixed-bed reactor. J Catal 242(2):299–308. doi:10.1016/j.jcat.2006.06.013

Chica A, Gatti G, Moden B, Marchese L, Iglesia E (2006b) Selective catalytic oxidation of organosulfur compounds with tert-butyl hydroperoxide. Chem Eur J 12(7):1960–1967. doi:10.1002/chem.200500858

Collins FM, Lucy AR, Sharp C (1997) Oxidative desulphurisation of oils via hydrogen peroxide and heteropolyanion catalysis. J Mol Catal A Chem 117(1–3):397–403. doi:10.1016/s1381-1169(96)00251-8

Conference EOR & Exhibition (2000) Conference proceedings, Berlin, Germany, 29th & 30th June, WEFA

Daage M, Chianelli R (1994) Structure-function relations in molybdenum sulfide catalysts: the "rim-edge" model. J Catal 149(2):414–427

Dai Y, Qi Y, Zhao D, Zhang H (2008) An oxidative desulfurization method using ultrasound/ Fenton's reagent for obtaining low and/or ultra-low sulfur diesel fuel. Fuel Process Technol 89 (10):927–932. doi:10.1016/j.fuproc.2008.03.009

de Souza WF, Guimarães IR, Guerreiro MC, Oliveira LCA (2009) Catalytic oxidation of sulfur and nitrogen compounds from diesel fuel. Appl Catal A Gen 360(2):205–209. doi:10.1016/j.apcata.2009.03.023

Deshpande A, Bassi A, Prakash A (2004) Ultrasound-assisted, base-catalyzed oxidation of 4,6-dimethyldibenzothiophene in a biphasic diesel−acetonitrile system. Energy Fuel 19 (1):28–34. doi:10.1021/ef0340965

Dooley KM, Liu D, Madrid AM, Knopf FC (2013) Oxidative desulfurization of diesel with oxygen: reaction pathways on supported metal and metal oxide catalysts. Appl Catal A Gen 468:143–149

Fan J, Wang G, Sun Y, Xu C, Zhou H, Zhou G, Gao J (2010) Research on reactive adsorption desulfurization over Ni/ZnO− SiO$_2$− Al$_2$O$_3$ adsorbent in a fixed-fluidized bed reactor. Ind Eng Chem Res 49(18):8450–8460

Fukunaga T, Katsuno H, Matsumoto H, Takahashi O, Akai Y (2003) Development of kerosene fuel processing system for PEFC. Catal Today 84(3):197–200

Furimsky E (1996) Spent refinery catalysts: environment, safety and utilization. Catal Today 30 (4):223–286. doi:10.1016/0920-5861(96)00094-6

Gao J, Wang S, Jiang Z, Lu H, Yang Y, Jing F, Li C (2006) Deep desulfurization from fuel oil via selective oxidation using an amphiphilic peroxotungsten catalyst assembled in emulsion droplets. J Mol Catal A Chem 258(1–2):261–266. doi:10.1016/j.molcata.2006.05.058

Gaofei Z, Fengli Y, Wang R (2009) Research advances in oxidative desulphurization technologies for the production of low sulfur fuel oils. Pet Coal 51(3):196–207

García-Gutiérrez JL, Fuentes GA, Hernández-Terán ME, Murrieta F, Navarrete J, Jiménez-Cruz F (2006) Ultra-deep oxidative desulfurization of diesel fuel with H$_2$O$_2$ catalyzed under mild conditions by polymolybdates supported on Al$_2$O$_3$. Appl Catal A Gen 305(1):15–20. doi:10.1016/j.apcata.2006.01.027

García-Gutiérrez JL, Fuentes GA, Hernández-Terán ME, García P, Murrieta-Guevara F, Jiménez-Cruz F (2008) Ultra-deep oxidative desulfurization of diesel fuel by the Mo/Al$_2$O$_3$-H$_2$O$_2$ system: the effect of system parameters on catalytic activity. Appl Catal A Gen 334 (1–2):366–373. doi:10.1016/j.apcata.2007.10.024

García-Gutiérrez JL, Laredo GC, García-Gutiérrez P, Jiménez-Cruz F (2014) Oxidative desulfurization of diesel using promising heterogeneous tungsten catalysts and hydrogen peroxide. Fuel 138:118–125

Gates BC, Topsøe H (1997) Reactivities in deep catalytic hydrodesulfurization: challenges, opportunities, and the importance of 4-methyldibenzothiophene and 4,6-dimethyldibenzothiophene. Polyhedron 16(18):3213–3217. doi:10.1016/S0277-5387(97)00074-0

González-García O, Cedeño-Caero L (2009) V-Mo based catalysts for oxidative desulfurization of diesel fuel. Catal Today 148(1–2):42–48. doi:10.1016/j.cattod.2009.03.010

González-García O, Cedeño-Caero L (2010) V-Mo based catalysts for ods of diesel fuel. Part II. Catalytic performance and stability after redox cycles. Catal Today 150(3):237–243

Guo W, Wang C, Lin P, Lu X (2011) Oxidative desulfurization of diesel with TBHP/isobutyl aldehyde/air oxidation system. Appl Energy 88(1):175–179. doi:10.1016/j.apenergy.2010.08.003

Gyanesh PK, Engelbert RD, Cass BW (2000) US Patents 6056871. U. Patents

Haji S, Erkey C (2003) Removal of dibenzothiophene from model diesel by adsorption on carbon aerogels for fuel cell applications. Ind Eng Chem Res 42(26):6933–6937

Hao L, Benxian S, Zhou X (2005) An Improved desulfurization process based on H2O2/formic acid oxidation system followed by liquid-liquid extraction. Part 1. Coker gas oil feedstocks. Pet Sci Technol 23(7-8):991–999. doi:10.1081/lft-200034498

Hernández-Maldonado AJ, Yang RT (2002) Desulfurization of liquid fuels by adsorption via π complexation with Cu(I)−Y and Ag−Y zeolites. Ind Eng Chem Res 42(1):123–129. doi:10.1021/ie020728j

Hernández-Maldonado AJ, Yang RT (2003a) Desulfurization of commercial liquid fuels by selective adsorption via π-complexation with Cu(I)−Y zeolite. Ind Eng Chem Res 42 (13):3103–3110. doi:10.1021/ie0301132

Hernández-Maldonado AJ, Yang RT (2003b) Desulfurization of liquid fuels by adsorption via π complexation with Cu(I)−Y and Ag−Y zeolites. Ind Eng Chem Res 42(1):123–129. doi:10.1021/ie020728j

Hernández-Maldonado AJ, Yang RT (2004a) Denitrogenation of transportation fuels by zeolites at ambient temperature and pressure. Angew Chem Int Ed 43(8):1004–1006. doi:10.1002/anie.200353162

Hernández-Maldonado AJ, Yang RT (2004b) Desulfurization of diesel fuels by adsorption via π-complexation with vapor-phase exchanged Cu(I)−Y zeolites. J Am Chem Soc 126 (4):992–993. doi:10.1021/ja039304m

Hernández-Maldonado AJ, Yang RT (2004c) New sorbents for desulfurization of diesel fuels via π-complexation. AIChE J 50(4):791–801. doi:10.1002/aic.10074

Hernández-Maldonado AJ, Stamatis SD, Yang RT, He AZ, Cannella W (2004) New sorbents for desulfurization of diesel fuels via π complexation: layered beds and regeneration. Ind Eng Chem Res 43(3):769–776. doi:10.1021/ie034108+

Hernández-Maldonado AJ, Yang FH, Qi G, Yang RT (2005) Desulfurization of transportation fuels by π-complexation sorbents: Cu(I)-, Ni(II)-, and Zn(II)-zeolites. Appl Catal B Environ 56 (1–2):111–126. doi:10.1016/j.apcatb.2004.06.023

Huang L, Wang G, Qin Z, Dong M, Du M, Ge H et al (2011) In situ XAS study on the mechanism of reactive adsorption desulfurization of oil product over Ni/ZnO. Appl Catal B Environ 106 (1–2):26–38. doi:10.1016/j.apcatb.2011.05.001

Imtiaz A, Waqas A, Muhammad I (2013) Desulfurization of liquid fuels using air-assisted performic acid oxidation and emulsion catalyst. Chin J Catal 34(10):1839–1847. doi:10.1016/S1872-2067(12)60668-8

Irvine RL, Benson BA, Varraveto DM (1999) IRVAD™ process—low cost breakthrough for low sulphur gasoline. Paper AM-99-42, paper presented at the NPRA 21–23 March 1999, Annual meeting, San Antonio, Texas

Ishihara A, Wang D, Dumeignil F, Amano H, Qian EW, Kabe T (2005) Oxidative desulfurization and denitrogenation of a light gas oil using an oxidation/adsorption continuous flow process. Appl Catal A Gen 279(1–2):279–287. doi:10.1016/j.apcata.2004.10.037

Javadli R, de Klerk A (2011) Desulfurization of heavy oil–oxidative desulfurization (ODS) as potential upgrading pathway for oil sands derived bitumen. Energy Fuel 26(1):594–602. doi:10.1021/ef201448d

Javadli R, Klerk A (2012) Desulfurization of heavy oil. Appl Petrochem Res 1(1-4):3–19. doi:10.1007/s13203-012-0006-6

Jiang X, Li H, Zhu W, He L, Shu H, Lu J (2009) Deep desulfurization of fuels catalyzed by surfactant-type decatungstates using H2O2 as oxidant. Fuel 88(3):431–436. doi:10.1016/j.fuel.2008.11.010

Jiang Z, Lü H, Zhang Y, Li C (2011) Oxidative desulfurization of fuel oils. Chin J Catal 32 (5):707–715. doi:10.1016/S1872-2067(10)60246-X

Joensen P, Frindt R, Morrison SR (1986) Single-layer MoS2. Mater Res Bull 21(4):457–461

Kim JH, Ma X, Zhou A, Song C (2006) Ultra-deep desulfurization and denitrogenation of diesel fuel by selective adsorption over three different adsorbents: a study on adsorptive selectivity and mechanism. Catal Today 111(1):74–83

Knudsen KG, Cooper BH, Topsoe H (1999) Catalyst and process technologies for ultra low sulfur diesel. Appl Catal A Gen 189(2):205–215. doi:10.1016/s0926-860x(99)00277-x

Komintarachat C, Trakarnpruk W (2006) Oxidative desulfurization using polyoxometalates. Ind Eng Chem Res 45(6):1853–1856. doi:10.1021/ie051199x

Kou J, Lu C, Sun W, Zhang L, Xu Z (2015) Facile fabrication of cuprous oxide-based adsorbents for deep desulfurization. ACS Sustain Chem Eng 3(12):3053–3061. doi:10.1021/acssuschemeng.5b01051

Kubota T, Miyamoto N, Yoshioka M, Okamoto Y (2014) Surface structure and sulfidation behavior of Co-Mo and Co-W sulfide catalysts for the hydrodesulfurization of dibenzothiophene. Appl Catal A Gen 480:10–16. doi:10.1016/j.apcata.2014.04.033

Larking I, Stomberg R (1972) Studies on peroxomolybdates. IX. The crystal structure of potassium diperoxoheptamolybdate (VI) octahydrate, K6Mo7O22 (O2) 2 8H2O. Acta Chem Scand 26:3708–3722

Lesieur, R. R., Teeling, C., Sangiovanni, J. J., Boedeker, L. R., Dardas, Z. A., Huang, H., et al (2002). Method for desulfurizing gasoline or diesel fuel for use in a fuel cell power plant: Google patents.

Li C, Jiang Z, Gao J, Yang Y, Wang S, Tian F et al (2004) Ultra-deep desulfurization of diesel: oxidation with a recoverable catalyst assembled in emulsion. Chem Eur J 10(9):2277–2280. doi:10.1002/chem.200305679

Li C, Gao J, Jiang Z, Wang S, Lu H, Yang Y, Jing F (2005) Selective oxidations on recoverable catalysts assembled in emulsions. Top Catal 35(1-2):169–175. doi:10.1007/s11244-005-3821-5

Lipsch J, Schuit G (1969) The CoO MoO3 Al2O3 catalyst: III. Catalytic properties. J Catal 15 (2):179–189

Liu Z, Zhang L, Jiang J, Bian C, Zhang Z, Gao Z (2013) Advancement of hydro-desulfurization catalyst and discussion of its application in coal tar. Adv Chem Eng Sci 3(1)

Long DL, Burkholder E, Cronin L (2007) Polyoxometalate clusters, nanostructures and materials: from self assembly to designer materials and devices. Chem Soc Rev 36(1):105–121

Long DL, Tsunashima R, Cronin L (2010) Polyoxometalates: building blocks for functional nanoscale systems. Angew Chem Int Ed 49(10):1736–1758

Lü H, Gao J, Jiang Z, Jing F, Yang Y, Wang G, Li C (2006) Ultra-deep desulfurization of diesel by selective oxidation with $[C_{18}H_{37}N(CH_3)_3]4[H_2NaPW_{10}O_{36}]$ catalyst assembled in emulsion droplets. J Catal 239(2):369–375. doi:10.1016/j.jcat.2006.01.025

Lu H, Gao J, Jiang Z, Yang Y, Song B, Li C (2007) Oxidative desulfurization of dibenzothiophene with molecular oxygen using emulsion catalysis. Chem Commun 0(2):150–152

Lu Y, Wang Y, Gao L, Chen J, Mao J, Xue Q et al (2008) Aerobic oxidative desulfurization: a promising approach for sulfur removal from fuels. ChemSus Chem 1(4):302–306. doi:10.1002/cssc.200700144

Lu H, Zhang Y, Jiang Z, Li C (2010) Aerobic oxidative desulfurization of benzothiophene, dibenzothiophene and 4,6-dimethyldibenzothiophene using an Anderson-type catalyst $[(C_{18}H_{37})_2N(CH_3)_2]5[IMo_6O_{24}]$. Green Chem 12(11):1954–1958

Ma X, Sakanishi K, Mochida I (1994) Hydrodesulfurization reactivities of various sulfur compounds in diesel fuel. Ind Eng Chem Res 33(2):218–222. doi:10.1021/ie00026a007

Ma X, Sun L, Song C (2003) Adsorptive desulfurization of diesel fuel over a metal sulfide-based adsorbent. Prepr Pap-Am Chem Soc Div Fuel Chem 48(2):522

Ma X, Sprague M, Song C (2005a) Deep desulfurization of gasoline by selective adsorption over nickel-based adsorbent for fuel cell applications. Ind Eng Chem Res 44(15):5768–5775

Ma X, Velu S, Kim JH, Song C (2005b) Deep desulfurization of gasoline by selective adsorption over solid adsorbents and impact of analytical methods on ppm-level sulfur quantification for

fuel cell applications. Appl Catal B Environ 56(1–2):137–147. doi:10.1016/j.apcatb.2004.08.013

Ma X, Zhou A, Song C (2007) A novel method for oxidative desulfurization of liquid hydrocarbon fuels based on catalytic oxidation using molecular oxygen coupled with selective adsorption. Catal Today 123(1–4):276–284. doi:10.1016/j.cattod.2007.02.036

Maciuca A-L, Ciocan C-E, Dumitriu E, Fajula F, Hulea V (2008) V-, Mo- and W-containing layered double hydroxides as effective catalysts for mild oxidation of thioethers and thiophenes with H_2O_2. Catal Today 138(1–2):33–37. doi:10.1016/j.cattod.2008.04.031

Mayo S, Plantenga F, Leliveld B, Miyauchi A (2001) Paper presented at the national petrochemical & refiners association (NPRA) annual meeting, AM-01-09, New Orleans, 18–20 March, 2001

McKinley SG, Angelici RJ (2003) Deep desulfurization by selective adsorption of dibenzothiophenes on Ag^+/SBA-15 and Ag^+/SiO_2. Chem Commun 20:2620–2621

Meng X, Huang H, Weng H, Shi L (2012) Ni/ZnO-based adsorbents supported on Al_2O_3, SiO_2, TiO_2, ZrO_2: a comparison for desulfurization of model gasoline by reactive adsorption. Bull Kor Chem Soc 33(10):3213–3217

Mikhail S, Zaki T, Khalil L (2002) Desulfurization by an economically adsorption technique. Appl Catal A Gen 227(1–2):265–278. doi:10.1016/S0926-860X(01)00937-1

Murata S, Murata K, Kidena K, Nomura M (2003) A novel oxidative desulfurization system for diesel fuels with molecular oxygen in the presence of cobalt catalysts and aldehydes. Energy Fuel 18(1):116–121. doi:10.1021/ef034001z

Neumann R, Khenkin AM, Dahan M (1995) Hydroxylation of alkanes with molecular oxygen catalyzed by a new ruthenium-substituted polyoxometalate, [WZnRu 2III (OH)(H2O) (ZnW9O34) 2]$^{11-}$. Angew Chem Int Ed Eng 34(15):1587–1589

Olguin E, Vrinat M, Cedeño L, Ramirez J, Borque M, López-Agudo A (1997) The use of TiO_2—Al_2O_3 binary oxides as supports for Mo-based catalysts in hydrodesulfurization of thiophene and dibenzothiophene. Appl Catal A Gen 165(1–2):1–13. doi:10.1016/S0926-860X(97)00184-1

Otsuki S, Nonaka T, Takashima N, Qian W, Ishihara A, Imai T, Kabe T (2000) Oxidative desulfurization of light gas oil and vacuum gas oil by oxidation and solvent extraction. Energy Fuel 14(6):1232–1239. doi:10.1021/ef000096i

Owens P, Amberg C (1961) Thiophene desulfurization by a microreactor technique. Adv Chem Ser 33:182

Pettersson L, Andersson I, Taube F, Toth I, Hashimoto M, Howarth O (2003) 17O NMR study of aqueous peroxoisopolymolybdate equilibria at lower peroxide/Mo ratios. Dalton Trans 1:146–152

Putaj P (2012) Applications of polyoxometalates in heterogenous catalysis. Université Claude Bernard-Lyon I, Villeurbanne

Rakesh Kumar D, Srivastava VC (2012) Studies on adsorptive desulfurization by activated carbon. Clean–Soil Air Water 40(5):545–550

Riad M, Mikhail S (2012) Oxidative desulfurization of light gas oil using zinc catalysts prepared via different techniques. Cat Sci Technol 2(7):1437–1446. doi:10.1039/C2CY20064C

Saleh TA (2015) Applying nanotechnology to the desulfurization process in petroleum engineering. IGI Global, Hershey

Salem ABSH (1994) Naphtha desulfurization by adsorption. Ind Eng Chem Res 33(2):336–340. doi:10.1021/ie00026a025

Salem ABSH, Hamid HS (1997) Removal of sulfur compounds from naphtha solutions using solid adsorbents. Chem Eng Technol 20(5):342–347. doi:10.1002/ceat.270200511

Sampanthar JT, Xiao H, Dou J, Nah TY, Rong X, Kwan WP (2006) A novel oxidative desulfurization process to remove refractory sulfur compounds from diesel fuel. Appl Catal B Environ 63(1–2):85–93. doi:10.1016/j.apcatb.2005.09.007

Sano Y, Choi K-H, Korai Y, Mochida I (2004a) Adsorptive removal of sulfur and nitrogen species from a straight run gas oil over activated carbons for its deep hydrodesulfurization. Appl Catal B Environ 49(4):219–225

Sano Y, Choi K-H, Korai Y, Mochida I (2004b) Selection and further activation of activated carbons for removal of nitrogen species in gas oil as a pretreatment for its deep hydrodesulfurization. Energy Fuel 18(3):644–651

Segawa K, Takahashi K, Satoh S (2000) Development of new catalysts for deep hydrodesulfurization of gas oil. Catal Today 63(2–4):123–131. doi:10.1016/S0920-5861(00)00452-1

Shafi R, Hutchings GJ (2000) Hydrodesulfurization of hindered dibenzothiophenes: an overview. Catal Today 59(3–4):423–442. doi:10.1016/S0920-5861(00)00308-4

Song C, Ma X (2003) New design approaches to ultra-clean diesel fuels by deep desulfurization and deep dearomatization. Appl Catal B Environ 41(1):207–238. doi:10.1016/s0926-3373(02)00212-6

Sundararaman R, Ma X, Song C (2010) Oxidative desulfurization of jet and diesel fuels using hydroperoxide generated in situ by catalytic air oxidation. Ind Eng Chem Res 49(12):5561–5568. doi:10.1021/ie901812r

Takahashi A, Yang FH, Yang RT (2002) New sorbents for desulfurization by π-complexation: thiophene/benzene adsorption. Ind Eng Chem Res 41(10):2487–2496

Tang X-l, Meng X, Shi L (2011) Desulfurization of model gasoline on modified bentonite. Ind Eng Chem Res 50(12):7527–7533. doi:10.1021/ie200475x

Tawara K, Nishimura T, Iwanami H (2000) Ultra-deep hydrodesulfurization of kerosene for fuel cell system.(Part 2): Regeneration of sulfur-poisoned nickel catalyst in hydrogen and finding of auto-regenerative nickel catalyst. Sekiyu Gakkai Shi 43(2):114–120

Tawara K, Nishimura T, Iwanami H, Nishimoto T, Hasuike T (2001) Ultra-deep hydrodesulfurization of kerosene for fuel cell system.(Part 3) Development and evaluation of Ni/ZnO catalyst. Sekiyu Gakkai Shi 44(1):43–51

Te M, Fairbridge C, Ring Z (2001) Oxidation reactivities of dibenzothiophenes in polyoxometalate/H_2O_2 and formic acid/H_2O_2 systems. Appl Catal A Gen 219(1–2):267–280. doi:10.1016/S0926-860X(01)00699-8

Thian TC (2008) Effects of catalyst morphology on hydrotreating reactions. J Eng Sci Technol 3(2):117–123

Tian F, Li C, Jiang Z, Weicheng WU (2005) Adsorption of sulphur containing compounds from FCC gasoline on cerium-exchanged Y zeolite. Chin J Catal 26(9):734–736

Triantafyllidis KS, Deliyanni EA (2014) Desulfurization of diesel fuels: adsorption of 4,6-DMDBT on different origin and surface chemistry nanoporous activated carbons. Chem Eng J 236:406–414. doi:10.1016/j.cej.2013.09.099

Trysberg L, Stomberg R (1981) Studies on peroxomolybdates. 10. The crystal-structures of (NH4) 4 [MO3O7 (O2) 4]. 2H2O, K5 [MO7O21 (O2) 2 (OH)]. 6H2O AND (NH4) 4 [MO8O24 (O2) 2 (H2O) 2]. 4H2O-A Preliminary-Report (vol. 35, pp. 823–825): Munksgaard Int Publ Ltd 35 Norre Sogade, Po Box 2148, DK-1016 Copenhagen, Denmark

Turk B, Gupta R (2001) RTI's trend process for deepdesulfurization of naphtha. Paper presented at the abstracts of papers of the American Chemical Society

Tuxen A, Kibsgaard J, Gøbel H, Lægsgaard E, Topsøe H, Lauritsen JV, Besenbacher F (2010) Size threshold in the dibenzothiophene adsorption on MoS2 nanoclusters. ACS Nano 4(8):4677–4682

Ullah R, Bai P, Wu P, Zhang Z, Zhong Z, Etim U et al (2016) Comparison of the reactive adsorption desulfurization performance of Ni/ZnO–Al2O3 adsorbents prepared by different methods. Energy Fuel 30(4):2874–2881

Vasudevan PT, Fierro JLG (1996) A review of deep hydrodesulfurization catalysis. Catal Rev 38(2):161–188. doi:10.1080/01614949608006457

Velu S, Ma X, Song C (2003) Selective adsorption for removing sulfur from jet fuel over zeolite-based adsorbents. Ind Eng Chem Res 42(21):5293–5304. doi:10.1021/ie020995p

Venkateshwar Rao T, Sain B, Kafola S, Nautiyal BR, Sharma YK, Nanoti SM, Garg MO (2007) Oxidative desulfurization of HDS diesel using the aldehyde/molecular oxygen oxidation system. Energy Fuel 21(6):3420–3424. doi:10.1021/ef700245g

Vergara-Méndez BZ, García-Gómez ÁA, Poisot M, Ramírez-Galicia G (2011) Theoretical study of peroxo-and diperoxomolybdate formation as catalysts in the oxidative desulfurization of diesel. Top Catal 54(8-9):527–534

Wang D, Qian EW, Amano H, Okata K, Ishihara A, Kabe T (2003) Oxidative desulfurization of fuel oil: Part I. Oxidation of dibenzothiophenes using tert-butyl hydroperoxide. Appl Catal A Gen 253(1):91–99. doi:10.1016/S0926-860X(03)00528-3

Wang R, Zhang G, Zhao H (2010) Polyoxometalate as effective catalyst for the deep desulfurization of diesel oil. Catal Today 149(1–2):117–121. doi:10.1016/j.cattod.2009.03.011

Watanabe S, Ma X, Song C (2004) Selective sulfur removal from liquid hydrocarbons over regenerable CeO2-TiO2 adsorbents for fuel cell applications. ACS Div Fuel Chem 49 (2):511–513

Wen Y, Wang G, Wang Q, Xu C, Gao J (2012) Regeneration characteristics and kinetics of Ni/ZnO–SiO$_2$–Al$_2$O$_3$ adsorbent for reactive adsorption desulfurization. Ind Eng Chem Res 51 (10):3939–3950. doi:10.1021/ie202730w

WS (2001) Paper presented at the national petrochemical & refiners association (NPRA) annual meeting, AM-01-29, 18–20 March, 2001, New Orleans

Xue-Min Y, Jia-Heng L, Dan L, Yang-Chun W, Guo L-P (2007) Oxidative desulfurization of diesel oil using mesoporous phosphotungstic acid/SiO2 as catalyst. J Chin Chem Soc 54:911–916

Yan XM, Lei JH, Liu D, Wu YC, Guo LP (2007) Oxidative desulfurization of diesel oil using mesoporous phosphotungstic Acid/SiO2 as catalyst. J Chin Chem Soc 54(4):911–916

Yang RT, Hernández-Maldonado AJ, Yang FH (2003) Desulfurization of transportation fuels with zeolites under ambient conditions. Science 301(5629):79–81. doi:10.1126/science.1085088

Yang L, Li J, Yuan X, Shen J, Qi Y (2007) One step non-hydrodesulfurization of fuel oil: catalyzed oxidation adsorption desulfurization over HPWA-SBA-15. J Mol Catal A Chem 262 (1–2):114–118. doi:10.1016/j.molcata.2006.08.058

Yazu K, Yamamoto Y, Furuya T, Miki K, Ukegawa K (2001) Oxidation of dibenzothiophenes in an organic biphasic system and its application to oxidative desulfurization of light oil. Energy Fuel 15(6):1535–1536. doi:10.1021/ef0101412

Yazu K, Furuya T, Miki K, Ukegawa K (2003) Tungstophosphoric acid-catalyzed oxidative desulfurization of light oil with hydrogen peroxide in a light oil/acetic acid biphasic system. Chem Lett 32(10):920–921

Yazu K, Makino M, Ukegawa K (2004) Oxidative desulfurization of diesel oil with hydrogen peroxide in the presence of acid catalyst in diesel oil/acetic acid biphasic system. Chem Lett 33 (10):1306–1307

Yazu K, Sato S, Yoshikazu S (2007) Tungstophosphoric acid–catalyzed oxidative desulfuriazation of naphtha with hydrogen peroxide in naphtha/acetic acid biphasic system. J Jpn Pet Inst 50 (6):329–334

Yu G, Lu S, Chen H, Zhu Z (2005) Diesel fuel desulfurization with hydrogen peroxide promoted by formic acid and catalyzed by activated carbon. Carbon 43(11):2285–2294. doi:10.1016/j.carbon.2005.04.008

Zhang YW, Shen J, Yuan XD (2005) Desulfurization by catalytic oxidation and adsorption over Ti3(PW12O)4. Pet Process Petrochem 36(3):20–24

Zhang Y, Lü H, Wang L, Zhang Y, Liu P, Han H et al (2010) The oxidation of benzothiophene using the Keggin-type lacunary polytungstophosphate as catalysts in emulsion. J Mol Catal A Chem 332(1–2):59–64. doi:10.1016/j.molcata.2010.08.021

Zhang M, Zhu W, Xun S, Li H, Gu Q, Zhao Z, Wang Q (2013) Deep oxidative desulfurization of dibenzothiophene with POM-based hybrid materials in ionic liquids. Chem Eng J 220:328–336. doi:10.1016/j.cej.2012.11.138

Zhou A, Ma X, Song C (2006a) Liquid-phase adsorption of multi-ring thiophenic sulfur compounds on carbon materials with different surface properties. J Phys Chem B 110 (10):4699–4707. doi:10.1021/jp0550210

Zhou X, Zhao C, Yang J, Zhang S (2006b) Catalytic oxidation of dibenzothiophene using cyclohexanone peroxide. Energy Fuel 21(1):7–10. doi:10.1021/ef060441p

Zhou X, Gai H, Wang J, Zhang S, Yang J, Zhang S (2009a) Oxidation of benzothiophenes using tert-amyl hydroperoxide. Chin J Chem Eng 17(2):189–194. doi:10.1016/S1004-9541(08)60192-5

Zhou X, Li J, Wang X, Jin K, Ma W (2009b) Oxidative desulfurization of dibenzothiophene based on molecular oxygen and iron phthalocyanine. Fuel Process Technol 90(2):317–323. doi:10.1016/j.fuproc.2008.09.002

Zhu W, Huang W, Li H, Zhang M, Jiang W, Chen G, Han C (2011) Polyoxometalate-based ionic liquids as catalysts for deep desulfurization of fuels. Fuel Process Technol 92(10):1842–1848. doi:10.1016/j.fuproc.2011.04.030

Chapter 9
Role of Nanomaterials as an Emerging Trend Towards the Detection of Winged Contaminants

Santanu Patra, Rashmi Madhuri, and Prashant K. Sharma

Abstract Hydrocarbons are very important as efficient energy sources in our day-to-day life. But apart from their application point of view, the most concerned area is their toxicity. A large number of literatures are being reported describing the toxicity from the last few decades. Polycyclic aromatic hydrocarbons (PAHs) and volatile organic compounds (VOCs) are the most common type of toxic hydrocarbons, most abundantly found in nature. Exhaust gas from motorbikes, combustion of coal, wood, and petroleum products are the major sources of those hydrocarbons. They are entering into the human or animal body by means of breathing, through skin, food, and water samples and caused various diseases including cancer. This makes their detection and extraction very much important. In this chapter, we have tried to sum up the source, contamination, and health effects of those hydrocarbons along with their detection and extraction techniques in combination with nanomaterials, reported so far. Major emphasis has been given on nanostructure-based sensing technique due to additional advantages and future point of view.

Keywords Polycyclic aromatic hydrocarbons • Volatile organic compounds • Nanomaterials • Sensing • Extraction

1 Introduction

The chemistry of hydrocarbon is very popular in organic chemistry. Hydrocarbons are known to be the simplest type of organic compounds containing only hydrogen and carbon in their structure. They are quite abundant in modern society, in which most commonly ingested hydrocarbons include gasoline, lubricating oil, motor oil,

S. Patra • R. Madhuri (✉)
Department of Applied Chemistry, Indian Institute of Technology (Indian School of Mines),
Dhanbad, Jharkhand 826 004, India
e-mail: rshmmadhuri@gmail.com

P.K. Sharma
Functional Nanomaterials Research Laboratory, Department of Applied Physics, Indian
Institute of Technology (Indian School of Mines), Dhanbad, Jharkhand 826 004, India
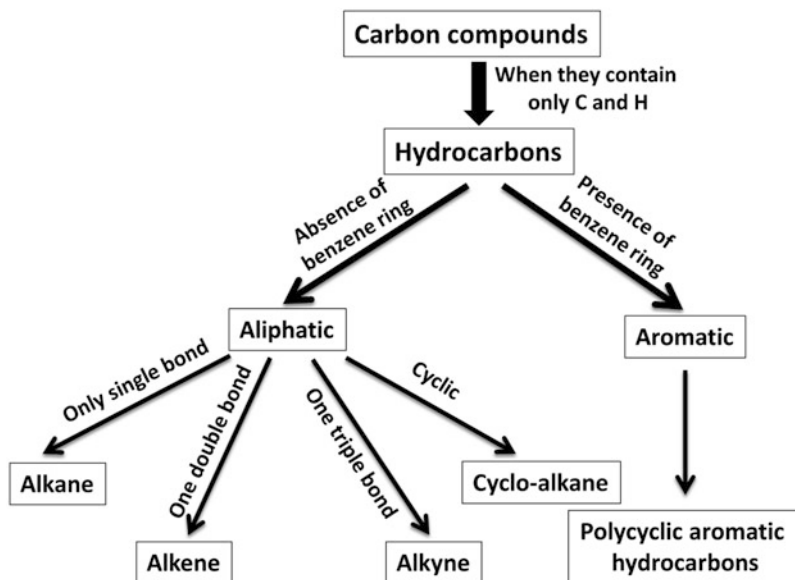
Fig. 9.1 Flowchart showing the general classification of hydrocarbons

mineral spirits, lighter fluid/naphtha, lamp oil, and kerosene. Basically, hydrocarbons can be divided into two categories: aliphatic and aromatic, depending on the presence of benzene ring (Fig. 9.1). Aliphatic hydrocarbon is of three types depending on the nature of bonding (Olah and Molnar 2003). That is, if only single bonds are present in the backbone, this is known to be an alkane, if a double bond is present, it will be known as alkene and in the case of a triple bond, it will be alkyne. After bonding, if they form a cycle, then they will be called as cycloalkanes. They can also be classified as saturated and unsaturated hydrocarbons (Olah and Molnar 2003). Saturated hydrocarbon has only single bonds in the structural backbone and contains the maximum number of hydrogen atoms for each carbon atom. Unsaturated hydrocarbons contain multiple bonding and contain less than the maximum number of hydrogens per carbon. These are major classes of hydrocarbons and will be found in detail in any basic organic chemistry books. Halogenated hydrocarbons are a subgroup of aromatic hydrocarbons, in which one of the hydrogen molecules is substituted by a halogen group. The most important halogenated hydrocarbons include carbon tetrachloride, trichloroethylene, tetrachloroethylene, trichloroethane, chloroform, and methylene chloride.

Apart from their classification and structure, they are very important in our day-to-day life as efficient energy sources. The majority of hydrocarbons found on this planet are coming from the crude oil, where decomposed organic matters provide an abundance of carbon and hydrogen, which after bonding forms limitless chains (Speight 2011). Basically, natural gas, petroleum, and coal are the three major sources of these hydrocarbons. Natural gas is very popular for generation of

temperature and it is a powerful domestic cooking and heating fuel. It is a fossil fuel formed when layers of buried plants, animals, and gases are exposed to intense heat and pressure for thousand years. The energy obtained by plants from the sun is stored in the form of chemical bonds in natural gas. Natural gas basically a hydrocarbon gas consists of methane (major composition) with varying amounts of other higher alkanes and even a lesser percentage of carbon dioxide, nitrogen, and hydrogen sulfide (Smil 2015). In many developed countries, it is supplied through pipes to home, where it is used for many household purposes. Petroleum is the mixture of a large number of different hydrocarbons, most commonly alkanes (paraffins), cycloalkanes (naphthalene), aromatic hydrocarbons, and complicated chemicals like asphaltenes (Petrov 1987). The alkanes from pentane (C_5H_{12}) to octane (C_8H_{18}) are refined into petrol and from nonane (C_9H_{20}) to hexadecane ($C_{16}H_{34}$) into diesel fuel, kerosene, and jet-fuel (Simanzhenkov and Idem 2003). Alkanes with more than 16 carbon atoms can be refined into fuel oil and lubricating oil. Paraffin wax and asphalt are such types of alkanes with 25 and 35 carbon atoms, respectively (Simanzhenkov and Idem 2003). The shortest molecules with four or fewer carbon atoms are in the gaseous state at room temperature. They are known as petroleum gases.

The third form of hydrocarbon or coal is a fossil fuel and is the altered remains of prehistoric vegetation that originally accumulated in swamps and peat bogs. The energy we get from coal today comes from the energy that plants absorbed from the sun millions of years ago. Coal combustion is another source of hydrocarbons. During coal gasification, it produces syngas. Methanol, hydrogen, carbon monoxide with certain olefins, acetic acid, formaldehyde, ammonia, urea, and others are present in the produced syngas. With respect to natural resources, vegetation is the main emitter of hydrocarbons, with compounds such as ethylene, isoprene, and monoterpenes.

Despite their natural origin and seems to be eco-friendly nature of hydrocarbons, their toxicity and their evil effects to the atmosphere are widely reported. The hydrocarbons which are abused for euphoric effects via the respiratory route of exposure (e.g., toluene) are named inhalants (Tormoehlen et al. 2014). Toxicity is related to the dose, and the chemical characteristics of volatility, lipid solubility, viscosity, and surface tension. Those with higher volatility could be better absorbed after inhalation. Lipophilic hydrocarbons cross the blood–brain barrier more readily and able to effect central nervous system (CNS) more often. Hydrocarbons with low viscosity and low surface tension may result in aspiration (Mowry et al. 2013). There are some types of hydrocarbon exposures including:

- Children with usually unintentional ingestion of household hydrocarbons
- Workers with dermal or inhalational occupational exposures
- Adolescents and young adults with intentional inhalational abuse

Hydrocarbons are present as trace gases in the atmosphere, with methane as the predominant hydrocarbon molecule with an approximate concentration 1.7 ppmv (parts per million by volume) (Dewulf and Langenhove 2009). Besides methane, other hydrocarbons are in the parts per billion or parts per trillion ranges. The main

toxicity of these hydrocarbons lies in the photochemical air pollution. It is being reported and examined that methane and hydrocarbons have a high contribution to global warming, ozone depletion and acute, chronic toxicity with carcinogenicity (Tormoehlen et al. 2014). In addition to the environmental side effects, hydrocarbons also play a critical role in the atmospheric chemistry and atmospheric hydrocarbons have a high environmental relevance. The most important contributors in this regard can be categorized into two major classes: (1) polycyclic aromatic hydrocarbons (PAHs) and (2) volatile organic compounds (VOCs). Herein, we have compiled the detection techniques used so far for detection of these compounds using the help of nanotechnology.

2 Polycyclic Aromatic Hydrocarbons (PAHs)

Polycyclic (Polynuclear) aromatic hydrocarbons (PAHs) are a class of complex organic chemicals, containing carbon and hydrogen with a fused ring structure with at least two benzene rings (Abdel-Shafy and Mansour 2016). They may have also additional fused rings that are not six-sided. Benzopyrene is most popular among all the PAHs, containing five rings. They have a very low vapor pressure and present both as gas and in associated form with particles, at ambient temperature in air. The lighter PAHs, like phenanthrene, are present mostly in gas phase whereas the heavier PAHs like benzopyrene are almost totally adsorbed onto particles (Ravindra et al. 2008). Additionally, these types of compounds are carcinogenic in nature and known as one of the first atmospheric pollutants, suspected to have a carcinogenic effect (Ravindra et al. 2001). It has also been reported that, with an increase in the molecular weight, the carcinogenicity of PAHs also increases, and their acute toxicity decreases. Benzopyrene is important for being the first chemical carcinogen to be discovered (Ravindra et al. 2008). Benz[a]anthracene and chrysene, benzo[k]fluoranthene, benzo[b]fluoranthene, indeno[1,2,3-cd]pyrene, benzo[j]fluoranthene, and dibenz[a,h]anthracene are identified as highly carcinogenic and teratogenic materials. They appear as mostly colorless or sometimes white or pale yellow-green solids. The structures of most common PAHs are shown in Fig. 9.2.

2.1 Sources of PAHs

The best possible sources of PAHs are the incomplete combustion of fossil fuel (petroleum, natural gas, and coal) and burning vegetation. They are always found in a complex mixture and commonly not exist as a single product. Other important sources of PAHs are from oil seepage, petroleum spills, and diagenesis of organic matter in anoxic sediments. They can also be found in coal tar, roofing tar, creosote, and crude oil. Few of the PAHs are used in medicine or to make plastics, dyes, and
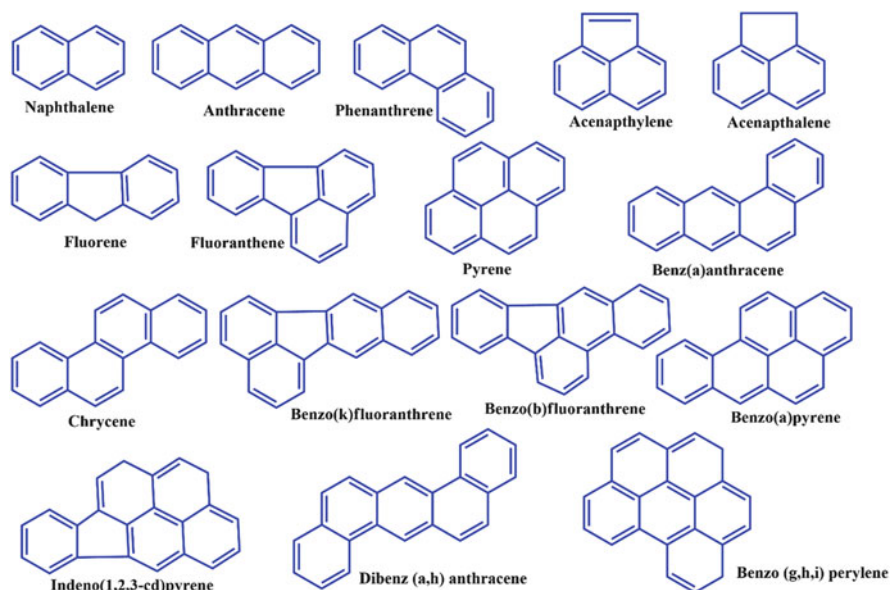
Fig. 9.2 Structures of toxic and commonly reported PAHs

pesticides. Naphthalene, anthracene, phenanthrene, fluorene, fluoranthene, and pyrene are prepared in chemical laboratories for their commercial use. According to Ravindra et al., the sources of PAHs can be classified into five major categories: domestic, mobile, industrial, agricultural, and natural (Wing and Bada 1992). Beegle et al. have proposed some cosmic sources of PAHs also (2001). Domestic emissions are mostly associated with the burning of coal, gas, oil, garbage, and some other organic substances like tobacco or char broiled meat. According to WHO, wood, dried animal-dung-cake, and crop waste from agricultural residue are widely used as fuel for cooking in the developing nations. According to that report, ~75% people in India, China, and South East Asia, and 50–75% people from South America and Africa are using these solid fuels for their daily cooking. The partial combustion of coal (a hydrogen-to-carbon ratio <1) is a major source of PAH compounds. According to Bostrom et al. wood burning is being reported to contribute 430 kg benzopyrene, whereas gasoline and diesel vehicles together were estimated to contribute up to 320 kg benzopyrene in Sweden (1999). Schauer and Cass reported the similar results for Los Angeles city (Schauer and Cass 2000). Mobile sources of PAHs are the emission from vehicles such as aircraft, railways, shipping, off-road vehicles, automobiles, and machinery. According to Paturel et al. the emission of PAHs from these sources is a function of engine type, load and age, fuel type and quality (1996). For gasoline automobiles, it has been reported that the production of PAHs is mostly depended on the air/fuel ratio. It has also been found that the amount of PAHs in engine exhaust decreases with a leaner mixture. In their experiments, Jones et al. (2004) found that with the increase in air/fuel combustion

ratio, the high molecular weight PAHs diminished rapidly (Jones et al. 2004). The use of diesel and diesel/electric locomotives in rail transportations is also important sources of PAHs emission. It is also reported that ~139 tons of PAHs are emitted by the creosoted ties of the Swiss railway network (Kohler and Kunniger 2003). The primary aluminum production (mainly by Soderberg process), coke production, waste burning, creosote and wood preservation, petrochemical and related industries, cement manufacture, rubber tire manufacturing, bitumen and asphalt industries, and commercial heat/power production are known as the best possible industrial source of PAHs (Ravindra et al. 2008). In a study, carried out by Pisupati et al. only acenaphthene, fluoranthene, and naphthalene were detected with their emission factors ranged from 85 to 320 mg/kg of fuel fired in water boiler (2000). The open burning of agricultural biomass is the main agricultural PAHs source. The emission factor as determined by Jenkins et al. is highest among all and it varied from 5 to 683 mg/kg (1996). Natural sources of PAHs can be divided into two categories: terrestrial origin and cosmic origin. Nonanthropogenic burning of forests, woodland, and moorland due to lightning strikes and volcanic eruptions come under the terrestrial sources. Whereas, carbonaceous chondrites, originated in the main asteroid belt, which are not associated with life is reported as the cosmic sources of PAHs.

2.2 Contamination of PAHs in Atmosphere, Soil, Sediments, and Food Samples

After the emission of PAHs from the abovementioned sources, they mainly contaminate the atmospheric air. In the atmosphere, PAHs are mainly found in two separate phases, a vapor phase and a solid phase in which the PAHs are sorbet onto particulate matter. It has been found that hydrophobic organic chemicals with a low vapor pressure (here PAHs) will sorbet to particulate matter with high efficiency than the chemicals with a high vapor pressure (like benzene). It has been found that the relative distribution of PAHs in two phases will be different for the given air samples, as different PAHs have different molecular weight, which in turn have different vapor pressure (Abdel-Shafy and Mansour 2016). The adsorption of PAHs is also depended on the types of suspended particulates (e.g., soot, fly ash, dust, pollens, and pyrogenic metal oxides). Literatures have reported the continuous deposition of PAHs to the earth surface by dry or wet deposition processes. After deposition to the earth's surface, PAHs can become mobile and the majority of PAHs in the soil will be bound to soil particles (Masih and Taneja 2006). The mobility of PAHs on earth surface, i.e., in soil, is dependent on the sorbent particle size and the pore throat size of the soils. In a similar way as that of surface soils, PAHs are deposited to the sedimentary environment. In rural areas, the PAHs can settle on the surface of streams, lakes, and oceans by dry or wet deposition and eventually they become integrated with the sediment. When they enter to the

atmosphere or soil samples, it is evident that they should contaminate the food samples and will enter the human body. The existence of PAH in foods is administered mainly by similar physicochemical factors used to determine the absorption and distribution in man. That is the relative solubility of PAHs in organic solvents and water. This solubility will determine their capacity for transportation and distribution between different environmental compartments and finally their uptake and accumulation by living organisms (Abdel-Shafy and Mansour 2016).

2.3 Human Exposure to PAHs and Health Effects

PAHs are mainly entered into the human body by breathing contaminated air or eating food that may contain PAHs or smoking cigarettes, or by breathing smoke from open fireplaces. Tobacco smoke contains certain types of PAHs, which are suspected to be human carcinogens. For nonsmokers, the main route is exposure through food or contaminated air. High-temperature cooking (i.e., grilling, roasting, and frying) also formed PAHs, which may enter into the human body after accumulation. Sometimes PAHs are synthesized or absorbed by some crops like wheat, rye, and lentils via water, air, or soil. The intake of PAHs mainly occurs from the contaminated soil via ingestion, inhalation, or dermal (skin) exposure and from inhalation of PAH vapors. Mechanics, street vendors, motor vehicle drivers, and the workers of mining, oil refining, and metal working accumulate PAHs through breathing exhaust fumes (Abdel-Shafy and Mansour 2016).

The concentration of PAHs during exposure, the toxicity of the accumulated PAHs, the route of exposure (i.e., via inhalation, ingestion, or skin contact), and time and length of exposure are the main factors that determine the acute effects of PAHs. The short-term exposure to PAHs has been reported to cause impaired lung function in asthmatics and thrombotic effects in people affected by coronary heart disease. However, it cannot be identified which components of the mixture are responsible for that. The high levels of pollutant mixtures containing PAHs are known to cause symptoms like eye irritation, vomiting, diarrhea, and nausea. They sometimes cause skin irritation and inflammation to the human body. Benzopyrene and naphthalene are known to be direct skin irritants, while anthracene and benzo-pyrene are reported to be skin sensitizers, i.e., they may cause allergic skin response in animals and humans. As long-term health effects, increased risk of skin, lung, bladder, and gastrointestinal cancers are being reported. Pyrene and benzopyrene has been identified as the cause of cancer in laboratory animals. Wells et al. have reported the effects of PAHs in animals, which may not be detected in human body (2010). Further animal studies also confirm that some PAHs can affect the hematopoietic and immune systems producing reproductive, neurologic, and developmental effects. A number of laboratory studies have done, where animals were exposed to a certain concentration of some PAHs over long period of time and found that they have suffered from stomach cancer from ingesting PAHs in food, lung cancer from inhalation, and skin cancer from skin contact (US EPA 2008).

Benzo(a)pyrene is reported to be the most common PAH to cause cancer in animals. Kristensen et al. conducted some laboratory studies on mice and found that ingestion of high levels of benzo(a)pyrene during pregnancy resulted in birth defects and a decreased body weight in the offspring (1995). In human body, the long-term exposure to PAHs may form cataracts and cause kidney or liver damage and jaundice. Naphthalene can cause redness and inflammation of the skin after long time contact and after breathing, they may cause the breakdown of red blood cells. Till now, no study has performed to understand the human health effects following oral exposure to PAHs. Reactive metabolites like the epoxides and dihydrodiols of some PAHs have the potential to bind to cellular proteins and DNA with toxic effects and this becomes one of the major health concerns in recent days. These will result in a biochemical disruption and cell damage, which may also lead to mutations, developmental malformations, tumors, and cancer (Bach et al. 2003). Extensive studies confirm that the mixtures of PAHs are more carcinogenic to humans than individual PAHs. U.S. Environmental Protection Agency (US EPA 2008) have classified seven PAHs as probable human carcinogens: benzo(a)pyrene, indeno(1,2,3-cd)pyrene, benz(a)anthracene, dibenz(ah)anthracene, benzo(b) fluoranthene, benzo(k)fluoranthene, and chrysene. Workers from coal gasification, chimney sweeper, oil refining, and roofing have the common problems of skin cancer in most of the cases. According to Armstrong et al. excessively high rate (16-fold higher) of lung cancer was found in coke-oven workers and this is closely correlated with the time spent for working on top of ovens where a high benzopyrene concentration was obtained (2004).

2.4   Detection and Extraction of PAHs

As we discussed earlier, PAHs are very carcinogenic to animals and human being. The atmospheric air, soil, and food samples are being continuously contaminated by these PAHs mixtures, which makes their detection as well as extraction very important. Gas chromatography, gas chromatography-mass spectrometry (GC-MS), electrochemical bio-sensing, immunoassay, high-performance liquid chromatography (HPLC), and surface-enhanced Raman spectroscopy has been popularly applied for the determination of PAHs in various research articles. Very recently, Taniguchi et al. have reported the detection of PAHs and polychlorinated biphenyls (PCBs) in plastic pellets collected randomly from 41 beaches (15 cities) from the coast of the state of São Paulo, south eastern Brazil using GC-MS as the detection technique. The concentration for PAHs detection was found in the range from 192 to 13,708 ng g^{-1}. The area was affected by both waste disposal and industrial complex, which was reported to be the main cause of the contamination (Taniguchi et al. 2016). A similar GC-MS analysis method was reported by Bian et al. for the detection of PAHs in ambient air of Riyadh, Saudi Arabia. Sixteen particle-phase PAHs were reckoned in 167 samples. Among them, pyrene and fluoranthene were the most abundant PAH, with an average population

of 3.37 ± 14.01 ng m^{-3} and 8.00 ± 44.09 ng m^{-3}, respectively. The widespread contamination of PAHs can be attributed to the oil combustion, i.e., large annual production and consumption, in Saudi Arabia (Bian et al. 2016). One of the recent literatures has also reported the finding of PAHs in 23 farmland soil samples and 10 riverine sediment samples from Guiyu, China. Guiyu is known for the largest electronic waste (EW) in China and the PAHs contamination is due to their combustion of liquid fossil fuels or coal, for the purpose of incinerating EWs, rather than EW combustion itself. They have determined a PAH concentration of 56–567 ng/g in the soils and 181–3034 ng/g in the sediments (Xu et al. 2016a). Akhbarizadeh et al. have reported the quantification of aliphatic and polycyclic aromatic hydrocarbons in coastal water and sediments of Khark Island, SW Iran using a gas chromatography/flame ionization detector (GC-FID) for the quantification. Twenty six aliphatic hydrocarbons (AHs), 16 polycyclic aromatic hydrocarbons (PAHs), and total petroleum hydrocarbons (TPHs) were found in that particular area (Akhbarizadeh et al. 2016). Ohura et al. have determined the concentrations of PAHs and chlorinated PAHs (ClPAHs) in different seasons at five sampling stations in Nagoya, a Japanese megacity using a gas chromatographic technique. They have found an annual total PAH concentration of 5200–8570 pg/m^3 (Ohura et al. 2016).

The Himalayas is the highest mountain in the world, of world's highest peaks including Mount Everest, however, it is also not free from PAHs contaminations. Recent literatures have reported the contamination of surface soil of Himalayan region by PAHs, with a total concentration in the range of 15.3–4762 ng/g. PAHs benzo(a)pyrene (BaP), benzo(a)anthracene (BaA), benzo(b)fluoranthene (BbF), benzo(k)fluoranthene (BkF), chrysene (CHR), and indeno (1,2,3-cd) pyrene (IcdP) are known for their carcinogenic property and they all have been found in the Himalayan soils. It has been reported that the PAHs contamination at mountain surface soil is the result of atmospheric deposition and sources from nearby areas (Devi et al. 2016).

Dhanbad, Jharkhand is known for the coal city of INDIA and is one of the polluted cities also. Therefore, from our institute, a quantitative study was carried out to understand the PAHs concentration in the coal mines area. In the study, the concentration variation at different locations of the city depending on the vehicular traffic was monitored using HPLC technique. At traffic site, they have found a PAH concentration of 1.019–10.856 μg/g and in control/rural site, the concentration was 0.640 μg/g. The higher contaminated value is due to the vehicular emission and various coal mining activity in the surrounding area of Dhanbad city. Coal mining is known to be the major source of these PAHs along with associated emissions from automobile exhaust and industries, biomass burning, resuspended soil dust and earth crust, oil combustion, and fugitive emissions (Suman et al. 2016). Recent literatures have also reported the detection of PAHs in Tar ponds and surrounding environments adjacent to a former coking and steel manufacturing facility using fingerprinting technology (MacAskill et al. 2016). Fernandez-Amado has reported an online in-tube solid-phase microextraction (IT-SPME) coupled to HPLC-

photodiode array-fluorescence detection technique for the analysis of PAHs in low volume rainwater samples (Fernández-Amado et al. 2016).

In the case of sensing or extraction, nano-sized materials are a good choice, due to their physicochemical properties, i.e., small size of nanomaterials, large surface-to-volume ratios, composition, shape, and unusual target binding characteristics (Patra et al. 2016). They can markedly improve the sensitivity and specificity of analyte detection. Herein for a better understanding of the readers, we have classified the nanoparticles-based sensing/extraction techniques into four different categories (Table 9.1):

1. Noble metal nanoparticles
2. Magnetic nanoparticles
3. Carbonaceous materials
4. Molecularly imprinted materials
5. Other nano-sized materials

2.4.1 Noble Metal Nanoparticles Based Extraction/Sensing Techniques

Noble metal nanoparticles are the most popular and widely studied colloidal systems in the field of nanoscience and nanotechnology. The popularity is mainly due to their unique characteristics like high surface-to-volume ratio, broad optical properties, easy synthesis, facile surface chemistry, and their versatile behavior in diagnostic assays (Conde et al. 2012). Gold (AuNPs) and silver nanoparticles (AgNPs) are the most popular among all noble metal nanoparticles. Numerous literature can be found on the different synthesis approaches and applications. Gold has been utilized in India since 1000–600 BC for medical purposes in the form of *swarna bhasma* (meaning, gold ash). In addition, role of gold nanoparticles as a sensing device has widely been reported.

Wang et al. have recently reported gold nanoparticles decorated hydrophobic porous polymer as surface-enhanced Raman spectroscopy substrate for the trace level detection of PAHs. For the preparation of the polymer, glycidyl methacrylate and ethylene dimethacrylate were used as monomers. The PAHs were adsorbed to the polymer matrix through presumed hydrophobic interaction, which brings the analytes close to the substrate. Anthracene, phenanthrene, and pyrene were selected as probe molecules for PAH detection and show the limit of detection (LOD) $= 0.93 \times 10^{-7}$, 4.5×10^{-7}, and 1.1×10^{-7} M, respectively. The substrate was reported to have high reproducibility and was applied for the rapid screening of PAHs in environmental water samples also (Wang et al. 2015a). A highly reproducible and portable surface-enhanced Raman scattering (SERS) sensor for PAH has been reported by Xu et al. using a new concept of coffee ring effect. It has been reported that this coffee ring effect could separate PAHs from the bulk solution and concentrate them on the closely packed AuNPs ring, which will enhance their Raman scattering (Xu et al. 2014). To confirm this, citrate-reduced and structurally unmodified AuNPs with 20 nm size were used. Due to this coffee ring effect, closely packed but not aggregated AuNPs arrays were formed, this facilitated the

Table 9.1 List of nanosensors reported for the detection/extraction of PAHs

S.N.	Materials	Analytical technique	PAHs detected	LOD	Real sample analyzed	Recovery (%)	References
1.	Au NP-GMA-EDMA	SERS	Anth, phen and pyrene	$0.93 \times 10^{-7}, 4.5 \times 10^{-7}, 1.1 \times 10^7$ M	Water samples	–	Wang et al. (2015a)
2.	Closely packed Au NP ring	SERS	Naph, anth, pyrene, BaP, BghiP, and IP	–	River water samples	–	Xu et al. (2014)
3.	Au NPs/Nickel foam	SERS	Pyrene	10^{-8} M	Tap water samples	94.4–115.0	Zhao et al. (2015)
4.	Au NPs/TiO$_2$ NTs	SERS	BaP	12.6 nM	Water samples	89.97–116.2	Sheng et al. (2012)
5.	CD-AuNPs	SERS	Anth, pyrene, chry, and tpy	100, 10, 100 and 1000 nM	–	–	Xie et al. (2011)
6.	Bare AuNPs coupled film system	SERS	BbF, fluo, BaA, and pyrene	$1.2 \times 10^{-8}, 2.0 \times 10^{-8}$, 5.5×10^{-8} and 6.3×10^{-8} M	Soil samples	–	Gu et al. (2016)
7.	CD-AgNPs	SERS	Pyrene and anth	7.5 and 10.0 μM	–	–	Xie et al. (2010)
8.	Ag NPs decorated humic acid	SERS	Anth, fluo, pyrene and 3,4-benzopyrene	$4.8 \times 10^{-7}, 1.3 \times 10^{-7}$, 5.5×10^{-7} and 1.3×10^{-7} M	Sludge samples from local river	–	Qu et al. (2013)
9.	Bromide-coated Fe$_3$O$_4$ NPs	UPLC-FLD	15 PAHs	$0.4–10.3$ ng L^{-1}	River water, wastewater, and tap water samples	59.23–87.95	Wang et al. (2015b)
10.	Fe$_3$O$_4$@MPS@IL NPs	mSPE-HPLC-FLD	7 PAHs	0.1–10 ng L^{-1}	Coffee and tea samples	87.5–104.5	Shi et al. (2016)
11.	Fe$_3$O$_4$@SiO$_2$@Flu	mSPE-GC-MS	16 PAHs	0.5–4.0 ng L^{-1}	Water samples	96.0–106.7	Cai et al. (2015)
12.	MNP-APTES-Chol	mSPE-GC-MS	16 PAHs	0.2–7.8 ng L^{-1}	Drinking water samples	80.9–98.2	Cai et al. (2016)

(continued)

Table 9.1 (continued)

S.N.	Materials	Analytical technique	PAHs detected	LOD	Real sample analyzed	Recovery (%)	References
13.	PDA@Fe_3O_4/ZIF-7	mSPE-GC-MS	Flu, anth, fluoranthene, pyrene, BbF and BbP	0.71–5.79 ng L^{-1}	Rain water samples	92.8–99.4	Zhang et al. (2016a)
14.	Ppy-PANI nanocomposite	MSBSE-GC-FID	Naph, acenaph, acenaphthene, phen, and anth	0.02–1.10 ng mL^{-1}	Wastewater, fountains water, and seawater samples	86–100	PAH magnetic SBSE Mollahosseini et al. (2016)
15.	Fe_3O_4-DVB-SO_3^-	mSPE-GC-MS	Naph, acenaphthene, fluo, phen, anth, fluoranthene and pyrene	1.1, 0.8, 1.1, 1.4, 0.6, 2.1, and 0.7 pg mL^{-1}	River and lake water samples	79.9–115.3	Xue et al. (2015)
16.	Thiol-modified Fe_3O_4@Ag	SERS	8 PAHs	10^{-5}–10^{-7} M	–	–	Du and Jing (2011)
17.	Fe_3O_4@Au	SERS	16 PAHs	5–100 nM	River water samples	–	Du et al. (2016)
18.	mCNTs	GC-MS	10 PAHs	0.05–0.42 µg L^{-1}	Lake water samples	80.5–110.2	Menezes et al. (2015)
19.	g-C_3N_4/Fe_3O_4	mSPE-HPLC-UV	7 PAHs	0.05–0.1 ng mL^{-1}	Environmental water samples	80.0–99.8	Wang et al. (2015c)
20.	Magnetic CN sheets	mSPE-GC-MS	8 PAHs	0.1–0.3 ng g^{-1}	Soybean oil samples	91.0–124.1	Zheng et al. (2016)
21.	Graphene/Fe_3O_4@polythiophene	mSPE-GC-FID	Naph, acenaphthene, fluo, phen, and anth	0.009–0.02 µg L^{-1}	Seawater samples	83–107	Mehdinia et al. (2015)
22.	Au-MNP-Silica	mSPE-LLME-GC	Fluo, phen, anth, fluoranthene and pyrene	0.002–0.004 µg L^{-1}	Seawater samples	91.4–104.2	Mehdinia et al. (2014)

No.	Material	Technique	Analytes	LOD	Sample	Recovery	Reference
23.	L-cysteine-capped CdSe/ZnSe/ZnS QDs-GO	PL	Phen, anth, pyrene and naph	~0.26 µg L^{-1}	—	—	Adegoke and Forbes (2016)
24.	BTMSI-IL-GO	SPME-GC-FID	9 PAHs	0.015–0.025 µg L^{-1}	Potatoes and food-wrap sample	89.1–101.3	Hou et al. (2016)
25.	GO-silica	GC-MS	14 PAHs	0.05–0.36 ng/cig	Mainstream cigarette smoke	—	Shi et al. (2015)
26.	CNTs	SFE-GC-MS	15 PAHs	1–10 ng mL^{-1}	Soil samples	62.9–111.8	Han et al. (2015)
27.	MWCNT-MMM and SLG-MMM,	MMMM-HPLC	8 PAHs	0.02–0.09 ng mL^{-1}	Sewage pond water samples	99.0–100.5	Mukhtar and See (2016)
28.	CD-silica microporous composite	SPE-HPLC	8 PAHs	0.03–0.8 ng mL^{-1}	River, well, rain and salty water samples	50–160	Mauri-Aucejo et al. (2016)
29.	Phenyl-functionalized TiO$_2$ NS	SPME-HPLC-UV	naph, phen, fluoranthene and BaP	0.008–0.043 µg L^{-1}	Environmental water samples	86.2–112.0	Guo et al. (2015)
30.	Bulk MIP	SPE-GC-MS	16 PAHs	5.2–12.6 ng L^{-1}	Seawater samples	83–113	Song et al. (2012)
31.	Nano-MIP	SPE-UHPLC	1-HP, 2-HF, 9-HF, 9-Phenanthrol, 1-Naphthol	0.33–2.6 ng mL^{-1}	Urine samples	78.22–95.41	Chauhan et al. (2015)

LOD Limit of detection, *Au NP* Gold nanoparticles, *GMA-EDMA* glycidyl methacrylate-ethylene dimethacrylate, *SERS* Surface enhanced Raman scattering, *Anth* Anthracene, *Phen* phenanthrene, *Naph* Naphthalene, *BaP* benzo[a]pyrene, *BghiP* benzo[g,h,i]perylene, *IP* indeno[1,2,3-cd]pyrene, *CD* cyclodextrin, *chry* chrysene, *tpy* triphenylene, *BbF* benzo[b]fluoranthene, *fluo* fluoranthene, *BaA* benzo[a]anthracene, *AgNPs* Silver nanoparticles, *UPLC* ultraperformance liquid chromatography, *FLD* fluorescence detection, *MPS* 3-(Trimethoxysilyl)propyl methacrylate, *IL* ionic liquid, *HPLC* High-performance liquid chromatography, *Flu* Fluorenyl, *Chol* cholesterol chloroformate, *mSPE* magnetic solid-phase extraction, *GC-MS* Gas chromatography-Mass spectrometry, *MNP* magnetic nanoparticles, *APTES* 3-aminopropyl triethoxy silane, *PDA* Polydopamine, *ZIF 7* zinc benzimidazolate, *Ppy* Polypyrrole, *PANI* Polyaniline, *mSBSE* magnetic stir-bar sorptive extraction, *BbP* benzo(b)pyrene, *acenaph* acenaphthylene, *DVB* Divinyl benzene, *mCNTs* magnetic carbon nanotubes, *CN* carbon nitride, *LLME* liquid–liquid microextraction, *PL* photoluminescence, *QD* quantum dot, *GO* graphene oxide, *BTMSI* Bis(trifluoromethanesulfonyl)imide, *SPME* solid-phase microextraction, *MMMM* Mixed Matrix Membrane Microextraction, *MWCNT* multiwalled carbon nanotube, *SLG* single layered graphene, *MIP* molecularly imprinted polymers, *1-HP* 1-Hydroxypyrene, *2-HF* 2-hydroxyfluorene, *3-HF* 3-hydroxyfluorene

separation and concentration of hydrophobic PAHs. The prominent SERS enhancement on the ring can be assigned to the electromagnetic mechanism. They have used a mixture of six PAHs with different numbers of benzene rings, namely, naphthalene, anthracene, pyrene, benzo[a]pyrene, benzo[g,h,i]perylene, and indeno[1,2,3-cd]pyrene and identified them in river water. Previously Zhao et al. and Sheng et al. have also reported the use of SERS technique towards PAH determination with AuNP/nickel foam and AuNP-TiO$_2$ nanocomposites. The AuNPs/nickel foam nanocomposite was prepared by a galvanic replacement reaction between nickel foam and auric chloride, followed by modification with long-chain alkyl mercaptan molecules. According to Zhao et al. as-prepared 3-D AuNPs/ nickel foam nanocomposite have super-hydrophobic properties, which may be used to detect PAHs via hydrophobic interactions (2015). The lowest detected concentration of PAH using AuNPs/nickel foam nanocomposite was reported to be 10^{-8} M. In another work, AuNPs-TiO$_2$ nanocomposite was prepared by photocatalytically depositing AuNPs inside the titania nanotubes. The detection limit was reported to be 12.6 nm with a recovery range of 89.97–116.2% for real water samples analysis (Sheng et al. 2012). Similarly, a per-6-deoxy-(6-thio)-β-cyclodextrin (CD-SH) modified AuNPs as a SERS sensor for PAH detection have also been reported. Here the quantitative detection of the PAHs was carried out using SERS technique on inclusion complexes with different concentrations. The sensing of PAHs was based on the matching relationship between the host and the guest, i.e., host–guest interaction mechanism (Xie et al. 2011). A bare AuNPs coupled film system for PAHs detection has been reported by Gu et al. They have a self-assembled smooth gold film (Au-film) with a hydrophobic layer of the alkyl chain to capture the PAHs molecules from bulk solution to the surface of Au-film. The lowest detection limits for the selected PAHs, i.e., benzo[b] fluoranthene, fluoranthene, benzo[a]anthracene, and pyrene, were found as 1.2×10^{-8}, 2.0×10^{-8}, 5.5×10^{-8}, and 6.3×10^{-8} M, respectively (Gu et al. 2016).

Like gold nanoparticles, silver has also been employed for the detection of PAHs. Xie et al. have reported a beta-cyclodextrin (β-CD) inclusion complex on AgNPs for the detection of PAHs by SERS. According to them, the designed system has the ability to bind anthracene and pyrene into the hydrophobic cavity of β-CD, which will cause the analytes to be closer to the surface of AgNPs, i.e., the zone of electromagnetic enhancement (Fig. 9.3). This will enable to detect SERS of PAHs and SERS spectra can easily distinguish the individual PAH compounds in a mixture by their characteristic peaks. As β-CD was used for detection, it has the feature of high selectivity due to its size of the cavity and will increase the sensitivity, selectivity, and analytical importance of the proposed sensing device (Xie et al. 2010). In another literature, Qu et al. have prepared humic acid decorated AgNPs with an average diameter of 50 nm for the detection of anthracene, fluoranthene, pyrene, and 3,4-benzopyrene. The adsorption of these aromatic molecules to the humic acid decorated AgNPs was explained by π–π stacking interactions between the adsorbate and adsorbent (Qu et al. 2013). Previously, Guerrini et al. have reported the preparation of dithiocarbamate-functionalized AgNPs for the detection of PAHs. The SERS spectra can inform the existence of the pollutant
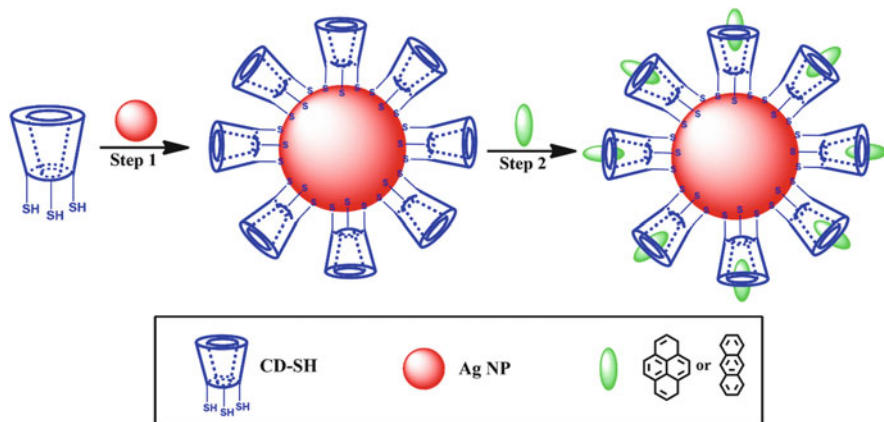
Fig. 9.3 Schematic representation of the procedure for detection of the PAHs using CD-Ag NPs (Redraw with permission from Xie et al. 2010)

by measuring its characteristic fingerprint vibrational features. In their study, they have used pyrene, benzo[c]phenanthrene, triphenylene, and coronene as model PAHs (Guerrini et al. 2009). A similar calix[4]arene-functionalized Ag NPs SERS sensor for PAHs has also been reported by Leyton et al. 2004). It was found that host–guest interaction mechanism took place through a π–π stacking, which leads to charge transfer between the complex and the metallic surface, resulting in modification of surface charge of the metallic Ag nanoparticles and enhanced SERS signals.

2.4.2   Magnetic Nanoparticles (MNPs) Based Extraction/Sensing Techniques

Iron oxide is the most popular among all metal oxide nanoparticles due to their excellent magnetic property, easy and bulk synthesis. They have become a useful member in biomedical fields as a magnetic resonance imaging contrast enhancement, in drug delivery, immunoassay, tissue repair, and hyperthermia, detoxification of biological fluids in cell separation, etc. Besides their biomedical applications, they are very popular for the fabrication of sensor or extraction devices also. The extraction can be easily and economically achieved through MNPs, just using the simple magnets.

Recently, Wang et al. have prepared a cetyltrimethyl ammonium bromide-coated Fe_3O_4 MNPs for the analysis of 15 PAHs in the aquatic environment by liquid chromatography in combination with fluorescence detection technique. They have used a solid-phase extraction (SPE) method for the extraction of PAHs and reached an enrichment factor of 800 within 5 min using 100 mg of Fe_3O_4 MNPs and 50 mg of CTAB. They have concluded that this SPE technique is more convenient, efficient, time-saving, and cost-effective than the conventional liquid–liquid

extraction technique or the C18 SPE cartridge. The LOD value for all the selected PAHs was found within 0.4–10.3 ng L^{-1}. The recovery value was found in between 59.23 and 87.95% for rainwater, upstream and downstream river water, wastewater, and tap water sample (Wang et al. 2015b). A magnetic SPE technique coupled with HPLC-Fluorescence detection has been reported recently for the determination of PAHs in coffee and tea samples. For this, they have synthesized a nano-adsorbent by combining ionic liquid, MNPs, and vinyl silane (trimethoxysilyl propyl methacrylate), i.e., Fe_3O_4@MPS@IL NPs, and applied it for the analysis of seven heavy molecular weight PAHs from coffee and tea samples. The full procedure has been discussed in Fig. 9.4. The material shows a good performance for the analysis of PAHs with the detection limits in the range of 0.1–10 ng L^{-1}. The spiked recoveries of the seven PAHs in coffee and tea samples were ranged in between 87.5 and 104.5%, with RSDs of less than 3.7% (Shi et al. 2016). A gas chromatography technique in combination with mass spectrometry and magnetic SPE has been reported for the analysis of 16 PAHs in drinking water samples. As a simple synthesis approach, they have prepared fluorenyl-functionalized superparamagnetic core/shell magnetic nanoparticles. The method was simple, fast, and environmentally friendly, i.e., does not require any organic solvent and have LOD value ranging from 0.4 to 4.0 ng L^{-1} (Cai et al. 2015). The recovery values in real water samples were found in the range of 96.0–106.7%. Later, the same group has reported another modified version of the material to improve the detection limit.
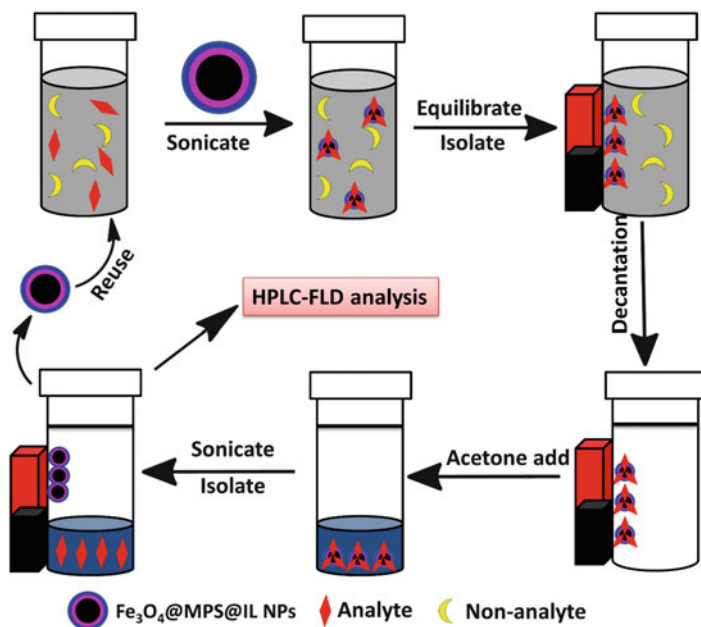
Fig. 9.4 Schematic representation showing the magnetic solid-phase extraction technique (Redraw with permission from Shi et al. 2016)

Here, they have coated the prepared MNPs with 3-aminopropyltriethoxysilane and modified with cholesterol chloroformate. The detection limit was lower than that of the previous one, ranging from 0.2 to 7.8 ng L^{-1} (Cai et al. 2016). A zeolitic imidazolate framework (ZIF) based magnetic SPE of polycyclic aromatic hydrocarbons from the air–water environment was reported in a recent article, published from Hangzhou Dianzi University, China. ZIF consists of metal nodes connected to imidazolate linkers, with both the properties of metal-organic frameworks (MOFs) and inorganic zeolites, known for their controlled pore sizes, high porosity, and high surface area (Zhang et al. 2016a). The synthesis procedure was simpler and was prepared by simply mixing ZIF-7 and polydopamine-coated Fe_3O_4 nanoparticles in solution phase. The functional groups like –OH and –NH_2 present at the surface of MNPs, get attracted and anchored to the ZIF-7 through non-covalent adsorption and covalent cross-link interactions. This promotes the complete magnetization of ZIFs and thereby enhances their stability and reusability. GC-MS was used as the main detection technique and applied for the analysis of PAHs from rainwater and air samples containing particulate matters. The detection limit was found in the range of 0.71–5.79 ng L^{-1} with limits of quantification = 2.50–19.2 ng L^{-1}. Similarly, Hong Kong University of Science and Technology (HKUST-1) based MOFs have also been prepared for magnetic SPE of eight heavy PAHs in waters and fruit tea infusions and analysis was performed by a combination of HPLC and fluorescence detection techniques. The method shows a new pathway for the preparation of adsorbent material (here simple mixing is used) and shows fast extraction (within $\sim$10 min) with a minimum amount of sorbent (20 mg of HKUST-1 and 5 mg of MNPs) and an organic solvent. The method possesses a lower LOD value of 0.8 ng L^{-1} with a recovery range of 75–94% in real sample analysis (Rocío-Bautista et al. 2016).

Nowadays, stir-bar sorptive extraction (SBSE) has become very popular in the field of extraction and ultra-trace level analysis. Recently, Mollahosseini et al. have reported the use of polypyrrole–polyaniline nanocomposite based conducting polymers as extraction phase for the analysis of PAHs through coupling of SBSE and GC. The method shows a good linear detection range in between 2 and 450 ng mL^{-1} with a LOD of 0.02–1.10 ng mL^{-1} for the selected PAHs. The recoveries of these compounds in spiked water samples were found in the range of 86–100% (Mollahosseini et al. 2016).

Xue et al. have reported the preparation of MNPs with both hydrophobicity and hydrophilicity for the extraction of PAHs from environmental water samples. MNPs with divinylbenzene (DVB) and sulfonate functionalities were prepared via "thiol-ene" click chemistry. Here, the hydrophobic DVB moieties were dedicated for extraction while the hydrophilic sulfonate groups were used for dispersing the MNPs in the aqueous sample solution. The method has shown a much lower LOD value of 1.1, 0.8, 1.1, 1.4, 0.6, 2.1, and 0.7 pg mL^{-1} for naphthalene, acenaphthene, fluorine, phenanthrene, anthracene, fluoranthene, and pyrene, respectively. Therefore, possess great potential in the pre-concentration of trace level analytes in the complex matrix (Xue et al. 2015).
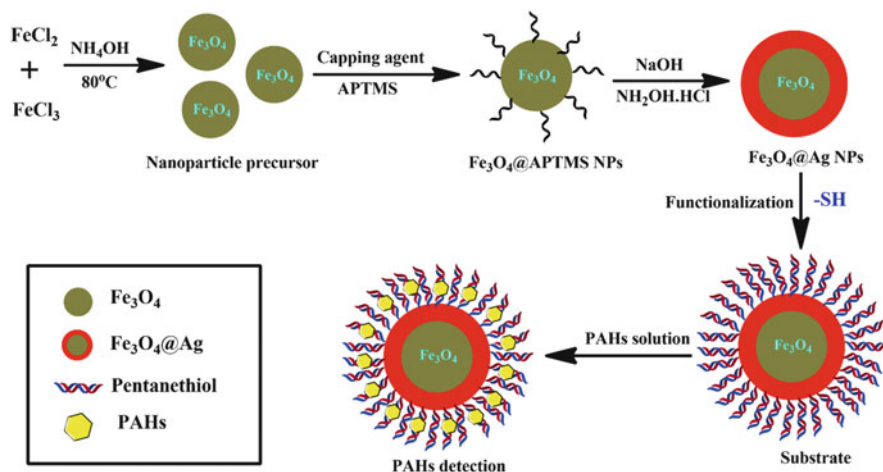
Fig. 9.5 Schematic diagram showing the SERS detection of PAHs using thiol-modified Fe₃O₄@Ag (Redraw with permission from Du and Jing 2011)

Besides single magnetic nanoparticles, some PAH sensor or extraction method has also reported the use of MNPs along with other nanostructures. Use of two nanostructures can enhance the effect of MNPs, due to the synergistic effect and employing the thought Du and Jing has reported the preparation of thiol-modified Fe_3O_4@Ag core–shell magnetic SERS probe for PAHs detection and identification (Fig. 9.5). The linear calibration range was obtained between 1 and 50 mg L^{-1} and the detection limit was in the order of 10^{-5}–10^{-7} M (Du and Jing 2011). Further, Du et al. have reported another SERS probe for the detection of 16 Environmental Protection Agency (EPA) priority PAHs using AuNPs-grafted Fe_3O_4. The approach does not require expensive instrumentation or large sample volumes and was very useful for identification of hydrophobic molecules like PAHs. They have achieved a LOD value of 100–5 nM and applied the approach for the rapid screening of PAHs in river water samples. Moreover, they have used a portable Raman spectrometer, which will be beneficial for the on-site monitoring of PAHs (Du et al. 2016).

A magnetic *N*-doped carbon nanotube (CNT) has been reported by another group for the identification and detection of PAHs in environmental water samples. The determination was done by GC-MS technique and according to authors, the method is more efficient than the use of SPME with polydimethylsiloxane fiber (Menezes et al. 2015). Wang et al. have recently reported the synthesis of g-C_3N_4/Fe_3O_4 nanocomposite and applied it for the solid-phase extraction of PAHs in water samples. g-C_3N_4 has a stacked two-dimensional sheet-like morphology and is made from simple precursors under ambient conditions at a low cost. Moreover, this is known to be the most stable allotrope of carbon nitride of a great potential to be used in environmental applications. The method shows a LOD of 0.05–0.1 ng mL^{-1} towards the detection of PAHs with a precision in the range of 1.8–5.3%. The technique also gives a high recovery value of 80.0–99.8% from real sample analysis

(Wang et al. 2015c). A similar magnetic SPE method has been proposed by Zheng et al. also, where low-cost carbon nitride nanosheets were prepared by urea and applied for the magnetic SPE of PAHs from edible oil. The obtained recoveries of PAHs for spiked soybean oil samples ranged from 91.0 to 124.1%, with RSDs of less than 10.2% (Zheng et al. 2016).

Like g-C_3N_4, graphene is another carbonaceous material of a 2-D sheet-like structure with a high adsorption and electronic property. Graphene has also been clumped with MNPs to provide the magnetic graphene. The magnetic graphene possesses high surface area, high adsorption capacity and also facilitates easy magnetic separation after adsorption of any environmental pollutant. Mehdinia has reported the use of polythiophene as a surface modifier of magnetic graphene. The detection limits were in the range of 0.009–0.02 μg L^{-1} in the real matrix with a recovery value in the range of 83–107% (Mehdinia et al. 2015). AuNPs-based magnetic mesoporous silica nanoparticle has been reported for the liquid–liquid microextraction and determination of PAHs by Mehdinia et al. (2014). For the incorporation of AuNPs, magnetic MCM-41 (mesoporous carbon) was functionalized with 3-aminopropyltriethoxysilane, which then interacted with AuNPs through the amine group. The π-system of PAHs and immobilized AuNPs on the surface of the sorbent can cause the electron donor–acceptor interactions. The detection was linear in the range of 0.01–50 μg L^{-1} with the detection limit of 0.002–0.004 μg L^{-1} for PAHs. The method was successfully applied for the analysis of PAHs in seawater samples with recovery value ranging from 91.4 to 104.2%.

2.4.3 Carbonaceous Materials Based Extraction/Sensing Techniques

Carbonaceous nanomaterials are regarded as the most studied nanomaterials of this era. Different forms of carbon nanomaterials (e.g., graphene, carbon nanotube, carbon nanospheres, carbon dots) have been explored and applied in the various field of analysis and extraction. Among them, graphene and CNTs are treated as the revolutionary invention with potential usefulness in almost all research fields. Sometimes to enhance their efficacy, they are being modified with some other nanomaterials also. Like, for the detection of PAHs, Adegoke and Forbes reported a simple procedure for the preparation of L-cysteine-capped core/shell/shell CdSeTe/ ZnSe/ZnS quantum dot–graphene oxide (GO) nanocomposite (Fig. 9.6). Phenanthrene, anthracene, pyrene, and naphthalene were chosen as model PAHs and technique shows the LOD of 0.19 μg L^{-1} for phenanthrene under optimum conditions, while the LOD of anthracene, pyrene, and naphthalene were estimated to be 0.26 μg L^{-1} (Adegoke and Forbes 2016). Hou et al. have reported a bis (trifluoromethanesulfonyl)imide-based ionic liquid-grafted GO-coated SPME fiber for extraction and enrichment of PAHs from potatoes and phthalate esters food wrap. The method was simple in application and shows the LOD value of 0.015–0.025 μg L^{-1} for PAHs detection (Hou et al. 2016). In another literature, the authors have reported the selective and sensitive determination of PAHs using
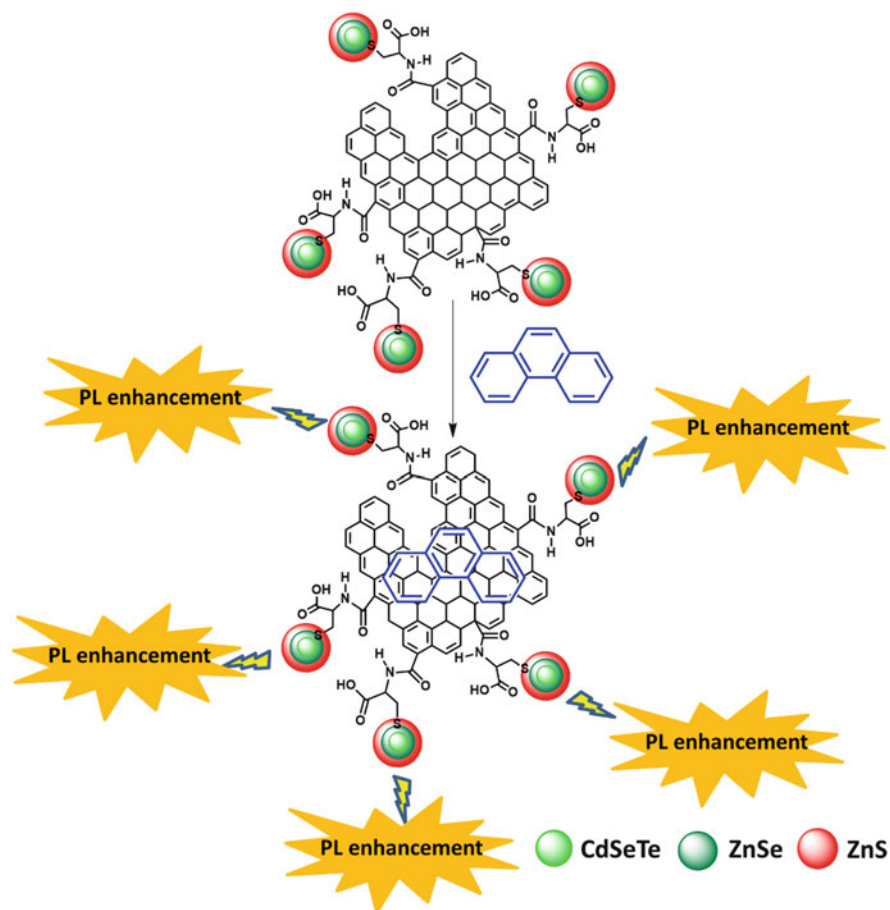
Fig. 9.6 Proposed fluorescence detection mechanism of phenanthrene using the QD-GO nanocomposite probe (Redraw with permission from Adegoke and Forbes 2016)

SPME and GC-MS technique in mainstream cigarette smoke. Graphene was used as a coating material for the SPME fiber. The prepared fiber has also been compared with commercially available 100-μm poly (dimethyl siloxane) (PDMS) fiber and found that graphene-based SPME fiber was advantageous than PDMS fiber in terms of their cleanup and pre-concentration efficiencies. The LODs and LOQs value of the selected 16 PAHs lies in between 0.02–0.07 and 0.07–0.22 ng/cigarette, respectively. The method was also advantageous in terms of their easy operation and good validation results (Wang et al. 2015d). A similar SPME fiber has also been reported for the extraction and detection of PAHs in cigarette smoke by Shi et al. (2015). This time, the authors have used GO-bound silica as SPE platform. The LODs and LOQs values were comparable as that of the previous one and were found in the range of 0.05–0.36 ng/cig and 0.17–1.19 ng/cig, respectively.

Besides GO, carbon nanotubes (CNTs) were also used for the analysis of PAHs. Han et al. have reported supercritical fluid extraction with CNTs as a solid collection trap for the analysis of PAHs. Fifteen typical PAH derivatives were selected for analysis and it was found that the material was most efficient trapping sorbent for the collection of PAHs and their nitro-, oxy- and alkyl-derivatives compared with liquid trapping and C18 solid-phase trapping. The method exhibited a recovery value of 62.9–111.8% for the real soil samples analysis with precisions [Relative standard deviation (RSD), intra-day] ranged from 1.9 to 13.7% (Han et al. 2015). Very recently, Mukhtar and See have reported the carbonaceous nanomaterials immobilized mixed matrix membrane microextraction technique for the determination of PAHs in sewage pond water samples. For the fabrication of carbonaceous materials, MWCNTs and single layered graphene nanoparticles were individually incorporated through dispersion in a cellulose triacetate polymer matrix. For the extraction, a small piece of the prepared membranes was dipped in the solution to initiate the analyte adsorption. After that, the analytes were desorbed by methanol and analyzed by HPLC. The LOD was in the range of 0.02–0.09 ng mL^{-1} with a pre-concentration factor of 54–100 for all PAHs (Mukhtar and See 2016).

2.4.4 Other Nano-sized Materials Based Extraction/Sensing Techniques

Besides noble metals, magnetic and carbonaceous nanomaterials, some other nano-sized materials have also been applied for PAH analysis. Very recently, Mauri-Aucejo et al. have reported the use of cyclodextrin-silica microporous composite for the determination of PAHs in water samples. SPE coupled with HPLC was chosen as the detection technique. Several parameters like amount of solid phase, the nature and volume of the eluent, and the sample volume and concentration were being evaluated, before their quantitative estimation. The quantification limits of the method were reported in the range of 0.09–2.4 μg L^{-1} (Mauri-Aucejo et al. 2016).

Titanium dioxide (TiO$_2$) nanoparticles are very popular for their excellent chemical and thermal stability, high corrosion-resistance, non-toxicity, low cost, and good biocompatibility. Over the past years, various size and shaped TiO$_2$ nanoparticles have been synthesized and applied in various research fields. Recently, Guo et al. have reported the preparation of phenyl-functionalized titanium dioxide-nanosheets for the analysis of PAHs in environmental water samples. Prior to the analysis, titanium dioxide-nanosheets were coated on a titanium wire for selective solid-phase microextraction of PAHs. The method exhibited high extraction capability, good selectivity, and rapid mass transfer for PAHs. The calibration graphs were linear over the range of 0.05–300 μg L^{-1} with the LOD of 0.008–0.043 μg L^{-1} (Guo et al. 2015). Another titania-based microextraction device was reported by Zhang et al. but here the analysis was performed by a coated-pore sintered titanium disk. Polydimethylsiloxane was used as the extraction phase and carcinogenic 16 types of polycyclic aromatic hydrocarbons were selected

as model analytes. The LODs and RSDs were found in the range of 0.06–3.20 ng L^{-1} and 0.57–7.08%, respectively (Zhang et al. 2016b).

2.4.5 Molecularly Imprinted Polymers (MIPs) Based Extraction/Sensing Techniques

MIPs are known to be a special class of polymers with a predetermined selectivity towards their target molecule (Patra et al. 2015). This phenomenon makes them useful materials in various fields like sensing, separation, drug delivery, etc. For the synthesis of MIPs, the monomer and templates (analytes) were taken simultaneously and after polymerization, the template molecules were extracted from the polymer matrix to leave a cavity selective and specific to that of the template molecule. For the synthesis of MIPs, selection of monomers, cross-linker, and the porogenic solvent is very important. For the polymerization, bulk polymerization, suspension polymerization, two-stage swelling, precipitation polymerization, and atom transfer radical polymerization techniques have been applied, in general. Due to the associated advantages, MIPs have also been applied for the extraction and determination of PAHs. Song et al. have reported the selective determination of 16 PAHs in seawater using MIP-based SPME technique and GC-MS was applied as the main detection technique. They have prepared the MIPs through non-covalent polymerization technique by using the 16 PAHs mixture as a template based on sol-gel surface imprinting process. They have also prepared same polymer matrix but with the absence of template molecules, termed as non-imprinted polymers (NIPs). Their as-prepared MIPs show a higher binding affinity (111.0–195.0 µg g^{-1}) than the NIPs with an imprinting factor of 1.50–3.12. With the high extraction efficiency of the MIPs, they can remove 93.2% PAHs from natural seawater. As a detection platform, they have achieved a LOD value of 5.2–12.6 ng L^{-1} (Song et al. 2012). An extraction technique by coupling GC-MS and MIPs together has also been reported for the sensitive determination of PAHs in ambient air dust. For their study, Chrysene (CHR), benzo[a]pyrene (BAP), benzo[b]fluoranthene (BBF), indeno[1,2,3-c,d]pyrene (ICP), and dibenzo[a,h]anthracene (DBA) were used as template molecules, 4-vinylpyridine as the functional monomer, ethylene glycol dimethacrylate (EGDMA) as the cross-linker, and 2,2′-azobis (2-isobutyronitrile) (AIBN) as the initiator. The recovery of PAHs from air dust was in the range of 85–97% with a detection limit of 0.15 ng L^{-1} (Krupadam et al. 2010). A similar extraction and determination method has been reported by Dravoba et al. for vegetable oil and tea samples (2012, 2013). In the first case, they have reached a recovery value of 70–99% with an LOQ of 0.1–0.3 µg kg^{-1} (Drabova et al. 2013). In the second case, they have reached a recovery value of 73–103% with an LOQ of 0.05–0.2 µg kg^{-1} (Drabova et al. 2012).

In bulk MIP, there is a general problem of template extraction, sometimes templates were not easily extracted from the polymer matrix. But in nano-sized MIPs, the surface-to-volume ratio increases, which overcome the problem associated with bulk MIP. Therefore, besides this bulk polymer matrix, some nano-sized

MIPs have also been fabricated to overcome the problem associated with bulk MIP. Chauhan et al. reported the preparation of nano-sized multi-template imprinted polymer for simultaneous extraction of PAHs using HPLC. For polymerization, they have used 1-naphthol, 9-phenanthrol, and 9-hydroxyfluorene as templates, methacrylic acid (MAA) as a monomer, EGDMA as a cross-linker, and AIBN as an initiator. The limit of detection (LOD) and limit of quantification (LOQ) value was much lower and was in the range of 0.33–2.6 and 0.99–8 ng mL^{-1} (Chauhan et al. 2015). Tiu et al. have reported the preparation of pyrene-imprinted polythiophene nanofilm by an electrochemical deposition method and used it for highly sensitive detection of pyrene and its analogues. The method shows good stability and reproducibility with a detected linear concentration range of 0.01–10 μM (Tiu et al. 2016). A molecularly imprinted titania microbead for the extraction of 1-hydroxy pyrene from urine using HPLC as detection technique has also been fabricated. As a typical synthesis process, they have prepared molecularly imprinted TiO_2 by polycondensation of titanium (IV) butoxide in the presence of the template, i.e., 1-hydroxy pyrene, and the resulting imprinted gel was deposited in the form of a thin film on a quartz support for the extraction and analysis of 1-hydroxy pyrene (Yang et al. 2016).

3 Volatile Organic Compounds (VOCs)

3.1 Source, Toxicity, Cause Behind Their Detection/ Extraction

In a simple definition, VOC can be defined as the organic chemicals with high vapor pressure at room temperature. Different kinds of VOCs can be found in the air, viz., alkanes, alkenes, alkynes, aromatic hydrocarbons, halogenated hydrocarbons, aldehydes, ketones terpenes, and alcohols (Kim et al. 2016). Maximum of them are toxic or carcinogenic, and therefore all of them have tolerance limit for their concentrations in the air. Because of their participation in photochemical reaction, especially the more reactive non-methane compounds are often regarded as precursors of ozone. They have a great influence on the tropospheric chemistry and can affect ozone formation (Chang and Chen 2008). Besides PAH, VOC can also be known as highly toxic materials mainly originated from the exhaust gas. Anthropogenic VOC sources include the combustion processes, the use of fossil fuels, solvents, industrial production processes, and biological processes. Robert Guicherit has previously carried out an extensive study to prove traffic as a source of VOCs in air (Guicherit 1997). Besides this, in residential or industrial areas, some other sources have been reported. The combustion of wood for cooking is known to emit several different VOCs (like halogenated hydrocarbons and oxygenated hydrocarbons) and other air pollutants. Pulp and paper manufacturing, biomass burning, industrial sources, and water treatment are the main global

anthropogenic sources of VOCs, while oceans, soil, termites, and microalgae are the main natural sources of these types of compounds. VOCs have been found to have serious toxic effects to the human body as that of PAHs. They may cause acute toxic effects (primarily neurological), cancer (such as leukemia), neurobehavioral effects, and adverse effects on the kidney (Mirzaei et al. 2016). The acute health effects associated with exposure to VOCs like benzene include muscle weakness, confusion dizziness, and incoordination. These effects mostly occur when their high concentration is present. In addition, they have also reported with the ophthalmic effects. The optic nerves may have been injured resulted from toluene as a metabolite. Toluene is the main cause behind the polyneuropathy in shoe factory workers. It is being reported that toluene in vapor phase has the ability to be absorbed rapidly from the lungs, and liquid toluene is taken up readily from the gastrointestinal tract, but poorly through the skin. Another VOC, xylene is responsible for the irritation to eyes, mucous membranes, and skin. These VOCs may cause sick building syndrome (SBS) also, which reported being associated with certain health issues like headaches, eye irritation, nausea, cough, etc. The concentration of toxic VOCs is low in motorcycle exhausted waste gas but it might affect the human health seriously due to long-term exposure and/or bioaccumulation (Mirzaei et al. 2016). Due to their high toxicity and adverse effects on health, major environmental safety agencies, like Environmental Protection Agency (EPA), National Institute of Occupational Safety and Health (NIOSH), and European Agency for Safety and Health at Work (EU-OSHA), have customized some guidelines regarding the limit of their exposure to human body in indoor and workplace. Therefore, from the perspective of air pollution control, the determination of these toxic VOCs is extremely crucial for taking actions that would be beneficial for our health. The effective methods to monitor VOCs in the complex matrix are in high demand for atmospheric environmental measurement and control as well as human well-being and health monitoring (Mirzaei et al. 2016).

3.2   Detection/Extraction of VOCs

Due to their widely reported heath hazardous effects, the detection of VOCs becomes a popular field. Numerous literatures have been reported towards their detection. Spectrophotometry, GC, and HPLC have been popularly applied for the quantification of VOCs. Initially, Xu et al. have reported a GC-MS-based method for the analysis of selected VOCs in Canada both in indoor and outdoor condition. The examined samples were collected in between September 2009 and December 2011 (Xu et al. 2016b). In another report, Vinci et al. have reported a headspace GC coupled to MS technique to study the occurrence of VOCs in foods purchased from the Belgian market and dietary exposure assessment. They have screened 377 food samples from the Belgian market and found the presence of 21 VOCs. The compounds with their respective percentages of occurrence were: chloroform (97%), toluene (95%), ethyl benzene (80%), o-xylene (79%), and benzene (58%)

(Vinci et al. 2015). Similarly, Cincinelli et al. have reported the analysis of VOCs in the libraries and archives in Florence (Italy). Among the detected VOCs, BTEXs (Benzene, Toluene, Ethylbenzene, Xylenes) being the most abundant, followed by cyclic volatile methylsiloxanes, aldehydes, terpenes, and organic acids (Cincinelli et al. 2016). An HPLC method was used for the determination of VOCs and others in mainstream cigarette smoke using a glass filter and a sorbent cartridge was reported recently. The sorbent cartridge was packed with Carboxen 572 (CX-572) and a Cambridge filter pad (CFP). For the determination, gaseous compounds collected with the CX-572 cartridge and total particulate matter (TPM) collected with the CFP are coeluted in the same vial and then analyzed by HPLC, GC-MS, and gas chromatograph–thermal conductivity detector (GC/TCD) (Uchiyama et al. 2015). These conventional methods and standard techniques have good accuracy and precision but suffer from some drawbacks like their cost, high power demand, lack of portability, and low throughput. Moreover, the use of such techniques sometime requires complex and time-consuming pretreatment steps and highly skilled operators also. The conventional method for monitoring the indoor VOCs is generally time-consuming and expensive because it requires on-site sampling of indoor air. This clearly suggests that this type of methods cannot be useful for the quantification of VOCs on a real-time basis. As we have discussed earlier, nanomaterials-based approach will be more advantageous and possess the opportunity for their real-time application in near future. Among the various nanomaterials used for sensing of VOCs, the metal oxide semiconductor materials are very popular in this field, which can be used to fabricate conductometric or resistive type devices. Here, the variation of electrical conductivity or resistivity of the sensitive element shows change or variation with a concentration of VOCs species, resulting in rapid and sensitive detection of these compounds (Table 9.2).

3.2.1 Noble Metal Nanoparticles Based Analysis

Some literatures have reported the use of noble metal-based nanoparticles in VOCs sensing. Like, Wang et al. have reported the preparation of unique $Au@In_2O_3$ core–shell nanostructure through a simple sol-gel method and applied for the selective detection of ethanol (Wang et al. 2015e). Another Au-loaded In_2O_3 nanofiber has also been reported for the sensing of ethanol. Here, electrospinning technique was applied for the fiber preparation. They have also changed the amount of Au during the fiber formation and compared their property for ethanol sensing. It was found that 0.2 wt.% Au-loaded In_2O_3 nanofiber shows the highest ethanol sensing property (Xu et al. 2011). Santhaveesuk et al. have also used AuNPs for VOCs sensing in combination with ZnO tetrapod sensor. They have also studied the enhancement of sensing performances after mixing of TiO_2. The synthesis was based on a simple thermal oxidation technique. The operating temperature was 260–360 °C with the ethanol concentration of 50, 100, 200, 500, and 1000 ppm (Santhaveesuk et al. 2010). Zhang et al. have reported the synthesis of Au-supported ZnO nanoplates and its applicability as ethanol sensor. They have also carried out a comparative gas

Table 9.2 List of nanosensors reported for the detection of VOCs

S.N.	Materials	VOCs	Concentration (ppm)	Temperature (°C)	Response time (s)	Recovery time (s)	Reference
1	Au@In$_2$O$_3$	Ethanol	100	160	4	2	Wang et al. (2015e)
2	Au-In$_2$O$_3$ nanofiber	Ethanol	500	140	12	24	Xu et al. (2011)
3	Au/TiZnO	Ethanol	50	240–340	–	–	Santhaveesuk et al. (2010)
4	Au/ZnO	Ethanol	5	300	13	–	Zhang et al. (2012)
5	Au/ZnO NW	Ethanol	100	380	5	6	Guo et al. (2014)
6	Au/ZnO NW	Ethanol	50	325	5	20	Ramgir et al. (2013)
7	AuPd-WO$_3$	Acetone	200	300	101	96	Kim et al. (2015)
8	In$_2$O$_3$/Au NRs	Acetone	50	250	10	18	Xing et al. (2015)
9	Au@SnO$_2$	Formaldehyde	50	RT	80	69	Chung et al. (2014)
10	Ag@SnO$_2$	Ethanol	200	RT	34	68	Wu et al. (2013)
11	Ag@TiO$_2$	Ethanol	<5	RT	52	63	Zhu et al. (2014)
12	Ag-TiO$_2$ nanobelts	Ethanol	500	200	1	2	Hu et al. (2010)
13	Ag@α-Fe$_2$O$_3$	Ethanol	100	250	5.5	16	Mirzaei et al. (2015)
14	CoFe$_2$O$_4$ NPs	Ethanol	50	150	50	60	Xiangfeng et al. (2006)
15	Ce-CoFe$_2$O$_4$ NPs	Acetone	2000	200	38	–	Khandekar et al. (2014)
16	Au-ZnO-Fe$_2$O$_3$	Acetone and n-butanol	100	225	57 and 113	–	Kaneti et al. (2015)
17	Hollow Fe$_2$O$_3$@SnO$_2$	Toluene	10	250	–	–	Zhang et al. (2013)
18	α-Fe$_2$O$_3$–Au nanospindles	Acetone	100	300	–	–	Zhang et al. (2011)
19	Nano-Fe$_2$O$_3$ films	Formaldehyde	100	320	–	–	Huang et al. (2013)
20	SnO$_2$/α-Fe$_2$O$_3$	Ethanol	10	250	1	–	Sun et al. (2014)
21	Fe$_3$O$_4$–NiO core–shell	Toluene	100	280	27	–	Qu et al. (2014)
22	SmFeO$_3$ NPs	Toluene	3	400	–	–	Mori et al. (2014)

23	3-D aloe-like SnO_2	Ethanol	50	285	1.2	76	Mei et al. (2012)
24	ZnO NW	Ethanol	1500	300	–	–	Hsueh et al. (2007)
25	PdO-decorated ZnO	Ethanol	100	320	1	7	Lou et al. (2013)
26	Pd-Ce-SnO_2	Ethanol	100	250	6	20	Bagal et al. (2015)
27	SnO_2@ZnO	Ethanol	400	400	–	–	Singh and Singh (2012)
28	MWCNTs-doped SnO_2	Formaldehyde	50	250	–	–	Wang et al. (2008)
29	Wormlike SnO_2	n-butanol	5	150	–	–	Wang et al. (2014)
30	Flower-shaped SnO_2	n-butanol	100	240	–	–	Huang et al. (2010)
31	ZnO-Graphene	Acetylene	100	250	100	24	Uddin and Chung (2014)
32	V_2O_5 NW microyarns	Ethanol	1000	330	–	–	Jin et al. (2015)
33	Sparked In_2O_3 films	Acetone	20,000	350	–	–	Inyawilert et al. (2014)

sensing studies between pristine ZnO and Au/ZnO nanoplates in order to investi-
gate the effect of Au nanoparticles on the sensor performance. The results demon-
strated that the Au/ZnO nanoplate sensor has the faster response and recovery
compared to the pristine ZnO sensor. The response time was 13 s for Au/ZnO
nanoplates, whereas, for pristine ZnO, it was 135 s (Zhang et al. 2012). ZnO
nanowires functionalized by AuNPs have been reported as a high-performance
ethanol sensor. In a typical synthesis procedure, AuNPs were successfully
immobilized onto the surface of ZnO nanorods by a facile solution reduction
process to serve as a sensitizer. The material was able to detect ethanol in a wide
concentration range and a high response, fast recovery time with good selectivity
and repeatability (Guo et al. 2014). A similar ethanol sensor has also been reported
by Ramgir et al. using Au and ZnO nanowire nanocomposites. For the synthesis of
desired material, they have modified the hydrothermally grown zinc oxide (ZnO)
nanowires network with thin Au layer ($\sim$10 nm). The reported response and
recovery times for Au-modified sensor films at 325 °C towards 50 ppm of ethanol
were found to be 5 and 20 s, respectively. This faster reaction kinetics was mainly
due to the role of Au in improving the sensing properties as per the electronic
sensitization mechanism and its nano-Schottky barriers type junction with ZnO
(Ramgir et al. 2013). Besides the ethanol, AuNPs have also been applied for
acetone sensing. Au- and Pd-decorated WO_3 nanorods have been employed as an
efficient acetone sensor. In a typical synthesis procedure, they have immersed the
prepared WO_3 nanorods in the mixture of acetone (25 mM), $HAuCl_4$ (25 mM) and
$PdCl_2$ solution followed by UV irradiation and annealing. The material exhibited a
far stronger response to acetone gas (Kim et al. 2015). Xing et al. have prepared a
series of In_2O_3/Au nanorods (AuNRs) and studied their gas sensing property. The
morphology of the prepared In_2O_3/Au nanorods has been shown in Fig. 9.7a, b, and
c with the selected area electron diffraction pattern (SAED) in the inset. All the
images suggested a rod-like morphology. The detection limit was found as 0.1 ppm
for acetone and 0.05 ppm for ethanol. In Fig. 9.7d, e, In_2O_3/Au NRs and pure In_2O_3
gas sensors response curves have been shown. For acetone, the concentrations were
0.1–50 ppm at 250 °C and for ethanol concentrations 0.05–650 ppm at 400 °C,
respectively. In the plot, the dots represent the experimental data and the straight
lines are representing the linear fitting functions. As an interesting study, In_2O_3/
AuNRs gas sensor can clearly distinguish the acetone and ethanol biomarkers in
human breath by humidity compensation method (Xing et al. 2015). Chung et al.
have prepared $Au@SnO_2$ core–shell nanostructure by sol-gel method and applied it
for the detection of formaldehyde at room temperature. The response and the
recovery times were reported as the 80 s and 62 s, respectively (Chung et al. 2014).

Besides gold, silver has also been used for the detection of VOCs by coupling
with metal oxides nanoparticles. Here we will discuss some earlier reported
approaches using silver-based metal oxide nanostructures for VOCs detection.
Wu et al. have prepared a nanocomposite core–shell $Ag@SnO_2$ material using
chemical reduction and carried out a comparative study to prove that core–shell
nanostructure is superior sensing material than normal nanohybrid. The material
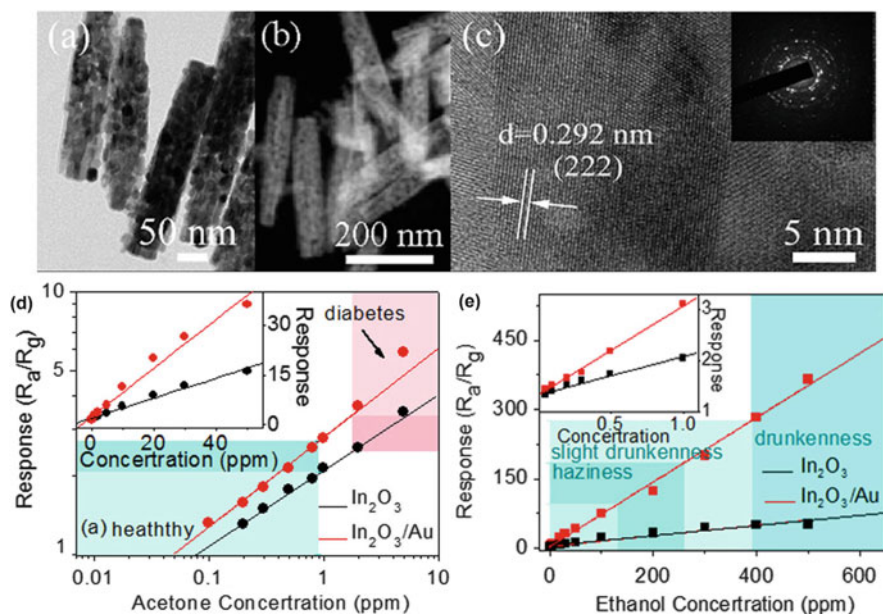
Fig. 9.7 (**a**) FE-TEM, (**b**) STEM, (**c**) HR-TEM image and SAED (inset of **c**) of In_2O_3/Au NRs sample, In_2O_3/Au NRs and pure In_2O_3 gas sensors response curves to different (**d**) acetone concentrations (0.1–50 ppm) at 250 °C and (**e**) ethanol concentrations (0.05–650 ppm) at 400 °C. The dots are experimental data and the *straight lines* are the linear fitting functions (Reproduced with permission from Xing et al. 2015)

shows a better sensor response towards ethanol detection with shortening response time (38 s) and recovery time (68 s). According to the authors, the sensing mechanism is based on its effective adsorption, the reaction on the surface and its fast desorption (Wu et al. 2013). Similarly, an Ag@TiO$_2$ core–shell nanoparticles based ethanol sensor has also been reported. The ethanol detection laboratory equipment diagram with its various parts is shown in Fig. 9.8. The sensor was reported to detect ethanol in the concentration range of 0.15–5 ppm. The sensor was reported to have very good selectivity and stability for ethanol gas (Zhu et al. 2014). Similarly, TiO$_2$ nanobelts based Ag-TiO$_2$ heterostructure has also been reported as ethanol sensor. For this, first TiO$_2$ nanobelt was prepared by hydrothermal method and was conjugated with silver by photo-reduction. The sensor performance towards ethanol vapor was examined and compared to electrical conductivity measurements at varied temperatures. The sensing mechanism was interpreted by surface depletion model (Hu et al. 2010).
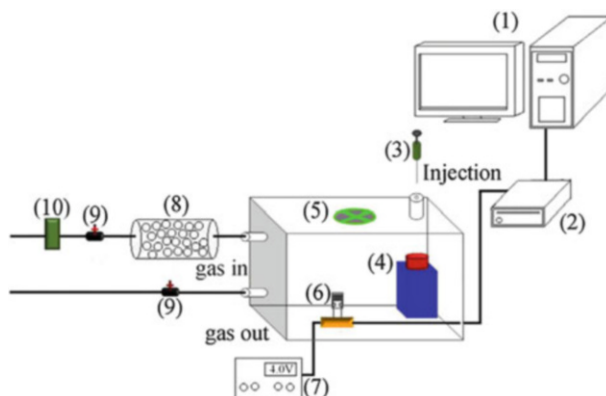
Fig. 9.8 Schematic representation showing the ethanol detection laboratory equipment diagram: (1) computer, (2) data acquisition system, (3) liquid injection, (4) heater, (5) fan, (6) sensing film, (7) power supply, (8) drying tube, (9) gas control valve, and (10) gas pump (Reproduced with permission from Zhu et al. 2014)

3.2.2 Magnetic Metal Oxide Nanostructures Based Analysis

The popular among all metal oxide nanostructure, the magnetic nanoparticles are very useful material in sensing and extraction of any compound. Several literatures have been reported to exhibit the use of magnetic nanohybrids for the analysis of VOCs. Recently, silver and iron oxide nanoparticles based core–shell structures have been reported as a gas sensing platform. The synthesis was based on two-step reduction sol-gel approach, where first AgNPs were synthesized using sodium borohydride as reducing agent and subsequently mixed with a Fe (III) sol for α-Fe_2O_3 coating. The material shows a better sensing performance than pristine α-Fe_2O_3 (Mirzaei et al. 2015). It is well known that spinel magnetic nanostructures are being prepared to improve the property of normal Fe_3O_4 nanostructure. Xiangfeng et al. have reported a hydrothermal technique for the preparation of $CoFe_2O_4$ nano-crystallines and applied for the ethanol sensing. The sensor was very useful for a trace amount of ethanol sensing and was also applied for the detection of triethylamine, when no ethanol was present in the atmosphere (Xiangfeng et al. 2006).

As we know, doping has a great ability to improve the performance of any nanostructure. Some literature has also reported the use of doped spinel structure for VOCs sensing. Very recently, Khandekar et al. have reported the preparation of Ce-doped $CoFe_2O_4$ nano-crystallines structure and study their gas sensing property towards reducing gases like liquefied petroleum gas (LPG), acetone, ethanol, and ammonia at 200–450 °C. As a research finding, they have reported that the material was sensitive and selective towards acetone as compared to other reducing gases (Khandekar et al. 2014). Besides this spinel structure, ZnO, SnO_2, and AuNPs modified MNPs for acetone sensing have also been reported extensively in the literature. Among them, recently Kaneti et al. have reported Au, ZnO, and Fe_2O_3 based magnetic nanocomposite for the detection of acetone and *n*-butanol. The

synthesis procedure was based on the hydrothermal approach and further surface coating by Au and ZnO. The comparative study also demonstrated that the ternary nanocomposite has the highest sensing ability than the binary and single α-Fe$_2$O$_3$. Higher sensitivity/response in ternary nanocomposite was observed towards the detection of acetone and *n*-butanol. The optimum temperature was also found very lower, i.e., ~225 °C, compared to the earlier reported methods. Chemical sensitization effect induced by the AuNPs is the main cause of their enhanced sensitivity, and the existence of conjugated depletion layers in the nanocomposites promotes a greater drop in resistance upon exposure to the gas (Kaneti et al. 2015). Similarly, Zhang et al. have reported the controlled synthesis of recyclable core–shell γ-Fe$_2$O$_3$@SnO$_2$ hollow nanoparticles of a high photocatalytic and gas sensing property. The synthesis technique was based on a low-cost and environmentally friendly seed-mediated hydrothermal method. First γ-Fe$_2$O$_3$ hollow NPs were synthesized by a template-free method and then they were used as a core for the growth of SnO$_2$ shells. By controlling the reaction time, the thickness of the shell can also be monitored. From the combination of a magnetic semiconductor like γ-Fe$_2$O$_3$ and wide band-gap semiconductor like SnO$_2$, it can be expected that the material will show an enhanced sensing performance. They demonstrated fast response and recovery rates, which imply their applicability as promising materials for gas sensors (Zhang et al. 2013). AuNPs-functionalized α-Fe$_2$O$_3$ nanospindles were prepared for enhanced gas sensing property and catalytic activity. The sensing property was much higher than pristine α-Fe$_2$O$_3$, which proves the effect of AuNPs on sensing ability once again (Zhang et al. 2011). Another literature has reported the use of Au, α-Fe$_2$O$_3$ and SnO$_2$ hybrid structures as an enhanced gas sensing material. The hybrid structure was made of α-Fe$_2$O$_3$ nanospindles as the core and Au-decorated SnO$_2$ coating as the shell. The higher gas sensing performances by means of their higher sensitivity and faster response-recovery were mainly due to special architectures and multiple compositions (Liu et al. 2012). Similarly, to increase the gas sensing property, nanocomposite of α-Fe$_2$O$_3$ and SnO$_2$ has also been reported in the literature. It was found that the ethanol sensing property was much higher in SnO$_2$/α-Fe$_2$O$_3$ than normal SnO$_2$ nanoparticles. Their study further demonstrated that the double shell structure was superior as a sensor than the single shell structure. At an ethanol concentration of 100 ppm, the response of nanocomposite was reported as 16 s, which is almost two times higher than normal SnO$_2$ nanoparticles. The response time for 10 ppm ethanol was reported to as low as 1 s at a temperature of 250 °C (Sun et al. 2014).

Besides the applicability of nanocomposite for ethanol and acetone sensor, they have also been applied as a potential sensing platform for formaldehyde, toluene, benzene, methanol, propanol, and butanol. In the year 2013, an in situ diffuse reflectance infrared Fourier transform spectroscopic study for the formaldehyde adsorption and reactions on nano-Fe$_2$O$_3$ films was reported by Huang et al. The method was simple in operation and the sensor fabrication was based on screen-printing technology (Huang et al. 2013). Another core–shell nanocomposite based on magnetic nanoparticles and NiO was prepared by a facile hydrothermal method in water-ethanol-butanol solvent without any templates. The morphological study

demonstrated that the porous architectures were assembled from Fe_3O_4 sphere core and NiO flower-like shells. The nanocomposite was applied as a chemical gas sensor for toluene detection. The sensor shows a high response, superior selectivity, and rapid response recovery towards toluene determination (Qu et al. 2014). Mori et al. have reported a perovskite-type $SmFeO_3$ oxide, a p-type semiconductor as a chemoresistive sensor material for VOC detection. For sensor fabrication, the $SmFeO_3$ particles were deposited on a comb-type Pt electrode printed on an alumina substrate. They have studied 15 kinds of VOCs (namely, methanol, ethanol, propanol, butanol, acetic acid, propionic acid, methyl acetate, ethyl acetate, acetone, methylethylketone, benzene, toluene, xylene, ethyl benzene, and chlorobenzene) using a single format sensing device. The concentrations were below 10 ppm and operating temperature was in the range of 350–500 °C. It was reported that the resistance of the sensor increased after the contamination of referenced air with the selected VOCs, which is used as sensing platform (Mori et al. 2014).

3.2.3 Other Metal Oxide Nanostructures Based Analysis

It can be found that among all the metal oxide nanostructures, SnO_2- and ZnO-based nanostructures have shown the most promising sensing performances towards the detection of VOCs. The shape is a useful characteristic towards the sensing property of a material. With the change in shape, an enormous change can be observed within a material. In addition to their combination with MNPs, their other 3-D structures and nanocomposites were also employed for VOCs sensing. Mei et al. have reported the synthesis of 3-D aloe-like SnO_2 nanostructures using a simple hydrothermal method. The aloe-like FESEM images are shown in Fig. 9.9. The developed sensor from this 3-D aloe-like SnO_2 can detect ethanol, even if the concentration is as low as 50 ppb at 285 °C with high sensitivity. The low ethanol concentration can be explained by the less agglomerative and thinner structure of aloe-like SnO_2 nanoparticles, together with the modulation of the conductance by the small nanosheets (Mei et al. 2012). Mesoporous wormlike SnO_2 nanostructure was employed as a highly selective sensor for n-butanol. The nanostructure was prepared using a simple combination of hydrothermal and annealing process, in the presence of various amount of soluble starch. The pore diameter of as-prepared SnO_2 nanostructure was reported as 6–15 nm and the modified sensor shows a linear detection limit in the range of 5–100 ppm (Wang et al. 2014). Huang et al. reported a flower shape SnO_2 nanostructure and applied as ethanol and 2-butanol sensor. The flower-like structures exhibited a good response and reversibility towards both the analytes. The sensor response at a concentration of 100 ppm ethanol and n-butanol was reported to be 42.6 s and 77.2 s, respectively, at a working temperature of 240 °C (Huang et al. 2010).

As that of SnO_2, laterally grown ZnO nanowires were also employed as ethanol sensor. According to their research findings, the growth direction of the ZnO nanowires was strongly depends on growth parameters and as an ethanol sensing

Fig. 9.9 FESEM images showing the morphological images of 3-D aloe-like SnO$_2$ nanostructures at (**a**) low and (**b** and **c**) high magnifications (Reproduced with permission from Mei et al. 2012)
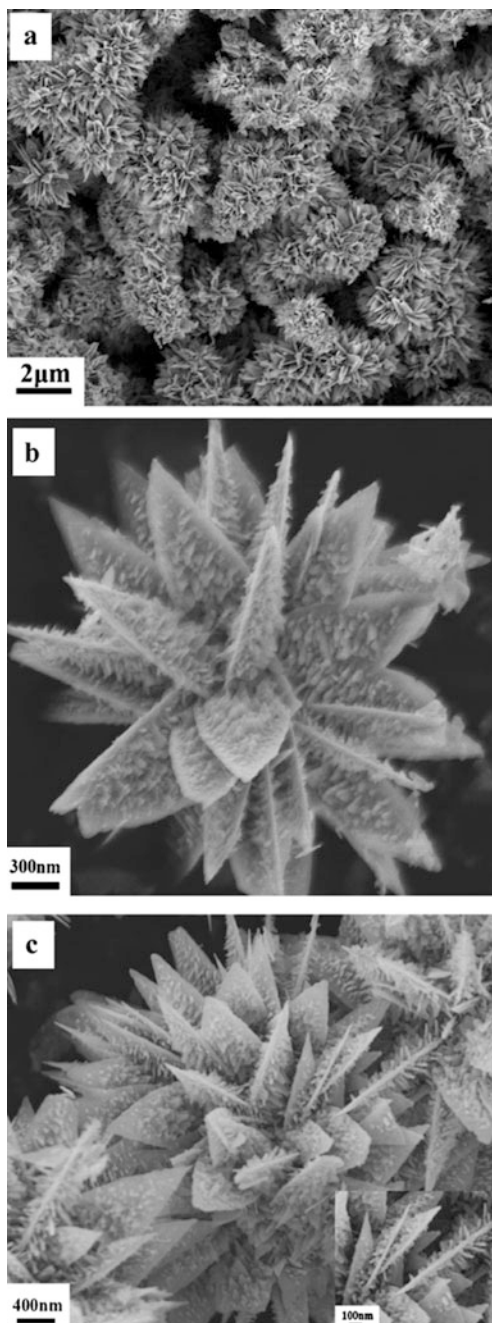
Fig. 9.10 FESEM images of flower-like ZnO and PdO-ZnO structures: (**a** and **c**) lower magnification; (**b** and **d**) higher magnification (Reproduced with permission from Lou et al. 2013)

platform, the resistivity of the reported sensor decreased upon ethanol gas injection (Hsueh et al. 2007). Similarly, flower-like pristine ZnO and PdO-decorated ZnO was prepared by a surfactant-free hydrothermal route and subsequent heat treatment. They have reported that PdO-ZnO based sensor displays the response for 100 ppm for heptane and ethanol. The FESEM and TEM images have been shown in Figs. 9.10 and 9.11, which clearly represent the flower-like morphology. The schematic diagram of the gas sensing mechanism has been shown in Fig. 9.12. The response was about 4–5 times higher than that of pristine ZnO at the optimal operating temperature of 240 and 320 °C (Lou et al. 2013). Bagal et al. have reported the effect of Pd and Ce doping on SnO_2 nanostructure for the sensing of ethanol. The amount of Pd and Ce was optimized and the prepared nano-crystalline powders were screen printed on the alumina substrates to form thick films, which were further used as a gas sensing platform. The material shows a quick response (6 s) and recovery (20 s) towards ethanol detection at an operating temperature of 250 °C (Bagal et al. 2015).

To increase the ethanol sensing response, combination of ZnO and SnO_2 was also employed. For this, first zinc oxide was synthesized by a chemical route and then deposited on an alumina substrate and lastly activated by tin dioxide (obtained by on-site oxidation of tin chloride) (Singh and Singh 2012). Similarly, a multiwalled carbon nanotube-doped SnO_2 sensor was also reported for the detection of low concentration of formaldehydes. For this type of low-level detection, they have employed an enrichment method with active carbon. The as-prepared nanocomposite was able to detect 0.03 ppm of formaldehyde (Wang et al. 2008). ZnO nanoparticles in combination with graphene oxide were used as acetylene
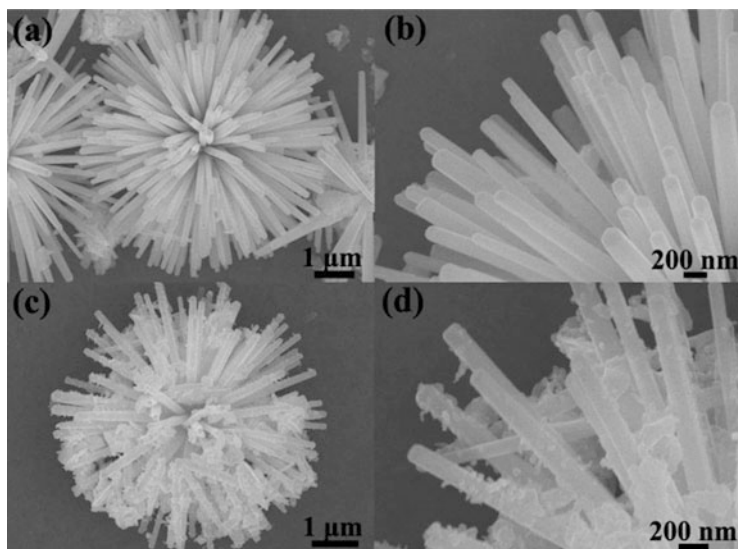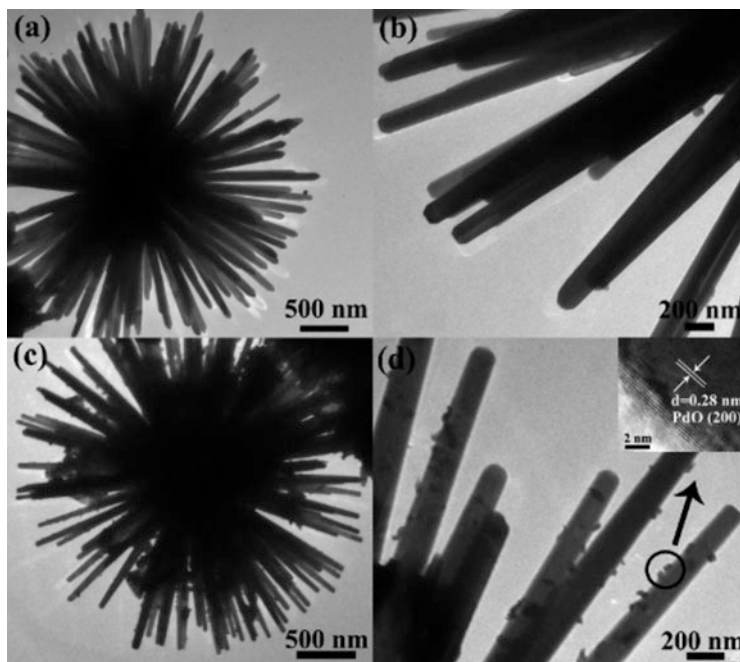
Fig. 9.11 TEM images of flower-like ZnO and PdO-ZnO structures: (**a** and **c**) low magnification and (**b** and **d**) high magnification (Reproduced with permission from Lou et al. 2013)
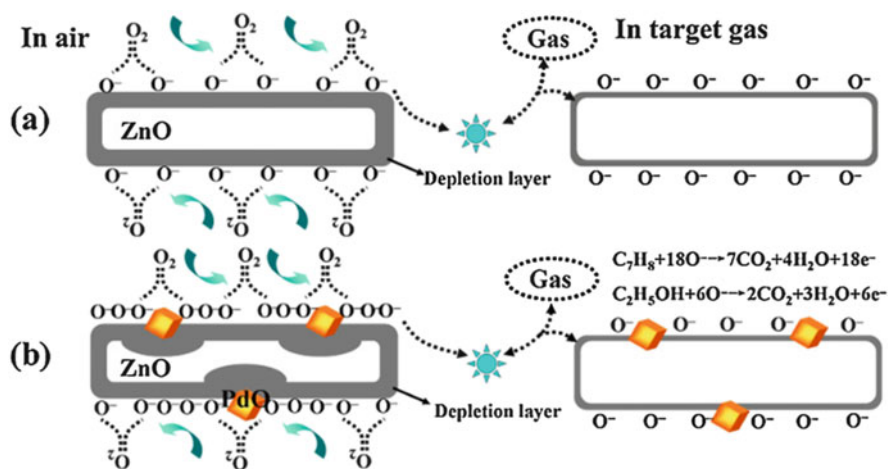
Fig. 9.12 Schematic diagrams on the gas sensing mechanism of (**b**) flower-like ZnO and (**c**) PdO-decorated ZnO structures (Reproduced with permission from Lou et al. 2013)

sensor. The material shows a maximum sensor response value of 143 for 1000 ppm acetylene at 250 °C with an optimized material ratio of ZnO and rGO (4:1). It was also concluded that improvement in sensor ability is mainly due to the incorporation of graphene (Uddin and Chung 2014). Besides ZnO and SnO_2 nanostructure, TiO_2 is equally useful material for gas sensing, therefore, also applied for VOCs detection, either individually or in combination with other nanoparticles. Recently, TiO_2 nanotubes have been synthesized and employed as a sensing material for ethanol (Kılınç et al. 2011). For the preparation of nanotubes, Ti thin films were anodized in a mixture of aqueous hydrofluoric acid (HF) (0.5 wt. %) and polar organic (0.5 wt.% NH_4F + ethylene glycol) electrolytes. The anodization potential was in between 5 and 20 V for HF and 20 and 60 V for polar organic electrolytes. As a sensing material, TiO_2 nanotubes show very high sensitivity towards VOCs in an operating temperature of 200 °C. Another report can be found in literature where TiO_2 nanotubular films were used as an improved VOC sensing material. It was reported that the prepared nanomaterial shows an improvement in sensing response and selectivity to toluene (50 ppm), after the ball-milling treatment for 3 h at the operating temperature of 500 °C. But, when the ball-milling treatment time was increased, it was unable to further enhance the original sensor response, which may cause a decrease in the porosity of the film (Seo et al. 2011).

One-dimensional vanadium oxide nanostructure is one of the potential gas sensing oxides and has applied by many researchers. For example, Jin et al. have reported the preparation of ordered V_2O_5 nanowire microyarns for the detection of ethanol, methanol, ammonia, and toluene. The response of the yarns shows a maximum value of 9.09–1000 ppm for ethanol at 330 °C. The finding value was around 3.5 times higher than that of other nanowires. On the contrary, the material shows a very little response towards methanol, ammonia and toluene; conclude the potential usefulness of V_2O_5 nanowire microyarns in selective sensing of ethanol (Jin et al. 2015). It is reported that one-dimensional (1D) metal oxide semiconductors nanostructures based sensors could exhibit excellent sensitivity to the detected gases. Among all the 1D metal oxides, much attention has been paid for the preparation of 1D In_2O_3 nanostructures such as nanowires, nanorods, nanotubes, and nanofiber mainly owing to their interesting optical and electrical properties. Driven by their advantageous effects, Zheng et al. have reported the preparation of In_2O_3 nanofibers with diameters of around 60 nm by electrospinning method. For electrospinning, they have used a solution of polyvinyl pyrrolidone and indium nitrate, which was further calcined at 700 °C in air. The as-prepared In_2O_3 nanofibers showed selectivity, fast response and recovery time towards ethanol gas (Zheng et al. 2009). In another report, sparked In_2O_3 sensing film was used for the VOCs sensing. For the preparation of sparked In_2O_3, two indium wires were sparked and scanned repeatedly above Al_2O_3 substrates. The Al_2O_3 substrates were well equipped with Au interdigitated electrodes at a sparking voltage of 4.5 kV for 10–200 cycles. The material was applied for the detection of ethanol and acetone within a concentration range of 50–1000 ppm and 100–2000 ppm, respectively, at 200–350 °C. The material was very useful as ethanol and acetone detectors for drunken driving detection and diabetes diagnosis (Inyawilert et al. 2014). Besides

the use of normal In_2O_3 nanostructures, other metal-based nanocomposites have also been reported. Recently, Karmaouni et al. have reported Pt-decorated In_2O_3 nanoparticles and applied it for the detection of acetone. The material was found very sensitive towards acetone and shows the LOD value of 10 ppb or less (Karmaoui et al. 2016). Mixture of indium and tin oxide (i.e., indium tin oxide, ITO) was also reported as an efficient toluene sensor in a current study (Vaishnav et al. 2015). The sensing mechanism was based on the redox reaction on the surface of ITO film. The sensor was very much sensitive and selective towards toluene with a linear detection range of 10–1000 ppm.

3.2.4 Molecularly Imprinted Materials Based Analysis

As we discussed earlier, MIP-based sensing devices are most popular in terms of their high selectivity. Due to their high selectivity, they are also termed as an artificial antibody or plastic antibody. MIPs as sensing material for VOCs are also reported in the literatures. Mostly ethanol, toluene, or acetone was used as template or target analytes during the MIP synthesis. Tan et al. have used a SnO_2-based MIP for the detection of ethanol. As expected, the material was highly selective towards ethanol (Tan et al. 2015a). Another SnO_2-based gas sensor for the detection of acetone was also reported, very recently. The method was optimized for the smooth adsorption and desorption of acetone gas (Tan et al. 2015b). In another report, ethanol sensing device was prepared by mixing MIP as recognition element, MWCNTs as conducting element, and poly(methyl methacrylate) (PMMA) as an adhesive substance. The sensor was very much selective and shows a good response towards ethanol with a response time ~1 min. The sensor was able to detect ethanol within a concentration range of 0.65–45.00 ppm with a LOD value of 0.5 ppm (signal to noise ratio = 3) (Alizadeh and Rezaloo 2013). A polymer membrane ion selective electrode based potentiometric sensing system for sensitive and selective determination of neutral vapors in the gas phase using MIP as a selective detection platform was also reported. For this, the MIP was incorporated into the membrane for selective adsorption of the analyte vapor from the gas phase into the sensing membrane phase. To study the change in MIP binding site, an indicator was used, which will have a similar structure as that of the selected analyte. In their report, they have used toluene as a model analyte and benzoic acid as the indicator. The sensing setup has been shown in Fig. 9.13. They were able to detect toluene up to parts per trillion level (Liang et al. 2015).

4 Conclusion and Future Scope

The sources, contamination, hazardous effects, various detection and extraction techniques of hydrocarbons have been presented in this chapter. The chapter comprises the efforts made by researchers in the past few years for the detection
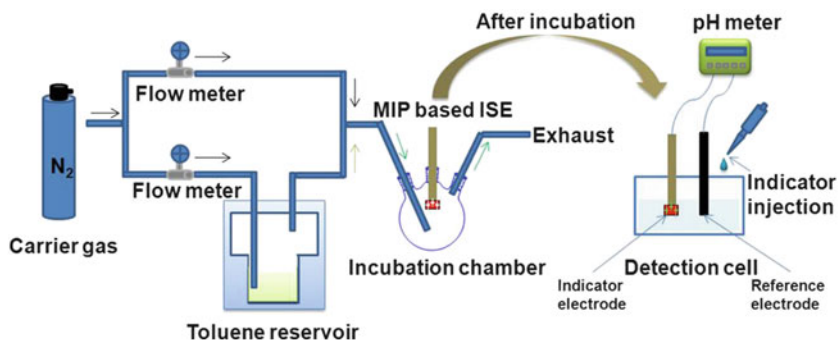
Fig. 9.13 Experimental setup for potentiometric detection of the toluene vapor (Reproduced with permission from Liang et al. 2015)

and extraction of two major toxic hydrocarbons (i.e., polycyclic aromatic hydrocarbons and volatile organic compounds) formulating the innovative and simpler way. The growing contamination of air, soil, and water samples from these types of hydrocarbons becomes major concern of these days. They are entering into the human and animal body through breathing, food, and water samples. Much development has been made so far for the preparation of nanosensor for their detection. But still, there is a need for more research to extend these sensors at the level of real-time applications in future. The reported techniques lack the feature of selectivity and much research has to be carried out for improving their detection limit in the range of parts per trillion or low. There is a high need for an efficient device for their trace level on-field detection by which we can efficiently detect the amount of atmospheric hydrocarbon level. In addition, some selective adsorbents with a high efficiency are also needed for their removal from atmosphere, soil or water samples, so that we can get a pollution-free earth in upcoming days.

Reference

Abdel-Shafy HI, Mansour MSM (2016) A review on polycyclic aromatic hydrocarbons: source, environmental impact, effect on human health and remediation. Egypt J Pet 25:107–123

Adegoke O, Forbes PBC (2016) L-Cysteine-capped core/shell/shell quantum dot–graphene oxide nanocomposite fluorescence probe for polycyclic aromatic hydrocarbon detection. Talanta 146:780–788

Akhbarizadeh R, Moore F, Keshavarzi B, Moeinpour A (2016) Aliphatic and polycyclic aromatic hydrocarbons risk assessment in coastal water and sediments of Khark Island, SW Iran. Marine Poll Bull 108:33–45

Alizadeh T, Rezaloo F (2013) A new chemiresistor sensor based on a blend of carbon nanotube, nano-sized molecularly imprinted polymer and poly methyl methacrylate for the selective and sensitive determination of ethanol vapour. Sens Actuators B 176:28–37

Armstrong BG, Hutchinson E, Unwin J, Fletcher T (2004) Lung cancer risk after exposure to polycyclic aromatic hydrocarbons: a review and meta-analysis. Environ Health Perspect 112:970–978

Bach PB, Kelley MJ, Tate RC, McCrory DC (2003) Screening for lung cancer: a review of the current literature. Chest 123:72–82

Bagal LK, Patil JY, Vaishampayan MV, Mulla IS, Suryavanshi SS (2015) Effect of Pd and Ce on the enhancement of ethanol vapor response of SnO_2 thick films. Sens Actuators B 207:383–390

Beegle LW, Wdowiak TJ, Harrison JG (2001) Hydrogenation of polycyclic aromatic hydrocarbons as a factor affecting the cosmic 6.2 micron emission band. Spectrochim Acta A 57:737–744

Bian Q, Alharbi B, Collett J Jr, Kreidenweis S, Pasha MJ (2016) Measurements and source apportionment of particle-associated polycyclic aromatic hydrocarbons in ambient air in Riyadh, Saudi Arabia. Atmos Environ 137:186–198

Bostrom CE, Gerde P, Hanberg A, Jernstrom B, Johansson C, Kyrklund T, Rannug A, Tornqvist M, Westerholm R, Victorin K (1999) Cancer risk assessment, indicators and guidelines for polycyclic aromatic hydrocarbons (PAH) in the ambient air. Swedish Environmental Protection Agency, Stockholm

Cai Y, Yan Z, Van MN, Wang L, Cai Q (2015) Magnetic solid phase extraction and gas chromatography–mass spectrometrical analysis of sixteen polycyclic aromatic hydrocarbons. J Chromatogr A 1406:40–47

Cai Y, Yan Z, Wang L, Van MN, Cai Q (2016) Magnetic solid phase extraction and static headspace gas chromatography–mass spectrometry method for the analysis of polycyclic aromatic hydrocarbon. J Chromatogr A 1429:97–106

Chang C-T, Chen B-Y (2008) Toxicity assessment of volatile organic compounds and polycyclic aromatic hydrocarbons in motorcycle exhaust. J Hazard Mater 153:1262–1269

Chauhan A, Bhatia T, Singh A, Saxena PN, Kesavchandran C, Mudiam MKR (2015) Application of nano-sized multi-template imprinted polymer for simultaneous extraction of polycyclic aromatic hydrocarbon metabolites in urine samples followed by ultra-high performance liquid chromatographic analysis. J Chromatogr B 985:110–118

Chung F-C, Wu R-J, Cheng F-C (2014) Fabrication of a $Au@SnO_2$ core–shell structure for gaseous formaldehyde sensing at room temperature. Sens Actuators B 190:1–7

Cincinelli A, Martellini T, Amore A, Dei L, Marrazza G, Carretti E, Belosi F, Ravegnani F, Leva P (2016) Measurement of volatile organic compounds (VOCs) in libraries and archives in Florence (Italy). Sci Total Environ 572:333–339

Conde J, Doria G, Baptista P (2012) Noble metal nanoparticles applications in cancer. J Drug Deliv 1–12. doi:10.1155/2012/751075.

Devi NL, Yadav IC, Shihua Q, Dan Y, Zhang G, Raha P (2016) Environmental carcinogenic polycyclic aromatic hydrocarbons in soil from Himalayas, India: implications for spatial distribution, sources apportionment and risk assessment. Chemosphere 144:493–502

Dewulf J, Langenhove HV (2009) Hydrocarbons in the atmosphere. In: Sabljic A (ed) Environmental and echological chemistry, vol II. Unesco, France, pp 1–23

Drabova L, Pulkrabova J, Kalachova K, Tomaniova M, Kocourek V, Hajslova J (2012) Rapid determination of polycyclic aromatic hydrocarbons (PAHs) in tea using two-dimensional gas chromatography coupled with time of flight mass spectrometry. Talanta 100:207–216

Drabova L, Tomaniova M, Kalachova K, Kocourek V, Hajslova J, Pulkrabova J (2013) Application of solid phase extraction and two-dimensional gas chromatography coupled with time-of-flight mass spectrometry for fast analysis of polycyclic aromatic hydrocarbons in vegetable oils. Food Control 33:489–497

Du J, Jing C (2011) Preparation of Thiol modified $Fe_3O_4@Ag$ magnetic SERS probe for PAHs detection and identification. J Phys Chem C 115:17829–17835

Du J, Xu J, Sun Z, Jing C (2016) Au nanoparticles grafted on Fe_3O_4 as effective SERS substrates for label-free detection of the 16 EPA priority polycyclic aromatic hydrocarbons. Anal Chim Acta 915:81–89

Fernández-Amado M, Prieto-Blanco MC, López-Mahía P, Muniategui-Lorenzo S, Prada-Rodríguez D (2016) A novel and cost-effective method for the determination of fifteen polycyclic aromatic hydrocarbons in low volume rainwater samples. Talanta 155:175–184

Gu H-X, Hu K, Li D-W, Long Y-T (2016) SERS detection of polycyclic aromatic hydrocarbons using a bare gold nanoparticles coupled film system. Analyst 141:4359–4365

Guerrini L, Garcia-Ramos JV, Domingo C, Sanchez-Cortes S (2009) Sensing polycyclic aromatic hydrocarbons with dithiocarbamate-functionalized ag nanoparticles by surface-enhanced Raman scattering. Anal Chem 81:953–960

Guicherit R (1997) Traffic as a source of volatile hydrocarbons in ambient air. Sci Total Environ 205:201–213

Guo J, Zhang J, Zhu M, Ju D, Xu H, Cao B (2014) High-performance gas sensor based on ZnO nanowires functionalized by Au nanoparticles. Sens Actuators B 199:339–345

Guo M, Song W, Wang T, Li Y, Wang X, Du X (2015) Phenyl-functionalization of titanium dioxide-nanosheets coating fabricated on a titanium wire for selective solid-phase microextraction of polycyclic aromatic hydrocarbons from environment water samples. Talanta 144:998–1006

Han Y, Ren L, Xu K, Yang F, Li Y, Cheng T, Kang X, Xu C, Shi Q (2015) Supercritical fluid extraction with carbon nanotubes as a solid collection trap for the analysis of polycyclic aromatic hydrocarbons and their derivatives. J Chromatogr A 1395:1–6

Hou X, Guo Y, Liang X, Wang X, Wang L, Wang L, Liu X (2016) Bis(trifluoromethanesulfonyl) imide-based ionic liquids grafted on graphene oxide-coated solid-phase microextraction fiber for extraction and enrichment of polycyclic aromatic hydrocarbons in potatoes and phthalate esters in food-wrap. Talanta 153:392–400

Hsueh T-J, Hsu C-L, Chang S-J, Chen I-C (2007) Laterally grown ZnO nanowire ethanol gas sensors. Sens Actuators B 126:473–477

Hu P, Du G, Zhou W, Cui J, Lin J, Liu H, Liu D, Wang J, Chen S (2010) Enhancement of ethanol vapor sensing of TiO_2 nanobelts by surface engineering. ACS Appl Mater Interfaces 2:3263–3269

Huang J, Yu K, Gu C, Zhai M, Wu Y, Yang M, Liu J (2010) Preparation of porous flower-shaped SnO_2 nanostructures and their gas-sensing property. Sens Actuators B 147:467–474

Huang K, Kong L, Yuan F, Xie C (2013) In situ diffuse reflectance infrared Fourier transform spectroscopy study of formaldehyde adsorption and reactions on nano γ-Fe_2O_3 films. Appl Surf Sci 270:405–410

Inyawilert K, Wisitsora-at A, Tuantranont A, Singjai P, Phanichphant S, Liewhiran C (2014) Ultra-rapid VOCs sensors based on sparked-In_2O_3 sensing films. Sens Actuators B 192:745–754

Jenkins BM, Jones AD, Turn SQ, Williams RB (1996) Emission factors for polycyclic aromatic hydrocarbons from biomass burning. Environ Sci Technol 30:2462–2469

Jin W, Yan S, An L, Chen W, Yang S, Zhao C, Dai Y (2015) Enhancement of ethanol gas sensing response based on ordered V_2O_5 nanowire microyarns. Sens Actuators B 206:284–290

Jones CC, Chughtai AR, Murugaverl B, Smith DM (2004) Effects of air/fuel combustion ratio on the polycyclic aromatic hydrocarbon content of carbonaceous soots from selected fuels. Carbon 42:2471–2484

Kaneti YV, Moriceau J, Liu M, Yuan Y, Zakaria Q, Jiang Z, Yu A (2015) Hydrothermal synthesis of ternary α-Fe_2O_3–ZnO–Au nanocomposites with high gas-sensing performance. Sens Actuators B 209:889–897

Karmaoui M, Leonardi SG, Latino M, Tobaldi DM, Donato N, Pullar RC, Seabra MP, Labrincha JA, Neri G (2016) Pt-decorated In_2O_3 nanoparticles and their ability as a highly sensitive ($<$10 ppb) acetone sensor for biomedical applications. Sens Actuators B 230:697–705

Khandekar MS, Tarwal NL, Mullad IS, Suryavanshi SS (2014) Nanocrystalline Ce doped $CoFe_2O_4$ as an acetone gas sensor. Ceram Int 40:447–452

Kılınç K, Şennik E, Öztürk ZZ (2011) Fabrication of TiO2 nanotubes by anodization of Ti thin films for VOC sensing. Thin Solid Films 520:953–958

Kim S, Park S, Park S, Lee C (2015) Acetone sensing of Au and Pd-decorated WO_3 nanorod sensors. Sens Actuators B 209:180–185

Kim K-H, Szulejko J, Kwon E, Deep A (2016) A critical review on the diverse preconcentration procedures on bag samples in the quantitation of volatile organic compounds from cigarette smoke and other combustion samples. Trends Anal Chem 85:65–74

Kohler M, Kunniger T (2003) Emission of polycyclic aromatic hydrocarbon (PAH) from creosoted railroad ties and their relevance for life cycle assessment. Holz Roh Werkst 61:117–124

Kristensen P, Eilertsen E, Einarsdóttir E, Haugen A, Skaug V, Ovrebo S (1995) Fertility in mice after prenatal exposure to benzo[a]pyrene and inorganic lead. Environ Health Perspect 103:588–590

Krupadam RJ, Bhagat B, Khan MS (2010) Highly sensitive determination of polycyclic aromatic hydrocarbons in ambient air dust by gas chromatography-mass spectrometry after molecularly imprinted polymer extraction. Anal Bioanal Chem 397:3097–3106

Leyton P, Sanchez-Cortes S, Garcia-Ramos JV, Domingo C, Campos-Vallette M, Saitz C, Clavijo RE (2004) Selective molecular recognition of polycyclic aromatic hydrocarbons (PAHs) on Calix[4]arene-functionalized Ag nanoparticles by surface-enhanced Raman scattering. J Phys Chem B 108:17484–17490

Liang R, Chen L, Qin W (2015) Potentiometric detection of chemical vapours using molecularly imprinted polymers as receptors. Sci Rep 5:12462

Liu X, Zhang J, Guo X, Wang S, Wu S (2012) Core–shell α–Fe2O3@SnO2/Au hybrid structures and their enhanced gas sensing properties. RSC Adv 2:1650–1655

Lou Z, Deng J, Wang L, Wang L, Fei T, Zhang T (2013) Toluene and ethanol sensing performances of pristine and PdO-decorated flower-like ZnO structures. Sens Actuators B 176:323–329

MacAskill ND, Walker TR, Oakes K, Walsh M (2016) Forensic assessment of polycyclic aromatic hydrocarbons at the former Sydney Tar Ponds and surrounding environment using fingerprint techniques. Environ Pollut 212:166–177

Masih A, Taneja A (2006) Polycyclic aromatic hydrocarbons (PAHs) concentrations and related carcinogenic potencies in soil at a semi-arid region of India. Chemosphere 65:449–456

Mauri-Aucejo A, Amorós P, Moragues A, Guillem C, Belenguer-Sapiña C (2016) Comparison of the solid-phase extraction efficiency of a bounded and an included cyclodextrin-silica microporous composite for polycyclic aromatic hydrocarbons determination in water samples. Talanta 156-157:95–103

Mehdinia A, Khojasteh E, Kayyal TB, Jabbari A (2014) Magnetic solid phase extraction using gold immobilized magnetic mesoporous silica nanoparticles coupled with dispersive liquid–liquid microextraction for determination of polycyclic aromatic hydrocarbons. J Chromatogr A 1364:20–27

Mehdinia A, Khodaee N, Jabbari A (2015) Fabrication of graphene/Fe_3O_4@polythiophene nanocomposite and its application in the magnetic solid-phase extraction of polycyclic aromatic hydrocarbons from environmental water samples. Anal Chim Acta 868:1–9

Mei L, Deng J, Yin X, Zhang M, Li Q, Zhang E, Xu Z, Chen L, Wang T (2012) Ultrasensitive ethanol sensor based on 3D aloe-like SnO_2. Sens Actuators B 166-167:7–11

Menezes HC, de Barcelos SMR, Macedo DFD, Purceno AD, Machado BF, Teixeira APC, Lago RM, Serp P, Cardeal ZL (2015) Magnetic N-doped carbon nanotubes: a versatile and efficient material for the determination of polycyclic aromatic hydrocarbons in environmental water samples. Anal Chim Acta 873:51–56

Mirzaei A, Janghorban K, Hashemi B, Bonavita A, Bonyani M, Leonardi SG, Neri G (2015) Synthesis, characterization and gas sensing properties of Ag@α-Fe$_2$O$_3$ core–shell nanocomposites. Nanomaterials 5:737–749

Mirzaei A, Leonardi SG, Neri G (2016) Detection of hazardous volatile organic compounds (VOCs) by metal oxide nanostructures-based gas sensors: a review. Ceram Int 42:15119–15142

Mollahosseini A, Rokue M, Mojtahedi MM, Toghroli M, Kamankesh M, Motaharian A (2016) Mechanical stir bar sorptive extraction followed by gas chromatography as a new method for determining polycyclic aromatic hydrocarbons in water samples. Microchem J 126:431–437

Mori M, Itagaki Y, Iseda J, Sadaoka Y, Ueda T, Mitsuhashi H, Nakatani M (2014) Influence of VOC structures on sensing property of SmFeO$_3$ semiconductive gas sensor. Sens Actuators B 202:873–877

Mowry JB, Spyker DA, Cantilena LR, Bailey JE, Ford M (2013) 2012 annual report of the American association of poison control centers' National Poison Data System (NPDS): 30th annual report. Clin Toxicol 51:949–1229

Mukhtar NH, See HH (2016) Carbonaceous nanomaterials immobilised mixed matrix membrane microextraction for the determination of polycyclic aromatic hydrocarbons in sewage pond water samples. Anal Chim Acta 931:57–63

Ohura T, Kamiya Y, Ikemori F (2016) Local and seasonal variations in concentrations of chlorinated polycyclic aromatic hydrocarbons associated with particles in a Japanese megacity. J Hazard Mater 312:254–261

Olah GA, Molnar A (2003) Hydrocarbon chemistry, 2nd edn. Wiley, New Jersey

Patra S, Roy E, Madhuri R, Sharma PK (2015) Imprinted ZnO nanostructure-based electrochemical sensing of calcitonin: a clinical marker for medullary thyroid carcinoma. Anal Chim Acta 853:271–284

Patra S, Roy E, Madhuri R, Sharma PK (2016) A technique comes to life for security of life: the food contaminant sensors. In: Grumezescu AM (ed) NanoBioSensors, vol 8. Academic Press, Natherland, pp 713–772

Paturel L, Saber A, Combet E, Joumard R (1996) Analysis of PAH emissions from passenger cars by high resolution Shpol'skii spectrofluorimetry. Polycycl Aromat Compd 9:331–339

Petrov AA (1987) Petroleum hydrocarbons. Springer, New York

Pisupati SV, Wasco RS, Scaroni AW (2000) An investigation on polycyclic aromatic hydrocarbon emissions from pulverized coal combustion systems. J Hazard Mater 74:91–107

Qu L-L, Li Y-T, Li D-W, Xue J-Q, Fossey JS, Long Y-T (2013) Humic acids-based one-step fabrication of SERS substrates for detection of polycyclic aromatic hydrocarbons. Analyst 138:1523–1528

Qu F, Wang Y, Liu J, Wen S, Chen Y, Ruan S (2014) Fe$_3$O$_4$–NiO core–shell composites: hydrothermal synthesis and toluene sensing properties. Mater Lett 132:167–170

Ramgir NS, Kaur M, Sharma PK, Datta N, Kailasaganapathi S, Bhattacharya S, Debnath AK, Aswal DK, Gupta SK (2013) Ethanol sensing properties of pure and Au modified ZnO nanowires. Sens Actuators B 187:313–318

Ravindra K, Mittal AK, Van Grieken R (2001) Health risk assessment of urban suspended particulate matter with special reference to polycyclic aromatic hydrocarbons: a review. Rev Environ Health 16:169–189

Ravindra K, Sokhi R, Grieken RV (2008) Atmospheric polycyclic aromatic hydrocarbons: source attribution, emission factors and regulation. Atmos Environ 42:2895–2921

Rocío-Bautista P, Pino V, Ayala JH, Pasáz J, Ruiz-Pérez C, Afonso AN (2016) A magnetic-based dispersive micro-solid-phase extraction method using the metal-organic framework HKUST-1 and ultra-high-performance liquid chromatography with fluorescence detection for determining polycyclic aromatic hydrocarbons in waters and fruit tea infusions. J Chromatogr A 1436:42–50

Santhaveesuk T, Wongratanaphisan D, Choopun S (2010) Enhancement of sensor response by TiO$_2$ mixing and Au coating on ZnO tetrapod sensor. Sens Actuators B 147:502–507

Schauer JJ, Cass GR (2000) Source apportionment of wintertime gas-phase and particle-phase air pollutants using organic compounds as tracers. Environ Sci Technol 34:1821–1832

Seo M-H, Yuasa M, Kida T, Huh J-S, Yamazoe N, Shimanoe K (2011) Microstructure control of TiO_2 nanotubular films for improved VOC sensing. Sens Actuators B 154:251–256

Sheng P, Wu S, Bao L, Wang X, Chen Z, Cai Q (2012) Surface enhanced Raman scattering detecting polycyclic aromatic hydrocarbons with gold nanoparticle-modified TiO_2 nanotube arrays. New J Chem 36:2501–2505

Shi R, Yan L, Xu T, Liu D, Zhu Y, Zhou J (2015) Graphene oxide bound silica for solid-phase extraction of 14 polycyclic aromatic hydrocarbons in mainstream cigarette smoke. J Chromatogr A 1375:1–7

Shi Y, Wu H, Wang C, Guo X, Du J, Du L (2016) Determination of polycyclic aromatic hydrocarbons in coffee and tea samples by magnetic solid-phase extraction coupled with HPLC–FLD. Food Chem 199:75–80

Simanzhenkov V, Idem R (2003) Crude oil chemistry. CRC Press, Taylor and Francis Group, New York

Singh O, Singh RC (2012) Enhancement in ethanol sensing response by surface activation of ZnO with SnO_2. Mater Res Bull 47:557–561

Smil V (2015) Natural gas: fuel for the 21st century. Wiley, New Jersey

Song X, Li J, Xu S, Ying R, Ma J, Liao C, Liu D, Yu J, Chen L (2012) Determination of 16 polycyclic aromatic hydrocarbons in seawater using molecularly imprinted solid-phase extraction coupled with gas chromatography-mass spectrometry. Talanta 99:75–82

Speight JG (2011) Handbook of industrial hydrocarbon processes. Elsevier, Natherland

Suman S, Sinha A, Tarafdar A (2016) Polycyclic aromatic hydrocarbons (PAHs) concentration levels, pattern, source identification and soil toxicity assessment in urban traffic soil of Dhanbad, India. Sci Total Environ 545-546:353–360

Sun P, Zhou X, Wang C, Shimanoe K, Lu G, Yamazoe N (2014) Hollow SnO_2/α-Fe_2O_3 spheres with a double-shell structure for gas sensors. J Mater Chem A 2:1302–1308

Tan W, Yu Q, Ruan X, Huang X (2015a) Design of SnO2-based highly sensitive ethanol gas sensor based on quasi molecular-cluster imprinting mechanism. Sens Actuators B 212:47–54

Tan W, Ruan X, Yu Q, Yu Z, Huang X (2015b) Fabrication of a SnO2-based acetone gas sensor enhanced by molecular imprinting. Sensors 15:352–364

Taniguchi S, Colabuono FI, Dias PS, Oliveira R, Fisner M, Turra A, Izar GM, Abessa DMS, Saha M, Hosoda J, Yamashita R, Takada H, Lourenço RA, Magalhães CA, Bícego MC, Montone RC (2016) Spatial variability in persistent organic pollutants and polycyclic aromatic hydrocarbons found in beach-stranded pellets along the coast of the state of São Paulo, southeastern Brazil. Mar Pollut Bull 106:87–94

Tiu BDB, Krupadam RJ, Advincula RC (2016) Pyrene-imprinted polythiophene sensors for detection of polycyclic aromatic hydrocarbons. Sens Actuators B 228:693–701

Tormoehlen LM, Tekulve KJ, Nañagas KA (2014) Hydrocarbon toxicity: a review. Clin Toxicol 52:479–489

Uchiyama S, Hayashida H, Izu R, Inaba Y, Nakagome H, Kunugita N (2015) Determination of nicotine, tar, volatile organic compounds and carbonyls in mainstream cigarette smoke using a glass filter and a sorbent cartridge followed by the two-phase/one-pot elution method with carbon disulfide and methanol. J Chromatogr A 1426:48–55

Uddin ASMI, Chung G-S (2014) Synthesis of highly dispersed ZnO nanoparticles on graphene surface and their acetylene sensing properties. Sens Actuators B 205:338–344

US EPA (Environmental Protection Agency) (2008) Polycyclic aromatic hydrocarbons (PAHs)- EPA fact sheet. National Center for Environmental Assessment, Office of Research and Development, Washington, DC

Vaishnav VS, Patel SG, Panchal JN (2015) Development of indium tin oxide thin film toluene sensor. Sens Actuators B 210:165–172

Vinci RM, Jacxsens L, Meulenaer BD, Deconink E, Matsiko E, Lachat C, de Schaetzen T, Canfyn M, Overmeire IV, Kolsteren P, Loco JV (2015) Occurrence of volatile organic

compounds in foods from the Belgian market and dietary exposure assessment. Food Control 52:1–8

Wang J, Liu L, Cong S-Y, Qi J-Q, Xu B-K (2008) An enrichment method to detect low concentration formaldehyde. Sens Actuators B 134:1010–1015

Wang H, Qu Y, Chen H, Lin Z, Dai K (2014) Highly selective n-butanol gas sensor based on mesoporous SnO_2 prepared with hydrothermal treatment. Sens Actuators B 201:153–159

Wang M, Cui S, Yang X, Bi W (2015a) Synthesis of g-C_3N_4/Fe_3O_4 nanocomposites and application as a new sorbent for solid phase extraction of polycyclic aromatic hydrocarbons in water samples. Talanta 132:922–928

Wang H, Zhao X, Meng W, Wang P, Wu F, Tang Z, Han X, Giesy JP (2015b) Cetyltrimethylammonium bromide-coated Fe_3O_4 magnetic nanoparticles for analysis of 15 trace polycyclic aromatic hydrocarbons in aquatic environments by ultraperformance, liquid chromatography with fluorescence detection. Anal Chem 87:7667–7675

Wang X, Hao W, Zhang H, Pan Y, Kang Y, Zhang X, Zou M, Tong P, Du Y (2015c) Analysis of polycyclic aromatic hydrocarbons in water with gold nanoparticles decorated hydrophobic porous polymer as surface-enhanced Raman spectroscopy substrate. Spectrochim Acta 139:214–221

Wang X, Wang Y, Qin Y, Ding L, Chen Y, Xie F (2015d) Sensitive and selective determination of polycyclic aromatic hydrocarbons in mainstream cigarette smoke using a graphene-coated solid phase microextraction fiber prior to GC/MS. Talanta 140:102–108

Wang Y, Lin Y, Jiang D, Li F, Li C, Zhu L, Wen S, Ruan S (2015e) Special nanostructure control of ethanol sensing characteristics based on Au@In_2O_3 sensor with good selectivity and rapid response. RSC Adv 5:9884–9890

Wells PG, McCallum GP, Lam KC, Henderson JT, Ondovcik SL (2010) Oxidative DNA damage and repair in teratogenesis and neurodevelopmental deficits. Birth Defects Res C Embryo Today 90:103–109

Wing MR, Bada JL (1992) The origin of polycyclic aromatic hydrocarbons in meteorites. Orig Life Evol Biosph 21:375–383

Wu R-J, Lin D-J, Yu M-R, Chen MH, Lai H-F (2013) Ag@SnO_2 core–shell material for use in fast-response ethanol sensor at room operating temperature. Sens Actuators B 178:185–191

Xiangfeng C, Dongli J, Yu G, Chenmou Z (2006) Ethanol gas sensor based on $CoFe_2O_4$ nanocrystallines prepared by hydrothermal method. Sens Actuators B 120:177–181

Xie Y, Wang X, Han X, Xue X, Ji W, Qi Z, Liu J, Zhao B, Ozaki Y (2010) Sensing of polycyclic aromatic hydrocarbons with cyclodextrin inclusion complexes on silver nanoparticles by surface-enhanced Raman scattering. Analyst 135:1389–1394

Xie Y, Wang X, Han X, Song W, Ruan W, Liu J, Zhao B, Ozaki Y (2011) Selective SERS detection of each polycyclic aromatic hydrocarbon (PAH) in a mixture of five kinds of PAHs. J Raman Spectrosc 42:945–950

Xing R, Xu L, Song J, Zhou C, Li Q, Liu D, Song HW (2015) Preparation and gas sensing properties of In_2O_3/Au nanorods for detection of volatile organic compounds in exhaled breath. Sci Rep 5:10717

Xu X, Fan H, Liu Y, Wang L, Zhang T (2011) Au-loaded In_2O_3 nanofibers-based ethanol micro gas sensor with low power consumption. Sens Actuators B 160:713–719

Xu J, Du J, Jing C, Zhang Y, Cui J (2014) Facile detection of polycyclic aromatic hydrocarbons by a surface-enhanced Raman scattering sensor based on the Au coffee ring effect. ACS Appl Mater Interfaces 6:6891–6897

Xu J, Szyszkowicz M, Jovic B, Cakmak S, Austin CC, Zhu J (2016a) Estimation of indoor and outdoor ratios of selected volatile organic compounds in Canada. Atmos Environ 141:523–531

Xu P, Tao B, Ye Z, Zhao H, Ren Y, Zhang T, Huang Y, Chen J (2016b) Polycyclic aromatic hydrocarbon concentrations, compositions, sources, and associated carcinogenic risks to humans in farmland soils and riverine sediments from Guiyu, China. J Environ Sci 48:102–111

Xue S-W, Tang M-Q, Xu L, Shi Z-G (2015) Magnetic nanoparticles with hydrophobicity and hydrophilicity for solid-phase extraction of polycyclic aromatic hydrocarbons from environmental water samples. J Chromatogr A 1411:9–16

Yang D-H, Shin MJ, Kim M, Kim Y-D, Kim H, Shin JS (2016) Molecularly imprinted titania microbeads for extraction of the metabolite 1-hydroxypyrene from urine prior to its determination by HPLC. Microchim Acta 183:1601–1609

Zhang J, Liu X, Wang L, Yang T, Guo X, Wu S, Wang S, Zhang S (2011) Au-functionalized hematite hybrid nanospindles: general synthesis, gas sensing and catalytic properties. J Phys Chem C 115:5352–5357

Zhang J, Liu X, Wu S, Cao B, Zheng S (2012) One-pot synthesis of Au-supported ZnO nanoplates with enhanced gas sensor performance. Sens Actuators B 169:61–66

Zhang S, Ren F, Wu W, Zhou J, Xiao X, Sun L, Liu Y, Jiang C (2013) Controllable synthesis of recyclable core–shell γ-Fe_2O_3@SnO_2 hollow nanoparticles with enhanced photocatalytic and gas sensing properties. Phys Chem Chem Phys 15:8228–8236

Zhang S, Yao W, Ying J, Zhao H (2016a) Polydopamine-reinforced magnetization of zeolitic imidazolate framework ZIF-7 for magnetic solid-phased extraction of polycyclic aromatic hydrocarbons from the air-water environment. J Chromatogr A 1452:18–26

Zhang Y, Wu D, Yan X, Guan Y (2016b) Rapid solid-phase microextraction of polycyclic aromatic hydrocarbons in water samples by a coated through-pore sintered titanium disk. Talanta 154:400–408

Zhao H, Jin J, Tian W, Li R, Yu Z, Song W, Cong Q, Zhao B, Ozaki Y (2015) Three-dimensional superhydrophobic surface enhanced Raman spectroscopy substrate for sensitive detection of pollutants in real environments using an oil-water separation system. J Mater Chem A 3:4330–4337

Zheng W, Lu X, Wang W, Li Z, Zhang H, Wang Y, Wang Z, Wang C (2009) A highly sensitive and fast-responding sensor based on electrospun In_2O_3 nanofibers. Sens Actuators B 142:61–65

Zheng H-B, Ding J, Zheng S-J, Zhu G-T, Yuan B-F, Feng Y-Q (2016) Facile synthesis of magnetic carbon nitride nanosheets and its application in magnetic solid phase extraction for polycyclic aromatic hydrocarbons in edible oil samples. Talanta 148:46–53

Zhu Z, Kao C-T, Wu R-J (2014) A highly sensitive ethanol sensor based on Ag@TiO_2 nanoparticles at room temperature. Appl Surf Sci 320:348–355

Chapter 10
Biogas Produced from Different Feedstocks in Anaerobic Digesters

Grazia Leonzio

Abstract Anaerobic digestion is a useful method for producing clean fuel from renewable feedstocks. It is a biological process where biodegradable matter is degraded or decomposed by the activity of specific microorganisms in the absence of oxygen, producing biogas used for electricity and heat generation. The anaerobic digestion is affected by the type of raw materials. Co-digestion, the simultaneous digestion of a mixture of two or more substrates, is a technique, by which the bioconversion rate, as well as the methane yield, can be increased. The same effects are produced by the pretreatment of the biomass as pretreatments make the organic substance of smaller size more accessible to microorganisms and methane production. An important parameter used to evaluate the efficiency of anaerobic digestion is the bio-methane potential. Others are the gross energy yields, the cumulative energy demand, the net energy yield, and the energy efficiency. In this chapter, a literature analysis about the diet of anaerobic digestion and related methods to improve the process is carried out. Works report that energy crop is the most used substrate for the biogas production. Mechanical, chemical, thermal, thermochemical, and biological pretreatments can be used. Also, the different configuration of anaerobic digester can be developed to improve the efficiency of the process.

Keywords Biogas • Anaerobic digestion • Co-digestion • Pretreatment of biomass • Bio-methane potential • Configuration of anaerobic digestion

1 Introduction

Policy makers from around the world show an increase in energy consumption, by promoting the conversion from an economy based on fossil sources to renewable sources (Richardson 2012). The agricultural sector participates in it, by providing biomasses that must be transformed into various forms of energy.

G. Leonzio (✉)
Department of Industrial and Information Engineering and Economics, University of L'Aquila,
Via Giovanni Gronchi 18, 67100 L'Aquila, Italy
e-mail: grazia.leonzio@graduate.univaq.it

In this context, the use of anaerobic digesters feed by biomasses for biogas production and ultimately also for bio-methane production is increasing. These are important strategies to reduce gaseous emissions produced by fossil fuels, in compliance with the Kyoto Protocol and therefore with the EU Directive 209/28, which considers the 20% of energy consumption deriving from renewable sources by 2020. Within the European Union, biogas production is increased by about six times from 1990 to 2005 (Murphy et al. 2011) reaching a value of 10.9 million tons of oil equivalent in 2020. Anaerobic digestion is currently widely promoted by businesses, research, and market policy (Callahan 2011).

At first, anaerobic digestion was used to handle sludge deriving from wastewater treatment systems. Recently, this technique has been extended to an animal, agricultural and industrial by-products, and sludge of wastewater treatment (González-Fernández et al. 2008).

The advantages that can be gained are the reduction of volatile suspended solids and odors, the destruction of pathogenic organisms, and the energy production from renewable sources. Then, anaerobic digestion offers the possibility of giving to biomass an added value by converting it into energy, as methane and organic soil (digestate), that is rich in nutrients, water, and organic matter.

Furthermore, it is a technologically process with low energy demand; it is possible to obtain simultaneously an organic waste treatment and stabilization, energy production, emissions reduction (including natural carbon), and liquid fertilizers production (Müller 2007). It is also possible to obtain the recirculation of nutrients and organic materials, by minimizing the need for external input. However, the CO_2 released in the digestion process cannot be considered a greenhouse gas emission because carbon is used by plants for photosynthesis and is released into the atmosphere, as part of the carbon cycle.

In waste management, anaerobic digestion is more favorable than aerobic treatment, due to a better emission control and the energy recovery in the form of biogas. Variations in the net energy consumption and in energy efficiency are related to raw material properties and design of anaerobic digester.

To achieve an excellent biogas yield, it is necessary to provide an accurate nutritional target and a suitable feeding.

Biogas plants treat different kinds of organic compounds that include wastewater, food industry and agricultural residues, sewage and energy crops. Although sewage allows having more energy enhancement through anaerobic digestion (Marañón et al. 2012), biogas plants are mainly fed by energy crops.

In the literature, there are several works related to biogas production from energy crops. Only a few works combine the specific methane yield and the crop yield, by assigning a methane yield per hectare (Bauer et al. 2010).

Multiannual crops are *Arundo donax* L. (Arundo, also known as Giant Reed), *Panicum virgatum* L. (switchgrass) cv. Alamo, the inter-specific hybrid Sorghum arundinaceous Stapf × (Sorghum halepense Pers. × Sorghum roxburghii Stapf), known as Silk Sorghum (S. Silk). Among these, switchgrass (Panicum virgatum) has been recently reassessed for methane production (Frigon et al. 2012), while Arundo is subject to most recent experimentations (Di Girolamo et al. 2013).

Annual energy crops are: sorghum [*Sorghum bicolor* (L.) Moench] genotypes, namely fiber (Biomass 133; B 133), sweet (SUCROS 506; S506) and forage hybrid (Trudan Headless; Trudan H.), a hybrid corn (Klips, FAO 700 maturity).

Among multiannual species, Arundo is a promising crop in Southern Europe from the point of view of energy (Lewandowski et al. 2003); switchgrass is used overall in the USA (Monti et al. 2011); Sorghum Silk should combine the better forage sorghum characteristics (thin-stemmed "Sudan" genotypes) with its multiannual production (Corleto et al. 2009). Barbanti et al. (2014) evaluate crop diversity in quantity (biomass yield) and in quality (analytical characteristics), reflecting on their performance in the specific methane yield and in gross energy efficiency. Corn is the most important energy crop for biogas production with the highest yield in central Europe. Silage cereals are mainly used in Italy and in other parts of Europe.

In addition to corn, that is the main contact among energy crops, different varieties of sorghum (Sorghum bicolor) are used, hybrids including fiber, sweet and forage genotypes, for which methane production is evaluated (Jerger et al. 1987; Bauer et al. 2010; Sambusiti et al. 2013). The comparison between the velocity of the recirculated and measured liquid phase and the experimental is shown in Fig. 10.1.

2 Parameters Related to Diet of Anaerobic Digester to Evaluate the Efficiency of the Biogas Production

In processes of anaerobic digester, different parameters are used to evaluate the efficiency of biogas production.

The methane yields are in general evaluated in batch reactors under mesophilic conditions (35 °C), with an inoculum that has the following characteristics: TS of 36 mg g^{-1}, VS of 22.6 mg g^{-1}, TOC of 11.2 mg g^{-1}, TKN of 3.5 mg N g^{-1}, low C/N ratio equal to 3.2, total alkalinity of 28.2 g CaCO$_3$ l^{-1}. The content of NH$_4^+$–N is high enough (2.77 mg g^{-1}). Biogas is measured at each sampling time and it is aggregated as ml g^{-1} VS. CH$_4$ production is calculated based on volume displacement and percent methane content at each current and previous reading as the following equation (Lou et al. 2012) (Eq. 10.1).

$$CH_4(ml) = \left[\frac{(A+B)\cdot\%CH_{4t}}{100}\right] - \left[\frac{B\cdot\%CH_{4(t-1)}}{100}\right] \qquad (10.1)$$

where A is the displaced gas volume, B is the headspace gas volume, t is the current sampling time; $t-1$ is the previous sampling time. The specific methane yield is accumulated over time by adding up the amount of methane produced at each date at the net of the inoculum, expressed as ml CH$_4$ g^{-1} VS as in the following equation (10.2):
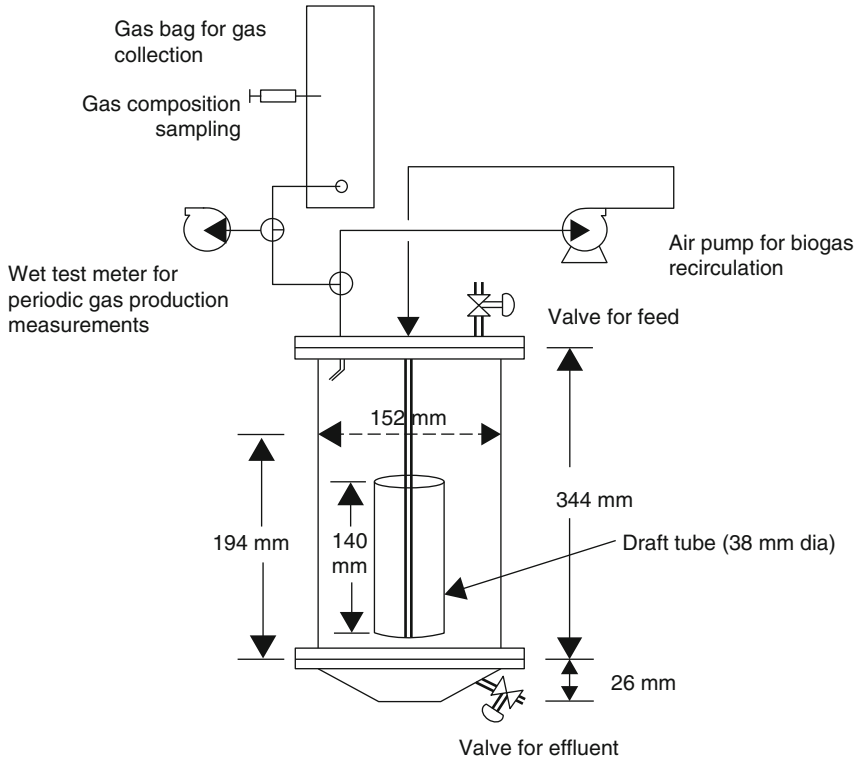
Fig. 10.1 Schematic diagram of the experimental setup of the anaerobic digester (Karim et al. 2005)

$$\text{specific yield} = \frac{\left(V_{\text{biogas sample}} \cdot CH_{4,\text{sample}}\right) - \left(V_{\text{biogas inoculum}} \cdot CH_{4,\text{inoculum}}\right)}{VS}$$

$$(10.2)$$

where $V_{\text{biogas sample}}$ and $V_{\text{biogas inoculum}}$ are biogas volume in sampling and in the inoculum, $CH_{4,\text{samples}}$ and $CH_{4,\text{inoculum}}$ are the methane percentages contained in the sample and in the inoculum. Energy crops have different specific methane yields and they are different from corn. The specific methane yields are evaluated in 58 days of incubation, and it is observed that they follow three different fields. Corn is characterized by a greater nation destination, so that it reaches greater methane potential yields equal to 316 ml g^{-1} VS. The three hybrid sorghums and S. Silk show an intermediate response with a median value of 262 ml CH_4 g^{-1} VS.

The difference in the potential methane yield, among energy crops and maize, are reported in the literature. As concerns sorghum, the highest values are often observed, with +16% as mean value (Sambusiti et al. 2013) in forage $\times$ fiber genotypes (251 ml CH_4 g^{-1} VS in Trudan Headless), or +15% as mean value (Jerger et al. 1987), but also +35% (Bauer et al. 2010). Yields of 400 g ml^{-1} VS are

evaluated for the 506 SUCROS sorghum (Jerger et al. 1987), but also of 303 ml g^{-1} VS (Sambusiti et al. 2013) and 345 ml g^{-1} VS. For these experiments, the incubation period varies from a minimum of 21 days (Mahmood and Honermeier 2012) to a maximum of 60 days (Jerger et al. 1987).

Switchgrass is collected mostly still green in the summer and therefore with lower lignification, specific methane yield and a low fiber content. Massé et al. (2011) find methane yield values between 169 and 252 ml CH$_4$ g^{-1} VS according to the climatic season. Frigon et al. (2012) identify wider range: 95–152 ml CH$_4$ g^{-1} VS, according to the climatic season and to the pretreatment used in feeding. Barbanati et al. (2014) find values of 216 ml CH$_4$ g^{-1} VS despite having been raised in senescence with an advanced stage of lignification. Arundo has methane yield values of 260 ml CH$_4$ g^{-1} VS (Ragaglini et al. 2014). Values of 273 ml CH$_4$ g^{-1} VS are achieved with experiments without pretreatment (Di Girolamo et al. 2013). The difference can be attributed to the different conditions in which the experiments are conducted: thermophilic and mesophilic at 53 and 35 °C in the first and in the second experiment.

Some evaluations about potential methane yields, with regard to the methane yield at the end of incubation, can be predicted through the Gompertz function. A first-order kinetics is particularly used to fix data, by leading the methane cumulative yield to a slight overestimation at the end of incubation, as the following equation (10.3):

$$CH_4 = CH_4O \cdot e^{-\frac{x-x_o}{b}} \qquad (10.3)$$

where CH$_4$ is the specific methane yield at t time (ml g^{-1} VS), CH$_4$O is the potential methane yield that is the asymptote, x is the speed of substrate degradation, x_o is the inflection point, and b the speed of substrate degradation. Some differences in the behavior of seven energy crops can be observed in the speed of substrate degradation (b parameter) and in the inflection point x_o: the shortest time indicating the easiest substrate degradation is recorded by corn (b and x_o, 5.6 and 5.9 days). The three hybrid sorghums S. Silk and Arundo, exhibit a slight decrease in both parameters (b between 8.2 and 9.5 days; x_o between 8.7 and 9.4 days) (Barbanati et al. 2014). Switchgrass shows slower kinetics (b and x_o, 11.4 and 11 days). Corn reaches the highest peak in the daily methane yield after 6 days of incubation (20.4 ml CH$_4$ g^{-1} VS d^{-1}). Three annual hybrids sorghums and S. Silk obtain an intermediate peak (with a mean value of 11.4 ml CH$_4$ g^{-1} VS d^{-1}) in a longer time, after 10 days of incubation. Arundo and switchgrass receive the lowest peaks (8.3 and 7 ml CH$_4$ g^{-1} VS d^{-1}) at the same time of sorghums variety, Fig. 10.2.

The gross energy yields per unit crops area (GE) measured in GJ ha^{-1} can be calculated as follows (Eq. 10.4):

$$GE = DBY \cdot VS \cdot CH_4O \cdot 0.03402 \qquad (10.4)$$

with 0.03402 GJ Nm^{-3} that is equal to the lower heat of methane (CTI 2009). The amount of consumed energy per unit crops area is evaluated by the Cumulative
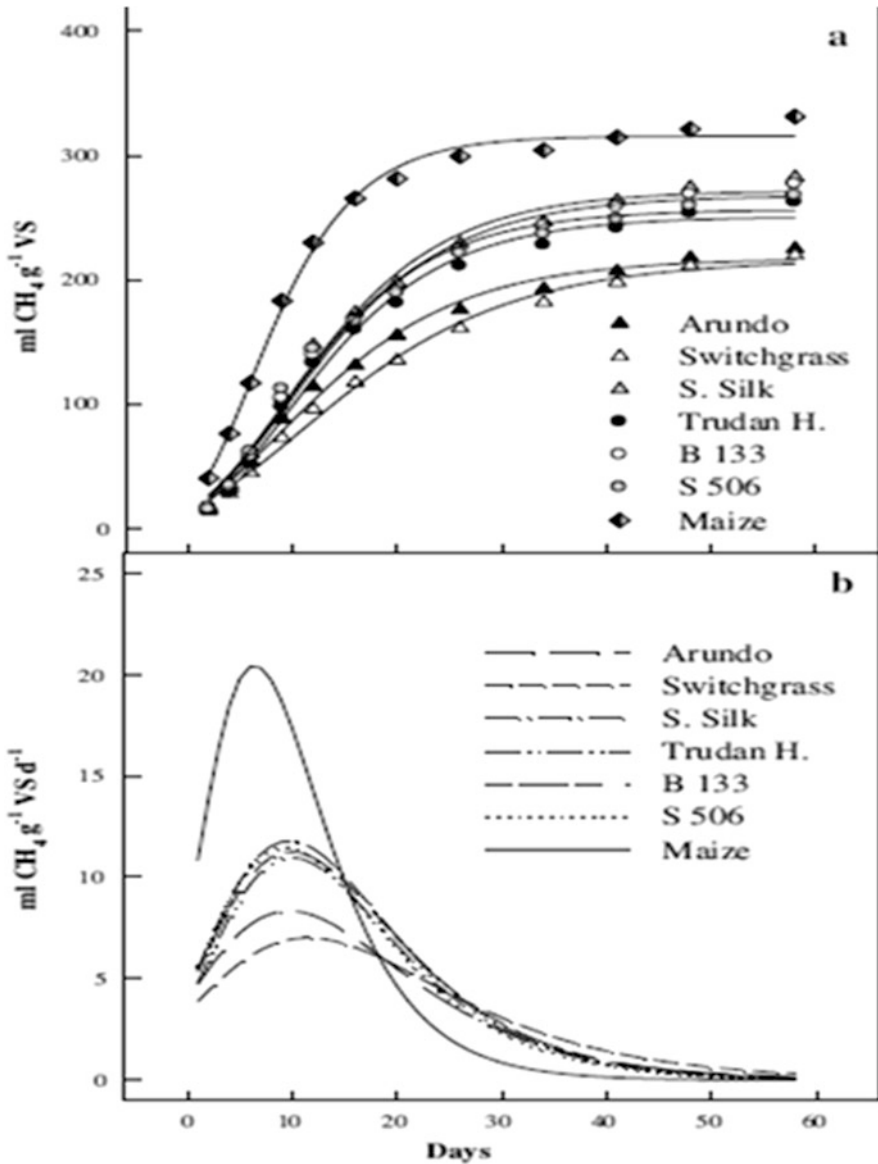
Fig. 10.2 Cumulative methane yield during the anaerobic digestion of seven crop samples (*symbols*) and fitted functions (*lines*) (**a**), and daily methane yield (**b**) estimated as the first derivative of fitted functions (Barbanti et al. 2014)

Energy Demand (CDE) through an analysis based on life cycle (Frischknecht and Jungbluth 2003). It briefly takes into account the amount of energy of the products used in the agricultural process (fertilizers, fuel, etc.) or small fractions attributed to the process (farms or equipment).

Other indicators to assess the energy efficiency of energy crops are net energy yield NE, as the difference between produced and consumed energy GE–CED, the energy efficiency EE as report GE/CED.

The GE values have a range between 286 GJ ha^{-1} for maize and 158 GJ ha^{-1} for switchgrass and S. Silk. This value corresponds to a methane production between 4600 and 8400 Nm^3 ha^{-1}. The two varieties of B133 and S 506 hybrid sorghum are lower than maize by 10% and 20%. The Cumulative Energy Demand varies between 39 GJ ha^{-1} for corn and 15 GJ ha^{-1} for the three multiannual species. The three hybrid sorghums show intermediate values of CED of 21 GJ ha^{-1}.

Net energy yield describes the same pattern as gross energy yield. The two aforementioned sorghum hybrids are not significantly different from maize. From experimental results, NE values encompass a range of net methane output between 4200 and 7000 Nm^3 ha^{-1}.

Unlike GE and NE, maize shows lower values of energy efficiency. The three heterogeneous energy crops, switchgrass, S. Silk, and S 506, show intermediate values of energy efficiency of 10.3 GJGJ^{-1}. Arundo and B133 have the highest energy efficiency, an average of 10.3 GJGJ^{-1}, due to the lower value of CED.

Significant differences are reported in the literature about the gross energy yield and the methane yield per hectare, as reported in Fig. 10.3. A methane yield of 7288 Nm^3 ha^{-1} which corresponds to values of GE 248 GJ ha^{-1} is measured for the sorghum silage, presumably a hybrid biomass (fibers or sweet), in Austria (Bauer et al. 2010); this value is very close to that obtained for the B133 sorghum and for SUCROS 506, an average equal to 237 GJ ha^{-1} (Barbanati et al. 2014). In other experiments, forage sorghum (genotype × fibers) reaches a value of 175 GJ ha^{-1} (Mahmood and Honermeier 2012). As regards switchgrass, the GE values vary in the range between 20 and 46 GJ ha^{-1} (Massé et al. 2011) and between 34 and 85 GJ ha^{-1} (Frigon et al. 2012), depending on the harvest time and on the used pretreatment. For switchgrass that has not received a pretreatment, there are values of 158 GJ ha^{-1}, which largely exceed the values indicated above, thanks to a higher biomass yield per hectare. No data on the energy yield or on the methane yield per hectare are present for Silk Sorghum.

Arundo has a value of methane yield equal to 9500 Nm^3 ha^{-1} (Ragaglini et al. 2014). Arundo suffers a wide gap from maize in both gross and net energy yield. The perspective of replacing corn with Arundo is associated with the possibility of its cultivation with the use of a few inputs (water, fuels, etc.). So pretreatments are an efficient method to improve the modest biodegradability of Arundo and to fill the gap with maize. Also, energy efficiency emphasizes a good chance for energy crops to be used. The multiannual energy crops and particularly Arundo seem to be the best candidates (EE average + 48% above the corn). As regards maize, the energy demand for irrigation (4.5 GJ ha^{-1}) and the N additional supply (8.6 GJ ha^{-1}) represents a constraint that energy crop cannot exceed. For these reasons, it is better to choose energy crops for biogas production.

Energy crops that require little energy can be a source of more sustainable energy than corn in areas where there is a greater surplus of land. Especially multiannual species are a viable alternative to corn (Lewandowski et al. 2003).
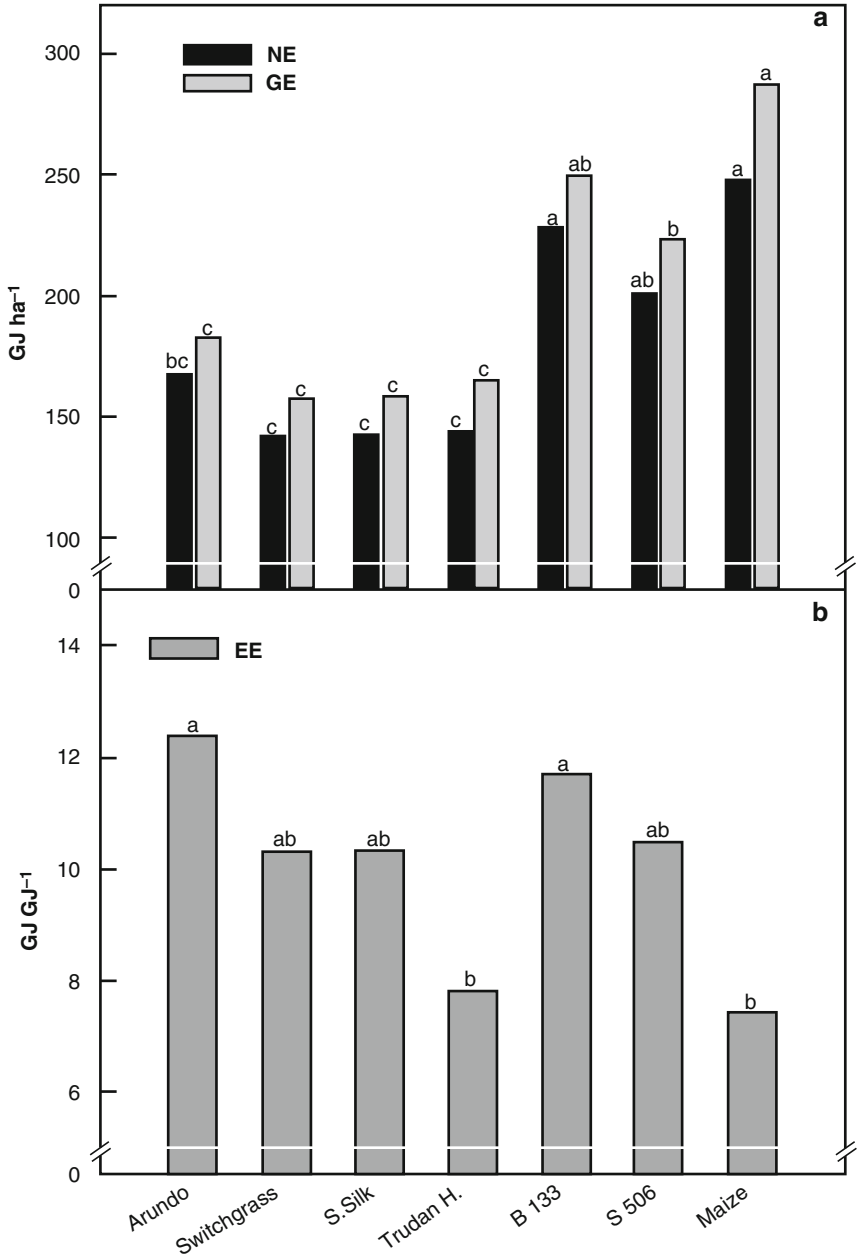
Fig. 10.3 Gross energy yield (GE) and net energy yield (NE) (**a**) and energy efficiency (EE) (**b**) in the seven biomass crops. ANOVA analysis significant at $P \leq 0.01$. In each trait, different letters indicate statistically different means (SNK test; $P \leq 0.05$) (Barbanti et al. 2014)

For the sorghum silage, a hybrid biomass (fibers or sweet), it is possible to have a methane yield of 7288 Nm ha^{-1} which corresponds to GE to 248 GJ ha^{-1} (Bauer et al. 2010).

These values are similar to other types of sorghum: 237 GJ ha^{-1} for B133 and SUCROS 506 in average. For the forage sorghum genotype fibers, there are values of 129 GJ ha^{-1}, whereas genotype fibers scored 175 GJ ha^{-1} (Mahmood and Honermeier 2012). Two varieties of hybrid sorghum, B 133 and S 506, have yields of about 10% and 20% that are lower if compared to corn.

There are open issues concerning the feeding of biogas plants: the required quality, the minimizing of the environmental impact, and the maximizing of the energy yield. The content and the availability of substrates that are capable of producing biogas are affected by variety, cultivation, and maturation stage.

Chandler et al. (1983) find different correlations between the biodegradability stage and the substrate composition. An esteem of the potential to produce methane from manure and energy crops is essential. The maximum methane yield requires adequate and effective nutrients that are supplied to microorganisms in the digester.

Literature reports studies on the digesters diet, analyzing how this can affect the amount of produced biogas and methane. The knowledge of potential biogas is important for decisions about size, design, and economic management of biogas plants.

A first-order kinetics model is used to evaluate the performance of biogas and methane production in different conditions (Sánchez et al. 1996; Pagés et al. 2011) (Eq. 10.5):

$$y(t) = y_{\max} \cdot \left(1 - e^{-k \cdot t} \right) \tag{10.5}$$

where $y(t)$ is the cumulative methane curve (CH_4 ml g^{-1} VS^{-1}), $y_{\max}$ is the final methane yield in an infinite residence time, k is the kinetic constant (d^{-1}), and t is time (days). Productivity is modeled in accordance with the following equation (10.6):

$$r_{(st)} = y_{\max} \cdot \frac{b \cdot c^b \cdot t^{b-1}}{\left(c^b + t^b \right)^2} \tag{10.6}$$

where $y_{\max}$ is the final methane yield (ml CH_4 g^{-1} VS^{-1}), t is time (days), and b and c are the equation coefficients. The experimental data are fixed by a nonlinear regression analysis. The theoretical methane yield from untreated sludge is calculated by using Busswel equation. When the experimental value is known, the total efficiency of the anaerobic digestion process is calculated by the following equation (10.7):

$$\eta = \frac{y_{\text{methane}}^{\text{exp}}}{y_{\text{methane}}^{\text{theo}}} \cdot 100 \tag{10.7}$$

3 Bio-methane Potentials for Anaerobic Digestion

Different methods are used to evaluate the effectiveness of a digester's diet, especially for expensive dedicated crops. One of them, as reported in the literature, is the bio-methane potentials (BMP), that is used to measure the potential production of methane from the substrate, under optimal conditions using laboratory scale tests (Hansen et al. 2004).

In particular, the bio-methane potential is a method, initially developed by Owen et al. (1979), to determine the conversion rate of organic waste into methane and to evaluate the maximum anaerobic biodegradability of an organic substrate. Through this parameter, it is possible to assess a given substrate and optimize an anaerobic digestion process (Raposo et al. 2011). Recently, there is a relative increase about BMP studies on different substrates, including agricultural crop straws, urban solid waste, and raw manures (Angelidaki et al. 2009). Many studies are conducted to evaluate the anaerobic biodegradability of a lignocellulosic substance by its chemical composition.

The features that influence the degradation degree of a lignocellulosic material are lignin content, hemicellulose, mannose, cellulose, cellulose crystallinity, and the association degree between lignin and carbohydrates (Chandler et al. 1980; Gunaseelan 1997; Tong et al. 1990). Some researchers try to define a mathematical model to estimate anaerobic biodegradability according to the lignocellulosic content of the substrate.

BMP is used for decades, however, researchers are considering further simplifications for further optimizations of the process (Colleran and Pender 2002; Rozzi and Remigi 2004a). Colleran and Pender (2002) evaluate the necessity to harmonize the anaerobic biodegradation, the activity, and inhibition assay, especially in the standardization of the test inoculum, test conditions, and the duration of the biodegradability tests.

Other researchers measure the pH influence, the temperature, the type, and concentration of biomass hydrolysis on BMP (Gunaseelan 1997; Rozzi and Remigi 2004a).

The inoculum source may have different bacterial populations, substrate adaption, and remains of substrates that are anaerobically biodegradable. Different inocula include sludge coming from industrial treatment plants, granular sludge from anaerobic digesters that treat brewery wastewater, animal manure, and sludge from municipal water treatment plants.

For the influence of the substrate/inoculum (S/I) ratio of the BMP value, results suggest an increase of the biodegradability, with the decrease of the S/I ratio, as reported by Hashimoto (1989). The first author reports a reduction of biodegradability when the S/I ratio increases, digesting ball-milled straw using a cattle manure inoculum. At an alkalinity level of 37 mg $NaHCO_3$ g COD^{-1}, they find that biodegradability and the speed of biodegradability decrease when the S/I ratio increases from 0.5 to 1 although there are strong influences on the performances of a granular inoculum. The decrease of BMP with the increase of S/I could be

attributed to luxury substrate uptake or storage under conditions of the high substrate (Chudoba et al. 1992). A further explanation about the decrease of BMP with the increase of S/I is due to the pH value for the VFA release.

In literature, a formula to estimate the value of BMP is present.

BMP expressed in liters of methane at standard conditions for amounts of added volatile solid substrate is calculated from the maximum methane production through the "sample bottle" and it is corrected by the maximum methane production through the "empty bottle." The biggest quantities of produced methane are calculated using the equation of state for gases at the increase of pressure and by multiplying the amounts of biogas with methane percentage in the headspace. The quantity is converted into liters, according to the following equation (10.8):

$$\text{BMP} = \frac{\left[\left(\frac{(P_s + P_{atm}) \cdot V_s}{RT}\right) \cdot \frac{\%CH_{4s}}{100}\right] - \left[\left(\frac{P_{bl} + P_{atm}}{RT}\right) \cdot V_{bl} \cdot \frac{\%CH_{4bl}}{100}\right]}{S_o} \cdot 22.4 \qquad (10.8)$$

where P_s is the pressure in the sample (in Pa), P_{atm} is the atmospheric pressure (in Pa), P_{bl} is the pressure in the headspace, V_s is the headspace volume of the test bottle (in m^3), V_{bl} the headspace volume of the blank bottle (in m^3), T is the temperature of 308.16 K, R is the universal gas constant equal to 8.3114 (in Pam^3 mol^{-1} K^{-1}), CH_{4s} is the methane percentage in the sample, CH_{4bl} is the methane percentage in the bottle blank, and S_o is the amount of added substrate (in GVS). BMP underestimations can take place in the presence of inhibitors with pH values outside the optimal value. In fact, the stable pH maintenance is the greatest problem for the digestion of the lignocellulosic material, due to its buffer capacity and volatile fatty acids accumulation (Banks and Humpreys 1998).

The biodegradability (B_o), as a maximum percentage of COD that is added and converted to methane, is calculated as the ratio between the maximum COD of methane, added as methane, and the biggest amount of COD, added in the sample (Eq. 10.9):

$$B_o = \frac{CH_{4,max}}{S_o} \cdot \frac{2.86}{COD_s} \cdot 100 \qquad (10.9)$$

where $CH_{4,max}$ is the maximum amount of methane produced in the digester in the last phase, S_o is the quantity of added substrate (in GVS), 2.86 corresponds to COD, that is the equivalent of 1 l of methane under standard temperature and pressure conditions (in g COD l^{-1}) and COD_s is referred to COD within a sample, (in g COD GVS^{-1}). Although B_o refers to the substrate converted into methane, a portion of the substrate that remains in the form of biomass is present: this quantity cannot be measured directly but it must be estimated.

However, the materials are mainly composed of soluble substances and different types of structural materials (lignin, cellulose, and hemicellulose). In the past, lignin is considered as an indicator for estimating the biodegradability of the material (Chandler et al. 1980; Tong et al. 1990). The impact of lignin on the

biodegradability of organic matter is associated with its role in the lignocellulosic complex: it is reported to hamper the degree and the rate of degradation of degradable hollocellulosic components (Selinger et al. 1996). The mechanism according to that lignin influences the hollocellulosica decomposition can take place by blocking the access to the microorganism in more biodegradable areas or through inhibitory effects starting from lignocellulose-containing compounds or by their hydrolysis.

It has been observed that lignin and cellulose can better describe the biodegradability of organic matter. Buffiere et al. (2006) find a relationship between the amount of lignin and cellulose and the biodegradability of organic matter although no statistical analysis is reported about it. The B_o value of different species of energy crops can be approximated, using simple linear models. Sutaryo et al. (2012) find a relationship between lignin and cellulose biodegradability (Eq. 10.10):

$$B_o = 086 - 0.92 \cdot (L + C) \tag{10.10}$$

where L and C are lignin and cellulose measured in GVS g^{-1}. Some interactions between lignin and cellulose can be statistically evaluated by considering an additional term that takes the product between the two variables into account (Eq. 10.11):

$$B_o = 081 - 0.69 \cdot (L + C) - 1.87 \cdot (L \cdot C) \tag{10.11}$$

Considering cellulose, hemicellulose, and soluble cells, the biodegradability of an organic substance can be found with the following relationship (Eq. 10.12):

$$B_o = (B_{oc} \cdot C \cdot C_{av}) + (B_{oh} \cdot H \cdot H_{av}) + (B_{ocs} \cdot CS) - X_b \tag{10.12}$$

where B_{oc} is the biodegradability of cellulose, B_{oh} is the biodegradability of hemicellulose, B_{ocs} refers to soluble cells, and X_b is the amount of converted biomass. Other models are showed in Table 10.1.

The model I and II are considered as approximation into an individual quantitative relation between the biodegradability of the fractions of cellulose and lignin, and hemicellulose and lignin. Model III considers both cellulose and hemicellulose to act as one entity. Model IV considers the relation between lignin and hollocellulose availability (CH_{av}) to be surface related (Conrad et al. 1985). The table also reports four statistical performance models.

The maximum biodegradability of a substance is calculated by the following equation (10.13):

$$B_p = \frac{COD_{methane, t=max} + COD_{s, t=max} - COD_{s, t=0}}{COD_{in} - COD_{s, t=0}} \tag{10.13}$$

where $COD_{methane, t=max}$ is the COD concentration that is equivalent to the amount of methane produced in the final digestion time, $COD_{s, t=max}$ is soluble COD at the

Table 10.1 Equations, number of parameters (p), coefficient of determinations (R^2), and significance (t values) for the estimation of anaerobic biodegradability based on a deterministic approach

Model	Equation	Assumption tested	R^2	RSS	F_{pr}
I	$B_o = [0.22 \cdot C_i \cdot C_{av}] + (1.01 \cdot (NDS_i + H_i)] - 0.17$	$C_{av} = (C - L)/C$	86	0.006	<0.001
II	$B_o = (0.58 \cdot C_i \cdot C_{av}) + (0.85 \cdot (H_i) \cdot H_{av}) \cdot (1.14 \cdot NDS_i) - 0.25$	$C_{av} = (C - L)/C$ $H_{av} = (H - L)/H$	81	0.016	<0.001
III	$B_o = (0.74 \cdot (C_i + H_i) \cdot CH_{av}) + (1.04 \cdot NDS_i) - 0.25$	$CH_{av} = (C + H - L)/(C + H)$	73	0.011	<0.001
IV	$B_o = (0.86 \cdot (C_i + H_i) \cdot CH_{av}) + (1.07 \cdot NDS_i) - 0.28$	$CH_{av} = [1 - (L^{2/3}/NDF^{2/3})]$	75	0.011	<0.001

C cellulose, *H* hemicellulose, *L* lignin, *av* available, *NDS* neutral detergent solubles

final digestion time (in g COD l^{-1}), $COD_{s,t=0}$ is the soluble COD concentration at the zero digestion time (in g COD l^{-1}), and COD_{in} is the initial total COD concentration in the sample (Table 10.2).

The B_S value, that is the portion of soluble COD converted into methane at the end of digestion, can be calculated in the following way (Eq. 10.14):

$$B_s = \frac{COD_{s,t=0} - COD_{s,t=\max}}{COD_{s,t=0}} \qquad (10.14)$$

According to BMP, a simple stoichiometric calculation of the maximum potential is used for gas production: theoretical or stoichiometric methane potential, TBMP (Møller et al. 2004; Raposo et al. 2011; Triolo et al. 2011). However, the TBMP values obtained by stoichiometric calculations are greater than the methane potential which is influenced by recalcitrant carbon (Triolo et al. 2011). So TBMP is not used as a potential indicator of biogas production but as a parameter to evaluate the biodegradability of a substrate.

A developed method to determine BMP is the near-infrared spectroscopy technology (NIRS). It allows the reduction of time measurement. In fact, the traditional measurement systems are expensive and require too much time, so are not advantageous for large-scale operating digesters. Triolo et al. (2014), in particular, test a partial least square (PLS) model for a rapid determination of BMP by using NIRS. A total of 88 plant biomass samples of a wide variety is used for model prediction. The standard error of the best PLS model is 37 CH$_4$NL kg^{-1} VS, where the BMP of the test set is between 136.2 and 477.9 CH$_4$NL kg^{-1} VS, the coefficient of determination and residual prediction deviation is 0.84 and 2.49. This shows that NIRS has some success in various applications and might be an alternative tool to traditional measurement systems. In various experiments, BMP values are determined by VDI 4630 regulations: Lesteur et al. (2011) and Doublet et al. (2013) apply this technology to municipal solid waste plants.

Table 10.2 BMP and biodegradability as assessed from batch digestion of 15 European species

Species	BMP (lCH_4 g VS^{-1})	BMP (lCH_4 g COD^{-1})	B_o (%COD)	B_p (%pCOD)	B_s (%sCOD)
Yellow lupin	0.26 ± 0.01	0.16 ± 0.01	47	36	92
Vetch	0.29 ± 0.02	0.2 ± 0.01	56	43	99
Carrot	0.31 ± 0.01	0.23 ± 0.02	66	31	100
Spartina	0.29 ± 0.01	0.21 ± 0.03	59	52	97
White lupin	0.26 ± 0.01	0.18 ± 0.04	52	35	100
Triticale	0.29 ± 0.00	0.20 ± 0.00	57	52	86
Braken	0.18 ± 0.01	0.12 ± 0.01	34	22	92
Sweet clover	0.29 ± 0.01	0.18 ± 0.01	53	42	88
Winter barley	0.30 ± 0.01	0.21 ± 0.01	60	51	93
Winter bea	0.35 ± 0.02	0.23 ± 0.02	66	55	89
Sweet pea	0.37 ± 0.03	0.24 ± 0.02	70	61	93
Oil seed rape	0.29 ± 0.02	0.18 ± 0.01	51	59	90
Buckwheat	0.32 ± 0.02	0.22 ± 0.01	63	54	98
Rosebay willow	0.20 ± 0.01	0.13 ± 0.01	37		
Quinoa	0.33 ± 0.02	0.24 ± 0.01	70		

B_o: Proportion of total COD converted into methane by the end of the digestion time; B_p: Proportion of the particulate COD that was mechanized by the end of the digestion time; B_i: Proportion of the soluble COD that was methanized by the end of the digestion time

4 Co-digestion Methods in Anaerobic Digesters to Produce Biogas

The definition of co-digestion is a treatment that combines different types of substrates with the aim of improving methane production (Cuetos et al. 2011). This strategy may increase the methane production by balancing the content of nutrients for substrate and by reducing the negative effects of substrate inhibitors in the anaerobic digestion process (Cuetos et al. 2011).

Co-digestion of organic residues can ensure the feasibility of the process and in many cases, biogas yields are increased due to the synergistic effect of the use of co-substrates that provides any missing nutrients (Mata-Alvarez et al. 2000). An economic balance of anaerobic digesters shows that substrate must have a methane yield greater than 20 $m^3CH_4t^{-1}$ as biomass to be cheap. For examples, sewage has a methane yield included in a range between 10 and 20 $m_3CH_4t^{-1}$, while for industrial organic by-products the range varies from 30 to 500 $m^3CH_4t^{-1}$. Besides the increase of methane production, the addition of by-products can stabilize the process, if added in a controlled manner. For example, co-digestion of sewage and industrial by-products appears to be an attractive method to make biogas plants economically feasible. However, in Denmark, the availability of organic by-products is limited if compared to the amount of slurry and the high prices of

this biomass made co-digestion not economically attractive (Ward et al. 2010). For this reason, Hamelin et al. (2011) propose some strategies to overcome this problem: a carbon external source in the form of energy crop as co-substratum, by using a digester with a larger residence time to compensate for lower methane yields of animal sewage.

Co-digestion has several other advantages: the dilution of toxic substances which come from used substrates, the synergistic effects of microorganisms, a greater speed of digestion, a possible detoxification based on the co-metabolism process (Montusiewicz and Lebiocka 2011). However, both the supplied load and the hydraulic residence time increase (Cecchi et al. 1996).

Trying to get a co-substrates mixture as optimal conditions that allow the maximum biogas yield without compromising the stability of the process is critical.

Generally, co-digestion of sewage sludge takes place with organic substrates such as the organic fraction of municipal solid waste (Bolzonella et al. 2006), food waste (Iacovidou et al. 2012), agricultural waste (Marañón et al. 2012), and wastewater from butchery activities (Cuetos et al. 2008).

Anaerobic co-digestion of agricultural waste and energy crops, in particular, can be one of the main alternatives in this sector, as stated by the United Nations Development Programme (UNDP), which considers this technology as one of the most useful decentralized sources of energy supply, especially when used with energy crops and with all substrates that can be easily found on many farms (Cavinato et al. 2010).

Sewage is a readily available source on farms, but the reduced biogas yield does not justify the capital costs of plants. So the biogas yield can be increased by placing co-substrates that are rich in energy such as corn, grass, fruit, and bread. Different experiences show that in co-digestion thermophilic temperatures are preferred to mesophilic (Mladenovska and Ahring 2000; Van Lier et al. 2001; Angelidaki et al. 2006). However, in co-digestion systems, the addition of the organic load radically alters the process management. In fact, the stability of the process becomes much more difficult to keep, due to the greater variability of the characteristics of the process and the balance that must be maintained between acid hydrolysis reactions and methanogenesis. The maintenance of the fed composition, the pH value control, and a possible recirculation are important.

Other studies in the literature report that silage can increase the biogas yield through co-digestion of corn and clover (Amon et al. 2007). Vinasse biomass is co-digested with pigs manure in laboratory scale and in five mesophilic digesters that work almost continuously for 640 days. The performances of the process are monitored by using chemical parameters and quantitative analyzes on acidogenesis populations and methane genesis. Through vinasse utilization, the process shows instability after 120 operating days. However, anaerobic digestion of sewage sludge has a low solids content, lower than 10%, so there are low methane yields compared to other organic substrates such as energy crops. To overcome this limitation and to increase methane production from the slurry, co-digestion of slurry is carried out with different substrates (Ward et al. 2008). Co-digestion of animals slurry clearly shows improvements in biogas production, in process stability and an increase in

methane yield compared to theoretical values. The methane yield at an organic loading rate (OLR) of 2.8 g VS/(lxg) and at a residence time of 45 days with a substrate mixture formed by 85% of vinasse and 15% of liquid manure is equal to 0.31 NlCH$_4$/g VS.

Bułkowska et al. (2012) study co-digestion of corn silage (*Zea mays* L. and *Miscanthus sacchariflorus*) with 0%, 7.5%, 12.5%, 25% of PS used as co-substrate in a perfect mixing reactor, with a hydraulic residence time of 45 days and an organic loading rate of 2.1 g l^{-1} d^{-1}. A correlation matrix between produced biogas/methane and the parameters that describe anaerobic digestion is created to study the stability of the process. The values of the correlation coefficients indicate that the greater anaerobic digestion stability is achieved with the 7.5% and 12.5% of slurry. A positive correlation between ammoniacal nitrogen and volatile fatty acids concentration, composed by 25% of sewage sludge, shows the instability of the process.

PCR results show clear changes in the quantitative composition of bacterial consortia for each fermenter.

Co-digestion is a method for the optimization of biogas production in Zimbabwe and in rural areas where the amount of liquid manure produced is not sufficient to satisfy the annual biogas production (Raphael et al. 2009). The advantages are as follows:

- It provides a better balance of nutrients from a variety of substrates which helps to maintain the performance of a digester at stable levels and therefore to produce a good quality fertilizer.
- It enables the optimization of rheological qualities when wastewater with bad properties are mixed with sewage or sewage sludge.
- Biogas production from the slurry is not profitable according to current oil prices (it has a low gas yield) so the addition of co-digested with a high methane potential intensifies the gas yields.

Fountoulakis et al. (2008) study biogas production from co-digestion of olive oil mills wastes (SW), marc (WGR), and from meat by-products (OMW). Olive oil mills wastes are taken from Stavrakia, Crete, and Greece after a three-phase centrifugation process. The experiments are conducted in continuous digesters at two different temperatures: 35 and 55 °C. The addition of SW to anaerobic digestion to OMW or WGR increases the methane yield and stabilizes the internal process. Results indicate that co-digestion with 50% of OMW and 50% of SW, with 50% of OMW and 50% of WGR, and with 50% of WGR and 50% SW give a methane yield of 170, 163, and 191 kg lCH$_4$$^{-1}$ per kg of COD added. This increases the methane yield by 23–36%, compared to that obtained by digestion of only OMW and WGR. The final methane yield of OMW, from co-digestion of OMW: SW, OMW:WGR, and WGR:SW under mesophilic conditions is estimated at 184, 214, and 188 kg lCH$_4$$^{-1}$ per kg of COD added. Co-digestion of OMW:SW, OMW:WGR, and WGR:SW under thermophilic conditions produces an increase of 34.5%, 28.9%, and 14.1%, respectively. The use of SW as co-substratum in anaerobic digestion of OMW and WGR has many advantages: improves the

methane yields, provides to the system all the missing nutrients. The results of this experiment suggest that co-digestion of these organic residues is very promising.

In general, anaerobic digesters for food waste are not very stable and efficient due to the volatile fatty acids accumulation. Small fruit and vegetable wastes can be found in the low value of the *C/N* ratio. So co-digestion of fruit and vegetable wastes with other organic waste materials such as municipal sludge, sewage, agricultural biomass become widespread (Bouallagui et al. 2009). Fruit and vegetable wastes (FVW) and food wastes (FW) are two FORSU in China and their lowest *C/N* ratio can cause a rapid acidification and release ammonia which can create problems of methanogenesis inhibition in the digester. Co-digestion of FVW:FW can be a solution to this problem although limited research has been conducted on it.

Lin et al. (2011) calculate the biochemical methane potential for fruit and vegetable wastes (FVW) and food waste (FW) from a northern city in China of 12.30, 0.56 m^{3}CH$_4$/kg VS (volatile solids) with a biodegradability of 59.3% and 83.6%. The experimental tests for anaerobic digesters in laboratory scale at a temperature of 35 °C are conducted with an organic loading (OLR) of 3 kg VS/(m^3 day) for FVW and FW. For FVW, the process is stable with a 2.17 m^3/(m^{3}day) biogas production rate and with a methane yield of 0.42 m^3 CH$_4$/kg VS. Anaerobic digestion of FW fails due to the accumulation of fatty acids. The effects of the FVW:FW ratio on the co-digestion stability and performances are analyzed with the same value of OLR. For values of FVW:FW equal to 2:1 and 1:1, the performance and operation of the digester are maintained stable, without volatile fatty acids (VFA) and ammonia accumulation. An FVW:FW ratio equal to 1:2 causes an increase in the concentration of VFA to 1100–1200 mg/l, while methanogenesis is slightly inhibited. At the 1:1 ratio for co-digestion of FVW with FW, the methane production yield is 0.49 m^{3}CH$_4$/kgVS and the efficiency in the removal of the volatile solids and chemical demand for soluble oxygen are of 74, 9% and 96.1%. Co-digestion of FVW and FW cannot only achieve the highest biogas yields, but also high efficiency in the organic matter removal.

Chiu et al. (2013) carry out some studies with different organic loads that are relative to anaerobic co-digestion of kitchen wastes and sludge from animals, fruit and vegetable wastes. In kitchen wastes, the Total Chemical Oxygen Demand (TCOD), oils and fats, and moisture content (MC) are calculated to be 101.5 g/l, 33.0 g/l, and 82.7%, respectively. In swine wastewater, TCOD/TKN is 4.56–43.9 and TCOD/TP is 2.02–31.8. Some biodegradability tests on fruit and vegetable wastes show that COD removal exceeds 56% and methane recovery exceeds 80%. Co-digestion of these three organic wastes proves that the system works steadily until an OLR of 9.52 g COD/ld and at a hydraulic retention time (HRT) of 5 days. When OLR increases to 12.54 g COD/ld, the efficiency in COD and volatile suspended solids (VSS) removal decreases from 90% to 76.5% and from 93% to 76.5%. The analyzed ammoniacal nitrogen concentration is 28% lower than the stoichiometry concentration planned. The discrepancy may be due to different biodegradability of the substrate, to sampling and analysis procedures of TKN, and to the parameters used for stoichiometric calculations.

Sewage is an abundant substrate for anaerobic digestion (Kaparaju and Rintala 2005; Nasir et al. 2012). In Denmark, the methane potential energy, annually generated through anaerobic digester is equal to 30 petjoule (PJ) and sewage contributes 80% to this potential.

It is estimated that liquid manure production in the future will continue to increase. This phenomenon is inevitable since the improvement in well-being and in standard social life is followed by a dietary change from carbohydrate sources to protein sources. The consequence of this is a strong demand for animal products, especially in developed countries. For example, sewage handling, through anaerobic digesters, particularly in Denmark is in line with the objective of using 50% of the produced slurry as a substrate for anaerobic digesters and therefore producing renewable energy in the form of biogas by 2020 (Aftale om Grøn Vækst 2009).

Sewage is an advantageous substrate for anaerobic digestion processes since it has a high water content that ensures dilution and it allows to avoid problems with the pumping; it contains a wide range of nutrients that promote the growth of microorganisms. However, there are also some limitations to its use. High water content means that there is little easily biodegradable carbon to produce sufficient methane per unit volume (Hamelin et al. 2011); therefore, much more energy is required to maintain the temperature inside the digester, and there are further costs related to sewage transportation in the biogas plant (Asam et al. 2011).

Methane production from sewage in terms of volatile solids (VS) is about $290 \ 1 \ kg^{-1}$ for slurry and $210 \ 1 \ kg^{-1}$ for cow manure (Burton and Turner 2003). Since the concentration of VS is lower than 5–7% for PS and then 7–9% for cow manure, methane production is low. This makes anaerobic digestion uneconomical. The main problems occurring with digestion of sewage in an anaerobic digestion process are the high water content and the low biodegradability of slurry due to the high content of fibers that are constituted mainly by lignocellulosic material (Hamelin et al. 2011). The biodegradability of the slurry is about 32%, 69%, and 52% for cow manure, and sow slurry. The presence of fibers hinders the hydrolysis processes (González-Fernández et al. 2008).

However, slurry is considered a very good substrate for anaerobic digestion due to its buffering capacity and its high content of a wide range of nutrients. But it has a low biogas yield, 20–30 m^3/ton (Angelidaki et al. 2003) and a high concentration of ammonia nitrogen (2–3 $gN-NH_4^+$/l). For this reason, co-digestion of wastewater with a high content of carbon is preferable, not only to increase the C/N ratio but also to increase biogas production by making the process economic.

Co-digestion of pig slurry (PS) with fish waste (FW) and biodiesel waste (BWs) is evaluated by Regueiro et al. (2012) and compared with the sole digestion of PS. The results demonstrate that co-digestion of PM with FW and/or BWs is possible only if the concentration of ammonia nitrogen and fatty acids remain below the inhibition level, by modifying some operating parameters such as feeding composition, the organic loading rate (OLR), and the hydraulic residence time. Co-digestion of PM and FW is possible with an OLR of 1–1.5 g COD/ld, in a biogas production of 0.4–0.6 L/L with a COD removal efficiency of 65–70%. As regards BW, good results (biogas production of 0.9 L/L d and COD elimination of 85%) are

achieved with a feeding concentration lower than 5%. However, if we operate at the same OLR, biogas production and methane content in co-digestion are increased if compared to the sole digestion.

Ogunwande et al. (2013) conduct studies about co-digestion of swine manure (SM) and chicken manure (CM) to optimize biogas production. Five different mixtures are considered with the SM/CM ratio of 0:1, 3:1, 7:1, 7:3, and 1:0, and they are digested in batch reactors for 63 days. The results show that co-digestion has a significant effect on the temperature of the substrate, on pH, and on the produced biogas. The average temperature of the substrate and the pH value during the digestion are 28.5 ± 2.5 °C and 6.8 ± 0.55. The biogas obtained from the mixture ratio 0:1 and 1:0, produce 0.52 and $0.38 \, l \, kg^{-1} \, VSfedday^{-1}$ on average per day. A value of ratio equal to 1:1 allows to obtain a biogas production higher than 69.2% and 131.6% if compared to ratio equal to 0:1 and 1:0.

Gomec and Ozturk (2013) evaluate biogas production from co-digestion of two different slurries (pork and chicken) in an anaerobic digester under mesophilic conditions. To increase biogas production, silage corn is added and the total produced energy (heat and electricity) is 1.2 times increased by a cogeneration system. The amount of produced methane is calculated as 5800 and 6580 m^3/day, while total energy is equal to 45.05103 and 51.05103 kWh, without or with the addition of corn silage.

Miao et al. (2014) observe as that co-digestion of blue algae with PS allows having the highest methane content equal to $212.7 \, ml \, g^{-1}$ with a ratio between the two substrates (blue algae/liquid manure) equal to 2. However, pH values, ammonia nitrogen, ammoniacal nitrogen, and volatile-free fatty acids do not show a significant difference between the single digestion and co-digestion. This confirms the stability of the process. The results demonstrate that this system is promising for energy production from renewable sources and for solid waste treatment.

Cavinato et al. (2010) study co-digestion of manure and other organic waste. If the temperature rises to 55 °C, biogas production is increased from 0.45 to 0.62 m^3/kg VS, compared to normal thermophilic conditions of 47 °C (typical of European co-digesters). Also methane content increases from 52% to 61%. With a higher stability of the parameters (pH, ammonia, VFA content), a general improvement of the digester is obtained. They also study the economic feasibility of such plant, considering the use of a co-generator of 1 MW for electricity and heat generation and a system for nitrogen removal. The simulations show PB values of 2.5 years, and 3 and 5 years, in a biogas plant with or without the nitrogen removal process.

Nges et al. (2012) show that the co-digestion of industrial and energy crops wastewater allows an increase in the produced methane yield per ton of power. The system also avoids the need for micronutrients that digestion of energy crops normally requires. Batch co-digestion is used to predict some results which can be obtained on a large scale, using a CSTR digester: the *C/N* ratio increases while the concentration of fatty acids decreases. Moreover, the economic feasibility of the system improves under these conditions.

Pastor et al. (2012) study the co-digestion of mud and oil used for a semicontinuous digester, in a pilot plant and under mesophilic conditions (38 °C).

They find that the addition of 0.5% of oil allows doubling the biogas production. The optimum percentage of oil in the mixture is 19%. The process of co-digestion improves the volatile substance removal (greater than 11%, if compared to the case where co-digestion is not used) and also the biogas production (greater than 23.5%, if compared to the case where co-digestion is not used). The efficiency of the produced biogas is the same in the presence or absence of co-digestion because the same kilowatts of energy per m^3 of biogas are produced by means of cogeneration.

Thy et al. (2005) conduct experimental tests in a farm in Cambodia that last 150 days and consist of five treatments with proportions between pig and cattle liquid manure equal to 100:0, 75:25, 50:50, and 25:75. Plug flow digesters, with a volume of 640 l and a residence time of 20 days, using a polyethylene tubular film are used. They verify that when the proportion of PS increases, the amount of produced gas increases more than 50%. The proportion of N in N total ammonia is also increased. The N experimental measurements are conducted with the Kjeldahl method. Instead, ANOVA analysis is used to describe the gas production trends, the characteristics of slurry, sludge, and effluents. They conclude that cattle manure produces less biogas and less valuable fertilizers if compared to manure.

Agricultural substrates such as fruits and easily biodegradable vegetables with a low nitrogen content are appropriate for co-digestion, and they can ensure a good methane production with animal organic waste. (Bouallagui et al. 2009; Dinuccio et al. 2010). Moreover, the use of agricultural substrates in co-digestion is a viable solution for its disposal in areas of high agricultural production. So the combination of PS and carbon-rich substrates can lead to better performance than digestion of PS only. Furthermore, co-digestion can lead to a reduction in the concentration of some compounds (such as ammonia and volatile fatty acids) that are present in the slurry and which may be toxic in the anaerobic digestion process (Murto et al. 2004). Agricultural substrates may have a different effect in the presence of other substrates (Fountoulakis et al. 2008).

Gelegenis et al. (2007) show that mills wastes may inhibit some microbial groups in anaerobic reactors, during co-digestion with chicken manure. These authors report that the presence of phenols and aromatic oils in agricultural substrates could inhibit the development of the populations of Archea in methanogenic consortia. Furthermore, methanogen populations and their domains are poorly understood by adding a substrate for the co-digestion with PS (Yue et al. 2013).

Ferrer et al. (2014) evaluate the effect of four different agricultural substrates (tomato, pepper, peach, and persimmon) on the biochemical methane potential (BMP) in an anaerobic digester during co-digestion of PS. The study is focused on optimizing the combination which improves the CH_4 production, and it may be a PS management in high livestock density areas. The experiments are conducted in plastic bottles for 100 days, under mesophilic conditions (35 $\mp$ 1 °C). The bottles are prepared to reach a certain homogeneity in volatile solids (1.3 g VS + manure from agricultural substrates + inoculum) as well as the amount of the inoculum (33.6 ml per bottle). On the basis of volatile solids, the inoculum-substrate ratio is equal to 0.7 in all combinations; therefore, the variation of the volatile solids in the composition is only attributed to the agricultural substrate. The concentration of

methane in the produced biogas is analyzed by using Focus Gas Chromatograph, with a split/splitless injector and a flame ionization detector. From some experiment they find that: vegetable substrates (pepper and tomato) show a higher content of lipids, proteins, lignins, and cellulose compared to fruit substrates. However, the latter have a higher carbohydrate content. The highest BMP values are achieved with those substrates that have a protein content between 14 and 20 g 100 g^{-1} VS, lipids between 4 and 5 g 100 g^{-1} VS, and carbohydrate between 74 and 78 g 100 g^{-1} VSn of tomato and pepper.

Some differences, concerning BMP production and observed in the study, can be explained by the composition of the substrate. BMP depends on the amount of the following components: lipids, proteins, carbohydrates, and lignin. The CH_4 potential of these components is equal to 1014 lCH_4 kg VS^{-1} (lipids), 496 lCH_4 kg VS^{-1} (proteins), and 415 lCH_4 kg VS^{-1} (carbohydrates).

Molinuevo-Salces et al. (2010) achieve an increase in BMP of 27%, by using PS in co-digestion with fresh corn, carrots, peas, and leaks, at inclusion levels from 15% to 85%, measured in terms of percentage of TS of vegetable substrates in relation to the TS of the initial PS.

Riaño et al. (2011) raise the BMP value by 49% by adding winery wastewater to wastewater during co-digestion at a level from 15% to 85%, measured in terms of COD. The increase in BMP with increasing agricultural substrate inclusion level can be explained by the adaptation of the co-substrate mixture to the optimum characteristics for digestion as regards the biodegradable organic matter. This is confirmed by the co-digestion of animal manure and agricultural substrates in continuous experiments using a continuous flow stirred-tank reactor or similar configurations (Callaghan et al. 2002).

Scano et al. (2014) carried out experimental studies on an anaerobic digester in a pilot plant which uses fruit and vegetable wastes as substrates, coming from the Fruit and Vegetable Wholesale Market of Sardinia (Italy). The experimental study is conducted for a period of about 6 months to assess the most suitable operating parameters of the process, according to the availability of different types of fruit and vegetable wastes in different periods of the year. Overall, the optimal waste loading rate is 35 kg/every day, with a corresponding hydraulic residence time of 27 days. The optimal organic loading rate ranges from 2.5 to 3.0 kg VS/m^3 d, and the average specific biogas production is approximately 0.78 Nm^3/kg VS, with a specific methane yield of about 0.43 Nm^3/kg VS. The results of the experimental study are used for preliminary evaluations of the performances of anaerobic digestion plant, employed for the treatment of all wastes produced by fruits and vegetables coming from the Wholesale Market of Sardinia. The estimation of daily methane production (290 Nm^3/d) is sent to a cogeneration unit with an output of about 42 kW and an annual power generation of about 300 MW h/year (about 25% of the Wholesale Market electricity consumption). The plant also shows interesting economic features since the cost of energy production (about 150 €/MW h) is slightly lower than the energy purchase cost of the wholesale market (about 200 €/MW h). A return time of 7.25 years can be made if electrical energy is sent

to the national network. PBT decreases by about 5.4 years if 50% of available thermal energy is used to replace heat production from fossil fuel boilers.

Bouallagui et al. (2009) study anaerobic digesters fed with fruit and vegetable wastes (FVW). These wastes are characterized by a content between 8 and 18% of total solids (TS) and by 86 and 92% of total volatile solids (VS). The organic fraction includes about 75% of biodegradable matter (sugars and hemicellulose), 9% of cellulose, and 5% of lignin. Anaerobic digestion of FVW is studied under different operating conditions and using different types of bioreactors. The 70–95% of organic matter conversion into methane is reached, with a volumetric organic loading rate (OLR) from 1 to 6.8 g fed versatile solids (VS)/l day. There is an important limitation, in this case, that is a rapid acidification of these wastes, with a pH decrease in the reactor, and a higher volatile fatty acids (VFA) production, which inhibits the methanogenic bacterial activity. Systems with two continuous phases appear to be the most efficient technologies for anaerobic digestion of FVW: more than 95% of volatile solids is converted to natural gas with a volumetric loading rate of 5.65 g VS/l d. They find that the average methane production yield is equal to 420 l/kg added VS.

Sitorus et al. (2013) carry out studies on anaerobic digestion of a mixture of fruit and vegetable wastes, for 14 weeks and at room temperature. The mixed fruit and vegetable wastes, collected in a city of Pontianak, are used as substrates in a single batch phase for biogas production. The wastes are taken according to the sampling method, with a composition of ±78% of vegetable wastes, ±4% of tuber wastes, and ±18% of the fruit wastes. Once manually mixed, the total waste weight is 160 kg. They find that the maximum content of methane in biogas is 65% with a biogas flow of 20–40 ml/min.

As suggested by several authors, sewage produced by various kinds of livestock, subjected to different diets are a source of gaseous emissions.

Methane emissions are generally reduced during slurry storage and the quality of fertilizers obtained is high.

For example, the reduction of proteins and the addition of nutritional additives and enzymes to formulated diets for pigs is found to be effective in reducing nitrogen, phosphorus, calcium, and other nutrients excretion (Veum et al. 2006), thus helping to reduce the environmental impact. Likewise, the reduction of protein content, associated with an addition of amino acids or fiber to the diet allows the reduction of excreted nitrogen and, consequently, of ammonia emissions. Dietary modifications can also affect methane production from manure, but few studies about it are conducted. Velthof et al. (2005) show that the decrease of protein in a diet reduces methane production, while the addition of fibers increases it. The increase of fiber in swine diets shifts nitrogen from urine to feces, increases the excretion of a few fatty acids, and decreases the pH value of feces.

Amon et al. (2006) try to find a relationship between the dairy cattle diet, manure composition, and methane yield. They also try to optimize anaerobic digestion of PS with corn silage and with the addition of glycerin. The latter allows increasing the methane yield of an anaerobic digester fed by protein-rich substrates (corn silage, PS, rapeseed flour). As regards pig farms, protein, and fiber diets affect

ammonia and methane emissions (Dourmad and Jondreville 2007). High fiber and low protein diets can reduce ammonia emissions. But this has an effect on methane emissions, too. In fact, some studies show that the reduction of protein weakens the maximum amount of methane that can be produced (Velthof et al. 2005), while this potential is higher with high fiber diets (Velthof et al. 2005). The right content of fiber and protein can be achieved by providing less soymeal, by adding amino acids and by increasing the incorporation of protein and/or fiber-rich by-products (Jarret et al. 2011a). At the same time, the recent increase of by-products such as biofuels, wheat distiller's dried grains with solubles, rapeseed flour, and sugar beet pulp, could be an economic and ecological alternative resource for swine diet. In the last 10 years, thanks to the rapid growth of ethanol industry in Canada, North America, and Europe, the amount of corn and wheat distiller's dried grain with solubles increase. So many studies are aimed at evaluating the effect of different by-products (wheat DDGS, sugar beet, and rapeseed fatty meal) on the composition of sewage and on methane emissions.

Jarret et al. (2011b) use five different swine diets, with a different content of fiber and protein: two control diets, a control high protein (CHP), a diet with 17% of crude protein (CP), a low-protein control (CLP) diet with 14% of CP, and three experimental diets with 17.5% of CP, with 20% of (1) dried distillers grain with soluble (DDGS), (2) sugar beet pulp (SBP), or (3) fatty rapeseed meal (FRM). They use a CSTR digester with a 30-day residence time. They evaluate the B_o value (ultimate methane potential) and the methane conversion factor, which reflects the portion of B_o converted into methane, in the obtained slurry. They use two different methods to measure methane. The first measures the amount of B_o in sewage sludge through the bio-methanogenic potential (BMP) test. In particular, the quantity of emitted methane expressed in liters is calculated on the basis of the organic content (OM), the volatile solids content (VS), the methane conversion factor (MCF) that reflects the amount of B_o really converted into methane and the ultimate methane potential expressed in $lCH_4 \ kg^{-1}OM$ (Eq. 10.15).

$$CH_4 = B_o \cdot MCF \cdot OM \qquad (10.15)$$

The values of B_o and of methane conversion factors are reported in the IIPCC. The second type of measurement is based on different effluents: fresh mud, stored mud, and a mixture of stools and water. They observe that the kind of diet and effluents affect the methane production after 30, 50, and 100 days. The interaction between the type of diet and manure is significant for methane emissions and for the methane conversion factor. The BMP method registers a greater methane production, while the average methane production is 77%, 58%, and 64% of the ultimate methane potential for fresh mud, stored mud, and the mixture of stools and water. The results of the experiments show that the type of diet has a significant effect but that it is rather limited in the ultimate methane potential from the slurry. The effect of diet is much more evident on the methane conversion factor, with low levels of high protein diets and high levels for high fiber diets. The results obtained in the experimental tests can be used to improve dietary characteristics to limit

uncontrolled methane emission in the environment and to maximize methane production, when anaerobic digestion is used for energy production.

Jarret et al. (2011a) evaluate the effects of adding 25% of DDGS (dried distiller's grain soluble) to swine diet, on the excretion of organic matter, nitrogen, and carbon and on the methane potential emitted by feces and urine. They conduct eleven experiments: a control diet mainly based on cereals and soybean meal, and ten experimental diets obtained by adding to the control diet 25% of one of the ten samples of DDGS. The ultimate methane potential (B_o) of effluents is measured with an increased digestion time of 100 days, for each type of diet. The addition of DDGS increases the amount of the produced feces from 27% to 50% and that of urine from 7% to 50%, if compared to the base case. The amount of organic matter produced by feces and urine increases by 65% and 54%, if compared to the basic case. The B_o values measured in feces and in urine vary in a range between 202–294 and 278–368 LCH$_4$/kg OM. On average, these values are lower than those obtained in the basic diet.

Sorghum production increases significantly in Brazil, so it can be used in animal feeding since it has a good nutritional quality and can be a substitute for corn. According to it, the author assesses the quality and the amount of produced biogas, starting from a supply that consists in the initial, increasing and final decomposition of PS, deriving from a corn- and sorghum-based diet. Experimental tests are performed on 20 batch digesters with a 30-day residence time, a solids content between 4% and 6% and a volatile solids between 3.2% and 5.6%. They also find that the average biogas production is greater in digester fed with feces.

Jarret et al. (2012) show that the addition of high fiber biofuel in diet causes a displacement of nitrogen from urine to excreted feces, a decrease in slurry pH, and an increase in C compounds, OM, VFA in the latter. This causes a decrease in the speed of ammonia volatilization during storage and an increase of produced methane. Results show that the addition of fibers and a lower content of proteins have significantly reduced the amount of ammonia nitrogen accumulated and volatilized, while the speed of ammonia volatilization rose from 12% to 32% if compared to high protein diets. So diet composition and its effects on effluent quantity and characteristics should be considered in a context of optimization of wastewater treatment, by minimizing ammonia and methane emissions or, in other situations, by maximizing the uncontrolled methane emissions from sewage.

Möller et al. (2010) study the amount of produced biogas and greenhouse gas emissions from dairy cattle manure, produced by different diets. The experimental tests are carried out in CSTR digesters, with a volume of 7 l and under mesophilic (35 °C) and thermophilic (50 °C) conditions. Instead, the experimental batch tests are conducted without the inoculum at four different temperatures (10, 15, 20, 35 °C). They also conduct some tests with the inoculum and under thermophilic and mesophilic conditions to determine the final methane yield. The cows are fed with low-fat corn silage, with corn silage and crushed rapeseed or with corn silage and grass silage (low-fat clover). The amount of biogas produced from sewage is in the following order: corn + fat > corn > grass. They analyze methane emissions from untreated liquid manure at a low temperature and under anaerobic conditions,

in which it is possible to observe the bacterial degradation of organic matter. Thanks to the international IPPC method that is famous for methane emissions calculation; they find that these are higher at all temperatures with a high-fat diet and that there are much more benefits in biogas production with this diet if compared with other diets. Therefore, fats have a positive effect on biogas production.

Amon et al. (2007) optimize the biogas production in an anaerobic digester from corn and cattle slurry. In fact, there is a growing demand for biogas production from these substrates. The highest biogas yield is achieved by sewage deriving from cattle fed with a well-balanced diet. Methane production is measured for 60 days in a batch reactor and at a temperature of 38 °C. The highest methane yield achieved is of 166.3 NlCH$_4$ kg VS^{-1}. Thirteen different varieties of corn are cultivated: the methane yield decreases when crops approach ripeness and with late varieties, the methane yield is between 312 and 365 NlCH$_4$ kg VS^{-1} for milk stage, and it is between 268 and 286 NlCH$_4$ kg VS^{-1} for complete maturation. Corn silage can increase the methane yield by 25% if compared with the natural one. Corn silage yields are of 289 NlCH$_4$ kg VS^{-1}, whereas the natural one is 25% lower, 225 NlCH$_4$ kg VS^{-1}. During silage, lactic acid, acetic acid, alcohols, formic acid, H$^+$, and CO$_2$, that are important precursors for methane formation, are produced. Another reason may be the decomposition of fibers during the ensiling process that increases the availability of fibers for methanogenesis.

The importance of nutrition in biogas plants is also studied by Piccinini et al. (2008). They analyze some substrates such as manure, energy crops, and/or agro-industrial residues. In both cases, it is necessary to consider the specific characteristics of the used matrix to have a proper operation of the plant. For energy crops, product uniformity makes the construction more reliable, even if it requires a lesser complexity of the plant. The addition of agro-industrial residues determines issues about the supply continuity and quality variability. These problems can be overcome if the matrix undergoes a silage, or if the main load is energy crops.

The input energy of a digester also influences the energy efficiency of the process. Anaerobic digesters are a valiant option in wastewater treatment, but the use of biogas requires the maintenance of a positive life-cycle energy. Many studies about energy balance are focused on the used raw materials, biogas systems, different waste management strategies, and possible options for biogas use (Pöschl et al. 2010).

Pöschl et al. (2010) evaluate the food impact (single or co-digestion) of different strategies for downstream waste management and the energy balance of plants. The input data are obtained from biogas plants, knowledge on the anaerobic digestion process, and technology management. The energy balance is assessed using the Primary Energy Input to Output (PEIO) ratio. For single feeding, the Primary Energy Input to Output (PEIO) ratio varies between 10.5% and 64% depending on the energy required for the provision of raw materials. The energy balance becomes negative when the distance for cattle manure transport is greater than 22 km and that for municipal waste is greater than 345 km. The input energy is strongly influenced by raw materials characteristics. Agricultural wastes, for

example, in most cases do not require any pretreatment. The energy balance depends on the biogas yield, the efficiency, and the energy value of fossil fuels replaced by biogas. As concerns co-digestion with multiple feeding, the PEIO varies between 45.6–48.6% and 34.1–55% for the small and large scale of biogas plants. This suggests a greater stability in the co-digestion process. Results suggest that the energy efficiency can be increased by 5.1–6.1% through the recovery of biogas emitted from the stored digestate.

The energy and environmental efficiency of biogas plants, according to the matrix, are analyzed by Bacenetti et al. (2013). They evaluate the energy and environmental efficiency of three different biogas plants with different electrical power and different feeding. They observe that sludge allows lower emissions but a higher consumption of thermal energy for heating. The environmental impact and energy efficiency are evaluated through LCA analysis, by using the amount of produced biogas as a functional unit. Results suggest that biogas plants also require that the anaerobic digestion process reaches the highest methane yield according to the kind of feeding used and by ensuring the highest peak of produced energy. The input power also affects the economy of the process. A mathematical model, that is made to describe the stationary and temporary state of a digester, shows the existence of a residence time and a quantity of substrate input flux that are able to maximize methane production in the produced biogas (Balmant et al. 2014).

To keep the anaerobic process for biogas production stable and uniform, it is necessary to feed it with a certain quantity of substrate with a stable quality or by varying the quantity to obtain a specific quality. Fed quantities are manually changed with biogas flow variations. Continuous information on the substrate quality are not available and analyses on feeding are too much expensive. Jacobi et al. (2012) evaluate the feasibility of near-infrared spectroscopic (NIRS) for an online monitoring of the substrate quality to find a way to control biogas production. An NIRS sensor is designed, built, and calibrated for continuous monitoring of dry matter [0.75% fresh matter (FM)], volatile solids (0.74% FM), crude fat (12.09% FM), crude protein (12.22% FM), crude fiber (1.50% DM), and nitrogen-free extracts (0.93% FM) of maize silage.

Centralized anaerobic digesters are in general used, in co-digestion processes. Many farms cooperate to feed a large centralized digestion plant, powered by different substrates. It is a standard technology used in Europe, Asia, and in the USA. Thorin et al. (2012) conduct studies to improve biogas production from co-digesters in the Växtkraft plant in Vasteras. Organic waste coming from civilian homes and restaurants are mixed with pasture crops and with the process water which is recirculated and sent to the digester. Solid and liquid wastes are then co-digested in a digester, with an extension of 4000 m^3. Later, the produced biogas is purified and used for vehicles operations, while plant residues are then used as fertilizers. They evaluate that the pretreatment of feeding and the use of membranes for filtering the recirculated water, allow an increase in biogas production up to 30%.

4.1   Inhibition of Microorganisms During The Co-digestion Method of Anaerobic Digesters

To prevent the inhibition of microorganisms during the co-digestion process, substrates with high biogas potential must be carefully added to avoid the suboptimal digestion conditions caused by the inhibition of microbial activity.

Nielsen and Angelidaki (2008) report that in biogas plants used in Denmark, for animal and industrial organic by-products sewage treatment, a high concentration of ammonia and long-chain fatty acids are due to the inhibition of microorganisms. This inhibition is indicated by a decrease in the speed of methane production and by an accumulation of fatty acids in the digester. Some inhibitors and inhibitory thresholds are reported in the Table 10.3.

The inhibition of microorganisms in the anaerobic digestion process can be attributed to inadequate knowledge of the organic substance composition, insufficiency in the knowledge of the characteristics of substrate degradation, inadequate supervision of the process, especially as regards the VFA concentration, insufficient substrate storage, by causing an improper mixing and a lower degree of precision in the substrate dosage (Nielsen and Angelidaki 2008).

Ammonia is a product of biological degradation of organic substances with a nitrogen content, mainly in the form of proteins and urea (Kayhanian 1994). Ammonia is essential for microbial growth, but if it is present in a high concentration in the substrate, it can cause the inhibition of the digestion process. The inhibition threshold is reported in the table, and it is a combination of free ammonia nitrogen and ionized ammonia nitrogen (Kayhanian 1994).

Angelidaki and Ahring (1993) observe the performance of a digester treating cattle manure under thermophilic conditions when the concentration of free ammonia exceeds 7 g l^{-1}. Whittmann et al. (1995) propose a change in the pH intercellular value, an increase in the required energy demand, and the inhibition of the specific enzymatic reaction as a mechanism of ammonia inhibition. The ammonia inhibition experiments using urea as a source of ammonia are conducted with five different TAN values and with some digesters maintained at 50 °C for a

Table 10.3 Inhibitors and inhibition threshold in the AD process

No	Inhibitors	Inhibition threshold
1	Ammonia	TAN 2.5 g l^{-1} both mesophilic and thermophilic of AD processing cattle manure that not previously acclimated to high ammonia concentration; 4 g l^{-1} to previously acclimated with high ammonia concentration (Hashimoto 1989) Increasing FA: 0.55–0.65 g l^{-1} in thermophilic of AD causes decreasing methane yield by 25% of digester processing cattle manure (Angelidaki and Ahring 1993)
2	LCFAs	Oleic acid and lauric acid IC50 = 4.3 mM (Chen et al. 2008)
3	Sulfide	100–800 mg l^{-1} as dissolved sulfide or approximately 50–430 mg l^{-1} as undissociated H_2S (Parkin et al. 1990) C/SO_4^{2-} = 1.6 corresponding to 1400 mg SO_4^{2-} l^{-1} (Siles et al. 2010)

residence time of 4 h. They find a negative correlation between the methane yield obtained from cow manure and that with a concentration of TAN and VFA. Methane yields with a TAN of 2.93 g l^{-1} and an FA of 0.71 g l^{-1} are less than 23.6% if compared to those with TAN values of 2.15 g l^{-1} and FA of 0.48 g l^{-1}. Isobutyric and isovaleric acid are accumulated during the experiments so that they are indicators of ammonia inhibition.

Nakakubo et al. (2008) suggest that isobutyric, butyric, and isovaleric acid can be used as indicators of ammonia inhibition. After a period of ammonia inhibition, butyric and valeric acid gradually decrease and they suggest a conversion into isobutyric acid and then in propionic acid (Nielsen and Ahring 2007).

In the case of ammonia inhibition, VFA concentration, isobutyric acid, isovaleric acid, TAN values, and biogas production can be used as process indicators. Kayhainan (1994) suggest that to prevent ammonia inhibition the C/N value of the substrate must be kept between 22 and 35 and that the pH value inside the digester must be controlled. Chen et al. (2008) propose a method to obstruct ammonia inhibition by increasing the residence time of biomass in the digester, by switching off the stirrer half an hour before the addition of the substrate and by immobilizing microorganisms with inert material (clay, activated carbon, zeolite).

Slurry acidification with sulfuric acid can help to reduce ammonia emissions. Kai et al. (2008) find that this method can help to reduce ammonia emissions by 70% for PS. However, a high acid concentration may cause the inhibition of microorganisms in the anaerobic digestion process. The presence of sulfates in the acidified manure may help the growth of the sulfate-reducing bacteria (SRB) which compete with metanogeneci bacteria.

The ultimate methane yield of acidified cow manure is significantly less than 45%, compared to not acidified manure. Batch digestion that both raw and liquid-manure acidified fraction shows sulfide inhibition, but this does not happen while evaluating the solid fraction of acidified slurry. However, methane production from a solid fraction of the slurry is greater than the not acidified one, whereby the acidified solid fraction can be used for co-digestion to increase the methane yield (Sutaryo et al. 2012). So co-digestion of cow manure with the solid fraction appears a promising method to increase methane production. They show that there is not any negative effect in the acidification process of the solid fraction of cattle manure on the methane yield, but there is sulfide inhibition of the anaerobic digestion of acidified manure. To avoid this, some substrates with high biogas potential must be added carefully to prevent the suboptimal conditions of digestion that cause the inhibition of microorganisms.

Siles et al. (2010) evaluate sulfate inhibition using continuous flow reactors that process Na_2SO_4-fed glucose and they find that the inhibition ratio C/SO_4^{2-} is 1.6, which corresponds to 1400 mg l^{-1} SO_4^{2-}.

Moset et al. (2012) find a reduction in 18% of methane in an anaerobic digester, starting from a substrate that consists of 20% of acidified PS and in 80% of not acidified slurry. However, the concentration of sulfates in the substrate is of 730 mg l^{-1}.

Chen et al. (2008) propose a method to prevent and to reduce sulfide inhibition by including the substrate dilution and by reducing the concentration of sulfide in the substrate by means of stripping, coagulation, oxidation, precipitation, and partial oxidation.

The solid fraction of manure has a high potential in methane production per unit fresh weight, so it may be used as co-substrate for anaerobic digestion (Hjorth et al. 2010).

Sutaryo et al. (2012) assess co-digestion of not acidified cattle manure with its acidified solid fraction. They use three different concentrations of acidified solid fraction, that are equal to 10%, 20%, and 30%, in a thermophilic digester at a temperature of 50 °C. The acidified solid fraction of cow manure is obtained from a Danish farm, by using an acidification technology developed by InFarm A/S, Aalborg, Denmark. Solid-liquid manure separation is performed using the screw-press solid-liquid separation method with 0.5 mm screen size. They find that methane production per VS substrate gram decreases significantly as the concentration of the solid fraction in acidified cow manure increases. This phenomenon can be explained by the fact that the solid fraction of acidified cow manure is a recalcitrant part of animal sewage with a lower biodegradability. This result is in line with the reduction of the VS concentration as the solid fraction concentration of acidified cow manure increases. However, methane production from a power supply with 30% of acidified solids is about 50% greater than the base case model. Furthermore, digestate has a residual methane potential that is three times higher. So post-digestion of acidified digestate with a high concentration of solids is necessary to prevent methane emissions from digestate.

Co-digestion of acidified solids also allows having a stable methane production and a low concentration of VFA. Rasi et al. (2011) report that the H_2S concentration in biogas plants for common boilers and internal combustion engines should be smaller and it does not exceed 1000 ppm.

Sutaryo et al. (2012) determine the methane production from different acidified slurry fractions that are produced by different solid-liquid separation methods. The experiments are conducted in batch digesters under mesophilic conditions and for an incubation period of 90 days. The different substrates used in the experiments are: a fraction of acidified sow slurry that is subjected to separation by a screw press with four different screen sizes and two different dishes voltages, a fraction of acidified PS that is subjected to drum/rotating screen, and acidified cow manure not subjected to the separation process that is filtered press. The results show that the ultimate methane yield of the solid fraction of acidified PS increases significantly with a bigger screen size in screw press manure separation. The ultimate methane yield from the solid fraction of acidified PS through a separation process with the drum is higher compared to the solid fraction of acidified cow slurry, obtained from the screw press separation method. This is due to the different substrate composition.

4.2 C/N *Parameter for Co-digestion Processes of Anaerobic Digesters*

The C/N parameter is important in the optimization of an anaerobic digester diet.

Zeshan et al. (2012) evaluate the effects of the C/N ratio and the associated ammonia, in an anaerobic digester operating under thermophilic conditions. This parameter has a certain influence on the global methane yield (Guendouz et al. 2010). The ammonia nitrogen concentration prevents the reduction of biomass activities and avoids the inhibition of the anaerobic digestion process. In particular, ammonia nitrogen has a much more significant inhibitory effect on methane genesis that ionizes ammonium ion. This causes a considerable drop of pH and ammonia production.

Li et al. (2013) report that the optimal C/N values are in the range 20–30: higher values release a lower concentration of ammonia nitrogen in the digester. Different amounts of organic loading rate (OLRs) and recirculated digestate are set to improve the biogas recovery and to overcome the problem of ammonia nitrogen accumulation within the system (Table 10.4).

Wang et al. (2012) evaluate the possibility of improving methane yield from an anaerobic digester that is fed with a mixture of dairy slurry (DM), poultry manure (CM), and wheat straw (WS) optimized according to the C/N ratio. They show that as the C/N ratio increases, methane potential increases. Values equal to 25:1 and 30:1 allows to have the best digester performance with a stable pH and low concentrations of total ammonia nitrogen. The maximum methane potential is achieved with DM/CM equal to 40.3:59.7 and a C/N of 27.2:1, obtained through the optimization of response surface methodology.

Table 10.4 Factors that influence the thermophile digestion

Factors	Causes	Effects
C/N	Low C/N High C/N	Accumulation of TAN and VFA Rapid consumption of nitrogen by methanogens and low gas production
Total ammonia nitrogen	With 30% TS fed With 18% TS feed With 7% TS feed With 20% TS feed	Inhibition at 1200 mg TAN/l Inhibition at 3500 mg TAN/l Inhibition at 4000–5000 mg TAN/l No TAN inhibition, TAN: 2300 mg/l 17% loss in methane yield
Solid content	Increase from 20% to 30% of TS	14.4% decrease in organic removal
Inoculation and retention time	Less inoculums High inoculum	Needs high retention time Need less retention time, accelerated start-up High gas production rate
Temperature and retention time	High temperature	Free ammonia inhibition Needs low retention time

TAN Total ammonia-N, *VFA* Volatile fatty acid

Ye et al. (2013) study the optimal feeding for biogas production that consists of rice straw, manure, and kitchen wastewater. They use batch digesters in series, under mesophilic conditions. The optimal ratio, which is found for kitchen waste, manure, and rice straw, is 0.4:1.6:1 with a *C/N* ratio equal to 21.7. The methane yield of 674.4 l/kg VS is higher than the value equal to 71.67% and 10.41% obtained from digestion of rice straw and PS.

5 Pretreatments of the Biomass to Produce Biogas in Anaerobic Digesters

Different biomasses are used in the anaerobic digesters to produce biogas.

Low cost and low-value substrates that can be used in biogas plants in a sustainable way are the agricultural by-products such as slurry, straw, and energy crops. Unfortunately, these organic materials have a low biodegradability, so that their treatment is not cheap (Møller et al. 2007). A common way to solve this problem is to do a pretreatment to the substrate.

Currently, there are several pretreatments: mechanical, physical, thermal, chemical (alkali, acid, oxidative), and organic or a combination of them (Hendriks and Zeeman 2009).

An effective pretreatment may increase the area, by improving substrate accessibility to enzymes, or may minimize the loss of substrate and the formation of inhibitors.

For this reason, pretreatments make the organic substance of smaller size: it is more accessible to microorganisms and methane production is increased. Speed and degradation degree increase after size reduction especially for substrates with a high fibers content (Palmowski and Müller 2003). In fact, there are several factors that contribute to limit the enzymatic hydrolysis of biomass, like crystallinity, the degree of polymerization of cellulose, the presence of lignin, the cellulose protection from hemicellulose, and fiber strength (Mosier et al. 2005).

Pretreatment with lime is most promising because the levels of inhibitors (furfural, methyl furfural, and hydroxy soluble phenolic compounds) released during or after alkali pretreatment are low and the pH value is increased, by obstructing acid production in the reactor. Furthermore, this pretreatment dissolves lignin and removes about 33% and almost 100% of acetal groups. In addition, lime has reduced costs and a greater safety compared to other chemical compounds (Wyman et al. 2005).

In the literature, there are several examples of the positive effect of pretreatment on biogas production: the biogas yields of some substrates increase linearly with the increase of the surface area (Jedrczak and Krolik 2007). However, the fiber size cannot be directly correlated to the increase of biogas yield because there can be many shearing effects from treatment which cannot be measured only by the fiber size. Palmowski and Müller (2003) study the connection between the surface area

and the biogas yield through a kinetic model and they find a good relation between the model and the experimental data.

Alkaline pretreatments are used too. Alkaline pretreatment of wheat plant (WP), which includes grain and straw, is investigated under different conditions to ensure bio-methane production under mesophilic condition (López-Jiménez et al. 2015). Alkaline pretreatments are carried out using 8% of NaOH weight solution at different temperatures (0, 25, 50, 75, and 100 °C). The best performances are reached by a pretreatment at 75 °C for 60 min, giving a methane yield of 404 g ml^{-1} VS. Cumulative methane yield for pretreated WP at 25, 50, and 75 °C increases the methane yield of about 47.5%, 40.8%, and 54.5%. These values are greater than those obtained from untreated WP, whereas pretreatments at 0 and 100 °C do not guarantee an improvement in biogas production. Qualitative analysis obtained from WP pretreatment, by using the Scanning Electron Microscopy and the Fourier Transform Infrared show crystallinity reduction and surface layers of lignin and hemicellulose removal (Taherdanak and Zilouei 2014). Alkaline pretreatments are an effective method that can solubilize and also neutralize acids released by various lignocellulosic complexes (Hendriks and Zeeman 2009; Chen et al. 2012). However, the presence of small amounts of alkaline residues that remain in treated solids may be useful for preventing pH reduction during the subsequent phase of acidogenesis. For these reasons, alkaline pretreatment is much more effective and compatible when compared with other pretreatments, including the thermochemical ones.

Dererie et al. (2011) conduct some experimental tests for methane batch fermentation (at a mesophilic temperature of 37 °C) with a rice straw substrate. A 3% of NaOH solution as pretreatment is given to ground rice straw biomass for 120 h at 37 °C, while hydrothermal pretreatment is given for 10 min at 200 °C. It is observed that the addition of NaOH is a mandatory requirement to keep a suitable range of pH and for starting biogas production from pretreated rice straw slurry with the hydrothermal method. The concentration of the substrate during feeding are maintained at 5% TS (50 g TS/l). The study shows that 140.0 l/kg VSa biogas and 59.8 l/kg VSa methane are obtained from untreated rice straw substrate. However, substrate pretreatment with NaOH solutions results into 184.8 l/kg VSa biogas and 74.1 l/kg VSa methane. Hydrothermal pretreatment followed by the addition of 5% NaOH results into highest biogas and methane production yields as 315.9 l/kg VSa and 132.7 l/kg VSa. The pretreated substrate with NaOH shows an increase of 132.0% in biogas production and 123.9% in methane production relative to the untreated substrate. However, the hydrothermally pretreated substrate results into an increase of 225.6% in biogas production and 222.0% in methane production compared to untreated rice straw substrate.

Thermo alkaline pretreatments are usually conducted at temperatures between 100 and 150 °C with a load of lime of about 0.1 Ca(OH)$_2$ (Chang et al. 2011).

Gonzales et al. (2013) evaluate a thermos-alkaline pretreatment at 100 °C to ensure anaerobic digestion of press mud in terms of increased methane yield. The effects of lime are evaluated on COD solubilization and on volatile fatty acids production in different experimental conditions. BMP measurements are carried out

to evaluate the effect of alkaline pretreatment on methane yield during digestion of press mud. The measurements are conducted in batch assay under mesophilic conditions (37 ± 1) according to VDI 4630 standards (2006).

A type of pretreatment that is available and that can be installed for large-scale plants is mechanical pretreatment, which includes: milling, grinding, crushing, and chopping.

Methane production from substrates such as food waste, sisal fibers, sludge from wastewater treatment plants, paper, or tomatoes increased by 28%, 23%, 7%, 60%, and 100%, after mechanical pretreatment. (Kouichi et al. 2010). Although the positive effect of biogas production after the use of this pretreatment is evident, it is necessary to determine whether the increase in the quantity of gas compensates for the larger amount of input required energy.

Maibritt et al. (2011) study the use of an extruder to increase the methane yield in produced biogas. They analyze five different types of agricultural biomasses. The samples are analyzed at different temperatures, maximum particle sizes, biogas potentials, and energy consumption. The extruder treatment increases biomass temperature from 5 to 35 °C. Furthermore, extrusion accelerates the organic compounds degradation slowly and some organic compounds, that are not otherwise degradable, are degraded. The methane yield increased significantly from 18% to 70% after 28 days, and from 9% to 28% after 90 days. The additional electrical energy for the increased methane production is of 6–68%. After 90 days, the extrusion process of the analyzed biomass has an energy efficiency that is classified as follows: grass = straw = flocculated solid manure < solids pressure screw manure < littiera.

Two types of mechanical pretreatment, as Grubben deflaker (Gd) and a Krima disperser (Kd), are tested on a large-scale plant to evaluate their effect on particle size, methane potential, energy balance, and capacity. The results after 115 days of incubation in a batch reactor show that methane production is increased by 59% and 43%, after the grinding with Gd and Kd. In both pretreatments, 90% of the ley crop grow as particle sizes lower than 2 mm and more than 50% of the sample is reduced to particles that are smaller than 0.125 mm. The energy balance is positive for Gd and around the break-even point for Kd. Some analysis of the setup shows that Kd has a capacity that is almost twice than Gd capacity (Lindmark et al. 2012).

Usually, a chemical pretreatment with a Fenton reactor, for a nonselective degradation process of organic compounds is used (Karina et al. 2012). The greater effectiveness of this method depends on the formation and release of OH^- radicals generated during H_2O_2 degradation, in the presence of Fe_2^+ ions. The Fenton processes advantages are availability, simplicity, and low cost (Deng 2007; Torrades et al. 2008).

This process is studied by Karina et al. (2012) on Miscanthus giganteus biomass, Sida Hermaphrodite, and Sorghum Moensch for two hours and under optimal conditions (pH = 3, the mass ratio $[Fe_2^+]:[H_2O_2]$ equal to 1:25 for Miscanthus and Sorghum and 1:15 for Sida). The delignification degrees are 30.3%, 62.3%, and 48.1% for these three species. The lignification levels are low due to the chemical pretreatment and both cellulosic structure and hemicellulose are destroyed by

enzymes. Results show that this method has low ability to degrade cellulose which results in a low glucose content. The volatile fatty acids concentration after chemical pretreatment is high enough so that biogas has a high methane content (from Sorghum Moensch biomass it is possible to have biogas with a methane concentration of 75%). To have a high biogas concentration, there is no need for Fe_3^+ ions coagulation. Some studies show that the produced biogas is characterized by a higher energy level when Fenton process does not have a coagulation stage.

The oat straw is enriched with saccharine through enzymes and fermented to ethanol by thermochemical pretreatments and after its removal, the remaining material is subject to biogas digestion. A detailed calculation of the material balance shows that for steam explosion pretreatment, the combination of ethanol fermentation and biogas digestion converts the 85–87% of the higher heating value (HHV) of holocellulose (cellulose and hemicellulose) in the oat straw and into biofuel energy. The energy yields of ethanol and produced methane are of 9.5–9.8 MJ/(kg dry oat straw), which is 28–34% greater than the direct digestion of biogas, which shows a yield of 7.3–7.4 MJ/(kg dry oat straw). The speed of biogas formation from residues fermentation is even higher than that obtained from the corresponding, but not fermented pretreatment; this means that biogas digestion can be terminated only after 24 days and ethanol process acts as an additional pretreatment for the biological process.

Biogas production can be increased through biomass pretreatment with microwave irradiation, as studied by Zehra (2013), where electromagnetic energy is converted into heat energy. The advantage is that microwaves penetrate biomass, deposit energy, and generate heat through the treated material. Barley, corn, wheat, and straw from agriculture in Norway are considered as biomass. These are divided into two groups: the first contains minced straw while the second wet straw with deionized water. Both are subjected to irradiation with microwaves at a temperature between 200 and 300 °C. A group of 66 batch digesters is tested under mesophilic conditions for 60 days. Preliminary results show that the use of microwaves has no effect on biogas production. An increase of the process temperature of 300 °C leads to a lower biogas production. The specific methane yield is not improved by irradiation with microwaves and the author finds an inverse relationship between thermochemical conversion efficiency and cumulative biogas production.

Pilli et al. (2011) evaluate the benefits obtained by pretreatment of sludge with ultrasound, the effect of sonic parameters, the impact of the characteristics of mud on its disintegration, and consequently the increase of the biogas production in the anaerobic digester. The comparison between ultrasound and other pretreatments is necessary to evaluate the best pretreatment of sludge from both the environmental and economic point of view.

Braguglia et al. (2011) study how to maximize the biological digestion of sludge to clarify the feasibility of a new treatment to recover good quality mud for agricultural use. The combined effect of organic loading rates (from 0.7 to 2.8 g VS l^{-1} d^{-1}) and of the degree of dehydration by anaerobic digestion of sludge subjected to ultrasonic pretreatment are evaluated together with the thermal and energy balance. Despite the use of low sonic parameters, the performances of mud

digestion improved in terms of solids degradation and biogas production which depends on the organic load of soluble compounds. Biogas production from sludge pretreated by ultrasound is higher (over 30%) compared to the basic case. The improved filterability during digestion of sludge that is subjected to ultrasonic pretreatment at an average value of OLR due to a significant purpose dejection. Heat balances indicate that ultrasound could be a system to ensure the sustainability of mesophilic digesters. However, thickening is a prerequisite to achieving a positive energy balance.

Preliminary studies on the substrate for biogas production show that different types of pretreatments make the matter much more accessible to biological degradation after the breakdown of complex structures of organic materials, thereby their potential for biogas production is increased.

The biological degradation of sludge by means of ultrasound is extensively studied in full-scale laboratory experiments (Pilli et al. 2011). Kim et al. (2003) observe that the use of ultrasound allows increasing methane production by 34%.

Ultrasound is an emerging method and an effective mechanical pretreatment to ensure the biodegradability of sludge, and it could be useful in sewage and sludge treatment plants. Ultrasound increases sludge digestibility through the destruction of its physical, chemical, and biological properties. The degree of destruction depends on sonic parameters and on the characteristics of mud: the optimal evaluation of the parameters varies according to the type of sonic parameter used and the type of mud. Results show that ultrasound usage increases biogas production by 50% and some assessments on the energy balance show that the average ratio of the net gain of electric energy consumed by the ultrasound device is 2.5.

Pretreatments are ozonation and sonolysis. During ozonation, ozone decomposes and the radicals react with organic matter by making it soluble and reducing it in size: this makes it more biodegradable. Therefore, the final amount of mud and the digestion time can be reduced while the biogas production increases (Bougrier et al. 2006). The rate of digestion is increased by a factor equal to 2.2 by suggesting the possibility to have smaller residence time. Remarkable results in sludge solubilization are reported by Salsabil et al. (2010). Chu et al. (2008) find that ozone allows having an efficiency in solubilization between 25% and 40%. While ozonation and sonolysis are widely studied as pretreatment processes in anaerobic digesters, their use for an organic fraction of municipal solid waste (OFMSW) is not yet developed.

Cesaro and Belgiorno (2013) use sonolysis and ozonation to improve the biodegradability of OFMSW in anaerobic digesters to ensure a greater biogas production. The results show that both pretreatments may enhance the solubilization of organic solid waste. However, during ozonation experiments, no correlation is observed between increased solubilization and biogas production: the application of higher ozone doses led to the formation of by-products less biodegradable than untreated substrate. This evidence makes the ultrasound process more efficient than ozonation and addresses further studies for sonolysis optimization.

The structure and physical properties of zeolite make it ideal for the use in biological purification wastewater (Park et al. 2010). Therefore, the use of zeolite in

wastewater treatment is increased significantly in the past decade. The supports of zeolites ensure that the anaerobic digester contains a high level of biomass and that it can operate with a hydraulic retention time significantly reduced. Zeolites are used as supports to immobilize microorganisms in different reactors (fixed bed, fluidized bed, etc.) and consequently as ion exchangers for the removal of ammonia in anaerobic digesters for the presence of Na^+, Ca_2^+, and Mg_2^+ on its crystal structure. These properties make them useful in improving the performance of anaerobic digestion processes treating high nitrogen content wastewater, such as cattle and chicken wastes. At the same time, zeolites show a great capacity for the absorption of toxic metals that can inhibit the microorganisms responsible for anaerobic digestion.

Montalvo et al. (2012) conduct a review on the use of zeolites in anaerobic digestion processes evaluating the influence of size on mesophilic and thermophilic digesters. They also consider the role of zeolites in granulation and anaerobic oxidation processes and in sequential reactors such as hybrid moving bed biofilm reactors.

For biological pretreatments, the breakage of organic compounds into simple organic structures takes place through the action of enzymes that are produced by microorganisms inside the digester. In the case of lignocellulosic materials, the biodegradation process is facilitated by cellulose and hemicellulose (Parawira 2012). Three experiments are conducted:

- Thermophilic digester at 50 °C: a mixture of enzymes is added to dairy cattle manure and it is fed into the digester, both in the presence and absence of an enzymatic pretreatment.
- Mesophilic digester at 35 °C: a mixture of enzymes is added to dairy cattle manure and it is fed into the digester, both in the presence and absence of an enzymatic pretreatment.
- The mixture of enzymes is added to the solid fraction followed by a step of incubation at 35 °C for 20 h before being combined with the liquid fraction and then it is fed into the thermophilic digester. A mixture of the inactive enzyme is added for the control of the digester at 121 °C and for 30 min.

They find that the addition of enzymes to cow manure does not produce any significant effect on methane production in both mesophilic and thermophilic digesters. This is attributed to microorganisms in the digester degrading the ME since the substrate is fed into the digester immediately after mix with ME, and extracellular enzymes produced by microorganisms already present in the digester that are sufficient to facilitate the hydrolysis of the organic compounds in DCM (Romano et al. 2009). The addition of microorganism mixture followed by an incubation period at 50 °C for 3 days has a significant effect on increasing the methane yield. The addition of the enzyme mixture to solid fraction followed by an incubation period at 35 °C for 20 has a positive effect on methane yield produced by a substrate mixture (30% liquid fraction of cow manure and 70% solid fraction of cow manure treated with enzymes). However, compared to the previous case, there

are further costs for the application of enzymes and therefore it represents a limiting factor for large-scale biogas plants.

Zieminski et al. (2012) use an enzymatic pretreatment on sugar beet pulp and spent hops for their high fiber content. A 24-hour hydrolysis time with a mix of enzymatic preparations Celustar XL and Agropect pomace (3:1, v/v) with endoglucanase, xylanase, and pectinase activities prove to be the most efficient. The highest biogas yields are obtained from the enzymatic hydrolysis of sugar beet pulp (183.39 ml/d from 1 g COD at fermenter loading with organic matter of 5.43 gCOD/l-d). Methane fermentation of spent hops hydrolysate has a yield equal to 121.47 ml/d biogas from 1 g COD. These results show that enzymatic pretreatment improves biogas production.

Hydrothermal pretreatment provides an accelerated pre-hydrolysis of biomass that results in higher biogas and methane production yields. Energy analysis of the complete conversion of biomass into biogas process (impregnation; steam explosion; enzymatic hydrolysis; two-step anaerobic fermentation) is performed with an optimization of the thermochemical and biological process by Santarelli et al. (2012). The analyses are carried out on a pilot plant. They analyze the biogas-to-electricity phase, considering two different types of CHP and SOFC. The results show that the integration of the conversion process from biomass to electricity allows a positive electrical balance, but there is a deficit in heat balance. Finally, the comparisons show that the best performance is obtained from an integrated SOFT plant.

Thermal pretreatments have a positive effect on energy balance (Hendriks and Zeeman 2009). The substrates are heated and the composition of hemicellulose and the branching groups determine the effectiveness of the treatment (Hendriks and Zeeman 2009).

High-temperature thermal pretreatments in the range of 100–225 °C at 25 °C intervals for 15 min are performed by evaluating the biochemical methane potential (BMP) of cattle manure, dewatered manure, and chicken manure. Such pretreatment on cow manure to 175 and 200 °C for 15 min provides a significant increase in methane production after an incubation period of 90 days. In the 27th day, the improvements in methane production are 13% and 21% at 175 °C and 200 °C. For PS, methane production is increased at all temperatures between 125 and 200 °C with the greatest increase of 29% at 200 °C after 27 days.

A significant methane production of pretreated samples compared to not pretreated ones, in cattle manure, and in dehydrated, shedding indicates a change in the lignocellulosic structure of substrate by giving easier access to microbial enzymes (Bruni et al. 2010).

There is no positive effect of high-temperature thermal pretreatment on methane production from chicken manure. Even at 225 °C thermal pretreatment led to reducing methane by 18% compared to the basic case. The lack of a positive effect could cause an increase in the biodegradability of chicken manure, since there is no bedding material in the sample, thus providing limited potential for improving the methane production in the pretreated sample (Raju 2012).

Sutaryo et al. (2012) evaluate the effect of low-temperature pretreatments on the methane yield from PS and the solid fraction of PS in batch digesters. The use of such pretreatment is an interesting method since the required energy can be used by the surplus obtained from the cogeneration system.

Low-temperature thermal pretreatments are conducted from PS by Møller et al. (2004). In particular, four different treatments are conducted (from 65 to 80 °C with intervals of 5 °C) for 20 h and are applied to both raw and solid fraction manure. They find that such pretreatments provide a slight increase in pH and a large increase in VFA total concentration. Acetic acid and butyric acid in pretreated PS at 65 °C increase by 65% and 63%. For solid fraction of slurry, an increase of 63% and for acetic acid and butyric acid an increase of 126% are recorded, compared to non-pretreated specimens at a temperature of 80 °C. The pH increase is due to the solubilization of macromolecules (Carrère et al. 2010) or to the formation of some substances such as ammonia nitrogen, whereas an increase in VFA concentration can be determined by auto-hydrolysis (Bonmati et al. 2013). There is a significant increase in methane production from PS within a range of 9.5% and 26.4% for 11 days of incubation. So low-temperature thermal pretreatments may increase the reaction rate, but it has a little effect on the overall yield with an infinite residence time, as represented by B_o parameter. The use of low-temperature thermal pretreatments provides a significant increase in methane production for a solid fraction of the slurry. This happens in a linear fashion with pretreatment temperature. Energy balances show that high- and low-temperature thermal pretreatment is a useful method to increase methane production from liquid manure only when there is thermal energy available that can be used in the thermal pretreatment processes. In low-temperature thermal pretreatment, excess heat can be used by the cogeneration plant (Menardo et al. 2011).

6 Configuration of Anaerobic Digesters to Produce Biogas from Different Biomasses

Biogas production efficiency can be optimized by the use of two cascade digesters connected in series by using methane genesis microorganisms. Athanasoulia et al. (2012) consider residence times included between 12.3 and 19.7 days for both systems. For these two reactors that are in series, biogas production increases while the volatile suspended solids concentration decreases. Biogas production is increased from 9.5% to 40.1%; the biogas selectivity is estimated to be 0.49 ± 0.06 m³ biogas/kg TVSdegradato for the reactor in series and 0.44 ± 0.02 m³ biogas/kg TVSdegradato for the reactor at a single stage. As regards volatile suspended solids reduction, values between 31.5% and 33.8% for a single digester and values between 36.2% and 40.7% for a digester in series are obtained.

Ge et al. (2010) study two mesophilic digesters in series with a working volume of 4.6 l, treating primary sludge with a residence time of 2 and 14 days. The system

allows a volatile solids reduction of 44%, this is a lower value than that of 54%, which is reached under thermophilic-mesophilic conditions. The effects of residence time on the biogas yield and on volatile fatty acids concentration are examined.

Kaparaju et al. (2009) evaluate the possibility of optimizing biogas production from sewage through two methanogenesis CSTR digesters in series. They also estimate a single digester which operates at 55 °C with a residence time of 15 days and a working volume of 5 l. For the digesters in series, the working volume is distributed as 70/30%, 50/50%, 30/70%, and 13/78% between the methanogenesis digesters in series. The reactors in series can increase the biogas production, and the best results are obtained when the working volume is distributed as 70/30% and 50/50%; it is possible to have a biogas production that is 13–17.8% higher, a lesser volatile fatty acids content, and a minor loss of methane compared to a single CSTR digester. They estimate an increase in biogas production when the working volume is distributed as 30/70%, but the process is unstable. With a working volume distributed as 13/78%, differences in biogas production are not present and a lower methane production, compared to a single digester is present. Some experiments on laboratory scale show that with a distribution of working volume as 77/23%, biogas production can be increased by 1.9–6.1%, if compared to a single digester. The temperature between the methane genesis reactors must be similar. However, the highest biogas production must be economically evaluated together with the extra installation costs and the complexity of the process.

Ramakrishnan and Surampalli (2013) study the configuration of a hybrid anaerobic reactor that uses supports for biomass immobilization and biogas recycling to improve mixing. The reactor consists of sludge bed in the lower part and an anaerobic filter in the upper part and is fed with wastewater containing complex phenols. Four different biogas flow rates of 25.11, 16.87, 25.30, and 37.95 1^{-1} are recirculated for 100 days. Biogas recirculation ensures the residence time for solids and biomass. The removal of COD and phenols improves with the increase in biogas recirculation. With a residence time of 0.33 days, a removal of phenols and COD of 95% and 92% are obtained.

Lee et al. (2013) use in three experimental studies a biogas with a methane concentration of 73% produced at the Taiwan Sugar Swine Farm in Taichun. In the first study, they investigate the effect of biogas flow rate on the performance of generator at different excesses air. Then, the results of this study are compared to the results obtained from studies on biogas with a methane concentration of 60%. Finally, for biogas with a methane concentration of 73%, the effect on the performance of the generator with a preheated gas input (using a waste heat recovery system) at different temperatures is evaluated. Power generation increases with increasing methane concentration in biogas, except when excess air is less than 0.85. However, thermal efficiency increases with increasing methane concentration only when excess air is greater than 0.95. The best performance of the generator, obtained by preheating the inlet gas, are evident when excess air is relatively high, for example, 1.3.

Jung et al. (2013) develop a process for the conversion of solid organic waste (food waste and sewage sludge) in H_2 and CH_4. The first stage is formed by a dark fermentative hydrogen production (DFHP) without requiring the use of an inoculum. The second stage is constituted by a sequence of anaerobic digesters and batch reactors (ASBR) and an up-flow anaerobic sludge blanket reactor (UASBr) is used to treat H_2. The system (H_2+CH_4-ASBR) shows the best performance in terms of total biogas conversion (78.6%), while a higher biogas flow is obtained with the system (H_2+CH_4-UASBr). To reduce the addition of bases in DFHP process, the produced methane is used for water dilution. Effluents of ASBR and UASBr are effective to keep pH higher than 6 with no methane production.

References

Aftale om Grøn Vækst (2009) Danish Ministry of Food, Agriculture and Fisheries: Copenhagen Denmark. www.fvm.dk/Udspil_og_aftale.aspx?ID=42190. Assessed 12 Jun 2011

Amon B, Kryvoruchko V, Amon T, Zechmeister-Boltenstern S (2006) Methane, nitrous oxide and ammonia emissions during storage and after application of dairy cattle slurry and influence of slurry treatment. Agric Ecosyst Environ 112:153–162

Amon T, Amon B, Kryvoruchko V, Zollitsch W, Mayer K, Gruber L (2007) Biogas production from maize and dairy cattle manure—influence of biomass composition on the methane yield. Agric Ecosyst Environ 118:173–182

Angelidaki I, Ahring BK (1993) Thermophilic anaerobic digestion of livestock waste: the effect of ammonia. Appl Microbiol Biotechnol 38:560–564

Angelidaki I, Ellegaard L, Ahring BK (2003) Application of the anaerobic digestion of waste activated sludge. In: Ahring BK (ed) Biomethanation II. Springer, New York, pp 1–33

Angelidaki I, Chen X, Cui J, Kaparaju P, Ellegaard L (2006) Thermophilic anaerobic digestion of source-sorted organic fraction of household municipal solid waste: start-up procedure for continuously stirred tank reactor. Water Res 40:2621–2628

Angelidaki I, Alves M, Bolzonella D, Borzacconi L, Campos JL, Guwy AJ et al (2009) Defining the biomethane potential (BMP) of solid organic wastes and energy crops: a proposed protocol for batch assays. Water Sci Technol 59:927–934

Asam Z-u-Z, Poulsen TG, Nizami AS, Rafique R, Kiely G, Murphy JD (2011) How can we improve biomethane production per unit of feedstock in biogas plants? Appl Energy 88:2013–2018

Athanasoulia E, Melidis P, Aivasidis A (2012) Optimization of biogas production from waste activated sludge through serial digestion. Renew Energy 47:147–151

Bacenetti J, Negri M, Fiala M, González-García S (2013) Anaerobic digestion of different feedstocks: Impact on energetic and environmental balances of biogas process. Sci Total Environ 463–464:541–551

Balmant W, Oliveira BH, Mitchell DA, Vargas JVC, Ordonez JC (2014) Optimal operating conditions for maximum biogas production in anaerobic bioreactors. Appl Therm Eng 62:197–206

Banks CJ, Humphreys PN (1998) The anaerobic treatment of a ligno – cellulosic substrate offering little nature buffering capacity. Water Sci Technol 38(4/5):29–35

Barbanti L, Di Girolamo G, Grigattia M, Bertinb L, Ciavatta C (2014) Anaerobic digestion of annual and multi-annual biomass crops. Ind Crop Prod 56:137–144

Bauer A, Leonhartsberger C, Bösch P, Amon B, Friedl A, Amon T (2010) Analysis of methane yields from energy crops and agricultural by-products and estimation of energy potential from sustainable crop rotation systems in EU-27. Clean Technol Environ Policy 12:153–161

Bolzonella D, Pavan P, Battistoni P, Cecchi P (2006) Anaerobic co-digestion of sludge with other organic wastes and phosphorous reclamation in BNR wastewater treatment plants. Water Sci Technol 13(6–7):1437–1445

Bonmatí A, Sotres A, Mu Y, Rozendal R, Rabaey K (2013) Oxalate degradation in a bio-electrochemical system: Reactor performance and microbial community characterization. Bioresour Technol 143:147–153

Bouallagui H, Lahdheb H, Ben Romdan E, Rachdi B, Hamdi M (2009) Improvement of fruit and vegetable waste anaerobic digestion performance and stability with co-substrates addition. J Environ Manage 90:1844–1849

Bougrier C, Albasi C, Delgenes JP, Carrere H (2006) Effect of ultrasonic, thermal and ozone pre-treatments on waste activated sludge solubilisation and anaerobic biodegradability. Chem Eng Process 45:711–718

Braguglia CM, Gianico A, Mininni G (2011) Laboratory-scale ultrasound pre-treated digestion of sludge: heat and energy balance. Bioresour Technol 102:7567–7573

Bruni E, Jensen AP, Angelidaki I (2010) Comparative study of mechanical, hydrothermal, chemical and enzymatic treatments of digested biofibers to improve biogas production. Bioresour Technol 101:8713–8717

Buffiere P, Loisel D, Bernet N, Delgenes JP (2006) Towards new indicators for the prediction of solid waste anaerobic digestion properties. Water Sci Technol 53(8):233–241

Bułkowska K, Pokój T, Klimiuk E, Gusiatin ZM (2012) Optimization of anaerobic digestion of a mixture of Zea mays and Miscanthus sacchariflorus silages with various pig manure dosages. Bioresour Technol 125:208–216

Burton CH, Turner C (2003) Manure management treatment strategies for sustainable agriculture. Silsoe Research Institute, Silsoe

Callaghan FJ, Wase DAJ, Thayanithy K, Forster CF (2002) Continuous co-digestion of cattle slurry with fruit and vegetable wastes and chicken manure. Biomass Bioenergy 22:71–77

Callahan R (2011) Manure to power Indiana dairy farms' delivery trucks. Associated Press, New York

Carrère H, Dumas C, Battimelli A, Batstone DJ, Delgenès JP, Steyer JP, Ferrer I (2010) Pretreatment methods to improve sludge anaerobic degradability: a review. J Hazard Mater 183:1–15

Cavinato C, Fatone F, Bolzonella D, Pavan P (2010) Thermophilic anaerobic co-digestion of cattle manure with agro-wastes and energy crops: comparison of pilot and full scale experiences. Bioresour Technol 101:545–550

Cecchi F, Pavanb P, Mata-Alvarez J (1996) Anaerobic co-digestion of sewage sludge: application to the macroalgae from the Venice lagoon. Resour Conserv Recycl 17:57–66

Cesaro A, Belgiorno V (2013) Sonolysis and ozonation as pretreatment for anaerobic digestion of solid organic waste. Ultrason Sonochem 20:931–936

Chandler JA, Jewell WJ, Gossett JM, Van Soest PJ, Robertson JB (1980) Predicting methane fermentation biodegradability. Biotechnolo Bioeng Symp 10:93–107

Chandler JA, Hermes SK, Smith KD (1983) A low cost 75 kW covered lagoon biogas system. Paper presented at Energy from Biomass and Wastes VII. Lake Buena Vista, FL, USA

Chang CJ, Tyagi VK, Lo SL (2011) Effects of microwave and alkali induced pretreatment on sludge solubilization and subsequent aerobic digestion. Bioresour Technol 102:7633–7640

Chen Y, Cheng JJ, Creamer KS (2008) Inhibition of anaerobic digestion process: a review. Bioresour Technol 99:4044–4064

Chen BY, Chen SW, Wang HT (2012) Use of different alkaline pretreatments and enzyme models to improve low-cost cellulosic biomass conversion. Biomass Bioenergy 39:182–191

Chiu SF, Chiu JY, Kuo WC (2013) Biological stoichiometric analysis of nutrition and ammonia toxicity in thermophilic anaerobic co-digestion of organic substrates under different organic loading rates. Renew Energy 57:323–329

Chu CF, Li YY, Xu KQ, Ebie Y, Inamori Y, Kong HN (2008) A pH- and temperature-phased two-stage process for hydrogen and methane production from food waste. Int J Hydrog Energy 33:4739–4746

Chudoba P, Morel A, Capdeville B (1992) The case of both energetic uncoupling and metabolic selection of microorganisms in the OSA activated sludge system. Environ Technol 13:761–770

Colleran E, Pender S (2002) Anaerobic biodegradability, methanogenic activity and toxicity test systems: defining the test conditions. Institute for Environment and Sustainability. Joint Research Centre. European Commision, Lago d'Orta, Italy, pp 1–10

Conrad R, Phelps TJ, Zeikus JG (1985) Gas metabolism evidence in support of the juxtapositioning of hydrogen-producing and methanogenic bacteria in sewage sludge and lake sediments. Appl Environ Microbiol 50:595–601

Corleto A, Cazzato E, Ventricelli P, Cosentino SL, Gresta F, Testa G, Maiorana M, Fornaro F, De Giorgio D (2009) Performance of perennial tropical grasses in different Mediterranean environments in southern Italy. Trop Grasslands 43:129–138

Cuetos MJ, Gomez X, Otero M, Moran A (2008) Anaerobic digestion of solid slaughterhouse waste (SHW) at laboratory scale: influence of co-digestion with the organic fraction of municipal solid waste (OFMSW). Biochem Eng J 40:99–106

Cuetos MJ, Fernández C, Gómez X, Morán A (2011) Anaerobic co-digestion of swine manure with energy crop residues. Biotechnol Bioprocess Eng 16:1044–1052

Deng Y (2007) Physical and oxidative removal of organics during Fenton treatment of mature municipal landfill leachate. J Hazard Mater 146:334–340

Dererie DY, Trobro S, Momeni MH, Hansson H, Blomqvist J, Passoth V, Schnürer A, Sandgren M, Ståhlberg J (2011) Improved bio-energy yields via sequential ethanol fermentation and biogas digestion of steam exploded oat straw. Bioresour Technol 102:4449–4455

Di Girolamo G, Grigatti M, Barbanti L, Angelidaki I (2013) Effects of hydrothermal pre-treatments on Giant reed (Arundo donax) methane yield. Bioresour Technol 147:152–159

Dinuccio E, Balsari P, Gioelli F, Menardo S (2010) Evaluation of the biogas productivity potential of some Italian agro-industrial biomasses. Bioresour Technol 101:3780–3783

Doublet J, Boulanger A, Ponthieux A, Laroche C, Poitrenaud M, Cacho Rivero JA (2013) Predicting the biochemical methane potential of wide range of organic substrates by near infrared spectroscopy. Bioresour Technol 128:252–258

Dourmad JY, Jondreville C (2007) Impact of nutrition on nitrogen, phosphorus, Cu and Zn in pig manure, and on emissions of ammonia and odours. Livest Sci 112(3):192–198

Ferrer P, Cambra-López M, Cerisuelo A, Peñaranda DS, Moset V (2014) The use of agricultural substrates to improve methane yield in anaerobic co-digestion with PS: effect of substrate type and inclusion level. Waste Manage 34:196–203

Fountoulakis MS, Drakopoulous S, Terzakis S et al (2008) Potential for methane production from typical Mediterranean agro-industrial by-products. Biomass Bioenergy 32:155–161

Frigon JC, Mehta P, Guiot SR (2012) Impact of mechanical, chemical and enzymatic pre-treatments on the methane yield from the anaerobic digestion of switchgrass. Biomass Bioenergy 36:1–11

Frischknecht R, Jungbluth N (2003) Implementation of life cycle impact assessment Methods. Final report Ecoinvent 2000. Swiss Centre for LCI, Dubendorf(CH). www.ecoinvent.org. Last accessed 05.09.13.

Ge H, Jensen PD, Batstone DJ (2010) Pre-treatment mechanisms during thermophilic–mesophilic temperature phased anaerobic digestion of primary sludge. Water Res 44:123–130

Gelegenis J, Georgakakis D, Angelidaki I, Christopoulou N, Goumenaki M (2007) Optimization of biogas production from olive-oil mill wastewater, by codigesting with diluted poultry-manure. Appl Energy 84:646–663

Gomec C, Ozturk I (2013) Effect of maize silage addition on biomethane recovery from mesophilic co-digestion of chicken and cattle manure to suppress ammonia inhibition. Energy Convers Manage 71:92–100

González-Fernández C, León-Cofreces C, García-Encina PA (2008) Different pretreatments for increasing the anaerobic biodegradability in swine manure. Bioresour Technol 99:8710–8714

González-García S, Castanheira EG, Dias AC, Arroja L (2013) Environmental performance of a Portuguese mature cheese-making dairy mill. J Clean Prod 41:65–73

Guendouz J, Buffière P, Cacho J, Carrère M, Delgenes J (2010) Dry anaerobic digestion in batch mode: design and operation of a laboratory-scale, completely mixed reactor. Waste Manage 30:1768–1771

Gunaseelan VN (1997) Anaerobic digestion of biomass for methane production: a review. Biomass Bioenerg.:83–114

Hamelin L, Wesnæs M, Wenzel H, Peterson BM (2011) Environmental consequences of future biogas technologies based on separated slurry. Environ Sci Technol 45:5869–5877

Hansen TL, Schmidt JE, Angelidaki I, Marca E, Hansen JC, Mosbæk H, Christensen TH (2004) Method for determination of methane potentials of solid organic waste. Waste Manage 24:393–400

Hashimoto AG (1989) Effect of inoculum/substrate ratio on methane yield and production rate from straw. Biol Wastes 1989(28):247–255

Hendriks ATWM, Zeeman G (2009) Pretreatments to enhance the digestibility of lignocellulosic biomass. Bioresour Technol 100(1):10–18

Hjorth M, Christensen KV, Christensen ML, Sommer SG (2010) Solid-liquid separation of animal slurry in theory and practice, a review. Agron Sustain Dev 30:153–180

Iacovidou E, Ohandja DG, Voulvoulis N (2012) Food waste co-digestion with sewage sludge – realising its potential in the UK. J Environ Manage 112:267–274

Jacobi HF, Ohl S, Thiessen E, Hartung E (2012) NIRS-aided monitoring and prediction of biogas yields from maize silage at a full-scale biogas plant applying lumped kinetics. Bioresour Technol 103:162–172

Jarret G, Cozannet P, Martinez J, Dourmad JY (2011a) Effect of different quality wheat dried distiller's grain solubles (DDGS) in pig diets on composition of excreta and methane production from faeces and slurry. Livestock Sci 140(1):275–282

Jarret G, Cozannet P, Martinez J, Dourmad JY (2011b) Effect of different quality distiler's grain solubles (DDGS) in pig diets on composition of excreta and methane production from faeces and slurry. Livest Sci Amsterdam 140(1–3):275–282

Jarret G, Cerisuelo A, Peu P, Martinez J, Dourmad J-Y (2012) Impact of pig diets with different fibre contents on the composition of excreta and their gaseous emissions and anaerobic digestion. Agric Ecosyst Environ 160:5–58

Jedrczak A, Krolik D (2007) Influence of paper particle size on the efficiency of digestion process. Environ Prot Eng 33(2):147–155

Jerger DE, Chynoweth DP, Isaacson HR (1987) Anaerobic digestion of sorghum biomass. Biomass 14:99–113

Jung KW, Kim DH, Shin HS (2013) Application of a simple method to reduce the start-up period in a H2-producing UASB reactor using xylose. Int J Hydrog Energy 38:7253–7258

Kai P, Pedersen P, Jensen JE, Hansen MN, Sommer SG (2008) A whole-farm assessment of the efficacy of slurry acidification in reducing ammonia emmissions. Eur J Agric 28:148–154

Kaparaju P, Rintala J (2005) Anaerobic co-digestion of potato tuber and its industrial by-products with pig manure. Resour Conserv Recycl 43:175–188

Kaparaju P, Ellegaard L, Angelidak I (2009) Optimisation of biogas production from manure through serial digestion: lab-scale and pilot-scale studies. Bioresour Technol 100:701–709

Karim K, Klasson KT, Hoffmann R, Drescher SR, De Paoli DW, Al-Dahhan MH (2005) Anaerobic digestion of animal waste: effect of mixing. Bioresour Technol 96(14):1607–1612

Karina M, Krystian M, Liliana K, Stanisław L (2012) Influence of pretreatment with Fenton's reagent on biogas production and methane yield from lignocellulosic biomass. Bioresour Technol 119:72–78

Kayhanian M (1994) Performance of a high-solid anaerobic digestion process under various ammonia concentrations. J Chem Technol Biotechnol 59:349–352

Kim J, Park C, Kim T, Lee M, Kim S, Kim S, Lee J (2003) Effect of various pretreatments for enhanced anaerobic digestion with waste activated sludge. J Biosci Bioeng 95(3):271–275

Kouichi I, Yu-ki O, Norio N, Chiaki N, Shuichi Y, Tatsuki T (2010) Effects of particle size on anaerobic digestion of food waste. Int Biodeterior Biodegrad 64:601–608

Lee KH, Park KY, Khanal SK, Lee JK (2013) Effects of household detergent on anaerobic fermentation of kitchen wastewater from food waste disposer. J Hazard Mater 244–245:39–45

Lesteur M, Latrille E, Maurel VB, Roger JM, Gonzalez C, Junqua G et al (2011) First step towards a fast analytical method for the determination of biochemical methane potential of solid wastes by near infrared spectroscopy. Bioresour Technol 102:2280–2288

Lewandowski I, Scurlock JMO, Lindvall E, Christou M (2003) The development and current status of perennial rhizomatous grasses as energy crops in the USand Europe. Biomass Bioenergy 25:335–361

Li YQ, Zhang RH, Liu XY, Chen C, Xiao X, Feng L et al (2013) Evaluating methane production from anaerobic mono- and co-digestion of kitchen waste, corn stover, and chicken manure. Energy Fuels 27:2085–2091

Lin J, Zuo J, Gan L, Li P, Liu F, Wang K, Chen L, Gan H (2011) Effects of mixture ratio on anaerobic co-digestion with fruit and vegetable waste and food waste of China. J Environ Sci 23(8):1403–1408

Lindmark J, Leksell N, Schnürer A, Thorin E (2012) Effects of mechanical pre-treatment on the biogas yield from ley crop silage. Appl Energy 97:498–502

López-Jiménez A, Escudero-González J, Montoya Martínez T, Fajardo Montanana V, Gualtieri C (2015) Application of CFD methods to an anaerobic digester: the case of Ontinyent WWTP, Valencia, Spain. J Water Process Eng 7:131–140

Lou XF, Nair J, Ho G (2012) Influence of food waste composition and volumetric water dilution of methane generation kinetics. Int J Environ Prot 2:22–29

Mahmood A, Honermeier B (2012) Chemical composition and methane yield of sorghum cultivars with contrasting row spacing. Field Crop Res 128:27–33

Maibritt H, Kay G, Anders PSA, Henrik BM (2011) Extrusion as a pretreatment to increase biogas production. Bioresour Technol 102:4989–4994

Marañón E, Castrillón L, Quiroga G, Fernández-Nava Y, Gómez L, García MM (2012) Co-digestion of cattle manure with food waste and sludge to increase biogas production. Waste Manage 32:1821–1825

Massé D, Gilbert Y, Savoie P, Bélanger G, Parent G, Babineau D (2011) Methaneyield from switchgrass and reed canarygrass grown in Eastern Canada. Bioresour Technol 102:10286–10292

Mata-Alvarez J, Macé S, Llabrés P (2000) Anaerobic digestion of organic solidwastes: an overview of research achievements and perspectives. Bioresour Technol 74:3–16

Menardo S, Balsari P, Dinuccio E, Gioelli F (2011) Thermal pre-treatment of solid fraction from mechanically-separated raw and digested slurry to increase methane yield. Bioresour Technol 102:2026–2036

Miao H, Wang S, Zhao M, Huang Z, Ren H, Yan Q, Ruan W (2014) Codigestion of Taihu blue algae with swine manure for biogas production. Energy Convers Manage 77:643–649

Mladenovska Z, Ahring BK (2000) Growth kinetics of thermophilic Methanosarcina spp. isolated from full-scale biogas plants treating animal manures. FEMS Microbiol Ecol 31(3):225–229

Molinuevo-Salces B, Cruz Garcia-Gonzalez M, Gonzalez-Fernandez C, Jose Cuetos M, Moran A, Gomez X (2010) Anaerobic co-digestion of livestock wastes with vegetable processing wastes: a statistical analysis. Bioresour Technol 101:9479–9485

Møller HB, Sommer SG, Ahring BK (2004) Methane productivity of manure, straw and solid fractions of manure. Biomass Bioenerg 26:485–495

Møller HB, Nielsen AM, Nakakubo R, Olsen HJ (2007) Process performance of biogas digesters incorporating pre-separated manure. Livest Sci 112:217–223

Möller K, Rudolf S, Müller T (2010) Substrate inputs, nutrient flows and nitrogen loss of two centralized biogas plants in southern Germany. Nutr Cycl Agroecosyst 87:307–325

Montalvo S, Guerrero L, Borja R, Sánchez E, Milán Z, Cortés I, de la la Rubia MA (2012) Application of natural zeolites in anaerobic digestion processes: a review. Appl Clay Sci 58:125–133

Monti A, Barbanti L, Zatta A, Zegada-Lizarazu W (2011) The contribution of switchgrass in reducing GHG emissions. Glob Change Biol Bioenergy 4:420–434

Montusiewicz A, Lebiocka M (2011) Co-digestion of intermediate landfill leachate and sewage sludge as a method of leachate utilization. Bioresour Technol 102:2563–2571

Moset V, Cerisuelo A, Sutaryo S, Møller HB (2012) Process performance of anaerobic co-digestion of raw and acidified PS. Water Res. 46:5019–5027

Mosier N, Hendrickson R, Brewer M, Ho N, Sedlak M, Dreshel R, Welch G, Dien BS, Aden A, Ladisch MR (2005) Industrial scale-up of pH controlled liquid hot water pretreatment of corn fiber for fuel ethanol production. Appl Biochem Biotechnol 125:77–97

Müller C (2007) Anaerobic digestion of biodegradable solid waste in low- and middle-income countries: overview over existing technologies and relevant case studies. Eawag, Dübendorf, Switzerland

Murphy R, Woods J, Black M, McManus M (2011) Global developments in the competition for land from biofuels. Food Policy 36:S52–S61

Murto M, Björnsson L, Mattiasson B (2004) Impact of food industrial waste on anaerobic co-digestion of sewage sludge and pig manure. J Environ Manage 70:101–107

Nakakubo R, Möller HB, Nielsen AM, Matsuda J (2008) Ammonia inhibition of methanogenesis and identification of process indicators during anaerobic digestion. Environ Eng Sci 25:1487–1496

Nasir IM, Mond I, Omar R, Idris A (2012) Palm oil mill effluent as an additive with cattle manure in biogas production. Proc Eng 50:904–912

Nges IA, Escobar F, Fu X, Björnsson L (2012) Benefits of supplementing an industrial waste anaerobic digester with energy crops for increased biogas production. Waste Manage 32:53–59

Nielsen HB, Ahring BK (2007) Effect of tryptone and ammonia on the biogas process in continuously stirred tank reactors treating cattle manure. Environ Technol 28:905–914

Nielsen HB, Angelidaki I (2008) Codigestion of manure and industrial organic waste at centralized biogas plants: process imbalances and limitations. Water Sci Technol 58(7):1521–1528

Ogunwande GA, Osunade JA, Adeagbo AO, Fakuyi OF (2013) Effects of co-digesting swine manure with chicken manure on biogas production. Ife J Sci 15(1):1–8

Owen WF, Stuckey DC, Healy JB, Young IY, McCarty PL (1979) Bioassay for monitoring biochemical methane potential and anaerobic toxicity. Water Res 13:485–492

Pagés JD, Pereda IR, Lundin M, Sárvari IH (2011) Co-digestion of different waste mixtures from agro-industrial activities: kinetic evaluation and synergetic effects. Bioresour Technol 102:10834–10840

Palmowski LM, Müller JA (2003) Anaerobic degradation of organic materials: significance of the substrate surface area. Water Sci Technol 47(12):231–238

Parawira W (2012) Enzyme research and applications in biotechnological intensification of biogas production. Crit Rev Biotechnol 32:172–186

Park MJ, Jo JH, Park D, Lee DS, Park JM (2010) Comprehensive study on a two-stage anaerobic digestion process for the sequential production of hydrogen and methane from cost-effective molasses. Int J Hydrog Energy 35:6194–6202

Parkin GF, Lynch NA, Kuo W, Van Keuren EL, Bhattacharya SK (1990) Interaction between sulfate reducers and methanogens fed acetate and propionate. J Water Pollut Control Fed 62:780–788

Pastor L, Ruiz L, Pascual A, Ruiz B (2012) Co-digestion of used oils and urban landfill leachates with sewage sludge and the effect on the biogas production. Appl Energy 107:438–445

Piccinini S, Bonazzi G, Fabbri C, Sassi D, Schiff MC, Soldano M, Verzellesi F (2008) Energia dal biogas – prodotto da effluenti zootecnici, biomasse dedicate e di scarto. AIEL Editore, Legnaro

Pilli S, Bhunia P, Yan S, LeBlanc RJ, Tyagi RD, Surampalli RY (2011) Ultrasonic pretreatment of sludge: a review. Ultrason Sonochem 18:1–18

Pöschl M, Ward S, Owende P (2010) Evaluation of energy efficiency of various biogas production and utilization pathways. Appl Energy 87:3305–3321

Ragaglini G, Dragoni F, Simone M, Bonari E (2014) Suitability of giant reed (Arundodonax L.) for anaerobic digestion: effect of harvest time and frequency on the biomethane yield potential. Bioresour Technol 152:107–115

Raju, Ch (2012) Optimization of the anaerobic digestion process by substrate pretreatment and the application of NIRS. PhD thesis. Aarhus University, Denmark

Ramakrishnan A, Surampalli RY (2013) Performance of anaerobic hybrid reactors for the treatment of complex phenolic wastewaters with biogas recirculation. Bioresour Technol 129:26–32

Raphael S, Panoutsou C, Bauen A (2009) Reconciling bio-energy policy and delivery in the UK: will UK policy initiatives lead to increased deployment? Biomass Bioenerg 33:679–688

Raposo F, Fernandez-Cegri V, De la Rubia MA, Borja R, Beline F, Cavinato C et al (2011) Biochemical methane potential (BMP) of solid organic substrates: evaluation of anaerobic biodegradability using data from an international interlaboratory study. J Chem Technol Biotechnol 86:1088–1098

Rasi S, Läntelä J, Rintala J (2011) Trace compounds affecting biogas Energy utilisation–a review. Energy Convers Manage 52:3369–3375

Regueiro L, Carballa M, Alvarez JA, Lema JM (2012) Enhanced methane production from pig manure anaerobic digestion using fish and biodiesel wastes as co-substrates. Bioresour Technol 123:507–513

Riaño B, Molinuevo B, García-González MC (2011) Potential for methane production from anaerobic co-digestion of swine manure with winery wastewater. Bioresour Technol 102:4131–4136

Richardson B (2012) From a fossil-fuel to a bio-based economy: the politics of industrial biotechnology. Environ Plann C Gov Policy 30:282–296

Romano RT, Zhang R, Teter S, McGarvey JA (2009) The effect of enzyme addition on anaerobic digestion of Jose Tall Wheat Grass. Bioresour Technol 100:4564–4571

Rozzi A, Remigi E (2004a) Methods of assessing microbial activity and inhibition under anaerobic conditions: a literature review. Rev Environ Sci Biotechnol 3(2):93–115

Salsabil MR, Laurent J, Casellas M, Dago C (2010) Techno-economic evaluation of thermal treatment, ozonation and sonication for the reduction of wastewater biomass volume before aerobic or anaerobic digestion. J Hazard Mater 174:323–333

Sambusiti C, Ficara E, Malpei F, Steyer JP, Carrère H (2013) Effect of sodiumhydroxide pretreatment on physical, chemical characteristics and methane pro-duction of five varieties of sorghum. Energy 55:449–456

Sánchez E, Borja R, Lopez M (1996) Determination of the kinetic constants of anaerobic digestion of sugar mill-mud-waste (SMMW). Bioresour Technol 56:245–249

Santarelli M, Barra S, Sagnelli F, Zitella P (2012) Biomass-to-electricity: Analysis and optimization of the complete pathway steam explosion – enzymatic hydrolysis – anaerobic digestion with ICE vs SOFC as biogas users. Bioresour Technol 123:430–438

Scano EA, Asquer C, Pistis A, Ortu L, Demontis V, Cocco D (2014) Biogas from anaerobic digestion of fruit and vegetable wastes: experimental results on pilot-scale and preliminary performance evaluation of a full-scale power plant. Energy Convers Manage 77:22–30

Selinger LB, Forsberg CW, Cheng KJ (1996) The rumen: a unique source of enzymes for enhancing livestock production. Anaerobe 2:263–284

Siles J, Brekelmans J, Martin MA, Chicas A, Martin A (2010) Impact of ammonia and sulphate concentration on thermophilic anaerobic digestion. Bioresour Technol 101:9040–9048

Sitorus B, Sukandar, Panjaitan SD (2013) Biogas recovery from anaerobic digestion process of mixed fruit–vegetable wastes. Energy Proc 32:176–182

Sutaryo S, Ward AJ, Møller HB (2012) Thermophilic anaerobic co-digestion of separated solids from acidified dairy cow manure. Bioresour Technol 114:195–200

Taherdanak M, Zilouei H (2014) Improving biogas production from wheat plant using alkaline pretreatment. Fuel 115:714–719

Thorin E, Lindmark J, Nordlander E, Odlare M, Dahlquist E, Kastensson J, Leksell N, Pettersson CM (2012) Performance optimization of the Växtkraft biogas production plant. Appl Energy 97:503–508

Thy S, Preston TR, Borin K, Buntha P, Vanvuth T (2005) The optimization of gas production in tubular plastic biodigesters by charging with different proportions of pig and cattle manure. Livest Res Rural Dev 17(12)

Tong X, Smith LH, McCarty PL (1990) Methane fermentation of selected lignocellulosic materials. Biomass 21:239–255

Torrades F, Saiz S, García-Hortal JA, García-Montaño J (2008) Degradation of wheat straw black liquor by fenton and photo-fenton processes. Environ Eng Sci 25(1):92–98

Triolo JM, Sommer SG, Møller HB, Weisbjerg MR, Jiang XY (2011) A new algorithm to characterize biodegradability of biomass during anaerobic digestion: influence of lignin concentration on methane production potential. Bioresour Technol 102:9395–9402

Triolo JM, Ward AJ, Pedersen L, Løkke MM, Qu H, Sommer SS (2014) Near Infrared Reflectance Spectroscopy (NIRS) for rapid determination of biochemical methane potential of plant biomass. Appl Energy 116:52–57

van Lier JB, Tilche A, Ahring BK, Macarie H, Moletta R, Dohanyos M, Pol LWH, Lens P, Verstraete W (2001) New perspectives in anaerobic digestion. Water Sci Technol 43:1–18

Velthof GL, Nelemans JA, Oenema O, Kuikman PJ (2005) Gaseous nitrogen and carbon losses from pig manure derived from different diets. J Environ Qual 34:698–706

Veum TL, Bollinger DW, Buff CE, Bedform MR (2006) A genetically engineered Escherichia coli phytase improves nutrient utilization, growth performance and bone strength of young swine fed diets deficient in available phosphorus. J Anim Sci 84(5):1147–1158

Wang X, Yang G, Feng Y, Ren G, Han X (2012) Optimizing feeding composition and carbon–nitrogen ratios for improved methane yield during anaerobic co-digestion of dairy, chicken manure and wheat straw. Bioresour Technol 120:78–83

Ward AJ, Hobbs PJ, Holliman PJ, Jones DL (2008) Optimisation of the anaerobic digestion of agricultural resources. Bioresour Technol 99:7928–7940

Ward AJ, Møller HB, Raju CS (2010) Extreme thermophilic pre-treatment of manures for improved biogas production. In: Proceeding 14th ramiran international conference

Whittmann C, Zeng AP, Deckwer WD (1995) Growth inhibition by ammonia and use of pH-controlled feeding strategy for effective cultivation of Mycobacterium chlorophenolicum. Appl Microbiol Biotechnol 44:519–525

Wyman CE, Dale BE, Elander RT, Holtzapple M, Ladisch MR, Lee YY (2005) Comparative sugar recovery data from laboratory scale application of leading pretreatment technologies to corn stover. Bioresour Technol 96:2026–2032

Ye J, Li D, Sun Y, Wang G, Yuan Z, Zhen F, Wang Y (2013) Improved biogas production from rice straw by co-digestion with kitchen waste and pig manure. Waste Manage 33:2653–2658

Yue Z, Chen R, Yang F, MacLellan J, Marsh T, Liu Y, Liao W (2013) Effects of dairy manure and corn stover co-digestion on anaerobic microbes and corresponding digestion performance. Bioresour Technol 128:65–71

Zehra S (2013) The effect of microwave pretreatment on biogas production from agricultural straws. Bioresour Technol 128:487–494

Zeshan O, Karthikeyan P, Visvanathan C (2012) Effect of C/N ratio and ammonia-N accumulation in a pilot-scale thermophilic dry anaerobic digester. Bioresour Technol 113:294–302

Zieminski K, Romanowska I, Kowalska M (2012) Enzymatic pretreatment of lignocellulosic wastes to improve biogas production. Waste Manage 32:1131–1137